AN INVESTIGATION OF ION ACCELERATION AND ELECTRON-ION RECOMBINATION MECHANISMS IN HIGHLY IONISED PLASMAS

by

GEOFFREY JOHN PARKINSON

Thesis submitted to the University of London
for the
Degree of Doctor of Philosophy

November 1969

ABSTRACT

In Section I of this thesis, the Polytron device, comprising a toroidal discharge in the presence of a multi-cusp shaped magnetic field, is investigated. The design and construction of the apparatus and the properties of a preionisation discharge are reported. In the main discharge, the multi-cusp shaped magnetic field restricted axial electron motion in the plasma and Hall currents were established in the cusp regions. The ion Larmor radius was chosen to be larger than the axial separation of the cusps so that axial ion motion was unaffected. Measurements are presented of the magnetic field effects associated with the plasma Hall currents and of directed ion motion in the plasma. A study of the stability and confinement of the Polytron plasma is also given.

In Section II of this thesis, the decay of highly ionised plasma in the electron density range 10^{16} to 10^{13} cm^{-3} is investigated. Experimental measurements of electron densities and electron temperatures in 125 different hydrogen and rare gas afterglows are given. Plasma decay at high densities is shown to be dominated by the three body recombination process with an electron as the third body. The non-uniform distribution of plasma parameters in laboratory type afterglows, where the walls of the discharge vessel remain fixed at $300^{o}K$, is extensively investigated both experimentally and theoretically. Equations expressing the energy balance and recombination processes in non-uniform decaying plasmas are formulated and solved using a computer for the general case where the temperatures of all particle species in the plasma are treated as variables. Numerical estimates of the recombination coefficients for helium, neon, argon and krypton plasmas in the electron density range 10^{16} to 10^{13} cm^{-3} are presented. Good agreement is concluded between theory and experiment.

CONTENTS

SECTION I		PAGE
INTRODUCTION		2
CHAPTER 1	DESIGN AND CONSTRUCTION OF THE POLYTRON : 1	6
CHAPTER 2	DESIGN AND CONSTRUCTION OF THE POLYTRON : 2	41
CHAPTER 3	PROPERTIES OF THE PREIONISED PLASMA	73
CHAPTER 4	POLYTRON PLASMA DIAGNOSTICS	103
CHAPTER 5	POLYTRON EXPERIMENTAL RESULTS	116
CHAPTER 6	DISCUSSION AND CONCLUSIONS ON THE POLYTRON	151
SECTION II		
INTRODUCTION		159
CHAPTER 7	PLASMA DIAGNOSTICS WITH FAR INFRARED LASERS	162
CHAPTER 8	MICROWAVE TECHNIQUES FOR PLASMA DIAGNOSTICS	200
CHAPTER 9	REVIEW OF PLASMA RECOMBINATION PROCESSES	216
CHAPTER 10	DENSITY AND TEMPERATURE GRADIENTS IN AFTERGLOW PLASMAS	234
CHAPTER 11	EXPERIMENTAL STUDIES OF DECAYING PLASMAS	268
CHAPTER 12	COMPUTER SOLUTION OF THE CONSERVATION OF ENERGY - RECOMBINATION EQUATIONS IN A DECAYING PLASMA	315

		PAGE
CHAPTER 13	COMPARISON OF COMPUTED AND EXPERIMENTAL RESULTS	371
CHAPTER 14	DISCUSSION AND CONCLUSIONS ON AFTERGLOW PLASMA WORK	416
APPENDICES		421
REFERENCES		444
ACKNOWLEDGEMENTS		452

PREFACE

The contents of this thesis have been divided into two main sections, where each section is concerned with the study of plasmas possessing quite different physical characteristics. The main feature connecting the work described in sections I and II is that all the plasmas were produced in the same experimental apparatus.

A large number of diagrams, graphs and photographs have been presented in this thesis. In accordance with the thesis binding regulations, the sequence of page numbers includes both the diagrams and the text. This procedure has led to an extraordinarily long thesis solely in terms of page numbers.

SECTION I

SECTION I

INTRODUCTION

In this section, we are concerned with a plasma device called the Polytron. The concept of this device is due to Haines (1)(2), who proposed a toroidal discharge configuration with a superimposed multiple cusp shaped magnetic field. The Polytron proposal arose from an earlier experiment performed at Imperial College (3)(4), where a single coil was energised around a linear plasma discharge and axial motion of the plasma, in the direction of the applied electric field, was inferred from measurements made using piezo-electric and magnetic probes. In this linear experiment, the directed plasma motion was limited by the presence of electrodes and a toroidal discharge was proposed for the Polytron to eliminate this restriction.

The operation of the Polytron can be described in simple terms using cylindrical coordinates (r,θ,z) as follows. The radial component of each cusp field $\vec{B}_r$ interacts with the axial current $\vec{i}_z$ to produce an azimuthal Hall current. This Hall current in turn interacts with $\vec{B}_r$ to produce an $\vec{i}_\theta \wedge \vec{B}_r$ force which is independent of the direction of $\vec{B}_r$. Provided that the ion Larmor radius in the radial field $\vec{B}_r$ is large compared to the cusp coil separation, whilst the electron Larmor radius is small and that $\omega\tau$ for the electrons is $\gg 1$, then the $\vec{i}_\theta \wedge \vec{B}_r$ force preferentially accelerates the ions and the electrons remain trapped by the cusp fields. Once the directed ion velocity becomes greater than the ion thermal speed, radial

leakage of plasma out of the loss cones of the cusp fields is prevented. In addition, the increase in magnetic field presented to plasma moving away from the toroidal axis of the multiple cusp field system, provides the necessary condition for stability against plasma disturbances and it also acts to balance the centrifugal force of high speed ion motion.

Much of the work described in section I is concerned with the transformation of the theoretical outline for the Polytron proposed by Haines into a working plasma device. One of the aims of the experiment was to study the proposed plasma acceleration and containment mechanisms over a wide range of plasma conditions and, in general, a pragmatic approach was adopted towards the construction of the device. The highest values of induced axial electric field and cusp magnetic field that could reasonably be realised in practice were adopted, together with the maximum working range for these parameters. The diameter of the toroidal axis of the system was chosen to be exactly 50.8 cm (20 inches). The desire to keep the cusp field loss cones as narrow as possible dictated that the separation of the cusp coils should be kept to a minimum, and a total of 36 cusp coils were equally spaced around the toroidal axis. The electric field parallel to the toroidal axis was induced by a capacitor bank discharge through an eight rod system approximating in shape to a toroidal shell. The toroidal discharge chamber was made from fused silica and a bore of 44 mm was initially chosen, though later, this was increased to 71 mm. In describing the experimental work, the terms 'small torus' and 'large torus' are extensively used to distinguish between the two sizes of discharge vessel.

A schematic diagram of the Polytron assembly illustrating the description given above is shown in fig. (I.1). Also illustrated in this diagram are the additional features of a plasma preionisation system and

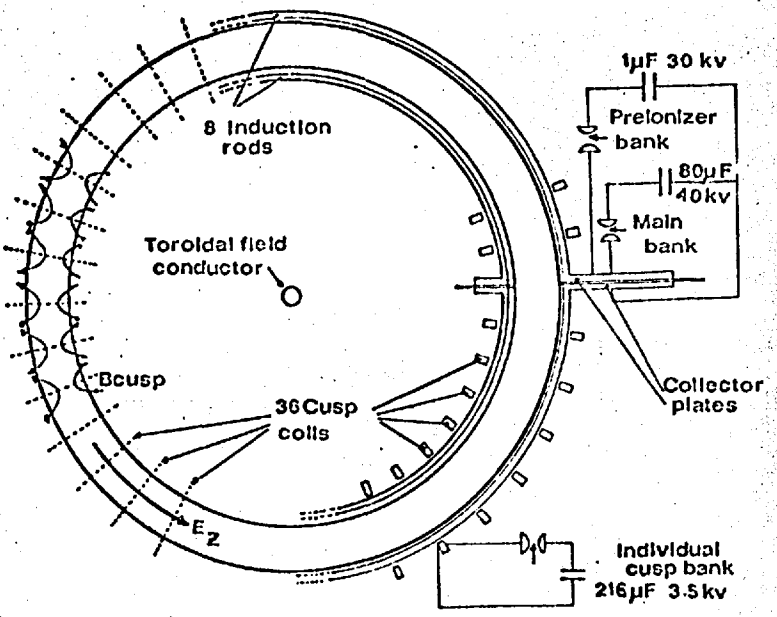

FIG. (I.1)

a central current carrying conductor producing a weak toroidal axial magnetic field.

In the first two chapters of section I the theory, construction and experimental testing of the various elements forming the Polytron assembly are described. The characteristics of the plasma produced by the preionisation system are

discussed in the third chapter. In the remaining chapters of section I, the results obtained from diagnosing Polytron plasmas using Rogowski coils, magnetic probes, flux loops, ion probes, spectroscopic measurements and an image convertor camera are presented. Some of these experimental results are compared with a computer study of a hydromagnetic Polytron plasma model performed by Dunnett (5)(6).

In an experiment as complex as the Polytron, the results presented for this first stage of its development were not expected to yield a complete description of the plasma acceleration and stability mechanisms. Rather, the aim of the work has been to verify the basic principles of the Hall acceleration mechanisms and to examine experimentally the stability and containment of the plasma.

CHAPTER 1

DESIGN AND CONSTRUCTION OF THE POLYTRON : 1

In this chapter, a description is given of the design, construction and experimental testing of the capacitor bank that provided the main induced electric field in the Polytron. This capacitor bank was called the main capacitor bank.

(1.1) OUTLINE FOR THE MAIN CAPACITOR BANK

The main capacitor bank has to satisfy the condition that, when coupled to the eight rod system enclosing the torus, it must produce a large sustained induced electric field inside the torus. This induced electric field, denoted by E_t, is in the absence of plasma proportional to the rate of change of current in the eight rod system, and for an undamped main bank discharge we can write

$$E_t \propto \frac{d}{dt}(i_{ROD}) = \frac{V_B}{L_1} \cos\left[\frac{t}{(L_1 C_B)^{\frac{1}{2}}}\right] \qquad (1.1)$$

where i_{ROD} = total current in eight rod system
V_B = initial charging voltage of main bank
L_1 = inductance of main bank and rod system
C_B = capacity of main bank.

The inductance of the eight rod system, L_{ROD} was fixed by the geometry of torus and was not easily varied. Detailed

calculations of L_{ROD} for the system used with the small torus, together with approximate calculations of L_{ROD} based on a closed outer shell, are given in appendix (A.1), where it is shown that

$$L_{ROD} \text{ (small torus system)} = 660 \text{ n.H.} \qquad (1.2)$$

In order to make the optimum use of the energy stored in the main capacitor bank, the inductance of the main bank system alone, denoted by L_B, should satisfy the condition

$$L_B \ll L_{ROD} \qquad (1.3)$$

A maximum main bank working voltage of 40 kilovolts was chosen, since switching and insulation at this voltage could easily be performed using standard techniques. Substitution into equation (1.1) shows that the maximum rate of rise of current in the small torus rod system was therefore $6.1\ 10^{10}$ amp.sec.$^{-1}$. Considerations of cost and safety dictated a maximum value for C_B of 80 μF. Hence, from equation (1.1) a unidirectional value of E_t can only be maintained for a period of time t_u where

$$t_u = \frac{\pi}{2} (L_{ROD}\ C_B)^{\frac{1}{2}} = 11.4\ 10^{-6} \text{ sec.} \qquad (1.4)$$

The time intervals t_u from the start of the main bank discharge was the most interesting period in the study of ion acceleration processes. Under ideal conditions, we would expect the ion directed velocity to be a maximum after a time t_u, and to fall back to zero after a time $2t_u$ due to the action of the reversed induced electric field in the second quarter period.

In order to satisfy condition (1.3), a main bank comprising many capacitors, spark gaps and cables connected in parallel to a low inductance collector plate was required. We chose to use an arrangement of forty 2 μF capacitors, 40 spark gaps and 160 connecting cables. The techniques of low inductance switching using parallel spark gaps were pioneered at A.W.R.E. by Fitch and McCormick (7). We chose to use a three electrode swinging cascade type spark gap and the requirements and performance of these spark gaps will be discussed in section (1.3). The forty capacitor spark gaps were triggered from a trigger pulse generator incorporating a single spark gap called the master gap. The requirements and performance of this trigger generator will be discussed in section (1.4). The trigger generator was itself charged from a 100 k.v. Marx type pulse generator, and the master gap was triggered by a 35 k.v. pulsed Blumlein cable generator. Using this triggered master gap arrangement, it was possible to trigger plasma diagnostic equipment (e.g. image convertor camera) with a jitter time of less than 20 n.second with respect to the firing of the main bank.

(1.2) MAIN BANK CAPACITORS

B.I.C.C. rapid discharge capacitors each of 2 μF and 40 k.v. working voltage were used. The internal inductance of each capacitor was quoted as 103 n.H. and the lifetime was rated at $> 10^5$ shots with an 80% voltage overswing. The capacitors were of cylindrical shape and leant themselves readily to direct connection with a coaxial design of spark gap. A framework was constructed to hold four rows each of ten capacitors: the latter being mounted at an angle of 10° to

the horizontal with the live termination lowest to avoid possible internal flashover problems. Pressure sensitive microswitches were incorporated in each capacitor and these were wired to an alarm circuit.

(1.3) MAIN BANK SPARK GAPS

A swinging cascade type of spark gap, consisting of three electrodes which form two gaps in series, was chosen as being the best possible spark gap for use in the main bank.

In the operation of the swinging cascade spark gap, the central electrode is initially held at a fraction of the capacitor charging voltage so that the electrical stresses in both gaps are the same. The spark gap is triggered by applying a high voltage pulse to the central electrode causing breakdown of one gap. This causes the full capacitor charging voltage to appear across the second gap which then breaks down. This mode of operation gives the swinging cascade spark gap two distinct practical advantages over a simple two electrode single triggered type of spark gap.

1. Since the breakdown of the second gap in the cascade spark gap is not caused by the applied trigger voltage, the latter is not fed directly onto the main cables connecting the capacitors to the load.

2. The cascade spark gap is capable of being adjusted to hold off large preioniser voltage fluctuations on the main load cables without increasing the minimum trigger voltage requirements of the spark gap. In the Polytron, where the preioniser and main bank discharges are both carried by the same collector plate and induction rod system, the above

feature was a vital factor in the choice of a cascade type of spark gap.

(1.3.1) Theory of the Swinging Cascade Gap

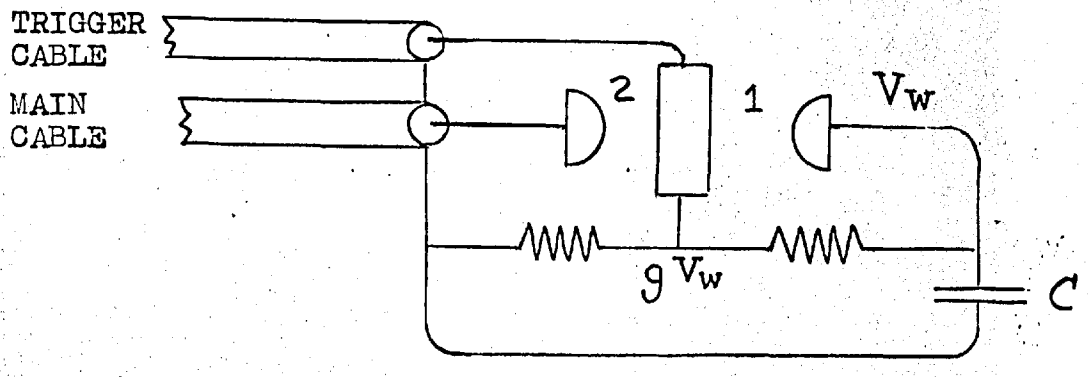

FIG. (1.1)

A schematic diagram of a swinging cascade spark gap is shown in fig.(1.1), where V_w is the capacitor working voltage. The central electrode is initially held at a voltage gV_w where g is chosen so that the electric fields in both gaps are equal

$$\therefore \quad \frac{g}{l_2} = \frac{(1-g)}{l_1} \qquad (1.5)$$

where l_1 = length of gap 1

l_2 = length of gap 2.

The breakdown field strength of air for a fast rising trigger voltage pulse ($\sim$ 2 k.v. per n.sec.) is about 1.4 X the

static breakdown field strength of air which we will call E_s. Hence, the trigger voltage V_{TIB} required to breakdown gap 1 in fig. (1.1), is given by

$$V_{TIB} = 1.4\, E_s l_1 - (1 - g)\, V_w \qquad (1.6)$$

As a precaution against self firing of the bank, l_1 and l_2 are chosen so that the static breakdown of gaps 1 and 2 occur at a voltage which is 20% higher than the maximum working voltage. Taking the latter value as 40 k.v. we can write

$$l_1 E_s = (1 - g)\, 48 \quad \text{k.v.} \qquad (1.7)$$

$$l_2 E_s = g\, 48 \quad \text{k.v.} \qquad (1.8)$$

The correct operational sequence of the spark gap requires that the trigger breaks down gap 1 in preference to gap 2, and this condition sets a minimum value on the capacitor working voltage given by

$$1.4\, E_s l_1 - (1 - g)\, V_w < 1.4\, l_2 E_s + g V_w$$

$$\therefore V_w > 1.4\, (l_1 - l_2)\, E_s \qquad (1.9)$$

or using equations (1.7) and (1.8)

$$V_w > 1.4\, (1 - 2g)\, 48 \quad \text{k.v.} \qquad (1.10)$$

Fitch and McCormick (7) have shown that the value of g corresponding to the optimum operating conditions is around 0.33 and in this case equation (1.10) predicts a working voltage range of

$$22.5 \leqslant V_w \leqslant 40 \quad \text{k.v.} \qquad (1.11)$$

The value of V_{TIB} given by equation (1.6) for V_w = 22.5 k.v. and g = 0.33 is 31.5 k.v. Thus, allowing a factor

of 20% for the fact that gap 1 should break down before the absolute peak of the trigger pulse is reached, the minimum trigger voltage required for consistent spark gap operation over the full working range is

$$V_T \text{ (min.)} \sim 40 \text{ k.v.} \qquad (1.12)$$

The breakdown of gap 2 depends on the inductive and capacitative properties of the spark gap, and these properties must be chosen to produce a high value for the voltage V_2 induced across the second gap after the first gap has been broken down. A high value for V_2 can be achieved in practice by capacitatively loading the central electrode to produce the maximum voltage overswing as the latter is charged up from the main capacitor.

Fitch and McCormick (7) have considered the case where the extra capacity was added directly across the second gap in fig. (1.1.). Since the transit time for the main cables is greater than the rise time of V_2, this situation corresponds to having the added capacity in series with the impedence of the main cable.

In the case we shall consider, the extra capacity added to the central electrode is in the form of short lengths of transmission cable connected in parallel, where the transit time for each short cable is very much less than the rise time of V_2. A schematic diagram for the system is shown in fig. (1.2) (a), where Z_2 and Z_3 are the trigger and main cable impedences respectively. The equivalent circuit of fig. (1.2)(a) is shown in fig. (1.2) (b) where L^* is the inductance of the capacitor and first gap in series and R^* is the resistance of the circuit. The analysis of the circuit shown in fig. (1.2)(b) can easily be performed by considering

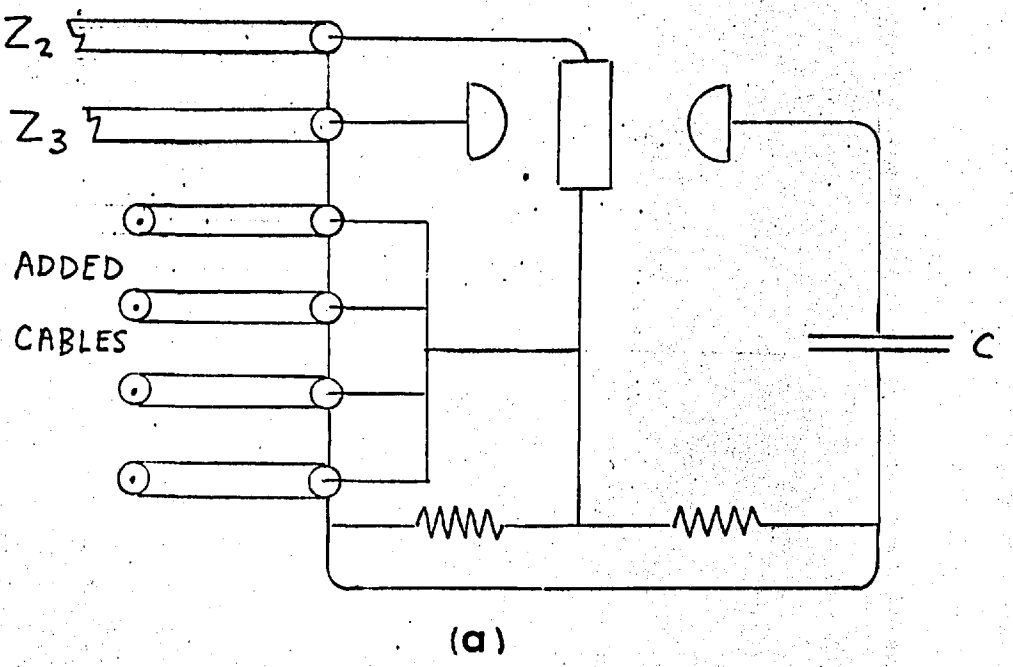

(a)

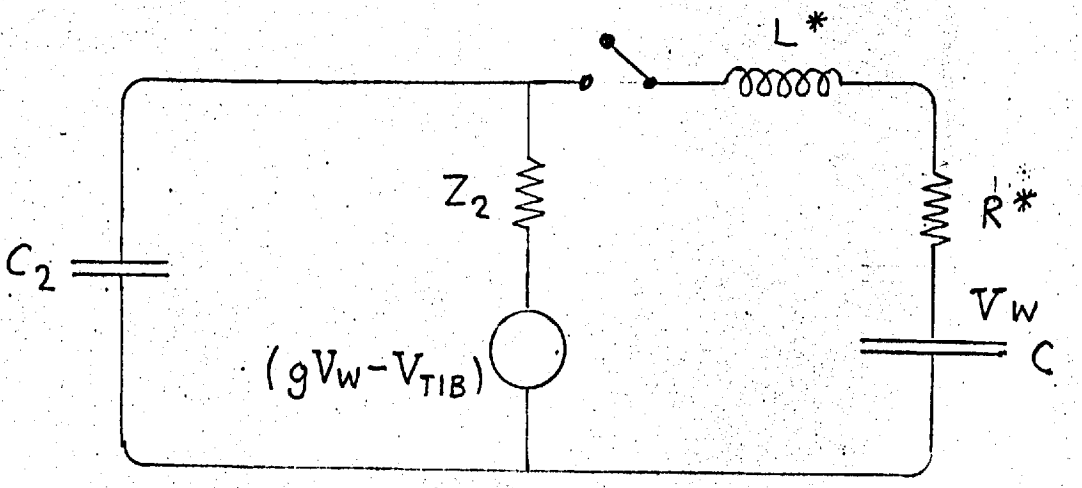

(b)

FIG (1.2) (a) Schematic diagram of a swinging cascade spark gap system.

(b) Equivalent circuit of the system.

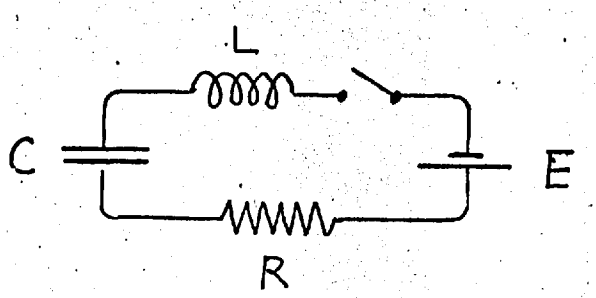

FIG. (1.3)

the analogy with the simple series LCR circuit shown in fig. (1.3). The oscillation of charge Q(t) on the capacitor in fig. (1.3) when the switch is closed is given for the case when $R/2L < (LC)^{-\frac{1}{2}}$ by Smythe (8) as

$$Q(t) = CE\left[1 - \exp\left\{\frac{-R}{2L}t\right\}\left(\cos\omega t + \frac{R}{2\omega L}\sin\omega t\right)\right] \qquad (1.13)$$

where $$\omega^2 = \frac{1}{LC} - \frac{R^2}{4L^2} \qquad (1.14)$$

For the equivalent circuit shown in fig. (1.2)(b) we have very similar conditions to those in fig. (1.3), except that $Q_2(0)$, the initial charge on the capacity C_2 added across gap 2, is given by

$$Q_2(0) = (gV_w - V_{TIB})\,C_2 \qquad (1.15)$$

Hence from equations (1.13) and (1.15) we can write the expression for $Q_2(t)$ as

$$Q_2(t) = C_2\left[V_w - (gV_w - V_{TIB})\right]\left[1 - \exp(-\alpha^* t)\left(\cos\omega t + \frac{\alpha^*}{\omega}\sin\omega t\right)\right] + Q_2(0) \qquad (1.16)$$

where $$\alpha^* = \frac{R^*}{2L^*} \qquad (1.17)$$

$$\omega^2 = \frac{1}{(L^* C_2)} - (\alpha^*)^2 \qquad (1.18)$$

The potential V_2 of the central electrode of the spark gap is simply given by

$$V_2(t) = \frac{Q_2}{C_2} \quad (t) \qquad (1.19)$$

and hence combining equations (1.15) (1.16) and (1.19) we obtain the equation for $V_2(t)$

$$V_2(t) = V_w - \left[V_w \quad (1 - g) + V_{TIB}\right] \exp(-\alpha^* t), \left[\frac{\alpha^*}{\omega} \sin \omega t + \cos \omega t\right] \qquad (1.20)$$

(1.3.2.) Design and Construction of the Spark Gaps

The following main requirements served as a basis for the design of the swinging cascade spark gaps.

1. The gaps should have a low inductance.
2. The gaps must be utterly reliable with respect to insulation and correct mode of operation.
3. The working life between cleaning should be at least several thousand shots.
4. The gaps must be easily and cheaply manufactured.

The spark gap design for the U.K.A.E.A. Culham Mega joule bank was considered but excluded because of condition 4.

The final design of spark gap is shown in the photograph of the main bank fig. (1.4). The gap was of coaxial design and it was mounted directly on the front of each capacitor with the six current return rods taking the weight of the gap and its associated cables. The gap was kept as short as possible being limited by insulation tracking lengths in dusty conditions. The end electrodes were hard steel balls and the

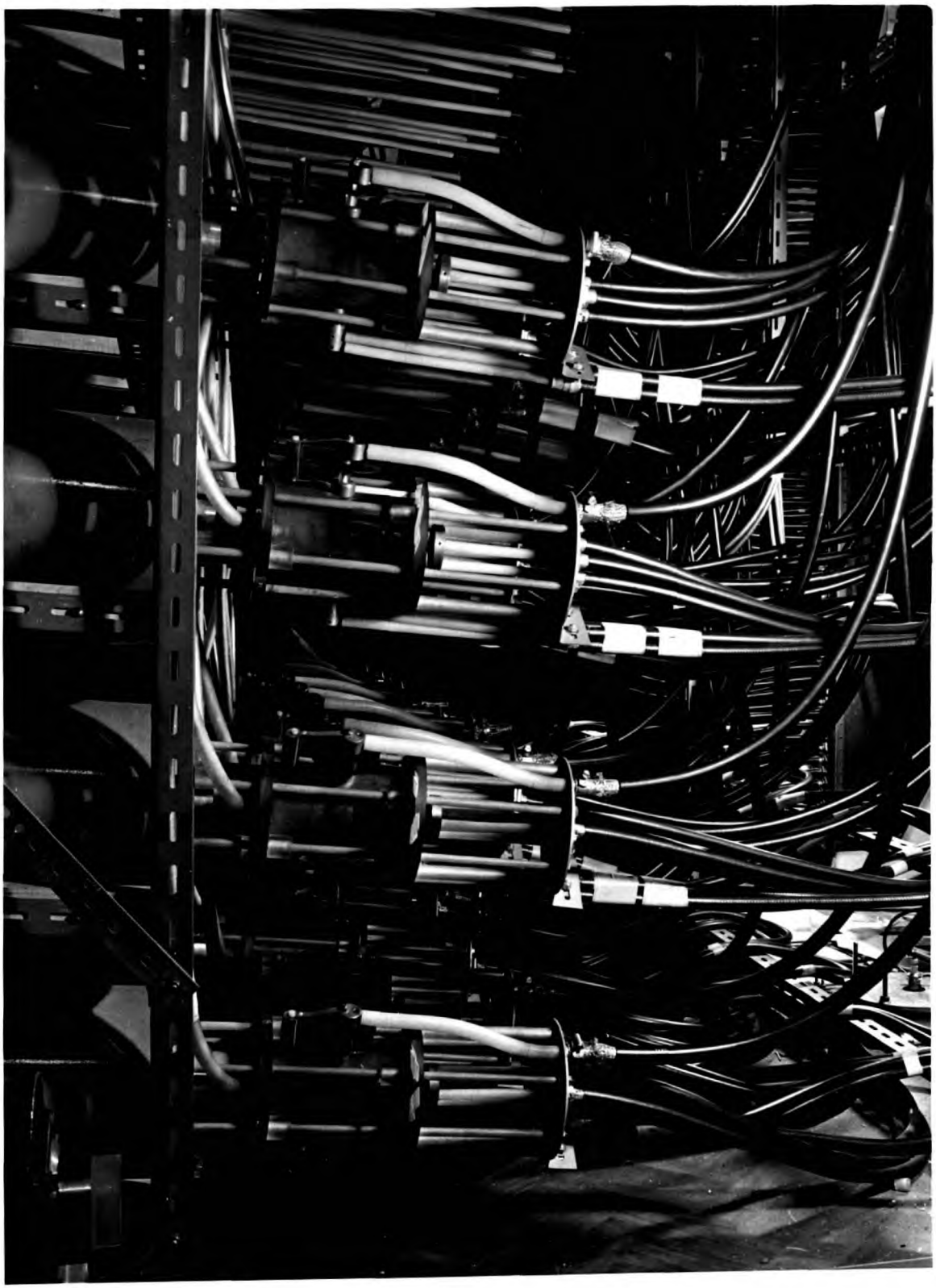

FIG (1.4)

central electrode was manufactured from copper rod. A tungsten irradiating pin was contained within the central electrode which served the function of providing an initial supply of electrons to both gaps as a result of an auxiliary discharge produced by the trigger pulse. A high inductance coil, connecting the irradiating pin to the surrounding electrode, ensured equipotential prior to triggering. U.R.74 cable was used for the trigger pulse cable and cable specially manufactured to be 2/3 the size of U.R.74 cable was used for each of the four main cables per gap. As a result of the experimental testing described in section (1.3.3.), the extra capacity added to the central electrode was achieved using two loops of main cable wound back on themselves. The insulation materials used in the construction of the gaps were tufnol, perspex, nylon and polythene. Prior to fixing in position, the first and second gaps were set on an insulation tester to have static breakdown voltages of 32($\pm$ 0.5) k.v. and 16($\pm$ 0.5) k.v. respectively.

(1.3.3) Experimental Testing of the Spark Gaps

Prior to batch manufacture of the forty spark gaps, experimental testing of prototypes was performed to check conditions 1 to 4 listed in section (1.3.2), and to check the mode of operation of the spark gaps with the theory presented in section (1.3.1.).

The circuit used for testing single spark gaps is shown schematically in fig. (1.5). As the master gap trigger generator was not constructed at this time, a Blumlein cable arrangement was used to provide the necessary fast rising trigger pulse. The upper frequency response of the electronic

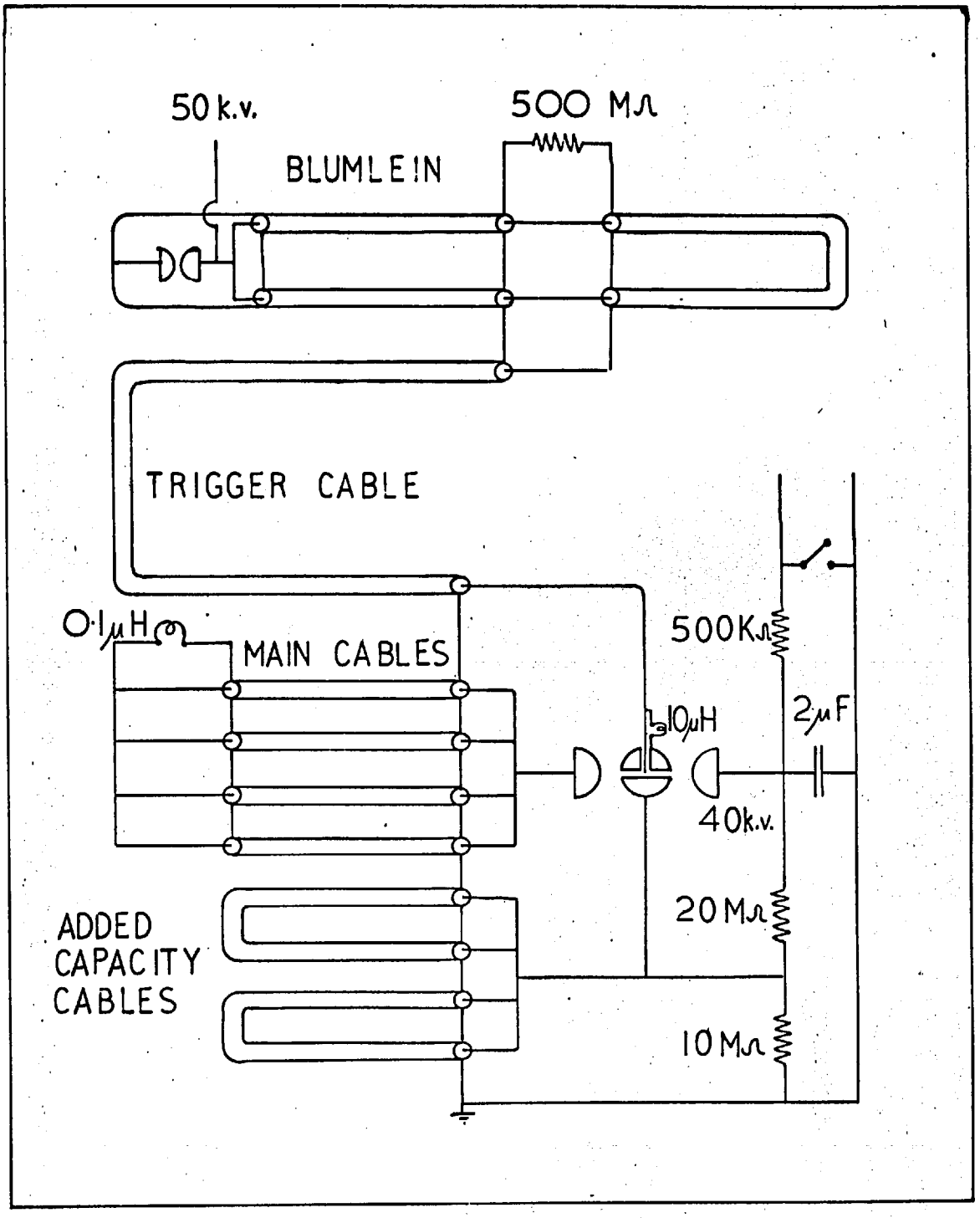

FIG (1.5) Spark gap test circuit.

system required to measure the voltage oscillations on the central electrode of the spark gap was estimated to be $\sim$ 50 MH_Z. This high frequency response was met by using an A.W.R.E. type 583 oscilloscope, where the signal was fed directly onto the C.R.T. deflecting plates so avoiding the usual pre-amplifier response limitation. The inherent rise time of the scope was $\sim$ 4 n.second and the fastest time base was $\sim$ 100 n.second full screen sweep. The sensitivity of the scope was $\sim$ 150 volt per cm. of screen and a 100 : 1 step down potentiometer was used to give a full screen deflection for the complete system around 60 k.v. In order to maintain the high frequency response of the system, the potentiometer was specially constructed to be of a coaxial design with the measuring resistor matched to the 50 Ω cable connection to the oscilloscope. The calculated total inductance of the potentiometer was $<$ 50 n.H. and the potentiometer ratio measured using a high frequency voltage generator was found to be 102 ($\pm$ 2) : 1. Since the central electrode of the spark gap was biassed above earth potential prior to triggering, a low inductance 5000 pF 60 k.v. blocking capacitor was inserted between the central electrode and the potentiometer. This blocking capacitor limited the low frequency response of the voltage measuring system and produced an extra calculated signal attenuation of $\sim$ 1% at 10 MH_Z and $\sim$ 10% at 1 MH_Z. A single turn loop of 0.1 μH. inductance was used as a load for the main capacitor discharge. Experiments were performed for first and second gap spontaneous break down settings of 32 k.v. and 16 k.v. respectively and with the central electrode at 1/3 the main capacitor voltage. Slits were cut into the perspex cover locating the central electrode in the spark gap so that either or both of the two gaps could be physically prevented

from breakdown by inserting sheets of polythene insulation.

With no extra capacity added to the central electrode, the triggering of the spark gap was observed to be uncertain at only a few k.v. below 40 k.v. Adding a 500 pF. 50 k.v. Visconal capacitor across the second gap did not improve the performance, no doubt due to the high inductance of this type of capacitor. However, when a ten foot length of U.R.74 cable was connected to the central electrode with the braid earthed, a working voltage range of 25 to 40 k.v. was found. A later cable capacitor system employed two 6 foot lengths of main cable where each cable was looped back so that there were four inner conductor connections at the central electrode and the outer braids were earthed. This later system avoided the flash over problems associated with stray open ends of cable, and yielded a working voltage range of 20 - 40 k.v.

The variation of the central electrode voltage with time, measured using the resistance potentiometer, for charging voltages of 40, 30, 20, 15 and 0 k.v. are shown in figs. (1.6) and (1.7). The waveforms shown are reproductions of oscilloscope photographs. Note that, in drawing the baselines for the waveforms shown in figs. (1.6) and (1.7), we have chosen the baseline voltage to be 0.33 Vw. The three traces at each voltage show the effects on the central electrode potential of successively (a) preventing breakdown in both gaps, (b) preventing breakdown in the second gap and (c) no prevention of breakdown in either gap.

The following comments are made from a visual inspection of the waveforms shown in figs. (1.6) and (1.7).

1. In case (b), where the second gap only is prevented from breaking down, V_2 oscillates about the mean working voltage V_w.

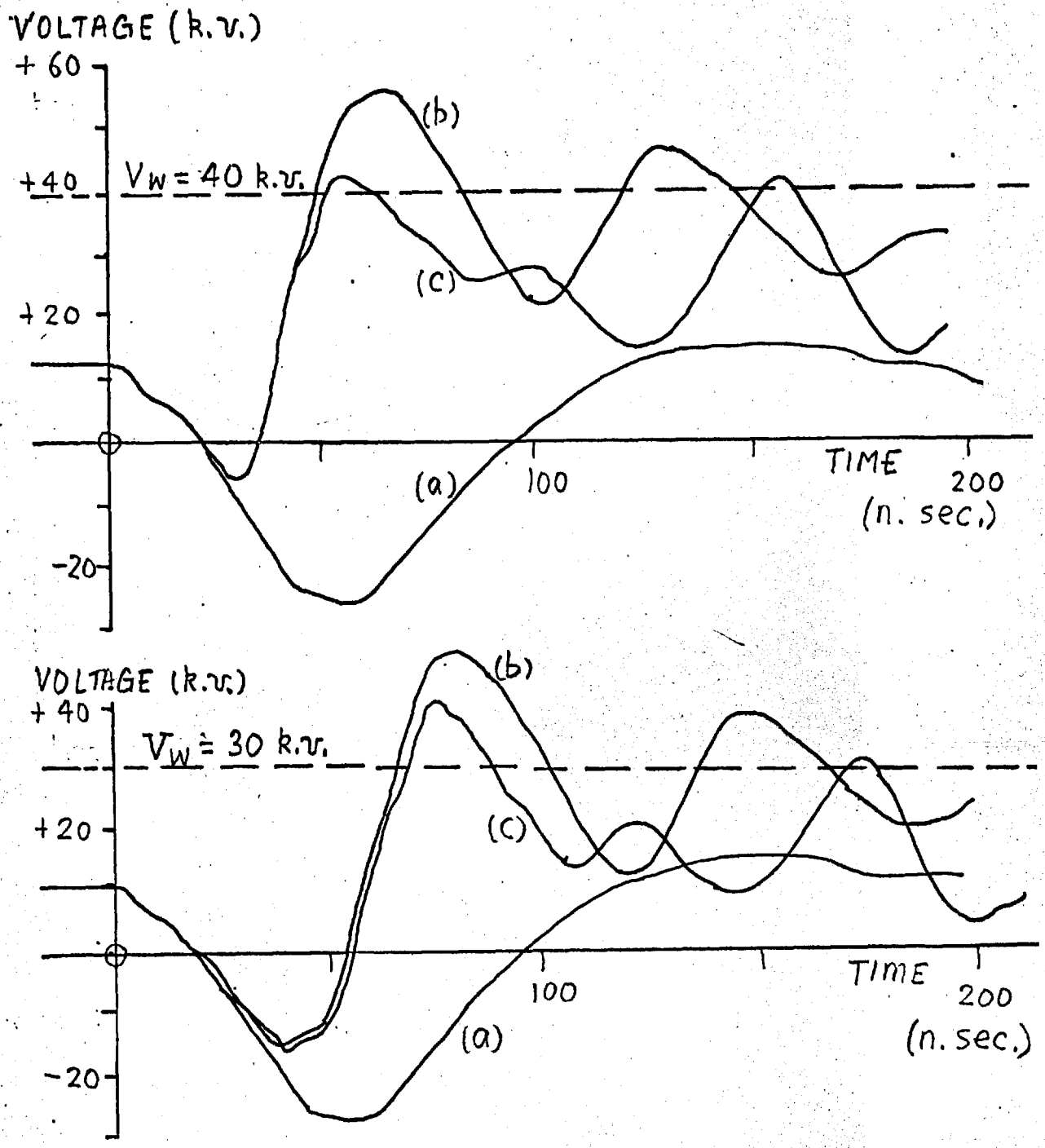

FIG (1.6) Spark gap central electrode voltage waveforms.

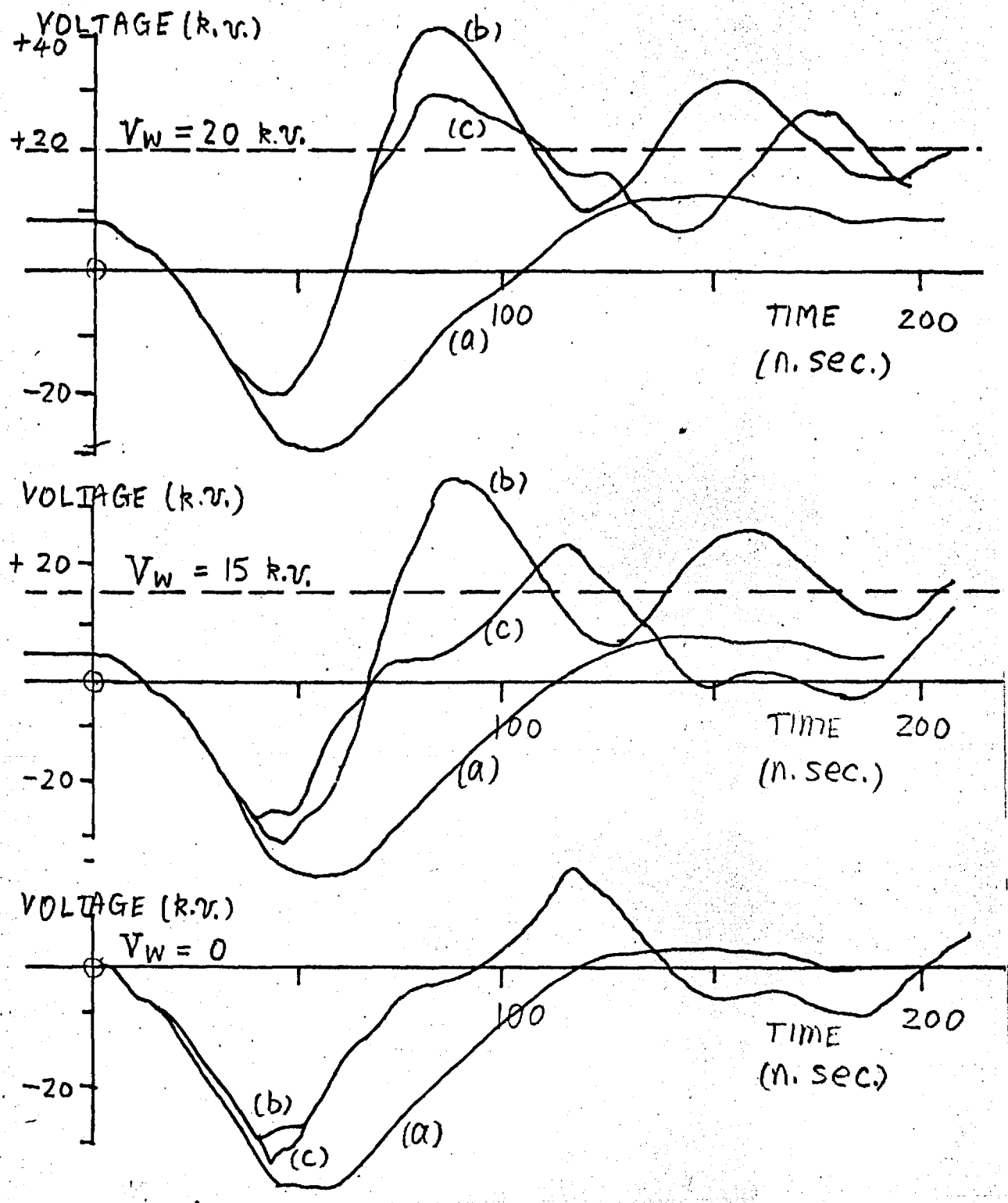

FIG (1.7) Spark gap central electrode voltage waveforms.

with damped harmonic motion.

2. The breakdown of the first gap requires larger trigger voltages and occurs at later times with decreasing V_w.

3. A comparison of the various waveforms corresponding to breakdown of both gaps shows that operation at 20 k.v. is satisfactory but that operation at 15 k.v. is not in the correct swinging cascade mode.

(1.3.4.) Comparison of Experiment with Theory

We now make a comparison of the central electrode voltage waveforms measured for the case (b), when gap 1 breaks down and gap 2 is prevented from breaking down, with the theoretical equation (1.20).

In practice, L^* in the equivalent circuit analysis, is the sum of three parts.

$$L^* = L_1^* + L_2^* + L_3^* \qquad (1.21)$$

where L_1^* = internal inductance of the main capacitor

L_2^* = inductance of gap 1

L_3^* = inductance of connections to cable capacitor.

L_1^* was given by the manufacturers as 103 n.H., and L_2^* and L_3^* were calculated from the geometry of the spark gap to be 84 n.H. and 65 n.H. respectively.

$$\therefore \quad L^* = 250 \text{ n.H.}$$

The capacity C_2 added to the central electrode was simply the capacity of 12 feet of 52 Ω cable

$$\therefore \quad C_2 = 360 \text{ p.F.}$$

The value for the circuit resistance R^* calculated with allowance for the skin effect was approximately

$$R^* \sim 5\,\Omega$$

Substitution of the above values for L^*, C_2 and R^* into equations (1.17) and (1.18) shows that

$$\frac{1}{L^*C_2} \gg (\alpha^*)^2 \qquad (1.22)$$

$$\text{and } \therefore \omega \simeq \frac{1}{(L^*C_2)^{\frac{1}{2}}} = 1.05\ 10^8 \text{ sec.}^{-1}$$

which corresponds to a theoretical period of oscillation of V_2 (around V_w) of 61 n.second. The experimentally measured periods of oscillation of V_2 (around V_w) for various values of V_w have been listed in table (1.1).

TABLE (1.1)

V_w (k.v.)	OSCILLATION PERIOD OF V_2 (n.second)
40	66
30	64
20	66
15	65

The voltage of the central electrode at the breakdown point of the first gap is

$$g V_w - V_{TIB}$$

$$= V_w - 1.4\ l_1 E_s \qquad \text{from equation (1.6)}$$

$$= (V_w - 45) \text{ k.v.} \quad \text{for } l_1 E_s = 32 \text{ k.v.} \qquad (1.23)$$

In table (1.2), this value of $(V_w - 45)$ is compared with the experimental value of the central electrode voltage at the breakdown point of the first gap as shown in figs. (1.6) and (1.7).

TABLE (1.2)

V_w (k.v.)	$(V_w - 45)$ (k.v.)	EXPERIMENTAL VALUE (k.v.)
40	-5	-7
30	-15	-16
20	-25	-22
15	-30	-29

From the damped harmonic oscillations of the voltage V_2 about the mean voltage V_w, the experimental value of α^* has been estimated as $6.6\ 10^6$ sec.$^{-1}$. From equation (1.17) and the value of L^* given above, this experimental estimate of α^* yields

$$R^* \text{ (experiment)} \sim 3.3\ \Omega$$

Finally the transit time for each of the two 6 foot cable loops forming C_2 is ~ 9 n.second, whereas the measured risetime of V_2 is ~ 17 n.second which satisfies the condition that the cable transit time $<$ rise time of central electrode voltage.

(1.4) MAIN BANK TRIGGER GENERATOR

(1.4.1) Theory

All trigger generators used for the simultaneous triggering of many parallel spark gaps must satisfy one basic condition. This condition is that all the spark gaps must be triggered within an interval of time which is less than the time that an electromagnetic wave takes to couple any two spark gaps via the common collector plate. This latter time we will call the characteristic time of the capacitor bank and we will denote it by t_B. For times $< t_B$, all the spark gaps are effectively decoupled and the initial charging voltage across each spark gap will be maintained. For times $> t_B$ after the firing of the first gap, the initial field across the gap falls rapidly and triggering may become impossible.

In order to keep the inductance of the main bank small (and to economise on cable) the main cable length was chosen as 15 feet which was the minimum length set by the size of the bank. The characteristic time for the main bank was therefore

$$t_B \simeq 45 \text{ n.second.}$$

The minimum trigger voltage for the maximum working voltage range of the bank was found in section (1.4.1) to be $\sim$ 40 k.v. Hence, if we aim for a rate of rise of trigger

voltage at the spark gaps around 2 k.v. per n.second, then we will easily satisfy the necessary triggering requirement stated above.

In practice, voltage pulses rising to 40 k.v. in times around 25 n.second can be produced by slowly charging up one set of coaxial cables and then rapidly discharging these cables into the set of trigger cables connected to each spark gap. The first set of cables we will call the discharge cables. In this type of pulse generator, the rate of rise of voltage in the trigger cables is determined by the inductance of the spark gap used for the switching of the discharge cables into the trigger cables. This spark gap is called the master gap.

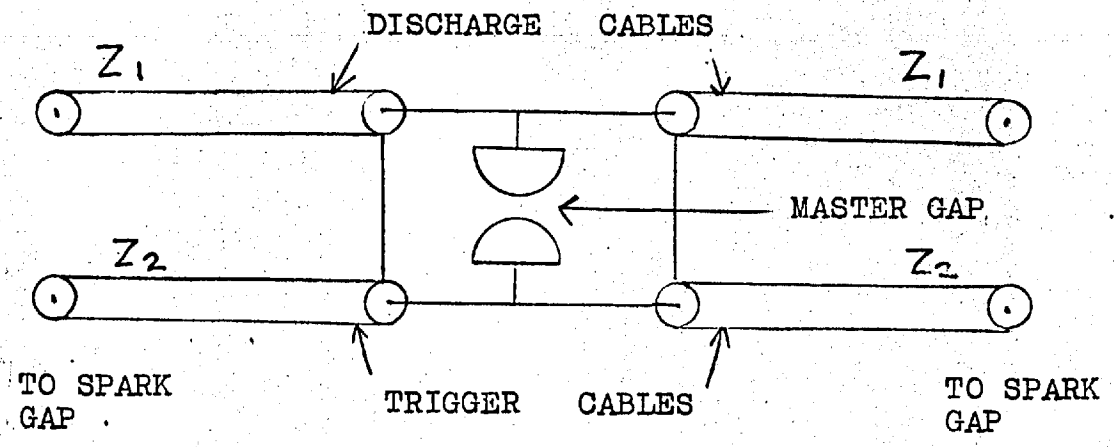

FIG. (1.8)

A schematic diagram of a cable trigger generator is shown in fig. (1.8), where the number of discharge cables is assumed to be equal to the number of trigger cables. For this trigger generator, the trigger voltage V_T at each spark gap is

given by

$$V_T = V_C \frac{Z_2}{Z_1 + Z_2} \left[1 - \exp\left(-\frac{t}{\beta}\right)\right] \quad (1.24)$$

where $$\beta = \frac{n_T L_G}{Z_1 + Z_2} \quad (1.25)$$

Z_1 = characteristic impedence of the discharge cables

Z_2 = characteristic impedence of the trigger cables

L_G = inductance of master gap

n_T = number of trigger cables

From equations (1.24) and (1.25) we will take the mean rate of rise of trigger voltage to be

$$\dot{V}_T \text{ (mean)} = \frac{0.6\, V_C\, Z_2}{n_T\, L_G} \quad (1.26)$$

In our case $n_T = 40$, $Z_2 = 52\ \Omega$ and an upper charging voltage limit for U.R.74 cable used under these pulsed conditions is ~ 75 k.v. Therefore substitution into equation (1.26) gives

$$\dot{V}_T \text{ (mean)} = \frac{58.5}{L_G} \text{ k.v. (n.sec)}^{-1} \quad (1.27)$$

hence for a mean rate of rise of trigger voltage around 2 k.v. (n.sec.)$^{-1}$

$$L_G \lesssim 30 \text{ n.H.} \quad (1.28)$$

By equating the maximum value of the trigger voltage given by equation (1.24) with the minimum estimated requirement of

40 k.v. we obtain

$$V_T \text{ (min.)} = 40 \leqslant V_C \cdot \frac{Z_2}{Z_1 + Z_2} \text{ k.v.} \qquad (1.29)$$

putting V_C equal to its maximum value of 75 k.v. gives the condition

$$Z_1 \leqslant 0.5\, Z_2 \qquad (1.30)$$

An easy way of achieving this impedence ratio, whilst using the same type of cable throughout, is to have twice the number of discharge cables as trigger cables connected to the same master gap.

The length of discharge cable is determined by the rule that the transit time t_D for the discharge cable should be at least 3β where β is given by equation (1.25). For the conditions $Z_2 = 2 Z_1 = 52\ \Omega$, $L_G = 30$ n.H., and $n_T = 40$, this rule yields a single discharge cable length of 16 feet. Both this rule and condition (1.30) can be satisfied by having 40 lengths of cable, each cable being 30 feet long, fastened in loops around the master gap with both free ends of each cable connected together. This arrangement avoids the flashover problems associated with open ended cables.

(1.4.2.) Construction of Trigger Generator

The extremely low inductance value of 30 n.H. dictated the use of a pressurised master spark gap. As only one spark gap was required, the considerations of cost and ease of manufacture were not as important as in the case of the swinging

cascade spark gaps, and a U.K.A.E.A. design of master gap was chosen. The master gap was identical to those employed as sub-master gaps on the U.K.A.E.A. Culham Mega-joule capacitor bank. This spark gap was designed to operate with 250 p.s.i. nitrogen gas but we used sulphur hexafluoride gas at 20 p.s.i. pressure. The outer earth ring used with the master gap was of our own design and consisted of a 4 foot diameter brass hoop suitably drilled to take the 120 cable ends. Particular care was taken to ensure that the inner surfaces of the earth ring and the flanges used for cable braid connections were smoothly finished. A photograph of the master gap and its associated cables is shown in fig. (1.9)(a).

The master gap discharge cables were pulse charged from a 100 k.v. Marx type generator (9). This generator was of conventional design and employed four 25 k.v. stages with the capacity of each stage being 0.35 μF. The time taken for the Marx generator to charge the discharge cables was ~ 1 μ.second. The main reason for choosing the U.K.A.E.A. design of master gap was that it contained an intermediate electrode by which the gap could be triggered. This direct triggering of the master gap, (rather than relying on the over-volting of the gap by the rising pulse from the Marx generator), enabled the jitter in the triggering of the main bank to be reduced to around 20 n.second. The master gap trigger was obtained from a Blumlein type cable arrangement charged to 50 k.v. The pulse from the Blumlein was timed to occur at 0.8 μ.second after the firing of the Marx generator. A schematic diagram of the complete master gap assembly, together with the equivalent circuit for the charging of the discharge cables from the Marx generator, is shown in fig. (1.10)

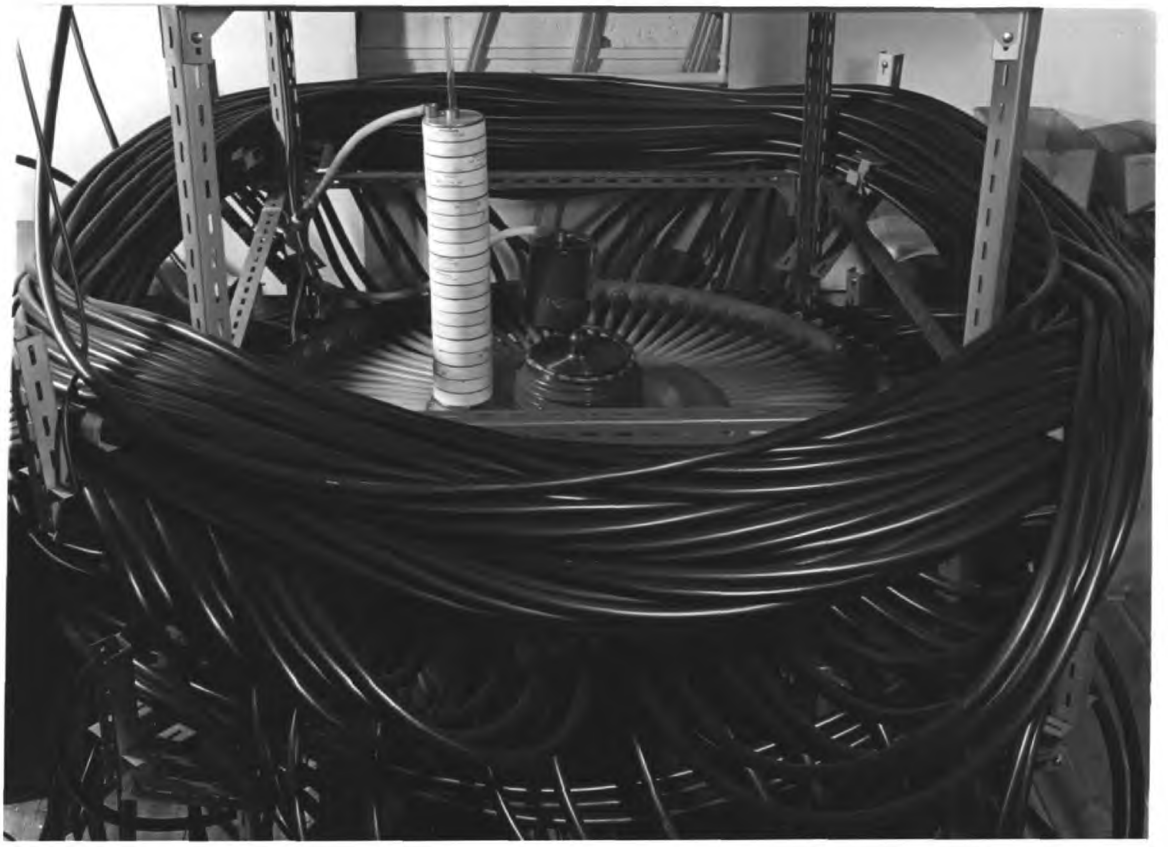

(a)

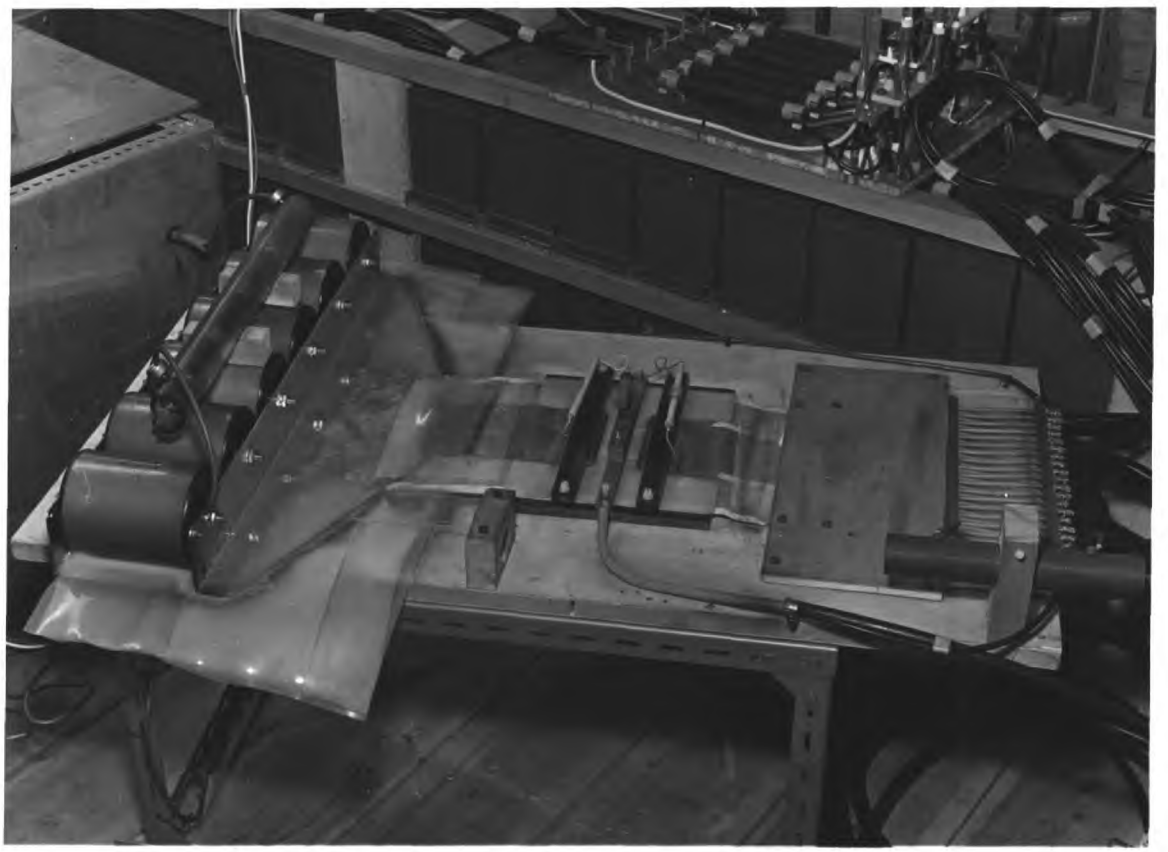

FIG (1.9) (b)

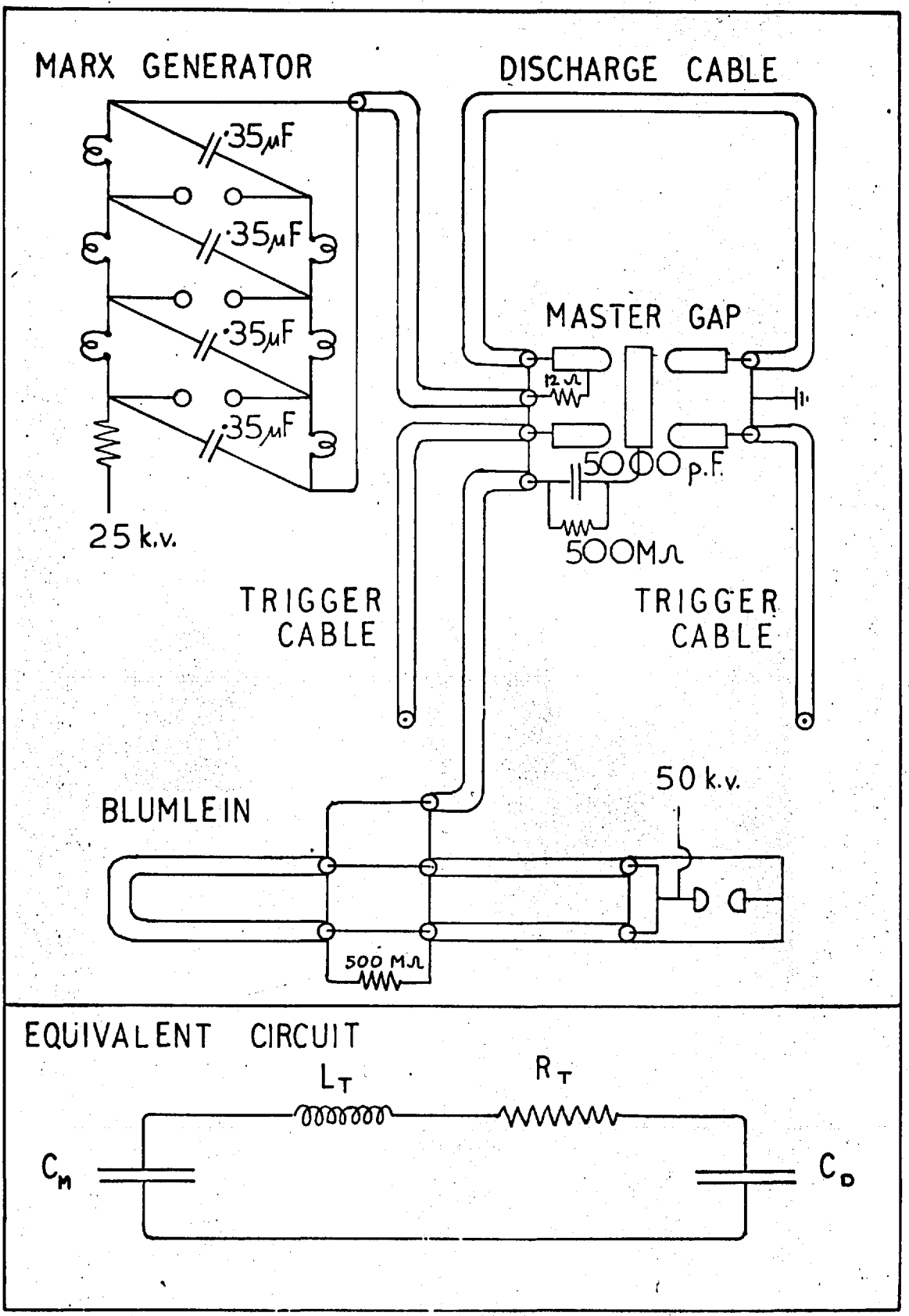

FIG (1.10) Trigger generator and equivalent circuit.

(1.4.3.) Performance of the Trigger Generator

The lifetimes of the U.R.74 discharge cables, when pulsed up to 75 k.v. from the Marx generator, are largely dependent on suppressing unwanted oscillations of voltage on these cables. The trigger cables to the spark gaps are pulsed to a voltage of 2/3 that for the discharge cables and are more lightly stressed. In order to minimise cable blow outs amongst the discharge cables, a critically damped Marx generator discharge is required. An experiment was performed where the Marx generator voltage was reduced to 12.5 k.v. and the Blumlein trigger was disconnected so that the oscillation of charge between the Marx generator and the discharge cables could be studied. In fig. (1.11) the voltage oscillations on the discharge cables for various series damping resistors between 0 and 20 Ω have been plotted. From these results a series damping resistor of 12 Ω was chosen.

The cable connecting the Marx generator to the discharge cables had a length of 10 feet and since this cable had a transit time $<<$ the rise time of the charging voltage, it acted as a series inductance during the charging period.

Therefore for the equivalent circuit shown in fig.(1.10)

$$L_T^* = L_{T1}^* + L_{T2}^* \qquad (1.31)$$

where L_{T1}^* = inductance of connecting cable (0.98 μH)

L_{T2}^* = series inductance of Marx generator capacitors and their connections ($\sim$ 2 μH)

$\therefore L_T^* \sim 3\ \mu H$

and C_m = series capacity of Marx generator

= 0.0875 μF

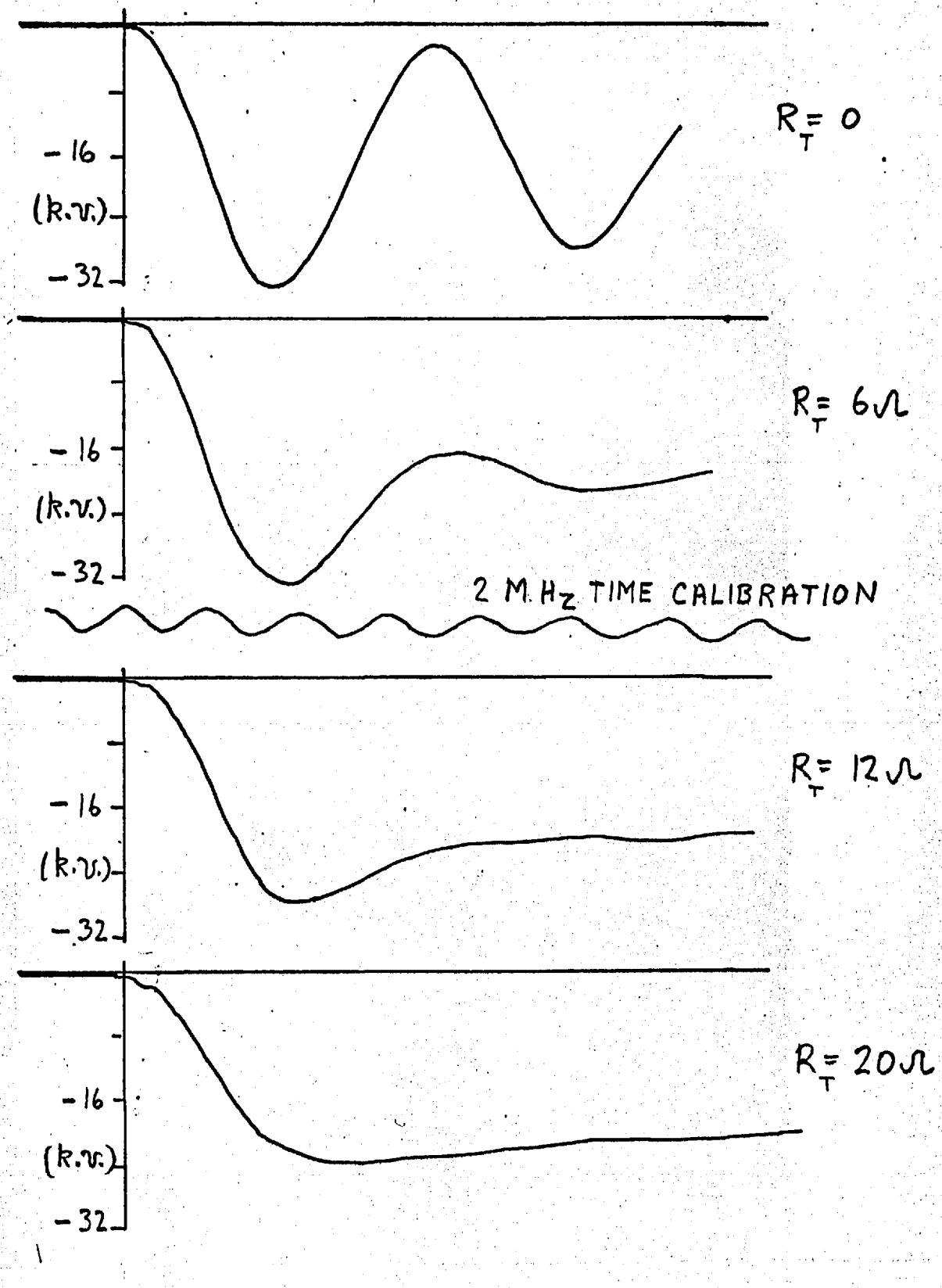

FIG (1.11) Trigger discharge cable voltage waveforms.

and C_D = total capacity of discharge cables

= 0.036 μF

The calculated period for lightly damped voltage oscillations on the discharge cables from the equivalent circuits fig.(1.10) using the above values is 1.74 μ.sec., which can be compared with a measured period of oscillation with no added damping resistor of ~1.7 μ.sec.

The maximum discharge cable voltage V_c for critically damped conditions is

$$V_c \text{ (max.)} = V_m \frac{C_m}{C_m + C_D} \qquad (1.32)$$

where V_m = Marx generator initial voltage. Combining equations (1.32) and (1.29) we obtain

$$V_T \text{ (min.)} \leqslant \left[\frac{Z_2}{Z_1 + Z_2}\right]\left[\frac{C_m}{C_m + C_D}\right] V_m \qquad (1.33)$$

Thus for a minimum trigger voltage of 40 k.v. the minimum required Marx voltage is ~85 k.v.

The rise of trigger voltage at the end of a trigger cable was measured by removing a cable from one main bank spark gap and connecting it to the resistance potentiometer described in section (1.3.3.). The voltage waveform is shown for two different time sweeps of the oscilloscope in fig. (1.12). No measurements were performed with the trigger cable connected to the spark gap.

The theoretical value of inductance for the master gap is given by

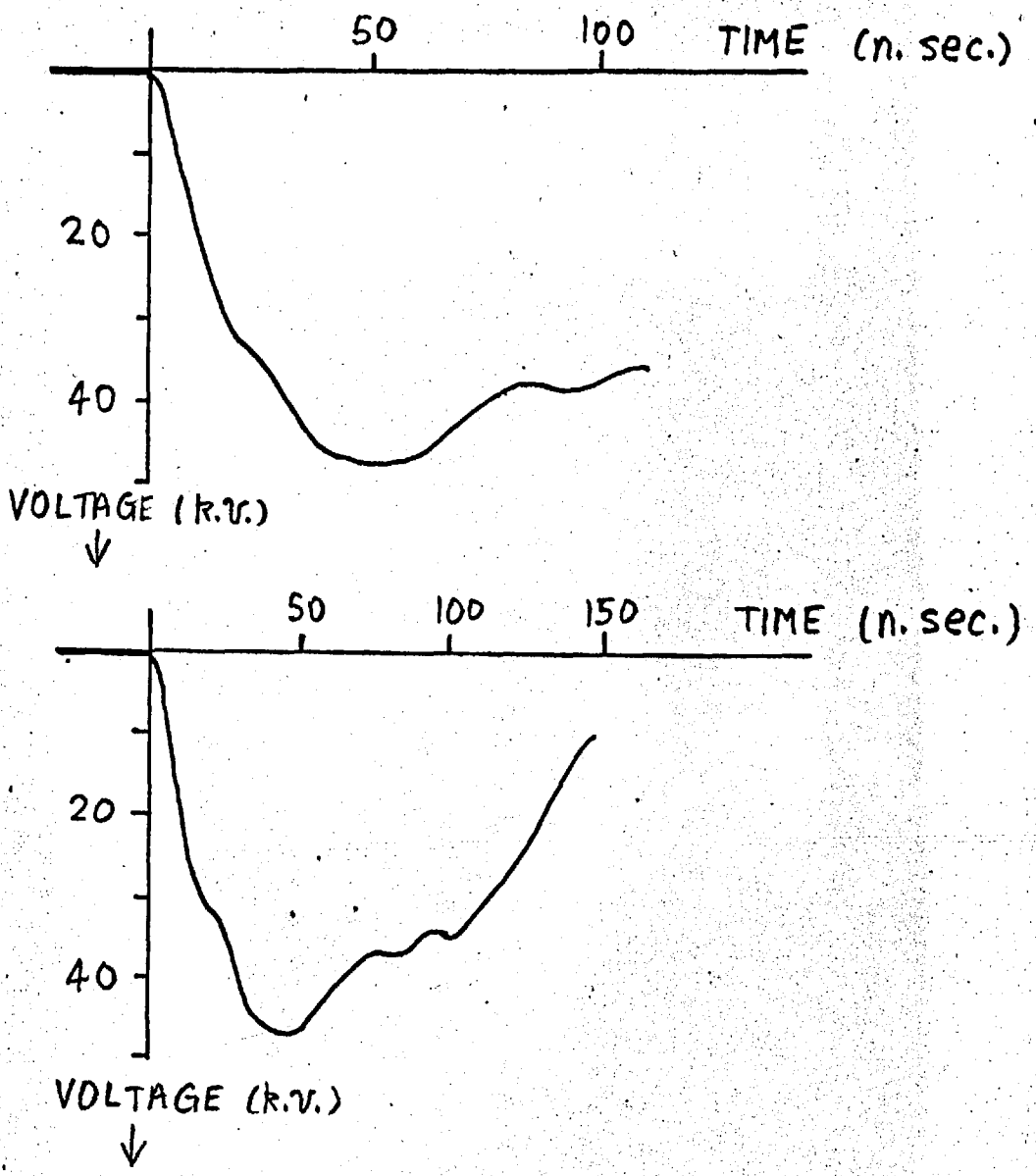

FIG (1.12) Trigger generator output waveforms.

$$L_G = 2\ 10^{-7}\ l_G\ \ln\left[\frac{R_G}{r_G}\right] \quad \text{Henries} \qquad (1.34).$$

where l_G = separation of the master gap electrodes (m.m.)
R_G = radius of earth ring
r_G = radius of master gap central electrode

Substitution of the appropriate physical dimensions into (1.34) gives L_G (theoretical) = 33 n.H.

From the equations (1.24) (1.25) and (1.32) we can write the initial rate of rise of trigger voltage as

$$\dot{V}_T(0)\ (\text{theoretical}) = \frac{Z_2\ C_m\ V_m}{40\ L_G\ (C_m+C_D)} \qquad (1.35)$$

which gives a theoretical value when V_m = 80 k.v. of

$$\dot{V}_T(0)(\text{theoretical}) = 2.2\ \text{k.v.}\ (\text{n.sec})^{-1}$$

The initial rate of rise of trigger voltage as measured from the experimental waveforms shown in fig. (1.12) is

$$\dot{V}_T(0)\ (\text{experimental}) = 1.9\ \text{k.v.}\ (\text{n.sec.})^{-1}$$

(1.6) CHARACTERISTICS OF THE MAIN BANK

The characteristics of the main capacitor bank as originally constructed for use in the Polytron experiment have been summarised in table (1.4).

TABLE (1.4)

MAIN BANK CHARACTERISTICS

Bank Capacitance	80 μF (given)
Maximum working voltage	40 k.v. (given)
Minimum working voltage	20 k.v. (measured)
Maximum bank energy	64 k.J. (given)
Bank inductance	12.8 n.H.(calculated)
Number of spark gaps	40 (given)
Master gap breakdown voltage	70 k.v. (measured)
Initial rise of trigger voltage	1.9 k.v./n.sec.(measured)
Characteristic time of bank	45 n.sec. (calculated)
Breakdown setting of gap 1	32 k.v. (measured)
Breakdown setting of gap 2	16 k.v. (measured)

(1.7) LATER MODIFICATIONS TO THE MAIN BANK

The initial experimental results obtained in the Polytron experiment indicated that the characteristics of the main capacitor bank, described in table (1.4), should be modified to satisfy the following two requirements.

1. The minimum working voltage of the bank should be reduced to well below 20 k.v. and an ideal working voltage range for the study of ion acceleration appeared to be 5 to 30 k.v.

2. The plasma conditions for ion acceleration appeared to

be more favourable with decreasing gas pressure, and the desire to work at the lowest possible gas pressures led to raising the preioniser voltage from 5 k.v. to 20 k.v. This increased preioniser voltage produced voltage oscillations on the main load cables, which broke down gap 2 of the main spark gaps and lead to the premature discharge of the main bank.

In order to meet both of these new requirements, thirty of the main bank spark gaps were modified by increasing the breakdown voltage of the second gap from 16 to 24 k.v. With our particular design of spark gap, this modification was very easily achieved without dismantling, by inserting fibreglass spacers of the appropriate thickness between the perspex cover locating the central electrode and the tufnol plate locating the end electrode. These spacers can be seen in position in the photograph of the modified main bank, fig. (1.4). Together with increasing the second gap, the central electrode bias was modified from being 1/3 the capacitor voltage to become zero, with the central electrode held at earth potential prior to triggering.

The results of both these modifications were that the second gap in the spark gap could withstand the full preioniser voltage of 20 k.v. for all main capacitor charging voltages and that the working range of the bank was altered to become 7.5 to 27.5 k.v. At the very low bank voltage of 7.5 k.v., on no occasion did one of the bank spark gaps fail to fire correctly. For bank voltages around 7.5 k.v., the spark gap mode of operation presumably tends towards the direct over-volting of both gaps 1 and 2 by the trigger pulse. The theoretical lower limit to this particular mode of operation for the modified spark gaps was calculated as 7 k.v.

In table (1.5), we have summarised the characteristics of the modified main bank which differ from those of the original main bank listed in table (1.4). This modified main bank was used for all the Polytron experiments described in Chapter 5.

TABLE (1.5)

MODIFIED MAIN BANK CHARACTERISTICS.

Bank Capacitance	60 μF	(given)
Maximum working voltage	27.5 k.v.	(measured)
Minimum working voltage	7.5 k.v.	(measured)
Maximum bank energy	23 k.J.	(calculated)
Bank inductance	17.3 n.H.	(calculated)
Number of spark gaps	30	(given)
Breakdown setting of gap 1	32 k.v.	(measured)
Breakdown setting of gap 2	24 k.v.	(measured)

CHAPTER 2

DESIGN AND CONSTRUCTION OF THE POLYTRON : 2

The design, construction and experimental testing of the elements comprising the Polytron assembly apart from the main bank are described in this chapter.

(2.1) OUTLINE FOR THE CUSP FIELD SYSTEM

The toroidal geometry of the apparatus will be described using the modified form of cylindrical coordinates shown in fig. (2.1). Thus, the magnetic field at any point (r, θ, z) can be described in terms of the three components B_r, B_θ and B_z. In general, each of these field components is a function of (r, θ, z). For the infinite cylinder approximation

$$R \gg a \qquad (2.1)$$

where R = radius of curvature of the z axis
a = radius of torus cross-section

The components of a cusped shaped magnetic field around the torus can be described, to a first order approximation, in terms of $B_r(r,z)$ and $B_z(r,z)$ only.

Using a very simple collisional plasma model, we will now estimate values of the cusp field components which correspond to the optimum ion acceleration in the Polytron device.

The first two conditions for ion acceleration are that:

for the electrons : $\ell_e < 0.5\, l_k$ (2.2)

for the ions : $\ell_i > 0.5\, l_k$ (2.3)

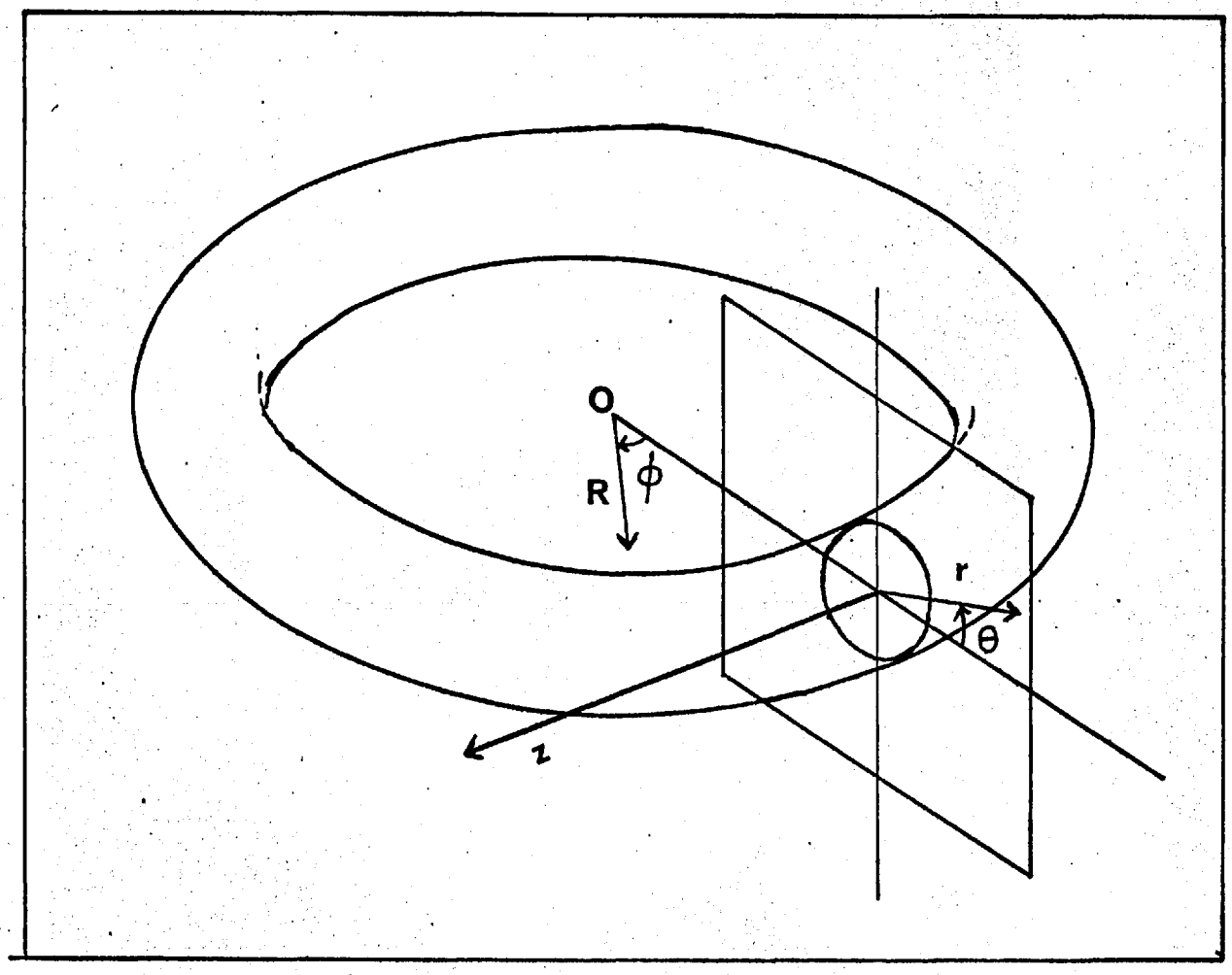

FIG (2.1) Toroidal coordinate system.

where ρ_e = electron Larmor radius in B_r
ρ_i = ion Larmor radius in B_r
l_k = cusp coil separation in the z direction

and that for the electrons

$$\omega_e \tau_e \gg 1 \qquad (2.4)$$

where ω_e = electron cyclotron frequency in B_r
τ_e = electron collision time

Provided plasma conditions (2.2) and (2.4) are both satisfied, then under the combined effects of the multi-cusped magnetic field and the applied electric field $\vec{E}_z$ in the z direction, the electrons are effectively trapped in the cusp regions as regards motion in the z direction, and they drift azimuthally in the $\vec{E}_z \wedge \vec{B}_r$ direction. This azimuthal electron drift gives rise to the so called Hall current in the plasma. For the ions, condition (2.3) shows that ionic motion from one cusp region to the next (where the sign of B_r reverses) is possible under the action of E_z without the ions performing a closed orbit. Thus, a single particle picture of ion motion around the torus under these conditions resembles a modified sine wave.

The starting point of the Polytron device corresponds to the firing of the main capacitor bank which immediately produces a large $\vec{E}_z$. At this time (t = o) we will assume that a quiescent nearly fully ionised plasma exists in the torus as a result of the preionisation process. We will now calculate the values of B_r which are optimum, under these initial conditions, for the inequalities (2.2), (2.3) and (2.4) to be satisfied.

The cyclotron frequencies ω_e for the electrons and ω_i

for the ions are given by

$$\omega_e = \frac{e B_r}{m c} \qquad (2.5)$$

$$\omega_i = \frac{e B_r}{M c} \qquad (2.6)$$

where m = electron mass

M = ion mass

For the highly ionised plasma produced by the preioniser, long range Coulomb collisions between particles dominate other collision mechanisms and the collision times for ions and electrons are related according to Spitzer (10) by

$$\tau_{ie} = \frac{M}{m} \tau_{ei} \qquad (2.7)$$

showing that at the start of the Polytron

$$\omega_e \tau_e \simeq \omega_i \tau_i \qquad (2.8)$$

Hence, condition (2.4) necessary for a small axial electron current means that

$$\omega_i \tau_i \gg 1 \quad \text{at time } t = o \qquad (2.9)$$

Because of condition (2.9) the magnitude of B_r at time $t = o$, denoted by $B_r(o)$, must satisfy the conditions (2.2) and (2.3) which, using equations (2.5) and (2.6), can be re-written as

$$\frac{m V_{eo} c}{e B_{r(o)}} \ll 0{\cdot}5 \ell_R < \frac{M V_{io} c}{e B_{r(o)}} \qquad (2.10)$$

where V_{eo} and V_{io} are the initial velocities of the electrons and the ions. Assuming a Maxwellian velocity distribution for each species, initially, with the electron and ion temperatures being both equal to a value T, we can write (2.10) as

$$\frac{2c\,(2mkT)^{1/2}}{e\,l_k} \ll B_r(0) < \frac{2c\,(2MkT)^{1/2}}{e\,l_k} \qquad (2.11)$$

or $B_{re}(0) \ll B_r(0) < B_{ri}(0)$

For the value of l_k = 4.4 cm corresponding to our experimental apparatus, the values of $B_{re}(0)$ and $B_{ri}(0)$ representing the lower and upper limits of the optimum initial value of B_r have been evaluated for initial temperatures of 2 and 20 e.v., and are given in table (2.1).

TABLE (2.1)

T (e.v.)	$B_{re}(0)$ (gauss)	$B_{ri}(0)$ (gauss)	
		Hydrogen	Argon
2	2.0	86	540
20	6.4	272	1720

For our multi-cusp shaped magnetic field, B_r is a strong function of both r and z and there is always a point near the z

axis where B_r passes through zero. Thus in the vicinity of the z axis there exists a region where $B_r(0) < B_{re}(0)$ and no electron trapping occurs in this region. We clearly require $B_r(0)$ to be as large as possible without causing ion trapping and from table (2.1) this suggests values of $B_r(0)$ of about several hundred gauss.

Once the ion acceleration process has led to the ions acquiring a directed velocity which is much greater than their initial thermal velocity, the threshold value of B_r for ion trapping is increased well above the values of $B_{ri}(0)$ given in table (2.1). The directed ion velocity at time t' from the start of the acceleration is given by

$$|V_i| = \int_0^{t'} \frac{e}{M} E_z(t)dt \qquad (2.12)$$

Where t' is very much less than the characteristic time τ_a for the acceleration process. Dunnett (5) has shown that, for most experimental conditions, the first quarter cycle time for E_z is $\ll \tau_a$. Thus the directed ion velocity at the end of the acceleration phase when E_z passes through zero is given by

$$|V_i| = \int_0^{\frac{\pi}{2\omega}} \frac{e}{M} E_{zo} \cos \omega t \, . \, dt \qquad (2.13)$$

where ω is the cyclic frequency of the main discharge oscillations and the condition for ion larmor radius $>$ cusp separation is

$$\frac{2M|V_i|c}{e B_r l_k} > 1 \qquad (2.14)$$

Combining expressions (2.13) and (2.14) we obtain the expression for the upper limit on B_r at the end of the first quarter cycle of the discharge as

$$B_r\,(\pi/2\omega) < \frac{2\,C\,E_{zo}}{\omega\,l_k} \qquad (2.15)$$

We note that expression (2.15) is independent of the charge or mass of the ion and for an initial induced voltage around the torus of 30 k.v. and for values of ω and l_k appropriate to our experiment, expression (2.15) has a numerical value

$$B_r\,(\pi/2\omega) < 62 \text{ k.gauss}$$

If during the acceleration process, we reach a situation where

$$\left.\begin{aligned} \omega_e \,.\, \tau_e &\gg 1 \\ \omega_i \,.\, \tau_i &\ll 1 \end{aligned}\right\} \qquad (2.16)$$

then the size of the magnetic field can be increased until $\omega_i\,\tau_i \sim 1$ without regard to the effect on the ion larmor radius.

(2.2) CONSTRUCTION OF THE MULTI CUSP COIL SYSTEM

The details of the cusp coil system that was constructed to provide the toroidal multi-cusp shaped magnetic field in the Polytron are summarised below.

1. Thirty six coils spaced at 10° intervals around the torus were used. Each coil was energised from eight 27 μF 5 k.v.

capacitors connected in parallel using one argon gas filled spark gap per coil. All connections between the capacitors and the coils were by copper and polythene strip leads. The physical arrangement of the spark gap and strip lead system is shown in fig. (2.2)(a).

2. The cusp coil spark gaps were triggered simultaneously from a trigger generator employing a surface tracking gap. Details of this low inductance trigger generator are given in section (2.2.1).

3. Each cusp coil consisted of a double turn coil and was formed by four components made from sheet brass and three insulating components made from sheet nylon. Details of the construction of each coil are given in section (2.2.2.).

(2.2.1.) Cusp Bank Trigger Generator

The cusp coil spark gaps were only coupled together via the cusp bank charging resistors and hence the triggering requirements were much more relaxed than those of the main capacitor bank described in section (1.4). For convenience, the trigger pulse was transmitted to each cusp spark gap along 50 Ω coaxial cable and since the impedence of the strip lead connections to each gap was $\sim 5\,\Omega$, this indicated the need for a 50 k.v. trigger generator.

The complete trigger generator is shown in fig. (1.9)(b). Six low inductance 5000 pF 60 k.v. capacitors connected in parallel were discharged using a surface tracking spark gap into the 36 trigger pulse cables. The surface tracking gap was the result of a lot of experimental development work. The final design consisted of a three electrode gap with fibreglass

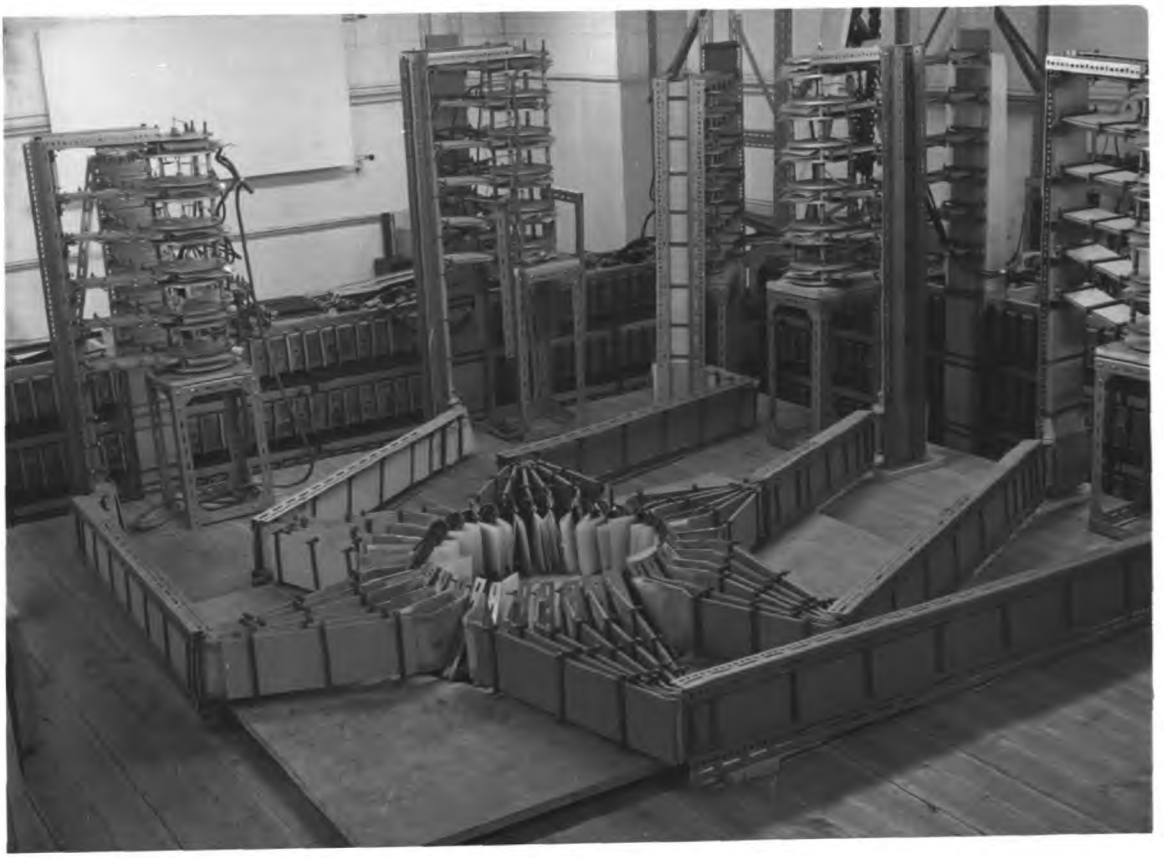

(a)

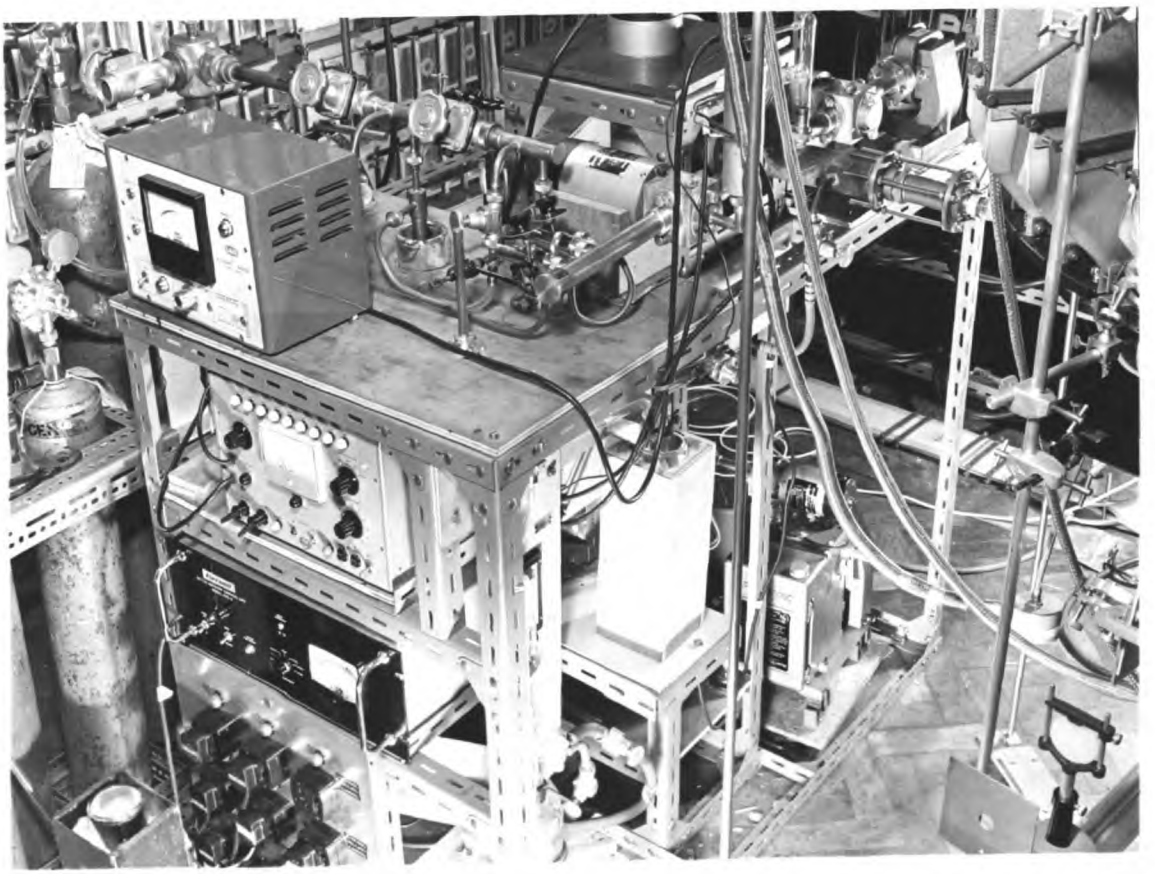

FIG (2.2) (b)

sheet as the tracking surface and the current return strip was situated immediately beneath the fibreglass. A schematic drawing of the gap and its triggering arrangement is shown in fig. (2.3)(a). The central electrode was initially held at half the capacitor charging voltage and both gaps were set equal. Triggering was effected by shorting the end of a long length of coaxial cable connected between the middle electrode and earth.

In fig. (2.3)(b), the maximum and minimum operating voltages of this system have been plotted as a function of the surface gap width of one gap. The upper limit corresponds to spontaneous gap breakdown and the lower limit to the minimum triggerable voltage. The working voltage range increased with voltage, since the initial voltage on the cable used for triggering was proportional to the charging voltage. For small gap widths $<$ 0.05 in., the gap behaved as an air gap, whilst for gap widths $>$ 0.05 in., the onset of surface tracking can be seen from the marked change in gradient of the plot shown in fig. (2.3)(b). There was negligible erosion of the copper electrodes after several thousand operations and cleaning of the fibreglass sheet was performed at very infrequent intervals.

(2.2.2.) CUSP COIL CONSTRUCTION

Several prototype forms of cusp coil were built and tested to meet the following specification.

1. The coil inductance should be much larger than the total inductance of the coil energising circuit comprising capacitors, spark gap and strip leads.

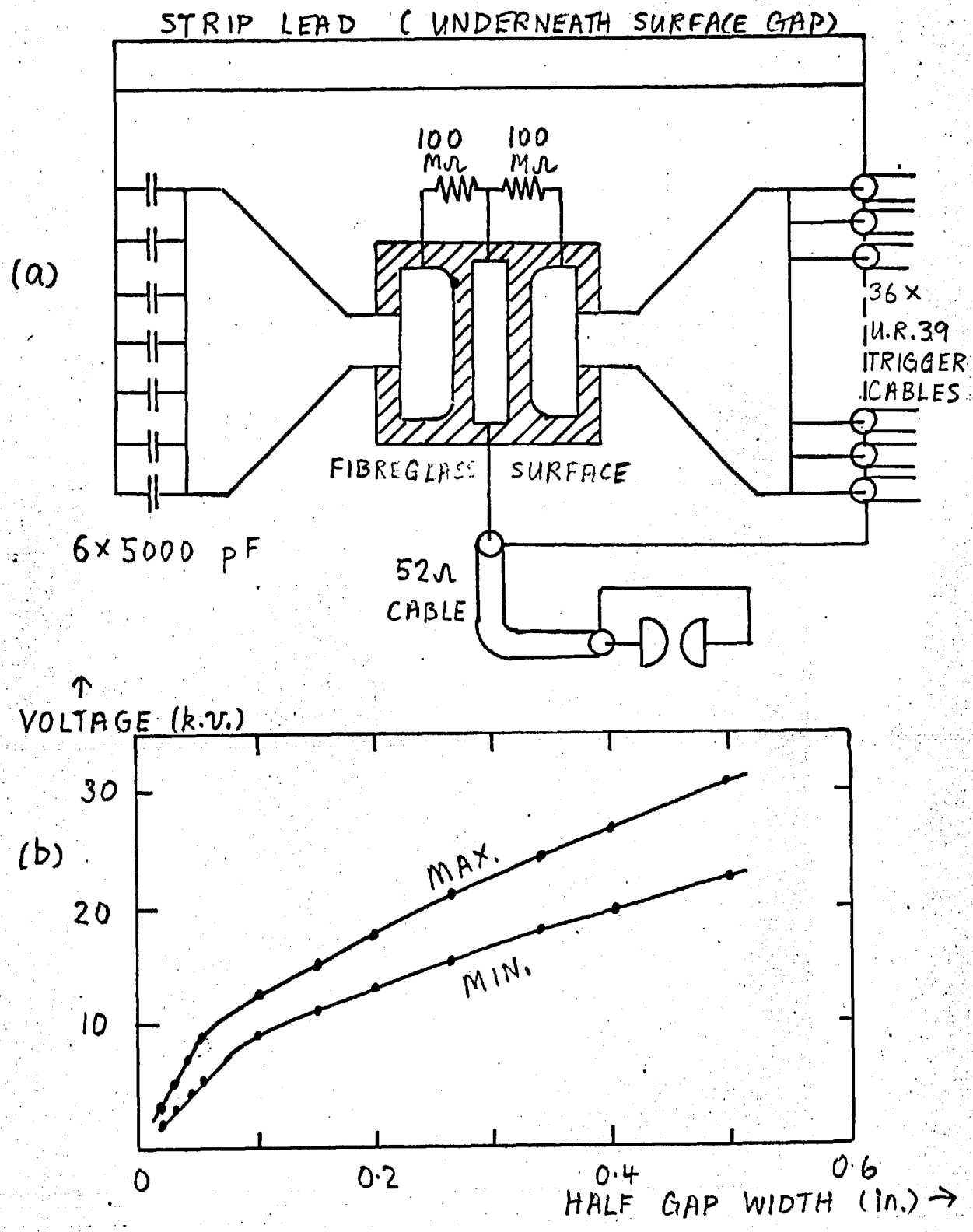

FIG (2.3) (a) Schematic diagram of cusp trigger generator.
(b) Breakdown characteristics of surface tracking gap.

2. The coil thickness had to be kept to the absolute minimum since the coils had to be evenly spaced around the torus and the collector plate had to fit between a pair of coils.

3. The coils and any insulation pieces had to be demountable for assembly around a complete torus.

4. The coils had to serve the purpose of aligning and holding the 8 induction rods in a fixed position around the torus, and consequently the coils had to be robust enough to withstand some of the forces on the induction rods as well as their own current forces.

A final design of coil meeting these requirements consisted of a double turn coil formed by four components made from 16 SWG hard brass sheet and three insulating components made from 16 SWG nylon sheet. Profiles of the components forming one coil are shown in fig. (2.4). The relative alignments of the brass components, under the action of the forces on the coil, were maintained using $\frac{1}{4}$ inch diameter steel pegs in the holes shown in these components in fig. (2.4). Clamps outside the coils prevented these steel pegs from dropping out and pressed the overlap areas of adjacent components together forming a good electrical connection. The clamps also secured the coils to the base plates of the apparatus.

(2.3) CUSP FIELD MEASUREMENTS

The radial and axial field components of the toroidal multi-cusp shaped magnetic field were measured with the cusp coils assembled and the discharge tube removed. A magnetic

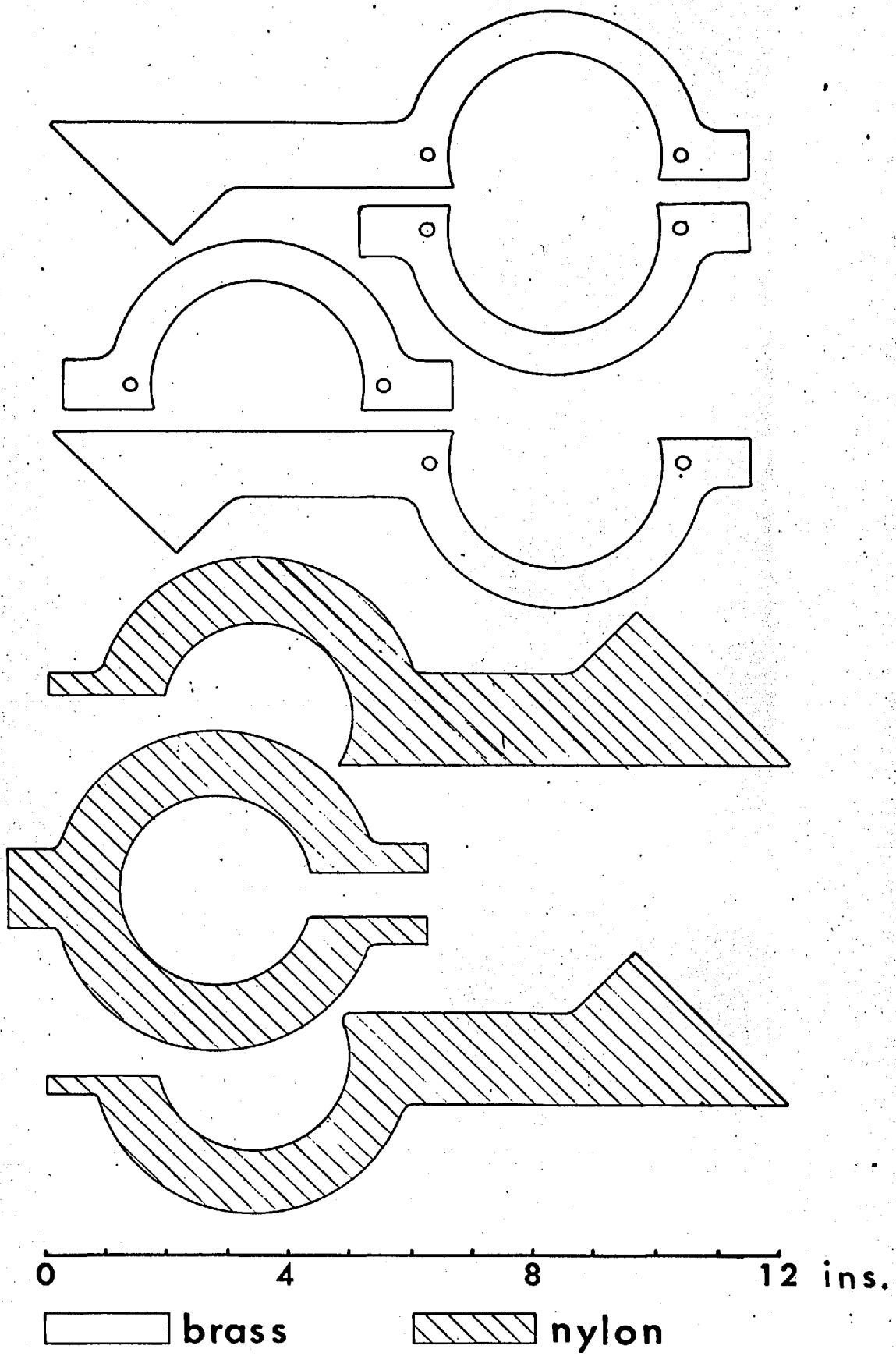

FIG (2.1) Coup coil components.

probe, having two coils with perpendicular axes, was moved using a three dimensional micrometer adjusted mount. B_r and B_z were recorded in planes passing through the toroidal z axis of the coil system which were perpendicular and parallel to the plane of the toroidal z axis. Because of the symmetry of the field system, only a region between the centre plane of a pair of cusp coils and one adjacent cusp coil plane was studied. Within this region, the profiles of B_r and B_z were measured along the paths shown in fig. (2.5). Plots of the experimentally recorded profiles corresponding to the peak first half cycle coil current for a capacitor charging voltage of 2.5 k.v. are shown in figs. (2.6) to (2.9). With reference to fig. (2.1), if we take the line from the centre of the coil system O to the midplane between coils to be $\phi = 0$, then the coil plane subtends an angle of $\phi = 5^\circ$, and the angles ϕ subtendend by the various paths shown on fig. (2.5) have experimentally measured values given by table (2.2).

TABLE (2.2)

PATH	ϕ	PATH	ϕ
AA'	5° 00'	ZZ'	5°00'
BB'	3° 45'	YY'	3°45'
CC'	2° 30'	XX'	2°30'
DD'	1° 15'	WW'	1°15'
EE'	0° 00'	VV'	0°00'

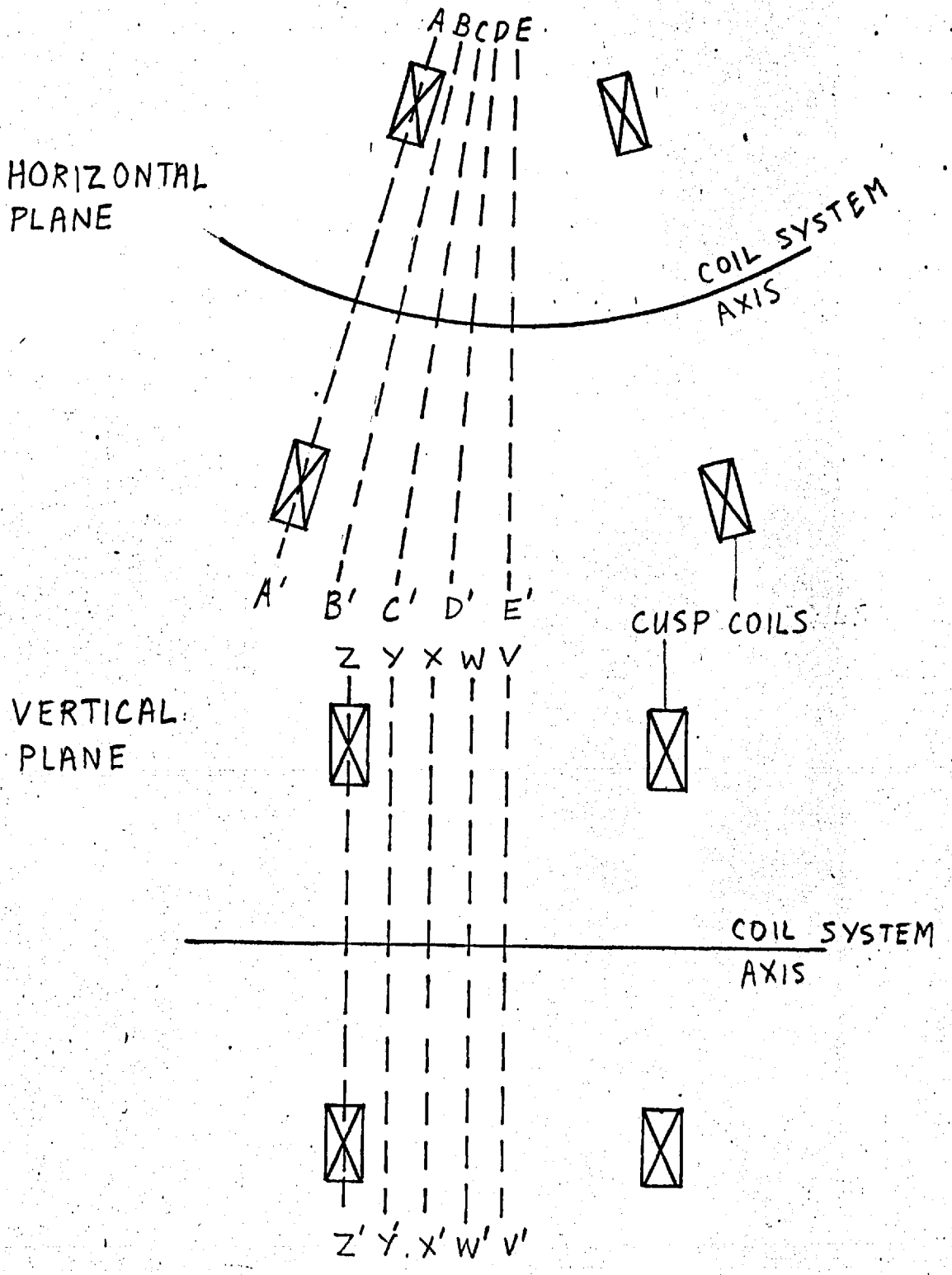

FIG. (2.5) Paths along which the cusp field components were measured.

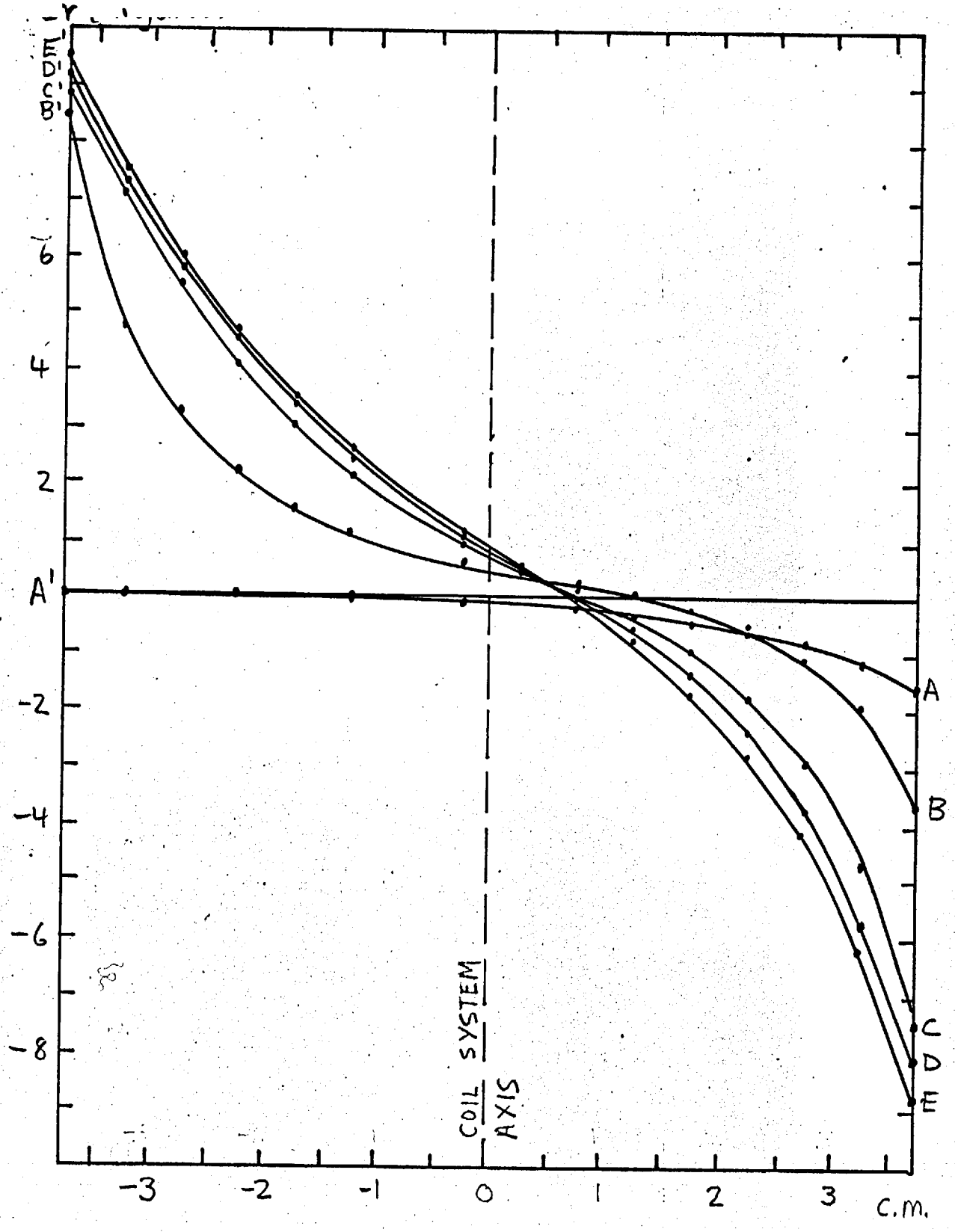

FIG (2.6) Radial cusp field components measured in the horizontal plane.

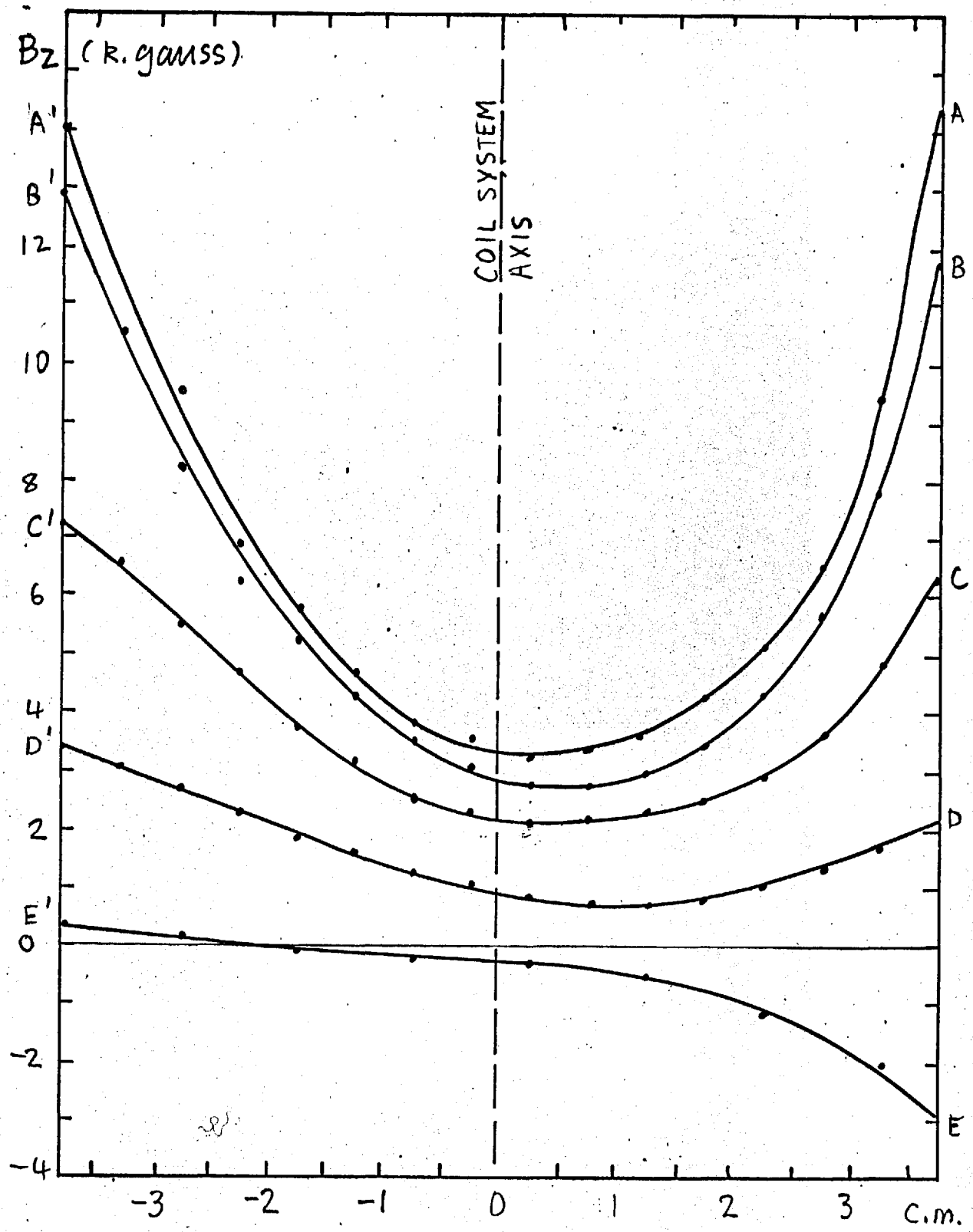

FIG (2.7) Axial cusp field components measured in the horizontal plane.

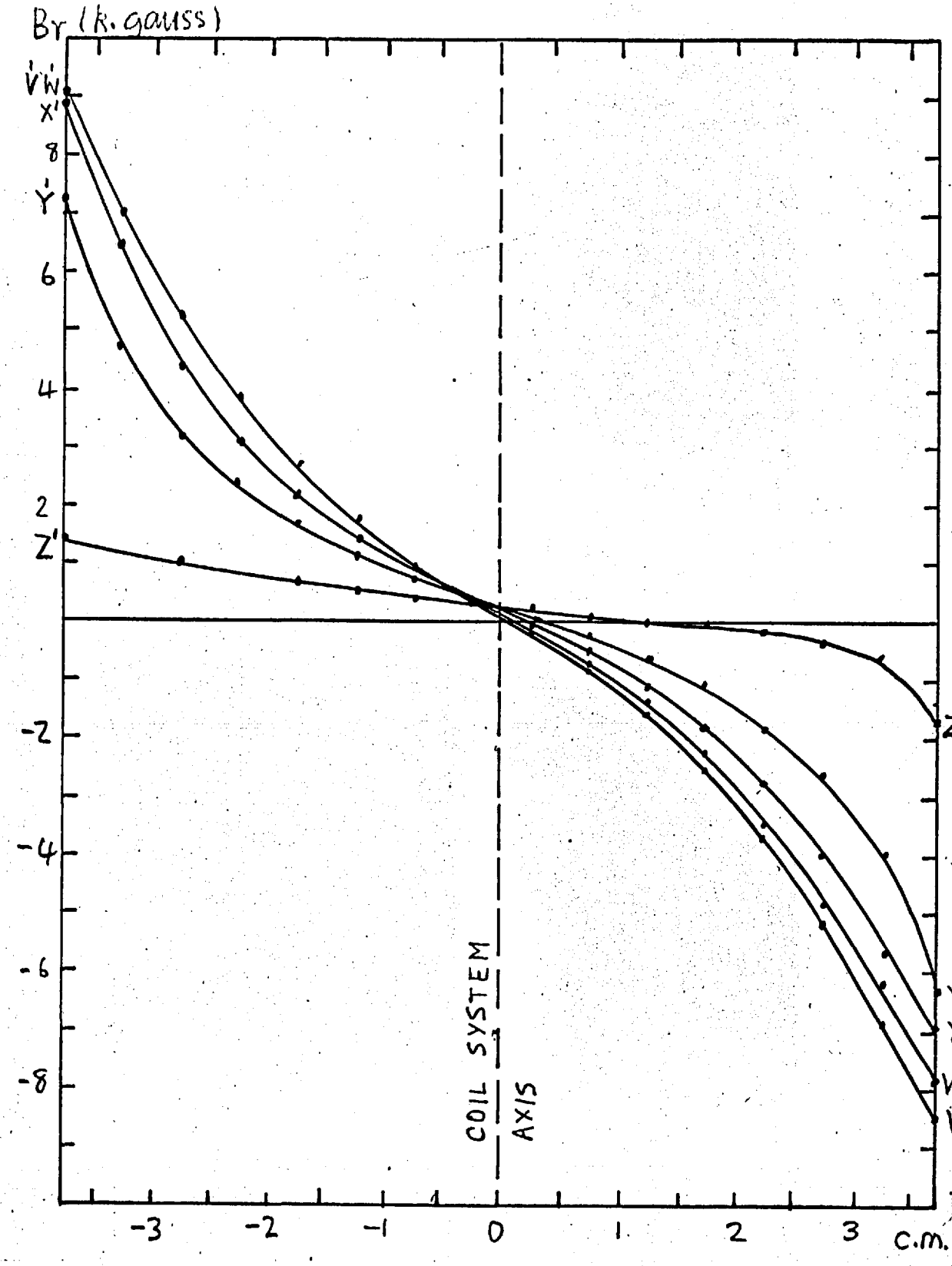

FIG (2.8) Radial cusp field components measured in the vertical plane.

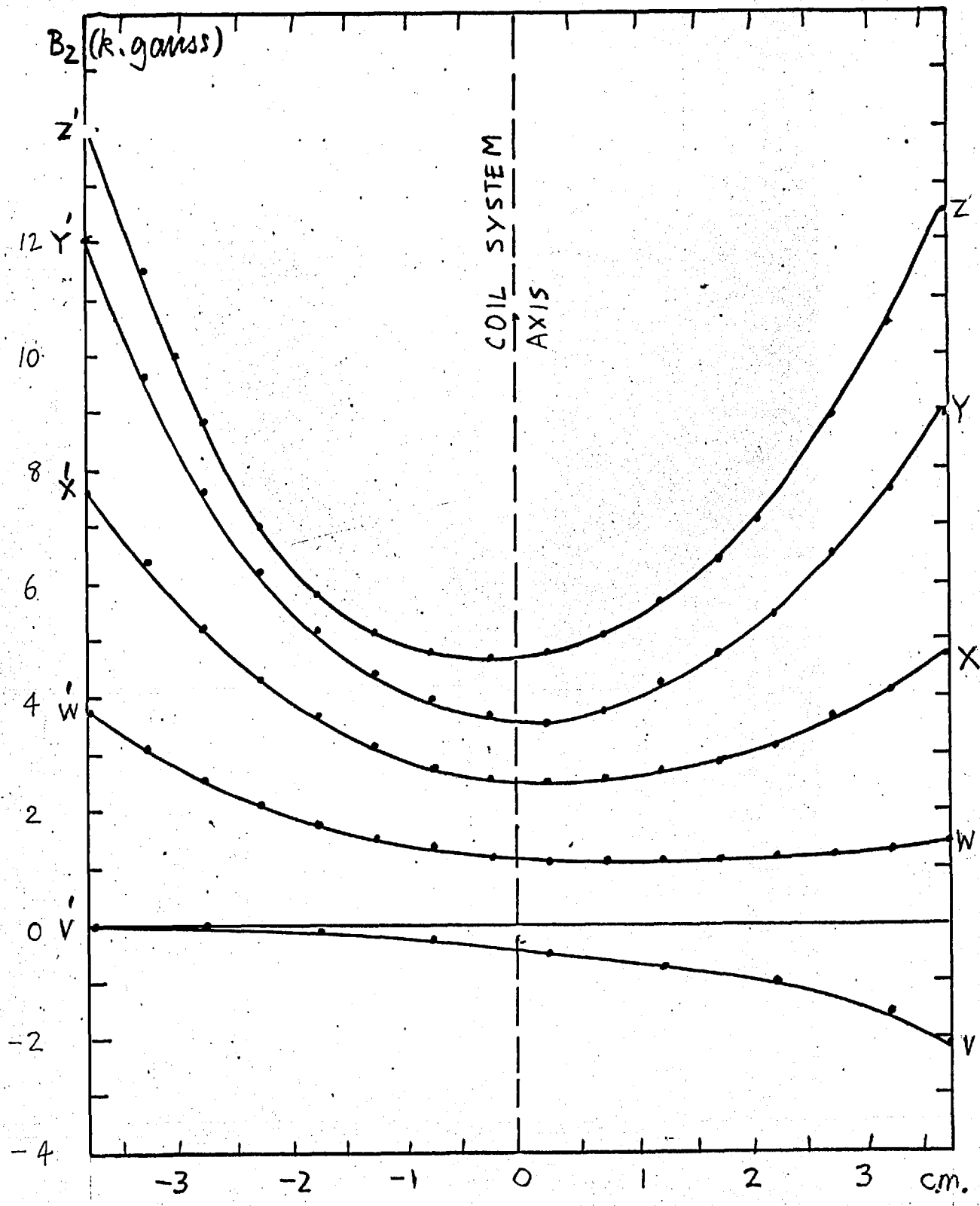

FIG (2.9) Axial components of cusp field measured in the vertical plane.

The following comments are made about the magnetic field component profiles shown in figs. (2.6) to (2.9).

1. The magnetic probe was moved along paths which were exactly perpendicular to the toroidal z axis of the coil system. The construction of each coil, employing four overlapping offset components, meant that the average plane of each coil was not exactly perpendicular to the toroidal z axis. This feature accounts for the large assymetries in the measured field components for paths close to the plane of the coil.

2. In the horizontal plane, fig. (2.6), the point where B_r passes through zero is shifted well inside the toroidal z axis of the coil system. This feature is caused by the curvature of the toroidal system and the fact that, in the horizontal plane, adjacent coils subtend an angle $\phi = 10^{\circ}$. In the vertical plane, fig. (2.8), the point where B_r passes through zero almost exactly coincides with the toroidal z axis of the coil system since the coils are parallel in the vertical plane.

(2.4) TOROIDAL AXIAL MAGNETIC FIELD SYSTEM

In operating the Polytron the need arose for an additional small magnetic field whose field lines should be parallel to the toroidal z axis. This magnetic field was required for two reasons

1. To enable the minimum gas pressure for breakdown by the preioniser to be lowered by channelling the initial ionising electrons around the torus.

2. To reduce plasma diffusion losses at the lower gas pressures in the interval between the end of the preioniser discharge and the establishment of the cusp magnetic field.

The system that was devised to produce the toroidal axial magnetic field, consisted of a 1800 μF 5 k.v. capacitor bank which discharged via a single spark gap through a rod passing perpendicularly through the centre of the plane of the torus. The return current was carried by four widely spaced rods outside the torus. The discharge was crow-barred by shorting the rod system using an additional spark gap at the time of the peak discharge current. The time taken for the peak current to be reached was ~100 μ sec. and the crow-barred current decay time was ~1.0 m.sec. Thus, over the time scale of the Polytron experiment, this system produced a virtually constant magnetic field.

The magnitude and uniformity of the toroidal axial field were measured using a magnetic probe for constant values of R, (see fig. (2.1)), around the torus. The measured variation of the axial field component B_z is shown in fig. (2.10). From these results, it can be seen that the four current return rods affected the homogeneity of the field by a factor of around 8%. Field measurements were not possible at the centre of the collector plate assembly, but from an extrapolation of the results shown in fig. (2.10), the magnetic field appears to be grossly distorted by the presence of the collector plate.

(2.5) THE PREIONISATION SYSTEM

The preionisation discharge for producing plasma in the

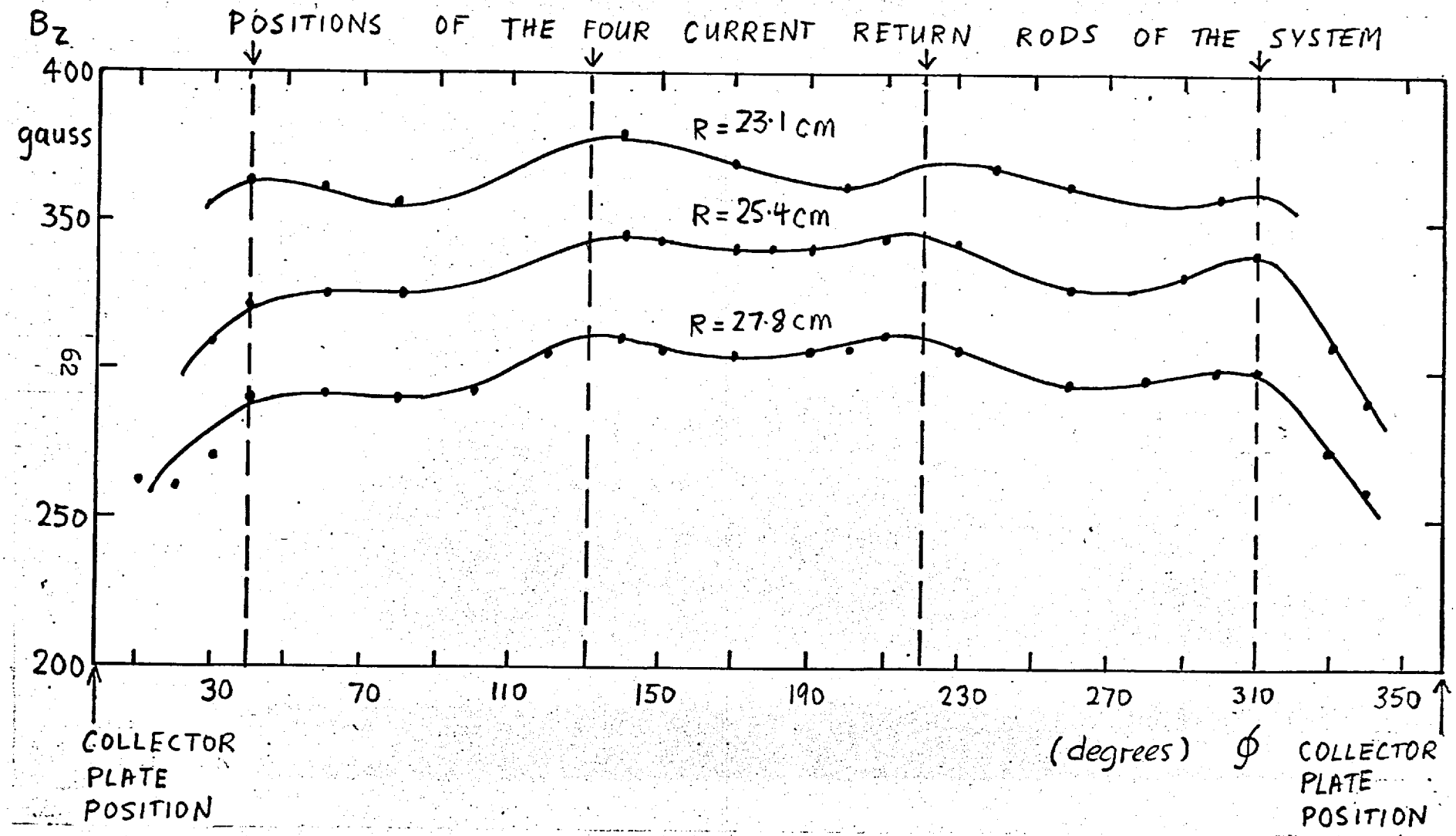

FIG. (2.10) Toroidal axial magnetic field components.

Polytron was passed through the same collector plate and eight rod induction system as was used for the main bank discharge. The preionisation system consisted of a single 40 k.v. rapid discharge capacitor connected via a single direct over-volted spark gap and sixteen 52 Ω coaxial cables in parallel to the collector plate. Triggering was performed by the usual thyratron and pulse transformer arrangement. For experiments with the small torus system, a 1 μF capacitor was used and the period of oscillation on load was $\sim$ 5 μ.sec. For experiments with the large torus system, both 1 μF and 2 μF capacitors were used and the periods of oscillation on load were 4.4 and 6.0 μ.sec. respectively. The total inductance of the capacitor + spark gap + cables was calculated to be around 230 n.H. and the normal operating voltage of the system was 20 k.v.

In table (2.3), we have listed the minimum gas pressures (in m.torr) for reliable gas breakdown for both the large and small torus systems with and without a toroidal axial magnetic field of 200 gauss, for a preioniser voltage of 20 k.v. The results show the effectiveness of a small axial magnetic field on lowering the working pressure limit.

TABLE (2.3)

MINIMUM GAS BREAKDOWN PRESSURES. (m.torr)

GAS	SMALL TORUS		LARGE TORUS			
	1μF		1μF		2μF	
	B_z=0	B_z=200	B_z=0	B_z=200	B_z=0	B_z=200
H	10	5	-	-	-	-
D	-	-	5.5	3.5	8.0	5.0
He	18	10	9.5	6.5	14	9.0
A	2.0	1.0	1.0	0.6	2.0	1.0

(2.6) THE TOROIDAL ASSEMBLY

A different configuration of the toroidal assembly was used with each of the two sizes of torus. For the small torus (minor diameter 44 mm) the eight induction rods were arranged to pass through the inside of the cusp coils, whilst for the large torus (minor diameter 71 mm) the eight induction rods passed outside the cusp coils. In both cases, the cusp coils used were identical, although the cusp coil clamps were changed. Illustrations of the small toroidal assembly are

shown in figs. (2.11) to (2.13) and of the large toroidal assembly in figs. (2.14) to (2.16). For both assemblies, the apparatus was built around a 5 inch diameter 'tufnol' cylinder suspended from a mezzanine floor. This 'tufnol' cylinder can be clearly seen in figs. (2.13) and (2.16). The collector plates were shaped roughly like equilateral triangles of side 6 feet. The 160 main cables were fed into one vertical side of the triangle and this can just be seen in the background of fig. (1.4). Both the live and earthed collector plates were made from $\frac{1}{4}$ inch thick brass sheet and the insulation was provided by 60 separate sheets of 2 thou. 'melinex' insulation. The apex of each collector plate was detachable and split horizontally for fitting around the torus. In both types of assembly, the eight rod induction systems were welded to flanges which were screwed to each collector plate. The collector plate feed in point to the rod system was a very carefully designed area because of the very small space available between a pair of cusp coils and because the torus passed through the centre of the region. Concentric polythene 'top hats' were used to prevent flashover between the collector plates, and the adjacent cusp coils were of modified design. Drawings of the feed in arrangement in both cases are shown in figs. (2.12) and (2.15). The maximum total outward force between the collector plates was estimated to be 3 tons wt. (full main bank at 40 k.v.) and large wooden clamps were used to hold the plates together during the main discharge. These wooden clamps can be seen in the background of figs. (2.13) and (2.16).

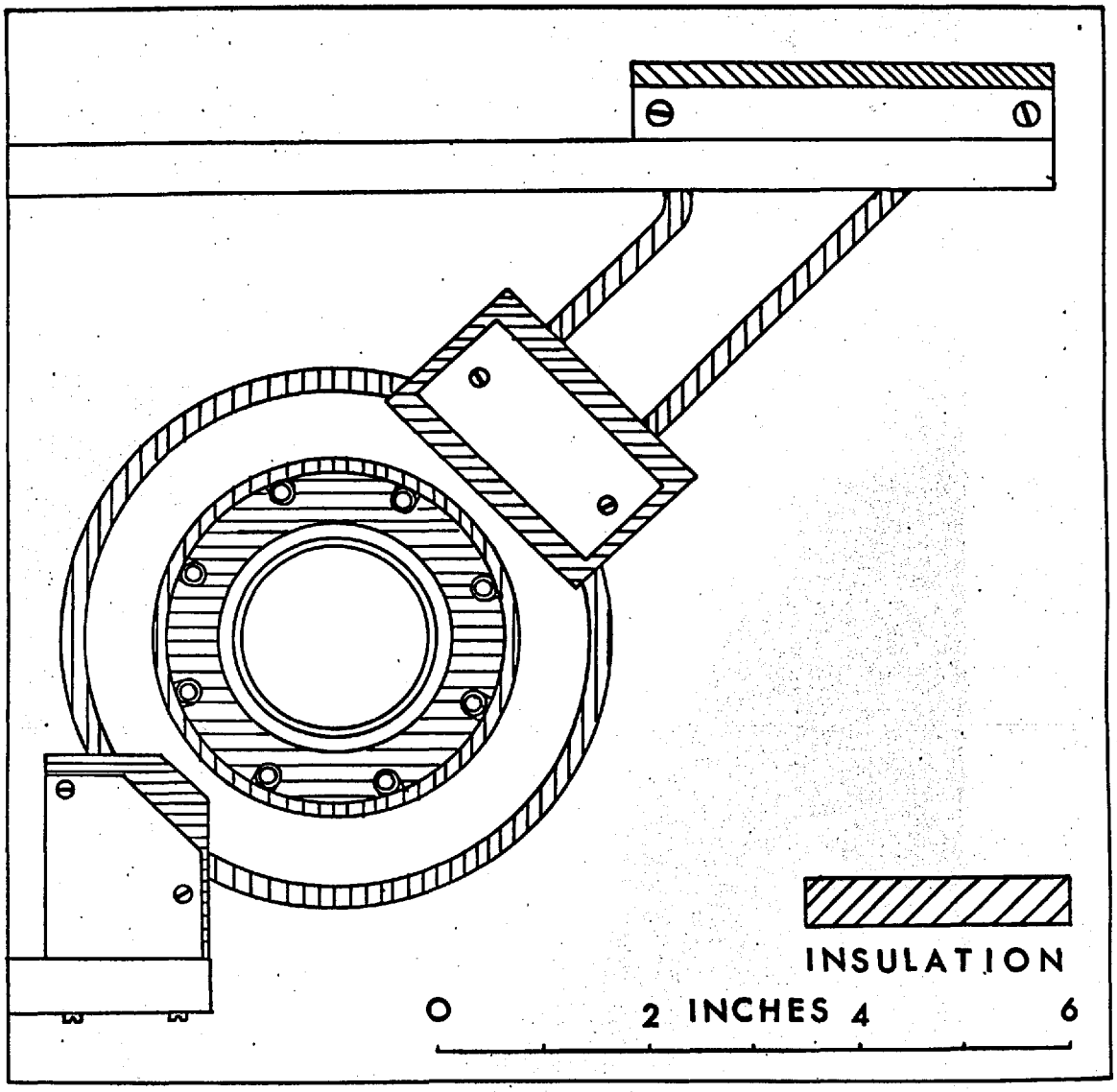

FIG (2.11) Small torus cusp coil assembly.

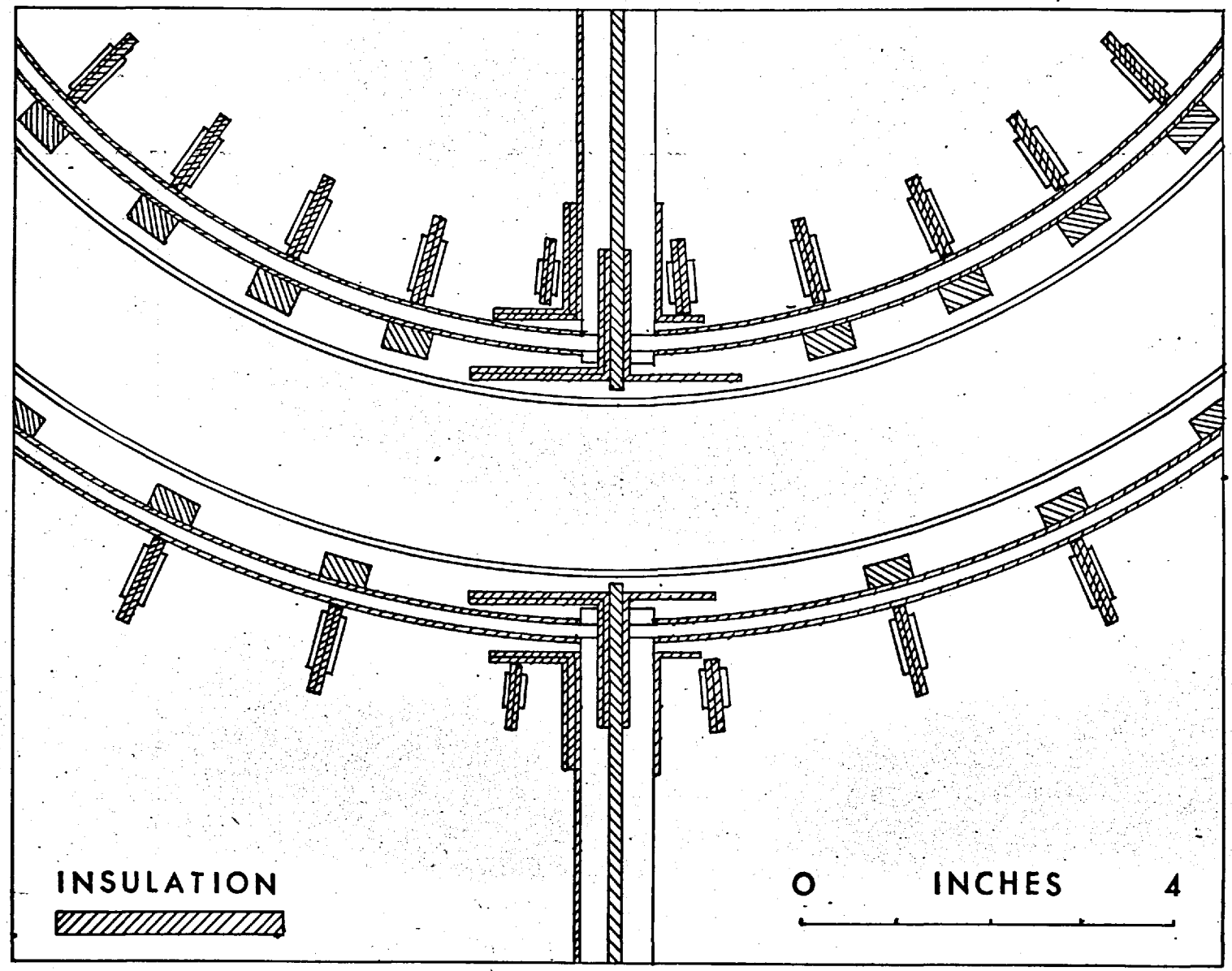

FIG (2.12) Small torus collector plate arrangement.

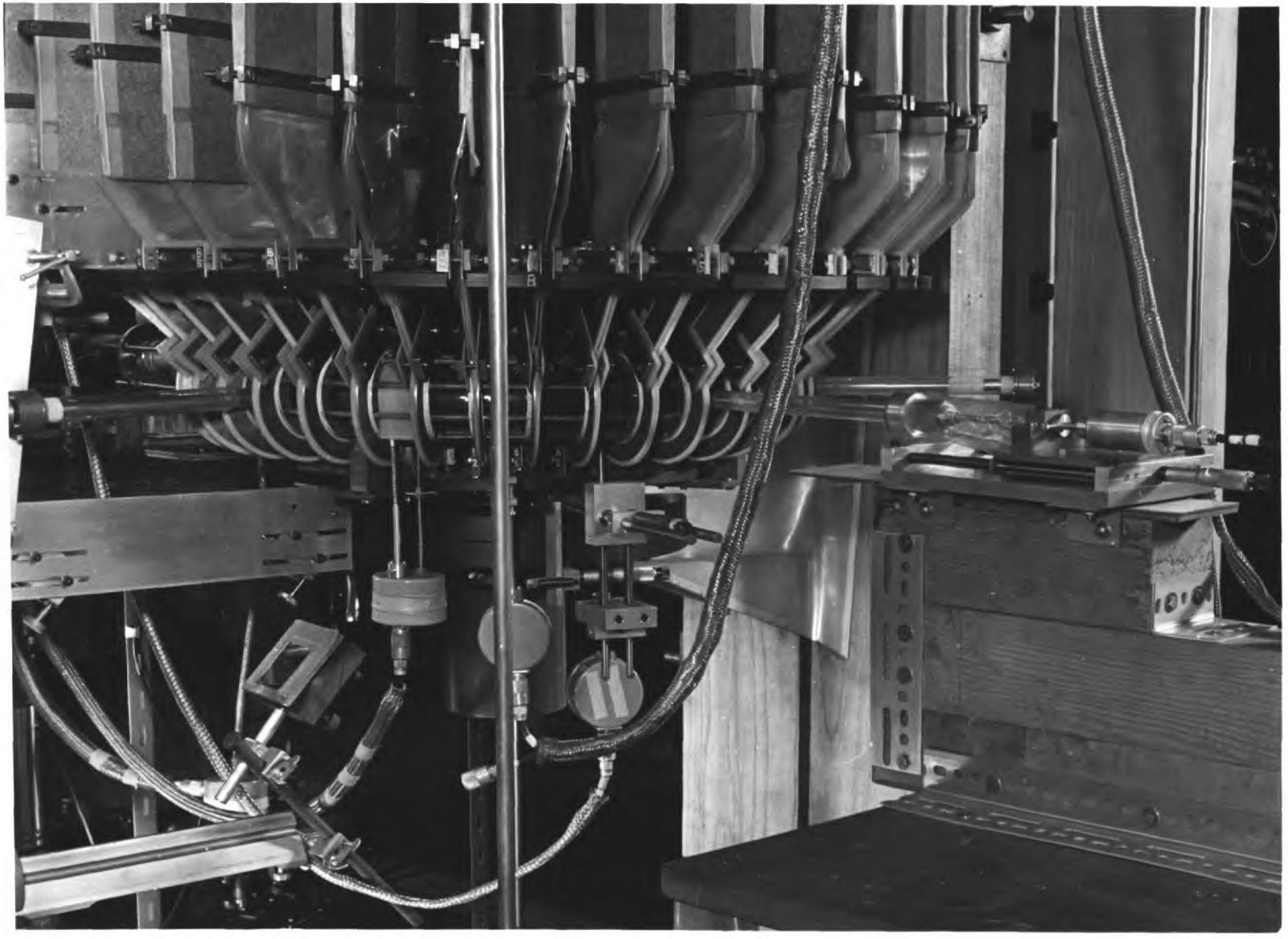

FIG. (2.13)

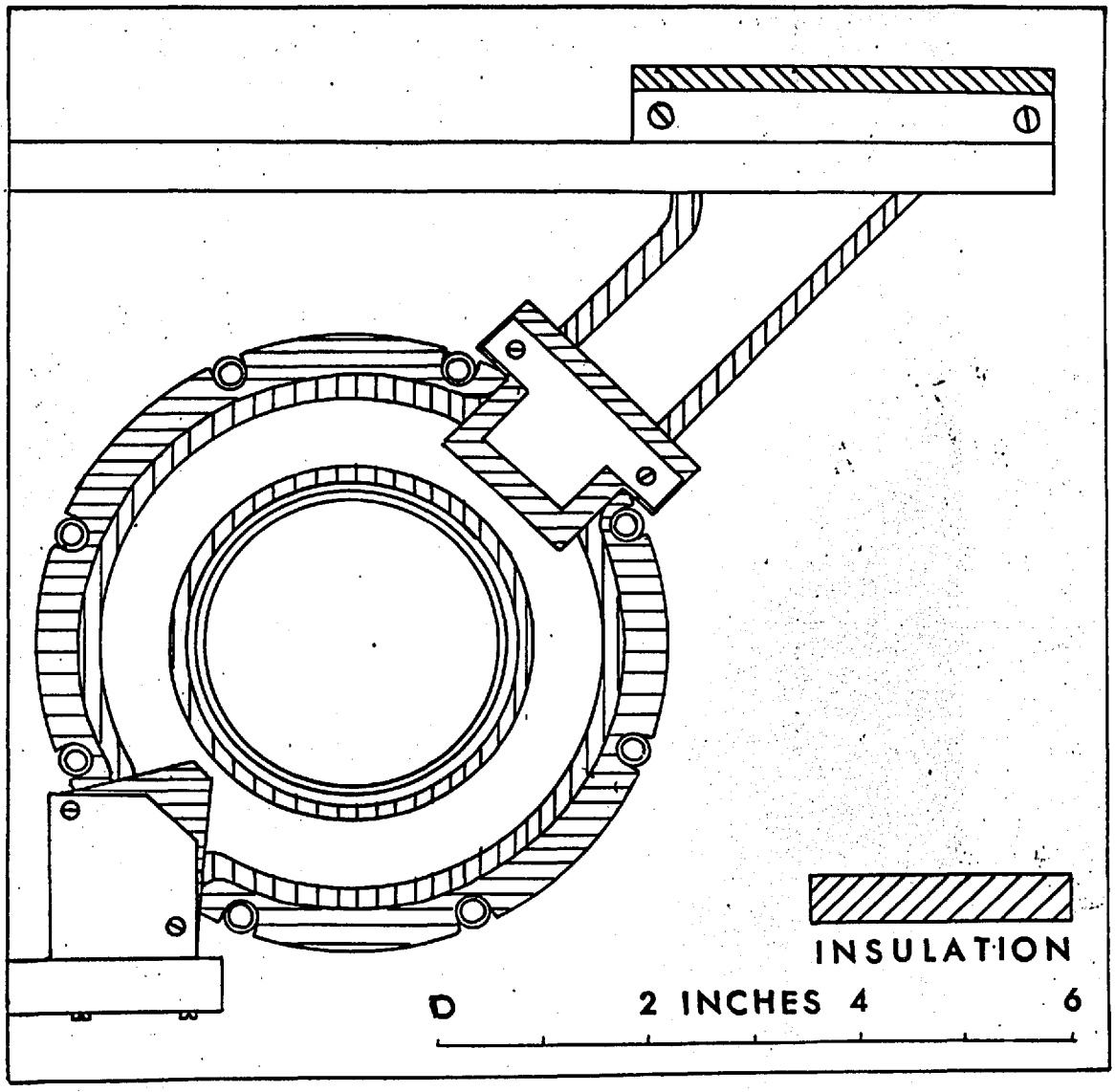

FIG. (2.14) Large torus cusp coil assembly.

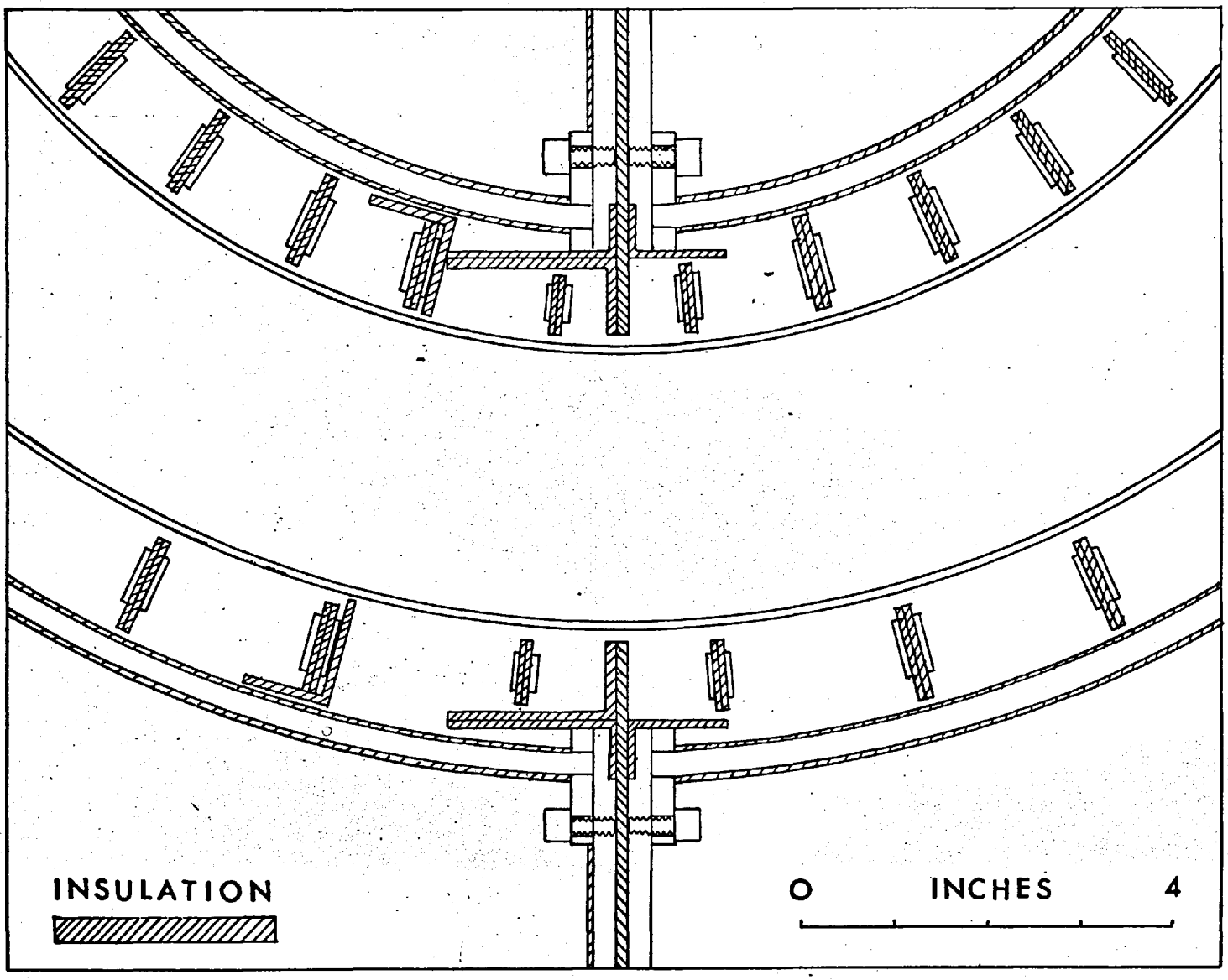

FIG. (2.15) Large torus collector plate arrangement.

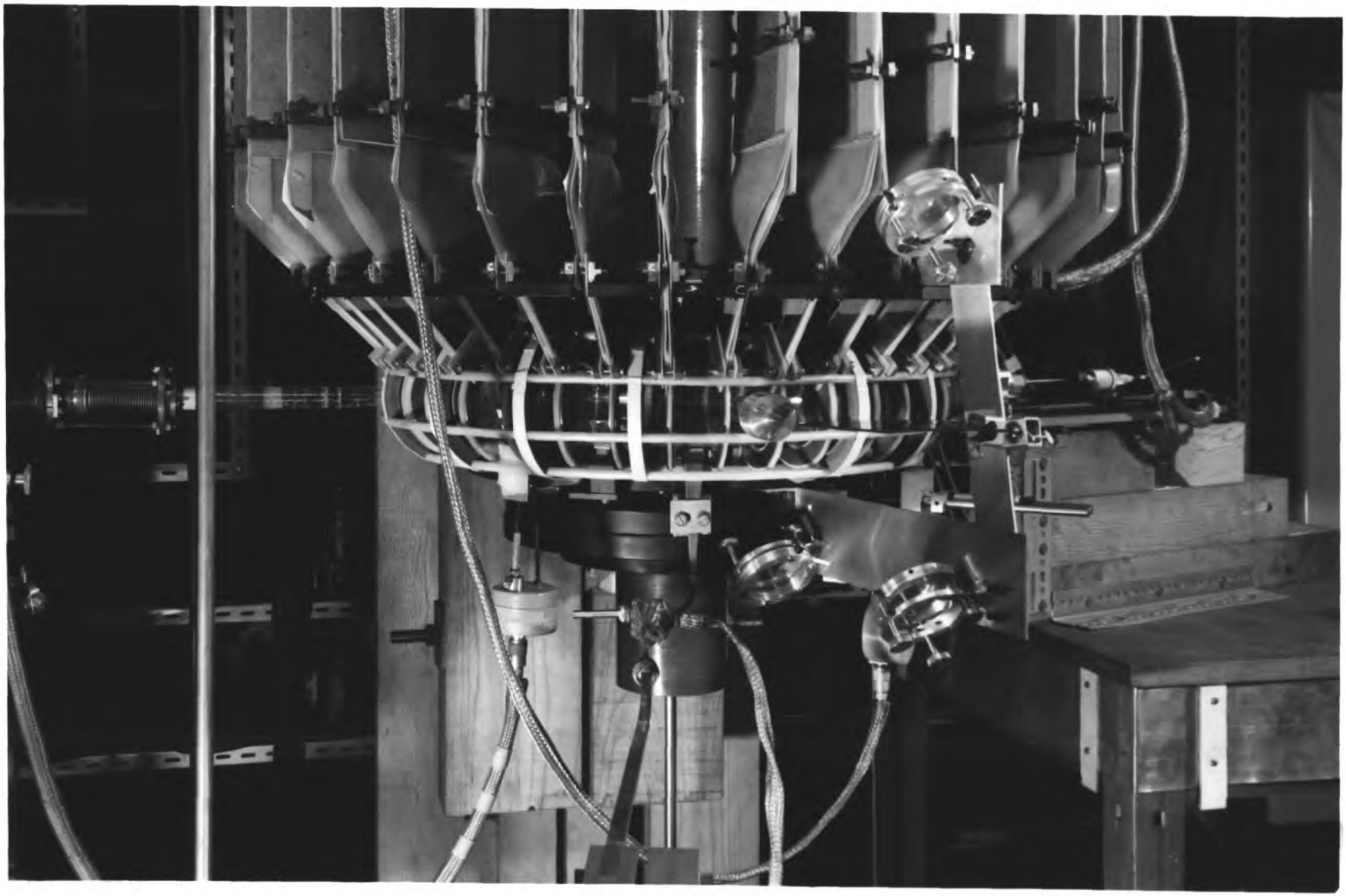

FIG (2.16)

(2.7) THE VACUUM EQUIPMENT

Conventional vacuum equipment was used in the experiment and the pumping system is shown in fig. (2.2)(b). A mercury vapour diffusion pump and liquid nitrogen cold trap was used to evacuate the torus and the vacuum was maintained overnight using an ion pump. The base pressure of the system was usually 5.10^{-7} to 10^{-6} torr and the leakage rate was $\sim$ 5.10^{-6} torr per minute. Two types of pressure gauges were employed: a Mullard ionisation gauge covered the pressure range 10^{-2} to 10^{-10} torr and an LKB Autovac gauge covered the range 10^{-3} to 10 torr. Both gauges were absolutely calibrated over the range 0 - 0.1 torr against a Mcleod gauge.

CHAPTER 3

PROPERTIES OF THE PREIONISED PLASMA

The properties of the plasma produced by the preionisation system described in section (2.5) are examined in detail to find the plasma conditions that exist in the torus when the Polytron main bank is triggered. These plasma conditions depend on the decay of plasma that has occurred following the end of the preioniser discharge current. The majority of Polytron experiments were performed at low gas pressures (<20 m.torr), where plasma diffusion in both the toroidal axial and multi-cusped magnetic fields to the walls of the torus was primarily responsible for the loss of plasma. With increasing gas pressure (>20 m.torr) plasma volume recombination made an increasing contribution to the overall decay of plasma and this subject forms the basis of the work described in section II.

A brief review of plasma diffusion is given at the start of this chapter, followed by a theoretical discussion and an experimental measurement of plasma decay in a toroidal axial magnetic field. Finally an experimental study of plasma in the toroidal multi-cusped magnetic field is presented.

(3.1) PLASMA DIFFUSION

The subject of plasma diffusion has been comprehensively reviewed by Chapman and Cowling (11) and by Golant (12).. Here we present a brief review of plasma diffusion which acts as a basis for subsequent theoretical and experimental discussions.

The equation which describes Γ the flux of particles of density n diffusing under the action of a density gradient is

$$\Gamma = -D \nabla n \qquad (3.1)$$

where D is called the diffusion coefficient.

Assuming no production or destruction of particles, the substitution of equation (3.1) into the usual continuity equation yields

$$\frac{\partial n}{\partial t} = D \nabla^2 n \qquad (3.2)$$

The solution of equation (3.2) for an infinitely long cylindrical chamber has the form

$$n(r,t) = \sum_{k=0}^{\infty} A_k \exp\left(\frac{-t}{\tau_k}\right) J_0\left(\frac{r}{\Lambda_k}\right) \qquad (3.3)$$

where $\Lambda_k = \frac{a}{\chi_k}$ = characteristic diffusion length of the k th mode

a = radius of cylindrical chamber

τ_k = characteristic decay time of the k th mode

$\chi_0 = 2.405$, $\chi_1 = 5.520$, $\chi_2 = 8.563$ ....

For an arbitary initial density distribution, the fundamental diffusion distribution $k = 0$ is established in a time $\sim \tau_0$ and subsequently, the density decay has a characteristic decay time given by

$$\tau_0 = \frac{\Lambda_0^2}{D} \quad \text{where} \quad \Lambda_0 = \frac{a}{2.405} \qquad (3.4)$$

Consider the case of a gas with particles of type α diffusing through a background of particles of type β which have no macroscopic velocity. In the absence of electric fields, the momentum transfer rate between particles is balanced by the pressure gradient, thus

$$n_\alpha m_\alpha \vec{u}_\alpha \nu_{\alpha\beta} = - \frac{d}{dx} (n_\alpha k T_\alpha) \qquad (3.5)$$

where $\nu_{\alpha\beta}$ is the collision frequency

x is the spatial coordinate

$\vec{u}_\alpha$ is the directed velocity of species α

and the other symbols have their usual meaning.

For a uniform temperature distribution, the diffusion flux Γ_α for particles type α is therefore

$$\Gamma_\alpha = n_\alpha \vec{u}_\alpha = - \frac{k T_\alpha}{m_\alpha \nu_{\alpha\beta}} \cdot \nabla n_\alpha \qquad (3.6)$$

Comparison of (3.6) with (3.1) gives the diffusion coefficient D_α for the type α particles as

$$D_\alpha = \frac{k T_\alpha}{m_\alpha \nu_{\alpha\beta}} \qquad (3.7)$$

In an ionised plasma where $T_e \sim T_i$ it can be seen from equation (3.7) that $D_e >> D_i$. Therefore, the simultaneous diffusion of electrons and ions in a plasma, whose Debye length << container dimensions, leads to the establishment of an electric field $\vec{E}$ which acts to retard electron diffusion and accelerate ion diffusion. This is

known as ambipolar diffusion and the expressions for the electron and ion fluxes in this case are

$$\Gamma_e = - D_e \nabla n_e - n_e \mu_e \vec{E} \qquad (3.8)$$

$$\Gamma_i = - D_i \nabla n_i + n_i \mu_i \vec{E} \qquad (3.9)$$

where μ_e = electron mobility $= \dfrac{e}{m_e \nu_e}$ (3.10)

μ_i = ion mobility $= \dfrac{e}{m_i \nu_i}$ (3.11)

Comparison of the expressions (3.10) and (3.11) with the expressions for D_e and D_i obtained from equation (3.7) gives the Einstein relationships

$$\frac{D_e}{\mu_e} = \frac{k T_e}{e} \quad \text{and} \quad \frac{D_i}{\mu_i} = \frac{k T_i}{e} \qquad (3.12)$$

The maintainance of quasi-neutrality throughout the plasma means that

$$n_e \simeq n_i \quad \text{and} \quad \nabla n_e \simeq \nabla n_i \qquad (3.13)$$

and eliminating $\vec{E}$ from the equations (3.8) and (3.9) yields the expression for the ambipolar diffusion constant D_a in the form

$$D_a = \frac{D_e \mu_i + D_i \mu_e}{\mu_i + \mu_e} \qquad (3.14)$$

Substitution of the Einstein relationships (3.12) into

expression (3.14) and making use of the fact that $\mu_e >> \mu_i$ gives

$$D_a \simeq D_i \cdot \left(1 + \frac{T_e}{T_i}\right) \qquad (3.15)$$

From equations (3.7) and (3.12)

$$D_i = \frac{\mu_i k T_i}{e} = \frac{k T_i}{m_i \nu_i}$$

The relevant collision frequency ν_i for ambipolar diffusion in strongly and weakly ionised gases is that due to ion-atom collisions ν_{ia}. At any fixed temperature

$$\nu_{ia} \propto \text{gas pressure } p \qquad (3.16)$$

and hence the product $(D_a.p)$ is a function of T_e and T_i only in most plasmas.

(3.2) PLASMA DIFFUSION IN A MAGNETIC FIELD

Golant (12) has performed calculations of plasma diffusion in magnetic fields based on the kinetic theory transport equations and the Boltzmann equation. He has shown that the averaged equation of motion for particles of speciés α in the plasma under equilibrium conditions can be written in the form

$$Z_\alpha e\left[\vec{E} + \frac{\vec{u}_\alpha \wedge \vec{H}}{c}\right] + kT_\alpha \frac{\nabla n_\alpha}{n_\alpha} - m_\alpha \sum \nu_{\alpha\beta}(\vec{u}_\alpha - \vec{u}_\beta) = 0 \qquad (3.17)$$

Where the temperature T_α is assumed to be constant throughout the plasma.

Solutions to equation (3.17) for plasmas consisting of ions of charge + Ze, electrons and atoms for various degrees of plasma ionisation have been found by Golant (12). These solutions are summarised in table (3.1) where the new symbols that are introduced have the meanings

$D_{\parallel}$ = diffusion coefficient parallel to the magnetic field
$D_{\perp}$ = diffusion coefficient perpendicular to the magnetic field
ω_e = electron cyclotron frequency
ω_i = ion cyclotron frequency.

(3.3) PLASMA DECAY IN A TOROIDAL MAGNETIC FIELD

The decay of plasma in a toroidal magnetic field was first studied experimentally by Bostock and Levine (13) who found that the diffusion coefficient in a helium plasma showed a pronounced minimum with increasing magnetic field around 600 gauss. This result was interpreted in terms of the anomolous diffusion described by Bohm (14).

Later, Golant, Danilov and Zhilinskii (15) showed that this minimum in the diffusion coefficient could be explained in terms of the drift of particles in the toroidal magnetic field due to the curvature of the field lines. These authors wrote the averaged equation of motion (3.17) in terms of toroidal coordinates and solved it for the case of toroidal drift superimposed on the normal diffusion that occurs in an infinite cylinder having the torus cross-section. After much

TABLE (3.1)

TYPE OF DIFFUSION	$D_{\parallel}$	$D_{\perp}$
Diffusion of electrons in a neutral gas	$\frac{k T_e}{m_e \nu_{ea}}$	$\frac{k T_e}{m_e \nu_{ea} \left(1 + \frac{\omega_e^2}{\nu_{ea}^2}\right)}$
Diffusion of ions in a neutral gas	$\frac{k T_i}{m_i \nu_{ia}}$	$\frac{k T_i}{m_i \nu_{ia} \left(1 + \frac{\omega_i^2}{\nu_{ia}^2}\right)}$
Ambipolar diffusion in a weakly ionised gas ($\nu_{ea} \gg \nu_{ei}$)	$\frac{k(T_i + Z T_e)}{m_i \nu_{ia}}$	$\frac{k (T_i + Z T_e)}{m_i \nu_{ia} \left(1 + \frac{\omega_e \omega_i}{\nu_{ea} \nu_{ia}}\right)}$
Diffusion in a fully ionised gas	--	$\frac{k (T_i + Z T_e) \nu_{ei}}{Z m_e \omega_e^2}$
Ambipolar diffusion in a highly ionised gas ($\nu_{ei} \simeq \nu_{ea}$)	$\frac{k(T_i + Z T_e)}{m_i \nu_{ia}}$	$\frac{k (T_i + Z T_e)}{m_i \nu_{ia} \left(1 + \frac{\omega_e \omega_i}{\nu_{ia}(\nu_{ei}+\nu_{ea})}\right)}$

manipulation of the equation, it was shown that the decay of plasma could be written in the form

$$\frac{\partial n}{\partial t} = D_{\perp} \nabla^2 n - |\vec{u}_d| \frac{\partial n}{\partial R} \qquad (3.18)$$

where R = radius vector from the centre of the torus plane (= radius of curvature of the field lines)

$|\vec{u}_d|$ = drift velocity of the plasma in the toroidal magnetic field

and the toroidal drift velocity was shown to have the form

$$|\vec{u}_d| = \frac{2 D_{\parallel}}{R} \qquad (3.19)$$

The diffusion coefficients $D_{\perp}$ and $D_{\parallel}$ are given, according to the plasma conditions, by table (3.1).

We will now derive the plasma drift velocity in the toroidal magnetic field by a much simpler method than that given by Golant et al. (15).

Spitzer (10) gives the drift velocity $\vec{v}_d$ of a single particle in a direction perpendicular to a curved magnetic field as

$$|\vec{v}_d| = \frac{1}{\omega_c R} \left[\frac{|\vec{v}_{\perp}|^2}{2} + |\vec{v}_{\parallel}|^2 \right] \qquad (3.20)$$

where ω_c = cyclotron frequency

R = radius of curvature of field lines

$\vec{v}_{\perp}$ = particle velocity $\perp$ field lines

$\vec{v}_{\parallel}$ = particle velocity $\parallel$ field lines

For a group of particles, of mass m, with a Maxwellian velocity distribution we can write

$$m\,|\vec{v}_{\perp}|^2 = 2kT \tag{3.21}$$

$$m\,|\vec{v}_{\parallel}|^2 = kT \tag{3.22}$$

and (3.20) can be re-written as

$$|\vec{v}_d|^2 = \frac{2kT}{m\,\omega_c\,R} \tag{3.23}$$

To find the plasma toroidal drift velocity, we first have to solve the equations for the macroscopic drift velocities $\vec{u}_{ed}$ and $\vec{u}_{id}$ for the electrons and ions respectively. In a strong magnetic field such that

$$\omega_i/\nu_i \gg 1 \quad , \quad \omega_e/\nu_e \gg 1 \tag{3.24}$$

the drift velocity equations are

$$\vec{u}_{ed} = \vec{v}_{ed} - \mu_e \vec{E} + \frac{\vec{E}\wedge\vec{B}}{|\vec{B}|^2} \tag{3.25}$$

$$\vec{u}_{id} = \vec{v}_{id} + \mu_i \vec{E} + \frac{\vec{E}\wedge\vec{B}}{|\vec{B}|^2} \tag{3.26}$$

where $\vec{v}_{ed}$ and $\vec{v}_{id}$ are the electron and ion particle drift velocities given by equation (3.23) and $\vec{E}$ is the electric field that is established to maintain charge neutrality. In equilibrium, the ambipolar fluxes of electrons and ions must be equal and a single plasma drift velocity $\vec{u}_d$ is established in the plasma where

$$\vec{u}_d = \vec{u}_{ed} = \vec{u}_{id} \qquad (3.27)$$

The particle drift velocities $\vec{v}_{ed}$ and $\vec{v}_{id}$ are in directions perpendicular to both $\vec{B}$ and $\vec{\nabla B}$, and, since the ions and electrons are oppositely charged, $\vec{v}_{ed}$ and $\vec{v}_{id}$ are in opposite directions. Hence the quasi-equilibrium electric field that is established in the plasma is in a direction perpendicular to $\vec{B}$ and to $\vec{\nabla B}$ and has a value given by equations (3.25) and (3.26) as

$$|\vec{E}| = \frac{|\vec{v}_{ed}| + |\vec{v}_{id}|}{\mu_e + \mu_i} \qquad (3.28)$$

We now resolve the plasma drift velocity $\vec{u}_d$ into two components $\vec{u}_{d1}$ and $\vec{u}_{d2}$ where

$\vec{u}_{d1}$ = drift velocity component $\perp$ to both $\vec{B}$ and $\vec{\nabla B}$

$\vec{u}_{d2}$ = drift velocity component $\perp$ to $\vec{B}$ and $\parallel$ to $\vec{\nabla B}$

From the discussion of the directions of the components of equations (3.25) and (3.26) given above, the magnitudes of $\vec{u}_{d1}$ and $\vec{u}_{d2}$ are

$$|\vec{u}_{d1}| = |\vec{v}_{ed}| - |\vec{v}_{id}| - \mu_e|\vec{E}| + \mu_i|\vec{E}|$$

$$= \frac{2\,\mu_i\,|\vec{v}_{ed}| - \mu_e\,|\vec{v}_{id}|}{\mu_i + \mu_e} \qquad (3.29)$$

$$|\vec{u}_{d2}| = \frac{|\vec{E}\wedge\vec{B}|}{|\vec{B}|^2} = \frac{|\vec{v}_{ed}| + |\vec{v}_{id}|}{(\mu_i + \mu_e)|\vec{B}|} \qquad (3.30)$$

In strong magnetic fields $|\vec{u}_{d1}| \ll |\vec{u}_{d2}|$ and the plasma drift is mainly in the direction of $-\nabla B$ (ie radially outwards in the plane of the torus) and the expressions for the electron and ion mobilities are

$$\mu_e = \frac{e}{m_e\nu_e\left[1 + \left(\frac{\omega_e}{\nu_e}\right)^2\right]} \approx \frac{e\,\nu_e}{m_e\,\omega_e^2} \qquad (3.31)$$

$$\mu_i = \frac{e}{m_i\,\nu_i\left[1 + \left(\frac{\omega_i}{\nu_i}\right)^2\right]} \approx \frac{e\,\nu_i}{m_i\,\omega_i^2} \qquad (3.32)$$

Substituting the expressions (3.31) and (3.32) into equation (3.30) and using the facts that

$$m_e\omega_e = m_i\,\omega_i$$

$$\nu_e/\omega_e \ll \nu_i/\omega_i$$

The equation for plasma drift velocity in the direction of $-\overrightarrow{\nabla B}$ becomes

$$[\overrightarrow{U_d}] = \frac{\omega_i}{\nu_i}\left[|\overrightarrow{v_{ed}}| + |\overrightarrow{v_{id}}|\right] \qquad (3.33)$$

and substituting for the particle drift velocities from equation (3.23) in (3.33) we obtain

$$|\overrightarrow{U_d}| = \frac{\omega_i}{\nu_i}\left[\frac{2k\,T_e}{m_e\omega_e R} + \frac{2k\,T_i}{m_i\omega_i R}\right] \qquad (3.34)$$

$$= \frac{2\,k\,(T_e + T_i)}{m_i\,\nu_i\,R}$$

$$= \frac{2\,D_{\parallel}}{R} \qquad (3.35)$$

where $D_{\parallel}$ is obtained from table (3.1).

The expression (3.35) is identical to the expression found for the toroidal plasma drift velocity by Golant et al as given by (3.19).

The toroidal drift velocity in weak magnetic fields such that

$$\omega_i/\nu_i \ll 1 \qquad \omega_e/\nu_e \gg 1 \qquad (3.36)$$

is given by solving the electron drift velocity equation (3.26) with a modified ion drift velocity equation of the form

$$\overrightarrow{U_{id}} = + \mu_i \overrightarrow{E} \qquad (3.37)$$

Solving (3.26) and (3.37), using the approximations given above, yields two different expressions (a) and (b) given below for the toroidal drift velocity:

(a) when $\mu_i \gg \mu_e$, the toroidal drift velocity simply equals the electron particle drift velocity given by equation (3.23)

(b) when $\mu_i \ll \mu_e$, the toroidal drift velocity is given by the expression

$$|\vec{u}_d| = \frac{\omega_e}{\nu_e} \cdot \frac{2 D_\parallel}{R} \qquad (3.38)$$

(3.4) SOLUTION OF THE TOROIDAL DECAY EQUATION

Using expressions (3.19) or (3.35) the equation (3.18) describing the decay of plasma in a toroidal magnetic field becomes

$$\frac{\partial n}{\partial t} = D_\perp \nabla^2 n - 2 D_\parallel \frac{\partial n}{\partial R} \qquad (3.39)$$

Golant et al. (15) have solved this equation with the boundary condition that the plasma density at the walls of the torus is zero. The general solution can be written in the form

$$n(R,t) = \sum_k D_k \exp\left[\frac{-t}{\tau_k}\right] S_k(R,z) \exp\left[\frac{D_\parallel r}{D_\perp R}\right] \qquad (3.40)$$

The form of equation (3.40) can be seen to be analagous to the form of the solution for plasma decay in an infinite straight cylinder given by equation (3.3.). The fundamental characteristic decay time of plasma τ_s corresponding to the solution of (3.40) for k = 0 is given by the sum of two terms. The first term corresponds to fundamental diffusion in an infinite cylinder and the second term corresponds to toroidal drift, thus,

$$\frac{1}{\tau_s} = \frac{D_\perp}{\Lambda_o^2} + \frac{|\vec{u}_d|^2}{4 D_\perp} \qquad (3.41)$$

which can be re-written as

$$\tau_s = \frac{\Lambda_o^2}{D_\perp} \cdot \frac{1}{\left[1 + \left[\frac{\Lambda_o}{R}\right]^2 \left[\frac{D_\parallel}{D_\perp}\right]^2\right]} \qquad (3.42)$$

Now, the fundamental density decay time τ_o due to plasma diffusion in the absence of a magnetic field is simply

$$\tau_o = \frac{\Lambda_o^2}{D_\parallel} \qquad (3.43)$$

and hence the change in plasma decay time due to diffusion when a toroidal magnetic field is applied is given by

$$\frac{\tau_s}{\tau_o} = \frac{D_\parallel / D_\perp}{1 + \left[\frac{\Lambda_o}{R}\right]^2 \left[\frac{D_\parallel}{D_\perp}\right]^2} \qquad (3.44)$$

The denominator in (3.44) represents the fractional reduction in the ratio τ_s/τ_0 due to the curvature of the field lines. For both torus dimensions (R = 25.4 cm, Λ_0 = 0.92 for the small torus and R = 25.4 , Λ_0 = 1.48 for the large torus) the quantity τ_s/τ_0 has been plotted as a function of $D_{\parallel}/D_{\perp}$ as shown in fig. (3.1). For the sake of comparison, the case of an infinite straight cylinder has been included on the plot. The theoretical plots in fig. (3.1) clearly show that the decay time in the toroidal magnetic field goes through a maximum value with increasing field (increasing ratio $D_{\parallel}/D_{\perp}$). The actual values of the maximum ratio of τ_s/τ_0 and the corresponding ratios of diffusion coefficients are given in table (3.2).

TABLE (3.2).

TORUS	$\left[\frac{\tau_s}{\tau_0}\right]_{max.}$	$\left[\frac{D_{\parallel}}{D_{\perp}}\right]$
LARGE	8.6	17
SMALL	13.9	27

(3.5) EXPERIMENTAL TOROIDAL PLASMA DECAY

An experimental investigation of plasma decay in a toroidal magnetic field was performed using the 1μF preionisation system with the small torus. The magnetic field was provided by the crowbarred bank system described in section (2.4). The

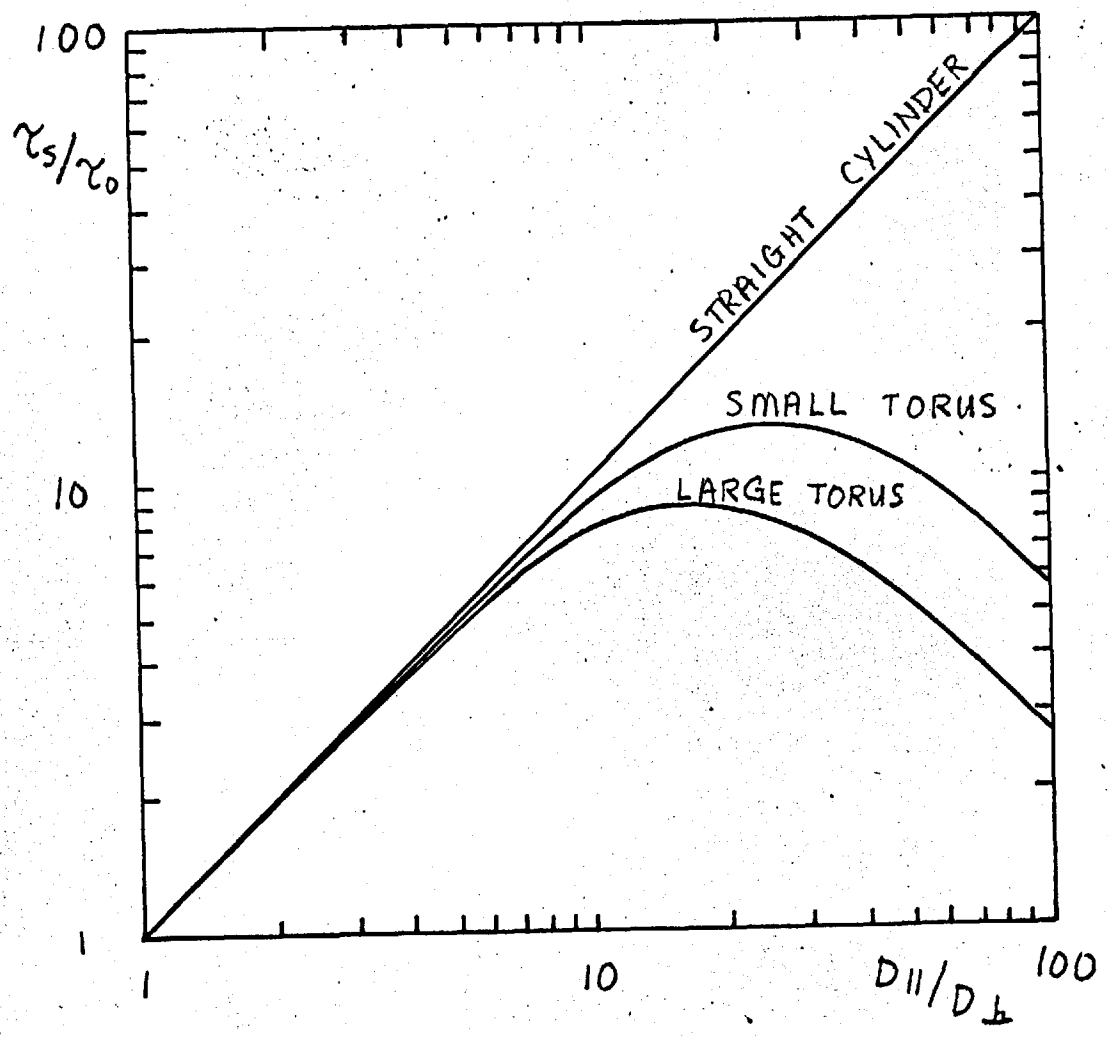

FIG (3.1) Plot of γ_s/γ_o versus $D_{\parallel}/D_{\perp}$ for the large and small tori and a straight cylinder.

electron density of the plasma was measured using the 70 GH_z microwave technique described later in chapter 8. An estimate of the electron density profile in the decaying plasma was made using a double electric probe.

The decay of electron density $\bar{n}$, averaged across the cross-section of the torus, which was obtained from the microwave results has been plotted in figs. (3.2) to (3.4) for low pressure hydrogen, helium and argon plasmas. The figures on each plot represent the magnetic field capacitor bank charging voltages which, for convenience, were used to describe the different magnitudes of magnetic fields in the torus. Since the crowbarred capacitor bank had a decay time $\sim$1 m.sec., the value of the magnetic field changed slightly over the period of the density measurements. Values of the magnetic field measured at the toroidal axis (R = 25.4 cm) as a function of time, for the various charging voltages shown on the plots (3.2) to (3.4), are given in table (3.3).

TABLE (3.3)

AXIAL MAGNETIC FIELD VALUES (gauss)

BANK VOLTAGE (k.v.)	TIME (μ. sec.)			
	50	100	150	200
0.75	98	84	74	63
1.0	131	111	99	85
1.5	196	174	156	137
2.0	265	220	195	183
2.5	329	297	267	239
3.0	401	352	319	287

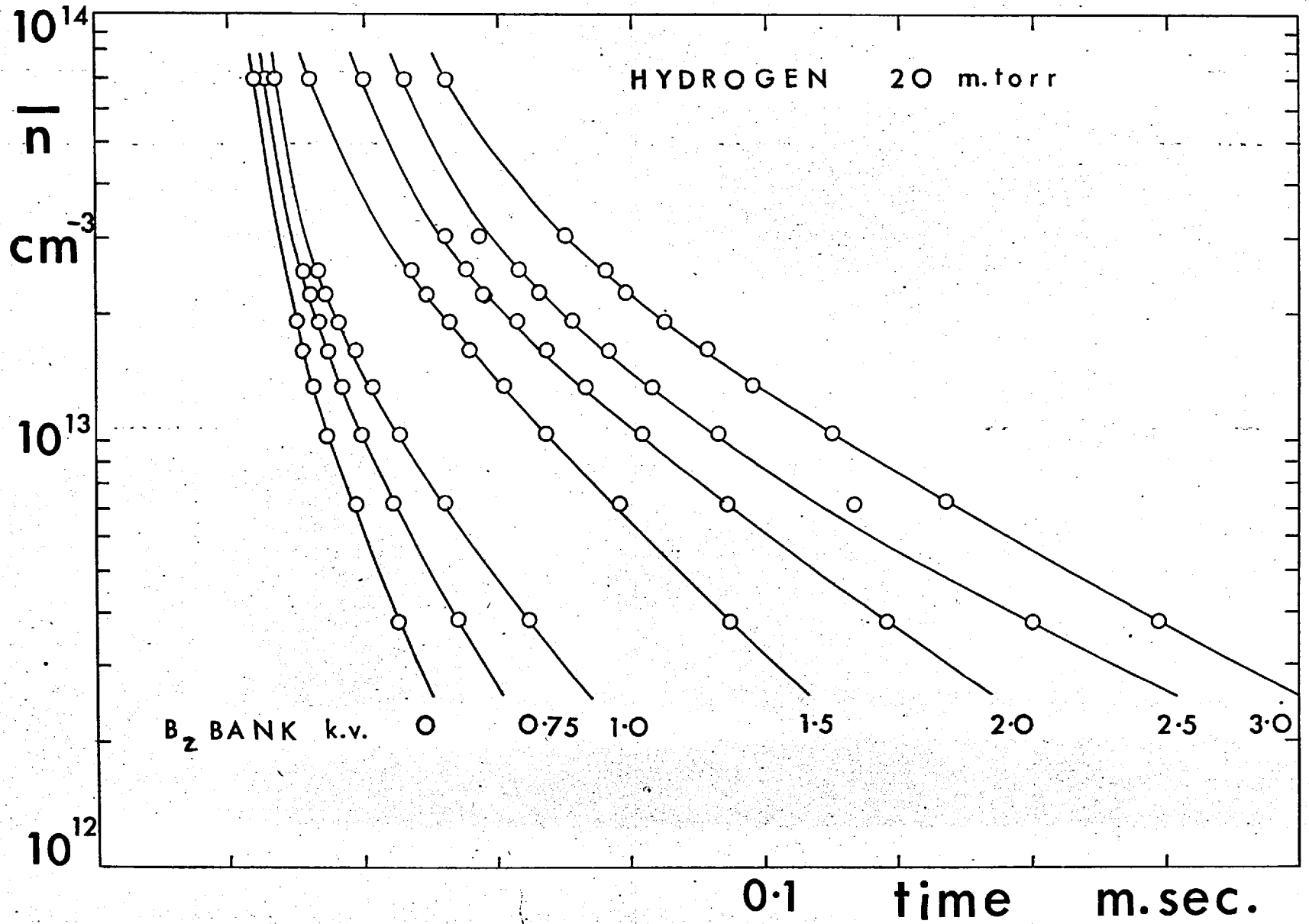

FIG (3.2) Electron density decay plots in 20 m.torr hydrogen plasmas.

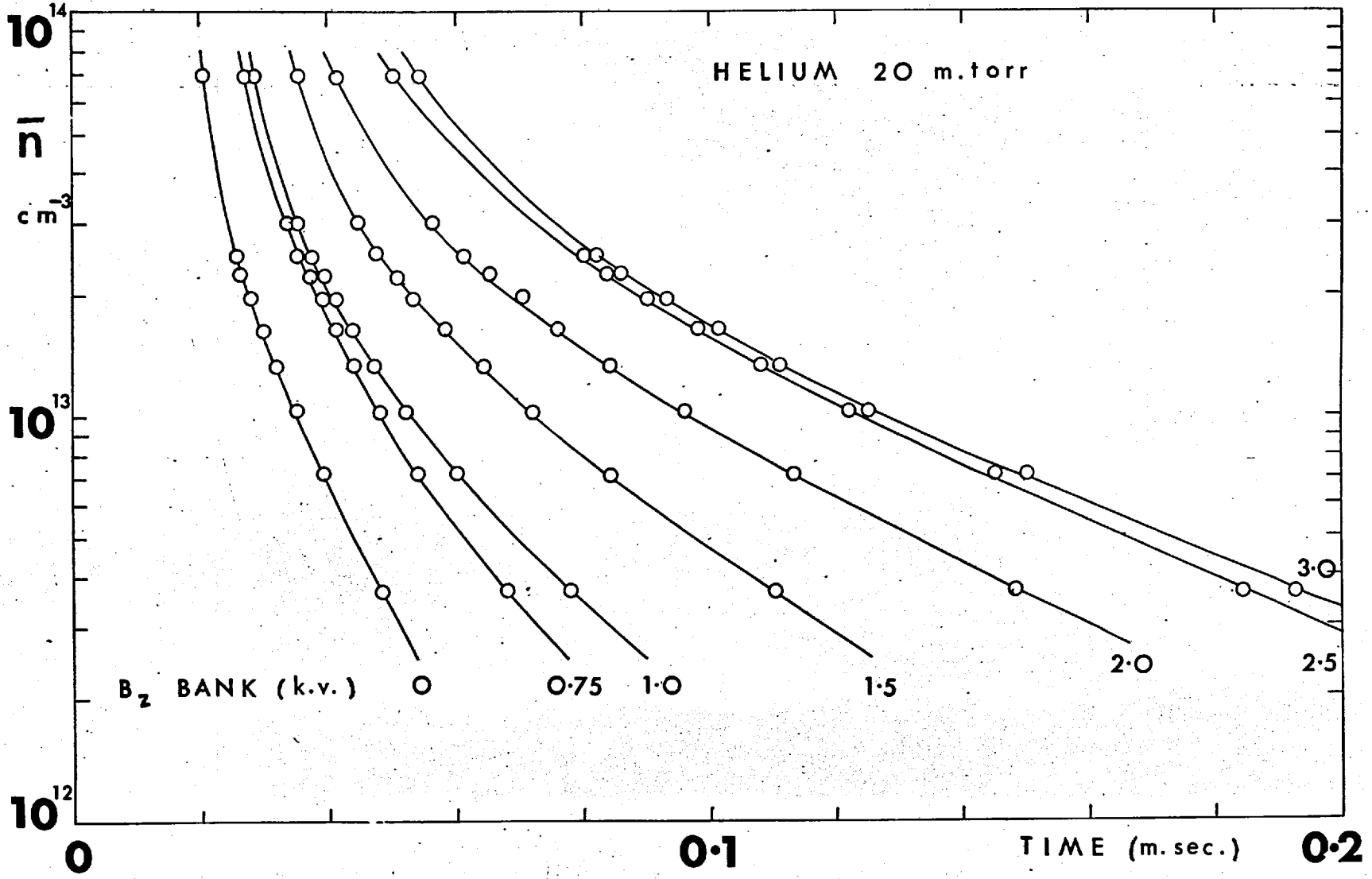

FIG (3.3) Electron density decay plots in 20 m.torr helium plasmas.

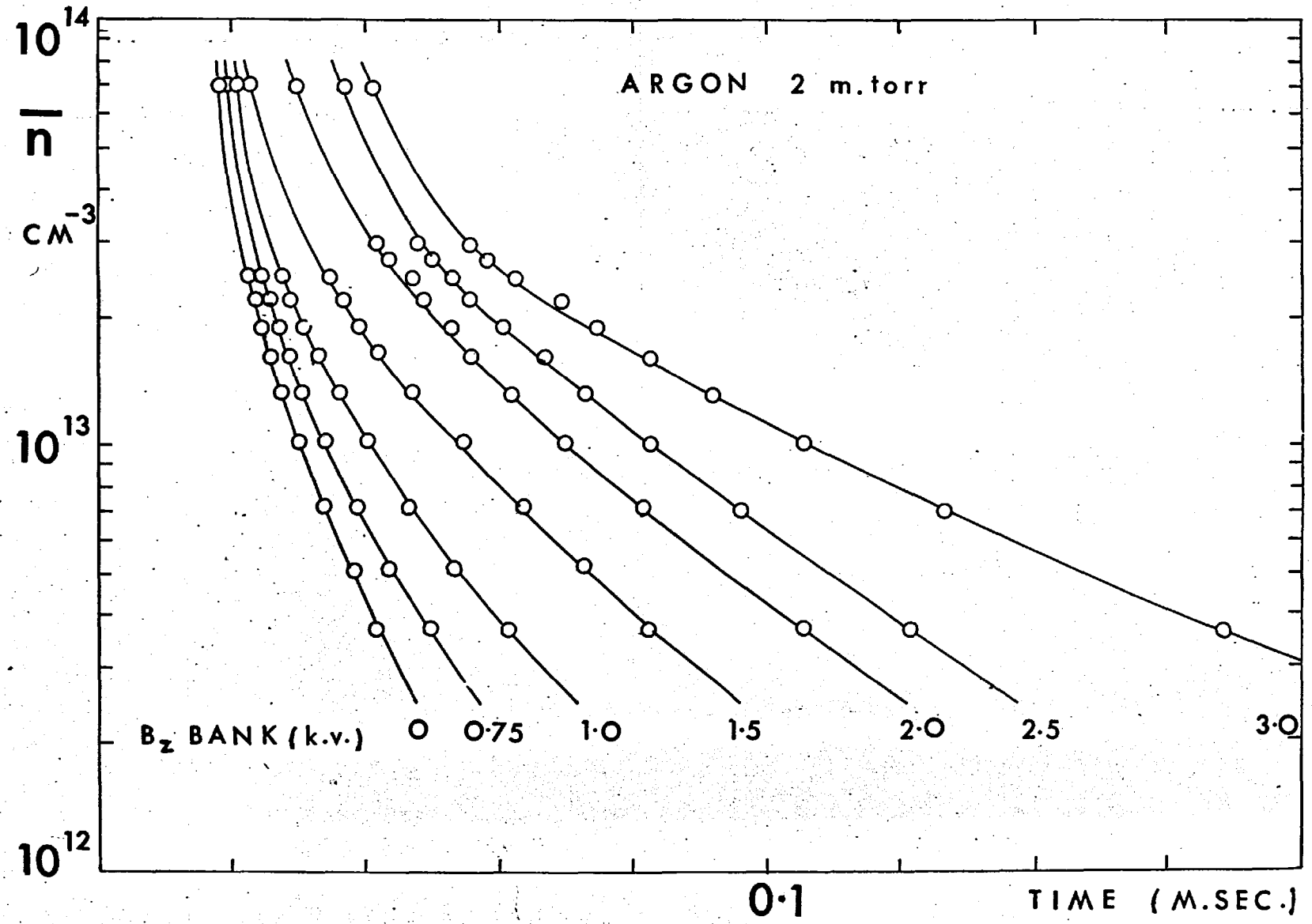

FIG (3.4) Electron density decay plots in 2 m.torr argon plasmas.

Of the different types of diffusion listed in table (3.1), ambipolar diffusion in a highly ionised plasma is the closest to our actual experimental conditions. Therefore we can write

$$\frac{D_{\parallel}}{D_{\perp}} = 1 + \frac{\omega_e \omega_i}{\nu_{ia}(\nu_{ea} + \nu_{ei})} = 1 + \frac{e^2 B^2}{m_e m_i c^2 \nu_{io}(\nu_{ea} + \nu_{ei})} \qquad (3.45)$$

The plasma decay times for the condition $\bar{n} = 10^{13}$ cm^{-3} were obtained from the gradients of the plots shown in figs. (3.2) to (3.4) and the average value of magnetic field at the time when $\bar{n} = 10^{13}$ cm^{-3} was obtained from table (3.3). In fig. (3.5) (a), (b) and (c) the experimental ratio of τ_s/τ_o has been plotted as a function of B^2 for each gas. At low magnetic fields, each plot shown in fig. (3.5) can be seen to approximate to decay in an infinitely long cylinder which has the form of equation (3.45). From the initial gradient of each plot and equation (3.44), the theoretical curves for τ_s/τ_o for plasma decay in a toroidal field have been worked out and these have been superimposed on each plot.

At the maximum applied magnetic fields, the distinction between infinite cylinder and toroidal diffusion is theoretically small and hence, verification of the toroidal expression (3.44) is difficult. Had it been possible to double the applied magnetic field, (with a four fold rise in B^2), the distinction between the two cases would have been very marked. However, the experimental plots of τ_s/τ_o do depart from a linear relationship with B^2. though this occurs at lower values of magnetic field than are predicted theoretically. This earlier

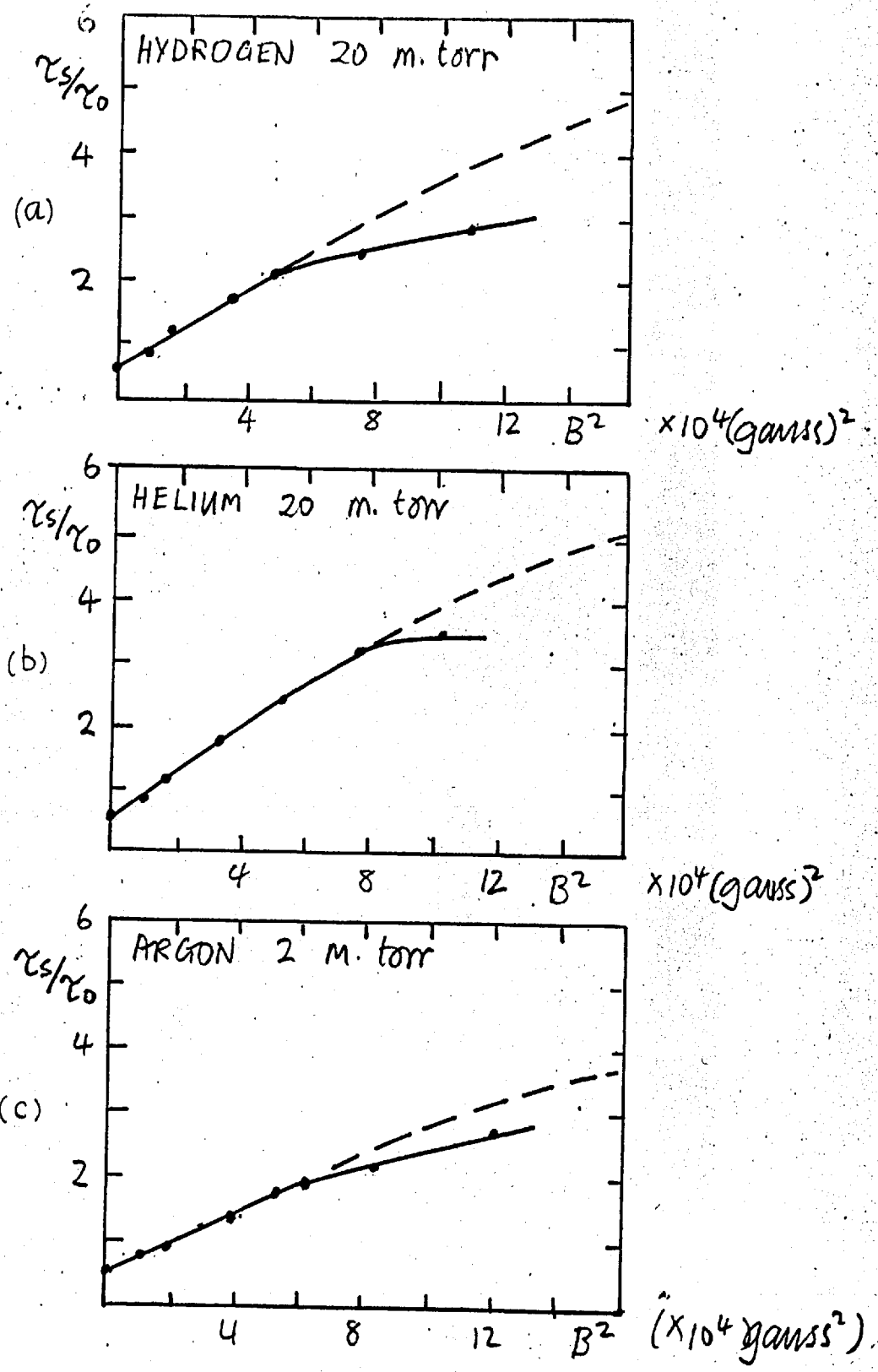

FIG (3.5) Plots of τ_s/τ_0 versus B^2 for (a) hydrogen, (b) helium and (c) argon plasma decays.

departure is possibly due to an upper limit on the plasma decay time being influenced by plasma volume recombination.

For the Polytron operation the main bank was usually triggered 40 μsec. after the preioniser. Hence, for the case of argon at 2.0 m.torr pressure, the degree of plasma ionisation at the start of the Polytron varied with the magnitude of the toroidal magnetic field according to table (3.4), where the effects of the cusp field (usually triggered 8 - 10 μ.sec before the main bank) have been ignored.

TABLE (3.4)

MAGNETIC FIELD BANK VOLTAGE	DEGREE OF IONISATION
0	0.08
1 k.v.	0.14
2 k.v.	0.45
3 k.v.	0.90

For the case of the helium discharge at 20 m. torr pressure and the toroidal field capacitor bank at 2.0 k.v., a double electric probe scan across the discharge yielded the profile shown in fig. (3.6). The probe bias voltage was kept constant and, from probe theory (16), the probe current is proportional to n and to the square root of T_e. Hence the profile shown in fig. (3.6) fairly accurately represents the electron density profile. It can be seen that the peak of the probe profile does appear to be shifted towards the outer wall of the torus

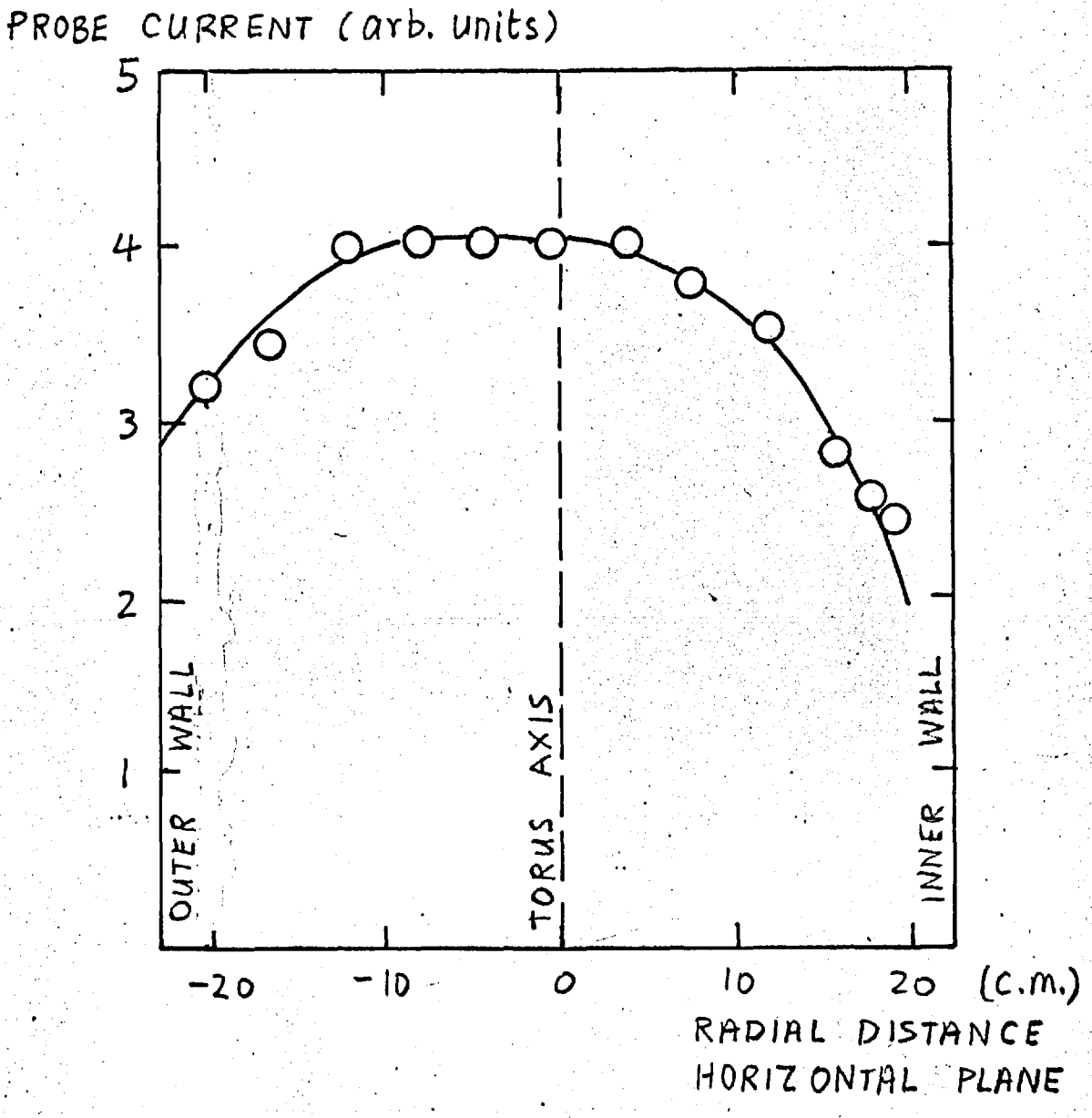

FIG (3.6) Double electric probe profile measured in a 20 m.torr helium plasma decay.

but this feature could possibly be due to plasma diffusing into the torus side port containing the probe as well as by any toroidal drift phenomena.

(3.6) PLASMA DECAY IN THE TOROIDAL MULTI-CUSPED FIELD

An experimental investigation was performed of the effect of the toroidal multi-cusped magnetic field upon the decay of preionised plasma. The cusp field had a half period of oscillation of 38 μ.sec. and it was usually triggered 30 μ.sec. after the preioniser and 10 μ.sec. before the main bank. The profiles of the B_r and B_z components of the cusp field given in figs. (2.6) to (2.9), show the large values of magnetic field associated with the peaks of the oscillatory cusp bank discharge. The experiments were aimed at determining whether the plasma diffusion loss was reduced by these large magnetic fields, or whether the loss cone regions of the cusp field produced an enhanced plasma loss compared to the diffusion loss in the weak toroidal axial magnetic field.

(3.6.1) Microwave Transmission Experiments

The spatial inhomogeneity of the cusp field made interpretation of the double electric probe data impossible and the plasma was studied only with a 70 GH_z microwave beam. In the first set of experiments, the microwave beam was transmitted directly across the plasma diameter at the mid-plane between a pair of cusp coils. The microwave system is described in detail in Chapter 8. A typical set of transmission profiles for various cusp bank charging voltages and constant plasma preionisation conditions is shown in fig. (3.7). The following comments are

Cusp bank voltage (k.v.)

0

1.5

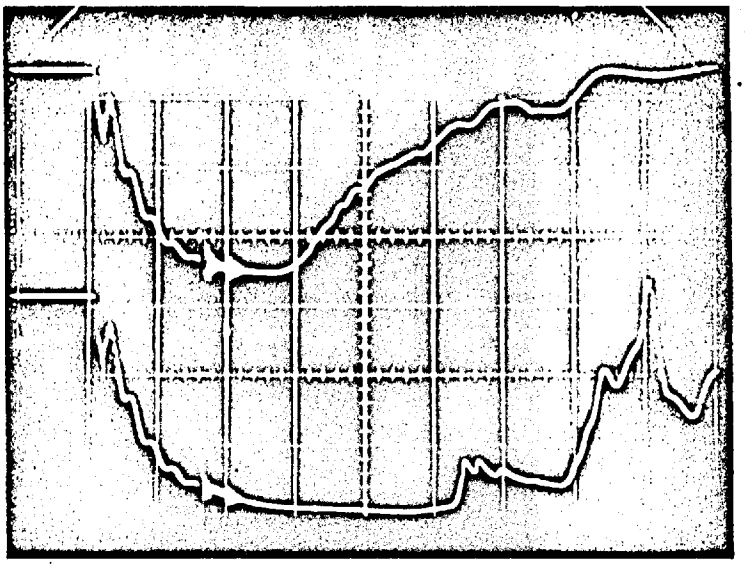

1.0

2.0

3.0

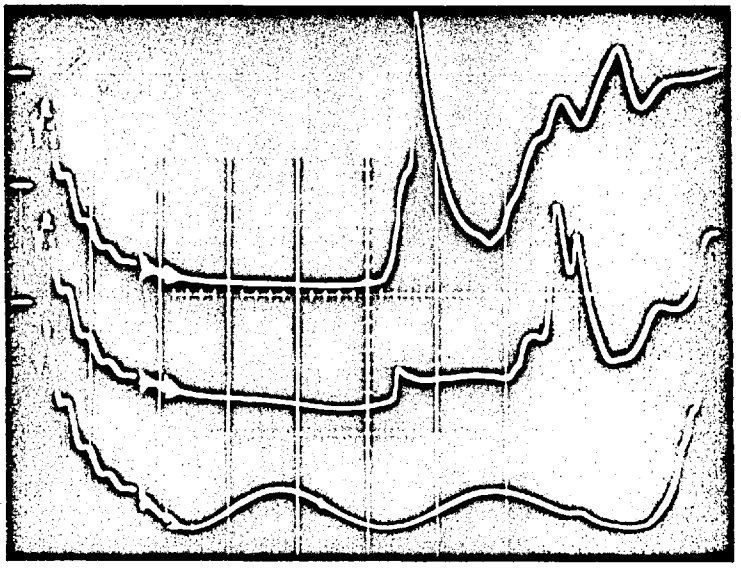

FIG (3.7) 70 GH_z microwave transmission signals in 5 m.torr pressure argon plasmas for cusp bank voltages 0 to 3 k.v. Transmitted signal displayed upwards and time base 20 μ sec./division.

made about these transmission profiles.

1. The microwave cut off region for zero transmission increased with increasing cusp bank voltage showing a general trend for the plasma diffusion loss to decrease with increasing cusp magnetic field.

2. The transmission of microwaves after the cut off region appeared, at first, in the form of transmission spikes corresponding to times when the cusp field passed through zero values. This feature is in agreement with plasma compression by the rising cusp fields and plasma expansion in the falling cusp fields.

3. Since plasma must be continuously decaying in the torus, the integral of electron density along the line of sight of the microwave beam must continuously decrease with time. Thus the spikes and the dips on the transmission profiles were due to changes in density distribution in the plasma, rather than by changes in the line averaged density value. Clearly without knowing the time history of the density profiles in the plasma, a detailed interpretation of the transmission profiles shown in fig. (3.6) is impossible.

(3.6.2) Microwave Reflection Experiments

In the second set of experiments, the microwave equipment was arranged so that the beam was reflected from the plasma in the mid-plane region between cusp coils. The reflection technique is described in detail in chapter 8. To a first approximation, the reflection of the microwave beam can be considered to take place at the plasma boundary where the electro

Cusp bank voltage (k.v.)

(a)

0

2



(b)

0

2

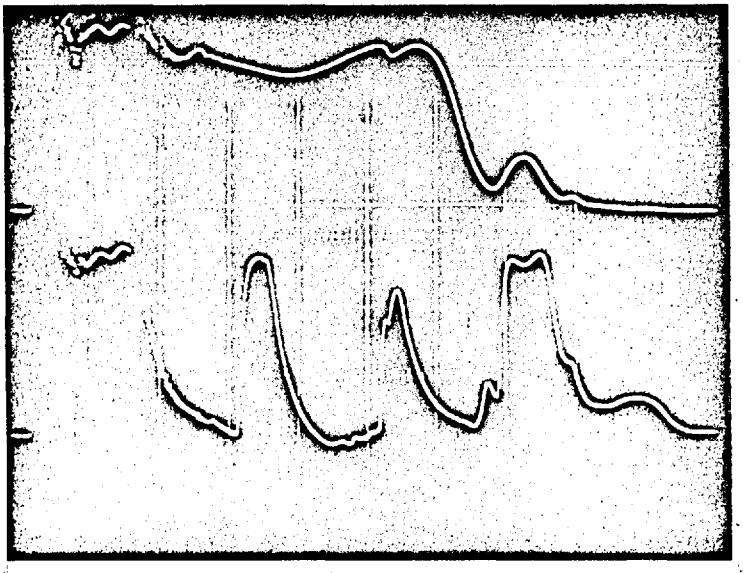

FIG (3.8) 70 GH_z microwave reflection signals.
Reflected signal displayed upwards.
(a) 5 m. torr argon plasma, time base 10 μ sec./div.
(b) 20 m. torr argon plasma, time base 20 μ sec./div.

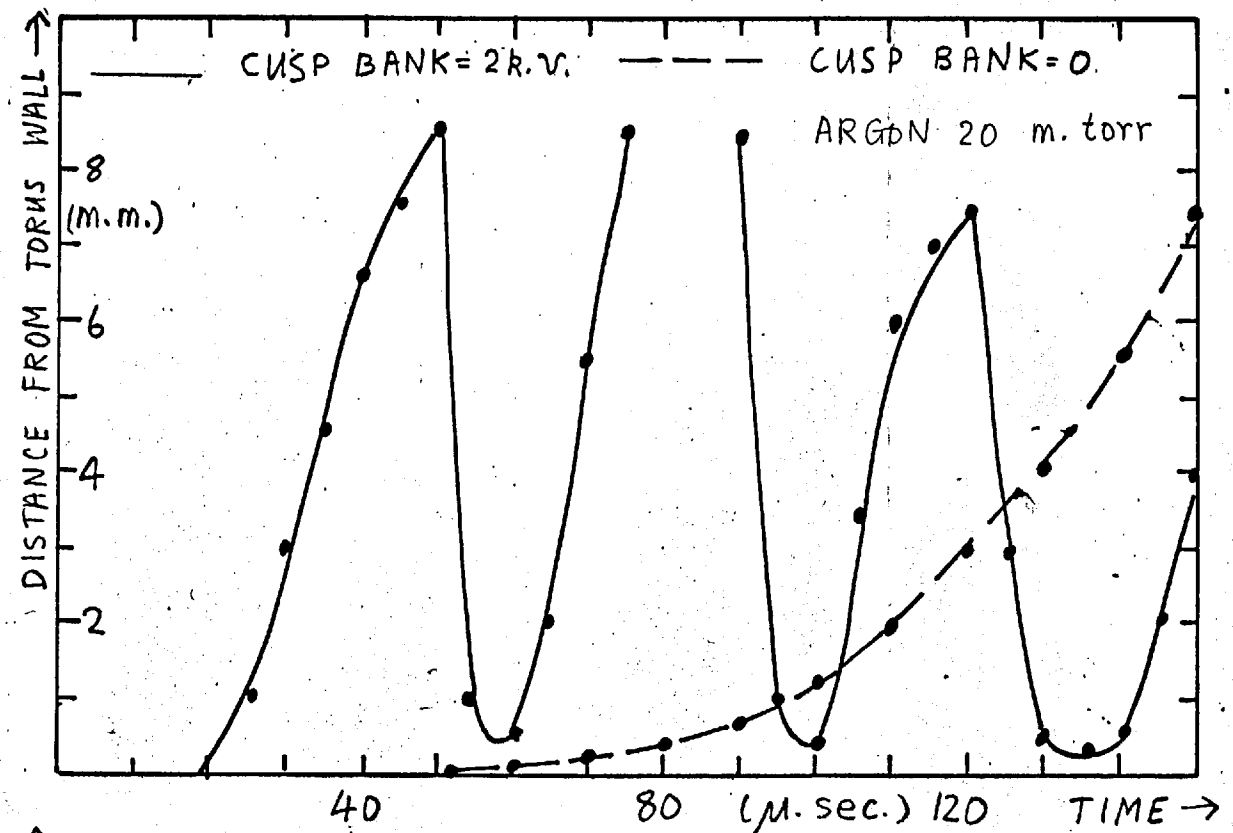

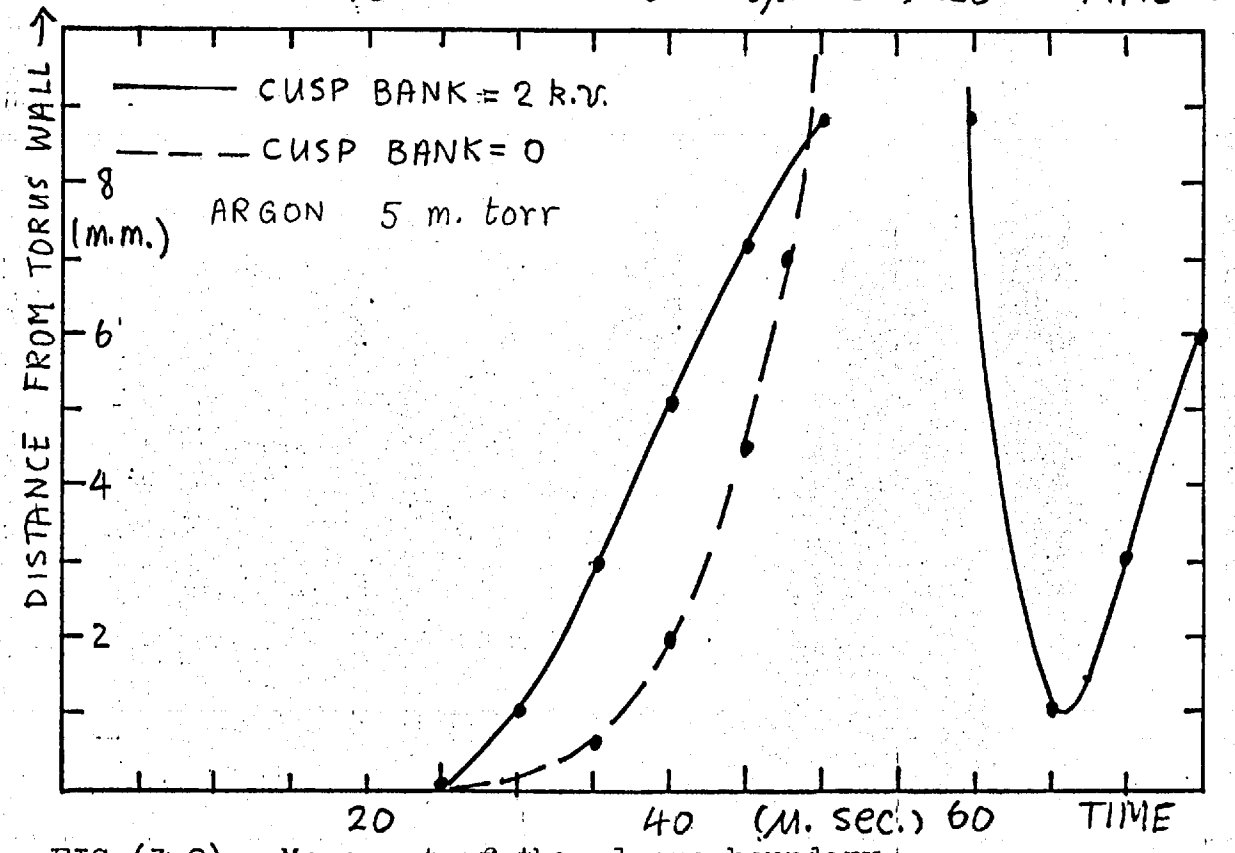

FIG (3.9) Movement of the plasma boundary $n = 6.1\ 10^{13}\ cm^{-3}$ inferred from the results shown in FIG (3.8).

density equalled the cut off density value for the 70 GH_z wave ($= 6.1\ 10^{13}\ cm^{-3}$). Examples of the signals reflected from the preionised plasma with and without the applied cusp magnetic field are shown in fig. (3.8). We make the following comments about these signals.

1. For both sets of results, the reflected signal can be seen to drop rapidly when the cusp field was applied and subsequently reappear strongly at each zero value of the cusp field. This behaviour is in agreement with the idea of plasma compression and expansion in unison with the cusp field oscillations.

2. From measurements made on the reflected signals shown in fig. (3.8), the movement of the plasma boundary $n = 6.1\ 10^{13}\ cm^{-3}$ with time has been worked out for plasma decays with and without the cusp field. Plots of the boundary movements are shown in fig. (3.9).

CHAPTER 4

POLYTRON PLASMA DIAGNOSTICS

Details of the plasma diagnostic techniques used in the Polytron experiment are given in this chapter. Some of the methods of plasma measurement (eg. Rogowski coils, magnetic probes) followed standard practice, whilst other methods (eg. ion probes) required some development work.

(4.1) CURRENT MEASUREMENTS

The currents in the plasma and in the eight induction rods were measured by integrating the output voltages of Rogowski coils (17) using a simple R.C. network. This technique is described in detail in (18) and the frequency response of the system has been discussed by Cooper (19). The Rogowski coils were of the compensated type, with the return wire of the coil brought back along the coil axis, to reduce voltages induced by cusp field oscillations.

(4.2) MAGNETIC FIELD MEASUREMENTS

A major Polytron diagnostic was the use of internal and external magnetic probes and flux loops to measure the magnetic fields in the plasma.

(4.2.1) Internal Magnetic Probes

The use of small coils surrounded by fused silica jackets in the probing of intense discharges has been described by several authors (20) (21) (22) (23). The requirements of high sensitivity, which varies as N x A (number of turns x coil area), and of low inductance, which varies as N^2A, indicate coils designed with the maximum allowable area and the minimum number of turns. A typical equivalent circuit for calculating the probe frequency response is shown in fig. (4.1)

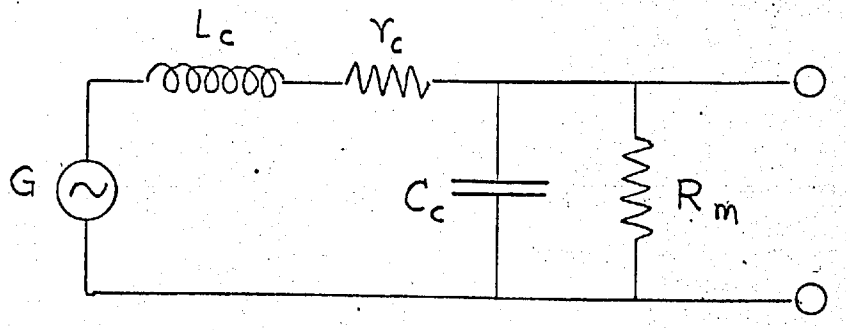

FIG. (4.1)

where G = coil voltage induced by magnetic field change
L_c = coil inductance
C_c = coil self capacitance
r_c = coil resistance
R_m = matching resistor of connecting cable

Segre and Allen (22) have shown that the condition for a flat frequency response of the equivalent circuit shown in fig. (4.1) is

$$R_m = \left(\frac{L_c}{C_c} \right)^{\frac{1}{2}} \qquad (4.1)$$

When the coaxial cable between the coil and oscilloscope is long such that the transit time of the cable is greater than the reciprocal of the highest frequency of interest, the equivalent circuit shown in fig. (4.2) is applicable

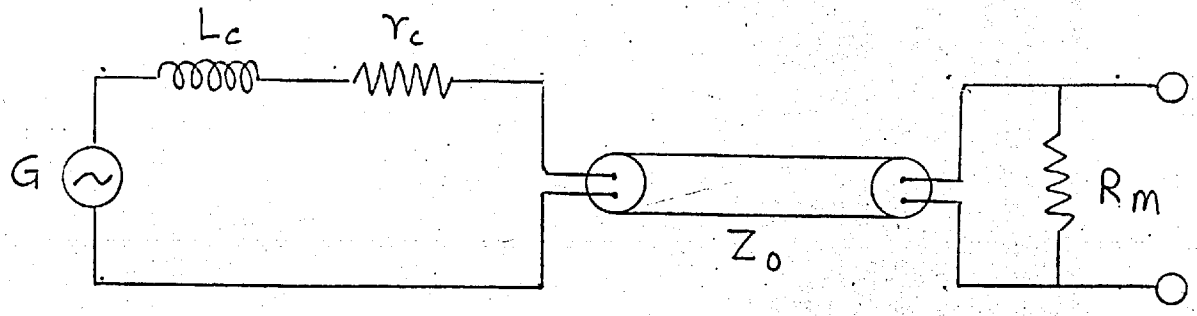

FIG. (4.2)

where Z_o = impedence of connecting cable.

Ashby et al. (23) have given an analysis of the equivalent circuit shown in fig. (4.2) and they showed that the frequency response of the system falls markedly when

$$\text{frequency } f \sim \frac{R}{2\pi L_c} \qquad (4.2)$$

and that neglecting the stray capacitance of the coil in the circuit analysis is valid provided

$$\left\{ \frac{L_c}{C_c} \right\}^{\frac{1}{2}} \gg R_m \quad \text{or} \quad Z_o$$

Herzog and Tischler (24) and Gautier (25) have given similar expressions for the magnetic field at a point using Taylor series expansions. They have shown that, when the spatial inhomogeneities of the magnetic field are comparable with the coil dimensions, an accurate measurement of the field component parallel to the coil axis at the centre of the coil can be obtained provided the coil dimensions satisfy the condition

$$\frac{\text{Length of coil}}{\text{Diameter of coil}} = 0.72 \qquad (4.4)$$

In the construction of the internal magnetic probe, the coil former was machined from P.T.F.E. rod to a diameter of 1 mm. The former was wound on a miniature coil winderwith 16 turns of 48 SWG 'Lewcosol' enamelled wire, so that the coil dimensions roughly conformed to expression (4.4). The winding was monitored under a microscope and the use of 'Loctite' adhesive was invaluable. The ends of the single layer coil were twisted together from the coil centre and the coil was glued to a 1 mm. o.d. 6 cm. long ceramic tube. Because of the long side ports on the small torus ($\sim$ 25 cm) a long probe was required, and the ceramic tube was fastened into a 30 cm. long stainless steel tube lined with P.V.C. sleeving. The whole assembly was sheathed in a fused silica tube whose tip was drawn out to provide the minimum wall thickness over the coil and ceramic tube. The outside diameter of the silica tube which entered the plasma was 2.5 mm. At the opposite end to the coil, the silica tube was 'araldited' inside a 6.3 mm. brass tube which made a sliding vacuum seal with a double Wilson seal attachment on the

torus port. The movement of the probe across the torus minor diameter was controlled by a micrometer adjusted spring loaded carriage, which was capable of reproducibly positioning the probe to within 0.05 mm. Amphenol twin UHF plugs and sockets and D.R. 68 coaxial cable were used to connect the probe to the integrating circuit at the oscilloscope. The magnetic probe in position in the small torus can be seen in fig. (2.13).

The inductance and stray capacitance of the probe were measured using a Marconi 'Q' meter type 329 G. The probe output socket was connected to the 'Q' meter using twisted leads and the resonant frequency found for various added capacitances across the circuit. The effects of the twisted test leads and sockets were eliminated by performing a second experiment with a shorted dummy socket. The resonant frequency f_χ of a test circuit was related to the added capacitance C_a across the circuit by the equation

$$\frac{1}{(f_\chi)^2} = 4\pi^2 (L_\chi + L_Q)(C_a + C_\chi) \qquad (4.5)$$

where L_χ = test inductance
C_χ = test capacitance
L_Q = internal inductance of 'Q' meter (0.05 μH)

Plots of the quantity $(f_\chi)^{-2}$ versus C_a for the two cases described above are shown in fig. (4.3). A value of the coil inductance was obtained from the gradients of the linear plots shown in fig. (4.3) and the intercept of the probe line with the $(f_\chi)^{-2}$ axis gave a value for the self capacitance of the coil according to equation (4.5).

The final test performed on the internal magnetic probe was the measurement of the turns-area of the coil using an

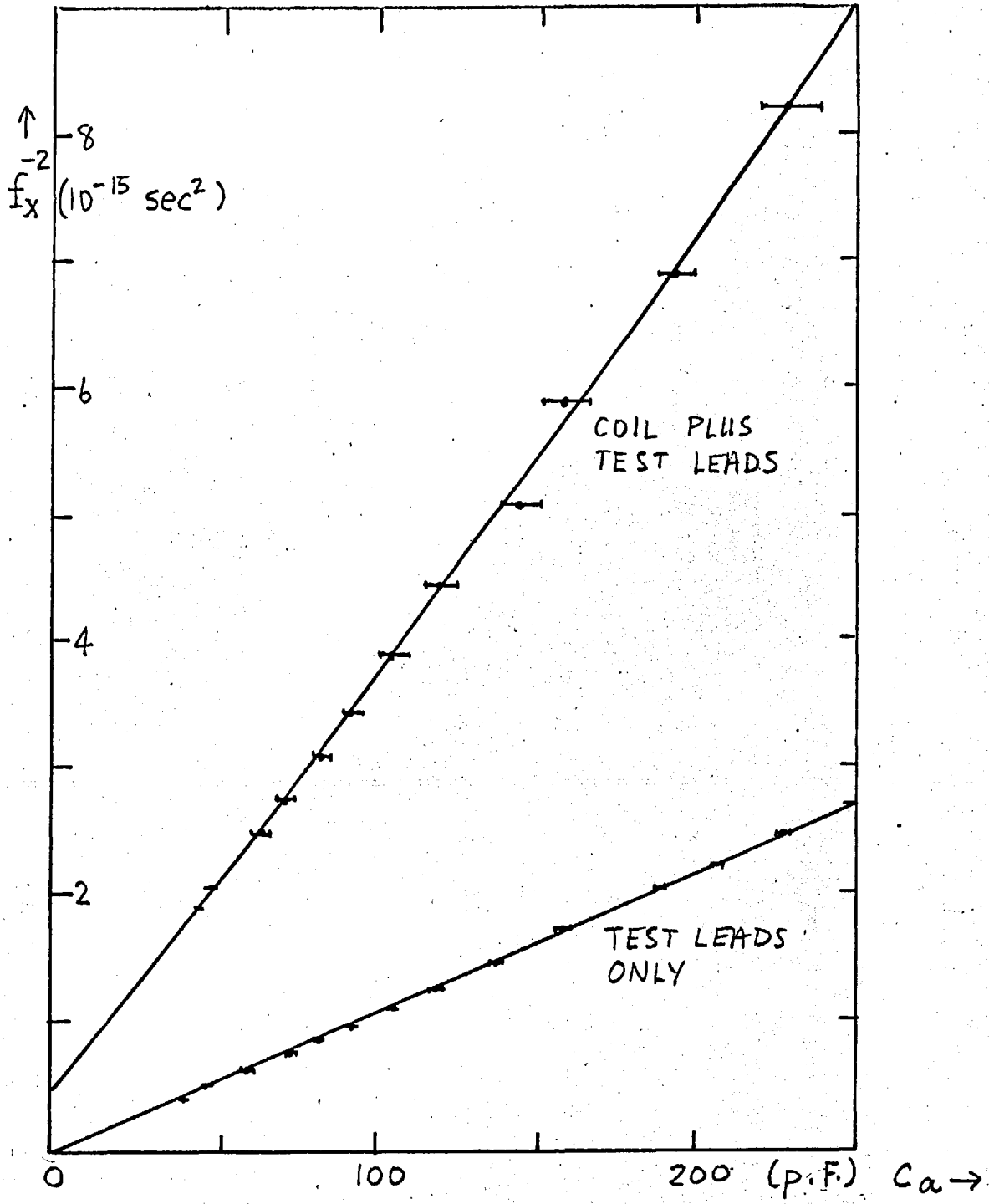

FIG (4.3) Plots of $(f_x)^{-2}$ versus C_a.

independently calibrated Helmholtz coil system.

A list of the internal probe characteristics based on the above measurements is given in table (4.1).

TABLE (4.1)

INTERNAL MAGNETIC PROBE CHARACTERISTICS

Probe inductance	0.57 (± 0.04)	μH
Probe self capacitance	8 (± 2)	pF
Probe resistance	14 (± 0.5)	Ω
Calculated turns-area	0.150	cm^2
Measured turns-area	0.146(± 0.005)	cm^2

From equation (4.1), the theoretical value of the matching resistance for a flat frequency response is therefore 189Ω, and the upper frequency response for the probe with the 100 Ω matching resistor actually used is, from equation (4.3), 28 $M.H_z$.

(4.2.2.) External magnetic Probe

A double coil external magnetic probe was constructed with the coils orientated at right angles to each other so that simultaneous measurements of the B_r and B_z components of the cusp magnetic field could be made. Each coil consisted of 40 turns of 47 S.W.G. wire on a 1.68 mm diameter former. As the centres of the coils were not coincident, (separation equalled 2 mm.), the field components obtained from the probe

measurements corresponded to different spatial regions of the cusp field and this fact had to be taken into account when making the field plots. The probe was accurately positioned using a three dimensional micrometer controlled carriage shown in fig. (2.13). This external probe was used to measure the cusp field components in the absence of plasma and the field components perturbed by Hall currents in the plasma.

(4.2.3.) External Flux Loops

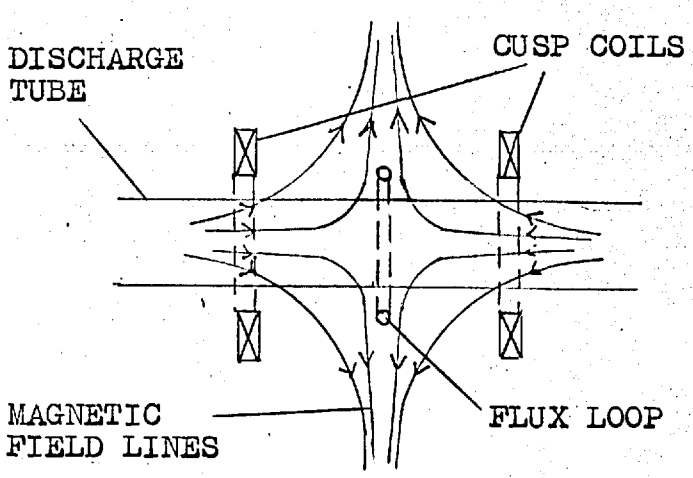

FIG. (4.4)

The external flux loop consisted of a single turn of wire placed in the mid plane between a pair of cusp coils as shown in fig. (4.4). The position of the loop was carefully adjusted so that in the absence of plasma, triggering the cusp field bank gave a negligible output signal (ie. no nett flux change across the loop). With the loop in this position, the presence

of azimuthal Hall currents in the Polytron plasma regime produced an easily detected change in flux across the loop. Because of the large area of the loop, the sensitivity of this flux loop system was several orders of magnitude greater than that for the internal magnetic probe system. One basic disadvantage of the flux loop measurement was that it gave only the value of the magnetic field change averaged across the area of the loop. In practice, the large area of the loop made the zero balance signal in the absence of plasma particularly sensitive to minor triggering differences in any one of ten cusp coils on either side of the loop. This factor set an upper limit to the level of sensitivity of the complete system.

The flux loop was constructed from 36 SWG piano wire and it was electrostatically screened using a split copper braid. The loop was pre-formed to the correct shape, before fixing in place underneath the induction rods system outside the torus. The loop was accurately positioned using the same three dimensional carriage as was used for locating the double external magnetic probe and it is just possible to see the flux loop in position around the small torus in fig. (2.13).

(4.3) DIRECTED ION VELOCITY MEASUREMENTS

Ion probes similar to the types developed at the U.K.A.E.A. Culham Laboratory by Ashby (26) (27) (28), were used to measure the directed ion velocity in the Polytron. A typical ion probe and its bias circuit is shown in fig. (4.5). The probes were designed to be scanned across the torus diameter to measure the directed ion velocity parallel to the toroidal z axis. The central electrode was negatively biassed (typically from -30 to

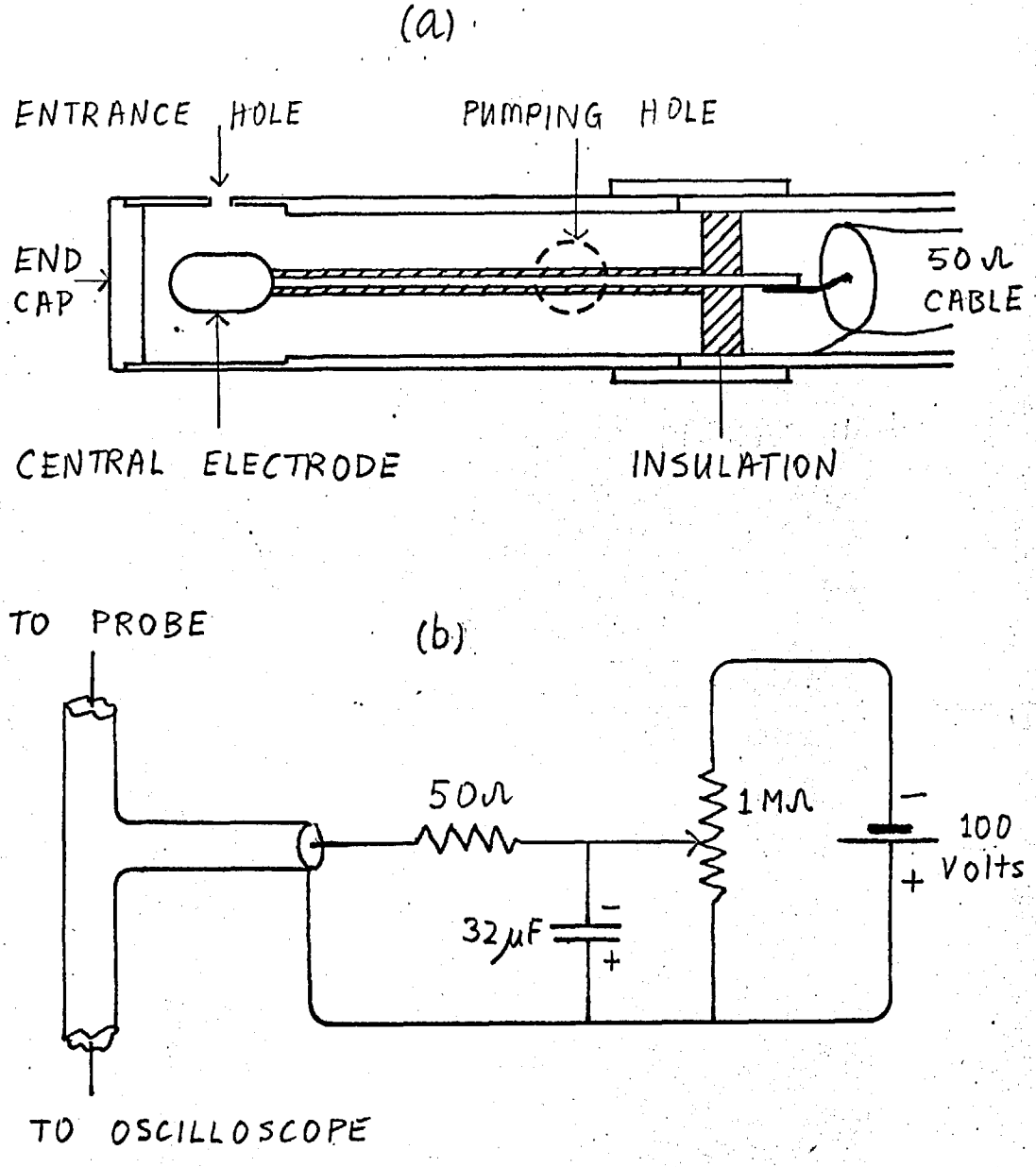

FIG (4.5) (a) Ion probe details.
(b) Bias circuit.

-100 volts) to repel electrons.

The theory of the probe operation is very simple when the directed velocity of the ions is much greater than their thermal velocity. In this case the probe current I due to ion collection is

$$I = n_i \, Z e \, |\vec{v_i}| \, A \qquad (4.6)$$

where n_i = ion density
$+ Ze$ = ionic charge
$\vec{v_i}$ = directed ion velocity
A = area of collecting hole normal to

Experimental arrangements have to be made so that the probe does not draw excessive current from the plasma due to the large area of contact between the metal probe outer surface and the plasma. This was achieved in practice by wrapping the coaxial cable connecting the probe to the oscilloscope several times around a ferrite transformer core. Over the time scale of the experiment, ($\sim$ 20 μ.sec.), the outer part of the probe was thus isolated by a large impedence and the probe could assume a potential near the plasma potential, whilst the transmission between the inner and outer of the coaxial cable was unaffected.

The outer part of the probe was constructed from stainless steel tube, and the tip of the probe containing the ion entrance hole was detachable. The tube wall was machined very thin ($\sim$ 0.1 mm.) in the region of the hole. The central collecting electrode was machined from copper. Experiments were performed under Polytron conditions, with entrance hole diameters varying from 0.1 to 0.75 mm and with varying distances between the hole and the collecting electrode, in order to arrive at a compromise between obtaining a large ion current signal and the prevention

of arcing inside the probe. In order to facilitate quick pump down of the probe and to prevent possible stagnation in the probe under plasma directed velocity conditions, two large exit holes, each 1.5 mm in diameter, were drilled into the outer wall of the probe in a position away from the discharge region. The central conductor to the collecting electrode was well insulated in the region opposite these pumping holes as a precaution against spurious signals.

The optimum probe characteristics that were found as a result of the above experimental work are listed in table (4.2).

TABLE (4.2)

ION PROBE CHARACTERISTICS

Probe outside diameter	3.95 mm
Probe wall thickness	0.1 mm
Entrance hole diameter	0.5 mm
Collecting electrode diameter	2.3 mm
Bias voltage	-50 volts.

(4.4) PLASMA PHOTOGRAPHY

Time resolved photography of the plasma was performed using a Telford Products image convertor camera which operated at framing intervals of 0.05 and 0.5 μ.sec.

(4.5) SCREENED ROOM FACILITIES

The screened room housing the oscilloscopes formed an essential part of the Polytron plasma diagnostics. The cables from the apparatus to the oscilloscopes were fed inside copper pipes earthed to the screened room and ferrite cores were extensively used for filtering out 'pick up' on the cable outer braids on entry into the screened room. The mains supply to the screened room was carefully filtered. Despite all these precautions, electrical 'pick up' from the main bank trigger generator was always apparent during the first two μ.sec. of Polytron operation. A major reduction in this 'pick up' was achieved by employing light beam triggering of the oscilloscopes. Gallium-phosphide emitters situated outside the screened room converted the timing unit pulses to each oscilloscope into light flashes which were transmitted to receivers inside the screened room using dielectric coated glass light pipes.

CHAPTER 5

POLYTRON EXPERIMENTAL RESULTS

The experimental results obtained from studying Polytron plasmas using the diagnostic equipment described in the previous chapter are now presented. The initial experiments were performed using the small torus (bore 44 mm) and the results indicated plasma leakage out of the cusped field. In an attempt to reduce the plasma leakage, the apparatus was modified to accept the larger torus (bore 71 mm) whilst retaining the same cusped field configuration. The small torus experiments were mainly directed towards a study of the basic ion acceleration mechanisms in the plasma whilst the large torus experiments were concentrated on a study of the stability and confinement of the plasma. Part of the work described in this chapter has already been published (139)(140).

(5.1) SMALL TORUS RESULTS

A typical timing sequence for the triggering of the various elements of the Polytron apparatus is shown in fig. (5.1), where the bottom waveform shows the variation of the plasma discharge current. The timing of the cusped field bank was chosen to produce the mean maximum cusp field over the first half cycle of the discharge current and this choice meant that the cusp field went through zero around the centre of the second half cycle of the discharge current. This coincidence of the zero cusp field and maximum induced electric

field at the centre of the second half cycle was responsible for the large current 'spike' shown in fig. (5.1). A comparison of the cusp field and discharge current waveforms shown in fig. (5.1) thus provides good evidence for electron trapping occuring at the times of large cusp field.

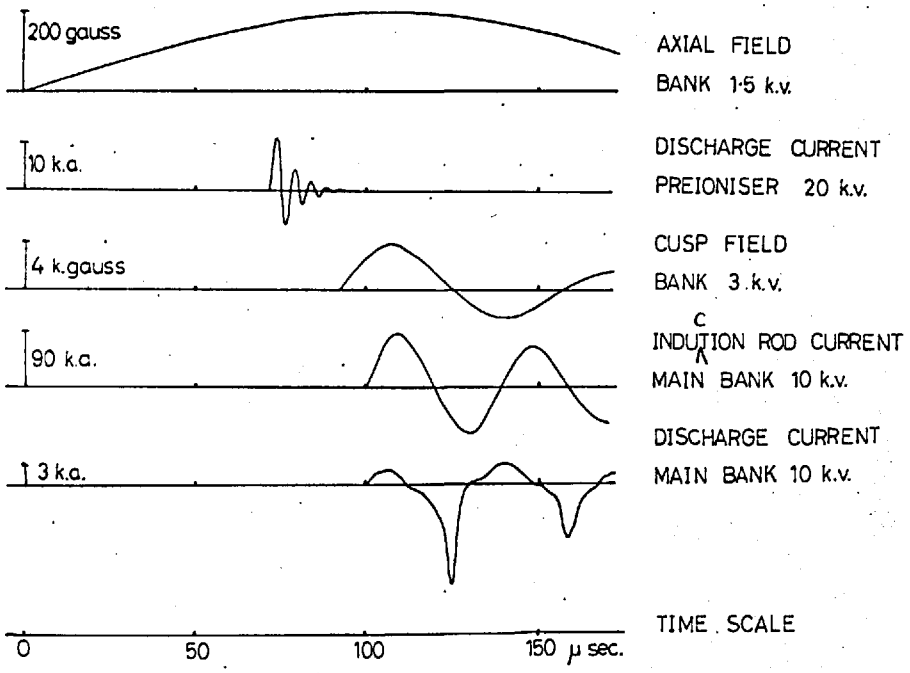

FIG. (5.1)

(5.1.1) Discharge Current Measurements

In order to evaluate the degree of electron trapping by the cusp field during the first half cycle of the discharge, the axial current was measured in two different plasma regimes:

(a) the Polytron regime with the applied cusp field and (b) a pinched discharge current regime with NO applied cusp field but where the conditions of gas pressure, preionisation and main bank voltage were the same as in regime (a). For regime (a) plasmas, the discharge current was assumed to be composed of ion current and leakage electron current. For regime (b) plasmas, the discharge current was assumed to be electron current which was usually inductively limited by the circuit conditions. Typical sets of discharge current waveforms obtained in an argon plasma at 10 m.torr pressure for both regimes are given in fig. (5.2). From a comprehensive series of measurements made in argon plasmas for main bank voltages 7.5 to 20 k.v. and gas pressures 2 to 500 m.torr, the peak values of the first half cycle discharge currents in both regimes have been plotted as a function of gas pressure for fixed main bank voltages as shown in fig. (5.3). On this plot, the plasma conditions which gave rise to a large difference between the peak current values in each regime were taken to correspond to a high degree of electron trapping and to be favourable for ion acceleration processes. Similarly the plasma conditions which gave rise to a small difference between peak current values in each regime were taken to be unfavourable for ion acceleration processes. Thus from fig. (5.3) the most favourable ion current conditions can be seen to correspond to low gas pressures and low main bank voltages. It is also clear from fig. (5.3) that the Polytron discharge current (case (a)) was a steadily increasing function of both gas pressure and main bank voltage and that there were no critical threshold values of these parameters marking a sharp dividing line between ion current and electron current regimes.

In the most favourable low gas pressure conditions, the

	Main bank voltage (k.v.)	Current sensitivity (k.a./div.)
(a)	7·5	6·6
	10·0	6·6
	12·5	13·1
	15·0	13·1
(b)	7·5	13·1
	10·0	13·1
	12·5	13·1
	15·0	13·1

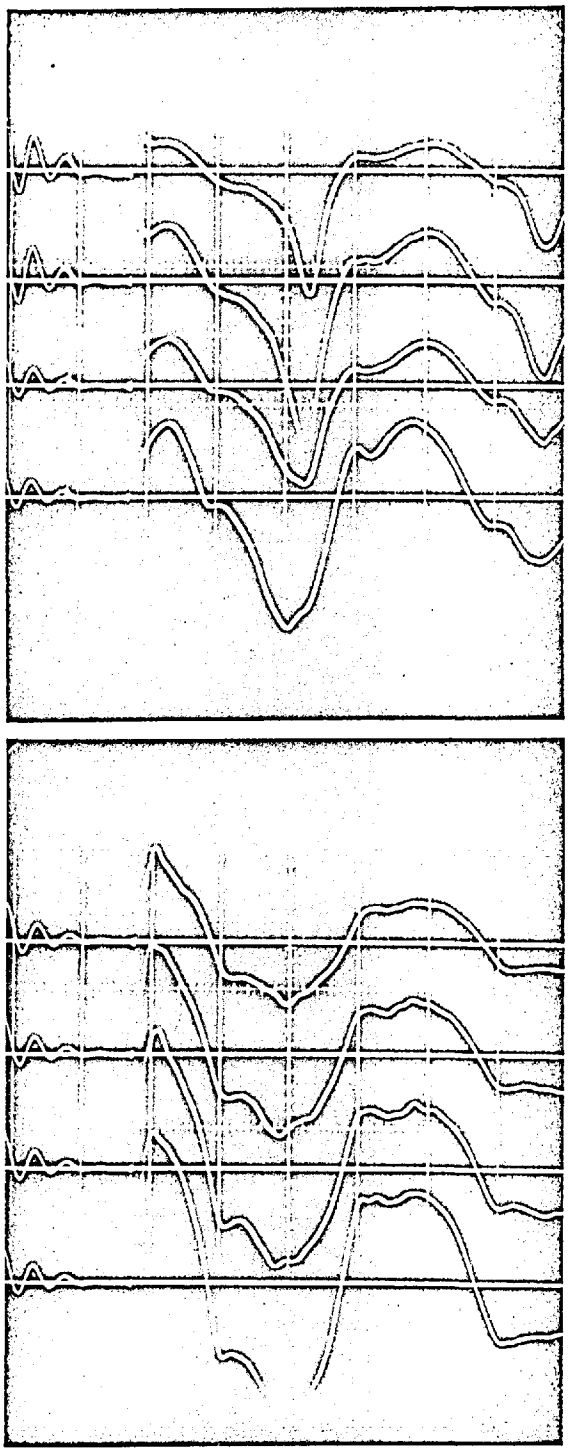

FIG (5.2) Discharge current waveforms in argon plasmas.
Time base 10 μ sec./div. Gas pressure 10 m. torr.
(a) cusp bank voltage = 3 k.v.
(b) cusp bank voltage = 0

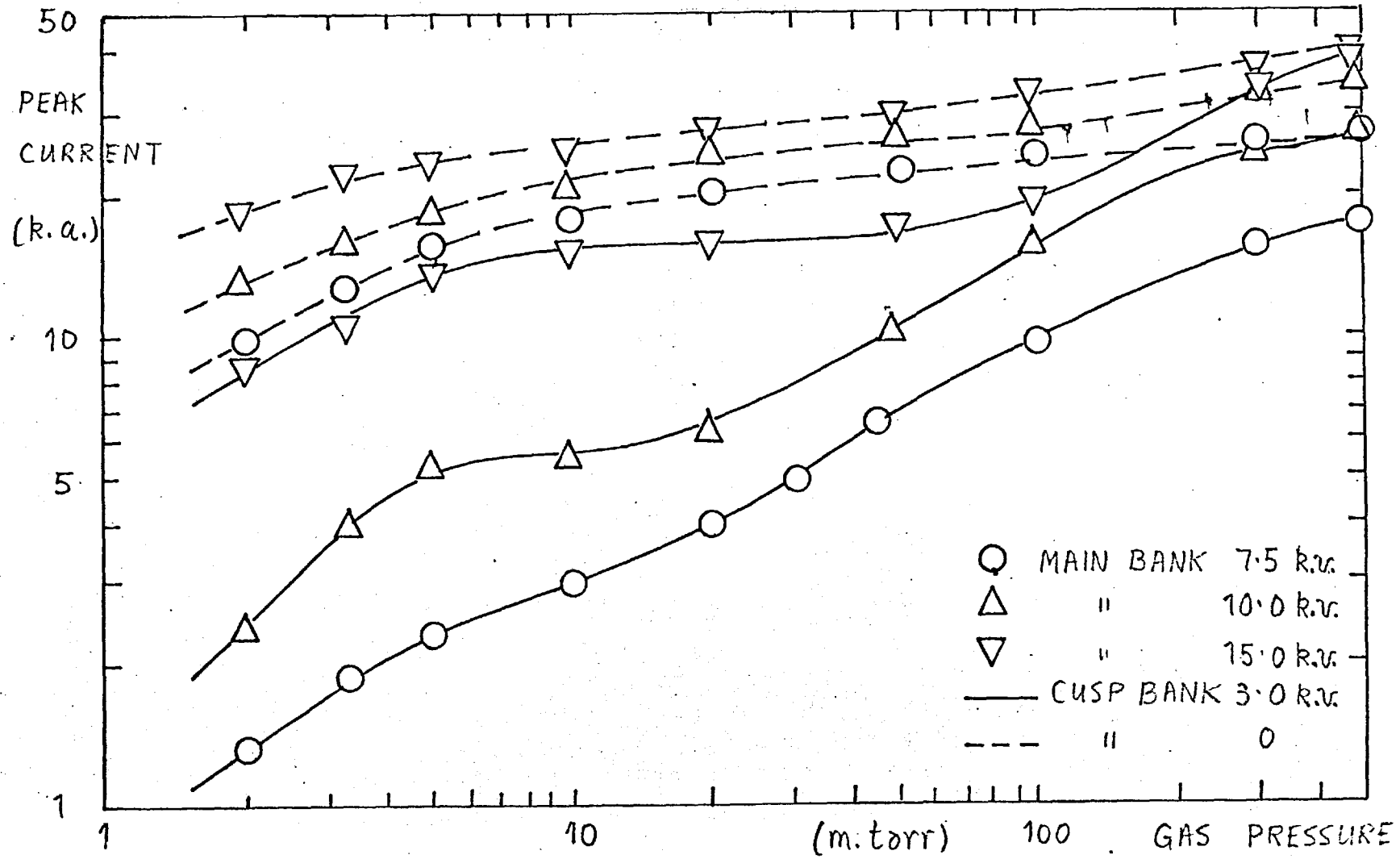

FIG (5.3) Plot of discharge currents in small torus argon plasmas.

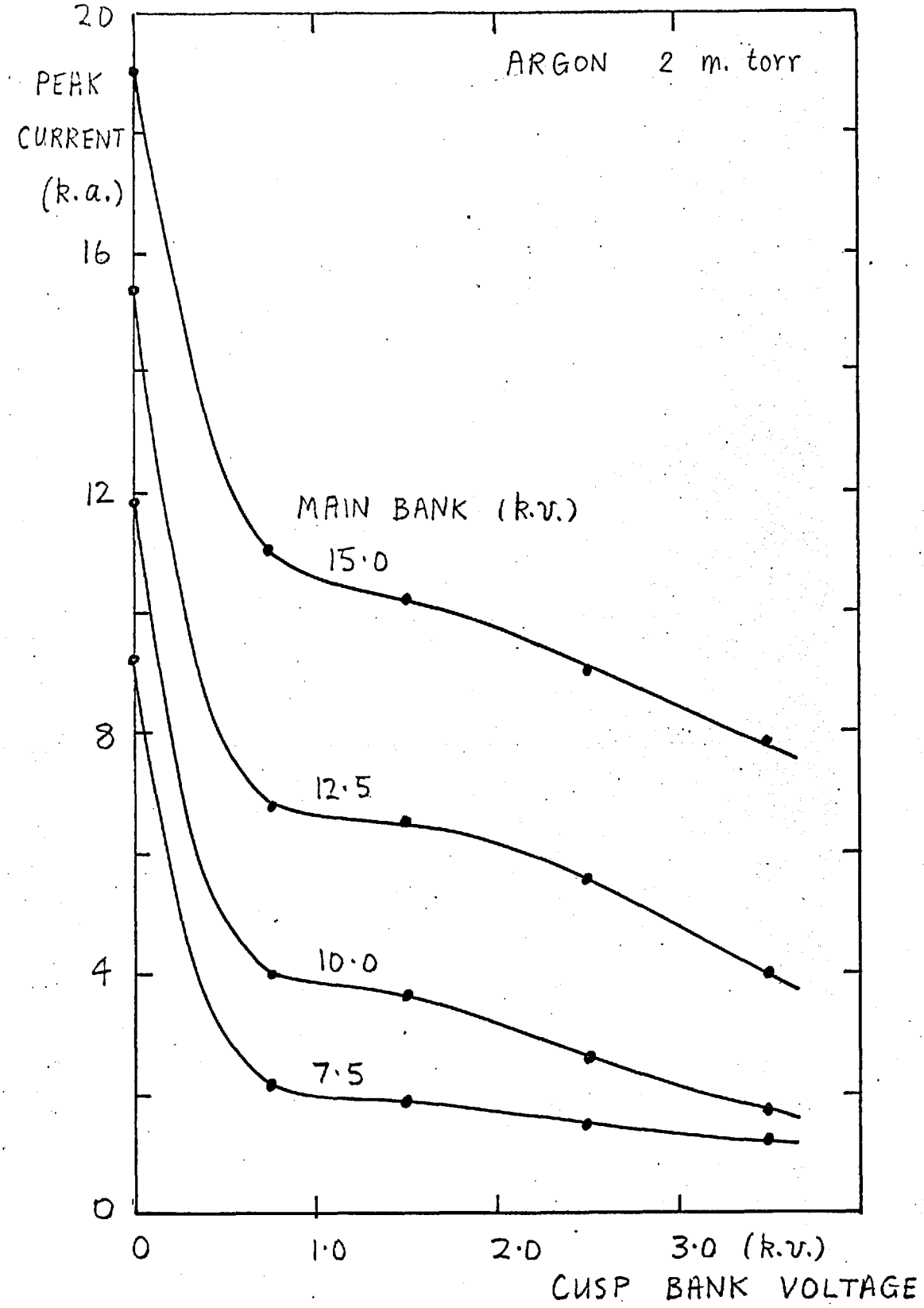

FIG (5.4) Plots of argon plasma discharge current versus cusp bank voltage.

discharge currents in 2 m.torr argon plasmas were measured as a function of cusp bank voltage for fixed values of the main bank voltage. The peak values of the first half cycle discharge currents are plotted versus cusp bank voltage in fig. (5.4). These plots show the large reduction in peak current values produced by a cusp bank voltage of 0.75 k.v. which confirms that B_r values of a few hundred gauss (corresponding to a bank voltage of 0.75 k.v.) were capable of trapping the majority of the electrons in agreement with the calculations presented in section (2.1). The comparatively small reduction in peak current values with increasing cusp bank voltage beyond 0.75 k.v. was taken to represent the reduction in electron leakage current in the vicinity of the plasma axis.

(5.1.2) Flux Loop Measurements

The flux loop described in section (4.2.3) provided a convincing demonstration of the presence of Hall currents in the Polytron plasmas.

In the first set of experiments, the flux loop signal was recorded for different main bank and cusp bank polarities and the resultant oscilloscope waveforms are shown in fig. (5.5). The directions of the flux loop signals were found to depend on the cusp bank and main bank polarities in a way which was consistent with electrons drifting azimuthally in the applied E_Z and B_r fields. A repeat of the above experiments with the weak toroidal axial magnetic field superimposed on the cusp field produced a nett shift in the baseline of the flux loop waveforms and no other effect. Thus it was concluded that the weak axial magnetic field had a negligible effect on electron

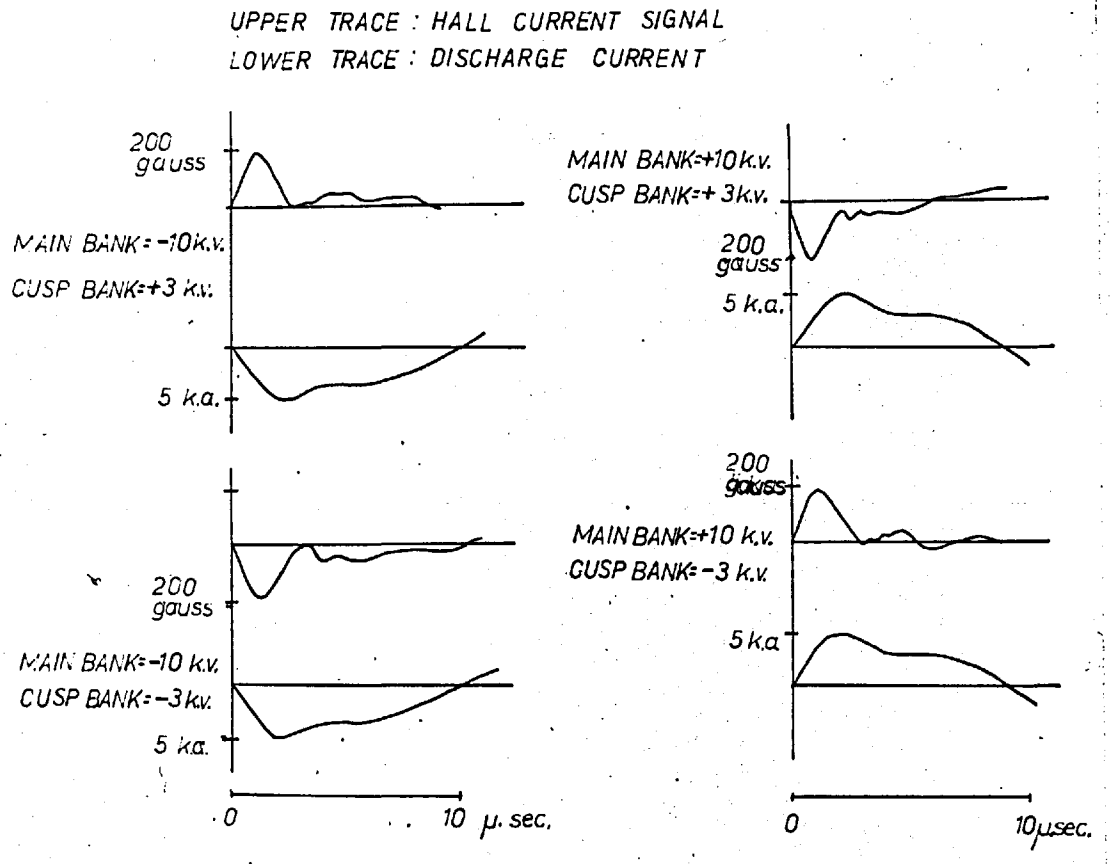

FIG (5.5) Variation of flux loop signal (Hall current signal) with main bank and cusp bank polarities.

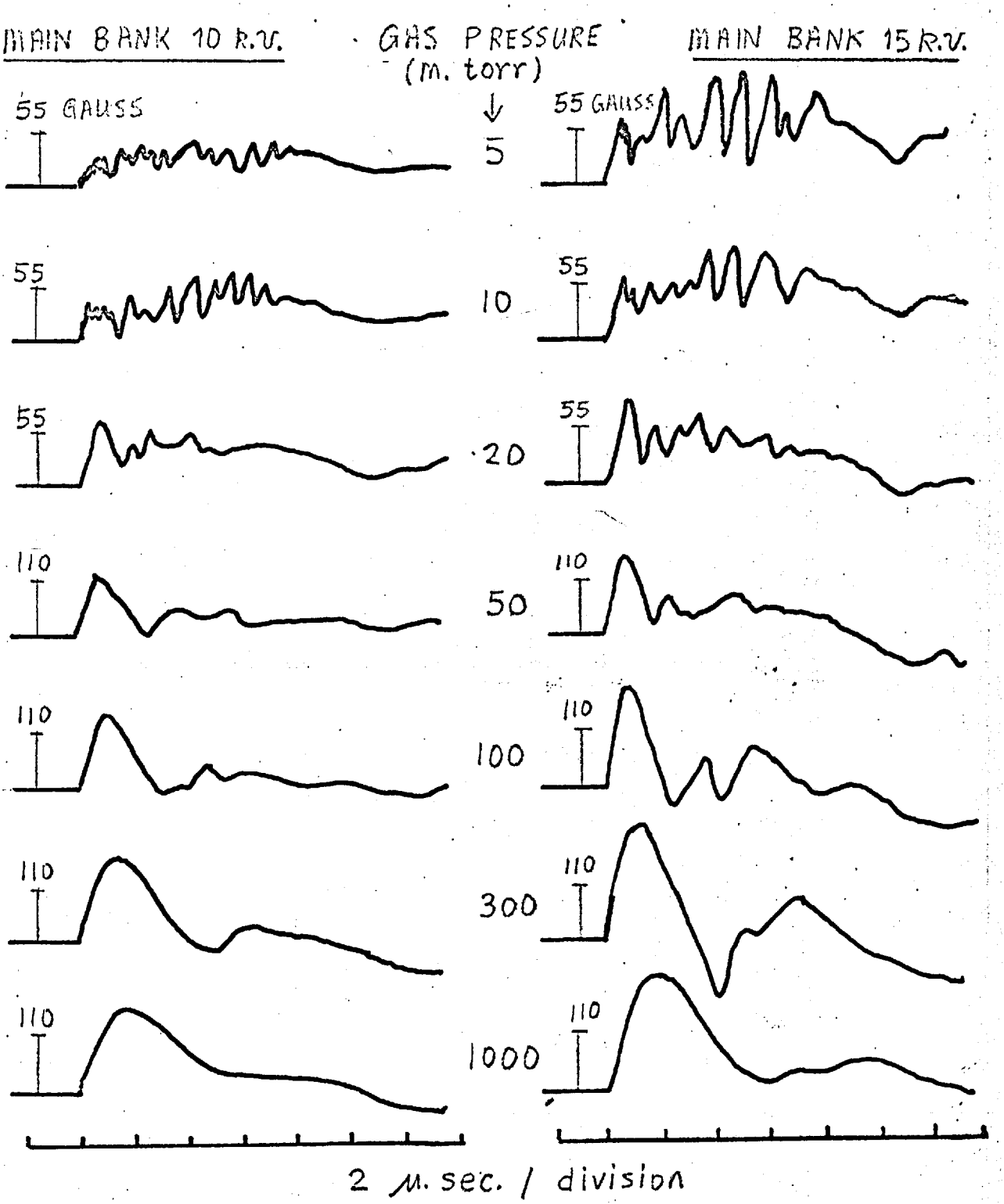

FIG (5.6) Variation of flux loop signal with main bank voltage and gas pressure in argon plasmas.

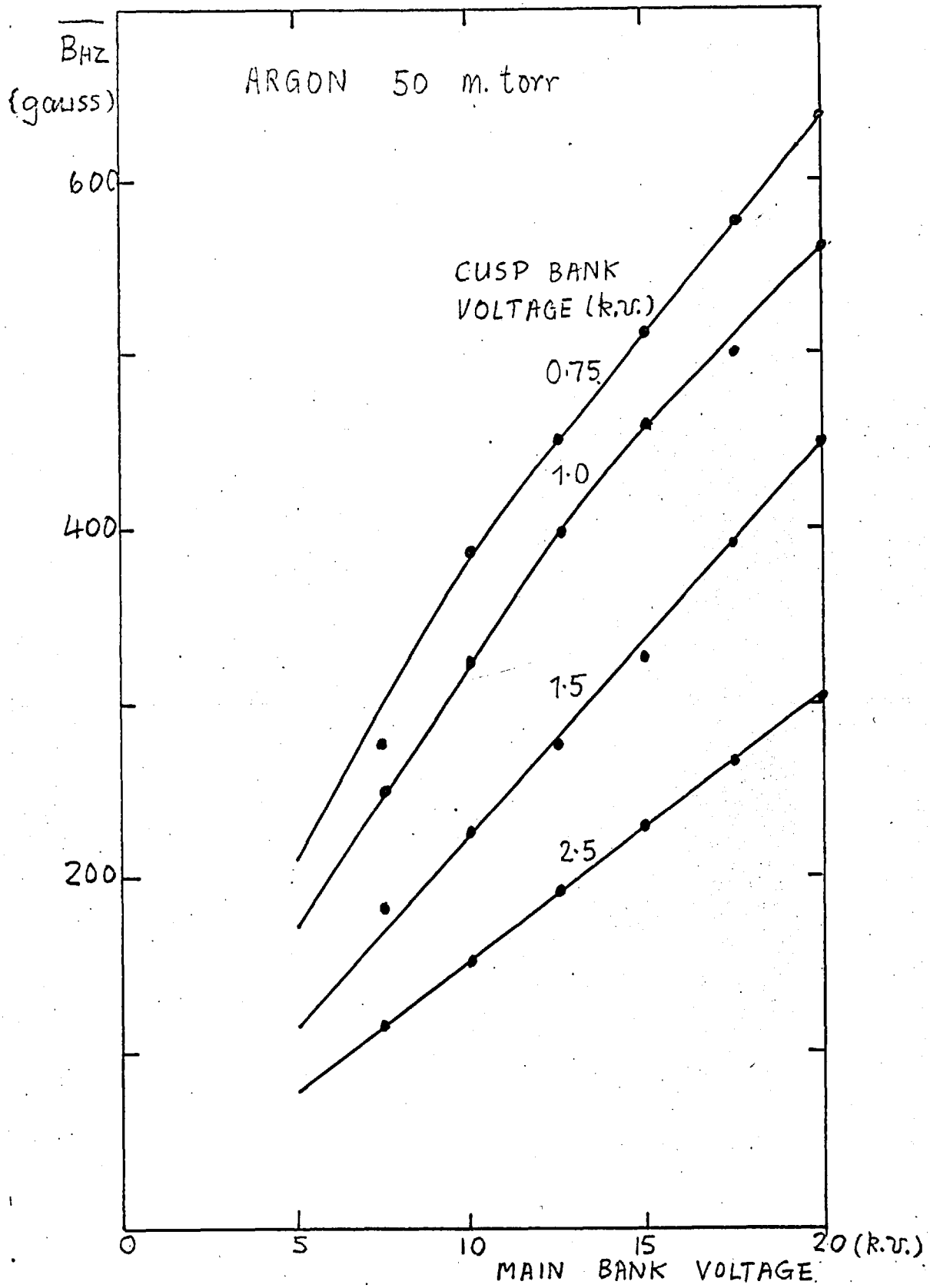

FIG (5.7) Plot of $\overline{B_{HZ}}$ versus main bank voltage for fixed values of cusp bank voltage.

trapping in the Polytron.

In the second set of experiments, the flux loop signals were recorded over a wide range of plasma conditions in argon discharges. The main bank range was from 10 to 20 k.v. and the gas pressure range from 0.003 to 1 torr. Some examples of the measured waveforms are reproduced in fig. (5.6), and we assume that these waveforms can be taken to represent the time behaviour of the Hall currents in the plasma. The interpretation of the fig. (5.6) waveforms is given later in section (5.1.7).

In the third set of experiments, the flux loop signals in 50 m.torr pressure argon discharges were recorded for cusp bank voltages from 0.75 to 2.5 k.v. and for main bank voltages from 7.5 to 20 k.v. The flux loop signals were converted into values of axial magnetic field averaged over the torus cross-sectional area using the known flux loop area and the integrating circuit parameters. We will denote these average values of axial magnetic field by $\overline{B}_{HZ}$ and we will assume that they represent the true average value of axial magnetic field due to the Hall currents

i.e. $$\overline{B}_{HZ} = \frac{2}{a^2} \int_0^a r\, B_{HZ}(r).\, dr \qquad (5.1)$$

where $B_{HZ}(r)$ = axial component of magnetic field produced by the Hall currents as a function of radial distance in the cusp coil mid-plane.

In fig. (5.7) the experimental peak values of $\overline{B}_{HZ}$ measured over the first half cycle of the discharge have been plotted versus the main bank voltage for fixed values of the cusp bank voltage. The plots shown in fig. (5.7) approximate closely to

straight lines showing that the magnitude of the Hall current was approximately proportional to the applied electric field. In table (5.1) the values of the reciprocal of the cusp bank voltage are compared with the values of the relative gradients of the plots shown in fig. (5.7) where the gradient of the plot corresponding to a cusp bank voltage of 1 k.v. has been normalised to unity.

TABLE (5.1)

CUSP BANK VOLTAGE (k.v.)	(CUSP BANK VOLTAGE)$^{-1}$ $(k.v.)^{-1}$	RELATIVE GRADIENTS OF PLOTS FIG.(5.7) (error $\pm$ 10%)
0.75	1.33	1.20
1.0	1.00	1.00
1.5	0.67	0.70
2.5	0.40	0.46

Table (5.1) shows that the gradients of the plots shown in fig. (5.7) are roughly proportional to the reciprocals of cusp bank voltages and we conclude therefore that, at fixed values of gas pressure and electric field, the magnitude of the Hall current was inversely proportional to the magnitude of the cusp field.

(5.1.3) Internal Magnetic Probe Measurements

The internal magnetic probe described in section (4.2.1) was used to measure the B_z and B_θ components of magnetic field in the plasma as a function of radial distance from the plasma

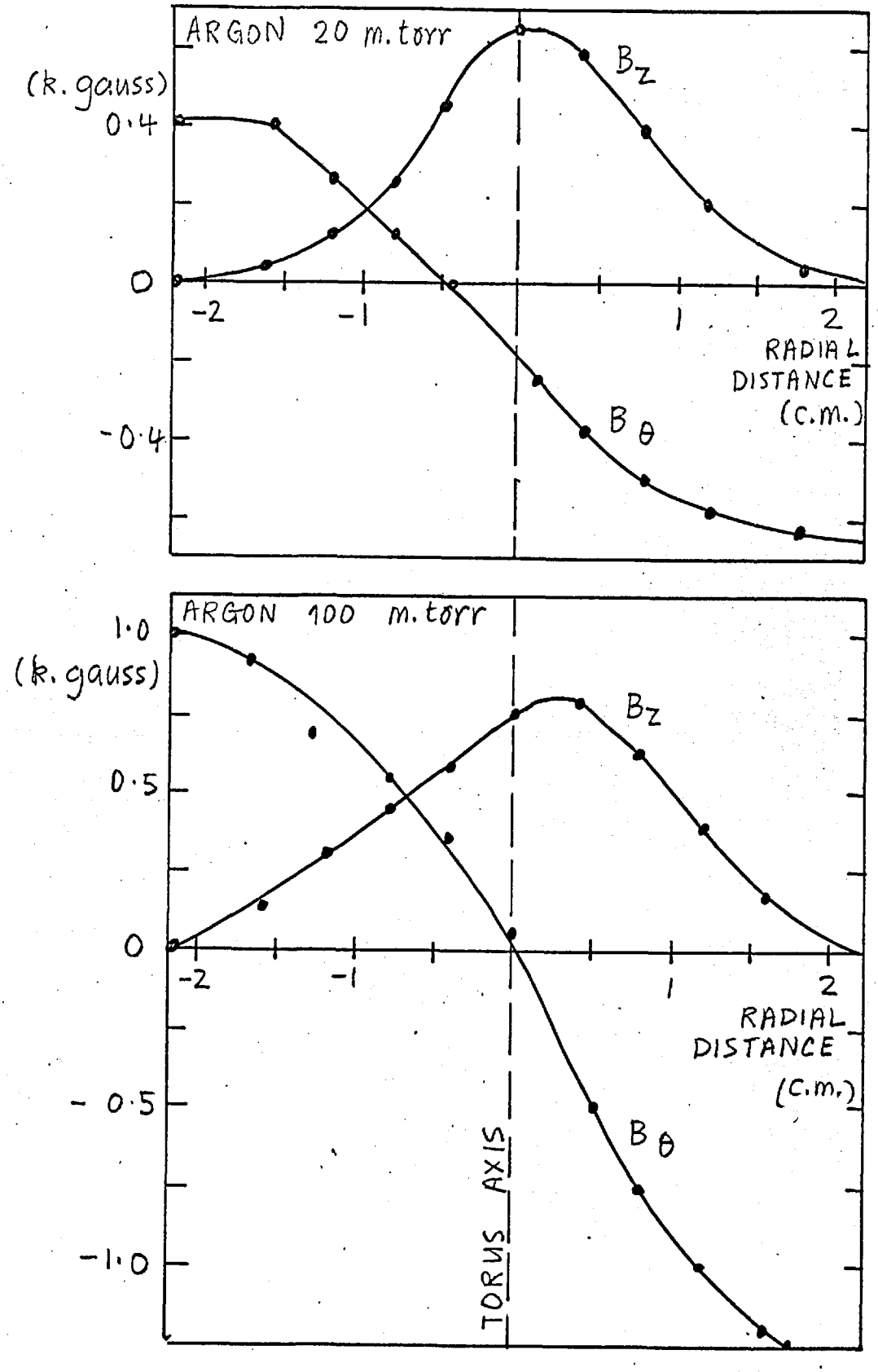

FIG (5.8) B_z and B_θ profiles.

axis in the mid-plane between a pair of cusp coils. In the Polytron discharges, the oscilloscope waveforms for the B_Z component measured with the internal probe and $\bar{B}_{HZ}$ measured with the flux loop were always of similar form for the same plasma conditions, although the value of the B_Z component at the plasma axis was always several times greater than the corresponding average value $\bar{B}_{HZ}$. The profiles for the B_Z and B_θ components measured at the times of peak Hall current signal in 20 m.torr and 100 m.torr pressure argon plasmas have been plotted in fig. (5.8). A detailed analysis of these magnetic field component profiles to yield the current distributions in the plasma has not yet been attempted, since it can only be satisfactorily performed in terms of a three dimensional cusp shaped plasma model. However, visual inspection of the profiles shown in fig. (5.8) suggests that the plasma discharge current was mainly confined to a region within 1.5 cm of the plasma axis at 20 m.torr pressure and that a near uniform distribution of discharge current occurred at 100 mtorr pressure. The profiles described above were measured from probe scans across the plasma diameter in the horizontal plane. A comparison of the profiles given in fig. (5.8) with the profiles for the radial components of the cusp field in the horizontal plane given in fig. (2.6) shows that the positions of peak B_Z component signals in fig. (5.8) almost exactly coincide with the positions of zero B_r cusp field components in fig. (2.11). Thus the distribution of the axial magnetic field produced by the azimuthal Hall currents in the plasma can be seen to be closely related to the distribution of the radial component of the applied cusp field.

A detailed comparison was made using the internal probe between B_Z component waveforms at the plasma axis in regime (a)

and regime (b) plasmas (see section (5.1.1) for the definition of plasma regimes). All the experiments were performed in the presence of the weak toroidal axial magnetic field. The regime (a) results were similar in form to those shown in fig.(5.6). The regime (b) results showed the usual axial field compression signals of a high conductivity pinched discharge, with a peak magnetic field compression ratio of about 20 to 1. One of several significant differences between the $B_Z(0)$ signals for regime (a) and regime (b) plasmas was that the former rose rapidly right from the start of the main bank triggering, whereas the latter only rose rapidly at the time when the current collapse neared the plasma axis.

(5.1.4) External Magnetic Probe Measurements

The external magnetic probe described in section (4.2.2) was used to measure the change in the radial and Z direction components of the cusp magnetic field external to the torus due to the magnetic fields produced by the Hall currents in the Polytron plasma. Etherington and Haines (137) have shown that it is possible to calculate the nett thrust acting on the plasma from the measured distortion of the cusp field. Their method of calculation involves the integration of the e.m. stress tensor around a surface enclosing a cusp coil but excluding the plasma and the eight induction rods. For the example of the linear approximation to the Polytron shown in fig. (5.9) where azimuthal symmetry is assumed, the nett axial e.m. force F_Z acting on the cusp coil can be written from the usual expression for the e.m. stress tensor (40) in terms of the line integral abcda around the cusp coil and the radial distances r_1 and r_2.

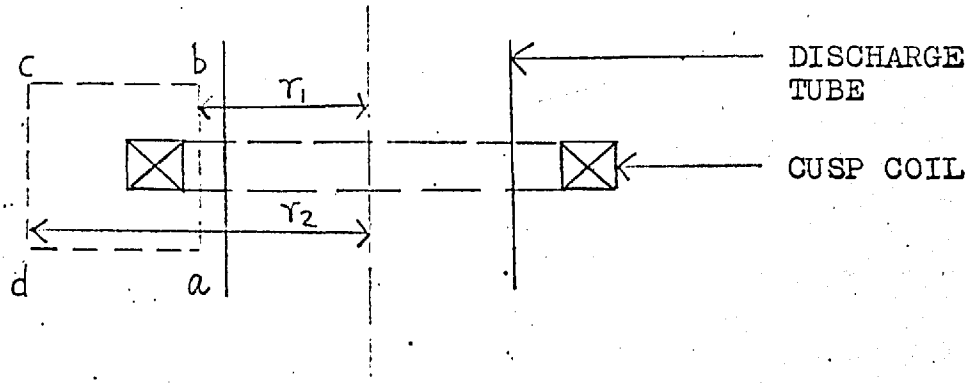

FIG. (5.9)

Etherington and Haines' work describes the evaluation of the stress tensor for a single coil placed around a linear discharge. For the case of the multi-cusp coil Polytron, provided we chose the distance a b in fig (5.9) to equal the axial separation of the cusp coils, the conditions for systematic behaviour in adjacent cusp regions means that the integrals along the paths b c and d a will make equal and opposite contributions to the stress tensor for all possible field perturbations. Also, by choosing the distances b c and d a to be very large, the contribution of the integral along c d to the stress tensor can be made negligibly small. Hence for the multi-cusp coil Polytron the expression for the nett axial force on the cusp coil reduces to

$$F_Z = -2\pi r_1 \int_a^b H_Z B_r \, d_Z \qquad (5.2)$$

where a b = cusp coil separation

r_1 = constant

In toroidal geometry, the curvature of the axis of the multi-cusp coil system means that at any fixed value r_1 of the radius vector, H_Z and B_r are functions of both Z and θ, and the

expression for the nett axial force for the toroidal system is therefore

$$F_Z = - r_1 \int_{\theta=0}^{2\pi} \int_{Z=a}^{b} H_Z(r_1,\theta,Z)\, B_r\,(r_1,\theta,Z)\, dz\, d\theta \qquad (5.3)$$

In the Polytron experiment, the amount of space available around the toroidal assembly prevented measurements over the full range of values of θ necessary for the complete evaluation of the expression (5.3). However an approximate estimation of F_Z was made by substituting the B_r and H_Z cusp field components measured in the vertical plane (ie. perpendicular to the torus plane) into the linear approximation expression (5.2). The experimental conditions chosen were an argon plasma with main bank voltage = 10 k.v., gas pressure = 50 m.torr and cusp bank voltage = 1.5 k.v. Since the Hall currents in the plasma varied inversely with cusp bank voltage (see section (5.1.2)) the fractional perturbation of the cusp field by the plasma Hall currents varied inversely with the square of the cusp bank voltage. The low value of the cusp bank voltage quoted above was chosen to make the cusp field perturbation as large as possible consistent with the plasma being in an electron trapping regime.

Plots of the values of the unperturbed and plasma perturbed H_Z and B_r cusp field components measured at a constant radial distance from the plasma axis r_1 = 2.4 cm at the time of peak Hall currents in the plasma (1.6 μ.sec) are shown in fig.(5.10). Plots of the product $H_Z\, B_r$ corresponding to the unperturbed and plasma perturbed components are shown in fig. (5.11). The nett areas under the plots shown in fig. (5.11) were substituted into the equation (5.2) and the following values for F_Z were found

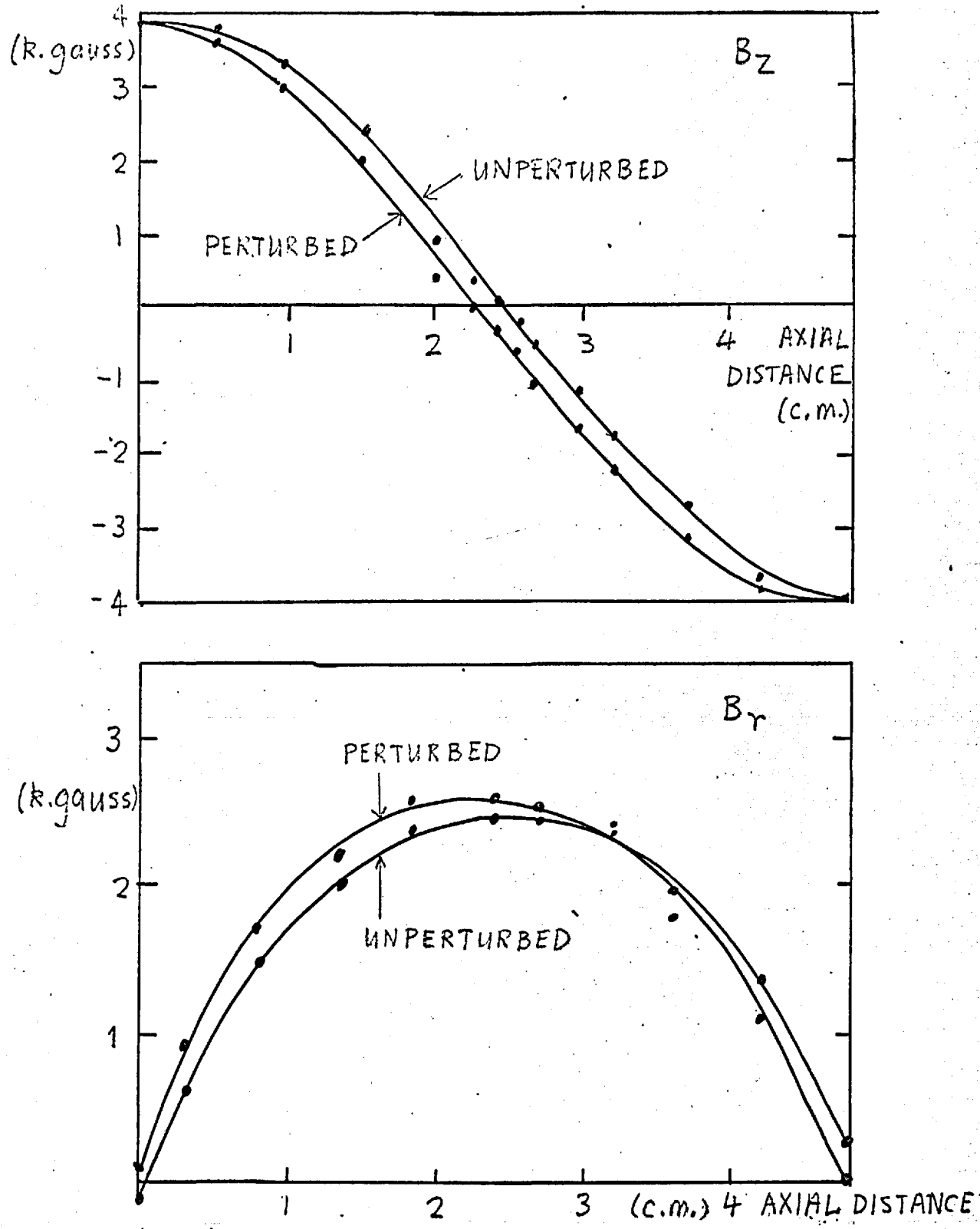

FIG (5.10) Plots of the unperturbed and plasma perturbed B_z and B_r cusp field components.

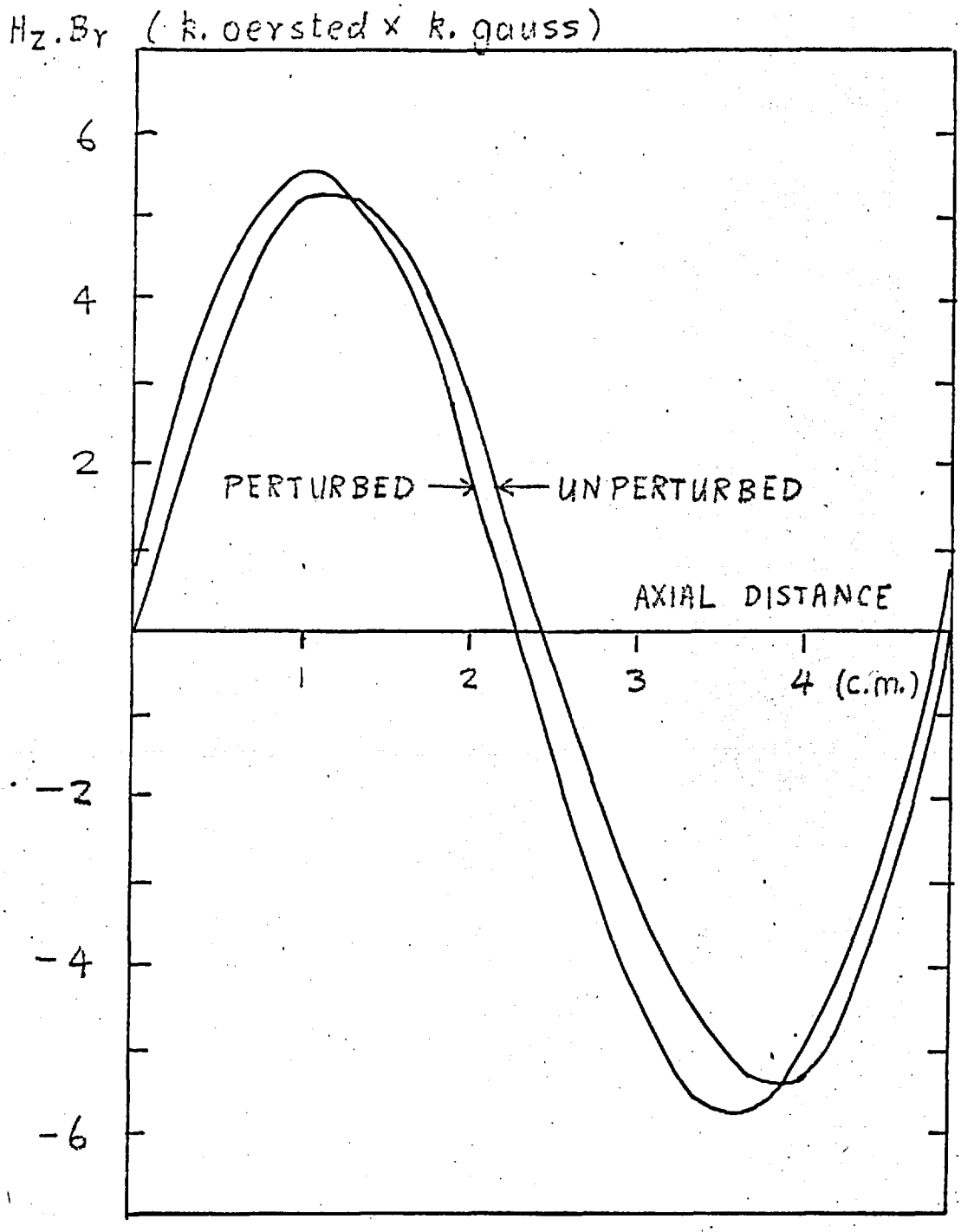

FIG (5.11) Plots of the product $H_Z.B_r$ versus axial distance based on the results shown in FIG (5.10).

$$\left.\begin{aligned} F_Z \text{ (perturbed)} &= 1.2 \text{ kg. wt.} \\ F_Z \text{ (unperturbed)} &= 0.08 \text{ kg. wt.} \end{aligned}\right\} \qquad (5.4)$$

The unperturbed value of F_Z was calculated to check the errors involved in the method of measurement since, by definition, the unperturbed value of F_Z must be zero. The direction of the force acting on the cusp coil in the plasma perturbed case was opposite to the direction of the induced electric field, consistent with the thrust on the plasma being in the same direction as the induced electric field.

(5.1.5) Ion Probe Measurements

The ion probe described in section (4.3) was scanned across the Polytron plasma from the torus wall to the plasma axis to yield a half profile for ion flux in a direction parallel to the toroidal Z axis of the system. Experiments were performed with the ion probe entrance hole alternately facing directions parallel and antiparallel to the induced electric field direction. These conditions were achieved using two methods: firstly the main bank polarity was kept fixed and the probe was alternately rotated through 180° and secondly the probe position was kept fixed and the main bank polarity alternately reversed. In all low pressure argon discharges, there was a significant systematic difference between the ion probe currents measured in the directions parallel and antiparallel to the electric field. Typical examples of the ion probe current waveforms are shown in fig. (5.12), where it can be seen that the probe current is much larger when the entrance hole faces a direction opposed to the electric field. These results are consistent with directed ion

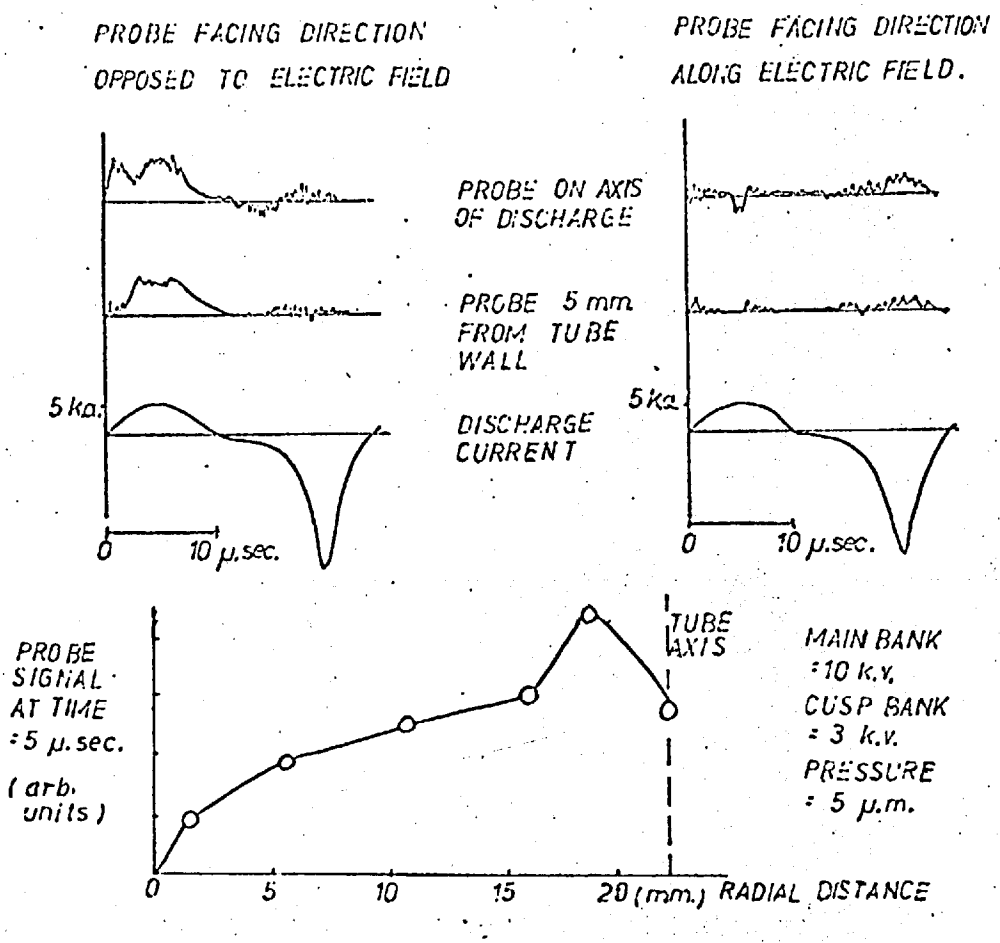

FIG (5.12) Ion probe waveforms and a half profile of ion probe current.

motion occuring within the plasma under the action of the induced electric field. From the ion probe scans across the plasma, the half profile for ion probe current shown in fig. (5.12) was constructed. This half profile has a maximum value occuring roughly 5 mm from the plasma axis, and the fall in probe current in the vicinity of the plasma axis (where B_r is small) has been tentatively ascribed to the effects of untrapped electron motion in this region.

Assuming a symmetrical profile for ion current about the plasma axis, the integral of the plot shown in fig. (5.12) has been converted into a value for total ion current in the plasma using the dimensions of the probe entrance hole and probe current measuring circuit parameters. The result together with the total discharge current measured using the Rogowski coil was

$$\left.\begin{array}{l}\text{Total ion current } (t = 5\ \mu\text{.sec.}) = 0.3 \text{ k.a.} \\ \text{Total discharge current } (t = 5\ \mu\text{.sec.}) = 5.1 \text{ k.a.}\end{array}\right\} \quad (5.5)$$

It is quite likely that the total ion current quoted in (5.5) is a gross underestimation of the true value of the total ion current, since the ion probe presented a large disturbance to the plasma and processes such as plasma stagnation and ion collisions occuring in the vicinity of the probe could easily have reduced the ion flux at the probe entrance hole. Assuming a fully ionised plasma with predominantly singly charged ions and applying equation (4.6) to the ion probe results gave an estimate of ion velocity in the region of 10^6 cm sec^{-1}.

Attempts were made to measure ion fluxes in both hydrogen and helium plasmas but the difference between the ion probe currents for probe directions parallel and antiparallel to the electric field was not significant.

As well as functioning as an ion flux detector, the ion probe described in section (4.3) also served as a detector of

plasma noise. The noise recorded in Polytron plasmas was of high frequency (10 MH_Z upwards) and presumably arose from fluctuating electric fields in the plasma. Marked changes in the noise levels for different regions of the plasma were observed. For the first half cycle of the discharge, the noise level was low at distances $>$ 1 cm from the plasma axis and increased rapidly for probe positions near the centre of the plasma. For the second half cycle of the discharge, the noise level was very large throughout the plasma around the time when the cusp field passed through zero. Thus it would appear that large noise levels were associated with plasma regions where axial electron motion was not impeded by the cusp field.

(5.1.6) Spectroscopic Measurements

The spectroscopic measurements performed on the Polytron plasmas were mainly concentrated on finding the Doppler shift of argon ion line emission in directions parallel and antiparallel to the plasma axis. A schematic drawing of the experimental arrangement is shown in fig. (5.13). The plasma radiation was sampled tangentially to the torus axis using a small mirror in a side port and a Hilger and Watts medium quartz spectrometer with scanning photomultiplier attachment was used to record the time histories and profile shapes of the line emissions. The dispersion characteristics of the spectrometer were such that the accuracy of line profile measurement increased with decreasing line wavelength and this feature dictated the use of a u.v. region line. The strongest line found experimentally in this region in argon plasmas was the argon IV 2809 Å line. The light gathering capacity of the mirror collecting system was only

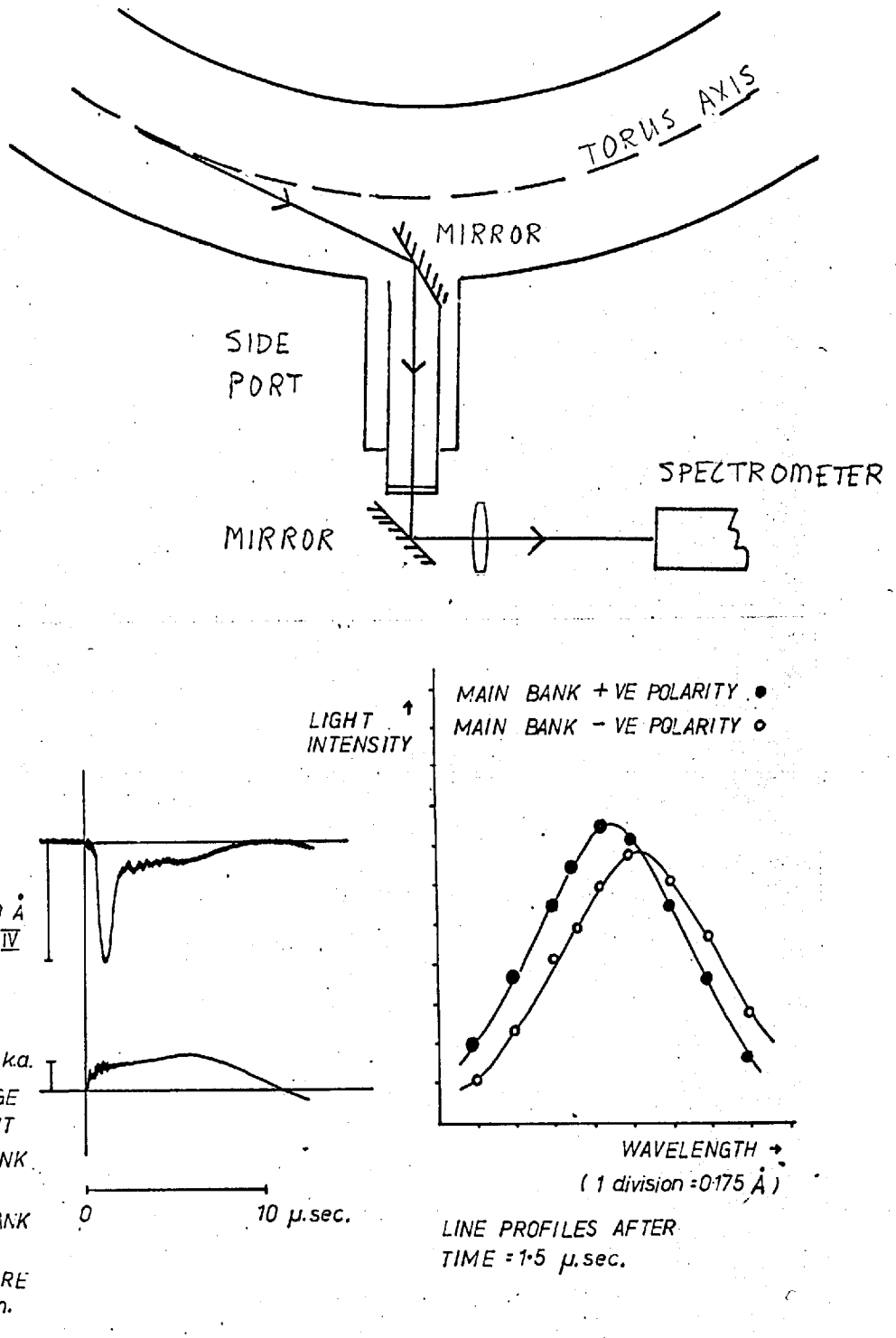

FIG (5.13) Upper: Experimental arrangement for tangential collection of light.
Lower: Time history of 2809 A line and plot of line profiles.

$\sim$ f/20 (mirror aperture divided by side port length) with the result that the spectrometer entrance slit had to be opened fairly wide to obtain a reasonable photomultiplier signal and the line profiles were mainly instrument broadened. In performing the Doppler shift measurement, the main bank polarity was reversed for each setting of the spectrometer scanning attachment to eliminate errors in reproducibly positioning the latter.

The time history of the 2809 A^{o} line in the Polytron discharge is shown in fig. (5.13) where the peak light intensity occurred 1.5 μ.sec. from the start of the discharge which roughly coincided with the time of peak Hall current in the plasma. The line profiles recorded at the time of peak light intensity for each main bank polarity are also shown in fig. (5.13) where a definite shift is discernable, although the instrumental width of each profile prevented the shift appearing as two separately resolved peaks when the two line profiles are superimposed. The direction of the shift of the profiles was in agreement with ion motion in the direction of the induced electric field. From the magnitude of the relative shift of the line profiles, a directed velocity of 1.1 10^{6} cm $sec.^{-1}$ with respect to the laboratory frame was calculated.

(5.1.7) Photography

Argon plasma discharges in the small torus were photographed over a wide range of Polytron conditions using an image convertor camera. Camera pictures of the region between a pair of cusp coils for discharges at 5, 50 and 300 m.torr pressure are shown in fig. (5.14), where the framing sequence is

MAIN BANK 10k.v.
CUSP BANK 3 k.v.
GAS PRESSURES (m.torr)

TIMING SEQUENCE

5



50

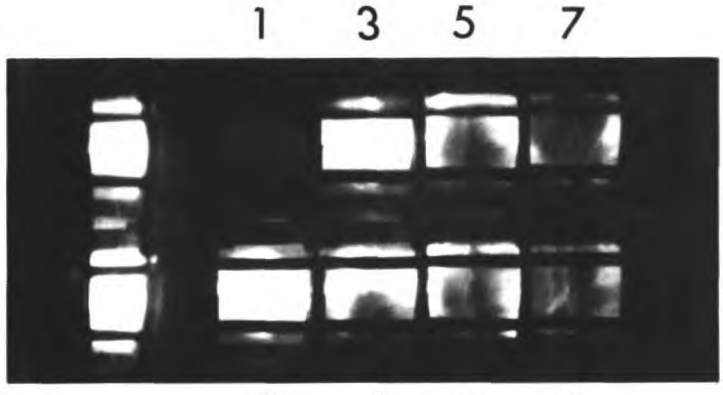

300

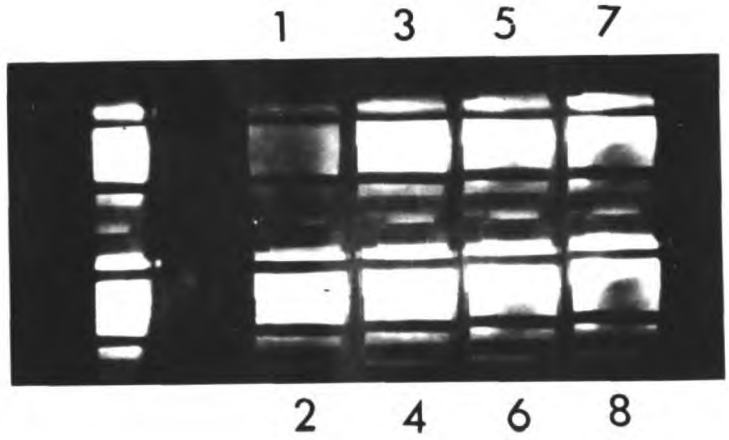

SMALL TORUS ARGON PLASMAS

FIG (5.14)

listed on each set of pictures and the framing interval is 0.5 μ.sec. The two bright images on the extreme left of each picture are parts of time integrated images and should be ignored. We have listed below some characteristics of plasma behaviour in the Polytron that were inferred from the camera pictures. The photographic information has also been related to the results of the flux loop diagnostics described in section (5.1.2).

1. Plasma leakage from the cusp field loss cone regions was visible at times > 0.5 μ.sec. after the initiation of the main discharge. The plasma leakage was clearly seen in the camera pictures as bright rings of light at the torus walls in the mid-plane between cusp coils.

2. In low pressure discharges (< 20 m.torr) the leakage of plasma out of the cusp field appeared to be the only cause of plasma loss and the plasma remained cusp shaped throughout the discharge first half cycle. However for main bank voltages of 15 and 20 k.v. the edges of the cusped plasma appeared ragged. In fig. (5.6) the flux loop signals (Hall current signals) at low pressures can be seen to be composed of oscillations, whose amplitude varies strongly with main bank voltage, superimposed on a background signal which varies in unison with the discharge current. These flux loop waveforms agree well with the camera pictures and suggest an instability oscillation inside the plasma where the amplitude of oscillation increased rapidly with applied electric field but where the oscillation was never large enough to change the overall shape of the plasma or completely destroy the Hall currents in the plasma.

3. For intermediate gas pressures (50 to 300 m.torr), camera pictures showed that a cusp shaped plasma only existed for an interval of time from 1.5 to 4 μ.sec. A comparison of the

camera pictures and flux loop waveforms for the same gas pressures showed excellent agreement between the lifetimes of the cusped plasmas and the duration of the Hall current signals. The termination of the cusp shaped plasma regime was characterised by the plasma moving as a whole in the direction of the applied electric field and the displacement was accompanied by the break up of plasma in a time $\sim$ 0.5 μ.sec. As the plasma broke up the Hall current signals were completely destroyed.

4. For high pressure discharges (> 500 m.torr), the camera pictures showed a plasma which was only slightly cusp shaped and which became more uniform with increasing gas pressure. No break up of plasma was observed and the Hall current signal was almost exactly proportional to the discharge current throughout the first half cycle.

(5.2) LARGE TORUS RESULTS

The small torus experiments described above have shown that ion acceleration mechanisms in the plasma were limited by the onset of plasma instabilities and that plasma leakage to the torus walls occurred. A significant feature of the small torus assembly was that the torus minor diameter (44 mm) was much less than the cusp coil diameter (89 mm) and thus it was difficult to achieve a small cusp field loss cone. In an attempt to overcome this difficulty, the torus minor diameter was increased to 71 mm whilst retaining the same cusp coil size. This modification of the apparatus increased the radial component of cusp field at the torus walls and reduced the size of the loss cone. Also, the minimum gas pressure for consistent

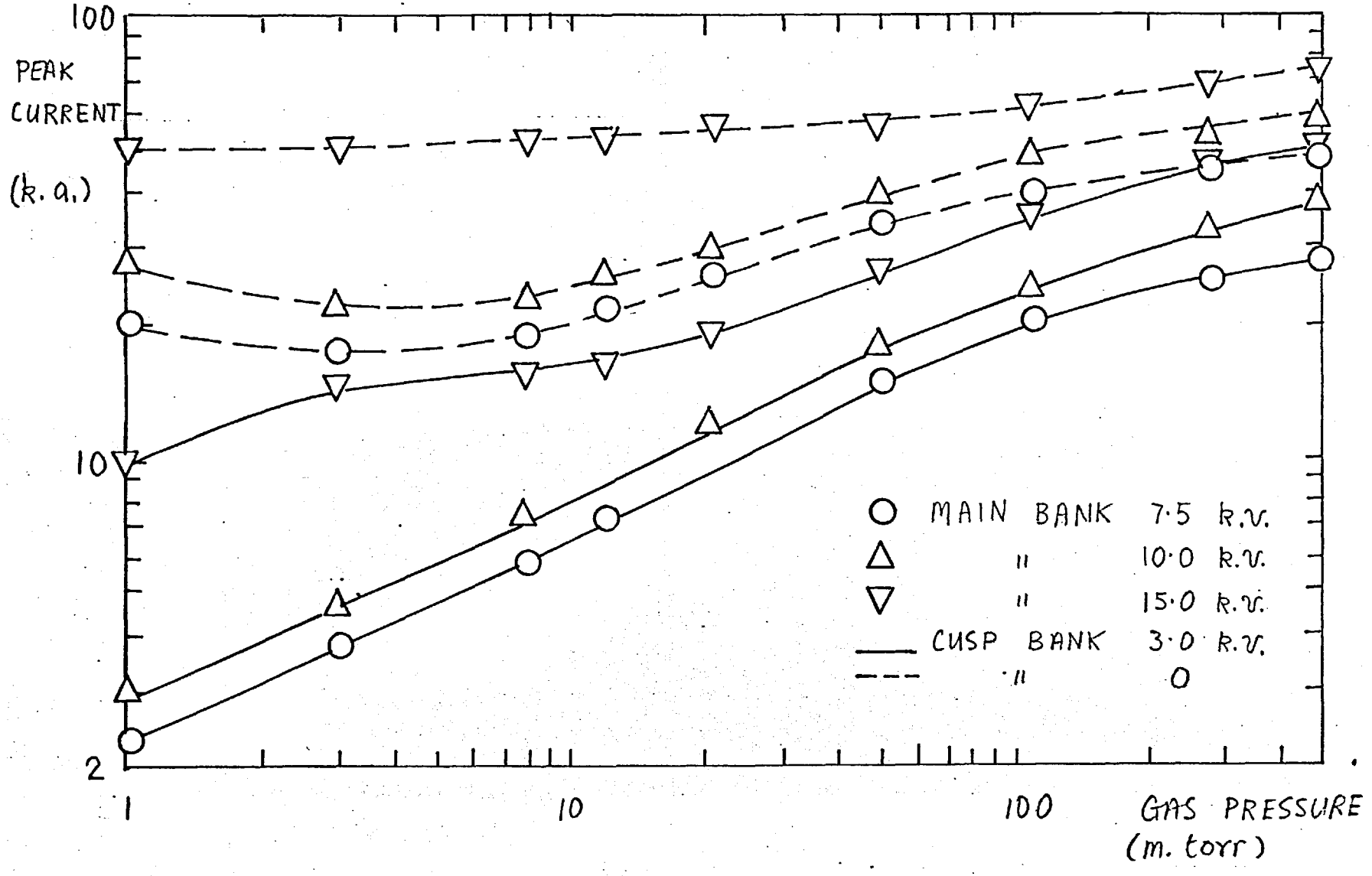

FIG (5.15) Plot of discharge currents in large torus argon plasmas.

plasma preionisation in the larger torus was about half that in the small torus (see table (2.3)). It was hoped that these two factors would produce a significant improvement in the stability and confinement of Polytron plasmas.

The wide range of diagnostics used on the small torus plasmas were not all applied to the large torus plasmas and a detailed study of argon, helium and deuterium plasmas was made using only the Rogowski coils and the image converter camera.

(5.2.1) Discharge Current Measurements

The experimental measurement of discharge currents in the large torus plasmas consisted of a repetition of the measurements described in section (5.1.1). A plot of the peak first half cycle currents in argon plasmas analagous to that shown in fig. (5.3) is given in fig. (5.15). A comparison of the above two plots shows that the cusp field produced a similar amount of electron trapping (impedence to axial electron motion) in both sizes of torus.

(5.2.2) Photography in Argon Plasmas

Camera pictures for argon discharges in the large torus at gas pressures of 1, 3, 10 and 50 m.torr are shown in fig.(5.16). These pictures were part of a wide range study of argon discharges and the following plasma behaviour was inferred.

1. The plasma leakage out of the cusp field loss cones was

slightly reduced compared to the small torus discharges, and was apparent after ~ 1 μ.sec. from the start of the main discharge.

2. At the lowest working pressure of 1 m.torr, cusp leakage appeared to be the only plasma loss mechanism and no gross plasma instabilities were observed.

3. For gas pressures between 3 and 50 m.torr, a cusp shaped plasma was initially produced which changed after a short interval to become an axial plasma filament (together with cusp leakage). The formation time for the central filament varied from 0.8 μ.sec. at 3 m.torr to 2 μ.sec. at 50 m.torr. The central filament was unstable and broke up by a kink type instability over a period of 2 to 3 μ.sec.

4. For gas pressures above 60 m.torr the Polytron discharge resembled a straightforward pinched discharge. A nearly uniform collapse of plasma occurred with no plasma leakage to the torus walls. The central pinched discharge showed the usual gross hydromagnetic instabilities.

A comparison of the above results with those described in section (5.1.7) shows the marked difference in the behaviour of argon plasmas in the large and small Polytron discharges.

(5.2.3) Photography in Deuterium and Helium Plasmas

Camera pictures of discharges in deuterium at 5, 15, 30 and 200 m.torr gas pressure are shown in fig. (5.17). From the range of discharges studied, the following plasma behaviour was interpreted.

MAIN BANK 10 k.v.

CUSP BANK 3 k.v.

GAS PRESSURES (m.torr)

TIMING SEQUENCE

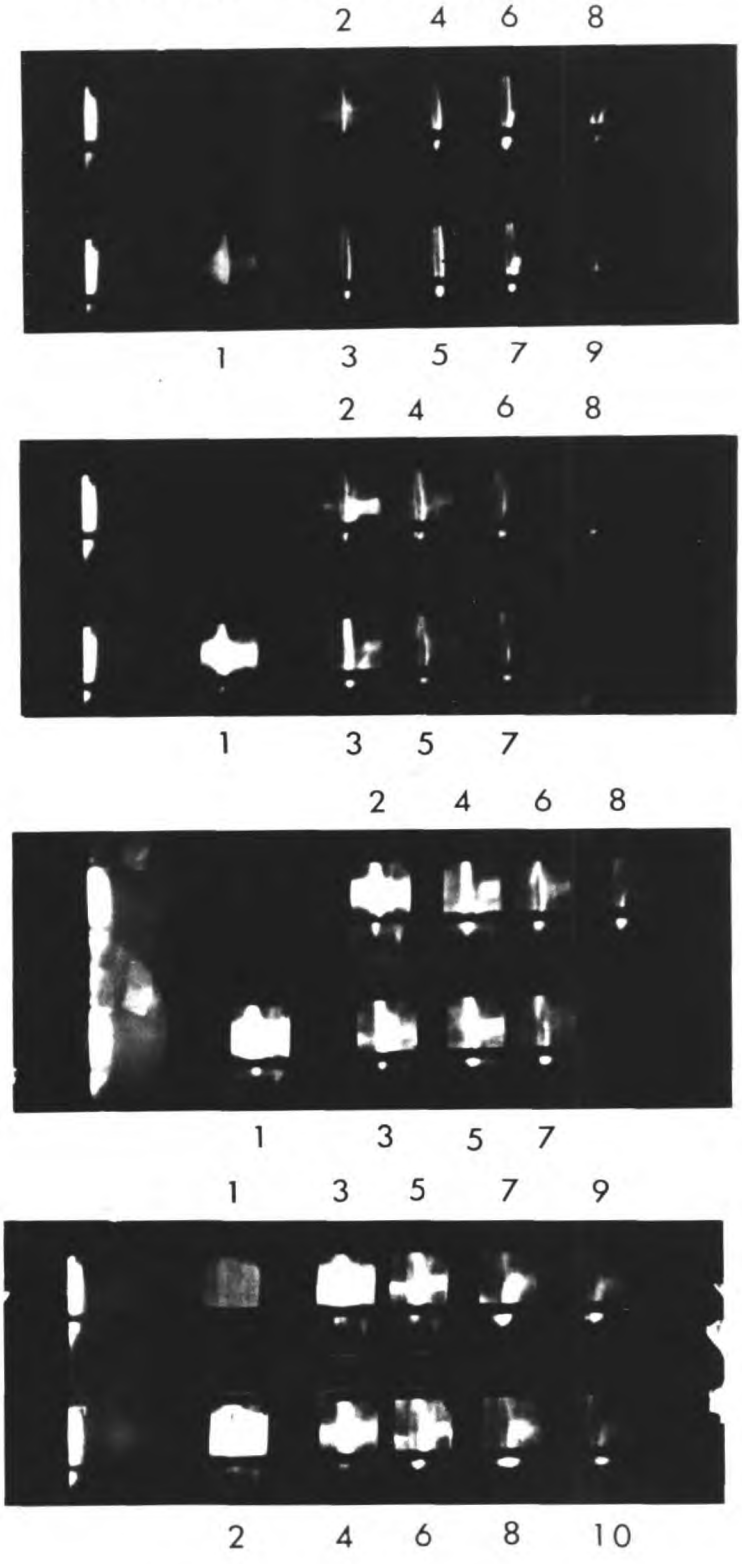

LARGE TORUS ARGON PLASMAS

FIG (5.16)

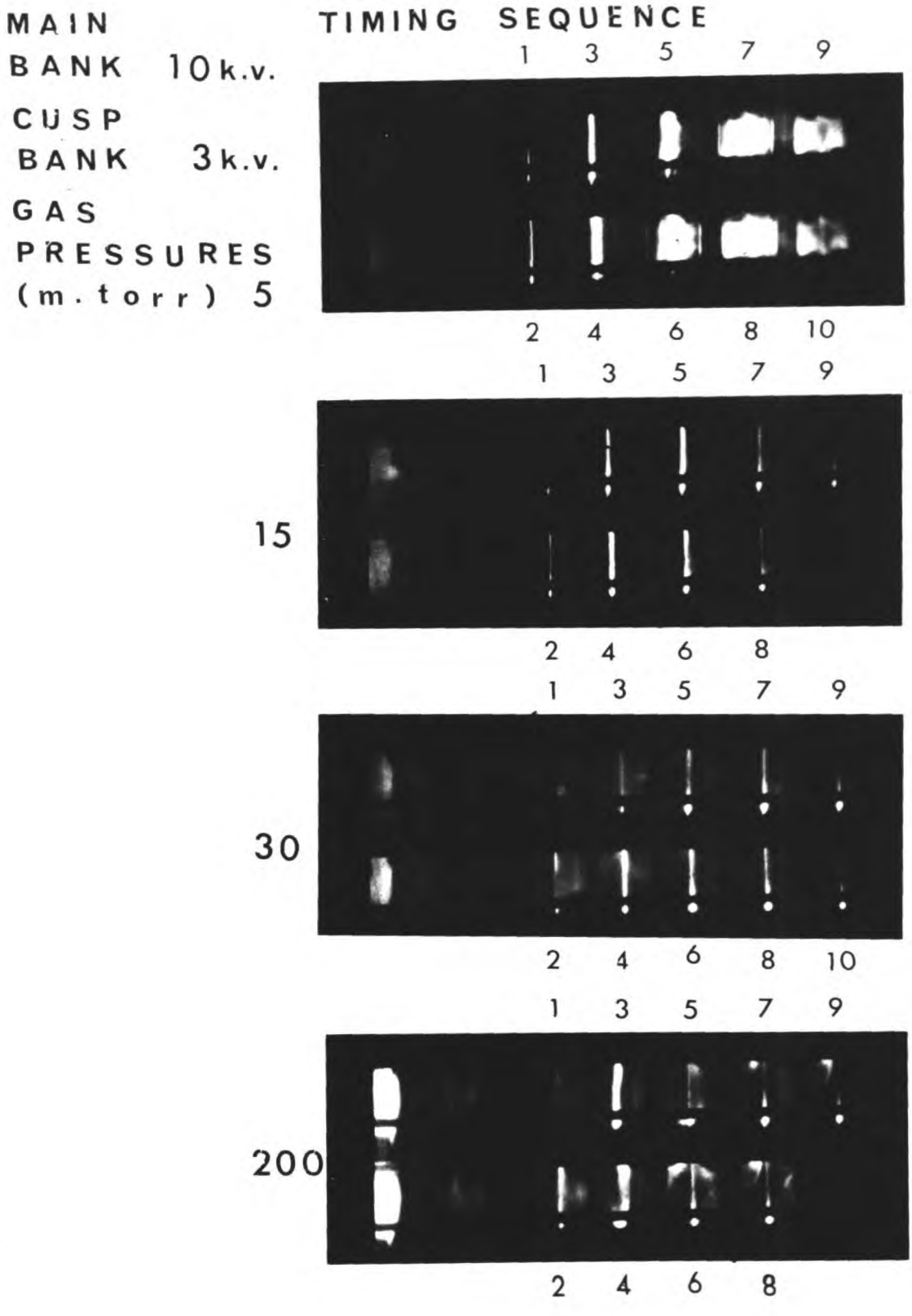

LARGE TORUS DEUTERIUM PLASMAS

FIG (5.17)

1. The low pressure discharges ($<$ 10 m.torr) showed plasma leakage from the cusp field loss cones growing rapidly from the start of the discharge. The width of the loss cone ring of light at the torus walls increased with time, leading to wide spread contact of plasma with the walls, after 2 to 3 μ.sec.

2. With increasing gas pressure in the range 20 to 100 m.torr, the plasma leakage became progressively smaller: the leakage at 100 m.torr being barely discernable. There was no formation of a central current filament or plasma break up over the discharge first half cycle.

3. For gas pressures above 200 m.torr the plasma appeared to be contained for 1 to 2 μ.sec. followed by strong plasma leakage out of the loss cones. After a further 2 μ.sec. this leakage led to the central cusp shaped region appearing dark surrounded by bright plasma: a negative image of the cusp region. This negative cusp image disappeared slowly towards the end of the first half cycle.

The overall behaviour of helium plasmas in the large torus was very similar to that described above for deuterium plasmas. The main difference in behaviour was that the rapid spread of plasma out of the cusp loss cone persisted to higher gas pressures ($\sim$ 50 m.torr).

From the whole range of camera pictures of large torus Polytron discharges, the gas pressure regions where the plasma appeared most stable and where plasma leakage was small have been listed in table (5.2).

TABLE (5.2)

GAS	OPTIMUM GAS PRESSURE FOR PLASMA STABILITY AND CONFINEMENT (m.torr)
A	< 3
He	50 - 150
D	20 - 100

CHAPTER 6

DISCUSSION AND CONCLUSIONS ON THE POLYTRON

In this chapter the theoretical studies on the Polytron that have been performed by Haines (1)(2) and Dunnett (5)(6) are reviewed. The results of Dunnett's calculations are compared with the experimental results presented in the previous chapter. A discussion of the confinement and stability of plasma is given and finally the overall conclusions on this initial experimental study of the Polytron are stated.

(6.1) REVIEW OF THEORETICAL WORK ON THE POLYTRON

Haines' original calculations on the Polytron (1)(2) were performed using a hydromagnetic plasma model possessing the following characteristics:

1. Infinite cylindrical geometry and azimuthal symmetry were assumed.

2. The radial motion of the plasma and radial currents in the plasma were neglected.

3. A uniform incompressible plasma of constant outer radius was assumed and the mass density, electron density and conductivity of the plasma were also taken to be constant.

4. The radial component of the multi-cusped magnetic field existing throughout the interior of the plasma was taken to be of the form

$$B_r = B_o \sin k_o Z \qquad (6.1)$$

where π/k_o = cusp coil separation

With these assumptions, Haines solved the hydromagnetic equation of plasma motion and the generalised Ohm's law equation (10) for the Polytron plasma and showed that it was possible for the ions to carry the axial current in the plasma in preference to the electrons. Haines also derived an expression for the characteristic time for the ion acceleration process and criteria for the prevention of runaway particles, the prevention of plasma leakage out of the cusp field and the balance of the plasma centrifugal force in toroidal geometry.

Dunnett (5)(6) has extended Haines' work by using a more realistic cusp field approximation. Dunnett again assumed the plasma characteristics 1 to 3 quoted above, but he represented the components of the multi-cusped magnetic field inside the plasma by the equations

$$\left.\begin{aligned} B_r &= \tfrac{1}{2} k_o \Upsilon \sin k_o Z \\ B_Z &= B_o + B_1 \cos k_o Z \end{aligned}\right\} \qquad (6.2)$$

Dunnett also made use of the work of Thonemann and Kolb (138) who have discussed the effects of Hall rotation in θ pinches, and an important addition to Haines' work was made by taking into account the effects of magnetic fields generated by the Hall currents in the plasma. In physical terms, the Hall currents that are established in the plasma regions between cusp coils are responsible for producing a secondary cusped magnetic field configuration which, in turn, is responsible for the generation of secondary Hall currents in the regions of the cusp coils themselves. These secondary Hall currents oppose the currents

flowing in the cusp coils and can lead to a situation where the original cusp field configuration in the plasma is nullified (ie. the cusp field is thrown out of the plasma). The expression for the critical electric field E_c which caused the cusp field to be thrown out of the plasma was found to be of the form

$$E_c = \text{constant} \frac{k_o (\overline{B_r})^2}{n} \qquad (6.3)$$

For a high upper limit to the applied electric field in the Polytron, equation (6.3) shows that large cusp fields and low plasma densities are necessary.

In order to relate the theoretical work as closely as possible to the experimental conditions, the electric field and cusp field used in the theoretical calculations were given time variations which closely resembled those measured for the oscillatory discharge of the main bank and cusp bank.

With the assumptions described above, Dunnett solved the hydromagnetic equations of plasma motion and the generalised Ohm's law equation using a computer to give theoretical waveforms for the discharge currents and the primary and secondary Hall currents in Polytron plasmas over a wide range of conditions.

(6.2) COMPARISON OF THEORY AND EXPERIMENT

The discharge current waveforms computed by Dunnett (5)(6) showed excellent qualitative agreement with those recorded in the experiment with small first half cycle values and large second half cycle values when the applied cusp field passed through zero. In fig. (6.1) the computed variations of the

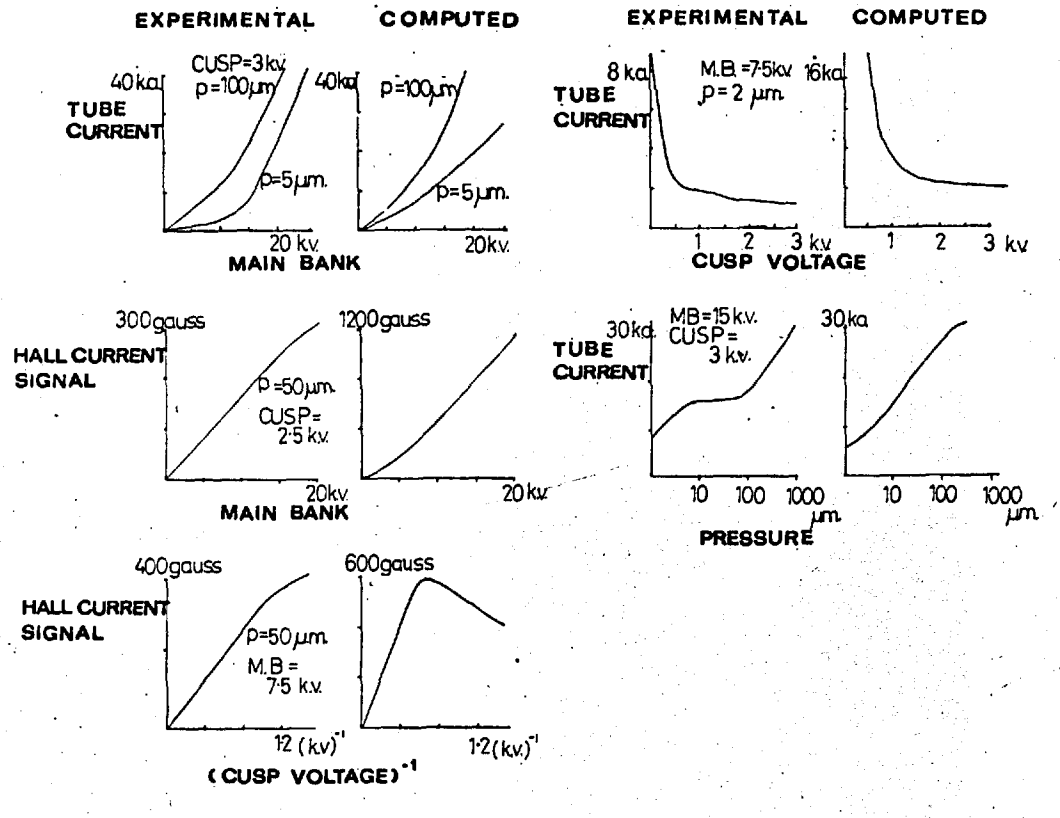

FIG (6.1) Comparison of experimental and computed results.

discharge current and Hall current signal (average magnetic field produced by Hall currents) with the main bank and cusp bank voltages have been compared with the experimentally measured variations of the same parameters. Since no reliable measurements of the conductivity, electron density or electron temperature of the plasma have been made in the Polytron, the plasma conductivity had to be assumed in the computer calculations. This assumption makes a quantitative comparison of the computed and experimental results rather meaningless, however good qualitative agreement between both sets of results can be seen in fig. (6.1).

(6.3) DISCUSSION ON PLASMA CONFINEMENT AND STABILITY

The camera pictures of the Polytron have shown plasma leakage out of the cusp fields in both sizes of torus at times 0.5 to 1 μ sec. after the start of the main discharge. In physical terms, plasma leakage in the Polytron is predicted unless the directed ion velocity in the plasma is greater than the ion thermal speed. Thus we conclude that, in the experimental discharges, the increase in ion thermal speed due to Ohmic heating effects outweighed the increase in directed ion velocity produced by the applied electric field. The fact that plasma leakage in both sizes of torus was observed so soon after the start of the main discharge suggested that the plasma preionisation conditions had a major effect on the Polytron behaviour. The microwave measurements made on the preionised plasma in the presence of the rising cusp field, described in section (3.6), showed that the plasma was compressed into the axial region of the torus. This plasma compression was undoubtably unfavourable towards the ideal operation of the

Polytron, since the bulk of the plasma was forced into a region where the radial component of the cusp field was small. Thus an enhanced electron discharge current and enhanced Ohmic heating effects were to be expected in the main discharge. Dispensing with the preionisation system and allowing the main discharge to ionise the plasma avoided the plasma compression problem, but this procedure was not successful in practice since the strong cusp fields inhibited gas breakdown except at high pressures.

With regard to the stability of the experimental Polytron discharges, it is very difficult to draw any definite conslusions from the results obtained. Disturbing features of the stability were the quite different behaviour of argon plasmas in the two sizes of torus and the fact that, with decreasing gas pressure, the stability improved in argon plasmas but became worse in helium and deuterium plasmas.

(6.4) CONCLUSIONS

The conclusions that have been drawn from the initial Polytron experiments described in the preceeding chapters are summarised as follows:

1. Discharges in the Polytron have been shown to be characterised by low values of the axial current consistent with the trapping of electrons by the multi-cusped magnetic field.

2. The drift of the trapped electrons under the action of the applied E_Z and B_r field components giving rise to azimuthal Hall currents has been verified from measurements of the

magnetic fields associated with the Hall currents. The magnitudes of the Hall currents have been shown to be roughly proportional to the applied electric field and inversely proportional to the applied cusp field.

3. Directed ion motion in the direction of the applied electric field has been measured in argon plasmas using ion probes and from the Doppler shift of ion line radiation emitted tangentially from the plasma. The results indicated an argon ion directed velocity around 10^6 cm sec^{-1} after 1.5 μ sec.

4. Camera pictures of the Polytron have shown plasma leakage out of the cusp field from the early stages of the main bank discharge. This plasma leakage has been tentatively ascribed to enhanced Ohmic heating in the main discharge as a result of plasma compression into the axial regions of the torus by the rising cusp fields.

5. Camera pictures and Hall current diagnostics have shown the presence of numerous instabilities in the Polytron discharges. Radically different plasma behaviour was observed in two different sizes of torus for otherwise identical discharge conditions. The growth of plasma instabilities was found to set an upper limit to the duration of the ion acceleration processes in the plasmas.

S E C T I O N II

SECTION II

INTRODUCTION

In this section, an experimental and theoretical study of highly ionised plasma decay in the electron density range 10^{16} to 10^{13} cm^{-3} is presented. This study arose directly from experiments performed on the preionisation discharge in the Polytron and a wide range of plasma afterglows have been investigated.

During the past ten years, a considerable amount of work has been published on the subject of plasma afterglows (most of the references from (62) to (102) inclusive). In almost all the experimental work that has been reported, electron density measurements have been made using microwave or 3.39 μm wavelength laser interferometers and electron temperature measurements have been made from the line intensities of radiative transitions. A main feature of our diagnostics of afterglow plasmas has been the use of a submillimetre wavelength (337 μm) continuous gas laser as the source of a Mach-Zehnder type interferometer. The 337 μm laser radiation enables plasma electron densities to be measured up to 10^{16} cm^{-3} (well above the upper density limit to microwave propogation) with a much greater accuracy than can be achieved using 3.39 μm laser radiation. The near parallel output beam of the 337 μm laser also makes measurement of the e.m. wave attenuation in the plasma relatively easy. In a highly ionised afterglow, an estimate of the plasma electron temperature can be obtained from the measured 337 μm wave attenuation using the electron-ion collision frequency relationship (10). With the 337 μm laser interferometer, measurements have been made on 125 different

afterglow plasmas of the decay of electron density in the range $5.\ 10^{15}$ to $5.\ 10^{13}$ cm^{-3} and the decay of electron temperature in the range $2.\ 10^{4}$ to $2.\ 10^{3}$ ^{o}K. The decay of electron density below $6.\ 10^{13}$ cm^{-3} in the afterglow plasmas has been measured using two types of 70 GH_Z microwave interferometer.

The decay of laboratory plasma in the electron density range 10^{16} to 10^{13} cm^{-3} is shown to be dominated by the three body recombination process with an electron as the third body. The value of the recombination coefficient for this three body process has been discussed by several workers (71)(80)(82) and it has been shown to be strongly dependent on the plasma electron temperature as well as the plasma electron density, so that the rate of plasma recombination is governed by the energy balance established in the plasma. In most afterglow conditions, the ionisation energy liberated when an electron and an ion recombine to form a ground state atom is much greater than the average thermal energy of each particle species in the plasma. Thus the recombination process can produce a considerable heating effect in a decaying plasma. A state of quasi-equilibrium is established in the plasma where the recombination rate is self adjusting, so that the rate of energy released by recombination plus the rate of change of thermal energy of the plasma equals the power radiated from the plasma plus the rate energy loss due to thermal conduction. It can be seen therefore that the decay rate of a highly ionised afterglow plasma can only be satisfactorily described by a detailed consideration of the complex physical processes occuring in the plasma.

In the theoretical work that is presented, the energy transport inside a cylindrical plasma afterglow contained in a discharge tube whose walls remain fixed at $300^{o}K$ is considered in detail. The above work serves as a basis for a new series of

computer solutions to the equations for the energy balance and recombination processes occurring in a non-uniform plasma. In solving the above equations, the temperatures of all particle species in the plasma appear as variables unlike previously published solutions (74)(75) to similar equations where the atom temperature was held fixed.

The results of preliminary measurements of electron densities and electron temperatures in afterglow plasmas using the 337 μm laser interferometer have been reported (141) in August 1968 and published (142) in October 1968.

CHAPTER 7

PLASMA DIAGNOSTICS WITH FAR INFRARED LASERS

The uses of far infrared gas lasers in the diagnostics of plasmas is discussed in this chapter. Detailed consideration is given to the design and construction of a plasma interferometer employing a 337 micron wavelength gas laser as the source of radiation. It is shown that far infrared gas lasers can play a unique and powerful role in diagnosing a wide range of laboratory plasmas.

(7.1) FAR INFRARED RADIATION SOURCES

The two main requirements for plasma interferometry which all sources of radiation must satisfy can be summarised:

(a) The source should be sufficiently powerful for the probing e.m. beam to be distinguished against the background of plasma emission in the source wavelength region.

(b) The source should be sufficiently coherent and monochromatic so as to enable phase shifts of at least several tens of wavelengths to be measured.

In the infrared wavelength region 50 to 1000 microns, possible sources of radiation are as follows:

1. Harmonics of klystron frequencies easily satisfy condition (b) above but power levels are extremely low due to inefficient frequency convertors. Also waveguide for true TE_{01} mode propogation in this wavelength region has an inherently high loss.

2. Some portion of the continuous emission spectrum obtained from a mercury lamp could be used. The luminance of a standard mercury lamp is $2.5\,\sigma^2$ nano watts per steradian per cm^2 of source where σ is the wave number in cm^{-1}. Condition (b) above means that the output of a mercury lamp usable for plasma interferometry is only a few microwatts per steradian per cm^2 of source.

3. Far infrared gas lasers have spectral widths limited by the Doppler broadened line width of the lasing transition and condition (b) above is easily satisfied. Power outputs of continuous wave (c.w.) lasers in this wavelength region are typically several tens of milliwatts (33), and pulsed laser operation can raise the power output to several watts.

From above it is clear that the gas laser is the best available source for plasma interferometry in the far infrared region. Also the fact that the laser radiation output is in the form of a nearly parallel beam makes the transmission of the e.m. beam through the plasma and the design of a plasma interferometer considerably easier in practice.

(7.2) FAR INFRARED GAS LASERS

Stimulated emission at far infrared wavelengths was first reported by Crocker et al. (29) for a pulsed water vapour laser. Several lasing wavelengths were found in the region between 23 and 118 microns, and the laser action was ascribed to vibrational or rotational transitions in the molecular vapour system. Soon afterwards, Gebbie et al. (30) reported pulsed laser operation at 337 microns wavelength in organic cyanide vapours. Matthias et al. (31) reported laser action at several

other wavelengths between 72 and 373 microns in pulsed organic cyanide vapours. Continuous wave laser action at 337 and 311 microns wavelength was first reported by Gebbie et al. (32), and Muller and Flescher (33) have described a comprehensive study of c.w. oscillation in gaseous compounds of C, N and H or D. The strongest lines for c.w. oscillation were found to occur at 311 and 337 microns wavelength.

The attenuation characteristics of the earth's atmosphere in the far infrared region are dominated by the absorption lines of water vapour (34), and one of the most favourable transmission 'windows' exists around 345 microns showing that the 337 micron laser line is well placed for low loss transmission. Borroughs et al. (35) have measured the attenuation index for 337 micron laser transmission in a clear atmosphere as 50 ($\pm$ 5) dB per km at 0°C and S.V.P.

Several explanations of the source of lasing action in organic cyanide vapours have been proposed (36) but the correct explanation of the origin of the 311 and 337 micron lines appears to be due to transitions amongst vibrational states of HCN molecules as proposed by Lide and Maki (37).

The absolute frequencies of the 311 and 337 micron transitions have been measured to accuracies of a few parts in 10^{7} by Hocker and Javan (38) (39) who frequency mixed the laser output with high order klystron harmonics. The measured frequencies were 964·3134 and 890·7607 $G.H_{Z}$ respectively.

(7.3) ELECTROMAGNETIC WAVE PROPOGATION IN A PLASMA

The propagation of electromagnetic waves through a plasma is described in many standard text books (40)(41)(42). We will

only be concerned here with picking out from the standard theory those quantities and equations that are required for subsequent calculations.

Manipulation of Maxwell's equations gives the harmonic wave equation for a uniform isotropic medium of finite conductivity and nett charge neutrality in the form

$$\nabla^2 \vec{E} + (k_o \mu^*)^2 \vec{E} = 0 \qquad (7.1)$$

where k_o = vacuum wave number = ω/c
ω = angular frequency of applied electric field $\vec{E}$
μ^* = complex refractive index of the medium

The complex refractive index μ^* can be written in the form

$$\mu^* = \left(1 - \frac{j\sigma^*}{\epsilon_o \omega}\right)^{\frac{1}{2}} \qquad (7.2)$$

$$\mu^* = \mu_r + j\,\mu_i \qquad (7.3)$$

where σ^* = electrical conductivity of medium (complex)
ϵ_o = vacuum permittivity
μ_r = real part of μ^*
μ_i = imaginary part of μ^*

The plane wave solutions of equation (7.1) for $\vec{E}$ are transverse in the form

$$\left|\vec{E}\right| = E_o \exp\left[j\,(\omega t - k_o \mu^* z)\right] \qquad (7.4)$$

indicating that the wavelength and attenuation in the medium are incorporated in the term for conductivity. An expression for conductivity can be derived in a simple form from the solution of the equation of motion for the electrons with added collisional damping

$$m \frac{d\vec{v}}{dt} + \nu m \vec{v} = -e \vec{E} \qquad (7.5)$$

where m = electron mass
$\vec{v}$ = electron drift velocity
ν = collision frequency for momentum transfer

The steady state solution of equation (7.5) for yields a complex conductivity of the form

$$\sigma^* = \frac{ne\vec{v}}{\vec{E}} = \frac{ne^2}{m(\nu + j\omega)} \qquad (7.6)$$

where n = electron number density.

The expression (7.6) for σ^* can be re-written in the form

$$\sigma^* = \epsilon_o \left[\frac{\omega_p^2}{\nu + j\omega} \right] \qquad (7.7)$$

where $\omega_p = \left[\frac{ne^2}{\epsilon_o m} \right]^{\frac{1}{2}}$ (7.8)

ω_p is the natural oscillation frequency of the free electron component and is called the plasma frequency. The cut-off electron density n_c for the upper boundary to wave propogation is defined by the inverse of equation (7.8)

$$n_c = \frac{\epsilon_o \omega^2 m}{e^2} \qquad (7.9)$$

Combining equations (7.2) (7.3) and (7.7) gives expressions for the real and imaginary parts of the complex refractive index as

$$\mu_r^2 = \frac{1}{2}\left\{1 - \frac{\omega_p^2}{\omega^2 + \nu^2}\right\} + \frac{1}{2}\left[\left\{1 - \frac{\omega_p^2}{\omega^2 + \nu^2}\right\}^2 + \left\{\frac{\omega_p^2}{\omega^2 + \nu^2} \cdot \frac{\nu}{\omega}\right\}^2\right]^{\frac{1}{2}} \qquad (7.10)$$

$$\mu_i^2 = -\frac{1}{2}\left(1 - \frac{\omega_p^2}{\omega^2+\nu^2}\right) + \frac{1}{2}\left[\left(1 - \frac{\omega_p^2}{\omega^2+\nu^2}\right)^2 + \left(\frac{\omega_p^2}{\omega^2+\nu^2}\cdot\frac{\nu}{\omega}\right)^2\right]^{\frac{1}{2}} \quad (7.11)$$

The indices μ_r and μ_i specify wave propogation in the plasma in terms of electron density and collision frequency.

It is often useful to specify the attenuation coefficient α and the phase coefficient β where

$$\alpha = \mu_i \omega/c \quad (7.12)$$

$$\beta = \mu_r \omega/c \quad (7.13)$$

α represents the wave AMPLITUDE attenuation coefficient defined on the usual exponential scale.

(7.4) E.M: WAVE PROPOGATION IN A LOW LOSS PLASMA

We will consider the form of e.m. wave propogation in a plasma below the cut off point, ie.

$$n < n_c \quad \text{or} \quad \omega > \omega_p \quad (7.14)$$

In this region, provided $\nu \ll \omega$, the plasma behaves as a low loss dielectric.

From equation (7.10) the form of the (real) plasma refractive index reduces to

$$\mu = \left[1 - \frac{\omega_p^2}{\omega^2}\right]^{\frac{1}{2}} \quad \text{or} \quad \left[1 - \frac{n}{n_c}\right]^{\frac{1}{2}} \quad (7.15)$$

We note that μ is very insensitive to ν when $\nu \ll \omega$.

The phase shift ϕ introduced by a uniform plasma in a transmission path is

$$\phi = (1-\mu)\frac{2\pi l}{\lambda} \quad (7.16)$$

where l = length of plasma.

Hence, from (7.15), when $n << n_c$

$$\phi \simeq \frac{\pi n \ell}{n_c \lambda} \qquad (7.17)$$

The quantity $(n_c \lambda)^{-1}$ therefore reflects the accuracy to which electron density can be measured in an interferometer, assuming that the minimum value of ϕ that can be measured is independent of λ. Table (7.1) shows a comparison between values of n_c and $(n_c \lambda)^{-1}$ corresponding to the HCN laser wavelength and the wavelengths used in conventional microwave and near infra-red laser interferometers.

TABLE (7.1)

WAVELENGTH	SOURCE	n_c (cm^{-3})	$(n_c \lambda)^{-1}$ (cm^2)
337 μm	HCN laser	$9.8\ 10^{15}$	$3.02\ 10^{-15}$
3.39 μm	He - Ne laser	$9.7\ 10^{19}$	$3.04\ 10^{-17}$
2.25 mm	Klystron	$2.2\ 10^{14}$	$2.02\ 10^{-14}$

From table (7.1), we can see that plasma electron densities can be measured with an HCN laser up to a cut off density value which is around 50 times larger than the upper limit of microwave diagnostics, and that the accuracy of electron density measurement is around 100 times better than can be achieved using a 3.39 micron helium-neon laser. Thus, the HCN laser wavelength of 337 micron ideally bridges the gap between the other two conventional wavelengths in terms of plasma electron density diagnostics.

From equations (7.11) and (7.12), when $n < n_c$ and $\nu \ll \omega$ we obtain an expression for the attenuation index as

$$\alpha = \frac{\nu}{2c} \frac{n}{n_c} \cdot \left[1 - \frac{n}{n_c} \right]^{-\frac{1}{2}} \qquad (7.18)$$

The characteristic attenuation length d for wave amplitude attenuation is defined by the inverse of equation (7.18)

$$d = (\alpha)^{-1} = \frac{2c}{\nu} \frac{n_c}{n} \left[1 - \frac{n}{n_c} \right]^{\frac{1}{2}} \qquad (7.19)$$

In a partially ionised gas, such as an afterglow plasma, the collision frequency ν is a combination of collisions of electrons with ions and neutrals.

The collision frequency ν_{ei} due to Coulomb collisions between electrons and ions has been worked out by Spitzer (10), in terms of the cumulative effect of many distant encounters as

$$\nu_{ei}_{\text{SPITZER}} = 2{\cdot}6 \; n Z \left[T_e \right]^{-3/2} \ln.\Lambda \qquad (7.20)$$

where Z = ionic charge

$\ln.\Lambda$ = Coulomb logrithm

Spitzer (10) has tabulated values of $\ln.\Lambda$ which show that it is a slowly varying function of plasma parameters n, T_e and has a value ~ 6 for afterglow plasma conditions giving

$$\nu_{ei}_{\text{SPITZER}} \simeq 15 \; n Z \; (T_e)^{-3/2} \quad \text{sec}^{-1} \qquad (7.21)$$

Ginzberg (42) has performed a similar calculation to Spitzer and he gives an expression for ν_{ei} when $T_e \neq T_i$ and $\omega_p \gtrsim \omega$ as

$$\nu_{ei}\ \underset{\text{GINZBERG}}{=}\ 5.5\ n\ Z\ (T_e)^{-3/2}\left[\ln.\left[\frac{280\ T_e}{Z\ n^{1/3}}\right]+\frac{1}{3}\ln.\left[\frac{T_i}{T_e}\right]\right] \qquad (7.22)$$

Heald and Wharton (41) have considered the relative contributions made by electron-ion and electron-neutral collisions to the total collision frequency. They have shown that for the common gases, electron-neutral collisions can be neglected provided:

$$\left.\begin{array}{l}\text{degree of ionisation} > 10^{-3} \text{ when } T_e = 10^4\ ^oK \\ \text{" " " } > 10^{-6} \text{ " } T_e = 300^oK\end{array}\right\} \qquad (7.23)$$

The plasma parameters associated with afterglow plasmas satisfy the conditions (7.23) for degrees of ionisation $> 10^{-4}$ indicating that Coulomb collisions dominate in highly ionised afterglow plasmas.

Hence, combining equations (7.19) and (7.21) with the value for cut off density associated with 337 microns wavelength (10^{16} cm^{-3}) we obtain an expression for the attenuation length of 337 microns radiation in a uniform plasma as

$$d_{337} \simeq 4.0\ 10^{25}\ (n)^{-2}\ (T_e)^{3/2} \quad \text{cm} \qquad (7.24)$$

(n cm^{-3}, T_e ^oK).

Fig. (7.1) shows a plot of electron densities and temperatures which give rise to attenuation lengths of 1, 10 and 100 cm according to equation (7.24). The effects of using the more comprehensive Ginzberg collision frequency have been included in fig. (7.1) where the attenuation lengths were calculated in terms of equation (7.22) instead of equation (7.21)

The values of d that can be found from an experimental measurement of the attenuation of a single transit of the e.m.

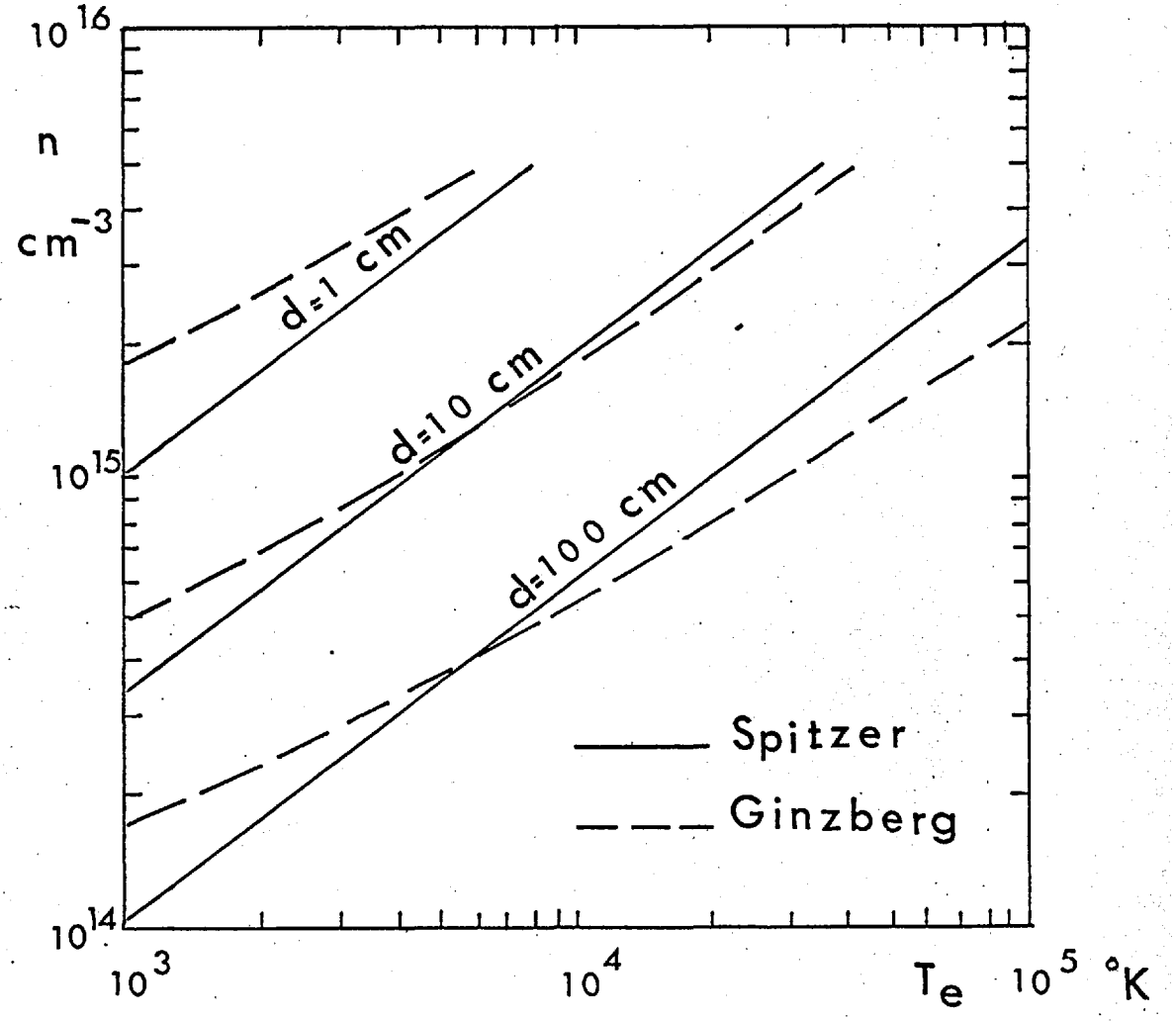

FIG (7.1) Plots of n versus T_e corresponding to fixed attenuation lengths of 337 μm radiation equal to 1, 10 and 100 cm in uniform plasma conditions.

beam across a plasma of thickness l lie between the limits

$$\chi < \exp\left\{-\frac{\ell}{d}\right\} < (1 - \chi) \qquad (7.25)$$

Where χ is the minimum fractional change in wave amplitude that can be measured against the background detector and/or plasma noise. In our experimental work, detector amplifier noise was the factor which determined the quantity χ. Table (7.2) shows upper and lower limits to the ratio of d/ℓ for values of χ of 0.05, 0.10 and 0.20.

TABLE (7.2)

χ	UPPER LIMIT TO d/ℓ	LOWER LIMIT TO d/ℓ
0.05	20.0	0.33
0.10	10.0	0.43
0.20	4.5	0.62

Taking the case of $\chi = 0.10$ as an example, this means that accurate measurements of d can be found from measured attenuations between 10% and 90% and this situation occurs for plasma conditions (n, T_e) lying between the lines d = 10 l and d = 0.43 l plotted on fig.(7.1). In designing an experiment to measure wave attenuation, one has to choose the number of beam transits across the plasma (ie. the plasma path length) so that the expected plasma properties lie within the region between the two lines defined above.

The values of (n, T_e) corresponding to afterglow plasmas are typically

$$\left.\begin{aligned} n &= 10^{15}\ \text{cm}^{-3}\ T_e = 10^4\ {}^{o}\text{K} \\ n &= 10^{14}\ \text{cm}^{-3}\ T_e = 3\ 10^3\ {}^{o}\text{K} \end{aligned}\right\} \qquad (7{:}26)$$

Taking conditions (7.26) in conjunction with fig. (7.1) and table (7.2) gives a predicted optimum plasma path length, for accurate attenuation measurements, of about 3 cm. This indicates that for our sizes of torus (minor radii 2.2 and 3.55 cm) a single transit of the laser beam diametrically across the plasma would be near optimum. It is also interesting to note that, in afterglow plasmas, n and T_e change in such a way that d follows a path on fig. (7.1) whose gradient is in the same sense as the d = constant lines, and this means that it is an inherent property of decaying plasmas that d can be measured over a wide range of the parameters (n, T_e).

(7.5) PLASMA REFRACTION

In order to make a valid calculation of the collisional attenuation experienced by a laser beam traversing a plasma from the experimentally measured transmitted laser power, we require that the effects of refraction, reflection and diffraction of the laser beam by the plasma should be negligible in comparison to the collisional attenuation. The refraction of an e.m. beam incident normally to a cylindrical plasma whose refractive index $\mu(r)$ varies with radius has been considered by Wort (43), who has derived and solved the equations for ray paths for several simple forms of $\mu(r)$. The refraction of microwave beams by uniform cylindrical plasmas has been discussed by Heald and Wharton (41).

In our experiment, the following physical parameters prevailed:

1. The outside diameters of the plasma were 4.4 and 7.1 cm respectively in the small and large tori.

2. The distance between the plasma and the screened room housing the far infrared detector was 5.5 m. This distance was chosen when the apparatus was operated in the Polytron regime.

3. The laser beam power output profile normal to the beam direction was roughly of Gaussian shape with a half width of 1 cm. (see section (7.8)).

4. A collecting lens of aperture 22 cm and focal length 39 cm was used to focus the laser beam onto a detector at the screened room.

For these physical conditions, a simple calculation of the refraction loss produced by a straightforward transmission of the laser beam across the plasma showed that the refraction loss was only small provided,

$$\left.\begin{aligned} n &< 0.045\ n_c \quad \text{small torus} \\ n &< 0.069\ n_c \quad \text{large torus} \end{aligned}\right\} \qquad (7.27)$$

where n_c = cut off density for laser beam frequency.

For electron density values above those given in (7.27) the refraction loss was a rapidly rising function of density.

In order to reduce the refraction losses inherent in the above system, two auxiliary lenses were introduced on either side of torus so that the laser beam was focussed to a point P near the plasma axis. The complete lens system is shown in fig.(7.2) where L_1 and L_2 are the auxiliary lenses and L_3 the collecting

lens. L_1 and L_2 were plano-convex lenses of aperture 5 cm . and focal length $\approx$ 50 cm.

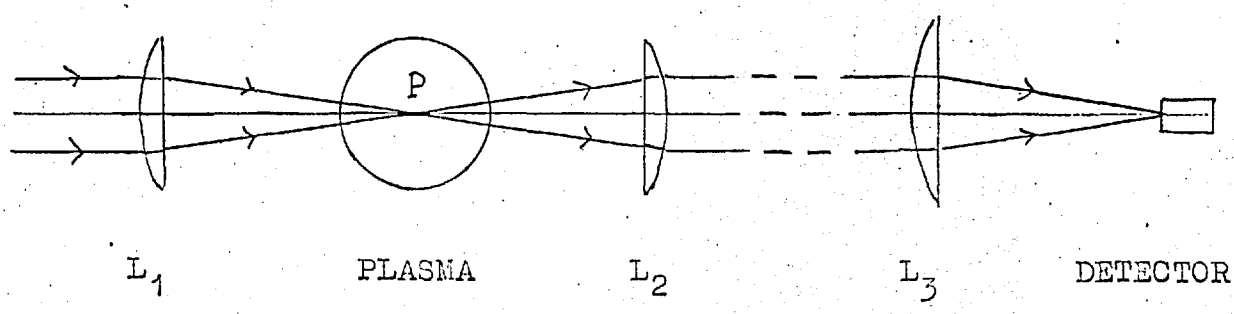

FIG. (7.2)

The lens system shown in fig. (7.2) was examined in detail with regard to the refraction losses that occur for movements of the focal point P away from the plasma axis. The calculations were performed using a cylindrical uniform plasma model, so that an estimate could be found for the accuracy of alignment of the focal point P inside the plasma for small refraction losses. The results obtained have been combined into the contour plot shown in fig. (7.3).. The contours shown in fig. (7.3) are for the limiting positions of the point P inside the plasma which gave rise to a zero refraction loss for fixed values of the ratio n/n_c. Fig. (7.3) was constructed for the large torus calculations but the results scale with very little error to

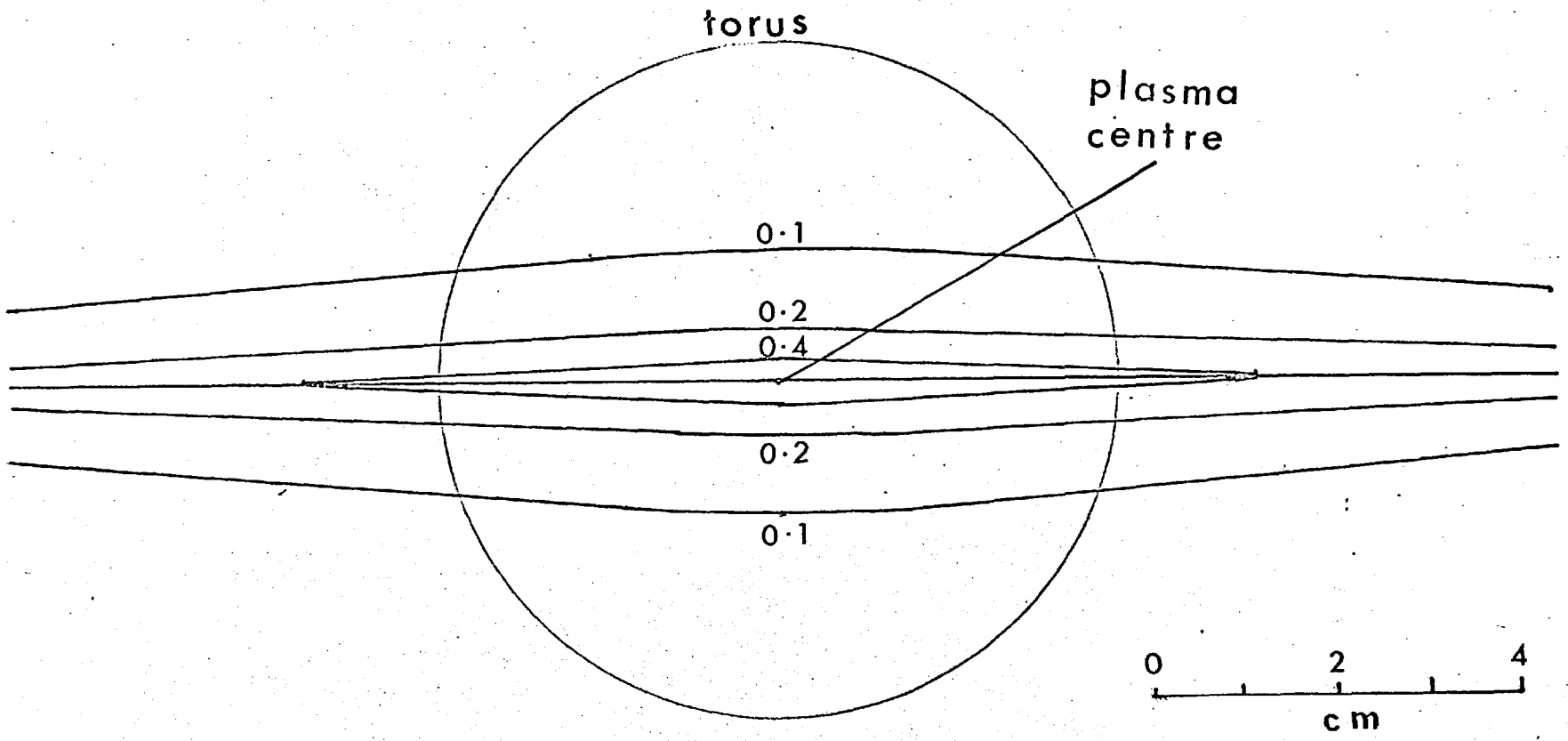

FIG (7.3) Contour plot showing the limiting positions of the focal point P for zero refraction loss as a function of n/n_c.

apply to the small torus case. For zero refraction losses at densities close to the cut off density, it can be seen from fig. (7.3) that the positioning of the laser beam axis relative to the plasma axis is very critical, whereas there is a fairly large tolerance on the coincidence of the focal point P on the laser axis with the plasma axis.

(7.6) PLASMA REFLECTION

From the electromagnetic theory presented in section (7.3) we can write the amplitude reflection coefficient for an e.m. wave at a homogenous plasma with a sharp boundary as

$$|R| = \left| \frac{1 - \mu^*}{1 + \mu^*} \right| \qquad (7.28)$$

where μ^* is the complex refractive index of the plasma. Using equation (7.3), we can re-write equation (7.28) as

$$|R| = \left[\frac{(1 - \mu_r)^2 + \mu_i^2}{(1 + \mu_r)^2 + \mu_i^2} \right]^{\frac{1}{2}} \qquad (7.29)$$

Numerical evaluation of μ_r and μ_i from equations (7.10) and (7.11) for the plasma conditions $\omega > \omega_p$, $\nu \gg \omega$ shows that $\mu_r \gg \mu_i$ and therefore we can write the power reflection coefficient R_p at the plasma boundary as

$$R_p = \left[\frac{1 - \mu_r}{1 + \mu_r} \right]^2 \qquad (7.30)$$

For a single transit of a laser beam across a plasma, the fractional power loss due to reflection at the boundaries (neglecting multiple reflections) is therefore

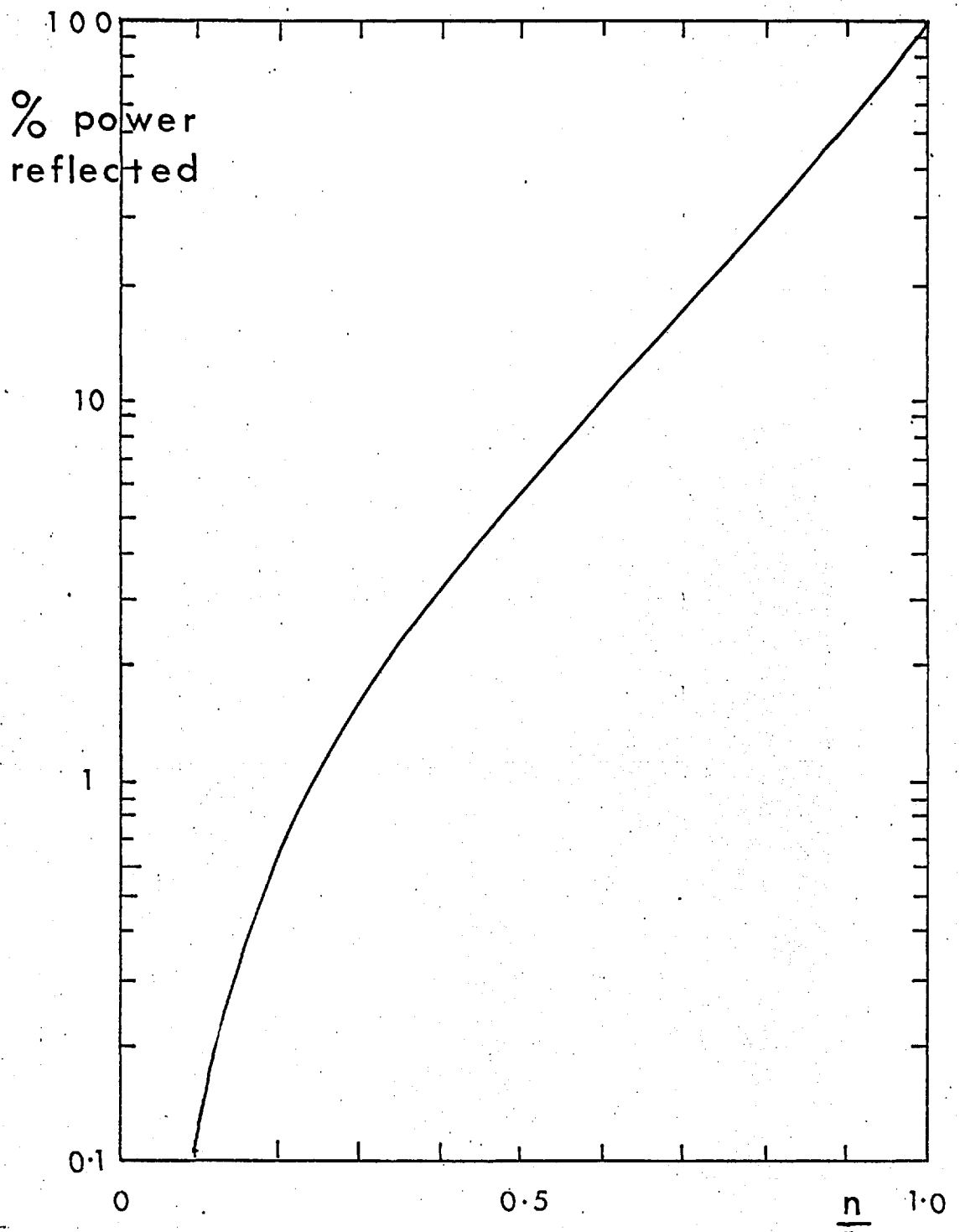

FIG (7.4) Percentage power loss due to e.m. wave reflection at a plasma plotted as a function of n/n_c.

$$1 - (1 - R_p)^2 = R_p (2 - R_p) \qquad (7.31)$$

Fig. (7.4) shows a plot of the percentage power loss due to reflection of the laser beam at the plasma boundaries based on equations (7.30), (7.31) and (7.15) where the percentage power loss has been plotted as a function of the ratio n/n_c. It can be seen that the reflection power loss is less that one per cent for $n < 0.25\ n_c$.

(7.7) THE HCN LASER

The HCN laser used in the experiment is shown in fig. (7.5). It was one of a batch of prototype c.w. lasers made at the National Physical Laboratory. The laser cavity wasof the usual Fabry-Perot type formed by two mirrors which appeared to be gold plated. The curvature of the mirrors was not known, but the mirror aperture was 5 cm. One mirror was fixed to a micrometer mount for axial cavity length adjustments and the separation of the mirrors was approximately one metre. Output power was coupled from the laser cavity by a 'Melinex' beam divider placed at 45° to the cavity axis. The fraction of energy removed from the cavity at each reflection was small, so that two nearly equal outputs in opposite directions at 90° to the cavity axis were obtained. Power was transmitted out of the laser through two 5 cm diameter 'Melinex' windows. The laser operated with a continuous flow of methyl cyanide vapour from the anode to the cathode of the gas discharge and the optimum working pressure was found to be about 0.7 torr. The cathode contained a heated filament to stabilise the arc discharge and typically 700 volts was dropped between anode and cathode for a current of 1 amp. A series ballast resistor was used to overcome the negative

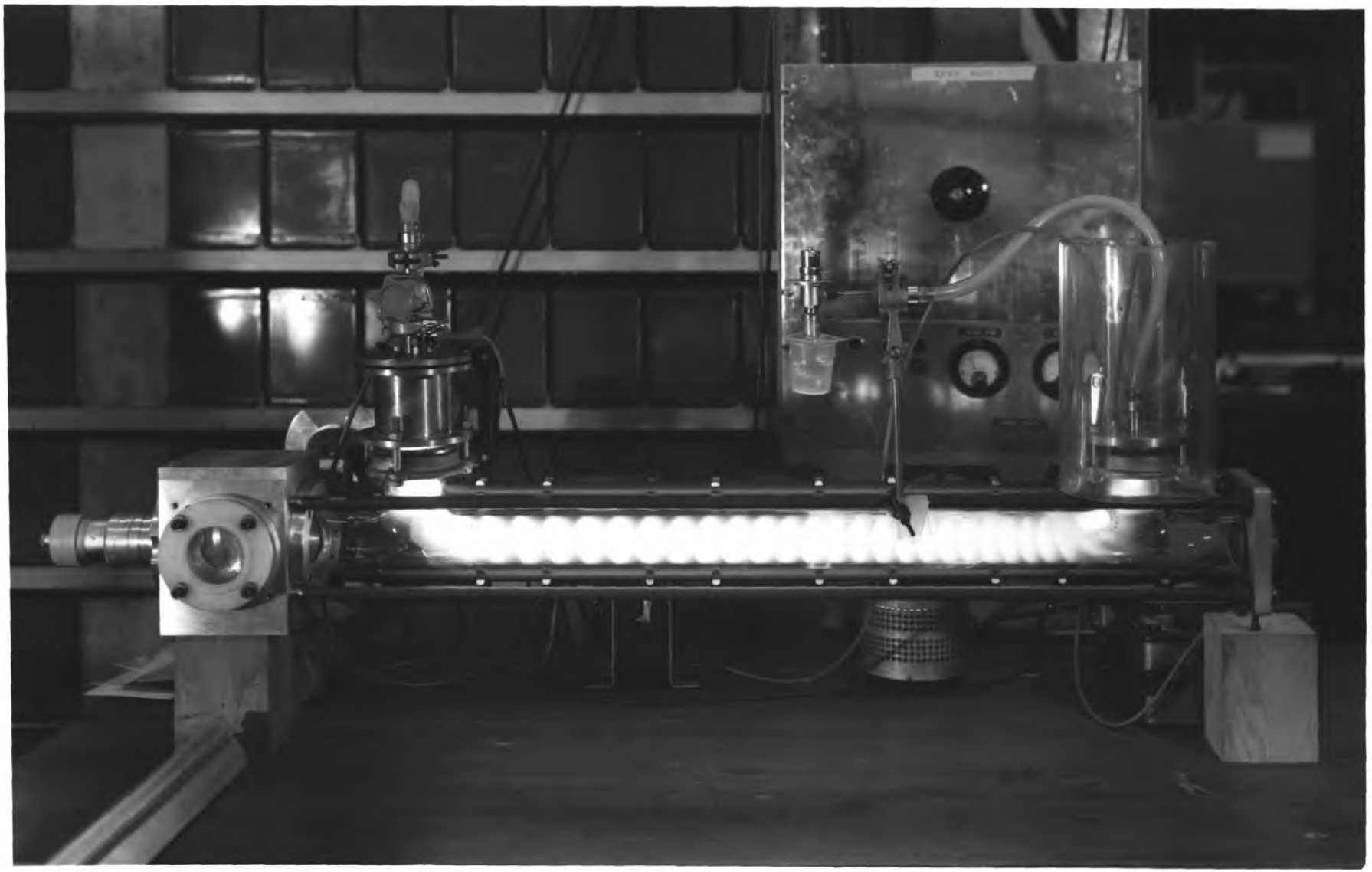

FIG (7.5)

resistance of the arc. The power dissipated by the discharge was removed by fan cooling the tube. A brown deposit, caused by breakdown of the organic cyanide, rapidly built up on the walls of the discharge tube which had to be cleaned every 100 hours running time to avoid excessive outgassing problems. For safety reasons, the exhaust from the vacuum pump was taken outside the lab.

(7.8) HCN LASER ANALYSIS

The Doppler broadened line width of the 337 micron transition was found experimentally to be about 4 M.H_Z from the variation of the laser output power with movement of the micrometer mounted mirror about a laser cavity resonance. The separation of the successive Fabry-Perot resonances of the laser cavity was about 150 M H_Z (corresponding to a 1 metre cavity) which showed that lasing action could only occur in a single axial mode. The drift of the cavity resonances relative to the laser frequency due to thermal expansion effects was small, after the initial heating up period, and the cavity needed re-tuning for optimum output about twice an hour.

The physical parameters which determine the properties of any laser are

R^* = radius of curvature of the mirrors
l^* = axial separation of the mirrors (the cavity length
b^* = radius of mirror aperture

and the quantities gain per unit length of the laser and coupling loss per transit.

The cavity diffraction loss for each laser mode is

determined by the Fresnel number N' of the cavity where

$$N' = \frac{b^{*2}}{l^{*}\lambda} \qquad (7.32)$$

Substitution of $b^{*} = 2.5$ cm, $l^{*} = 1$m and $\lambda = 337$ μm appropriate to our laser into (7.32) gives

$$N' = 1.85$$

In table (7.2), the percentage power loss due to diffraction for the two lowest transverse modes in a laser with $N' = 1.85$, $l^{*} = 1.0$m has been calculated for different values of R^{*} from the cavity theory of L_i(44). The results are presented for a symmetric cavity, but results for a half-symmetric cavity show a very similar trend with varying R^{*}.

TABLE (7.2)

PERCENTAGE POWER LOSS DUE TO DIFFRACTION : $N' = 1.85$, $l^{*} = 1.0$m

R^{*} (m)	TEM_{00}	TEM_{10}
∞	7.1	18
20	2.8	10
10	1.0	5.0
5	0.1	1.6
2	$\ll 0.1$	0.1

Table (7.2) shows that laser action will occur in more than one transverse mode for cavities anywhere near confocal.

The e.m. field distributions at the laser mirrors have been

calculated from a generalised cavity theory given by Boyd and Kogelnik (45). For near confocal cavities the TEM_{00} mode has a Gaussian distribution with an amplitude half width of $(b^{*2}/N'\pi)^{\frac{1}{2}}$. For changes in mirror radii towards near plane parallel cavities, there occurs an increase in the amplitude half width of about 50% compared to the near confocal case. In table (7.3) the [illegible] widths of the amplitude and power profile of the laser output, relative to the total mirror aperture, have been calculated as a function of mirror radius of curvature for a laser with $N' = 1.85$ and $l^* = 1.0$ m.

TABLE (7.3)

OUTPUT PROFILE [illegible] WIDTH RELATIVE TO MIRROR APERTURE

R^*(m.)	AMPLITUDE	POWER
∞	0.66	0.46
20	0.63	0.40
10	0.59	0.37
4	0.52	0.33
2	0.42	0.30
1	0.41	0.32

Experimental measurements of the laser power profiles were made by scanning a Golay detector (aperture diameter of 2.3 mm) across the laser output normal to the beam direction at distances of 0.1, 0.5, 1.0, 2.0 and 5.0 metres away from the

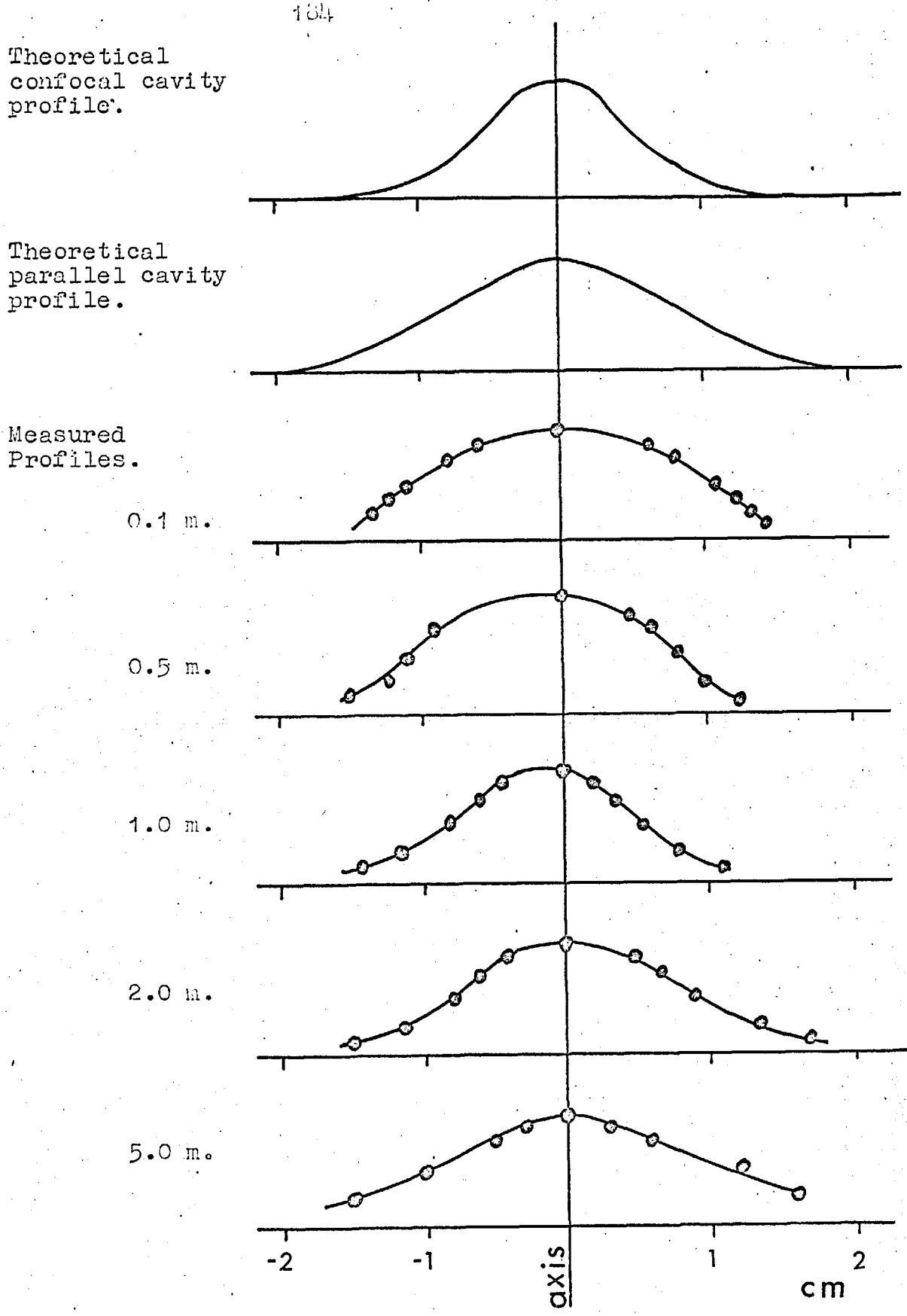

FIG (7.6) Plots of HCN laser power profiles measured at 0.1 to 5.0 m. from the laser.

laser output window. The arbitarily normalised power profiles together with the theoretical profiles calculated from (45) for near confocal and near plane parallel cavities are shown in fig. (7.6). Comparison of the theoretical and experimental profiles would suggest that the laser possessed plane mirrors.

The variation of laser power at the peak of the power profile with distance from the laser output window was measured on an optical bench using the Golay detector. The mechanical chopper used with this detector had a circular aperture of 3.1 cm, and two sets of measurements were made. In the first set, the chopper remained fixed at the centre of the laser output window, and in the second set, the chopper remained close to the detector. These experiments corresponded to laser output apertures of 3.1 and 5.0 cm respectively. The results obtained over distances up to 1 metre are shown in fig. (7.7). From Fresnel diffraction theory, the radii of Fresnel zones at a distance y from an aperture are given by

$$\varrho_m = [m \lambda y]^{1/2} \qquad (7.33)$$

where ϱ_m = radius of the m th zone

Substituting the values 3.1 and 5.0 cm for $2\varrho_m$ appropriate to each of the above experiments, the distances of the first three zones from the laser have been calculated from equation (7.33) as shown in table (7.4). The distances of the experimentally observed maxima and minima found from fig. (7.7) have also been given in the same table.

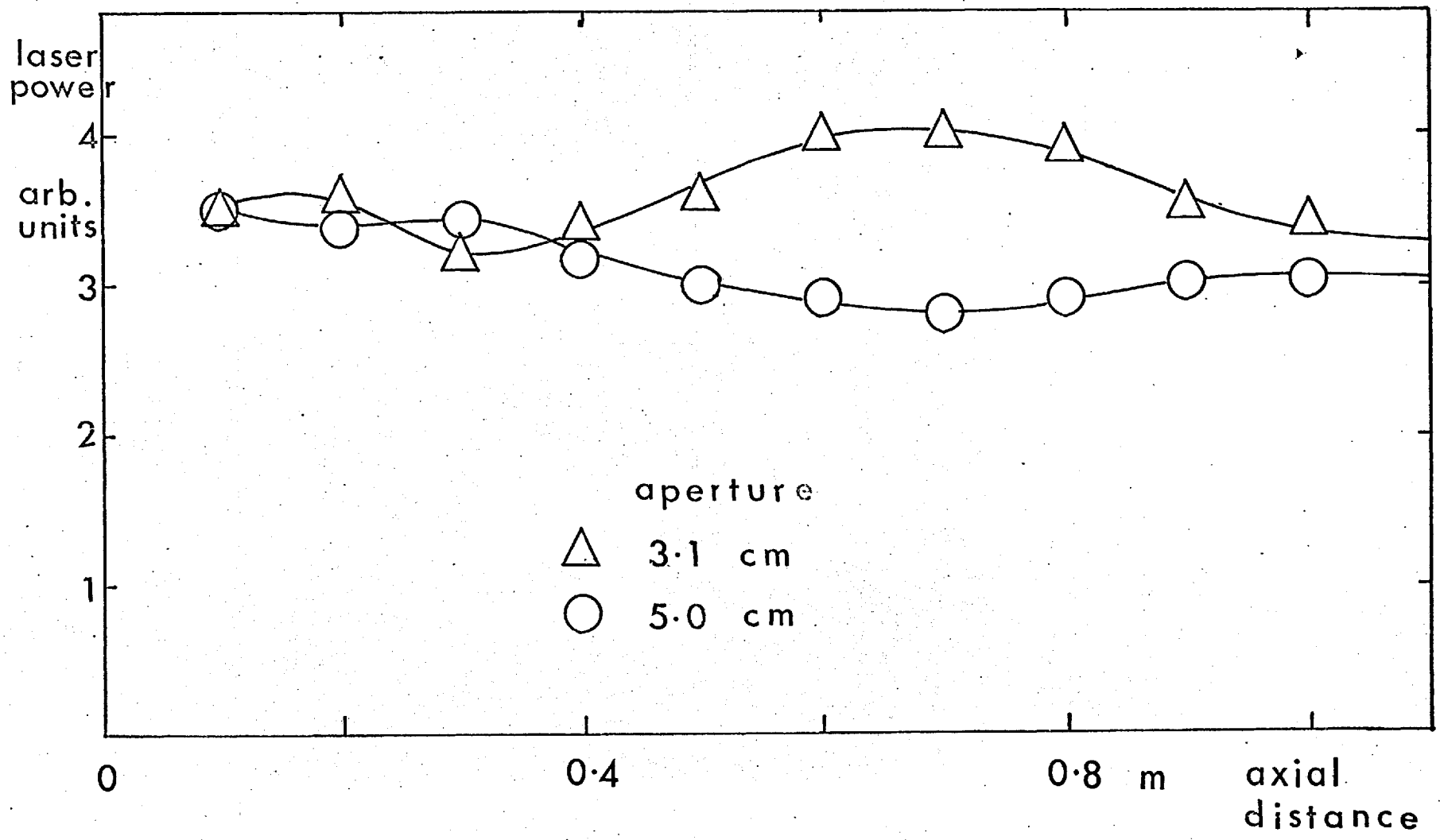

FIG (7.7) Plots of the relative laser power along the beam axis for laser apertures of 3.1 and 5.0 cm.

TABLE (7.4)

ZONE	APERTURE 3.1 cm		APERTURE 5.0 cm	
	CALCULATED y (cm)	MEASURED y (cm)	CALCULATED y (cm)	MEASURED y (cm)
1st (BRIGHT)	71.2	70($\pm$5)	150.1	-
2nd (DARK)	35.6	33($\pm$5)	75.1	70($\pm$5)
3rd (BRIGHT)	23.7	20($\pm$5)	50.0	30($\pm$5)

Comparison of the measured and calculated values of y in table (7.4) confirms the Fresnel diffraction theory presented. The fact that the variation of signal with distance y was much larger for the 3.1 cm aperture than for the 5.0 cm aperture is in agreement with the distribution of power across the laser profile discussed previously.

(7.9) INFRARED DETECTORS

In our experiment, the HCN laser radiation at 337 microns wavelength was detected using two quite different detectors: a Golay cell and a Putley indium antimonide detector.

The Golay cell (46) is a standard far infrared detector which operates at room temperature and requires the incident radiation to be chopped at 13 H_Z for its optimum performance. We used the Golay cell as a general purpose instrument for monitoring the laser output and aligning the interferometer.

The Putley detector (47)(48) consists of a sample of

n-type indium antinomide at a temperature of 1.7 ^{o}K and in a magnetic field of 7 kilogauss. The indium antimonide is biassed and acts in a photo-conductive mode. The peak detector response occurs at 1 mm wavelength with a nearly linear fall off in response down to 100 microns, so that at 337 microns the detector is not working with its optimum performance. Shaw and Putley[49] have shown that the intrinsic response time of the detector is around 0.5 μ.sec. At 1.7 ^{o}K, the resistance of the InSb sample is usually a few kΩ which means that to exploit the intrinsic response time of the detector, the InSb sample has to be shunted with a low resistance with a consequent drop in detector output. The equivalent noise resistance for the InSb sample at room temperature is only 20 Ω and hence the main source of noise is always in the amplifier used with the detector. In the experiment, the Putley detector was used to measure the interferometer output with the transient plasma.

The performances of the Golay and Putley detectors together with those for other far infrared detectors have been listed in table (7.5). The R.R.E. pyroelectric detector (50) was not used because of its inferior performance compared to the Putley detector, but it has the advantage of operating at room temperature. A similar argument applies to the diode detectors (51). The Bell Telephone pyroelectric detector (52) and the Josephson detector (53) are comparable or superior to the Putley detector at 337 microns but neither type was available at the time of the experiment.

TABLE (7.5)

DETECTOR TYPE	WAVELENGTH REGION (microns)	RESPONSIVITY (volt watt^{-1})	NOISE EQUIVALENT POWER 1 H_Z BANDWIDTH (watt)	RESPONSE TIME (sec.)
GOLAY CELL	0.4 - 5000	10^5	10^{-10}	10^{-1}
PUTLEY INDIUM ANTIMONIDE	200	200	$2\ 10^{-11}$	$5.\ 10^{-7}$
	500	500	$1\ 10^{-11}$	$5.\ 10^{-7}$
	1000	1000	$5\ 10^{-12}$	$5.\ 10^{-7}$
R.R.E PYROELECTRIC	1 - 5000	100	$5\ 10^{-8}$	$5\ 10^{-6}$
Ga As DIODE	100 - 2000	0.1	10^{-7}	10^{-8}
BELL TELEPHONE PYROELECTRIC	.1 - 5000	1000	$5\ 10^{-9}$	$5\ 10^{-8}$
JOSEPHSON EFFECT	250 - 5000	-	$5\ 10^{-13}$	10^{-8}

(7.10) DESIGN AND CONSTRUCTION OF THE HCN LASER INTERFEROMETER

The calculations performed in section (7.4) showed that a single transit of the laser beam across the plasma was optimum for making attenuation measurements. The calculations performed in section (7.5) showed that, for small refraction losses, the laser beam required to be focussed near the axis of the plasma. Combining these features, we obtain Mach-Zehnder type of interferometer shown schematically in fig. (7.8).

The efficiency of the Mach-Zehnder interferometer depends largely on the performance of the beam dividers used. Ideally, we want the power reflection and transmission coefficients to be both equal to 0.5 (and the attenuation loss to be zero). At submillimetre wavelengths, we have the choice of using either a dielectric film or a metallic mesh as a beam divider. Vogel and Genzel (54) and Moller and Ressler (55) have investigated woven and electroformed metallic meshes in the wavelength region 30 to 350 microns. Their results indicate that it is difficult to manufacture meshes that are accurate enough to give the desired properties at a given wavelength, and that a typical attenuation power loss in a mesh is around 50%. Chamberlain et al (56) have investigated dielectric film beam dividers in the far infrared region and they have shown that the performance of 'mylar' or 'Melinex' film is near ideal, because of its high refractive index (1.7 to 1.8) at these wavelengths. It is essential to choose the correct thickness of film for the angle of incidence and wavelength employed, since successive reflections between opposite faces of the film give rise to interference effects. The attenuation in 'Melinex' film is small, and it is best to choose the film thickness that gives rise to the first interference maximum. Chamberlain et al. (56) have shown that this occurs when

M_1-M_7 MIRRORS; L_1-L_4 POLYTHENE LENSES; D_1-D_3 BEAM DIVIDERS; W_1-W_2 MELINEX WINDOWS.

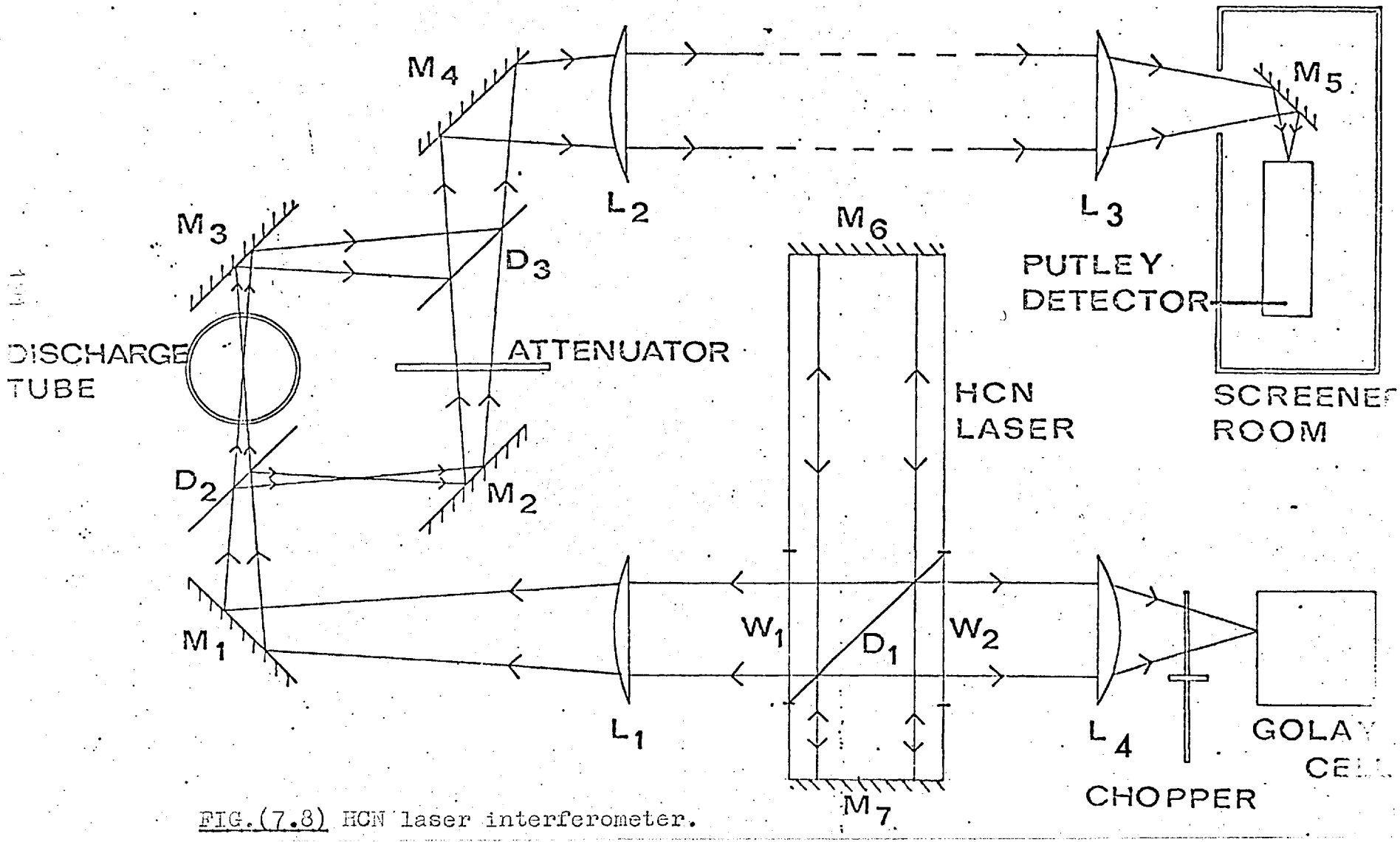

FIG.(7.8) HCN laser interferometer.

$$h' \sigma' n' \cos \theta' = 0.25 \qquad (7.34)$$

where h' = film thickness

σ' = wave number ($29.7\ cm^{-1}$ at 337 microns)

n' = refractive index of film (1.69 at 337 microns)

θ' = angle of refraction in the film

We want the beam splitters at 45° to the incident beam and this gives a value for θ' of $24^{\circ}\ 42'$, which when substituted into expression (7.34) gives $h' = 54.8$ microns. The nearest value to this figure in the standard range of 'Melinex' film is 200 gauge (51 microns). The transmission characteristic of a 50 microns thick 'melinex' film at 45° to the incident beam is shown in fig. (7.9) from the experimental measurements of Gebbie and Stone (57).

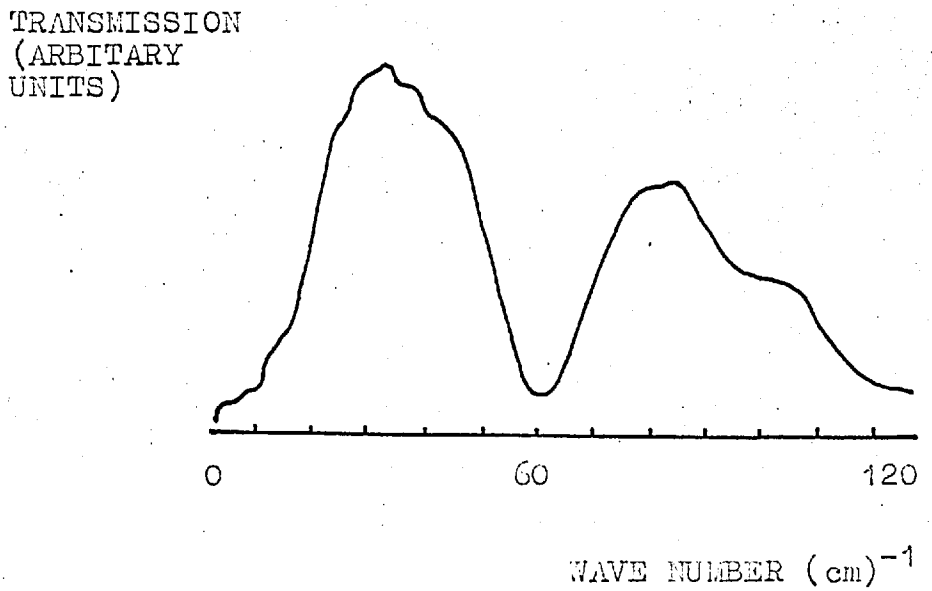

FIG. (7.9)

In practice, the beam dividers were constructed by sandwiching the 'melinex' film between two 6 cm diameter dural annuli which were clamped together by six 2BA screws. Applying hot air from a hair dryer evenly over the film for a few seconds caused it to shrink and produce a uniformly taut drum, which remained taut indefinitely. Each beam divider was adjustable using three 40 t.p.i. screws. The mirrors of the Mach-Zehnder interferometer were constructed in the same way as the beam dividers except that aluminium was vacuum deposited on the front surface of the film. A close up view of the mirrors and beam dividers in position around the torus can be seen in fig. (2.16).

The plano-convex lenses L_1 and L_2 were machined from a white polythene billet according to formulae given by Brown (106). The refractive index of white polythene at 337 microns wavelength is 1.50. The focal lengths of these lenses were measured on an optical bench using the laser as a source and the Golay cell as a detector. The results were

$$\text{focal length of } L_1 = 50.5\ (\pm\ 2.0)\ \text{cm}$$

$$\text{focal length of } L_2 = 48.5\ (\pm\ 2.0)\ \text{cm}$$

The collecting lens L_3 was obtained ready made with an aperture of 22 cm and a quoted focal length of 39.0 ($\pm$ 0.5) cm.

(7.11) EXPERIMENTAL ALIGNMENT OF THE INTERFEROMETER

The following procedure was employed in the alignment of the interferometer shown in fig. (7.8).

1. L_1, L_2 and L_3 were removed and the HCN laser beam direction

was defined using two 1 cm diameter apertures from measurements made with the Golay cell.

2. A He-Ne laser beam was directed through the output windows of the HCN laser and aligned with the two apertures.

3. Mirror M_1 was adjusted for visible laser light to pass diametrically across the torus which occurred when successive internal reflections from the torus walls were superimposed.

4. D_2, M_3, M_2 and D_3 were adjusted for superposition of the beams from each interferometer arm, and M_4 was roughly positioned for light to enter the screened room.

5. L_1, L_2 and L_3 were replaced, and the interferometer was adjusted for maximum 337 micron signal in the screened room by movement of M_4 only.

6. Compensation for 337 micron beam attenuation in the walls of the fused silica torus was made by inserting a combination of different thicknesses of black (carbon impregnated) polythene sheet into the reference beam arm, each arm of the interferometer being blanked off in turn to check signal equalisation.

7. Movement of M_2 normal to the mirror plane then produced successive interference maxima and minima with a visibility of better than 20 to 1. M_2 was finally adjusted for destructive interference in the absence of plasma.

8. For the study of plasma decay, the Golay cell was replaced by mirror M_5 and the Putley detector. The radiation input window on the Putley detector was $\sim$ 2 cm diameter so that the detector alignment was much less critical than with the Golay detector.

9. Setting up the Putley detector involved a long cooling procedure and the temperature of 1.7 ^{o}K was achieved by pumping

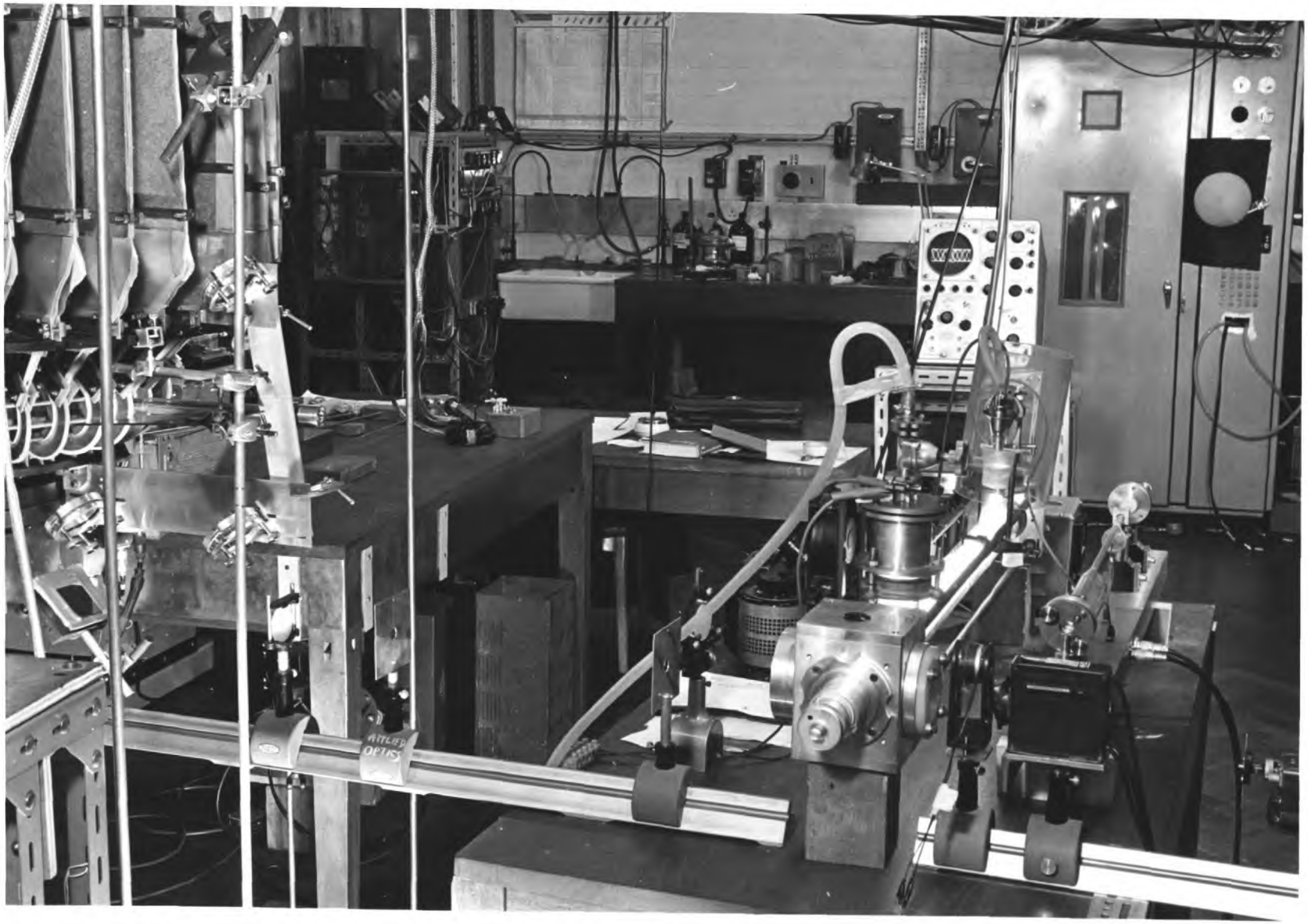

FIG (7.10)

liquid helium to a vapour pressure around 3.5 torr. The magnetic field of 7 kilogauss was supplied by a superconducting solenoid which was originally energised from a 12 volt accumulator. The detector low frequency response was checked by chopping the laser beam mechanically at 13 and 200 H_Z. The high frequency response was checked by recording fringe changes as the plasma was FORMED by the discharge at low gas pressures ($\sim$ 10 m.torr) in argon. From these measurements, the detector and its associated bias and amplifier circuits were shown to have a flat response from $< 100\ H_Z$ to $> 100\ kH_Z$.

A photograph showing most of the HCN laser interferometer set up around the torus is shown as fig. (7.10). The experimental results obtained with the interferometer are given in chapter 11.

(7.12) METHOD OF OBTAINING ϕ AND χ FROM INTERFEROMETER OUTPUT

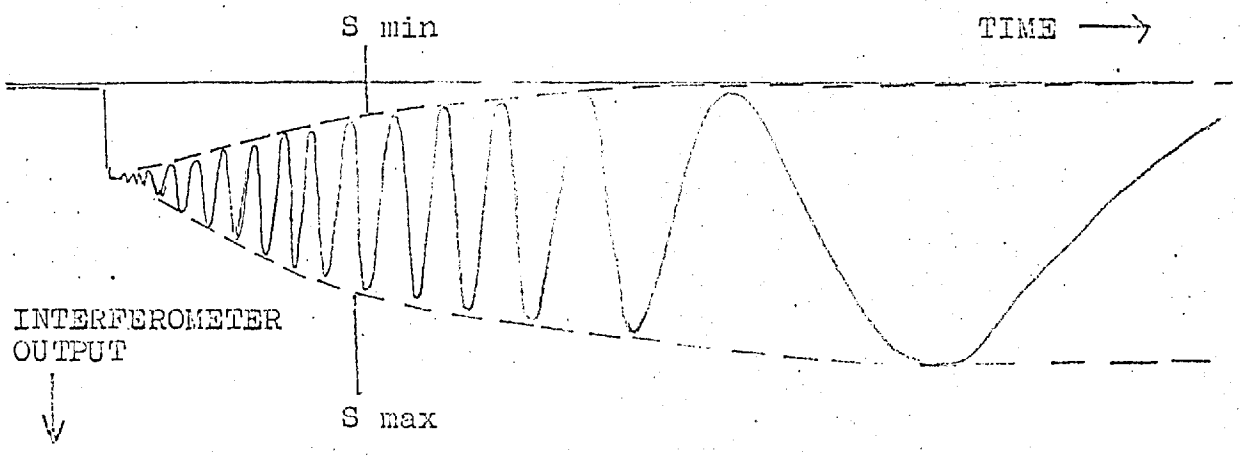

FIG. (7.11)

Fig. (7.11) shows schematically a typical interferometer output obtained in the study of plasma decay. Actual oscilloscope traces are shown later in figs. (11.2) and (11.3). The interferometer output is zero prior to plasma formation and also at the very end of the plasma decay because of the adjustment for destructive interference as described above.

The phase shift ϕ as a function of time is found in steps of π from the positions of the fringe maxima and minima on the trace working backwards in time from the last fringe in the usual way.

The interferometer output signal S is measured on a power detector and we can write

$$S = |A_1|^2 + |A_2|^2 + 2|A_1||A_2| \cos\phi \qquad (7.35)$$

where A_1 = wave amplitude of interferometer reference arm beam
A_2 = wave amplitude of interferometer discharge arm beam

In the absence of plasma, $|A_1| = |A_2|$ and $\phi = \pi$ giving $S = 0$. With plasma, A_1 is constant throughout and A_2 varies according to the plasma attenuation. From equation (7.35) the interferometer maximum and minimum outputs are related to A_1 and A_2 as

$$S_{max} = \text{max. output} = |A_1 + A_2|^2$$
$$S_{min} = \text{min. output} = |A_1 - A_2|^2$$
$$\therefore (S_{max} - S_{min}) = 4|A_1||A_2|$$
$$\therefore (S_{max} - S_{min}) \propto A_2$$

The average values of electron density of the plasma which correspond to the last fringe maximum in both sizes of torus are

$n = 8 \cdot 10^{13}$ cm^{-3} small torus
$n = 4.8 \cdot 10^{13}$ cm^{-3} large torus

The minimum electron temperature expected to exist at these values of electron density is $\sim 1000^{\circ}K$. Reference to equation (7.24) and the extrapolation of fig. (7.1) shows that for these conditions the plasma attenuation is always $< 1\%$ so that we can take the interferometer output at the last maximum to correspond to the unattenuated value of A_2. Hence, the e.m. wave amplitude attenuation in the plasma can be directly obtained from measurements of the fringe 'envelopes' of the recorded traces since

$$\left[\text{Wave Attenuation}\right]_p = \frac{|A_2|_1}{|A_2|_p} = \frac{|S\ \text{max} - S\ \text{min}|_1}{|S\ \text{max} - S\ \text{min}|_p} \qquad (7.36)$$

where the subscript p refers to the pth fringe. Note that the above method for measuring the attenuation does not depend on the exact equalisation of $|A_1|$ and $|A_2|$ in the experiment.

It is convenient to express the wave amplitude attenuation in terms of the quantity γ where

$$\gamma = \ln\ (\text{wave attenuation}) \qquad (7.37)$$

The quantities ϕ and γ, found from the oscilloscope traces as above, can be related exactly to electron density and electron temperature only when the distribution profiles $n(r)$, $T_e(r)$ are known. This operation is described in Chapter 10.

(7.13) USES OF FAR INFRA RED LASERS IN PLASMA DIAGNOSTICS

As a conclusion to this chapter, we review the possible application of far infra red lasers in the field of plasma diagnostics.

1. The use of a submillimetre laser (eg. HCN laser) as a source of an interferometer enables plasma electron densities in the region 10^{14} to 10^{16} cm^{-3} to be measured with an accuracy that is unequalled by any other method.

2. The attenuation of a far infra red laser beam in a plasma due to electron collisions can be measured with good accuracy, and from e.m. theory, this attenuation yields a direct measure of the electron collision frequency. In plasmas where the Spitzer formula (7.20) for electron collisions can be applied, values for the electron temperature can be estimated from the electron collision frequency. For certain plasmas, such that the electron drift velocity exceeds the thermal velocity, the electron collision frequency is enhanced above that given by the Spitzer formula. Under these conditions, the direct measurement of effective electron collision frequency can be used to check theories of enhanced resistivity.

3. Most far infrared lasers can operate simultaneously at more than one wavelength (eg. c.w. operation of the HCN laser at 128, 211, 311 and 337 microns wavelength is possible). Thus, we have a multifrequency parallel beam of radiation capable of making high spatial resolution measurements on a plasma. By frequency analysing a multifrequency laser beam after passage through a plasma, measurements of the plasma frequency over a wide range of conditions could be made. This type of experiment would represent a great advance over the frequency resolved measurement of the self absorption of plasma emission at far infra red wavelengths described by Kimmett and Niblett (58).

CHAPTER 8

MICROWAVE TECHNIQUES FOR PLASMA DIAGNOSTICS

The techniques employed in two novel types of microwave interferometers are described. Both these techniques rely upon the use of microwave reflection at the discharge tube walls or at the plasma boundaries as an integral part of the interferometers.

(8.1) MICROWAVE TRANSMISSION INTERFEROMETRY

The first attempt at measuring the plasma electron density using 70 GH_Z microwave equipment was made using a conventional reference arm type interferometer (41). As our tori were both made from fused silica, we chose to place the microwave transmitting and receiving horns outside the tori so as to avoid the difficulty of special ports and vacuum windows in the wave guides. This experiment showed several shortcomings, in particular, the performence of the hybrid tee junctions at 70 GH_Z was very imperfect and the reflection of microwaves at the walls of the tube grossly distorted the basic reference arm interference pattern. This last phenomenon gave rise to the idea of employing the successive reflection of microwaves between opposite torus walls as an interferometer in its own right and to dispence with the reference arm.

Experiments were initially performed using a short length of fused silica tube and polystyrene plasma models and these showed that the transmission was a superposition of the standing waves set up between the models, the tube walls and the horns

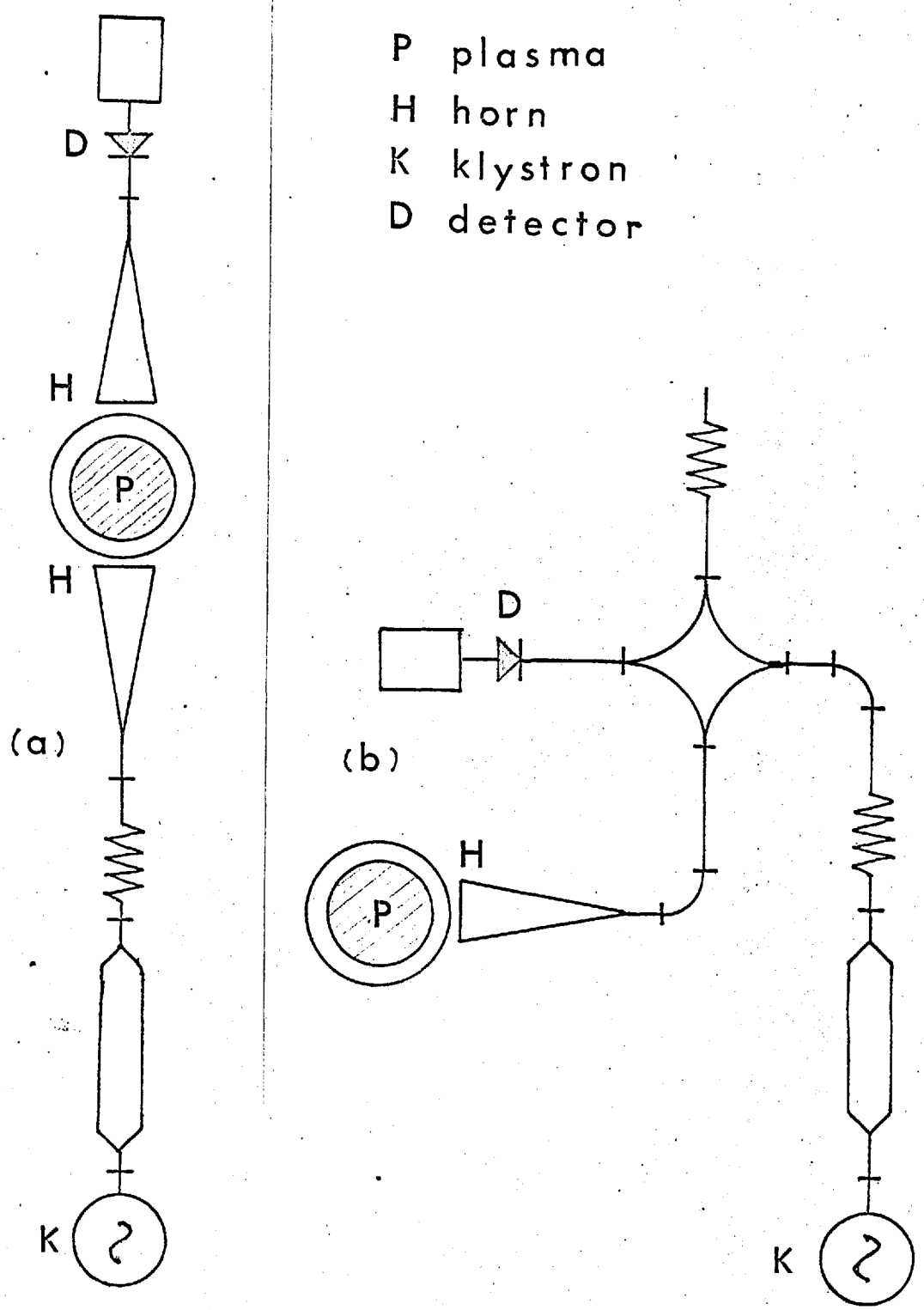

FIG (8.1) (a) Transmission interferometer.
(b) Reflection interferometer.

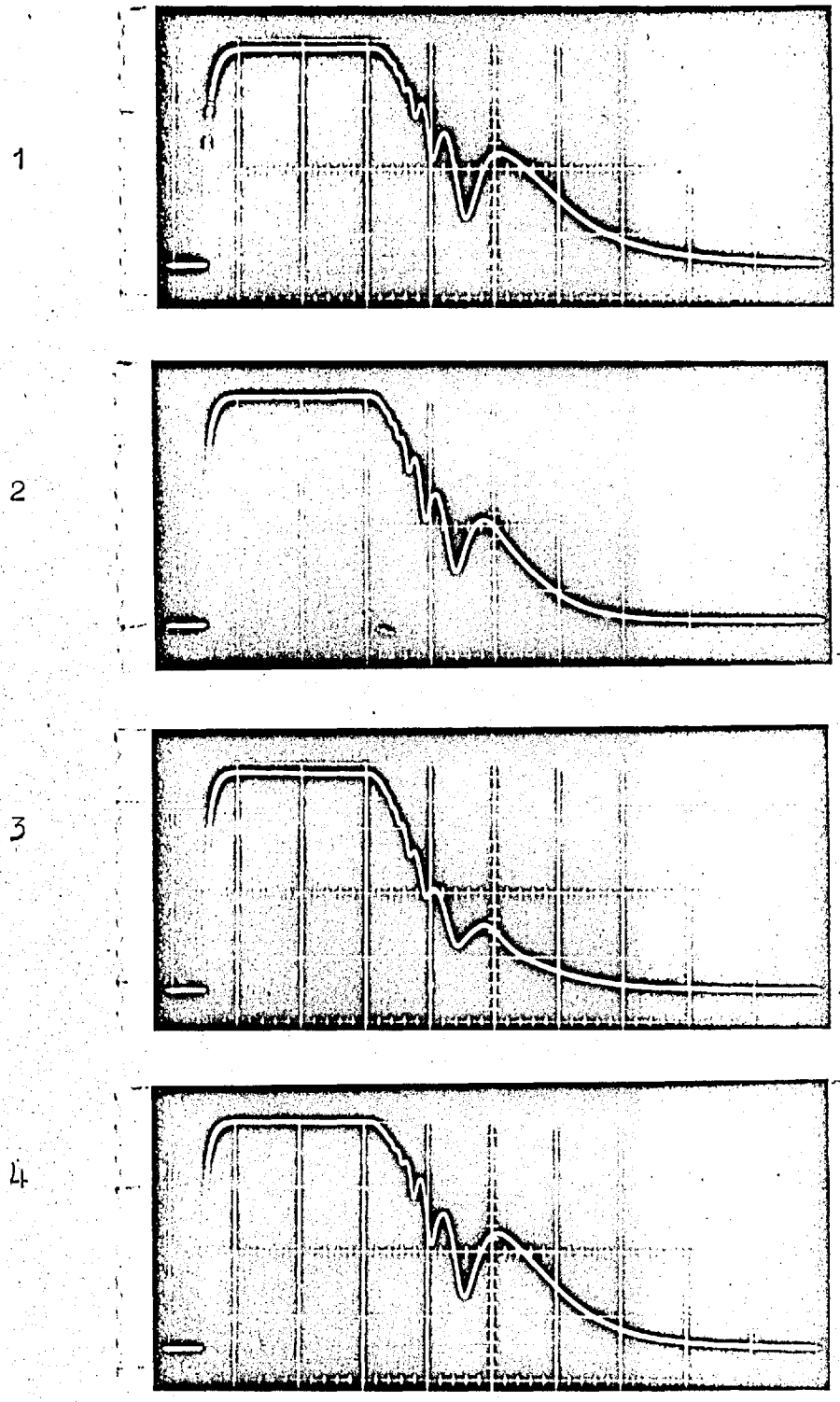

FIG (8.2) 70 GH_Z microwave transmission patterns recorded for successive movements of the transmitting horn away from the plasma in steps of 1/8 free space wavelength.

with a maximum signal modulation of about 5 : 1.

The experimental set up for the real plasma experiments is shown schematically in fig. (8.1)(a). The plasma was produced by the preionisation system described in section (2.5). Experiments were performed to investigate the variation in the transmitted microwave signal with the movement of the horns relative to the torus and plasma. We will denote the transmitting horn by H_1 and the receiving horn by H_2. In fig. (8.2) the microwave transmission patterns are shown when H_1 is successively moved in one eighth of a wavelength (0.5 mm) steps away from the torus with H_2 fixed. The transmission patterns were arbitarily normalised to produce the same cut off signal for each case, and the discharge conditions were kept constant. The following comments are made about the results shown in fig. (8.2).

1. In all cases an interference pattern can be seen superimposed on the straight forward transmission signal.

2. The amplitude of the interference pattern depends on the position of H_1 relative to the torus.

3. The positions in time of the corresponding interference maxima and minima depend hardly at all on the position of H_1 relative to the torus.

Observation 3. is particularly interesting since it shows that the interference pattern was caused by either successive reflections at the plasma boundaries or at the torus walls and not by successive reflections between the horns H_1 and H_2.

The transmission of microwaves through a plasma slab with finite density gradients has been studied by Jahn (130) Budden (131) and French et al. (133). Albini and Jahn (132) have

shown for a trapezoidal plasma profile (uniform slab bounded by linear ramps) that the modulation of transmitted power due to internal reflections across the plasma varies with the width of the boundary ramps as given in table (8.1) for the case when $n = 0.5\ n_c$ and plasma collisional attenuation is zero.

TABLE (8.1)

PERCENTAGE MODULATION OF TRANSMITTED POWER	BOUNDARY RAMP WIDTH (WAVELENGTHS)
36	0
33	0.1
23	0.25
10	0.5
<1	1.0

It is clear from table (8.1) and all the calculations in (130),(131),(132) that modulation of the transmitted beam due to successive reflections at the plasma boundary is only significant if the characteristic boundary width is much less than one microwave wavelength. The experimental measurements of the plasma density profiles existing in the plasma described in sections (3.5), (10.2) and (10.3) show that this clearly was not true in our experiment and so we conclude that the interference patterns shown in fig. (8.2) were caused by successive reflections between opposite walls of the torus. The above situation is analagous to a Fabry-Perot type of interferometer and the values of electron density corresponding to successive interference maxima and minima were worked out in the usual way from the internal diameter of the torus cross-section.

(8.2) MICROWAVE REFLECTION INTERFEROMETRY

In addition to the transmission experiments, a second set of experiments was performed using the microwave system shown in fig. (8.1)(b). Here a single microwave horn acted as both the transmitter of the incident beam and the receiver of any beams reflected from the plasma or the walls of the torus. The hybrid tee junction was arranged so that the single detector received most of the power reflected back into the horn together with a small amount of power straight from the klystron (the latter being due to imperfections in the junction.) Thus the complete system acted as an interferometer where the relative phase and amplitude of the signal reflected back into the horn could be measured.

Experiments were performed to investigate the variation of the reflection interferometer output with the movement of the horn relative to the torus. The interferometer patterns recorded for movements of the horn away from the small torus in steps of an eighth of a wavelength for constant plasma conditions are shown in fig. (8.3) and the following comments are made about these results.

1. The lower oscilloscope trace at each horn position shows predominantly the reflection interferometer output at the start of the plasma decay where the electron density at the plasma axis $n_o >$ the cut off density n_c. For these conditions, it is assumed that the microwave beam was reflected from the plasma boundary where

$$n = n_c \text{ (for 70 GH}_Z \text{ microwaves)} \qquad (8.1)$$
$$= 6.1 \ 10^{13} \text{ cm}^{-3}$$

As the plasma decay proceeded, the boundary region

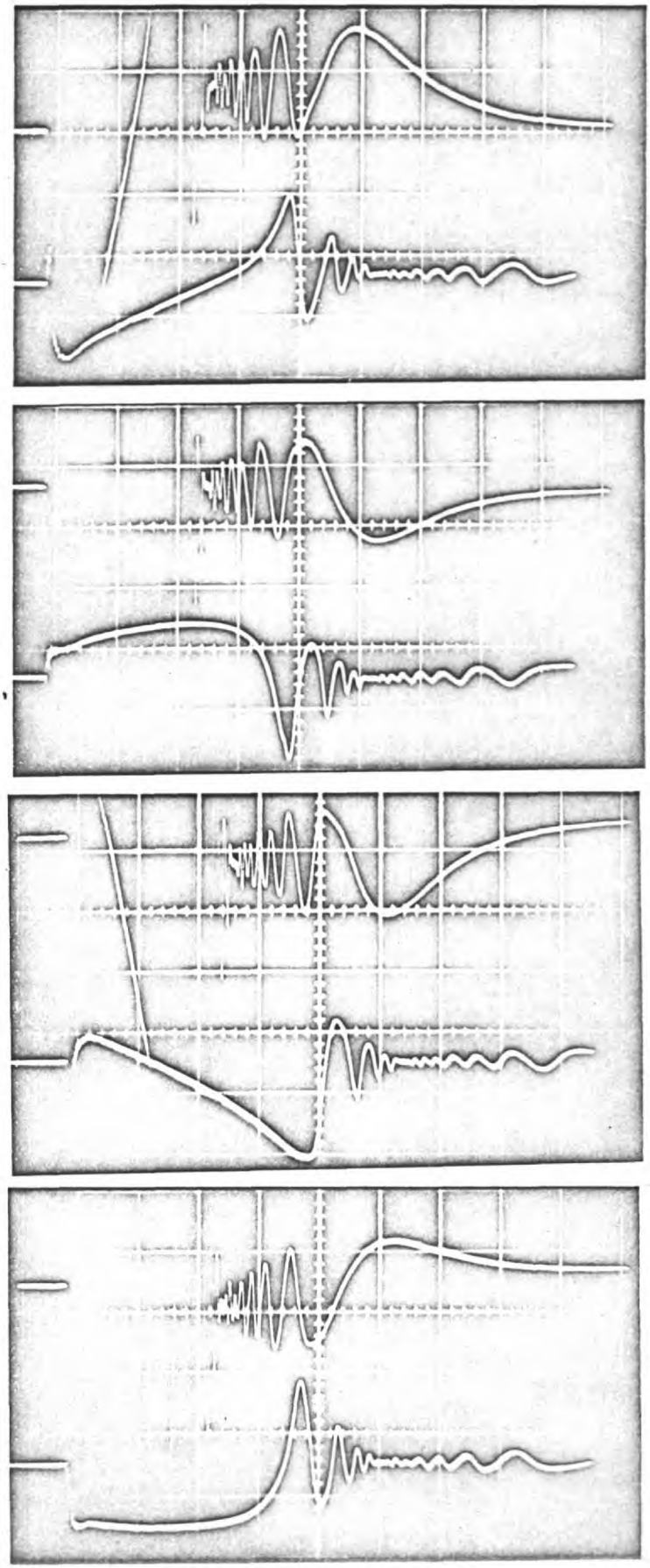

FIG (8.3) Reflection interferometer output for successive horn movements of 1/8 wavelength.

defined by equation (8.1) moved from the torus walls towards the plasma axis giving rise to the observed interference pattern.

2. The upper oscilloscope trace at each horn position shows predominantly the reflection interferometer output during the later stages of plasma decay where $n_o < n_c$. Here, it is assumed that the microwave beam traversed the whole plasma and was reflected from the far torus wall.

3. The interferometer patterns for both sets of traces shown in fig. (8.3) can be seen to be repetitive for successive half integral wavelength separations of the horn and torus. This feature is in agreement with the reflection explanations presented in 1. and 2. above.

(8.3) REFLECTION INTERFEROMETER $n_o < n_c$

In this case the horn and the far torus wall formed a Fabry-Perot type cavity enclosing the changing plasma. It was found in practice that in the large torus experiments the plasma density below cut off could be measured much more readily with this reflection technique than with the transmission technique described in section (8.1). In all experiments, the horn was positioned by performing experiments with the plasma and adjusting for the maximum unidirectional deflection of the last interferometer fringe. The electron density value corresponding to each interference maximum and minimum was found from the tube dimensions and the usual Fabry-Perot relationship.

(8.4) REFLECTION INTERFEROMETER $n_o > n_c$

In this case the interference pattern resulted from the phase change of the reflected microwave beam at the plasma boundary. In the afterglow plasma conditions, this phase change can be described in terms of a combination of two separate effects.

1. The movement of the plasma boundary defined by equation (8.1) affected the phase of the reflected beam (and hence the interference pattern) analagous to altering the separation of a Fabry-Perot type cavity.

2. For the plasma conditions:

collision frequency ν < wave frequency ω < plasma frequency ω_p (8.2)

the penetration of an e.m. wave into a uniform plasma possessing sharply defined boundaries is roughly equal to the free space wavelength corresponding to the PLASMA frequency. Thus there is an inherent change in the depth of penetration of an e.m. wave into the plasma (and hence change in phase of the reflected wave) with changing electron density independent of any plasma boundary movement.

We now evaluate the magnitude of the effect 2. described above by considering an e.m. wave incident normally to a sharply defined uniform plasma where $\omega < \omega_p$. The reflection coefficient R for the wave has been discussed in section (7.6) and it is given by equation (7.29). The expression for the phase change on reflection θ_R can be obtained from equation (7.28) as

$$\tan \theta_R = \frac{2 \mu_i}{1 - \mu_r^2 - \mu_i^2} \qquad (8.3)$$

For the conditions (8.2), corresponding to a low loss plasma beyond the cut off region, the expressions (7.10) and (7.11) for the real and imaginary parts of the complex refractive index approximate to

$$\mu_r = \frac{\nu\,\omega_p}{2\,\omega^2}\left[1 + \frac{5\,\nu}{8\,\omega^2} + \frac{\omega^2}{\omega_p^2}\right] \qquad (8.4)$$

$$\mu_i = \frac{\omega_p}{\omega}\left[1 - \frac{3\,\nu^2}{8\,\omega^2} - \frac{\omega^2}{2\,\omega_p^2}\right] \qquad (8.5)$$

Hence in the limit of zero attenuation loss $\nu \rightarrow 0$ we obtain

$$|R| = 1 \qquad (8.6)$$

and $$\tan\theta_R = \frac{-2\left[\omega_p/\omega\right]}{\left[\omega_p/\omega\right]^2 - 1} \qquad (8.7)$$

From (8.7) it can be seen that as the plasma density increases, $\tan\theta_R$ goes to smaller negative values corresponding to θ_R approaching π., which shows that the plasma behaves increasingly like a perfect conductor. A plot of equation (8.7) is given in fig. (8.4). From an experimental measurement of θ_R it is possible to calculate the electron density beyond the cut off limit for e.m. wave transmission. This type of measurement has been described by Takeda (134) (135). However, Kinney (136) has shown that the phase of the reflected e.m. wave is very dependent upon the actual electron density profile at the plasma boundary and consequently the estimation of electron density by this method is subject to large errors unless the electron density profile is also accurately measured and a suitable correction performed.

The variation of the reflection interferometer output

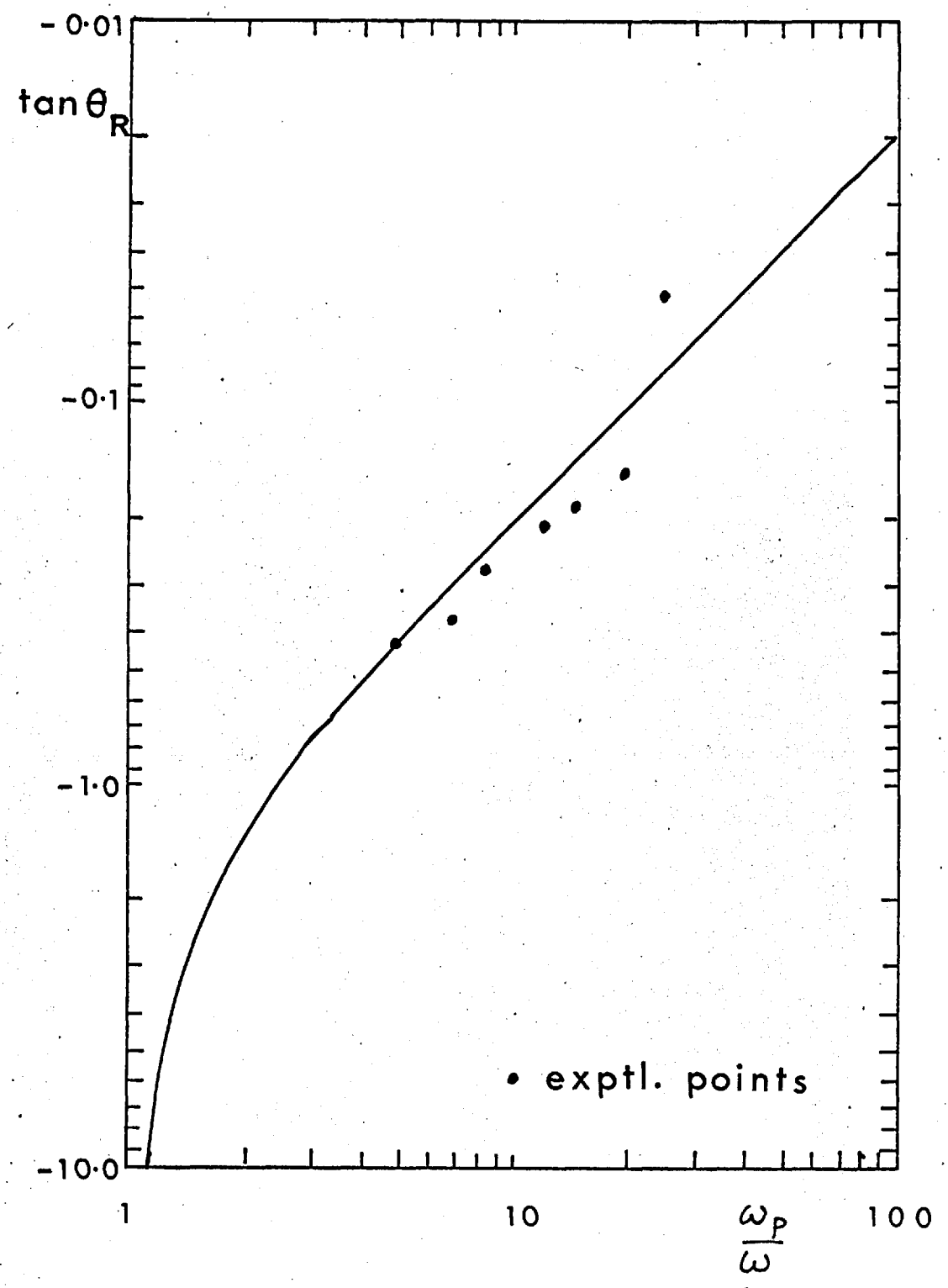

FIG (8.4) Plot of $\tan \theta_R$ versus ω_p/ω.

beyond cut off with changing gas pressure for argon plasma afterglows in the small torus is shown in fig. (8.5). It can be seen that at 50 m.torr gas pressure the reflected wave gave rise to a peak interferometer output at the start of the afterglow, and for the higher gas pressure results the peak signal was shifted to later times in the afterglow. The density profile across the plasma immediately at the start of each afterglow was likely to be uniform in all experiments and hence it was unlikely that the reflected e.m. wave phase changes were caused by plasma boundary movement in this initial region. Consequently the variation in the initial interferometer output with gas pressure shown in fig. (8.5) has been interpreted solely in terms of the variable depth of penetration of an e.m. wave into a static uniform plasma, and this explanation has been checked by two methods.

(a) According to equation (8.7), for a fixed e.m. wave frequency, θ_R is a function of only ω_p and hence the plasma electron densities existing at the times of the initial peak interferometer outputs should all be the same. Values of the average electron density $\bar{n}$ measured with the HCN laser transmission interferometer at the times of the initial peak reflection interferometer outputs are listed in table (8.2) where good agreement is confirmed

gas pressure (m.torr)	time base (μ sec./div.)
20	10
50	20
100	50
150	100
440	100
280	100

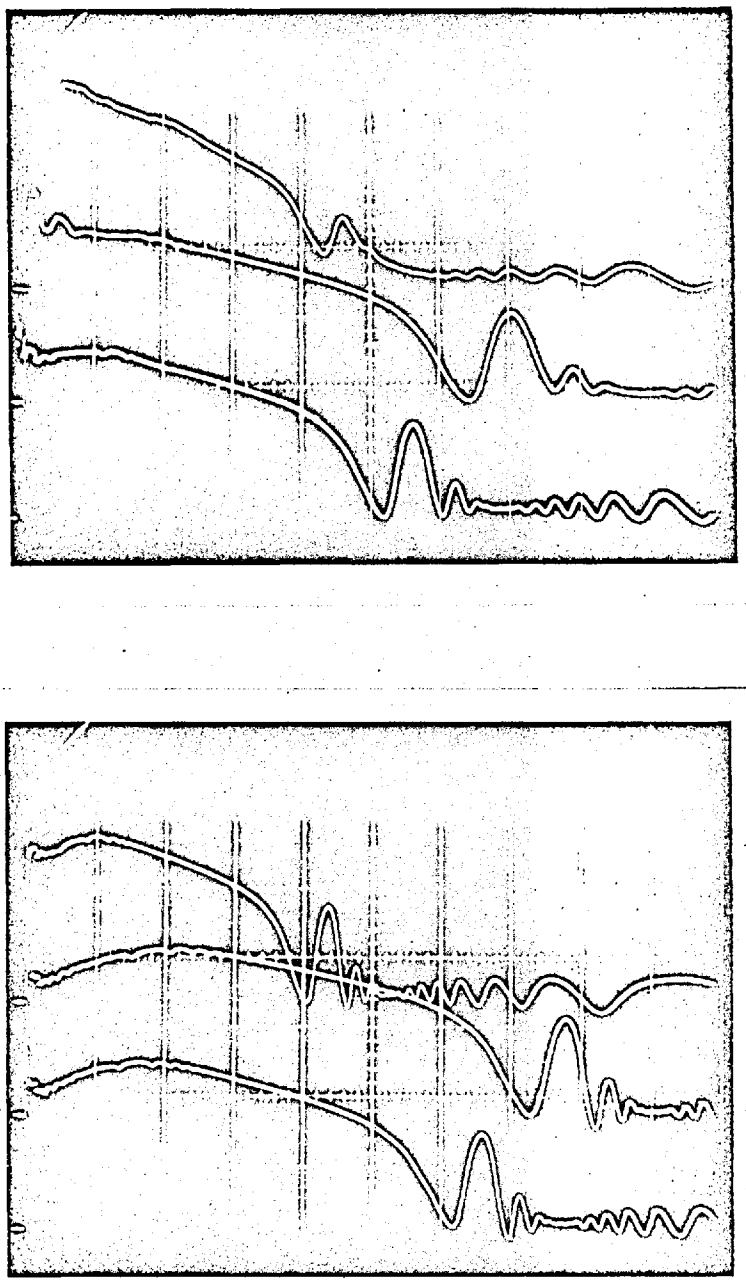

FIG (8.5) Reflection interferometer outputs for argon plasma afterglows.

TABLE (8.2)

GAS PRESSURE (m.torr.)	$\bar{n}$ CORRESPONDING TO PEAK REFLECTION (10^{15} cm^{-3})
50	1.3
100	1.2
150	1.6
280	1.3
440	1.9
880	2.3
1250	1.9

(b) From each set of interferometer outputs shown in fig.(8.5) the initial phase change on reflection relative to the 50 m.torr case was calculated. The plasmas were assumed to be fully ionised initially and the values of electron density (and hence ω_p) were found for each set of results from the gas pressures. The 50 m.torr.result was assumed to be in agreement with equation (8.7) and a theoretical value of θ_R ($\doteq 22^\circ\ 36'$) calculated from this equation was ascribed to this result. This theoretical value of θ_R was used as an absolute calibration of the reflected phases found for the other results. In fig. (8.4) the values of tan θ_R have been plotted versus ω_p/ω for each set of results shown in fig. (8.5), and it can be seen that the points above the 50 m.torr. case generally conform to the expected trend for variable e.m. wave penetration into a static plasma.

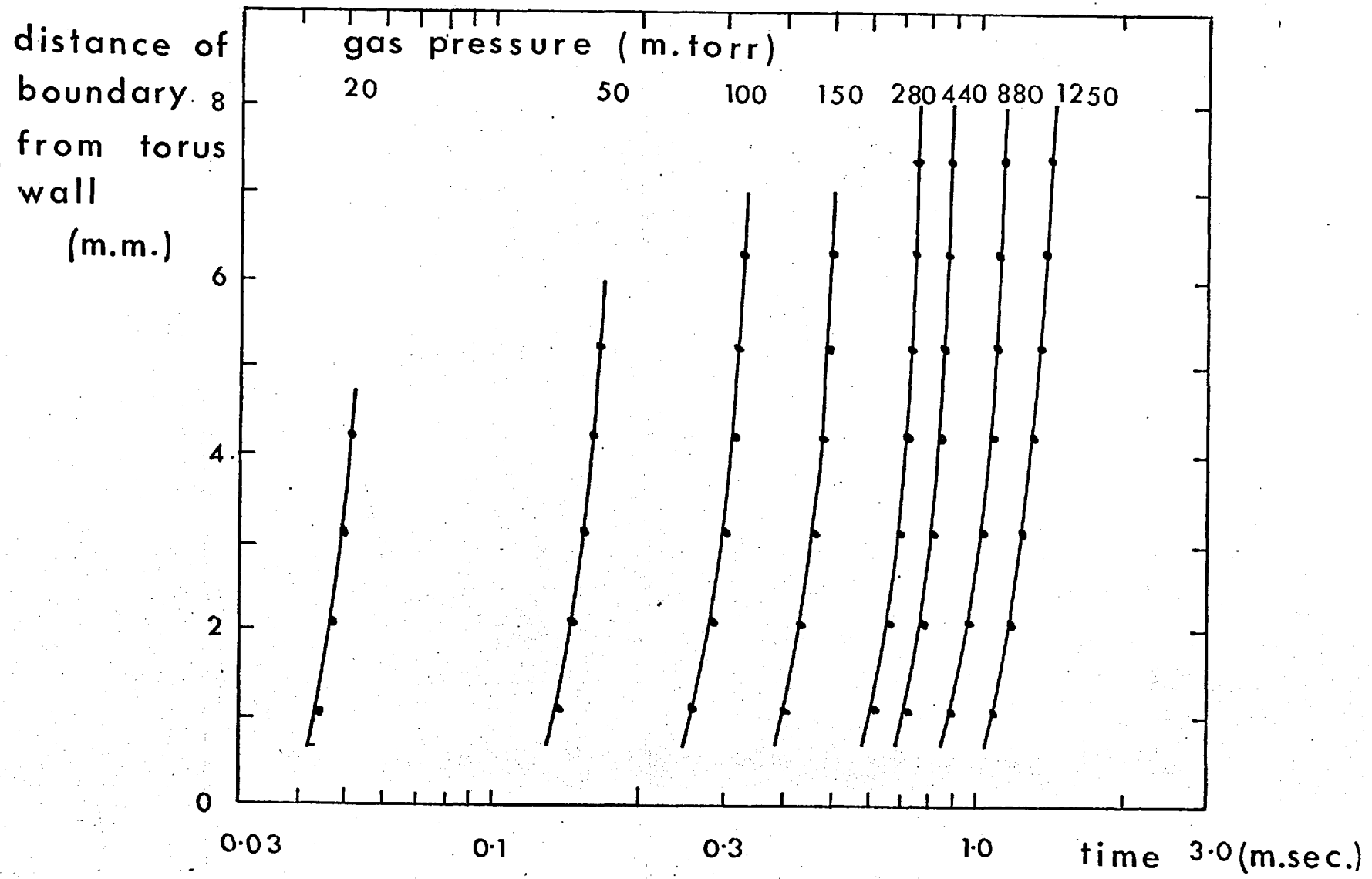

FIG (8.6) Movement of plasma region n = 6.1 10^{13} cm^{-3} in argon afterglows.

For each of the reflection interferometer outputs shown in fig. (8.5) AFTER the initial peak signal, the phase change of the reflected e.m. beam at the plasma was interpreted solely in terms of the movement of the cut off density region defined by equation (8.1). From this interpretation of the results, the distance of the cut off density boundary from the torus wall has been plotted as a function of time for each of the fig. (8.5) results as shown in fig.(8.6).

CHAPTER 9

REVIEW OF PLASMA RECOMBINATION PROCESSES

A review of the previously published work on the theory of plasma recombination and of the experimental measurements that have been made on decaying plasmas is given in this chapter.

(9.1) PLASMA RECOMBINATION

The term plasma recombination is applied to processes occuring within the body of the plasma leading to the recombination of electrons and ions. The recombination coefficient α is defined by the equation

$$\frac{dn_i}{dt} = -\alpha n n_i \qquad (9.1)$$

where n = electron density

n_i = ion density

Equation (9.1) is often written solely in terms of the electron density n since

$$n = Z n_i \qquad (9.2)$$

where Z = ionic charge

and it is often convenient to use the term recombination decay time = τ_R, in preference to α, where

$$\tau_R = (\alpha n)^{-1} \qquad (9.3)$$

(9.2) TWO BODY RADIATIVE RECOMBINATION

Two body radiative recombination refers to the process whereby an electron collides with an ion and is captured into a low lying orbit with the emission of a quantum of radiation. For the example of a helium plasma, this process can be written as

$$He^+ + e^- \longrightarrow He + h\nu \qquad (9.4)$$

Quantum mechanical calculations performed by Stuckelberger (59) and Cillié (60) have indicated values of

$$\alpha \text{ (two body radiative recombination)} \sim 10^{-12} \text{ cm}^3 \text{ sec}^{-1} \qquad (9.5)$$

The fact that two body radiative recombination plays only a minor role in the decay of dense plasmas ($n > 10^{11}$ cm^{-3}) was realised when experimental recombination coefficients of the order of 10^{-10} cm^3 sec^{-1} were found.

(9.3) THREE BODY RECOMBINATION

In order to explain the discrepancy between the experimental and two body recombination coefficients, D'Angelo (62) suggested a process where two electrons collide in the field of an ion leading to the transfer of one electron to a bound state of the ion. This process has been called three body recombination with an electron as the third body and it had been considered earlier by Giovanelli (63) in the study of stellar atmospheres. Taking a helium plasma as an example, the three body recombination process can be written as

$$He^+ + e^- + e^- \longrightarrow He^p + e^- \qquad (9.6)$$

where one electron has been captured into the pth quantum state of the ion to form a highly excited atom. Subsequently, the excited atom may be reionised by the reverse of process (9.6), or the electron may be transferred to other bound states in the atom (usually where $\Delta p = 1$) by further collisional or radiative transitions. The passage of the electron from the highly excited state near the continuum limit to the ground state of the atom, (when the recombination process is said to have occurred), can be described as a random walk in energy space and detailed consideration is given to this in section (9.6).

(9.4) THREE BODY RECOMBINATION IN A DENSE GAS

For cold dense plasmas, Bates and Khare (64) have presented a theory describing the recombination of electrons and ions in the presence of neutral atoms which act as the third bodies. The plasma electron density is assumed to be so low that three body recombination with an electron as the third body is negligible. For the example of a helium plasma we have

$$He^+ + e^- + He \longrightarrow 2\,He \qquad (9.7)$$

Calculations performed by Bates and Khare (64) showed that α can be very large (eg. $\alpha = 5.10^{-8}$ cm^3 $sec.^{-1}$ for an atom density of 10^{19} cm^{-3} at $250^{o}K$). Deloche (65) has computed the recombination coefficient for a plasma where the mechanisms of equations (9.6) and (9.7) occur simultaneously and the plasma conditions necessary for the dominance of process (9.7) over process (9.6) were found to be

$$\left.\begin{array}{c} 10 < \text{gas pressure} < 100 \text{ torr} \\ 10^{9} < n < 10^{11} \text{ cm}^{-3} \\ Te \sim 300^{\circ}K \end{array}\right\} \qquad (9.8)$$

(9.5) THREE BODY MOLECULAR ION FORMATION

The three body collision of an atomic ion with two neutral atoms leading to the formation of a molecular ion was first proposed by Bates (67). Taking a helium plasma as an example, the process can be written as

$$He^{+} + 2He \longrightarrow He_2^{+} + He \qquad (9.9)$$

The exact mechanism for the conversion of an atomic ion to a molecular ion is uncertain and Cronin and Sexton (66) have given a review of proposed mechanisms. However, the general conversion rate can be written in the form

$$\frac{dn}{dt}(ai) = \beta\, p_o^{2}\, n(ai) \qquad (9.10)$$

where $n(ai)$ = atomic ion density

β = ion conversion constant

p_o = gas pressure reduced to $273^{\circ}K$

As regards plasma recombination, the significance of molecular ion formation lies in the fact that the molecular ions are lost by the dissociative recombination process

$$He_2^{+} + e^{-} \longrightarrow He + He \text{ (excited atom)} + K.E. \qquad (9.11)$$

Bates' calculations (67) indicate values for the dissociative recombination coefficient around 10^{-7} cm^{3} sec^{-1} and experimental measurements (68) indicate values around 10^{-9} cm^{3} sec^{-1}. Hence, any molecular ion formed according to equation (9.9) recombines rapidly according to equation (9.11).

Oskam and Mittelstadt (68) have shown that these mechanisms, together with diffusion, are primarily responsible for plasma decay in the region

$$\left.\begin{array}{l} 0.01 < \text{gas pressure} < 10 \quad \text{torr} \\ 10^{9} < n < 10^{11} \quad \text{cm}^{-3} \\ T \sim 300^{\circ}\text{K} \end{array}\right\} \qquad (9.12)$$

Experimentally, molecular ion formation can be distinguished from three body recombination from the different forms of equations (9.10) and (9.1).

(9.6) COLLISIONAL-RADIATIVE RECOMBINATION

The parameters that are typical of the decay of highly ionised laboratory plasma lie in the ranges

$$\left.\begin{array}{l} 0.003 < \text{gas pressure} < 3 \text{ torr} \\ 10^{11} < n < 10^{16} \quad \text{cm}^{-3} \\ 300 < T_e < 30{,}000 \quad ^{\circ}\text{K} \end{array}\right\} \qquad (9.13)$$

These conditions enclose the full range of the parameters p, n and T_e encountered in our experimental work. From sections (9.2) to (9.5), it is clear that plasma recombination in the region described by conditions (9.13), will be due to the combined effects of three body collisional recombination with an electron as the third body, and two body radiative recombination. These two mechanisms are the basis of the collisional radiative (C.R.) recombination plasma model proposed by Bates, Kingston and McWhirter (69) (70) (71) (72). The theory of C.R. recombination enables equations to be formulated

which describe the population densities of the discrete energy levels in the recombining ion or atom.

We shall consider the recombination of electrons with bare nuclei N^{Z+} of charge +Ze to form hydrogen like ions or atoms of charge + (Z-1)e. Let p, q .... be the principal quantum numbers of the discrete levels with c for the continuum and let n(p), n(q) ... be the population densities of ions or atoms in the p, q .... levels. Let n be the free electron density and $n(N^{Z+})$ be the bare nuclei density. It is assumed that the free electrons have a Maxwellian velocity distribution. The collisional and radiative processes contributing to population and de-population of the energy levels are

(a) Three body recombination and the inverse process of ionisation by electron impact

$$N^{Z+} + e^- + e^- \rightleftharpoons N^{(Z-1)+}(p) + e^-$$

where the rate coefficients for these processes are denoted by K (c,p) and K(p,c) respectively.

(b) Collisional excitation from level p to level q by electron impact, and the inverse process of collisional de-excitation.

$$N^{(Z-1)+}(p) + e^- \rightleftharpoons N^{(Z-1)+}(q) + e^-$$

where the rate coefficients for these processes are K(p,q) and K(q,p) respectively.

(c) Spontaneous radiative decay from level p to level q and the inverse process of upward transition by photon absorption

$$N^{(Z-1)+}(p) \rightleftharpoons N^{(Z-1)+}(q) + h\nu$$

where the rate coefficients for these processes are A(p,q) and A(q,p) respectively.

(d) Radiative recombination of an electron with a bare nucleus to form an ion in level p,

$$N^{Z+} + e^{-} \rightleftharpoons N^{(Z-1)+}(p) + h\nu$$

where the rate coefficient for this process is $\beta(c,p)$. Note that the inverse of the above process, photoionisation, is negligibly small.

With assumptions (a) to (d), the set of equations describing the population rates of the bound levels can be written down. The equation for the level p is

$$\begin{aligned}\frac{d}{dt} n(p) = {} & n\, N^{Z+}\, K(c,p) - n\, n(p)\, K(p,c) \\ & - n\, n(p) \sum_{p \neq q} K(p,q) + n \sum_{q \neq p} n(q)\, K(q,p) \\ & + \sum_{q \neq p} n(q)\, A(q,p) - n(p) \sum_{p \neq q} A(p,q) \\ & + N^{Z+}\, n\, \beta(c,p) \qquad (9.14)\end{aligned}$$

Differential equations like (9.14) can be written down for each of the bound levels, but the large number of levels makes their simultaneous solution impossible without making further approximations.

(9.7) C.R. RECOMBINATION IN OPTICALLY THIN PLASMAS

For the case of an optically thin hydrogen-like plasma, photon absorption is negligible and in the summations for radiative transitions in equation (9.14), $q \neq p$ and $p \neq q$ should

be replaced by $q > p$ and $p > q$ respectively. As the rate coefficients $K(p,q)$ and $K(q,p)$ for the collisional processes increase rapidly with increasing principal quantum number due to the level spacing becoming closer, and the rate coefficient $A(p,q)$ for radiative de-excitation decreases with increasing quantum number, there exists a certain value of p denoted by p_s above which radiative processes play a negligible part in level population. This fact implies that the population densities of the levels with $p \geqslant p_s$ are close to theL.T.E. density values and can therefore be obtained from a modified form of Saha's equation (84).

$$\frac{n(p)}{g_p} = \frac{\text{const.}}{T_e^{3/2}} \frac{n(N^{Z+}) \cdot n}{g_{Z+}} \exp\left[\frac{\chi_p}{kT_e}\right] \qquad (9.15)$$

where g_p = statistical weight of the pth quantum state
g_{Z+} = statistical weight of the ground state of the ion of charge + Ze
χ_p = ionisation potential of the ion of charge +(Z-1)e in its pth quantum state.

Levels lying between the atom or ion ground state and the level p_s have population densities very much less than those predicted by equation (9.15) and therefore it follows that over a wide range of conditions,

$$n(p) \ll n \qquad p \neq 1 \qquad (9.16)$$

Another feature typical of afterglow plasmas is that the mean thermal energy is very much less than the energy gap between the ground state and the first excited level so that

$$n(p) \ll n(1) \qquad p \neq 1 \qquad (9.17)$$

Equations (9.16) and (9.17) indicate that the relaxation

times associated with the mechanisms for populating the excited levels are very much shorter than the relaxation times associated with the ground state population or the free electrons Thus, the excited level populations are close to their quasi-equilibrium values and we can put

$$\frac{dn}{dt}(p) = 0 \qquad p \neq 1 \qquad (9.18)$$

Equations (9.15) and (9.18) enable the set of simultaneous differential equations like (9.14) to be reduced to one rate equation (for the level p = 1), a set of (p_s-1) simultaneous equations and a number of Saha equations. McWhirter and Hearn (73), whilst performing a calculation of instantaneous population densities, assumed that level 20 and above had Saha populations and they showed that this assumption was justified for electron densities greater than $10^8 Z^7$ cm^{-3}.

Solutions to the set of equations for the energy level populations have been given by Bates et al (71) (72) and McWhirter and Hearn (73). The plasma recombination rate is put equal to the rate of change of atom ground state population and for the decay of singly charged hydrogen ions the decay equation has the form

$$\frac{dn}{dt} = n\, n(1)\, S(n,T_e) - n^2\, \alpha(n,T_e) \qquad (9.19)$$

where n = electron density
$n(1)$ = atom density
$S(n,T_e)$ = C.R. ionisation coefficient
$\alpha(n,T_e)$ = C.R. recombination coefficient

Numerical values for $S(n, T_e)$ and $\alpha(n, T_e)$ for optically thin hydrogen plasma conditions have been given in (71). For

values of n, T_e existing in afterglow plasmas, it is usually true that

$$S(n, T_e) \ll \alpha(n, T_e) \qquad (9.20)$$

(9.8) C.R. RECOMBINATION IN OPTICALLY THICK PLASMAS

Bates and Kingston (72) have considered C.R. recombination in hydrogen like plasmas that are (a) optically thick towards the Lyman series and (b) optically thick towards all line radiation. For total line absorption within the plasma, downward radiative transitions are exactly balanced by the inverse upward transitions. Therefore in case (a) all the spontaneous transition probabilities to the ground state A(p,1) are set equal to zero in the set of equations (9.14). In this case, level 2 cannot decay radiatively and, as a consequence, a quasi equilibrium population density is not rapidly established so that for case (a)

$$n(p) \ll n(1), \quad n(2) \quad \text{or} \quad n \qquad (9.21)$$
$$p \neq 1, 2$$

and the set of differential equations for population density reduce to two rate equations (for levels 1 and 2), a set of $(p_s - 2)$ simultaneous equations and the Saha equations.

For case (b) all the spontaneous transition probabilities in equations like (9.14) have to be set equal to zero and the level populations approach those given by equation (9.15) appropriate to an L.T.E. situation throughout. For both cases (a) and (b), Bates and Kingston (72) have solved the population levels density equations and values of n(2) and the C.R. recombination

coefficient have been given over wide ranges of n and T_e.

(9.9) C.R. RECOMBINATION IN NON-HYDROGEN LIKE PLASMAS

The treatment of C.R. recombination for hydrogen has been extended by Bates and Kingston (75) to include helium, where metastable levels associated with p = 2 are likely to occur. The relaxation times of populations in the metastable levels are likely to be of the order of that for the ground state population. Two cases have been considered in (75): (a) where the diffusion of metastable atoms to the walls of the discharge tube (where deactivation occurs) is rapid and (b) where metastable diffusion is slow and the plasma is simultaneously optically thick towards the transitions to the ground state. The results obtained for case (a) were similar to those for the optically thin hydrogen plasma and the results for case (b) were similar to those for the hydrogen plasma optically thick towards the resonance lines.

(9.10) DISCUSSION OF BATES et.al. TREATMENT OF C.R.RECOMBINATION

The extensive calculations performed by Bates et al. described above, where the recombination coefficient is found only after solving the equations for population density at each level, have only been applied to hydrogen and helium plasmas. The reason for this is that this method depends entirely on knowing accurately the relevant spontaneous transition probabilities and the rate coefficients for collisional processes for all the energy levels up to the Saha L.T.E. levels. For hydrogen and helium these rate coefficients can be

calculated from the work of Seaton (76) and Gryzinski (77), but for other elements, such as the rest of the rare gases, the errors involved in the rate coefficients are too large to justify solving the population level equations. Even for hydrogen and helium, the errors involved in the rate coefficients mean that otherwise exact calculations have a probable error of about 20%.

(9.11) THE WORK OF BYRON, STABLER AND BORTZ

Byron, Stabler and Bortz (78) have pointed out that, for the C.R. recombination process, there exists a minimum in the total rate of de-excitation of atoms as a function of the principal quantum number of the excited level. This minimum rate arises because the collisional de-excitation rate increases rapidly with increasing quantum number, whereas the radiative de-excitation rate decreases rapidly with increasing quantum number. The nett rate of recombination in equilibrium conditions is therefore limited by the rate of de-excitation of the crossing quantum level p_c at which the minimum occurs. In order to calculate the nett rate of recombination, it is necessary only to find the nett rate of de-excitation of the crossing level p_c due to electron collisions and radiative decay, together with the contributions due to radiative transitions directly from levels above p_c to levels below p_c. Using the same notation as in section (9.6), the nett recombination rate is given by the equation

$$\alpha . n^2 = n . n(p_c) . A(p_c) + n . n(p_c) . K(p_c, p_{c-1}) + \sum_{p=p_c+1}^{\infty} n(p) \sum_{q=1}^{p_c-1} A(p,q) \qquad (9.22)$$

where $A(p_c)$ = reciprocal mean life of level p_c.
Using collisional de-excitation cross-sections found from Gryzinski (77) and transition probabilities found from Salpeter (79), Byron et al. have solved the equation $d\alpha/dp_c = 0$ to obtain the crossing quantum number p_c which on substitution into (9.22) gave the recombination coefficient. The results obtained for hydrogen agreed excellently with Bates' calculations (71).

(9.12) THE WORK OF MAKIN AND KECK

Makin and Keck (80) have considered the recombination of an ion with two electrons in terms of a variational theory proposed by Keck (81), where the motion of the three bodies is described by a representative point in 18 dimensional phase space. A trial surface is chosen in this phase space separating the free and bound states and the rate at which representative points cross the surface in one direction is calculated. The surface is defined by the condition that the relative energy of the recombining electron-ion pair be E_c below the continuum level. The upper bound to the three body recombination rate is found to be of the form

$$\alpha . n^2 = n_i . n^2 . \text{const.}\ T^{1/2} . r_T^5 . \exp\left[\frac{E_c}{kT}\right] . \Gamma\left(\frac{E_c}{kT}\right) \qquad (9.23)$$

where r_T = Thomson's radius
$\Gamma\left(\frac{E_c}{kT}\right)$ = function $\left(\frac{E_c}{kT}\right)$

The function Γ is minimised with respect to E_c to obtain

a least upper bound to the recombination rate and it is shown that this occurs when

$$E_c = 2.5\ k\ T \qquad (9.24)$$

and the resultant upper bound to the recombination coefficient has the form

$$\alpha = 2.3\ 10^{-8}\ n[T_e]^{-4.5} \quad (n\ cm^{-3},\ T\ ^{o}K) \qquad (9.25)$$

(9.13) THE WORK OF D'ANGELO

As well as being the original proposer of three body recombination (62), D'Angelo in a subsequent paper (82) has shown that the recombination rate can be obtained from an elementary calculation based on a theory given by J.J.Thomson (83). According to Thomson's theory, recombination takes place when two oppositely charged particles lose enough of their energy by collision with a third body to describe a closed orbit, where the condition for a closed orbit is

$$r_T = \text{Thomson's radius} = \frac{2e^2}{3kT}$$

It is assumed that if either oppositely charged particle loses an amount of energy $\sim kT$ by collision whilst within a distance r_T of the other charged particle, then recombination occurs. Using this theory, D'Angelo has calculated the recombination rate to be of the form

$$\alpha = 3.9\ \ 10^{-9}.\ n[T_e]^{-4.5} \quad (n\ cm^{-3},\ T_e\ ^{o}K) \qquad (9.26)$$

Expression (9.26) is in close agreement with an earlier expression derived for α by Hinnov and Hirschberg (84), albeit by a somewhat doubtful method, which has the form

$$\alpha = 2.9 \ 10^{-9} \ n \left[T_e\right]^{-4.5} \quad (n \ cm^{-3}, \ T_e \ ^oK) \qquad (9.27) .$$

(9.14) EXPERIMENTAL STUDIES OF PLASMA RECOMBINATION

Experimental studies of plasma recombination have been reported within the density region

$$10^{11} < n < 3.10^{15} \quad cm^{-3}$$

for hydrogen and rare gas plasma afterglows, The types of plasma studied vary over a wide range including plasma jets, unconfined cylindrical plasmas and magnetically confined stellarator plasmas. The decay of electron density has usually been measured with microwave equipment and consequently there are few accurate density measurements for $n > 2. \ 10^{14} \ cm^{-3}$. Most of the electron temperature measurements have been performed spectroscopically in helium plasmas from the intensities of lines originating at upper levels which are assumed to have Saha-Boltzmann populations.

The first accurate measurement of electron-ion recombination in a plasma was reported by Kuckes et al.(85) in 1961, concerning the decay of magnetically confined helium plasma in the model B-1 stellarator. The density range was $5.10^{13} > n > 3. \ 10^{11} \ cm^{-3}$ and temperature range was $0.3 > T_e > 0.1$ e.v . Later, Hinnov and Hirschberg (84) and Hinnov (86) performed detailed spectroscopic measurements over the same range of plasma parameters in helium, using models B-1 and C stellarators. For all these experiments, the excellent charged particle containment reduced the effects of ambipolar diffusion to zero, and this work is probably the most accurate study of decaying helium plasma, in the density range indicated, that has so far been reported. The results have been used

extensively by theoretical workers (75) as a basis for the comparison of C.R. recombination theory with experiment.

Robben et al (87) have reported measurements made spectroscopically on decaying plasmas in a helium arc jet. Electron densities in the range $4 . 10^{14}$ to $4 . 10^{12}$ cm^{-3} and electron temperatures in the range 0.30 to 0.15 e.v.were inferred from absolute line intensity measurements.

Cooper and Kunkel (88) have reported on the decay of magnetically confined hydrogen plasma where spectroscopic techniques were used to study the decay region over the ranges $5\ 10^{15} > n > 10^{15}$ cm^{-3} and $3 > T_e > 1$ e.v.

Chen (89) (90) (91) has reported measurements made on hydrogen and rare gas plasma decays with microwave electron density measurements in the range $2\ 10^{14} > n > 10^{10}$ cm^{-3}. A triple electrostatic probe was used to measure electron temperature over the range $7000 > T_e > 300$ ^{o}K and a resistance thermometer was used to measure atom temperature over the range $800 > T_a > 300$ ^{o}K.

Newton and Sexton (92) (93) have reported on the decay of hydrogen, deuterium and helium plasmas in a cylindrical tube with no confining magnetic field. A combination of laser and microwave interferometers operating at 3.39 μm, 2.25 mm and 8.60 mm wavelengths were used to measure electron density over the range $2\ 10^{15} > n > 8\ 10^{11}$ cm^{-3}.

Collins and Hurt (94) (95) have studied the decay of helium plasma at densities $< 2\ 10^{13}$ cm^{-3} with particular emphasis upon the time dependent behaviour of the atomic light emitted in low pressure afterglows.

Gusinow and Gerado (96) (97) have reported a comprehensive study of helium and argon plasma decays in the density and temperature ranges $1.4\ 10^{15} > n > 5\ 10^{13}$ cm^{-3} and $7000 > T_e > 3000$ °K. Their plasma was contained in a tube with Brewster angled windows which formed part of a laser cavity and detailed profiles for electron and neutral atom density were obtained by movement of the cavity relative to the plasma.

Experiments of less significance, in which plasma decays have been studied, have been reported by Anisimov et al.(98), Quinn (99), Brand (100), Irons and Millar (101) and Aleskovskii and Granovskii (102).

It is very difficult to make a valid comparison between the recombination coefficient values found in each of the experiments reviewed above. For most of the hydrogen and helium experiments quoted, Newton (92) (93) has plotted the values of α versus n on a log scale. These plots showed an order of magnitude scatter in the values of α over the density range $10^{12} - 10^{16}$ cm^{-3}. The validity of plotting α versus n for experimental results measured in different sizes of decaying plasmas is very questionable. From equations (9.25) (9.26) and (9.27), the C.R. recombination coefficient can be seen to depend strongly on T_e as well as n, so that in a decaying plasma, α depends in a complex manner on the rate of energy loss from the plasma. The rate of energy loss, in turn, depends on such physical parameters as the plasma optical depth, thermal conductivity losses etc. all of which vary with the size and geometry of the plasma. Hence, it is to be expected that α, at a fixed value of n, varies quite markedly with the size of the decaying plasma. Only by considering the various complex physical processes that occur in afterglow plasmas in detail,

can a valid comparison of the results of the different experiments be made.

CHAPTER 10

DENSITY AND TEMPERATURE GRADIENTS IN AFTERGLOW PLASMAS.

This chapter is concerned with the density and temperature gradients existing in cylindrically symmetric afterglow plasmas. It is shown that these gradients are associated with the heat flux in the plasma and that the heat transport equation determines the overall decay rates of the plasma parameters as well as their distribution profiles. The theoretical work is aimed at evaluating mathematical functions for the distribution profiles and at deriving equations which can act as a basis for the energy balance in an afterglow plasma which is discussed in detail in Chapter 12. In the experimental work, time resolved measurements of electron density profiles in afterglow plasmas were found using two methods:(1) double electric probes and (2) an entirely new method involving the simultaneous plasma transmission and reflection of e.m. waves of two different frequencies. Finally, expressions are worked out for the total phase shift and total attenuation of an e.m. wave traversing the finite density and temperature profiles that are found in afterglow plasmas.

(10.1) TRANSPORT PHENOMENA IN AFTERGLOW PLASMAS

In deriving the heat transport equation for an afterglow plasma, we will consider an ideal plasma possessing the following properties.

1. The plasma is assumed to be cylindrically symmetric so that all profile functions for the plasma parameters can be written in terms of one variable : the radius vector r. The radius of the discharge tube is denoted by a and the tube walls are assumed to remain at a fixed temperature T_w which is close to $300^{\circ}K$.

2. The effects of diffusion and directed plasma motion upon the decay of plasma are assumed to be negligible in comparison to three body C.R. plasma recombination. According to the theory of C.R. recombination given in Chapter 9, and in particular equations (9.26) and (9.1), we will therefore write the electron density decay equation as

$$\frac{d}{dt} n(r) + C \frac{[n(r)]^3}{[T_e(r)]^{9/2}} = 0 \qquad (10.1)$$

where $C = 3.9\ 10^{-9}$ $(n\ cm^{-3},\ T_e\ ^{\circ}K)$

3. A highly ionised plasma is assumed with

$$10^{-5} < n/n(1) < 0.3 \qquad (10.2)$$

where $10^{17} < n(1) < 10^{15}$ cm^{-3} (10.3)

The above conditions correspond to those encountered in our experiments.

4. The thermal conductivities of hydrogen and rare gas plasmas are discussed in Appendices (A.2) and (A.3), where it is shown that over the temperature ranges encountered in plasma afterglows.

Atomic thermal conductivity $\gg$ Lorrentz gas plasma thermal conductivity (10.4)

Consequently, in afterglow plasmas the total thermal conductivity loss is almost entirely due to atomic thermal .

conduction effects.

In Appendix (A.2) we have shown that, over the afterglow temperature range, the coefficient of atomic thermal conductivity χ has the form

$$\chi = K T_a$$

where T_a = atom temperature

K = constant for a particular type of gas given by Table (A.2.2)

5. The total energy content per unit volume U of the plasma is taken to be equal to the sum of the thermal energy per unit volume of the plasma particles (assuming a Maxwellian velocity distribution for each particle species) and a fraction q of the total ionisation energy per unit volume of the plasma.

$$\therefore U = \sum_x \frac{3}{2} n_x(r)\, k\, T_x(r) + q\, I\, n(r) \qquad (10.6)$$

where x = particle species (electrons, ions, atoms).

I = Ionisation energy of atom

The factor q allows for the fact that, as the plasma recombines, part of the recombination energy escapes from the plasma in the form of radiation. A detaileddiscussion of the factor q will be given in Chapter 13.

6. We assume that no pressure gradients exist in the decaying plasma, which can be expressed mathematically by the equation

$$\frac{\partial}{\partial r} \sum_x n_x(r)\, k\, T_x(r) = 0 \qquad (10.7)$$

The transport equation for heat flow inside the plasma is

taken to be that given by the continuity equation with no external sources of heat.

$$\frac{\partial U}{\partial t} + \text{div } Q = 0 \qquad (10.8)$$

where Q = heat flux = $-K\, T_a(r)$ grad.$(T_a(r))$

In cylindrical coordinates equation (10.8) is written as

$$\frac{\partial U}{\partial t} - \frac{K}{r} \cdot \frac{\partial}{\partial r}\left[r.T_a(r).\frac{\partial}{\partial r} T_a(r) \right] = 0 \qquad (10.9)$$

Substituting expression (10.6) for U into equation (10.9) we derive the heat transport equation for a cylindrical afterglow plasma

$$\frac{\partial}{\partial t}\left[\sum_x \frac{3}{2} n_x(r) k T_x(r) \right] + q I \frac{\partial n(r)}{\partial t} = \frac{K}{r}\frac{\partial}{\partial r}\left[r.T_a(r).\frac{\partial T_a(r)}{\partial r} \right] \qquad (10.10)$$

Approximate solutions to equation (10.10) will now be found for the plasma conditions associated with the initial, intermediate, and final decay regions in plasma afterglows.

(10.1.1) Initial Decay Region

The initial decay region of high density plasma, such as was encountered in our experiments, has the following typical conditions

$$\begin{aligned} n &\geqslant 10^{15} \text{ cm}^{-3} \\ n(1) &\geqslant 3.10^{15} \text{ cm}^{-3} \\ T_e &\sim 10{,}000 \ ^{\circ}\text{K} \end{aligned} \qquad (10.11)$$

These conditions correspond to the situation where the electron, ion and atom temperatures are closely coupled so that the plasma can be described in terms of a single temperature T .

$$\text{i.e.} \quad T(r) = T_e(r) = T_i(r) = T_a(r) \qquad (10.12)$$

For these same conditions the factor q is close to unity (see Chapters 12 and 13) and since $I \gg kT$ we can write

$$q\, I\, n(r) \gg \sum_x \frac{3}{2} n_x\, k\, T_x(r) \qquad (10.13)$$

$$\text{subject to} \quad n \geqslant \frac{n(1)}{30} \qquad (10.14)$$

For approximation (10.13) the energy transport equation (10.10) reduces to

$$I \frac{\partial n(r)}{\partial t} = \frac{K}{r} \frac{\partial}{\partial r}\left[r . T(r) . \frac{\partial T(r)}{\partial r}\right] \qquad (10.15)$$

The electron density and temperature profile functions can now be obtained by solving equation (10.15) in together with equation (10.1). Unfortunately, it is not possible to find a general solution to this pair of non-linear equations. However, by a method of successive approximations, it is possible to find the profile functions and the density and temperature decay rates

that exist when a steady state has been established.

For the first order approximation we will assume that

$$\frac{\partial}{\partial t} n(r) = -L \tag{10.16}$$

where L is independent of r. Combining equations (10.15) and (10.16) we obtain

$$-L I = \frac{K}{r} \frac{\partial}{\partial r} \left[r . T(r) . \frac{\partial T(r)}{\partial r} \right] \tag{10.17}$$

Equation (10.17) shows that the first order approximation (10.16) is equivalent to assuming a uniform generation of heat throughout the decaying plasma.

Integrating equation (10.17) with the boundary conditions that $\partial T(r)/\partial r = 0$ at $r = 0$, gives

$$-\frac{L I}{K} r = 2 T(r) \frac{\partial}{\partial r} T(r) \tag{10.18}$$

Integrating equation (10.18) with the boundary conditions that $T(r) = T_o$ at $r = 0$ and $T(r) = Tw$ at $r = a$, gives

$$T(r) = \left[T_o^2 \left[1 - \left(\frac{r}{a}\right)^2 \right] + Tw^2 \left(\frac{r}{a}\right)^2 \right]^{\frac{1}{2}} \tag{10.19}$$

and $$T_o^2 = \frac{L I a^2}{2K} + Tw^2 \tag{10.20}$$

For this initial high density region, $T_o >> T_w$, and we can approximate (10.19) to

$$T(r) = T_o \left[1 - \left(\frac{r}{a}\right)^2 \right]^{1/2} \tag{10.21}$$

The first order approximation to the equation describing the decay of electron density is obtained from equations (10.16) and (10.20) as

$$-I \frac{dn}{dt} = \frac{2K}{a^2} (T_o^2 - T_w^2) \qquad (10.22)$$

The first order approximation to the electron density distribution profile is obtained by substituting the form of $T(r)$ given by (10.21) into equation (10.1) which yields

$$n(r) = n_o \left[1 - \left(\frac{r}{a}\right)^2\right]^{9/8} \qquad (10.23)$$

where n_o = electron density at $r = 0$.

To obtain a second order approximation for profiles $T(r)$, and $n(r)$, the first order approximation form of $n(r)$ has to be substituted into equation (10.15). Because of difficulties associated with the integration, the first order form of $n(r)$ given by equation (10.23) is slightly modified (with little loss in accuracy) to become

$$n(r) = n_o \left[1 - \left(\frac{r}{a}\right)^2\right] \qquad (10.24)$$

Thus the second order approximation to the energy transport equation (10.15) can be written as

$$\frac{I}{K} \frac{\partial n_o}{\partial t} . r . \left[1 - \left(\frac{r}{a}\right)^2\right] = \frac{\partial}{\partial r} \left[r . T(r) . \frac{\partial T(r)}{\partial r}\right] \qquad (10.25)$$

Integrating (10.25) twice with the boundary conditions as above and $T_o >> T_w$ yields

$$T(r) = T_o \left[1 - \frac{4}{3}\left(\frac{r}{a}\right)^2 + \frac{1}{3}\left(\frac{r}{a}\right)^4 \right]^{1/2} \qquad (10.26)$$

$$T_o^2 = -\frac{3\,a^2\,I}{8\,K}\left[\frac{\partial n_o}{\partial t}\right] \qquad (10.27)$$

and the corresponding second order approximation to the electron density profile is

$$n(r) = n_o \left[1 - \frac{4}{3}\left(\frac{r}{a}\right)^2 + \frac{1}{3}\left(\frac{r}{a}\right)^4 \right] \qquad (10.28)$$

Substituting (10.28) into (10.15) and repeating the above processes gives third order approximations of the forms

$$T(r) = T_o \left[1 - 1.42\left(\frac{r}{a}\right)^2 + 0.47\left(\frac{r}{a}\right)^4 - 0.05\left(\frac{r}{a}\right)^6 \right] \qquad (10.29)$$

$$T_o^2 = -0.35\,a^2\,\frac{I}{K}\left[\frac{\partial n_o}{\partial t}\right] \qquad (10.30)$$

$$n(r) = n_o \left[1 - 1.42\left(\frac{r}{a}\right)^2 + 0.47\left(\frac{r}{a}\right)^4 - 0.05\left(\frac{r}{a}\right)^6 \right] \qquad (10.31)$$

Plots of the profile distribution functions corresponding to the successive order approximation solutions to the energy transport equation in the initial decay region are shown in fig. (10.1).

(10.1.2) Intermediate Decay Region

We will now find solutions of the energy transport equation (10.10) for the approximation

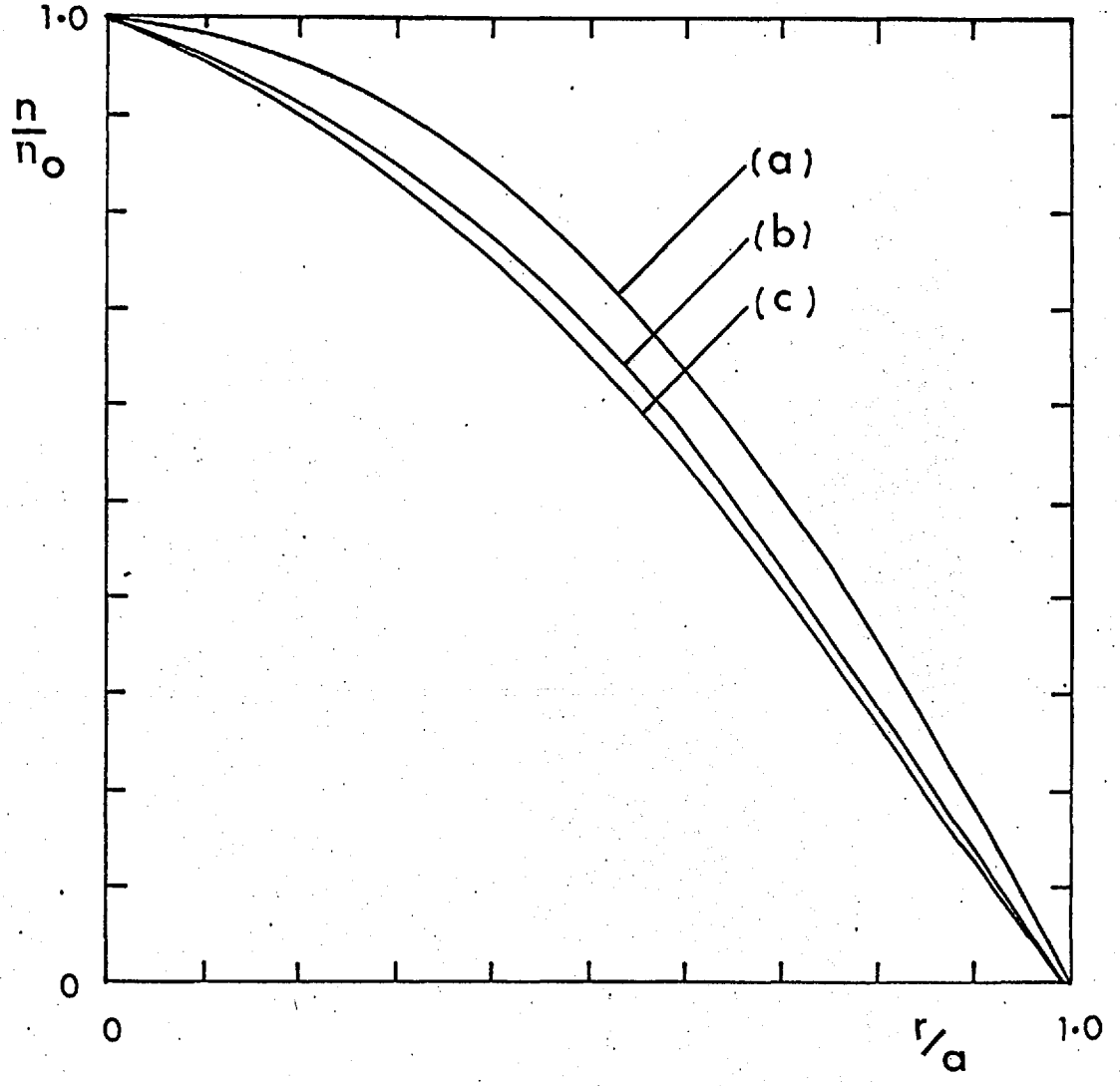

FIG (10.1) Plot of electron density profiles

(a) $n = n_o \left[1 - \left(\frac{r}{a}\right)^2\right]$

(b) $n = n_o \left[1 - \frac{4}{3}\left(\frac{r}{a}\right)^2 + \frac{1}{3}\left(\frac{r}{a}\right)^4\right]$

(c) $n = n_o \left[1 - 1.42\left(\frac{r}{a}\right)^2 + 0.47\left(\frac{r}{a}\right)^4 - 0.05\left(\frac{r}{a}\right)^6\right]$

$$q\, I n(r) \ll \left[\sum_x \frac{3}{2}\, n_x(r)\, k\, T_x(r)\right] \qquad (10.32)$$

Condition (10.32) applies to the intermediate electron density decay regions of high gas pressure plasma afterglows where typically

$$\left.\begin{aligned} 10^{13} < n < 10^{15} \ \mathrm{cm}^{-3} \\ n < \frac{n(1)}{30} \end{aligned}\right\} \qquad (10.33)$$

Using both inequalities (10.32) and (10.33) equation (10.10) reduces to

$$\frac{\partial}{\partial t}\left[\frac{3}{2}\, n(1)(r)\, k\, T_a(r)\right] = \frac{K}{r}\frac{\partial}{\partial r}\left[r \cdot T_a(r) \cdot \frac{\partial T_a(r)}{\partial r}\right] \qquad (10.34)$$

The assumption that no pressure gradients exist in the afterglow plasma as expressed in equation (10.7) means that the L.H.S. of equation (10.34) is always independent of the variable r. This condition is the same as that introduced into the heat transfer equation by the first order approximation (10.16) made in section (10.1.1). Hence the complete solutions to equation (10.34) have the same form as those found for the first order approximation in the initial decay region, so that for $T_a \gg T_w$ we can immediately write

$$T_a(r) = T_{ao}\left[1 - \left(\frac{r}{a}\right)^2\right]^{1/2} \qquad (10.35)$$

$$n(1)(r) = n(1)_o\left[1 - \left(\frac{r}{a}\right)^2\right]^{-1/2} \qquad (10.36)$$

and the equation describing the decay of atom temperature at the plasma axis is

$$-\frac{3}{2} n(1)_o k \frac{\partial T_{ao}}{\partial t} = \frac{2.K}{a^2} (T_{ao}^2 - T_w^2) \qquad (10.37)$$

In our experiments, the value of atom density was inferred from the gas filling pressure which gives the average value of atom density $\overline{n(1)}$ existing in the plasma. The relationship between $\overline{n(1)}$ and the axial value of atom density $n(1)_o$ is given, using equation (10.36), by

$$\overline{n(1)} = \frac{2\, n(1)_o}{a^2} \int_o^a \left[1 - \left(\frac{r}{a}\right)^2 \right]^{-1/2} . r . dr \qquad (10.38)$$

$$= 2\, n(1)_o \qquad (10.39)$$

Hence the equation for the decay of the axial value of atom temperature in terms of the average value of atom density in this intermediate decay region is

$$-\frac{3}{4} \overline{n(1)} k \frac{\partial T_{ao}}{\partial t} = \frac{2\,K}{a^2} (T_{ao}^2 - T_w^2) \qquad (10.40)$$

In this intermediate decay region, the coupling between T_e, T_i and T_a is not as strong as in section (10.1.1) so that the actual values of these parameters are not the same. However, the coupling is strong enough for the forms of the radial dependence of each of these parameters to be similar. Therefore the predicted forms of $n(r)$ and $T_e(r)$ for this intermediate decay region are

$$T_e(r) = T_{eo}\left[1 - \left(\frac{r}{a}\right)^2\right]^{1/2} \qquad (10.41)$$

$$n(r) = n_o\left[1 - \left(\frac{r}{a}\right)^2\right] \qquad (10.42)$$

(10.1.3) Final Decay Region

In the final decay region where typically

$$n \leqslant 10^{12} \quad \text{cm}^{-3} \qquad (10.43)$$

$$n(1) \geqslant 10^{15} \quad \text{cm}^{-3} \qquad (10.44)$$

there is only very weak coupling between T_e, T_i and T_a, and consequently no longer any relationship between the forms of $T_e(r)$ and $T_a(r)$. The atom temperature profile has the form

$$T_a(r) = \left[T_{ao}^2\left[1 - \left(\frac{r}{a}\right)^2\right] + T_w^2\left(\frac{r}{a}\right)^2\right]^{1/2} \qquad (10.45)$$

where $T_w < T_a < 3T_w$
and from (10.45), the profiles for $T_a(r)$ and its associated $n(1)(r)$ become more uniform the closer T_a approaches to T_w.

In a non-magnetically confined plasma the effects of diffusion are, in practice, likely to become more important in the final decay region, since the recombination time becomes very large at low electron densities, and the electron density profile is likely to become the steady state diffusion profile

$$n(r) = J_o\left(\frac{2{\cdot}405\,.\,r}{a}\right) \qquad (10.46)$$

(10.1.4) Validity of the Afterglow Equilibrium Profiles

The actual profiles of density and temperature present during the earliest stages in experimental afterglows lie somewhere between the profiles existing at the end of the discharge current heating phase and the equilibrium profiles found above. This region can only be studied theoretically by a full solution of equation (10.10) with the appropriate initial boundary condition. However, provided the relaxation time for the establishment of the plasma afterglow equilibrium is fairly rapid, we can afford to ignore the above very intractable region.

The relaxation times for the various plasma parameters are considered in detail in Chapter 12, from which we can state that: starting from a nearly fully ionised plasma, the afterglow equilibrium of all the plasma parameters is established by the time the degree of ionisation is less than 10%. Hence the solutions to the energy transport equations found in sections (10.1.1) to (10.1.3) should apply below this degree of ionisation.

(10.2) ELECTRON DENSITY PROFILE MEASUREMENTS USING ELECTRIC PROBES

A double electric probe (Langmuire probe) was scanned across the diameter of the plasma and the probe saturation ion current was recorded. Details of the experiment are as follows.

The probe consisted of two platinum wires 0.5 mm diameter, 1.5 mm separation fitted into a dual bore ceramic tube so that only the squared off ends of the wires were in contact with the

plasma. The bias circuit consisted of a 32 μF capacitor charged from a 60 volt battery and potentiometer arrangement. A series of dual ganged resistors R = 0.9, 2.5, 5.0 and 10.0 kΩ were used to measure the probe current. The probe was introduced into the torus using the same method as for the magnetic probes discussed in section (4.2.1). The probe was scanned horizontally across the torus diameter from a position 5 mm outside the line of the outer wall to a position within 2 mm of the inner wall. The probe was moved by steps of 4 mm in the small torus and 5 mm in the large torus. The bias voltage was chosen to be 40 volts so that the probe characteristic was always in the saturated ion current regime (ie. probe bias voltage $\gg T_e$ in e.v.). The bias voltage was kept constant throughout to avoid spurious results due to the change in probe sheath size in the plasma with changing bias.

The bore of the torus side port containing the probe was 18 mm and the measured probe current profiles were not symmetrical about the plasma axis. The asymmetry increased with increasing pressure of the gas, which suggested that it was not due to plasma diffusing into the side port, but rather due to the transport of energy to the boundary of the plasma. Because of the affects producedby the side port, only the half profiles measured from the tube axis to the inner wall were taken as being representative of the profiles existing in a perfect torus.

Comprehensive reviews of double electric probe methods have been given by Kagan and Perel (16), Jones and Saunders (103) and Johnson and Malter (104). From (16) we can write the saturation ion current i_p in the form

$$i_p = b\, n\, e \left(\frac{2kT_e}{M}\right)^{\frac{1}{2}} S(V) \qquad (10.47)$$

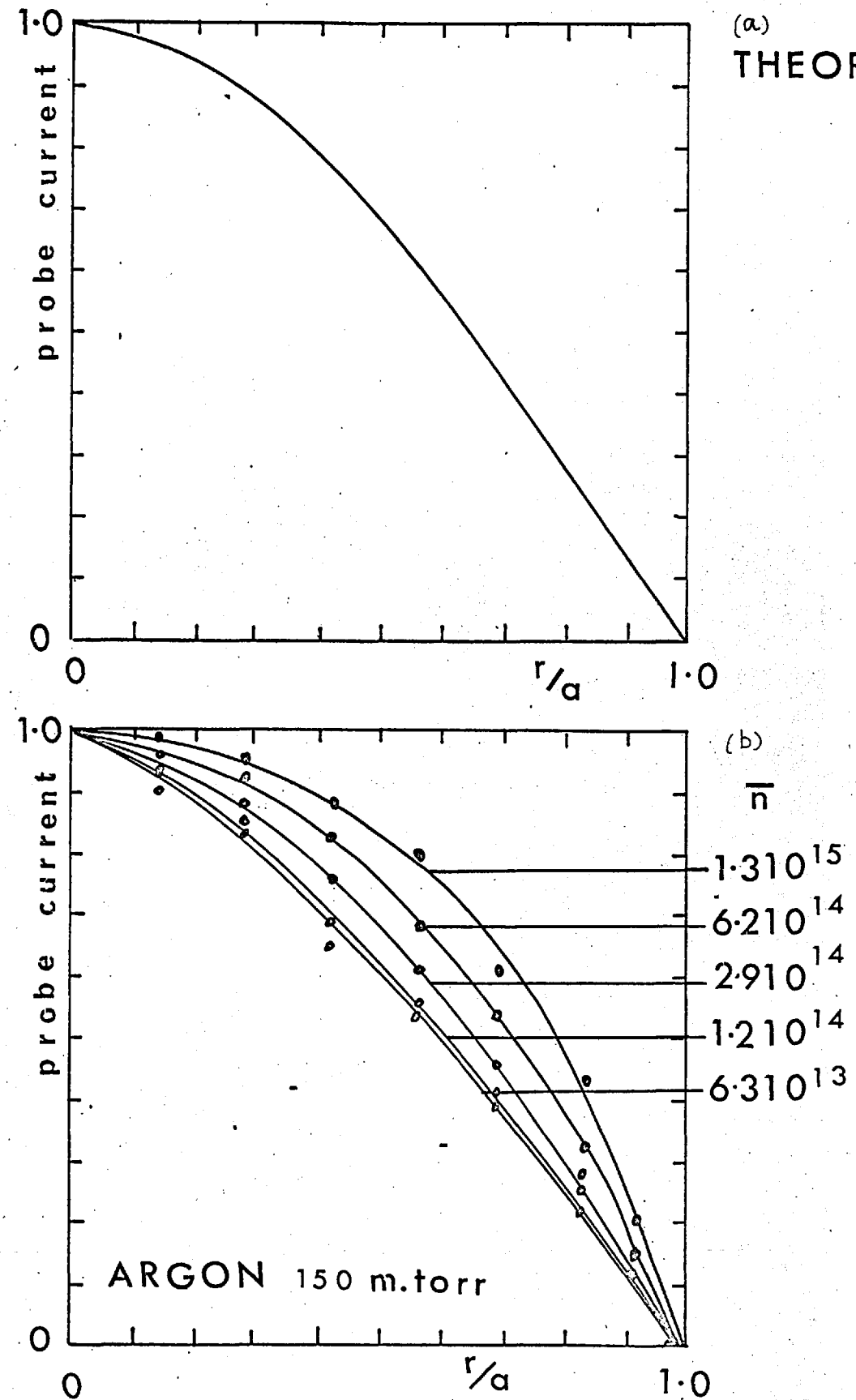

FIG (10.2) Theoretical and experimental double electric probe plots.

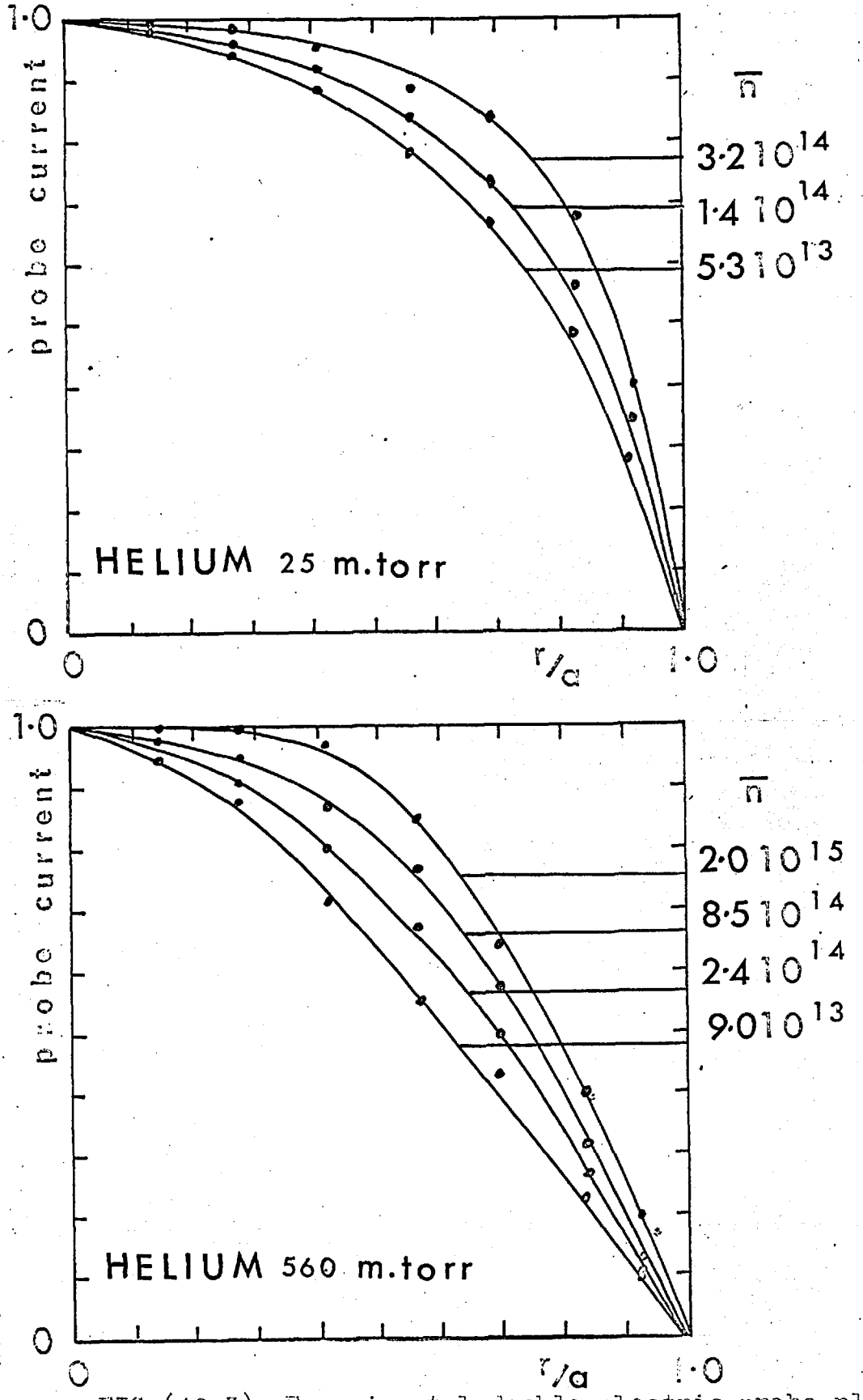

FIG (10.3) Experimental double electric probe plots.

where b = constant depending on probe geometry
S(V) = sheath area (a function of bias voltage V)
M = ionic mass.

From (10.47), for a given probe with a constant bias, the ion current profile $i_p(r)$ in a plasma possessing distributions $n(r)$ and $T_e(r)$ is therefore

$$i_p(r) = \text{constant.}\ n(r)(T_e(r))^{\frac{1}{2}} \qquad (10.48)$$

A plot of the normalised distribution profile for i_p based on equation (10.48) for the quasi-equilibrium afterglow plasma profiles (10.24) and (10.21) is shown in fig.(10.2)(a).

In fig. (10.2)(b) and fig. (10.3) plots of the saturation ion current profiles obtained experimentally are shown. Each graph shows the variation of the normalised probe profile in the decaying plasma. The average value of electron density (found from laser or microwave measurements) corresponding to each profile is indicated on the graphs. A comparison of these experimental results with fig. (10.2)(a) shows that the probe current profile existing in the plasma when a state of quasi-equilibrium is reached, (ie. when the profile shape ceases to change with average electron density), is in excellent agreement with the theoretical prediction.

Thus the electric probe saturation ion current measurements give good confirmation of the quasi-equilibrium solutions of the energy transport equation found in section (10.1).

(10.3) ELECTRON DENSITY MEASUREMENTS USING E.M. WAVES

In addition to the electric probe measurements, the time

history of the electron density profile in the decaying plasma was measured by a new technique involving electromagnetic wave diagnostics at only two different wave frequencies.

Previously reported measurements of electron density profiles using e.m. waves (98) (105) have relied on the simultaneous probing of the plasma with many different wave frequencies. Anisimov et al. (98) have described an experiment where several microwave frequencies were reflected from a plasma and the density profile was constructed from the relative positions of the reflection regions (cut off density value regions) for each wave frequency. Wharton and Slager (105) have described a microwave transmission experiment using five different wave frequencies. In this latter experiment, the density profile was inferred from the phase shifts integrated over the density profile for four of the wave frequencies at the cut off transmission point for the fifth wave frequency. (This latter wave frequency defined the peak density value of the profile).

Both the techniques (98) (105) described above suffer from the great disadvantage that the number of points that can be used to construct a density profile are equal to the number of different wave frequencies employed. Consequently, a vast quantity of expensive equipment is required to perform an accurate profile measurement. Also, the spread of the points corresponding to each wave frequency over the density profile depend on the absolute value of density. Therefore, for a range of wave frequencies covering, say, an order of magnitude, the profile can only be constructed over a very limited range of absolute density which is $<<$ an order of magnitude. As will be shown below, neither of these restrictions apply to our new technique.

In our new method of density profile measurement, we combine the measurement of the reflection of one (low) wave frequency at the plasma with the simultaneous measurement of the transmission of another (high) wave frequency across the plasma. We will assume that the plasma is cylindrically symmetric so that the plasma electron density as a function of position and time can be written in the form

$$n(r,t) = n_o(t) . f(x) \qquad (10.49)$$

where $n_o(t)$ = density at the plasma axis (as a function of time)

$f(x)$ = normalised density distribution profile

$x = \frac{r}{a}$ where a = tube radius, r = radial position

The transmission of the higher frequency e.m. wave across the plasma is used to find the value of electron density $\overline{n(t)}$ averaged across the whole density profile along the line of sight of the wave

ie. $$\frac{\overline{n(t)}}{n_o(t)} = \int_0^1 f(x)\, dx \qquad (10.50)$$

The reflection of the lower frequency e.m. wave at the plasma is used to measure the radial position r_b of the plasma boundary corresponding to the cut off density value n_c of the low frequency wave. The equation defining the variation of r_b with time in the decaying plasma is

$$n(r_b,t) = n_c \qquad (10.51)$$

and from equation (1049) this can be re-written in the form

$$n_o(t) . f(x_b) = n_c \qquad (10.52)$$

where $x_b = \frac{r_b}{a}$

For the simultaneous measurement of r_b and $\bar{n}$ we can eliminate $n_o(t)$ from equations (1052) and (10.50) to yield the relationship

$$f(x_b) = \frac{n_c}{\bar{n}} \int_o^1 f(x).dx \qquad (10.53)$$

Values of the integral appearing in (10.53) for several forms of normalised density distribution have been listed in table (10.1).

TABLE (10.1)

$f(x)$	$\int_o^1 f(x).dx$
UNIFORM = 1.0	1.0
$(1 - x^2)^{\frac{1}{2}}$	0.79
$(1 - x^2)^{\frac{3}{4}}$	0.74
$(1 - x^2)$	0.67
J (2.405x)	0.61

From equation (10.53) and table (10.1), the relationship between the quantities x_b and $n_c/\bar{n}$ was worked out for each of the profile functions listed. In fig. (10.4), the quantity $(1 - x_b)$ has been plotted versus the quantity $n_c/\bar{n}$ for each form of $f(x)$. The choice of the quantity $(1 - x_b)$ instead of x_b was made for convenience: $(1 - x_b)$ represents the fractional distance of the reflecting boundary from the wall of the discharge tube, whereas x_b represents the fractional distance of the

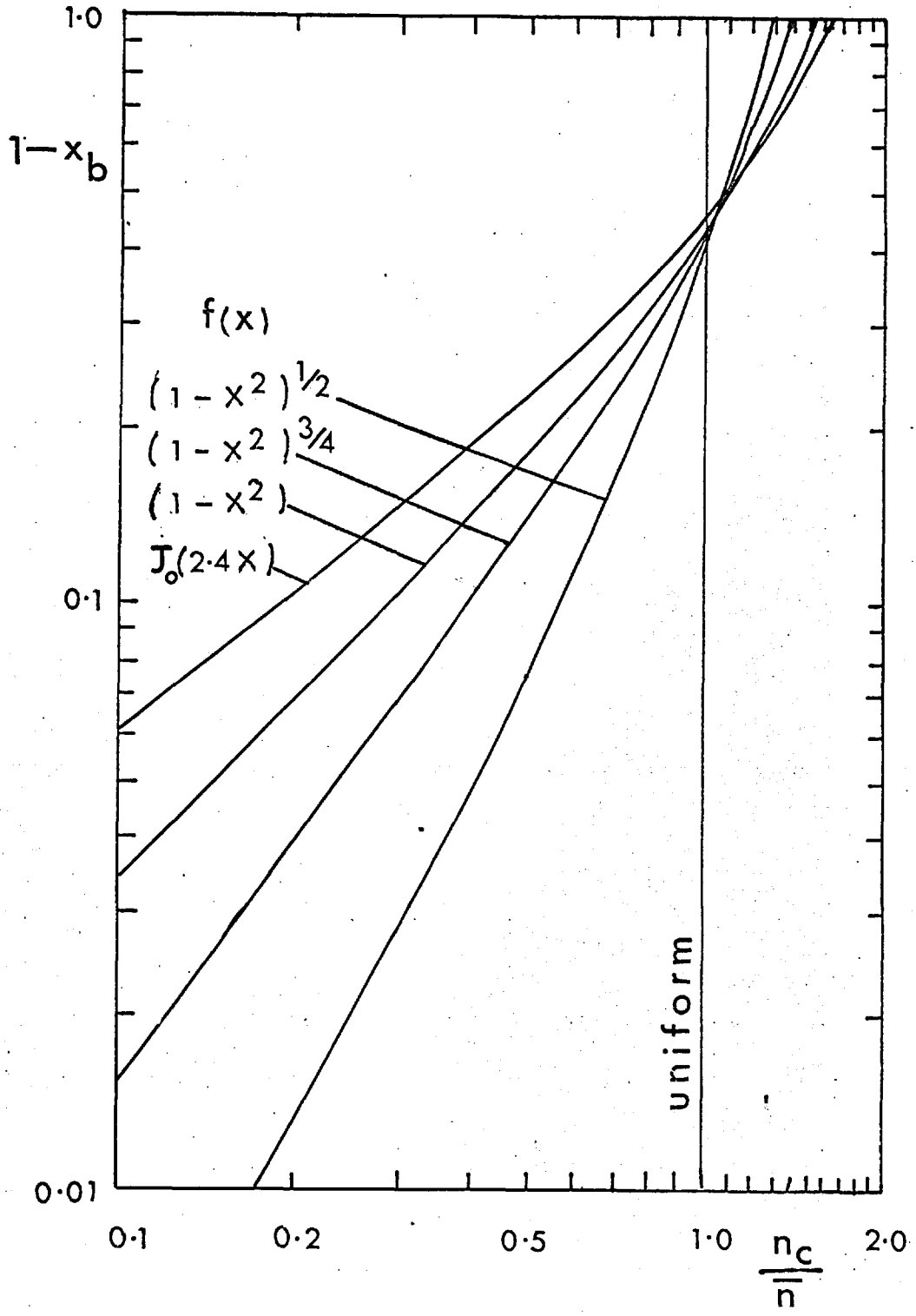

FIG (10.4) Theoretical plots of $(1 - x_b)$ versus $n_c/\bar{n}$ for various forms of the profile function f(x).

reflecting boundary from the axis of the tube. In the microwave reflection experiment, described in Chapter 8, the distance between the reflecting boundary and the wall was directly measured. We note that the quantity x_b is zero when the density at the plasma axis equals the cut off density of the lower wave frequency, and the values of the ratio $n_c/\bar{n}$ at this point are simply the reciprocals of the values listed in table (10.1).

In our experimental studies on decaying plasmas, the quantity $(1 - x_b)$ was found as a function of time from the 70 $G.H_z$ microwave reflection interferometer described in Chapter 8. The quantity $\bar{n}$ was found as a function of time from the HCN laser interferometer described in Chapter 7. In figs. (10.5) and (10.6), we have plotted the experimental values of $(1 - x_b)$ versus $n_c/\bar{n}$, where x_b and $\bar{n}$ correspond to coincident times throughout the plasma decay and n_c is the cut of density value for the 70 GH_z microwaves ($= 6.1\ 10^{13}\ cm^{-3}$). The relationships between $(1 - x_b)$ and $n_c/\bar{n}$ for the theoretical quasi-equilibrium profile function $f(x) = (1 - x^2)$ has also been included on each experimental plot. The following comments are made about these plots and this method of profile measurement in general.

1. A comparison of plots (10.5) and (10.6) with the plot (10.4) shows that in the decaying plasma the profile function $f(x)$ varies between the forms

$$(1 - x^2) < f(x) < (1 - x^2)^{\frac{1}{2}} \qquad (10.54)$$

All the experimental plots show that $f(x)$ tends towards the form $(1 - x^2)^{\frac{1}{2}}$ at high densities ($\bar{n} > 5 \cdot 10^{14}\ cm^{-3}$).

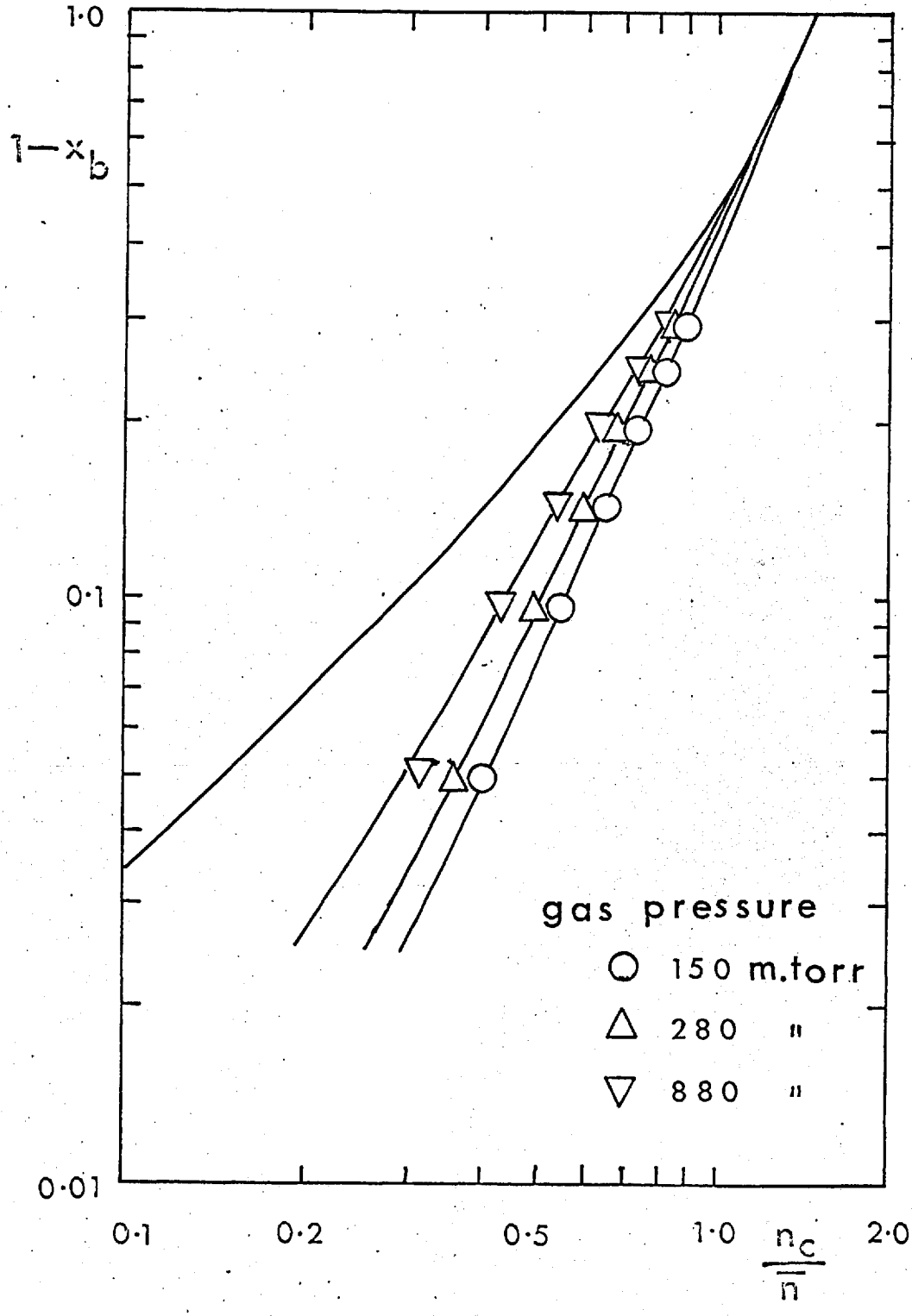

FIG (10.5) Experimental plots of $(1 - x_b)$ versus $n_c/\bar{n}$ for small torus argon afterglows.

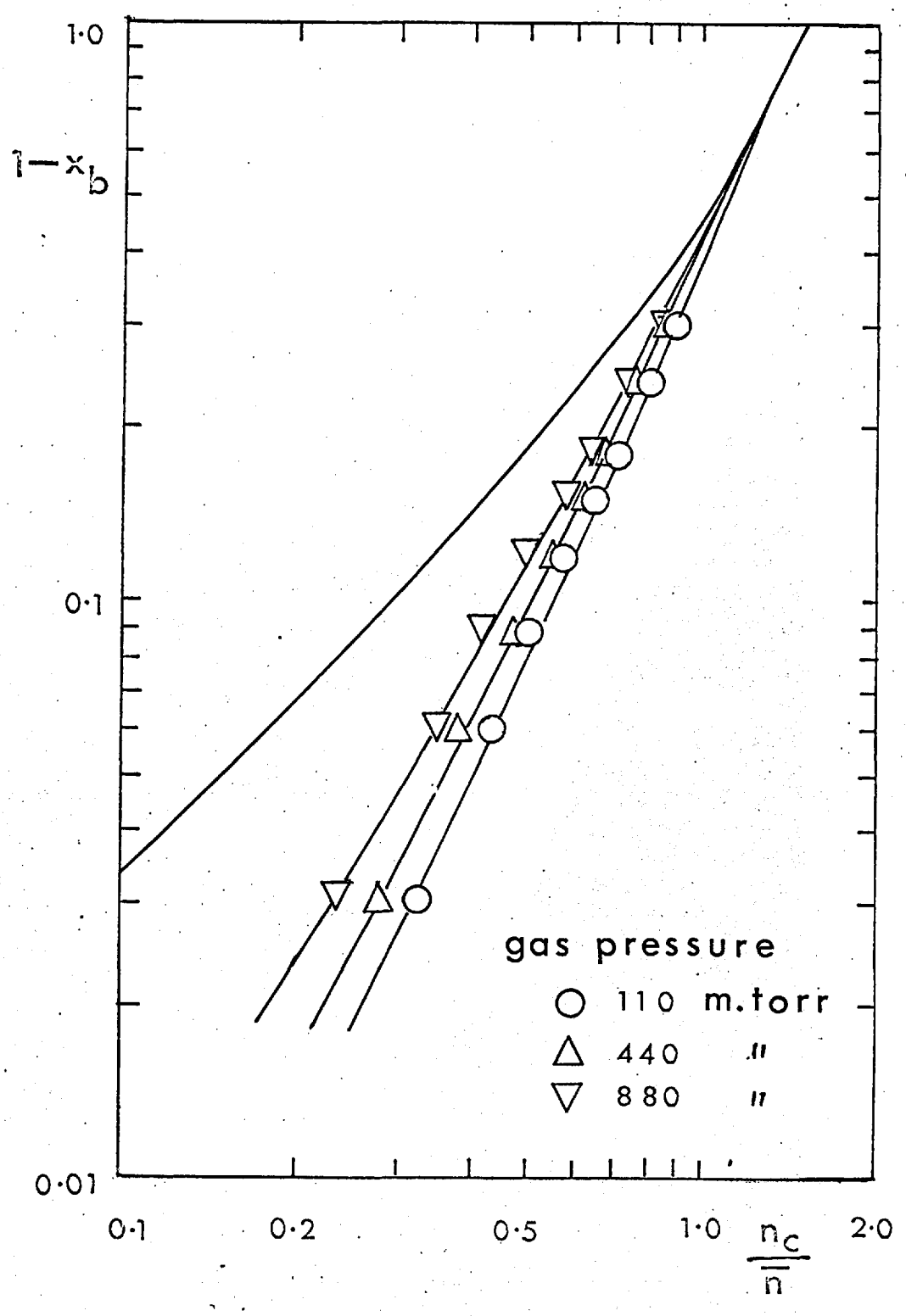

FIG (10.6) Experimental plots of $(1 - x_b)$ versus $n_c/\bar{n}$ for large torus argon afterglows.

2. For $\bar{n} > 2n_c$, the graph given in fig. (10.4) shows that there is a large difference between the plots for each form of the profile function f(x). Since, with the exception of the uniform profile, all these forms of f(x) are fairly similar, fig. (10.4) shows that this method gives a very accurate measurement of density profiles in the region $\bar{n} > 2n_c$.

3. The basic limitation on the absolute density range that can be studied using this method is that the electron density at the plasma axis must lie between the cut off density values of the two e.m. wave frequencies that are used. In our experiments we were fortunate in having a wide range between these limits (10^{16} - 6.1 10^{13} cm^{-3}).

4. For $\bar{n} < 0.2$ X (the cut off density of the higher e.m. wave frequency), the value of $\bar{n}$ is linearly related to the phase shift in the transmission interferometer and is independent of the form of f(x) existing in the plasma. This is discussed in detail in the next section. For $\bar{n}$ greater than the above limit, the actual form of f(x) has to be substituted into the integral expression for phase shift to derive the connection between $\bar{n}$ and the phase shift. This latter procedure makes the theoretical evaluation of the relationship between the transmitted wave phase shift and x_0 quite complicated, but it enables the accurate measurement of electron density profiles to be performed right up to the cut off point for transmission of the higher frequency e.m. wave.

(10.4) E.M. WAVE PHASE SHIFTS FOR VARIOUS DENSITY PROFILES

The phase shift ϕ experienced by an e.m. wave traversing normally across a cylindrical plasma diameter is given by

$$\phi = \frac{2\pi}{\lambda} \int_{-a}^{a} [1 - \mu(r)]\, dr \qquad (10.55)$$

where $\mu(r)$ is the plasma refractive index
λ is the e.m. wavelength in air

For a symmetrical density distribution in the plasma of the form (10.49) and the expression (7.15) for plasma refractive index, equation (10.55) can be re-written as

$$\phi = \frac{4\pi a}{\lambda} \int_{0}^{1} \left[1 - \left[1 - \frac{n_o}{n_c} f(x)\right]^{1/2}\right] dx \qquad (10.56)$$

where n_c is the cut off density value of the e.m. wave.

The solution of the integral expression (10.56) for various values of f(x) is considered below.

(10.4.1) Uniform Profile f(x) = 1.0

Evaluation of (10.56) with f(x) = 1.0 gives

$$H = \frac{n_o}{n_c} = \frac{\phi\lambda}{2\pi a}\left[1 - \frac{\phi\lambda}{8\pi a}\right] \qquad (10.57)$$

where H has been introduced to represent the ratio of n_o/n_c for a uniform density distribution f(x) = 1.0.

From equation (10.57) it can be seen that H varies almost linearly with ϕ for $H < 0.25$.

In most experiments, the form of the density profile f(x) is not known, or changes throughout the measurement period. In these cases, the measured value of ϕ can be substituted into equation (10.57) and the corresponding value of H calculated.

Except when f(x) = 1.0 in the experiment, the above procedure does not give the true value of n_o/n_c existing in the plasma, but it represents about the only way of analysing the experimental results. The deviation of H, found according to equation (10.57)., from the true value of n_o/n_c existing in a plasma possessing an arbitary density profile f(x) is discussed below.

(10.4.2.) f(x) = arbitary profile

We will define the quantity H′ by the equation.

$$H' = \frac{n_o}{n_c} \quad \text{for any arbitary profile } f(x) \neq 1.0 \qquad (10.58)$$

where n_o = axial value of electron density.

The phase shift ϕ experienced by an e.m. wave crossing the plasma is given by (10.56).

The value of H calculated from ϕ assuming a uniform profile is given by

$$\phi = \frac{4\pi a}{\lambda} \int_0^1 \left[1 - (1 - H)^{1/2}\right] dx \qquad (10.59)$$

Thus the relationship between H and H′ is given by equating (10.56) with (10.59), yielding

$$(1 - H)^{\frac{1}{2}} = \int_0^1 (1 - H' f(x))^{\frac{1}{2}} \, dx \qquad (10.60)$$

When H and H′ are small, say < 0.2, then expansion of equation (10.60) by the Binomial to include only the first order terms is permissable which gives

$$1 - \frac{H}{2} + \ldots = 1 - \frac{H'}{2} \cdot \int_0^1 f(x)\, dx + \ldots \qquad (10.61)$$

$$\therefore H \simeq H' \int_0^1 f(x)\, dx$$

But the true average value of density $\bar{n}$ of the arbitary density distribution is given by the equation

$$\bar{n} = n_o \int_o^1 f(x)\, dx \qquad (10.62)$$

Comparison of (10.61) with (10.62) and the definitions of H and H′ shows that

$$H \simeq \frac{\bar{n}}{n_c} \quad \text{for} \quad H < 0.2 \qquad (10.63)$$

Equation (10.63) shows that the value of electron density obtained from the measured value of the phase shift by assuming a uniform profile is always equal to the true average value of the density distribution for any arbitary profile function provided $\bar{n} < 0.2\, n_c$.

(10.4.3) $f(x) = (1 - x^2)$

This profile function is the quasi-equilibrium profile predicted for dense afterglow plasmas. The relationship between H and H′ is

$$(1 - H)^{\frac{1}{2}} = \int_0^1 (1 - H' + H' x^2)^{\frac{1}{2}}\, dx \qquad (10.64)$$

Numerical evaluation of the expression (10.64) shows that

as $H' \longrightarrow 1$ $\quad H \longrightarrow 0.750\, H'$

as $H' \longrightarrow 0$ $\quad H \longrightarrow 0.666\, H'$

The ratio of H′/H has been plotted versus H over the entire density region from e.m. wave cut off (H′ = 1) to zero density

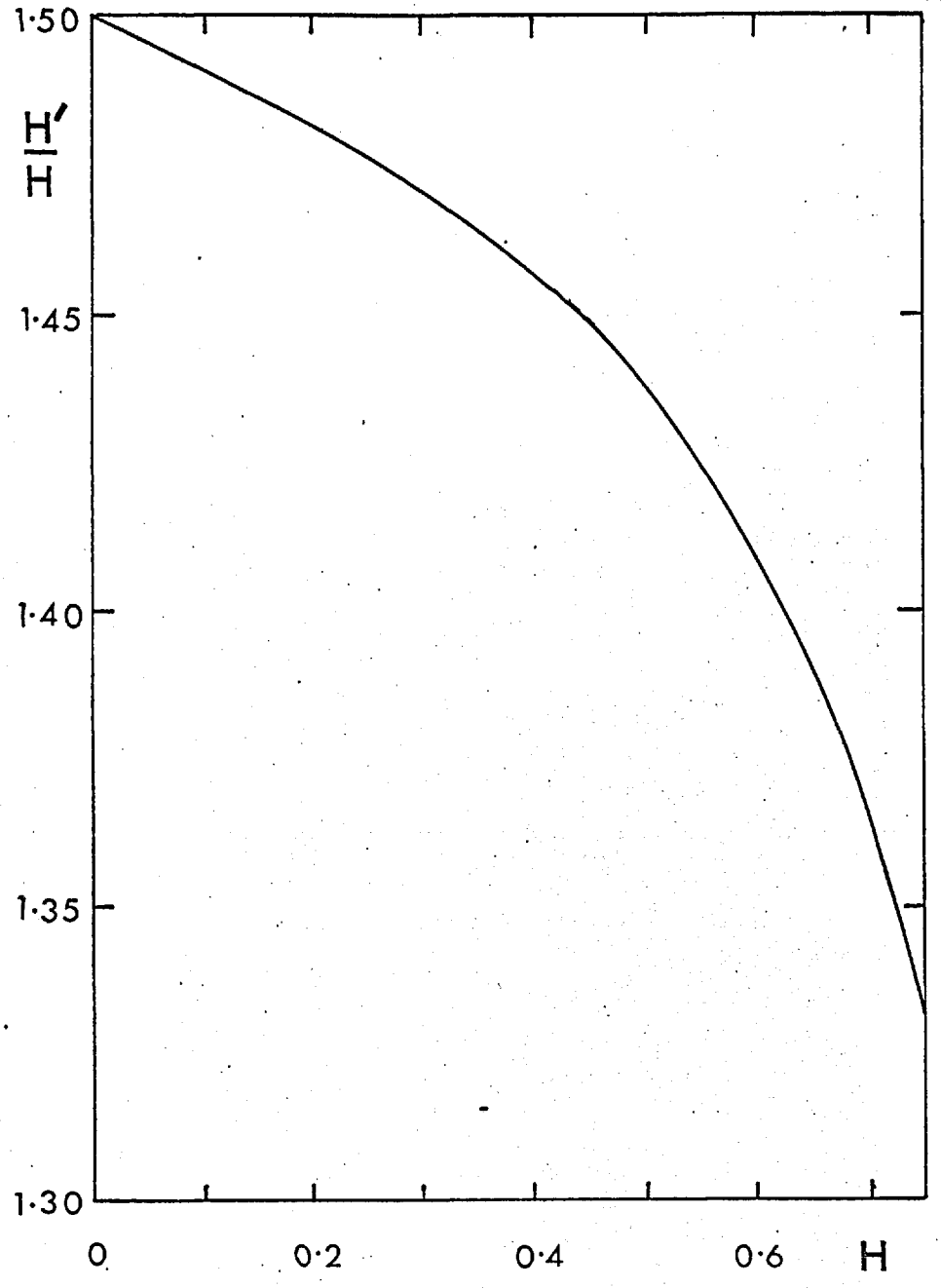

FIG (10.7) Plot of H'/H versus H for the profile function $f(x) = 1 - x^2$.

($H' = 0$) according to equation (10.64) and the result is shown in fig. (10.7). Using fig. (10.7), we can immediately convert the values of H found according to equation (10.57) into the corresponding values of H', which gives us the true value of axial electron density in a decay whose profile is $f(x) = (1 - x^2)$.

(10.5) E.M. WAVE ATTENUATION FOR VARIOUS DENSITY PROFILES

The attenuation experienced by an e.m. wave propogating through a plasma possessing an arbitary electron density profile function $f(x)$ and an arbitary electron temperature profile function $g(x)$ is now considered. We will only be concerned with dissipative attenuation and we neglect refraction and reflection effects.

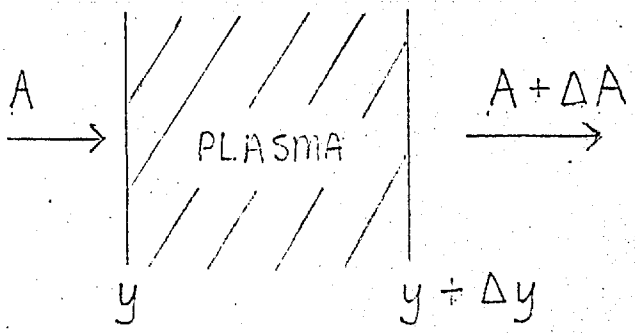

FIG. (10.8)

We consider the situation shown in fig. (10.8) where an e.m. wave passes through a thin slab of plasma of thickness Δy. If A is the amplitude of the incident wave and α the amplitude attenuation coefficient, then the expression for the change in amplitude = ΔA on traversing the plasma is

$$\Delta A = -\alpha A . \Delta y \qquad (10.65)$$

In the limit as $\Delta y \to 0$ we obtain from (10.65) the expression for the change in wave amplitude in going from y_1 to y_2 as

$$\int_{A_1}^{A_2} \frac{dA}{A} = \int_{y_1}^{y_2} -\alpha(y) \cdot dy \qquad (10.66)$$

Since in general α is a function of the spatial coordinate y in a non-uniform plasma.

In Chapter 7, the quantity γ was defined by equation (7:37) and from this equation and (10.66) we can write

$$\gamma = \ln\left[\frac{A_1}{A_2}\right] = \int_{y_1}^{y_2} \alpha(y)\, dy \qquad (10.67)$$

We assume that the wave attenuation is of the form discussed in section (7.4) so that α is given by equation (7.18) and the collision frequency by (7.20). Substitution of the above equations into (10.67) together with the density and temperature distributions of the forms

$$n(x) = n_o f(x) \qquad (10.68)$$

$$T_e(x) = T_o g(x) \qquad (10.69)$$

gives the expression for γ for an e.m. wave crossing a plasma diameter as

$$\gamma = \gamma_o \int_o^1 [f(x)]^2 [g(x)]^{-3/2} [1 - f(x)]^{-1/2} \cdot dx$$

$$\therefore \quad \gamma \simeq \gamma_o \int_0^1 [f(x)]^2 [g(x)]^{-3/2} \cdot dx \qquad (10.70)$$

where $$\gamma_o = \left\{ \frac{(2.6\, a\, \ln\Lambda\, n_o^2)}{c\, n_c\, T_o^{3/2}} \right\} \qquad (10.71)$$

Values of the integral in equation (10.70) have been worked out for the various forms of the profiles $f(x)$ and $g(x)$ and these are listed in table (10.2).

TABLE (10.2)

$f(x)$	$g(x)$	$\int_0^1 [f(x)]^2 . [g(x)]^{-3/2} dx$
1.0	$(1 - x^2)^{\frac{1}{2}}$	2.70
$(1 - x^2)^{\frac{1}{2}}$	$(1 - x^2)^{\frac{1}{2}}$	0.89
$(1 - x^2)^{\frac{3}{4}}$	$(1 - x^2)^{\frac{1}{2}}$	0.73
$(1 - x^2)$	$(1 - x^2)^{\frac{1}{2}}$	0.55
$J (2.405 x)$	$(1 - x^2)^{\frac{1}{2}}$	0.44

As was discussed in Chapter 7, from the interferometer output we obtain values for ϕ and γ and we want to relate these to the plasma properties of electron density and temperature. The method for relating ϕ to the electron density has already been discussed in section (10.4) where the procedure was adopted to firstly analyse ϕ in terms of a uniform density distribution profile. Here, we will adopt a similar procedure and firstly analyse the measured value of γ in terms of both uniform density and temperature distribution profiles. The value of electron temperature that is obtained from such an analysis we will call T_m. As was stated in section (10.4), the analysis of the experimental results in terms of uniform profile functions is about the only procedure that can be adopted when the profile functions are unknown or change throughout the measurement. We

will now work out correction factors relating T_m to the true value of axial electron temperature T_o existing in the plasma for the various forms of f(x) and g(x) listed in table (10.2).

From equations (10.70) and (10.71), T_m is connected to the measured value of γ by the equation

$$\gamma = \frac{2{\cdot}6\ a\ \ln\Lambda\ [n_m]^2[T_m]^{-3/2}}{c\ n_c} \qquad (10.72)$$

where n_m is the value of electron density obtained by substituting the measured value of ϕ into the uniform profile equation (10.57). The relationship between T_m and T_o is given by eliminating γ from equations (10.70) and (10.72), thus

$$(n_m)^2 . (T_m)^{-3/2} = (n_o)^2 . (T_o)^{-3/2} \int_0^1 (g(x))^{-3/2} . (f(x))^2 . dx \qquad (10.73)$$

For $n_m < 0.2\ n_c$, we have shown in section (10.4.2) that n_m is equal to the true average value $\bar{n}$ of the density profile and hence from equations (10.62) and (10.73) the relationship between T_m and T_o can be written in the form.

$$T_o = T_m \left[\frac{\int_0^1 [f(x)]^2 . [g(x)]^{-3/2} dx}{\int_0^1 [f(x)]^2 . dx} \right]^{2/3} \qquad (10.74)$$

Hence the relationship between T_o and T_m is obtained by substitution of the appropriate values from tables (10.1) and (10.2) corresponding to each set of f(x) and g(x) into equation (10.74). The results are shown in table (10.3) where values of the ratio T_o/T_m are listed.

TABLE (10.3)

f(x)	g(x)	T_o/T_m
1.0	$(1 - x^2)^{\frac{1}{2}}$	1.93
$(1 - x^2)^{\frac{1}{2}}$	$(1 - x^2)^{\frac{1}{2}}$	1.28
$(1 - x^2)^{\frac{3}{4}}$	$(1 - x^2)^{\frac{1}{2}}$	1.23
$(1 - x^2)$	$(1 - x^2)^{\frac{1}{2}}$	1.16
J (2.405x)	$(1 - x^2)^{\frac{1}{2}}$	1.11

For the intermediate three pairs of distribution profiles listed in table (10.3), which correspond closely to those found in afterglow plasmas, it can be seen that the correction factor T_o/T_m does not depend very strongly upon the different forms of the profiles. Hence calculating T_m from the experimentally measured value of γ and applying a correction factor of $\times$ 1.20 should give a value of T_o which is correct to within 10% (plus the experimental error on γ) throughout the whole afterglow period where significant changes in the density profiles occur.

CHAPTER 11

EXPERIMENTAL STUDIES OF DECAYING PLASMAS

In this chapter, most of the experimental measurements that were performed on decaying plasmas are described.

(11.1) GENERAL REMARKS ABOUT THE EXPERIMENTS

The decay of hydrogen, helium, neon, argon and krypton plasmas in both the large and small sizes of torus were studied for gas filling pressures between 10 m.torr and 1.7 torr. Approximately twelve values of pressure were chosen between these limits for each gas. The upper limit of pressure was set by the need to initially produce a hot highly ionised plasma and the lower pressure limit was set by reliable gas breakdown.

The discharge was produced by the preioniser system described in section (2.5), where a 1μF capacitor was coupled inductively to the torus for the small torus experiments and a 2μF capacitor was used for the large torus experiments. The discharges were not critically damped and a switched termination of the current pulse was not employed. An extensive study of the discharge currents was performed using the Rogowski coils and, in all cases, the plasma currents were shown to be predominantly inductively limited. Typical oscilloscope traces of the plasma currents for both sizes of torus are shown in fig. (11.1).

For the experiments performed using the small torus, the plasma decay at each gas pressure was measured both in the

Argon gas pressure
(m.torr)

(a)

22
55
100
280
660
1250

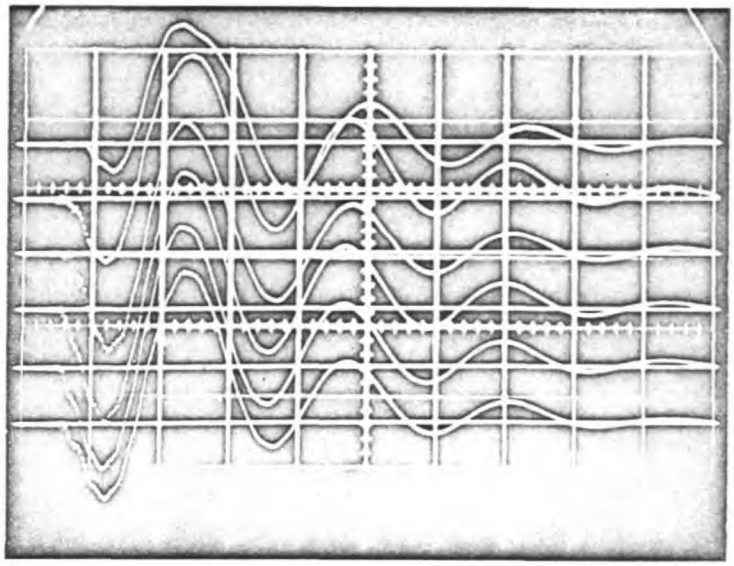

(b)

20
180
580
1250

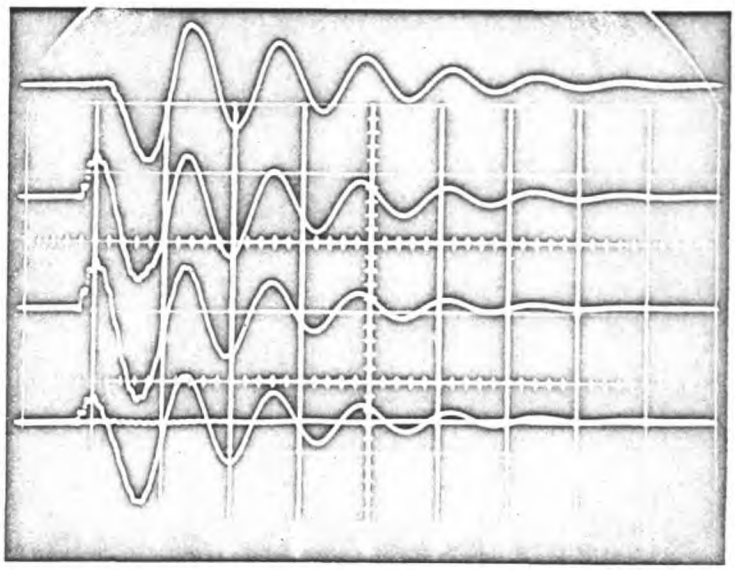

FIG (11.1) Discharge current waveforms.

(a) Small torus 1 μF capacitor, time base 2 μsec./div.

(b) Large torus 2 μF capacitor, time base 5 μsec./div.

absence of applied magnetic fields and in the presence of the toroidal axial magnetic field produced by the crowbarred bank and coil system described in section (2.4). The applied magnetic field was observed to produce a significant effect upon the decay of plasma at pressures $<$ 100 m.torr. All the experiments in the large torus were performed in the absence of applied magnetic field.

All the gases used were obtained from grade X (spectroscopically pure) gas flasks. No further purification of the gases was attempted in view of previously reported experiences. Hinnov and Hirschberg (84) have reported that adding 1% CO to a helium discharge did not produce any noticeable change in the behaviour of the afterglow plasma. Newton (93) has reported that further purification of grade X helium gas using a liquid nitrogen cooled charcoal trap did not alter the plasma behaviour. The base pressure in the evacuated toris varied from $5. 10^{-7}$ to 10^{-6} torr and the leakage rate was around $5. 10^{-6}$ torr per minute. The gas pressure in the experiments was monitored on an L.K.B. Autovac gauge which had two operating ranges 0 - 150 m.torr and 0.15 - 10.0 torr. Both these ranges were absolutely calibrated against two different Mcleod gauges covering the ranges 0 - 100 m.torr and 0 - 1.0 torr.

(11.2) LASER AND MICROWAVE INTERFEROMETRY

Some typical results that were obtained in afterglow plasmas using the HCN laser interferometer are reproduced in figs. (11.2) and (11.3). The upper oscilloscope trace in each case is a record of the interferometer output displayed downwards and the lower trace is a record of the plasma discharge current. The

Hydrogen

50 m.torr

20 μsec./div.

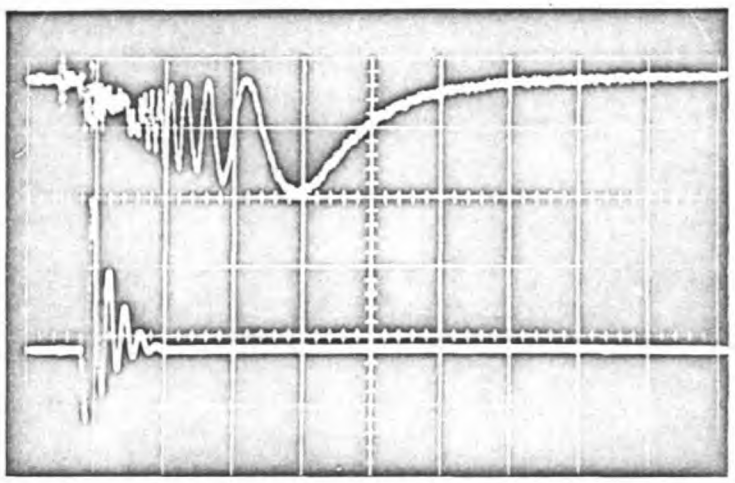

Hydrogen

640 m.torr

20 μsec./div.

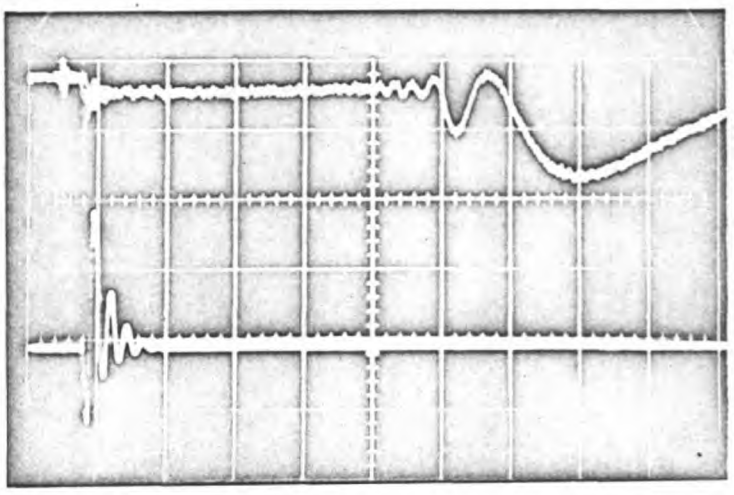

Argon

100 m.torr

50 μsec./div.

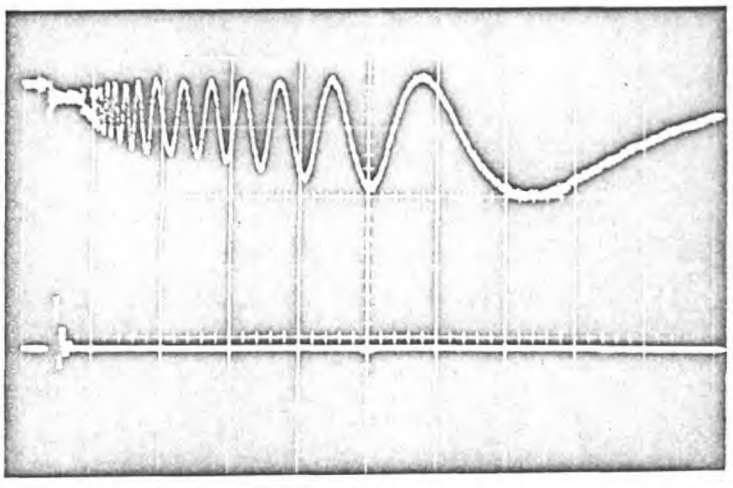

FIG. (11.2) HCN laser interferometer outputs in small torus afterglows.

Argon

440 m.torr

100 μsec./div.

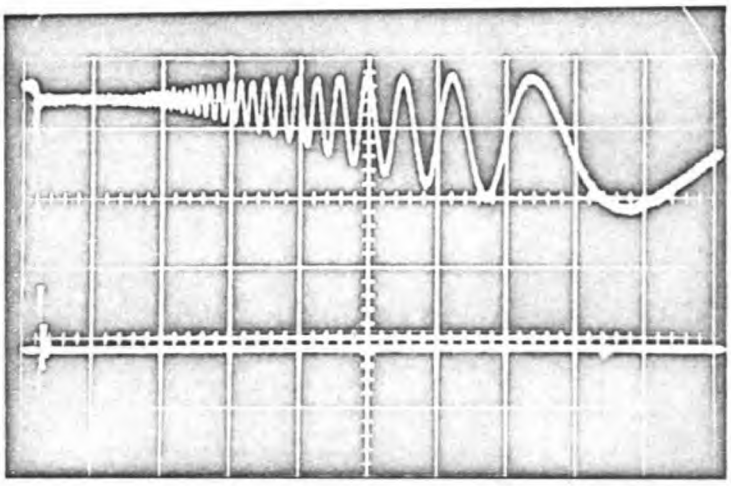

Krypton

50 m.torr

50 μsec./div.

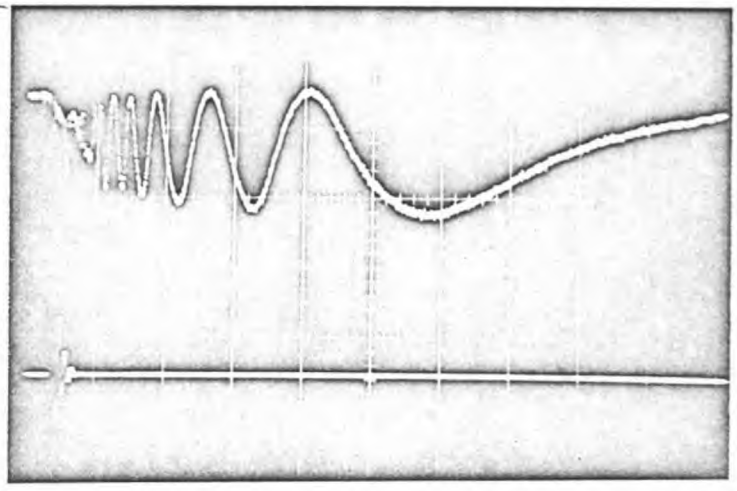

Krypton

100 m.torr

100 μsec./div.

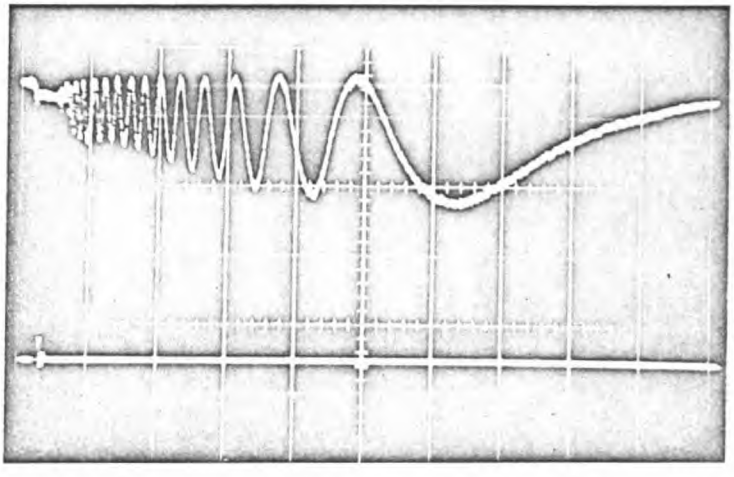

FIG (11.3) HCN laser interferometer outputs in small torus afterglows.

time scale goes from left to right in the conventional manner. The following points emerge from a visual inspection of these traces.

1. The amplitude of the interferometer output at any fixed value of gas pressure and fringe number (ie. at any fixed average values of atom and electron densities) increases with increasing atomic weight of the gas. This shows that the e.m. wave attenuation in the plasma at fixed $\bar{n}$, $\overline{n(1)}$ decreased going from hydrogen through to krypton.

2. The very small laser beam attenuation shown in fig.(11.3) for a low pressure krypton plasma demonstrates that refraction losses due to the plasma were indeed small. Now the plasma refraction loss is a function of electron density only and it is independent of parameters such as the type of gas and the gas pressure. The difference between corresponding fringe amplitudes in the low pressure krypton case and in the other cases shown in figs. (11.2) and (11.3) can therefore only be due to increased collisional attenuation of the laser beam by the plasma in these other cases.

3. At all gas pressures up to 1.5 torr, the plasma decay time, at any fixed value of electron density, was always observed to increase with increasing pressure. It is shown later, that correction for diffusion effects does not alter the above statement. Therefore, according to the theory of C.R. plasma recombination and equation (9.26) for the recombination coefficient, the equilibrium electron temperature existing in the plasma decay was also an increasing function of gas pressure.

4. An examination of the interferometer fringes for plasma decays over the whole gas pressure range 0.01 to 1.5 torr showed that the attenuation of the laser beam in the plasma

decreased slightly with increasing pressure up to ~ 100 m.torr in the small torus experiments and up to ~ 300 m.torr in the large torus experiments. Beyond these values of gas pressure, the plasma attenuation changed to become an increasing function of gas pressure: the increase in attenuation with pressure being much more rapid in hydrogen than in the rare gases. These latter results show that, at high gas pressures, the explanation of plasma attenuation solely in terms of electron-ion collisions is inadequate. According to equation (7.20), the Coulomb collision frequency is a decreasing function of electron temperature, and therefore from paragraph 3 above, we can see that Coulomb collisions become less frequent with increasing gas pressure. The experimentally observed increase in collisional attenuation with gas pressure beyond 0.3 torr is due to electron-neutral collisions making a significant contribution to the total electron collision frequency. The electron-neutral collision frequency is proportional to the gas pressure and in Appendix (A.6) we have shown that it is 1 to 2 orders of magnitude larger for hydrogen than for the rare gases.

Measurement of the times corresponding to successive interferometer maxima and minima, starting from the last fringe and working backwards in time, gave the temporal behaviour of the total e.m. wave phase shift ϕ produced by the plasma. These values of ϕ were analysed by the method outlined in section (10.4) to yield average values for the plasma electron density. Accordingly, plots of the decay of average plasma electron density with time have been made and these are shown in figs. (11.4) to (11.14). The estimated errors on the values of $\bar{n}$ and time are 10% and 3% respectively. For electron densities below $6 \cdot 10^{13}$ cm^{-3}, the plasma decay was measured using the 70 G H_z microwave interferometers described in chapter 8 . The

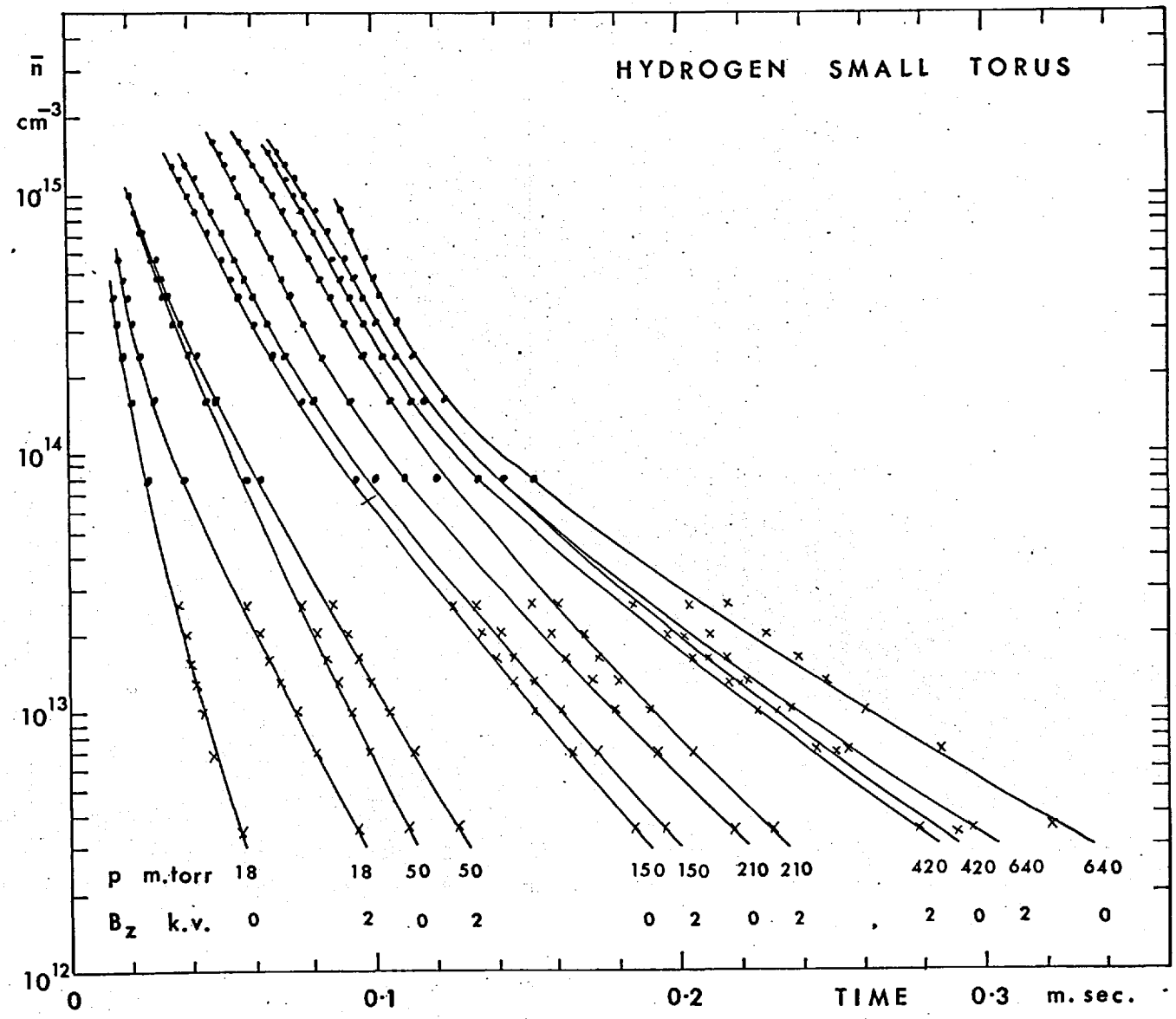
HYDROGEN SMALL TORUS
$\bar{n}$
cm^{-3}
10^{15}
10^{14}
10^{13}
10^{12}
p m.torr 18 18 50 50 150 150 210 210 420 420 640 640
B_z k.v. 0 2 0 2 0 2 0 2 2 0 2 0
0
0·1
0·2
TIME
0·3 m. sec.

FIG (11.11)

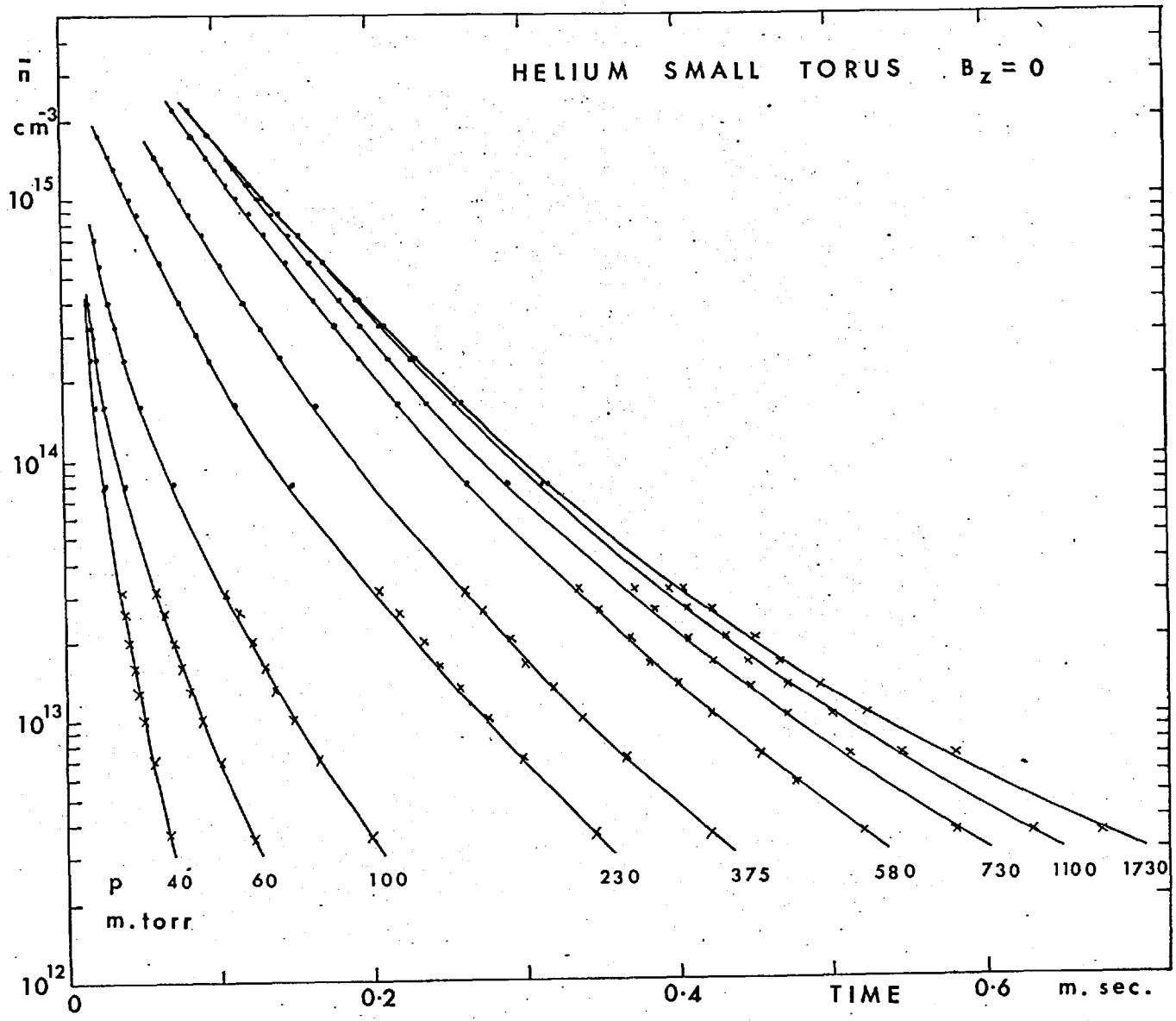
HELIUM SMALL TORUS $B_z = 0$
$\bar{n}$
cm^{-3}
10^{15}
10^{14}
10^{13}
10^{12}
p
m.torr
40
60
100
230
375
580
730
1100
1730
0
0·2
0·4
TIME
0·6
m. sec.

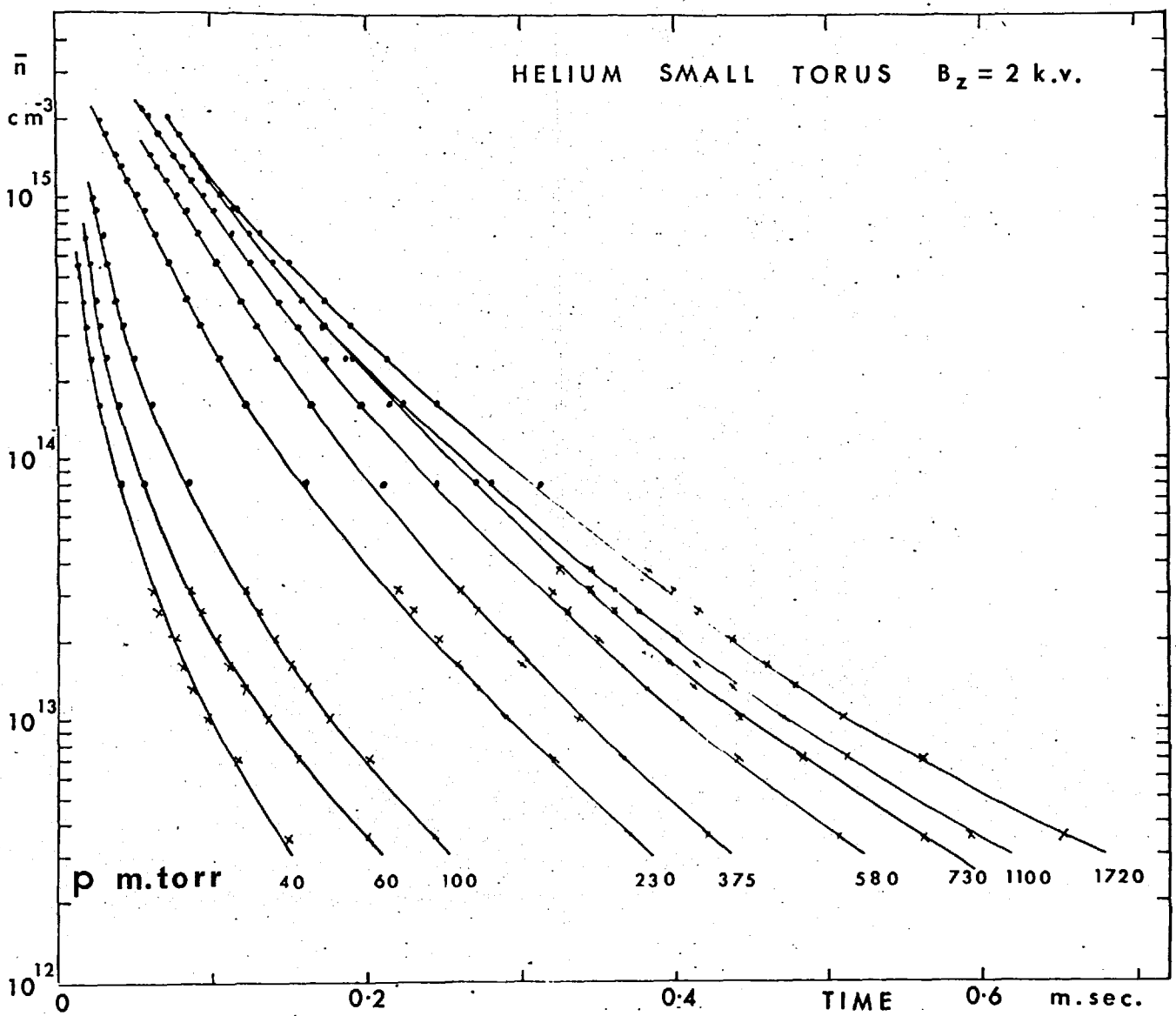
HELIUM SMALL TORUS B_z = 2 k.v.
$\bar{n}$
cm^{-3}
10^{15}
10^{14}
10^{13}
10^{12}
p m.torr
40
60
100
230
375
580
730
1100
1720
0
0·2
0·4
TIME
0·6
m.sec.

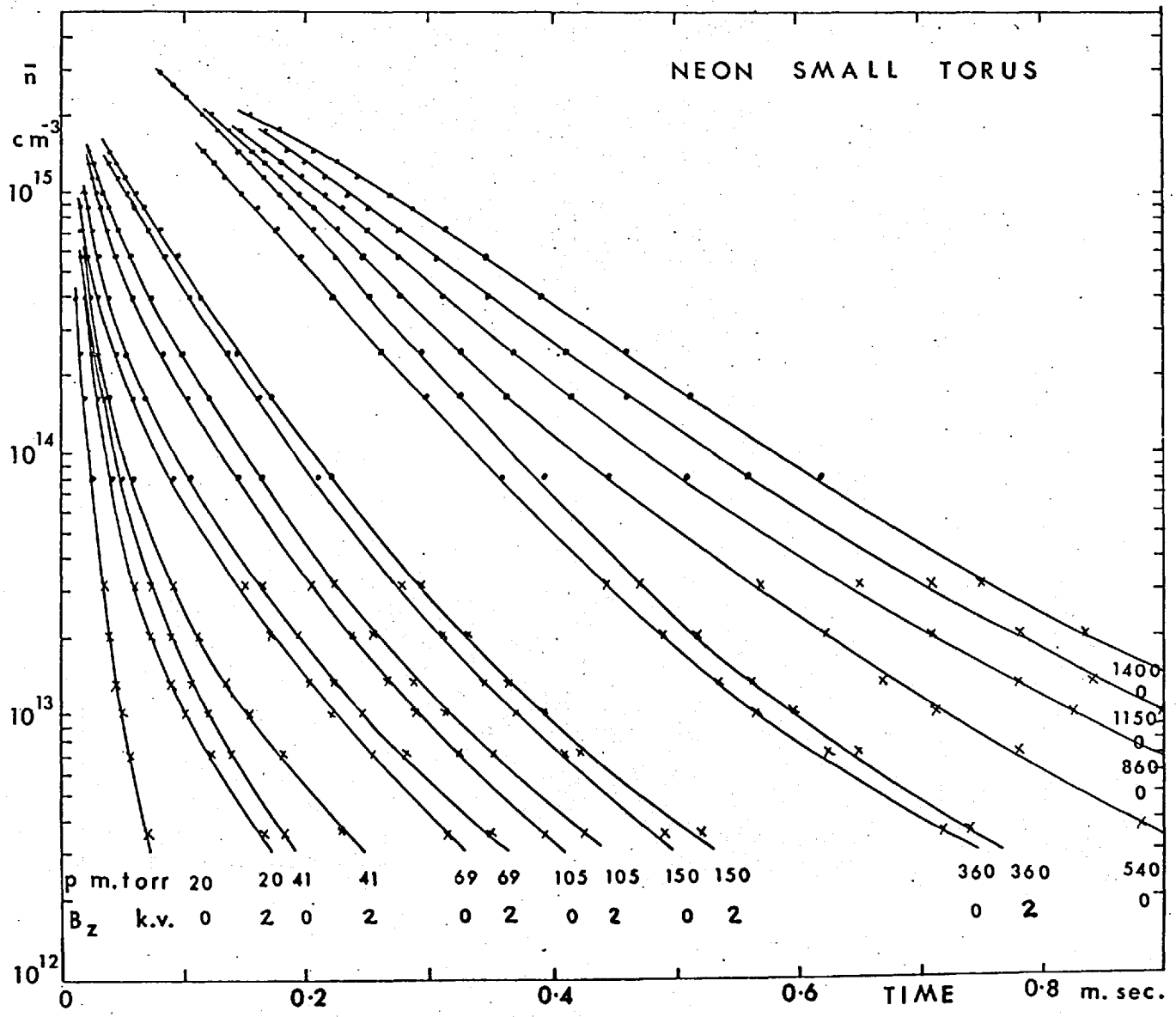
NEON SMALL TORUS
$\bar{n}$
cm^{-3}
10^{15}
10^{14}
10^{13}
10^{12}
p m.torr 20 20 41 41 69 69 105 105 150 150 360 360 540
B_z k.v. 0 2 0 2 0 2 0 2 0 2 0 2 0
1400
0
1150
0
860
0
0
0·2
0·4
0·6
TIME
0·8 m. sec.

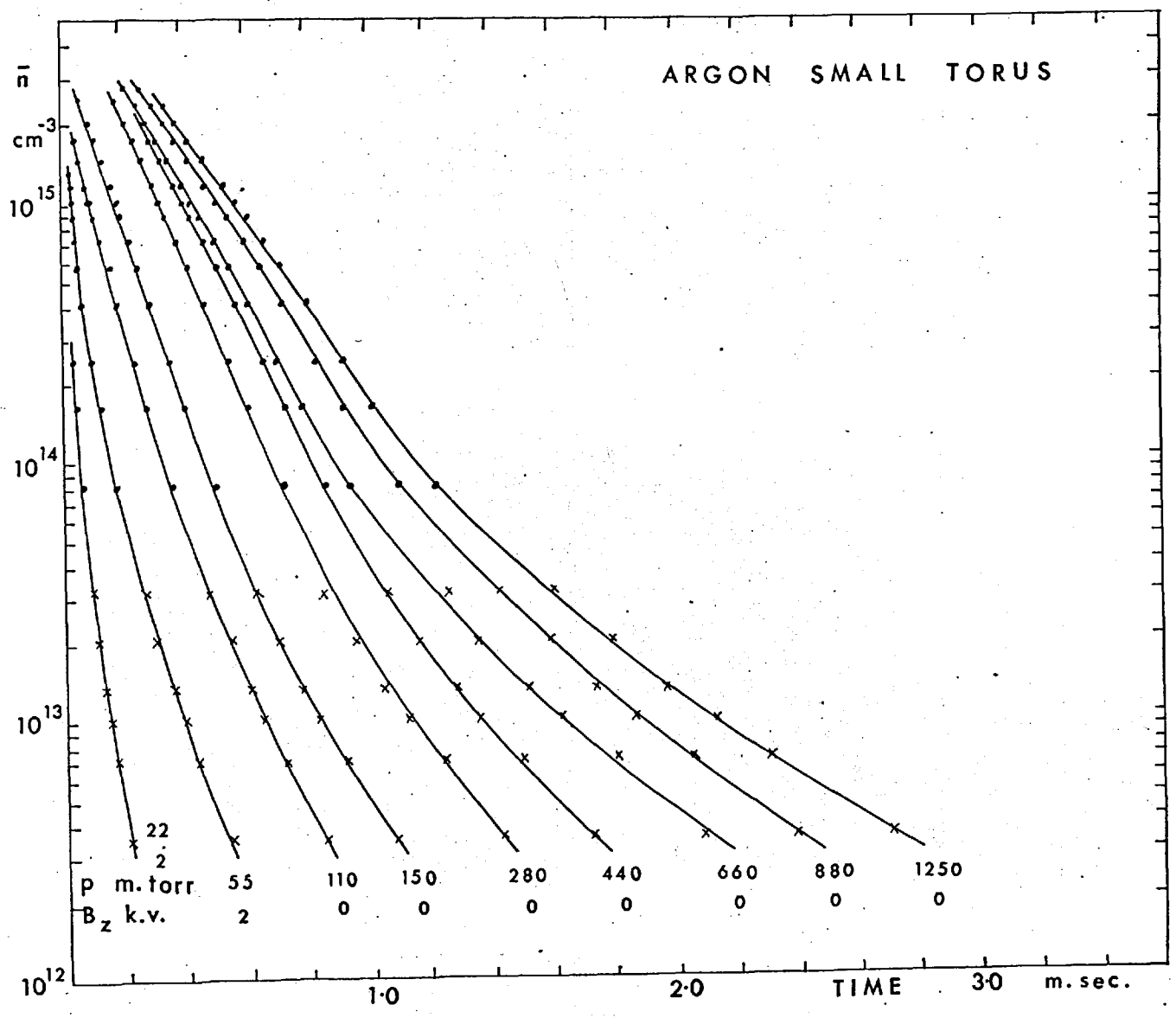
ARGON SMALL TORUS
$\bar{n}$
cm^{-3}
10^{15}
10^{14}
10^{13}
10^{12}
p m.torr 22 55 110 150 280 440 660 880 1250
B_z k.v. 2 2 0 0 0 0 0 0 0
1·0
2·0
TIME
3·0
m.sec.

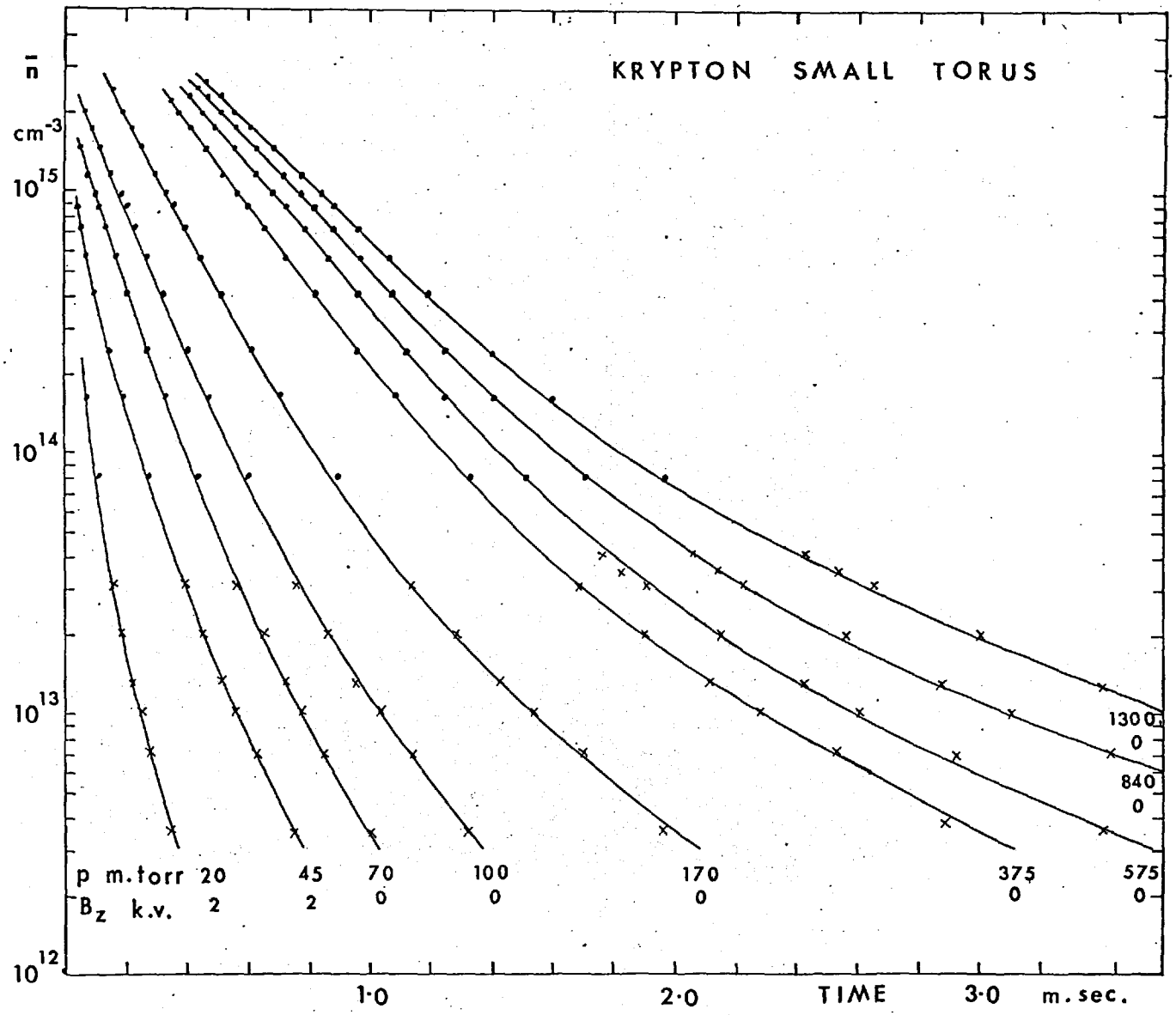
KRYPTON SMALL TORUS
$\bar{n}$
cm^{-3}
10^{15}
10^{14}
10^{13}
10^{12}
p m.torr 20 45 70 100 170 375 575
B_z k.v. 2 2 0 0 0 0 0
1300
0
840
0
1·0
2·0
TIME
3·0 m.sec.

FIG (11.9)

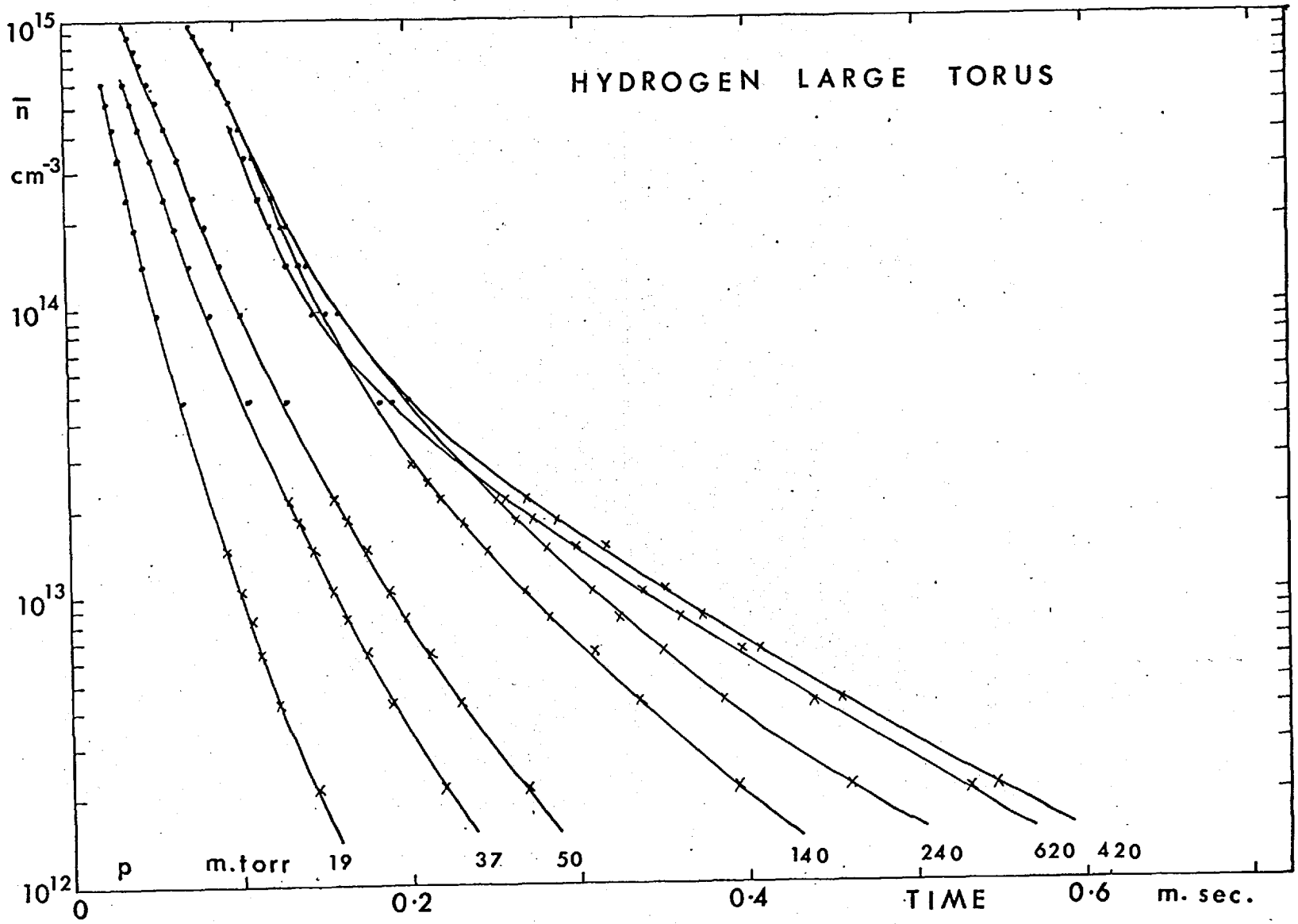
HYDROGEN LARGE TORUS
10^{15}
$\bar{n}$
cm^{-3}
10^{14}
10^{13}
10^{12}
p m.torr
19
37
50
140
240
620
420
0
0·2
0·4
TIME
0·6
m. sec.

Fig. (11.10).

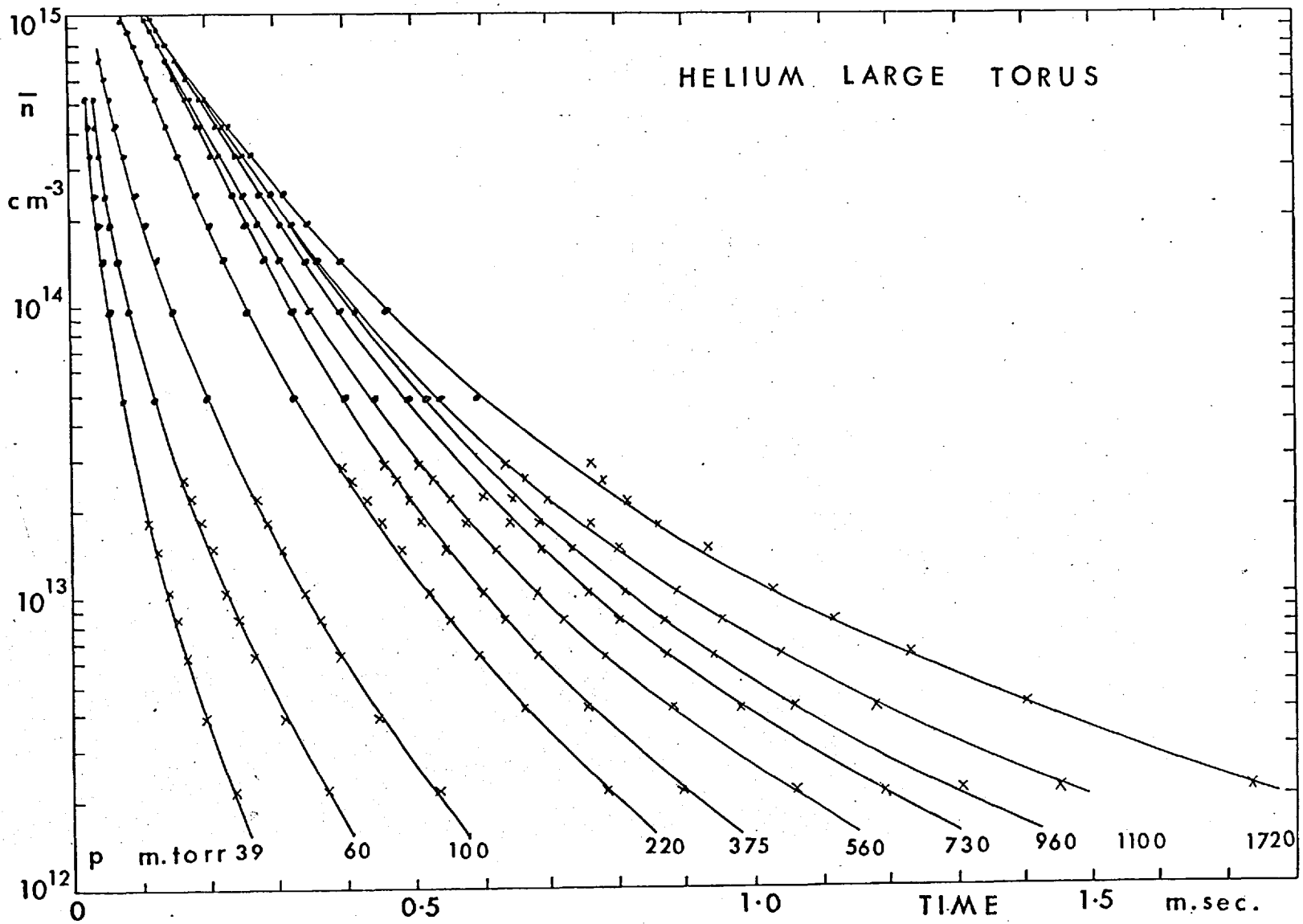
HELIUM LARGE TORUS
10^{15}
$\bar{n}$
cm^{-3}
10^{14}
10^{13}
10^{12}
p m.torr 39
60
100
220
375
560
730
960
1100
1720
0
0·5
1·0
TIME
1·5
m.sec.

FIG (11.11)

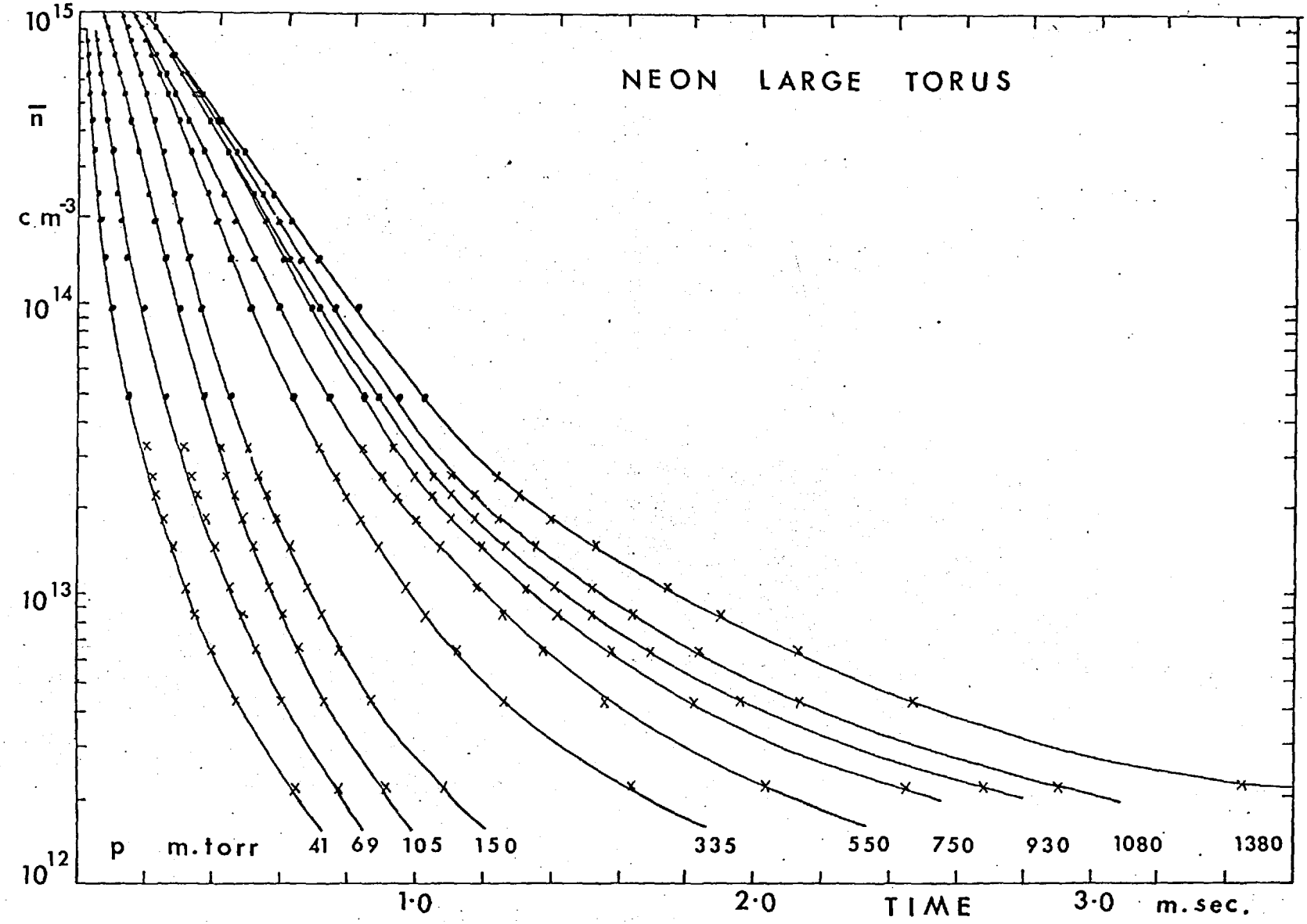
NEON LARGE TORUS
10^{15}
$\bar{n}$
c.m^{-3}
10^{14}
10^{13}
10^{12}
p m.torr
41
69
105
150
335
550
750
930
1080
1380
1·0
2·0
TIME
3·0
m.sec.

FIG. (11.12)

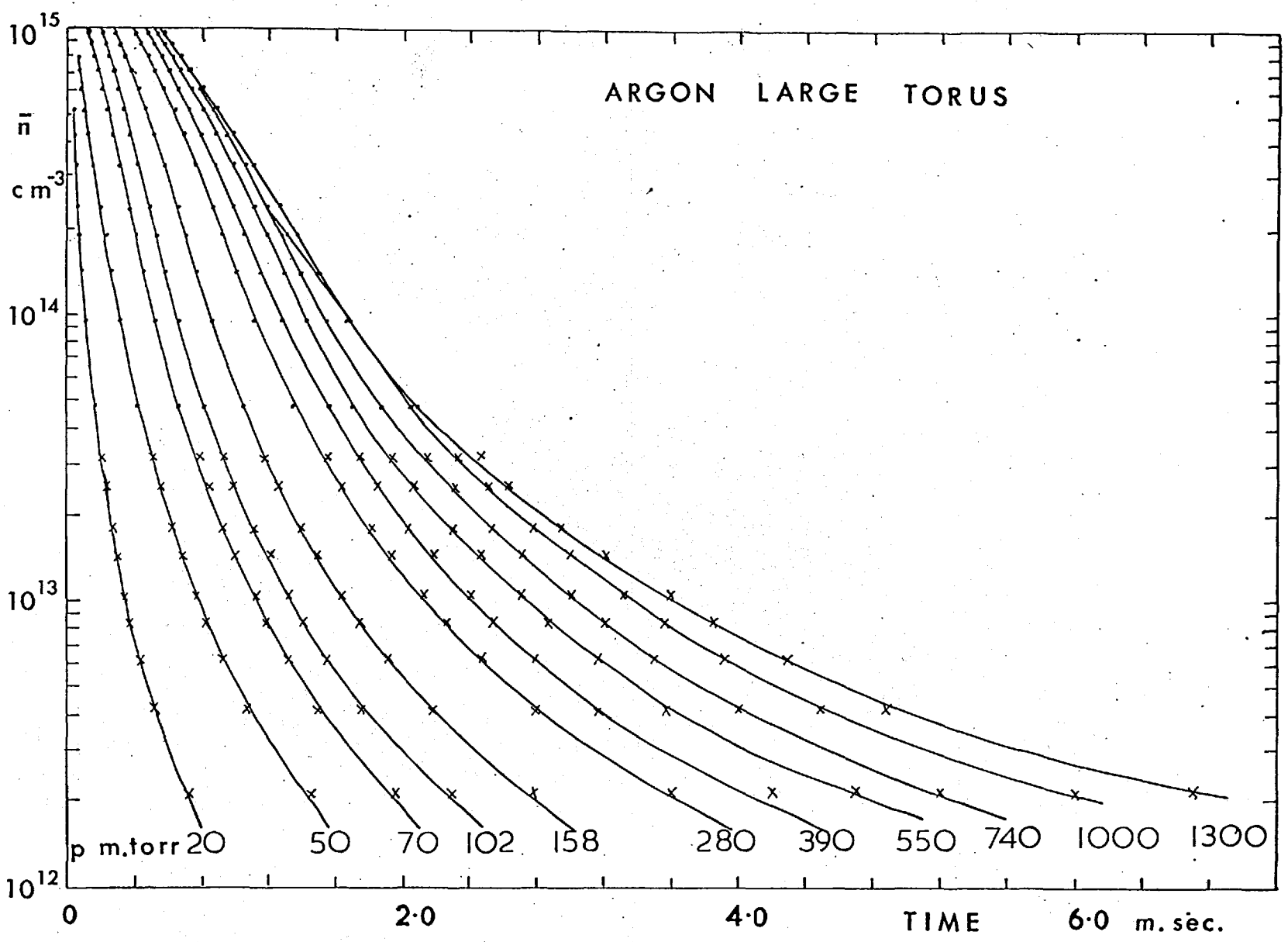
ARGON LARGE TORUS
10^{15}
$\bar{n}$
$c\,m^{-3}$
10^{14}
10^{13}
10^{12}
p m.torr 20
50
70
102
158
280
390
550
740
1000
1300
0
2·0
4·0
TIME
6·0 m. sec.

FIG (11.12)

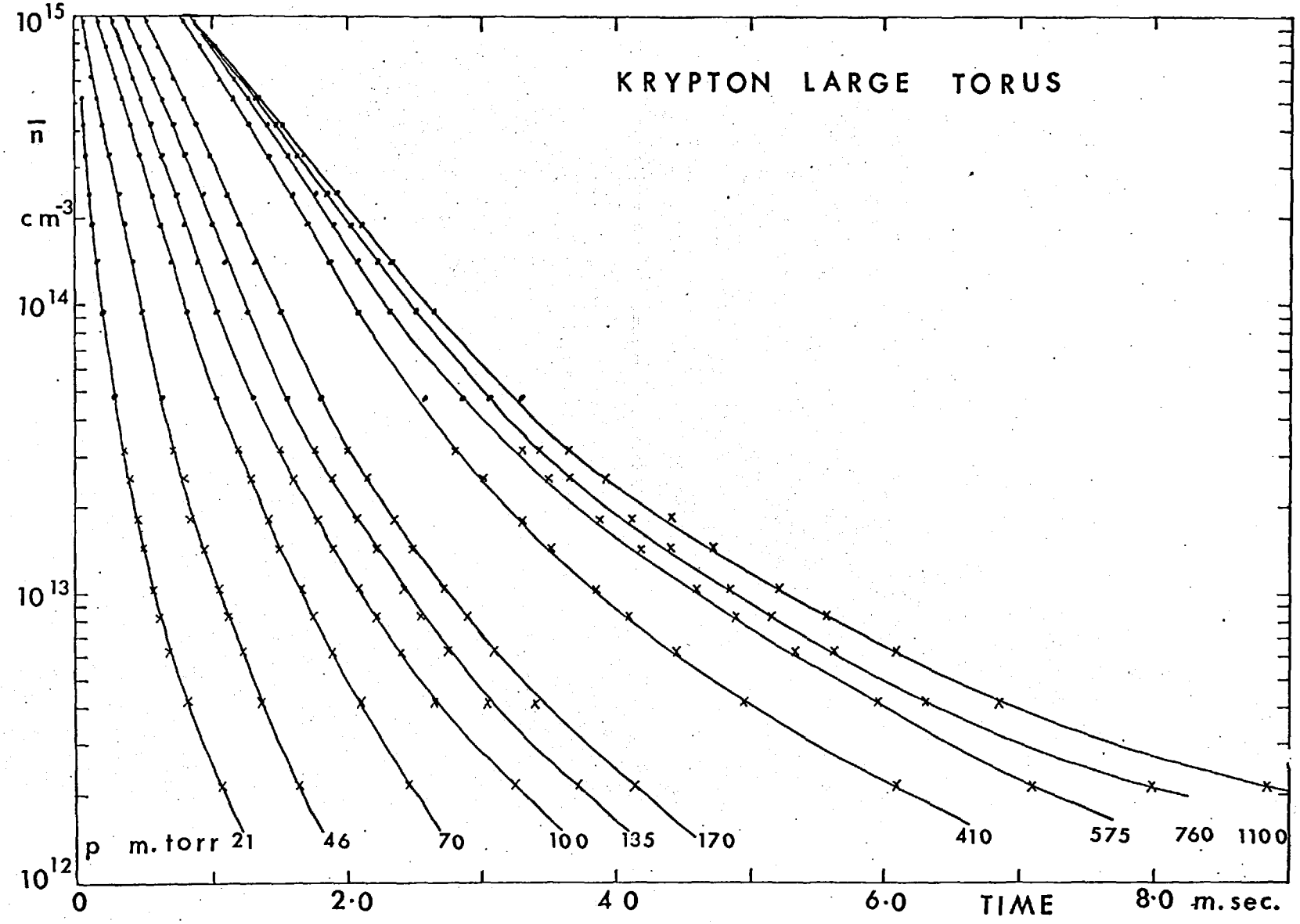
KRYPTON LARGE TORUS
10^{15}
$\bar{n}$
cm^{-3}
10^{14}
10^{13}
10^{12}
p m. torr 21
46
70
100
135
170
410
575
760
1100
0
2·0
4 0
6·0
8·0 m. sec.
TIME

microwave transmission interferometer was used for the small torus experiments and the tube wall reflection interferometer was used for the large torus experiments. In figs. (11.4) to (11.14) the HCN laser results are represented by full circles and the microwave results by crosses.

Measurements of the relative amplitudes of the HCN laser interferometer fringes were used to calculate the quantity γ according to equation (7.37). The only oscilloscope traces measured were those for discharges in the rare gases at low pressures, which corresponded to the case of Coulomb collisions dominating all other collision mechanisms. Analysis of the quantity γ together with the phase shift ϕ according to the method outlined in section (10.5) produced values for the axial electron temperature existing in the decaying plasmas.

In figs. (11.15) and (11.16), these calculated axial values of T_e have been plotted against calculated average values of n for each type of rare gas in each size of torus in the gas pressure region 50 to 200 m.torr. The estimated errors on the values of T_e and $\bar{n}$ are 30% and 10% respectively.

(11.3) ANALYSIS OF THE ELECTRON DENSITY DECAY PLOTS

We will define the plasma decay time by the equation

$$\tau = \left(\frac{d}{dt} \ln \bar{n} \right)^{-1} \qquad (11.1)$$

where $\bar{n}$ is the electron density averaged across the plasma diameter.

$$\bar{n} = \frac{1}{2a} \int_{-a}^{+a} n(r)\, dr \qquad (11.2)$$

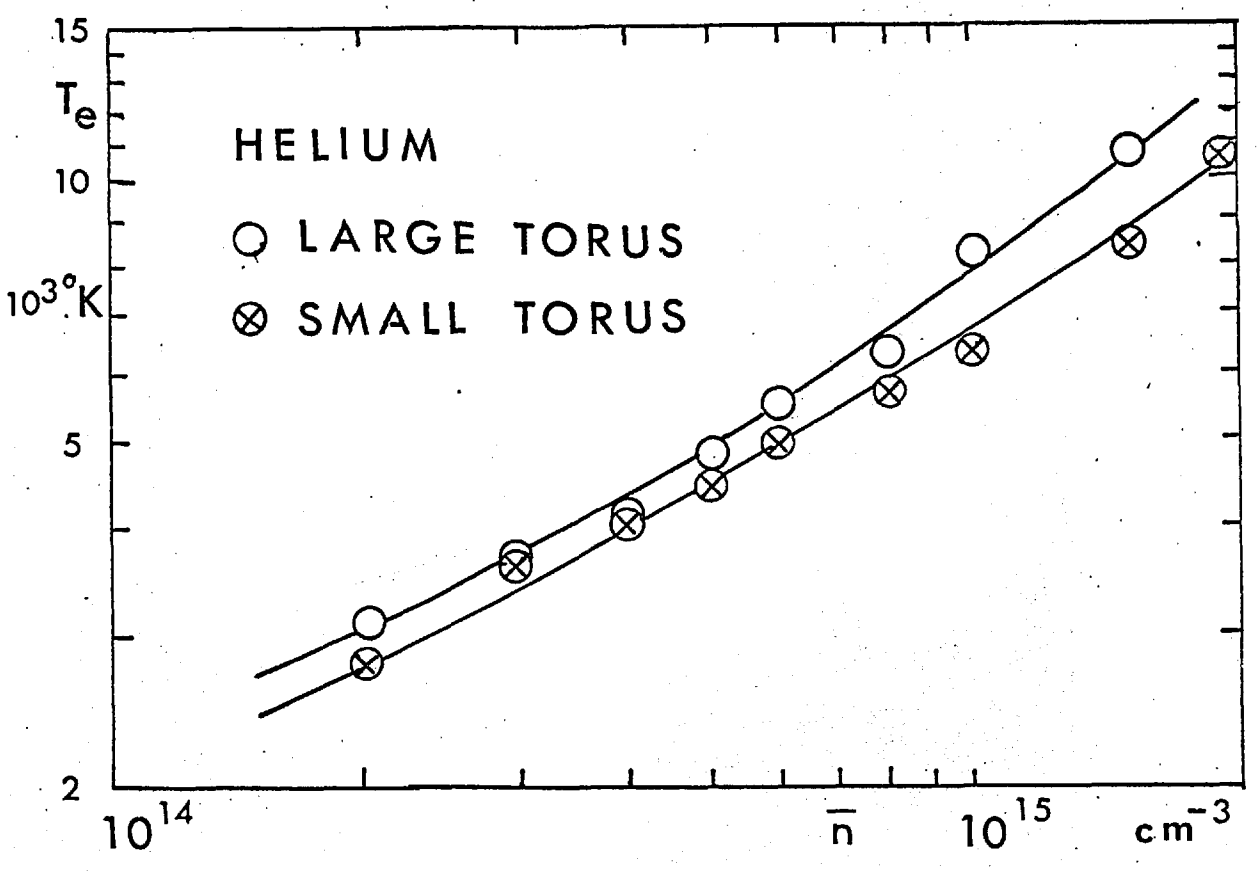

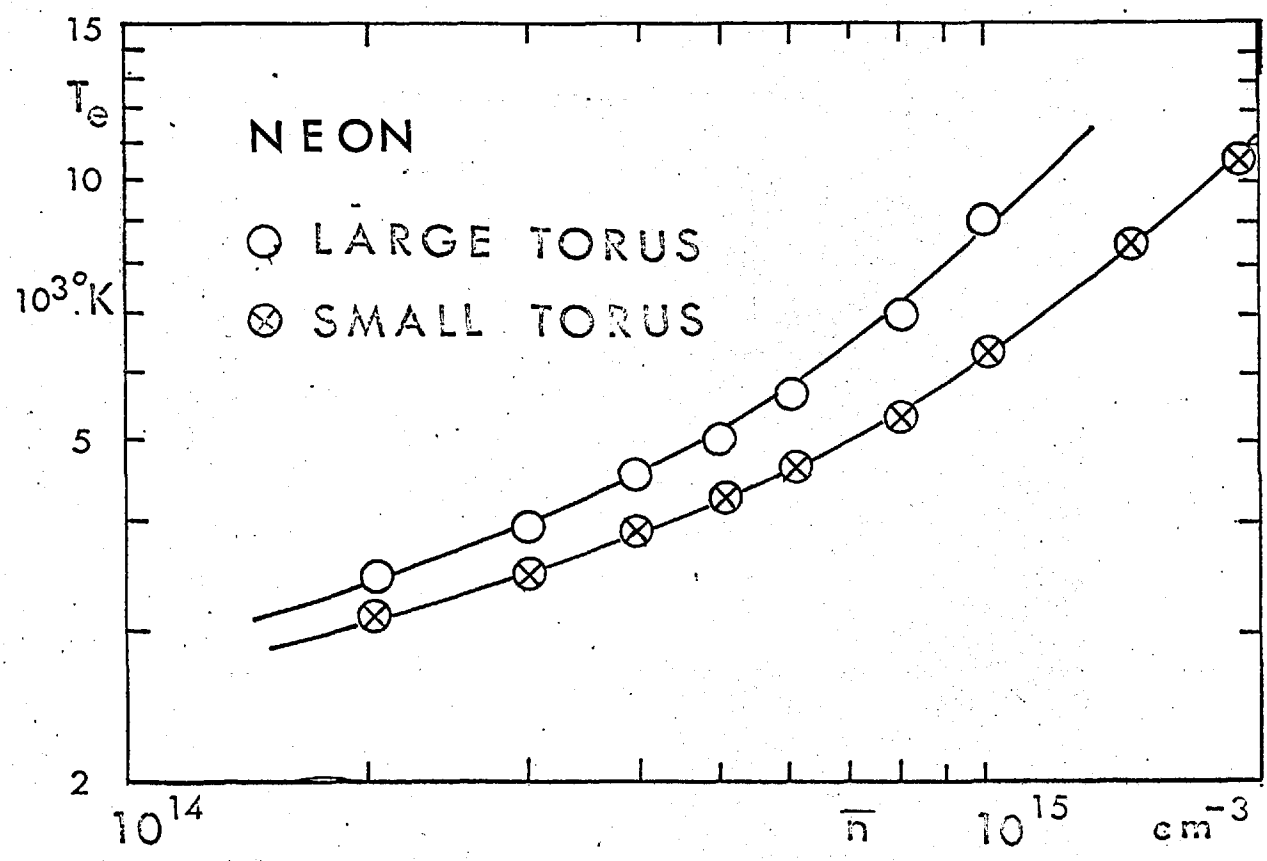

FIG (11.15) Electron temperature decay plots in low pressure afterglows.

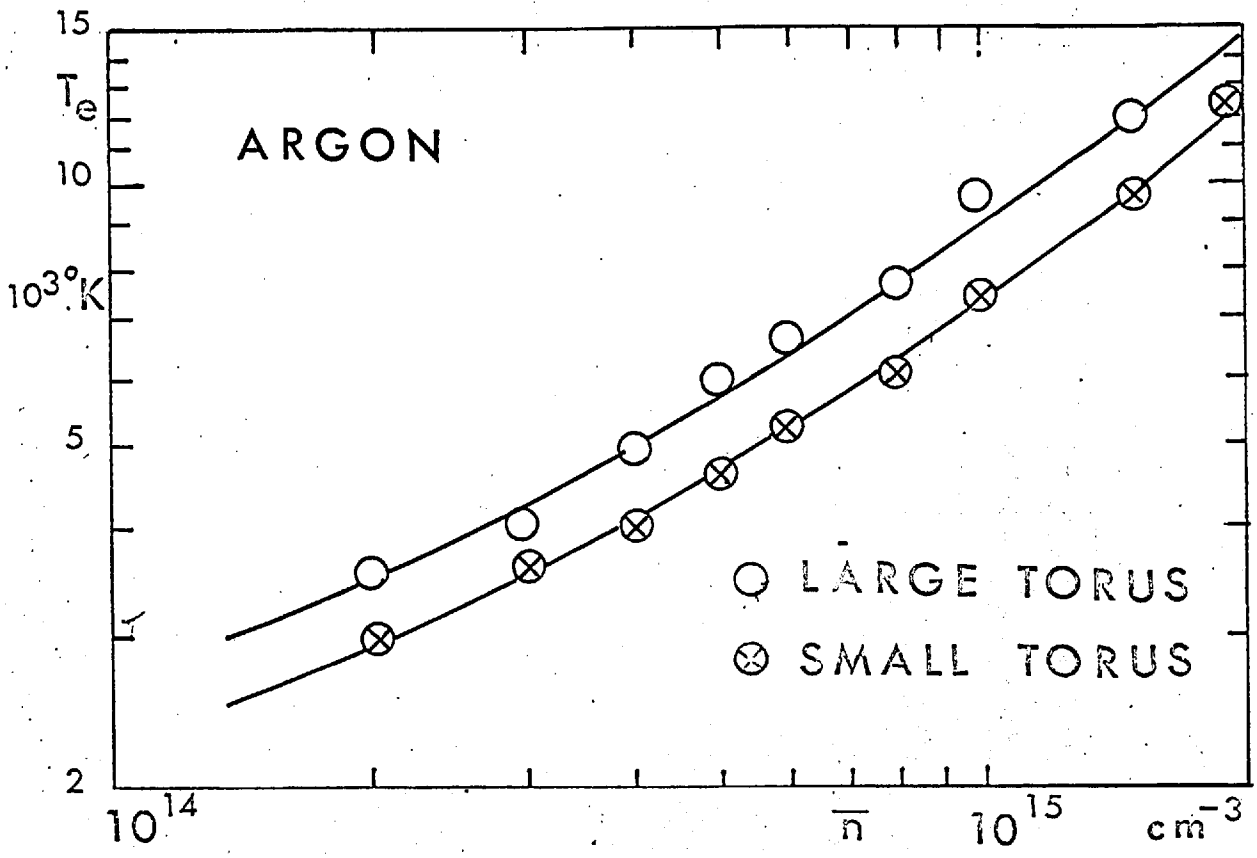

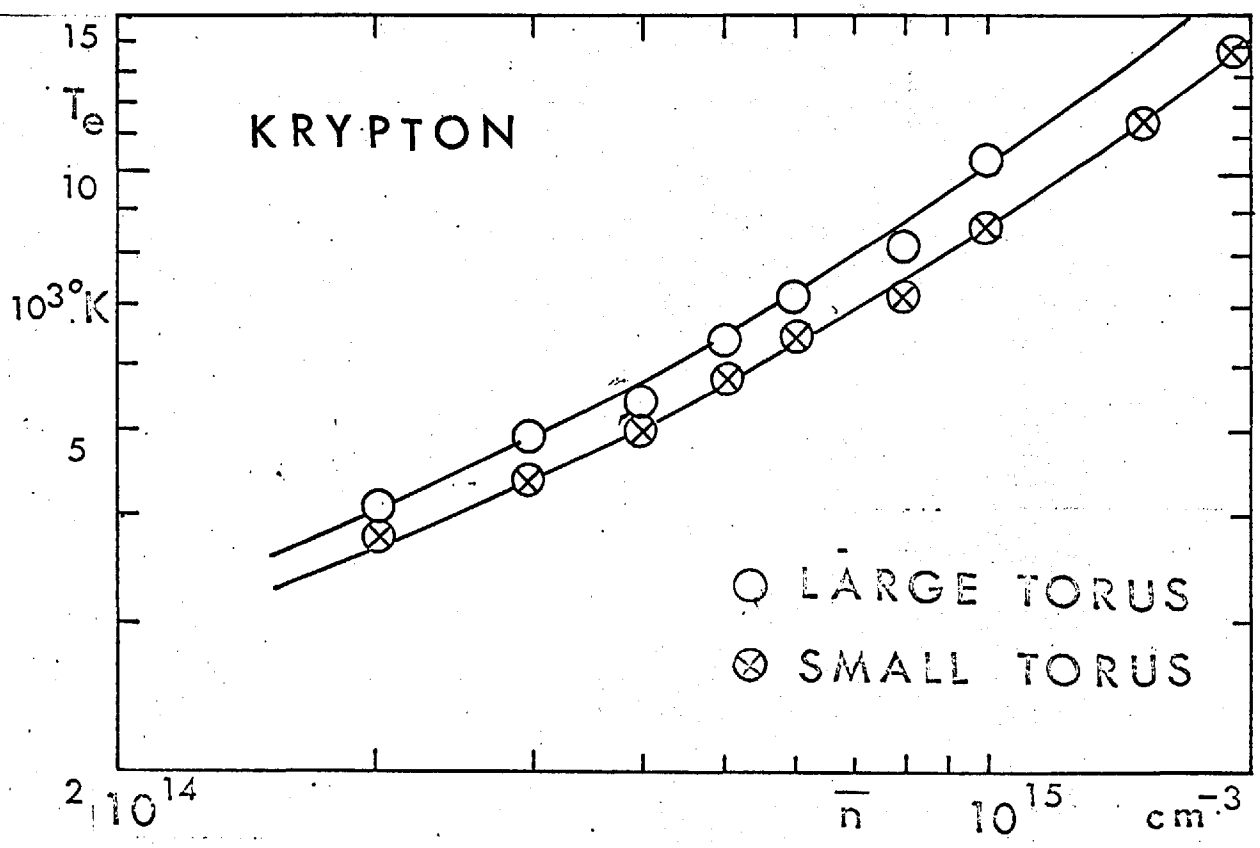

FIG (11.16) Electron temperature decay plots in low pressure afterglows.

Hence τ is obtained directly from the gradients of the decay plots of $\ell n.\bar{n}$ versus time shown in figs. (11.4) to (11.14).

In the absence of very strong magnetic fields and directed plasma motion, the plasma electron density decay is due to the combined effects of ambipolar diffusion and electron-ion recombination so that the decay equation can be written

$$\frac{dn}{dt} = -\alpha n^2 + D_a \nabla^2 n \qquad (11.3)$$

However, we have shown in Chapter 10 that the density and temperature distributions established in cylindrical afterglow plasmas are non-uniform and so equation (11.3) should be written in the form

$$\frac{d}{dt} n(r) = -\alpha\,(n(r), T_e(r)).n^2(r) + D_a(n(1)(r), T_e(r), T_i(r)).\nabla^2 n(r \qquad (11.4)$$

Equation (11.4) can only be solved in conjunction with the energy transport equations.

In analysing our experimental results, we are mainly interested in finding the contribution made by plasma recombination to the measured plasma decay time. For this purpose, we make the approximation of using average values of the parameters in equation (11.4) which yields the relationship

$$\frac{1}{\tau} = \frac{1}{\overline{\tau}_R} + \frac{\overline{D_a}}{\Lambda_o^2} \qquad (11.5)$$

where $\overline{\tau_R}$ and $\overline{D_a}$ are the average values of the plasma recombination time and ambipolar diffusion constant. Multiplying equation (11.5) throughout by gas pressure p, we obtain

$$\frac{p}{\tau} = \frac{p}{\overline{\tau}_R} + \frac{\overline{(D_a . p)}}{\Lambda_o^2} \qquad (11.6)$$

Equation (11.6) was first proposed by Anisimov et al (98) and has been used by other workers (92) as a means of distinguishing between diffusion and recombination.

Plots of the quantity p/τ versus p have been made for each set of experimental results, where τ was obtained from the density decay plots at certain fixed values of $\bar{n}$, and p was taken to be equal to the initial gas filling pressure. These plots of $p/\tau \leftrightarrow p$ are shown in figs. (11.17) to (11.27) and the following comments are made about them and equation (11.6).

1. The product $(\overline{D_a.p})$ is independent of pressure and is a function of electron and ion temperatures only. The intercepts of the plots of p/τ with the $p = 0$ axis enable the values of $(\overline{D_a.p})$ to be found as a function of $\bar{n}$ in the decaying plasma. Using the theory of ambipolar diffusion, estimates of the plasma electron temperature can be made from these values of $(\overline{D_a.p})$ as discussed in the next section.

2. According to equation (11.6) the plots of $p/\tau \leftrightarrow p$ are only straight lines when τ_R in the afterglow plasma is independent of gas pressure, and in this case, the value of τ_R is given by the gradient of the line. In figs. (11.17) to (11.27) it can be seen that the plots only approximate to straight lines at low values of p and high values of $\bar{n}$. A particularly interesting feature is the way the point of departure from the straight line relationship shifts to lower values of pressure with decreasing values of $\bar{n}$. This feature appears to be more pronounced for the large torus results than for the small torus results. At high values of p and low values of $\bar{n}$, the plots of p/τ with increasing pressure appear to assymptotically approach fixed values.

3. The $p/\tau \leftrightarrow p$ plot for helium plasma decay in the large torus,

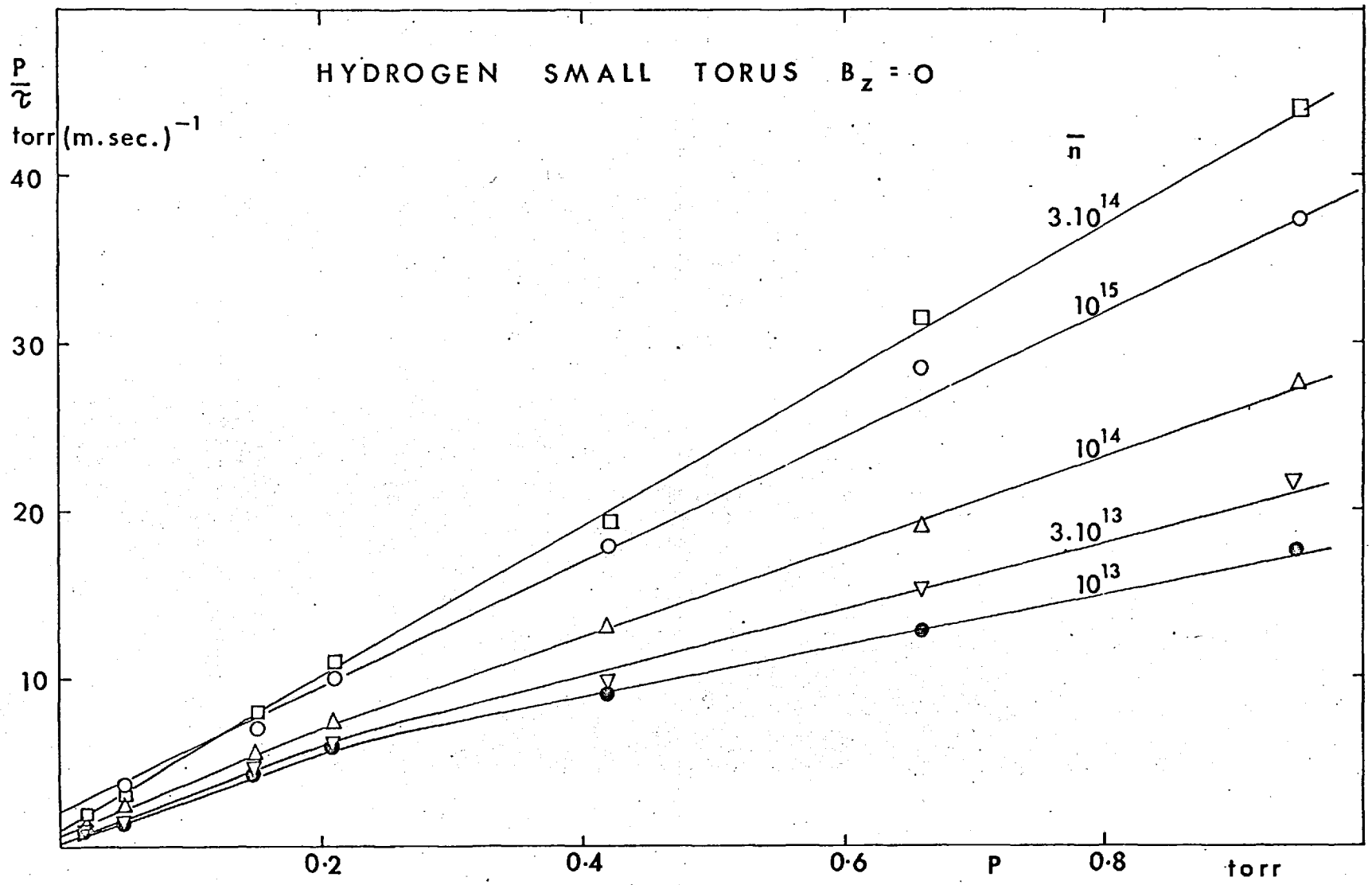
HYDROGEN SMALL TORUS $B_z = 0$
$\frac{P}{\tau}$
torr (m.sec.)$^{-1}$
40
30
20
10
$\bar{n}$
3.10^{14}
10^{15}
10^{14}
3.10^{13}
10^{13}
0·2
0·4
0·6
P
0·8
torr

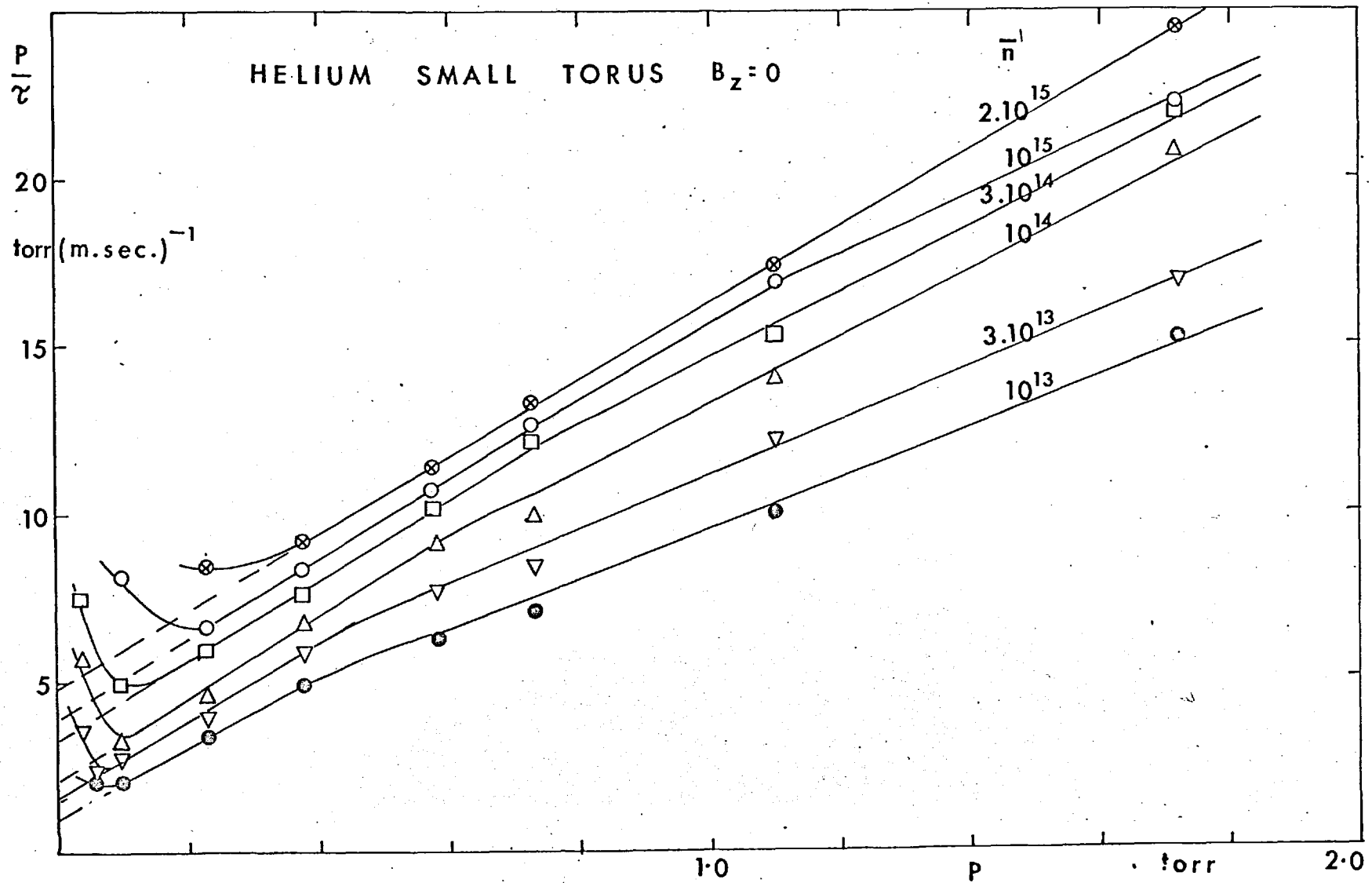
HELIUM SMALL TORUS $B_z = 0$
$\frac{P}{\tau}$
torr (m.sec.)$^{-1}$
$\bar{n}$
2.10^{15}
10^{15}
3.10^{14}
10^{14}
3.10^{13}
10^{13}
20
15
10
5
1·0
2·0
P torr

FIG (11.18)

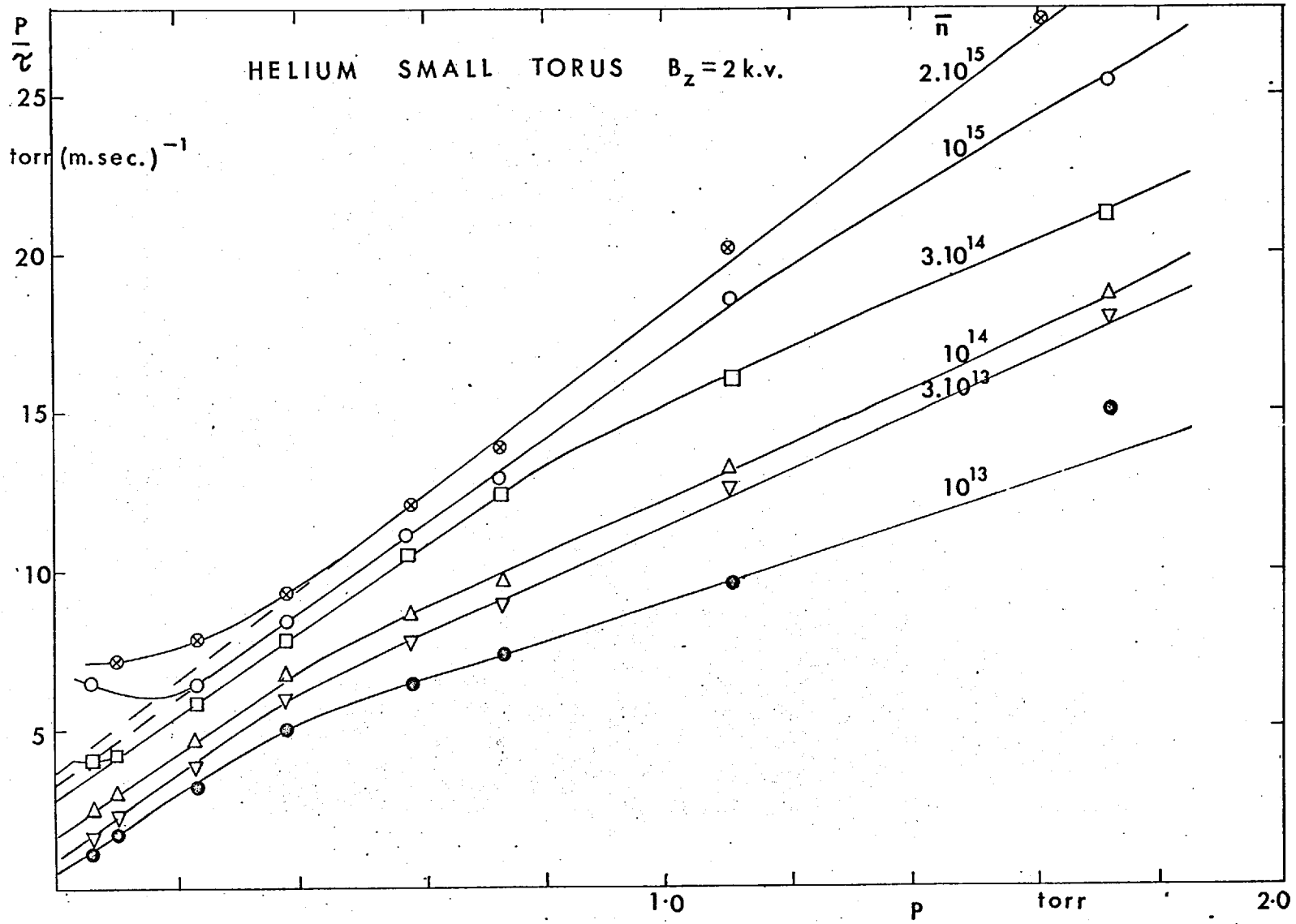
HELIUM SMALL TORUS $B_z = 2$ k.v.
$\bar{n}$
2.10^{15}
10^{15}
3.10^{14}
10^{14}
3.10^{13}
10^{13}
$\frac{P}{\tau}$
torr (m.sec.)$^{-1}$
25
20
15
10
5
1·0
P
torr
2·0

FIG. (11.19)

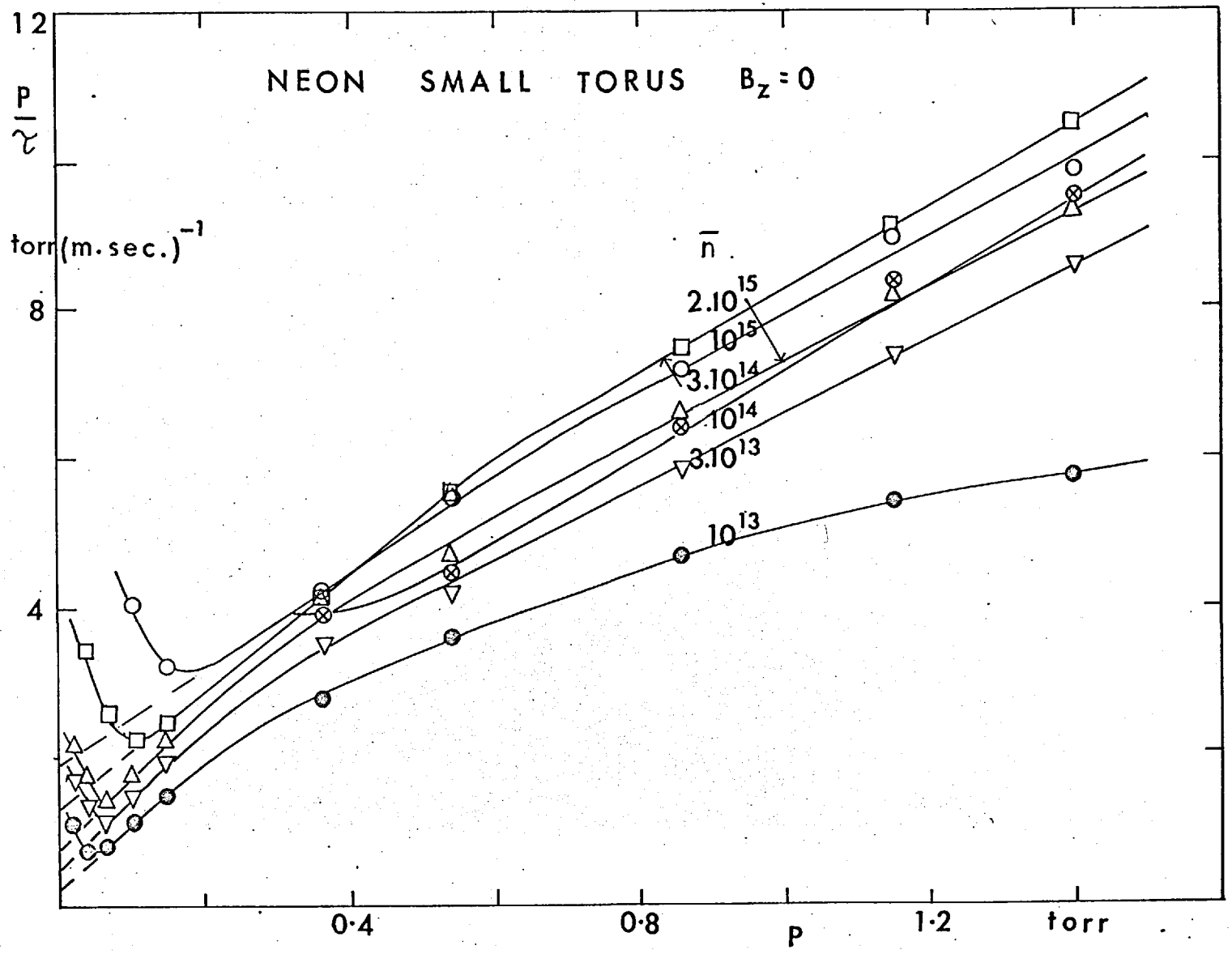
NEON SMALL TORUS $B_z = 0$
$\frac{P}{\nu}$
torr (m.sec.)$^{-1}$
$\bar{n}$
2.10^{15}
10^{15}
3.10^{14}
10^{14}
3.10^{13}
10^{13}
12
8
4
0·4
0·8
1·2
P
torr

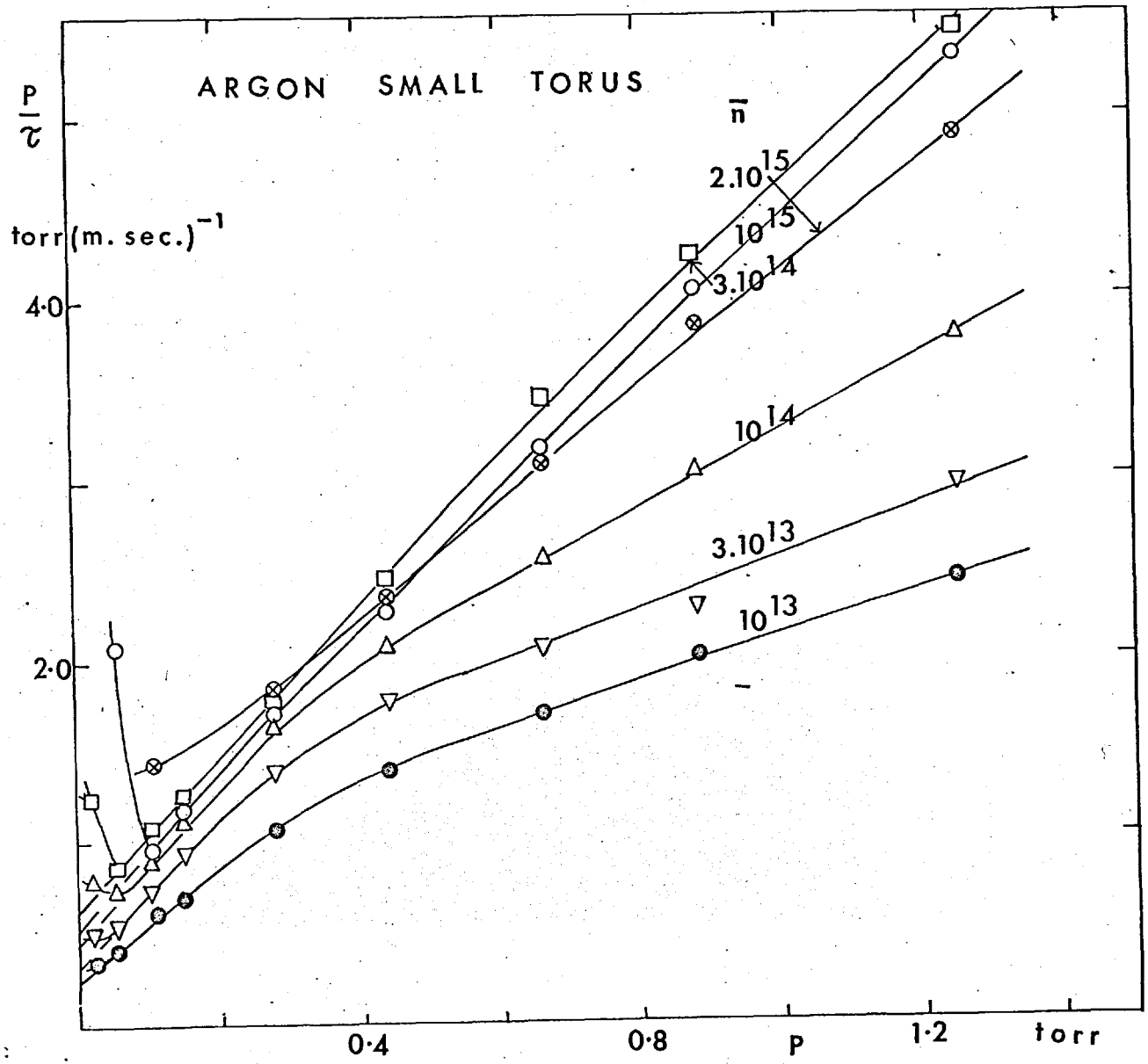
ARGON SMALL TORUS
$\frac{P}{\tau}$
torr (m. sec.)$^{-1}$
$\bar{n}$
2.10^{15}
10^{15}
3.10^{14}
10^{14}
3.10^{13}
10^{13}
4·0
2·0
0·4
0·8
P
1·2
torr

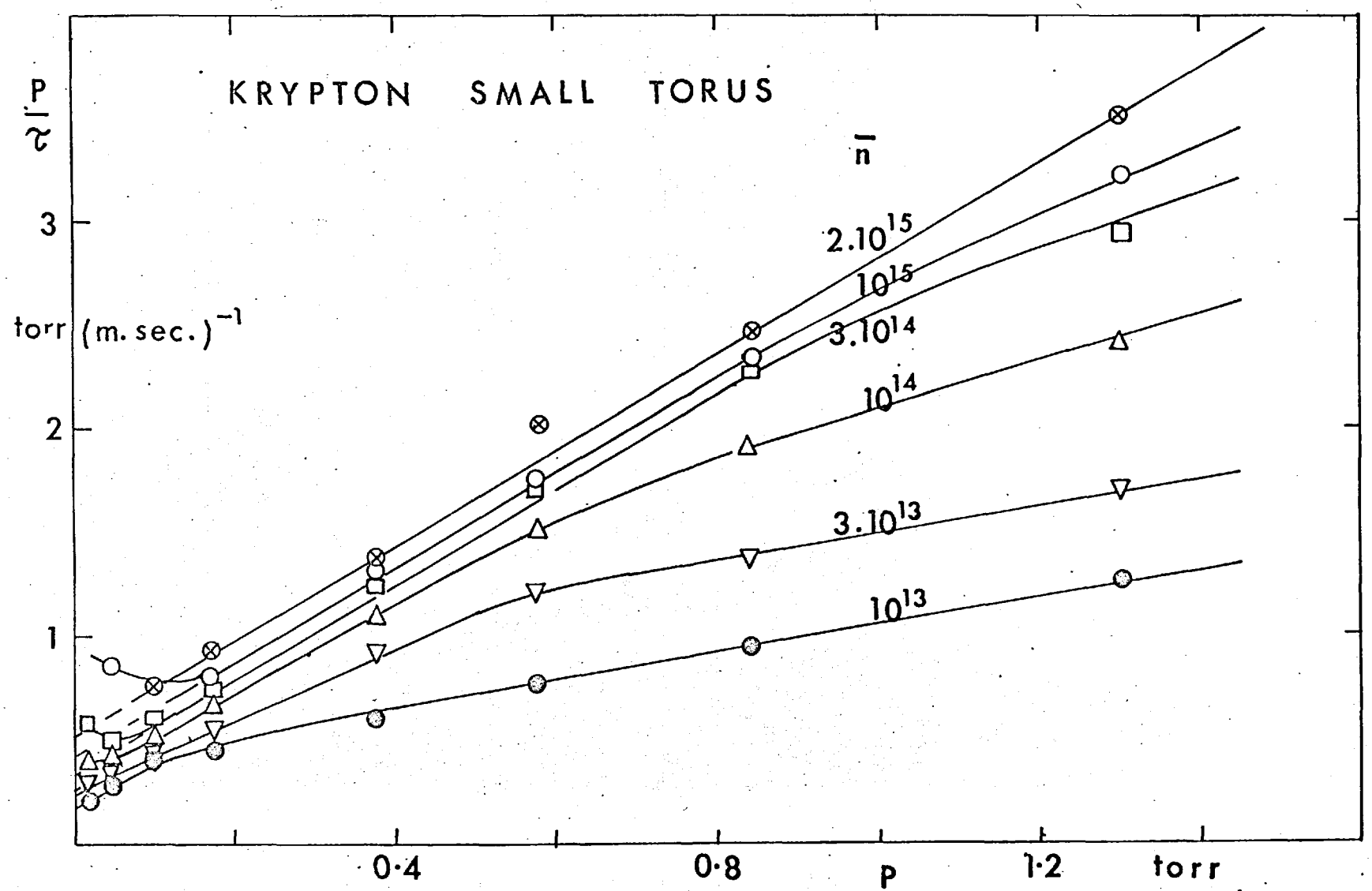
KRYPTON SMALL TORUS
$\frac{P}{\tau_i}$
torr (m.sec.)$^{-1}$
$\bar{n}$
2.10^{15}
10^{15}
3.10^{14}
10^{14}
3.10^{13}
10^{13}
3
2
1
0·4
0·8
1·2
P
torr

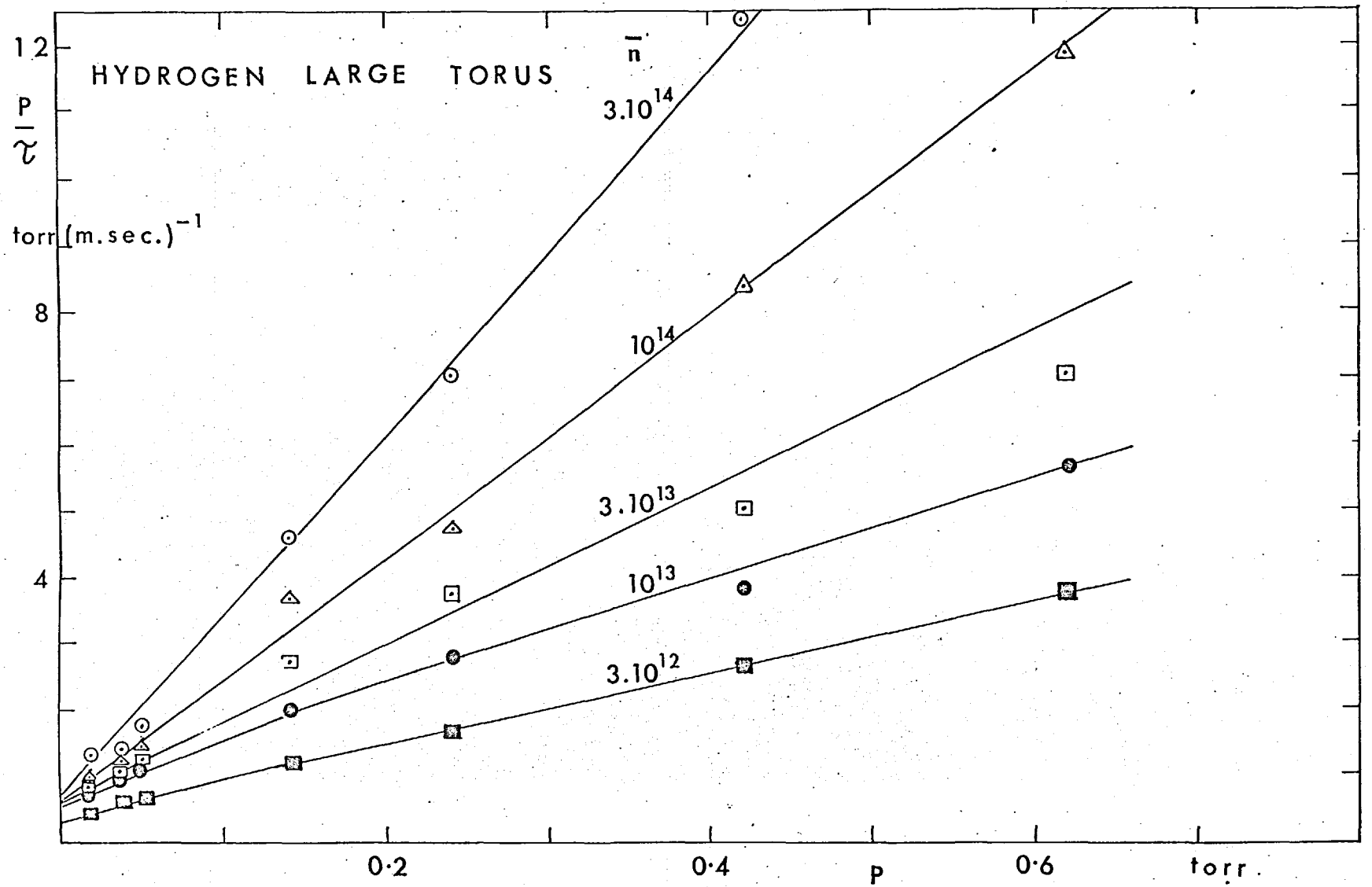
HYDROGEN LARGE TORUS
$\bar{n}$
3.10^{14}
10^{14}
3.10^{13}
10^{13}
3.10^{12}
$\frac{P}{\tau}$
torr (m.sec.)$^{-1}$
12
8
4
0·2
0·4
0·6
P
torr.

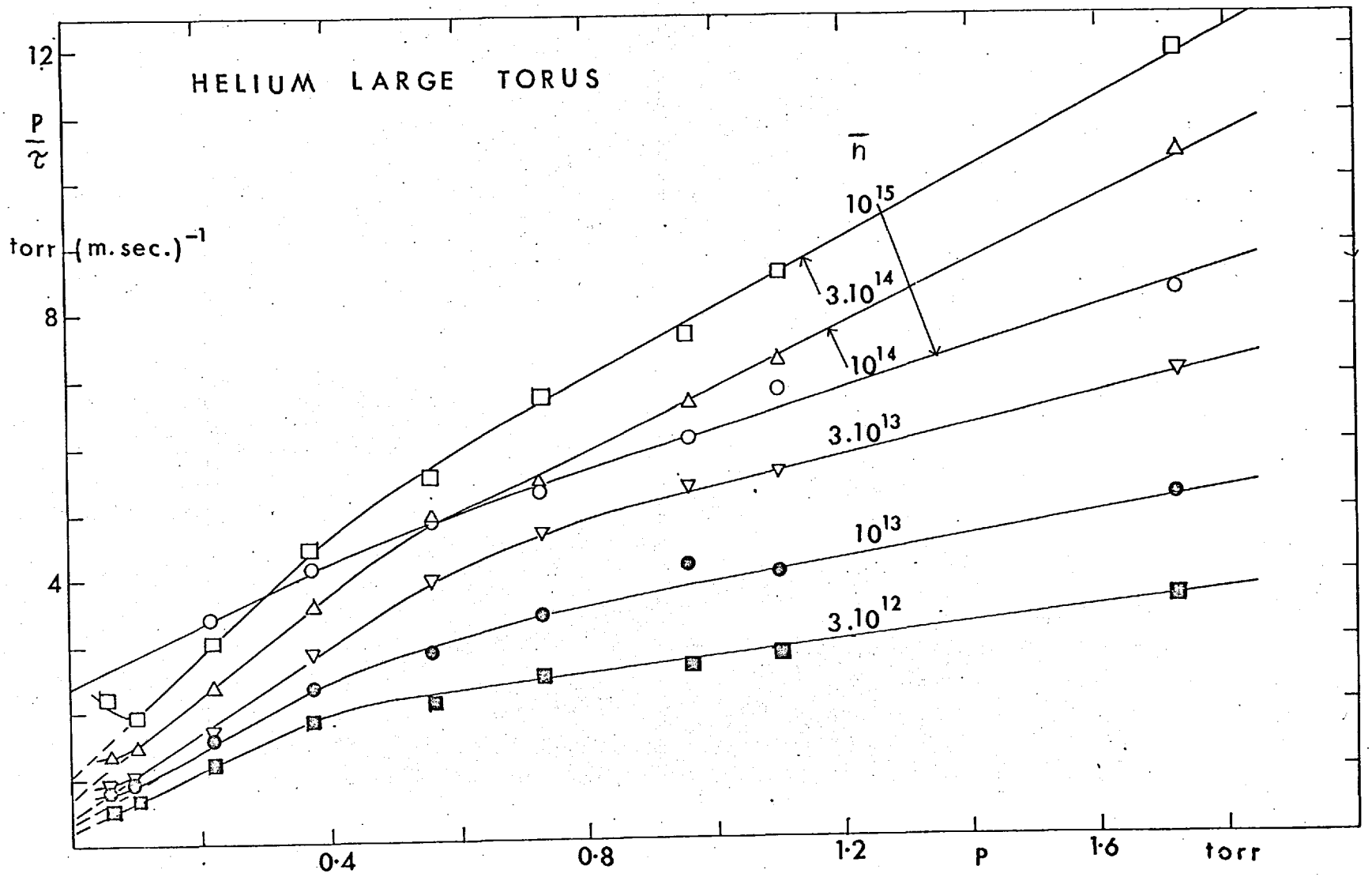
HELIUM LARGE TORUS
$\frac{P}{\tau}$
torr (m.sec.)$^{-1}$
$\bar{n}$
10^{15}
3.10^{14}
10^{14}
3.10^{13}
10^{13}
3.10^{12}
12
8
4
0·4
0·8
1·2
1·6
P
torr

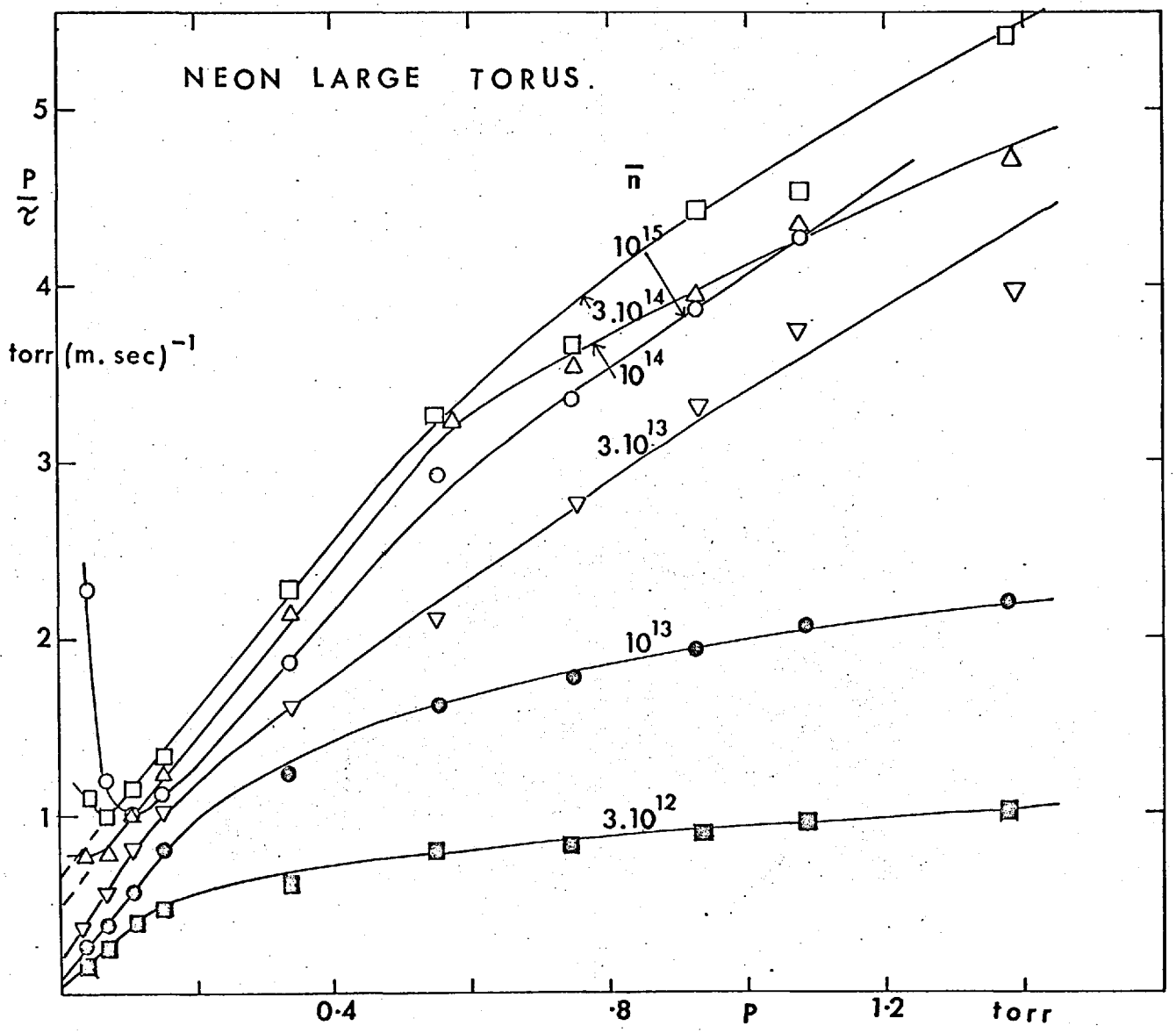
NEON LARGE TORUS.
$\frac{P}{\nu}$
torr (m. sec)$^{-1}$
$\bar{n}$
10^{15}
3.10^{14}
10^{14}
3.10^{13}
10^{13}
3.10^{12}
1
2
3
4
5
0·4
·8
P
1·2
torr

FIG. (11.25)

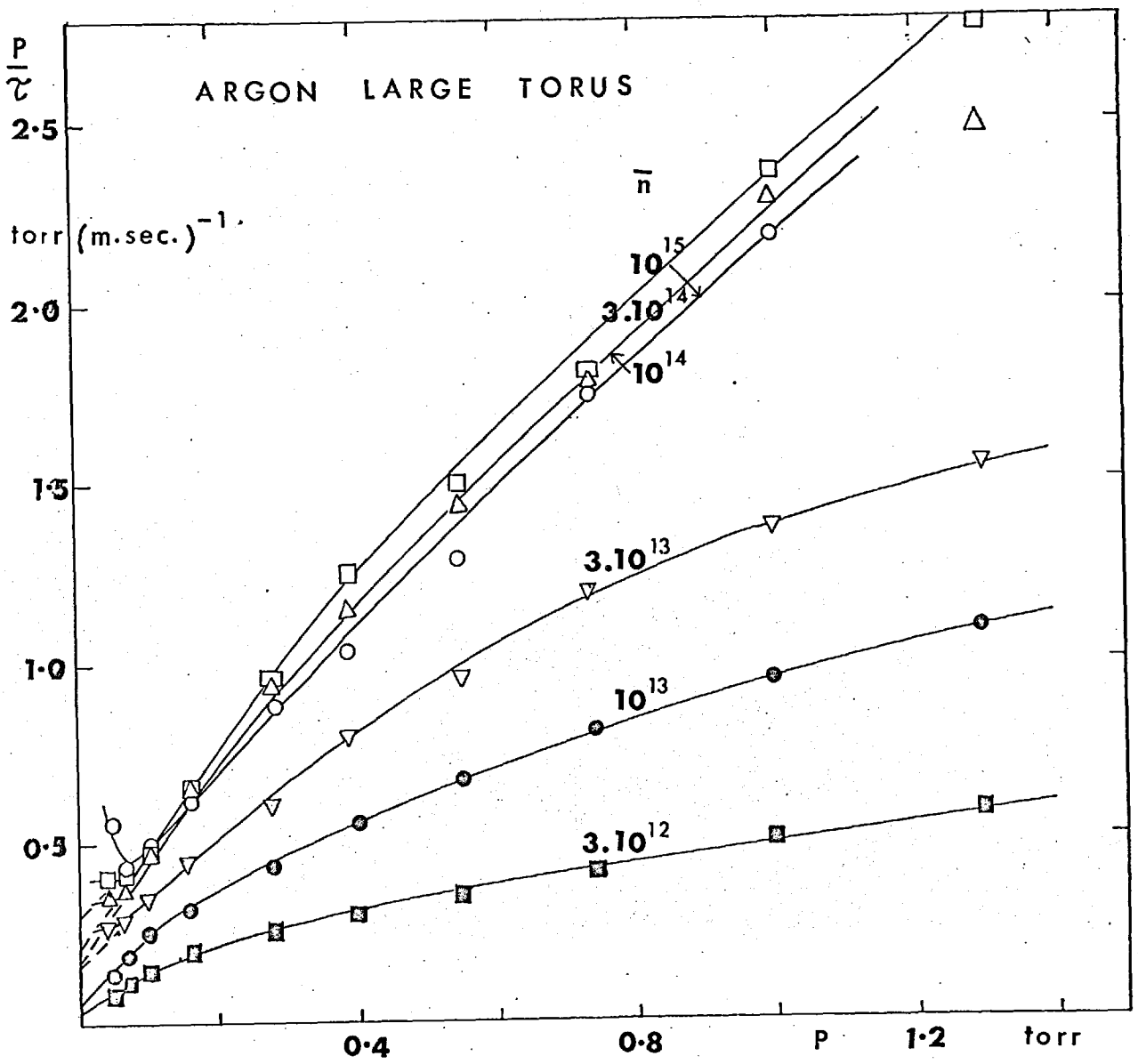
ARGON LARGE TORUS
P/τ
torr (m.sec.)⁻¹
n̄
10¹⁵
3.10¹⁴
10¹⁴
3.10¹³
10¹³
3.10¹²
2·5
2·0
1·5
1·0
0·5
0·4
0·8
P
1·2
torr

Fig. (11.26)

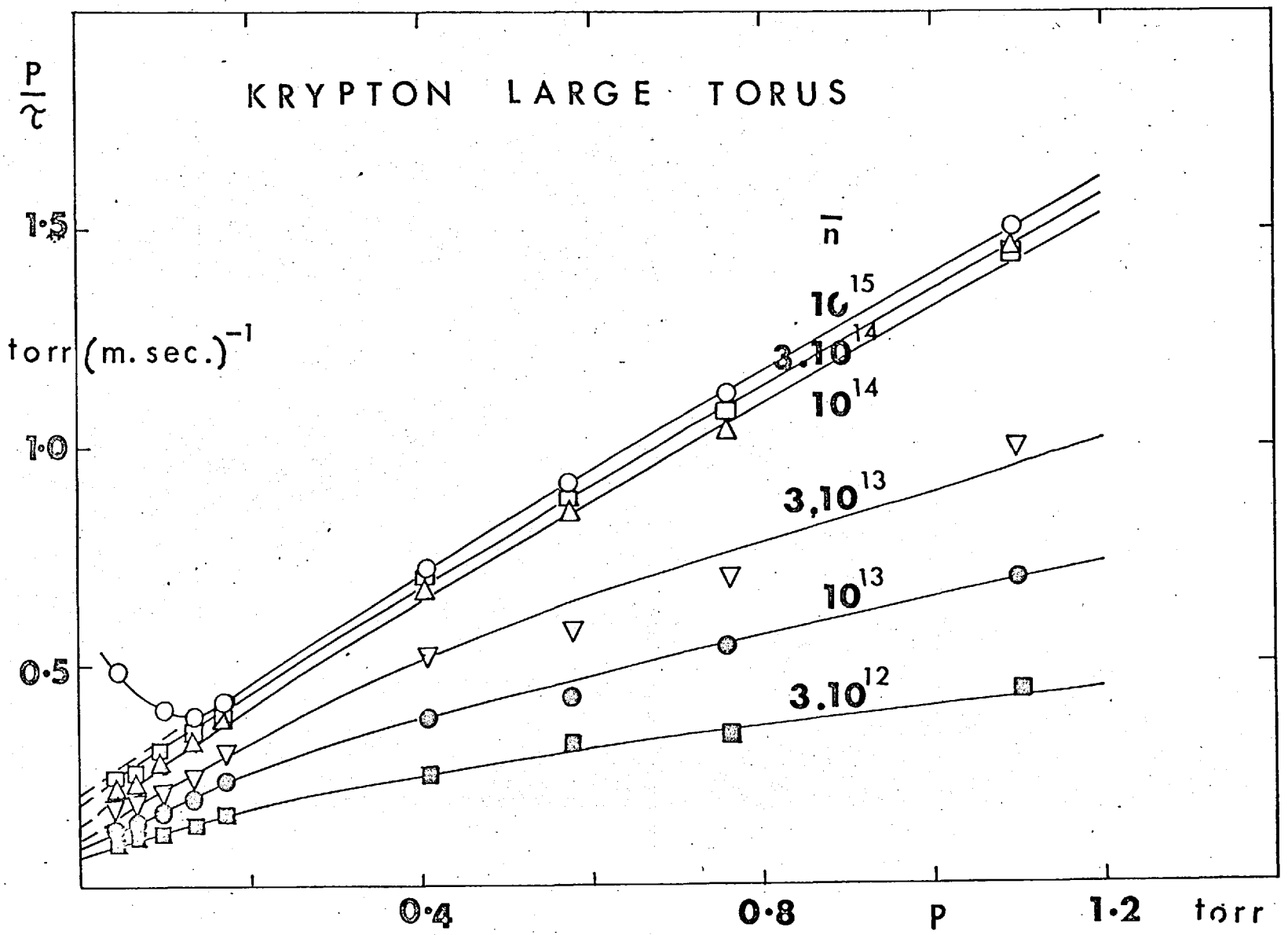
KRYPTON LARGE TORUS
P/τ
torr (m.sec.)⁻¹
1·5
1·0
0·5
n̄
10¹⁵
3.10¹⁴
10¹⁴
3,10¹³
10¹³
3.10¹²
0·4
0·8
p
1·2
torr

fig. (11.24), has been compared with a plot of the same quantities given by Newton (92)(93) for a helium plasma decay in a cylindrical discharge tube of radius 3.6 cm. Since our large torus minor radius was 3.55 cm, a comparison between both sets of results ought to be perfectly valid. However, Newton's plots, which were performed for values of $\bar{n}$ between 10^{12} and 10^{15} cm^{-3}, showed straight line relationships between p/τ and p throughout the entire pressure range of the experiment 0.05 to 1.7 torr. Clearly there is a large discrepancy between Newton's results and our present results.

4. The values of τ_R found from the gradients of the $p/\tau \leftrightarrow p$ plots at low gas pressures have been used to evaluate the ratio

$$\frac{\tau_{RL}}{\tau_{RS}} = \frac{\tau_R \text{ in large torus}}{\tau_R \text{ in small torus}} \qquad (11.7)$$

for all the types of gas over a wide range of plasma densities, where the values of τ_{RL} and τ_{RS} substituted into expression (11.7) corresponded to the same average value of electron density and the same type of gas. The results are shown in table (11.1)

TABLE (11.1)

RATIO τ_{RL}/τ_{RS}

GAS \ $\bar{n}$	10^{15}	$3\ 10^{14}$	10^{14}	$3\ 10^{13}$	10^{13}
H	-	1.7	1.5	1.7	1.9
He	1.4	1.7	2.0	2.5	2.9
Ne	2.0	2.0	1.9	1.9	1.9
A	1.6	1.6	1.5	1.8	1.5
Kr	1.5	1.4	1.4	1.7	2.0

The actual values of the decay times going from hydrogen to krypton change by more than an order of magnitude, and from table (11.1) it appears that the ratio τ_{RL}/τ_{RS} is independent of plasma density or the type of gas and is determined solely by the relative sizes of the two tori. The ratio of the torus minor radii was 1.60 ($\pm$ 0.05) and so it would seem that the dependence of the low pressure plasma recombination time upon the tube radius has the form

$$\tau_R \propto (\text{tube radius})^{1.0 \text{ to } 1.5} \qquad (11.8)$$

5. The values of τ_R found from the experimental decay plots and the p/τ - p plots are listed in tables (13.1) and (13.2) in Chapter 13 where a comparison with C.R. plasma recombination theory is performed.

(11.4) ANALYSIS OF THE TERM $(D_a.p)$

From the theory of plasma diffusion presented in Chapter 3, and in particular equations (3.12) and (3.15), the ambipolar diffusion coefficient can be written in the form

$$D_a = \frac{\mu_i \, k \, T_i}{e} \left\{ 1 + \frac{T_e}{T_i} \right\} \qquad (11.9)$$

Oskam and Mittelstadt (68) have determined the product $(D_a.p)$ from experiments performed in low density late period afterglows where $T_e = T_i = 300^{\circ}K$. We will denote their values for the product by $(D_a.p)_{300}$ and we will take these values, which have been listed in table (11.2), as comparison standards.

TABLE (11.2)

GAS	$(D_a.p)_{300}$ torr cm^2 sec^{-1}
H	538
He	460
Ne	174
A	69
Kr	39

Using equation (11.9) we can write an expression for the product $(D_a.p)$ in the form

$$(D_a.p) = (D_a.p)_{300} \left\{\frac{\mu_i}{\mu_{300}}\right\} \left\{\frac{T_e + T_i}{600}\right\} \qquad (11.10)$$

where μ_{300} = ionic mobility at $T_i = 300^oK$.

Substituting the experimentally measured values of $(D_a.p)$ into equation (11.10) together with the values of $(D_a.p)_{300}$ from table (11.2) enables calculations to be made of the electron temperature existing in the plasma afterglow for the two limiting cases (a) when $T_i = 300^oK$ and (b) when $T_i = T_e$.

(a) $T_i = 300^oK$

This case represents the lowest possible value for T_i in the plasma and equation (11.10) reduces to

$$(D_a p) = \frac{(D_a p)_{300}}{2} \left\{1 + \frac{T_e}{300}\right\} \qquad (11.11)$$

and an estimate for T_e can be directly found from equation (11.11)

(b) $T_i = T_e$

This case represents the highest possible value for T_i in the afterglow plasma and equation (11.10) reduces to

$$(D_a p) = (D_a p)_{300} \left\{ \frac{\mu_i}{\mu_{300}} \right\} \left\{ \frac{T_e}{300} \right\} \qquad (11.12)$$

The ratio of the ionic mobilities can be obtained from the theoretical work of Dalgamo (118), and a plot of this ratio applicable to singly charged hydrogen and rare gas ions moving in their parent gases over the temperature range 300°K to 10,000°K is shown in fig. (11.28). Using this plot an estimate for T_e can be found from equation (11.12).

In table (11.3) experimental values of the ratio $(D_a p) / (D_a p)_{300}$ have been given together with the values of T_e calculated by methods (a) and (b) above. These two values of T_e for each result represent the lower and upper limits to the range of possible values of T_e.

For rare gas plasma decays in the large torus, (especially the case of neon), the values for p/τ can be seen in figs. (11.23) to (11.27) to increase with decreasing pressure for the conditions

$$\left.\begin{aligned} \bar{n} &> 3 \times 10^{14} \quad \text{cm}^{-3} \\ p &< 150 \quad \text{m. torr} \end{aligned}\right\} \qquad (11.13)$$

This feature gives rise to a negative gradient of the p/τ plot for conditions (11.13) and extrapolation of this negative gradient line to the $p = 0$ axis gives rise to impossibly large

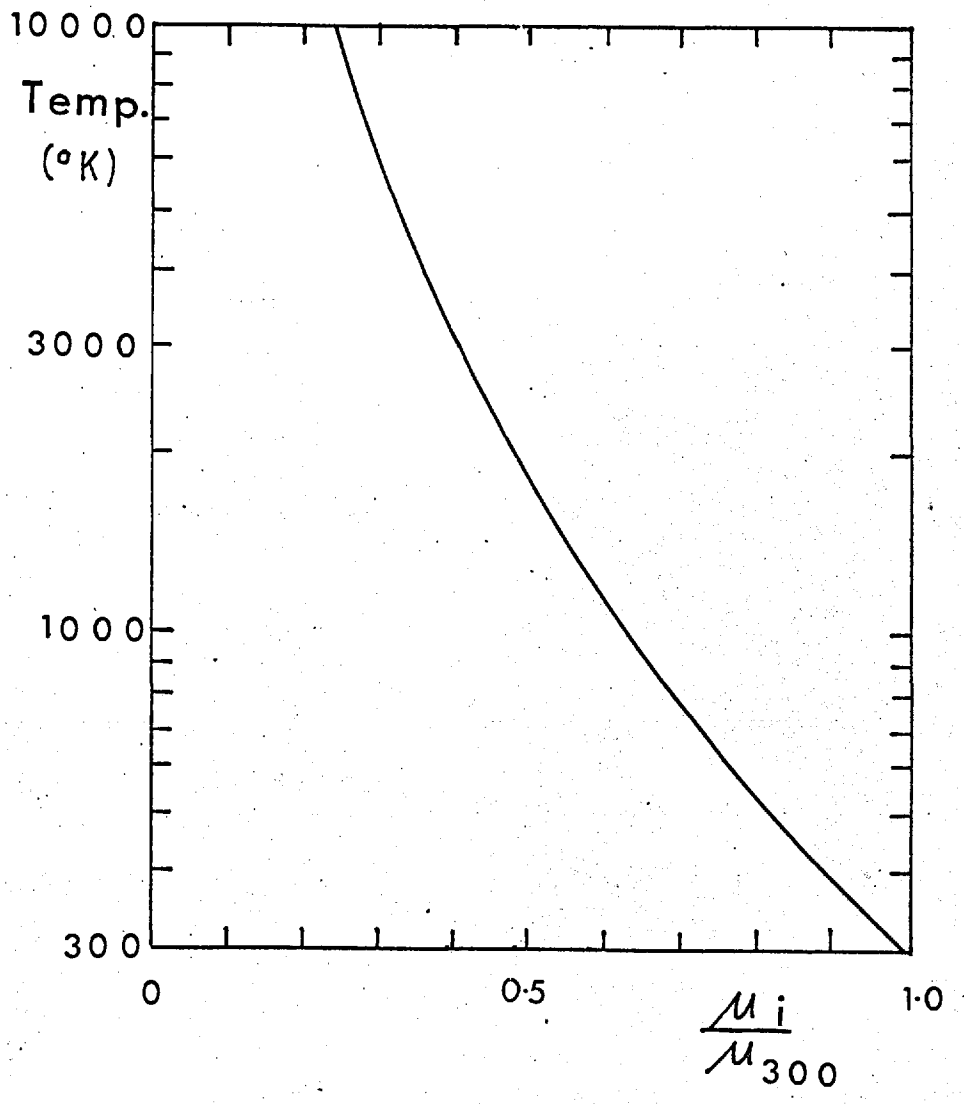

FIG (11.28) Plot of the relative mobility of singly charged ions moving in their parent gases over the temperature range 300°K to 10000°K.

TABLE (11.3)

AVERAGE ELECTRON DENSITY (cm^{-3})	LARGE TORUS			SMALL TORUS		
	$\frac{(D_a p)}{(D_a p)_{300}}$	T_e (T_i=300°K)	T_e (T_i=T_e)	$\frac{(D_a p)}{(D_a p)_{300}}$	T_e (T_i=300°K)	T_e (T_i=T_e)
HYDROGEN						
10^{15}				3.7	1900	2600
3 10^{14}	2.5	1200	1400	1.6	700	700
10^{14}	2.7	1300	1600	1.1	300	300
3 10^{13}	2.9	1500	1800			
10^{13}	2.7	1300	1600			
3 10^{12}	1.5	600	600			
HELIUM						
2 10^{15}				9.0	5100	10000
10^{15}	11.4	6500	14000	7.3	4100	7400
3 10^{14}	4.9	2600	4100	5.9	3300	5600
10^{14}	3.7	1900	2600	3.9	2000	2800
3 10^{13}	2.9	1500	1800	3.3	1700	2200
10^{13}	2.0	880	940	2.4	1100	1300
3 10^{12}	1.6	640	650			
NEON						
10^{15}	7.8	4400	8000	10.0	5700	12000
3 10^{14}	6.5	3600	5400	5.7	3100	5300
10^{14}	5.2	2800	4600	3.8	2000	2700
3 10^{13}	2.1	940	1100	2.1	980	1100
10^{13}	1.3	470	480	1.4	560	570

TABLE (11.3) CONTINUED

AVERAGE ELECTRON DENSITY (cm^{-3})	LARGE TORUS			SMALL TORUS		
	$\frac{(D_a p)}{(D_a p)_{300}}$	T_e (T_i=300°K)	T_e (T_i=T_e)	$\frac{(D_a p)}{D_a p)_{300}}$	T_e (T_i=300°K)	T_e (T_i=T_e)
ARGON						
$2\ 10^{15}$				10.1	5700	12000
10^{15}	10.4	6000	12800	7.7	4300	8000
$3\ 10^{14}$	9.5	5400	11000	7.7	4300	8000
10^{14}	7.8	4400	8100	6.0	3300	5700
$3\ 10^{13}$	5.2	2800	4700	3.8	2300	2800
10^{13}	3.6	1800	2500	3.3	1700	2100
$3\ 10^{12}$	2.6	1300	1500			
KRYPTON						
$2\ 10^{15}$				11.3	6500	15000
10^{15}	11.0	6300	14000	9.4	5300	11000
$3\ 10^{14}$	8.6	4900	9500	7.7	4300	7800
10^{14}	6.9	4200	6900	6.2	3400	6000
$3\ 10^{13}$	6.1	3300	5700	5.1	2800	4400
10^{13}	5.3	2900	4600	3.8	2000	2700
$3\ 10^{12}$	4.2	2200	3100			

values of $(D_a.p)$. Conditions (11.13) are those of very high degrees of plasma ionisation associated with the very early stages of the afterglow period. The explanation of the above phenomena is not obvious: it cannot be due to the effects of the 'tail' of the undamped discharge current producing plasma in the early afterglow, as this situation would yield an abnormally low value for p/τ. The only likely explanation of the high values of p/τ recorded, is that in the early highly ionised decay period, the plasma has not reached a state of quasi-equilibrium and is recombining very rapidly. The fact that the p/τ plots for weakly ionised plasma do not show this negative gradient is in agreement with the above conclusions. The negative gradients on the p/τ plots were therefore ignored and the intercepts with the $p = 0$ axis in figs. (11.17) to (11.27) at high electron densities were found by extrapolating the plots from the high pressure (low degree of ionisation) region.

(11.5). EXPERIMENTAL RELATIONSHIP BETWEEN n, T_e and τ_R.

By combining the experimental measurements of T_e as a function of n shown in figs. (11.15) and (11.16), with the experimental values of τ_R as a function of n, found in the same gas pressure region, we can find an experimental relationship between the parameters n, T_e and τ_R. We can also check the equation (9.26) for C.R. plasma recombination proposed by D'Angelo. From equation (9.26), we can write

$$n^2 \tau_R = \left(\frac{T_e}{C}\right)^{9/2} \qquad (11.14)$$

where $C = 3.9\ 10^{-9}$ $(n\ cm^{-3},\ T_e\ ^oK)$.

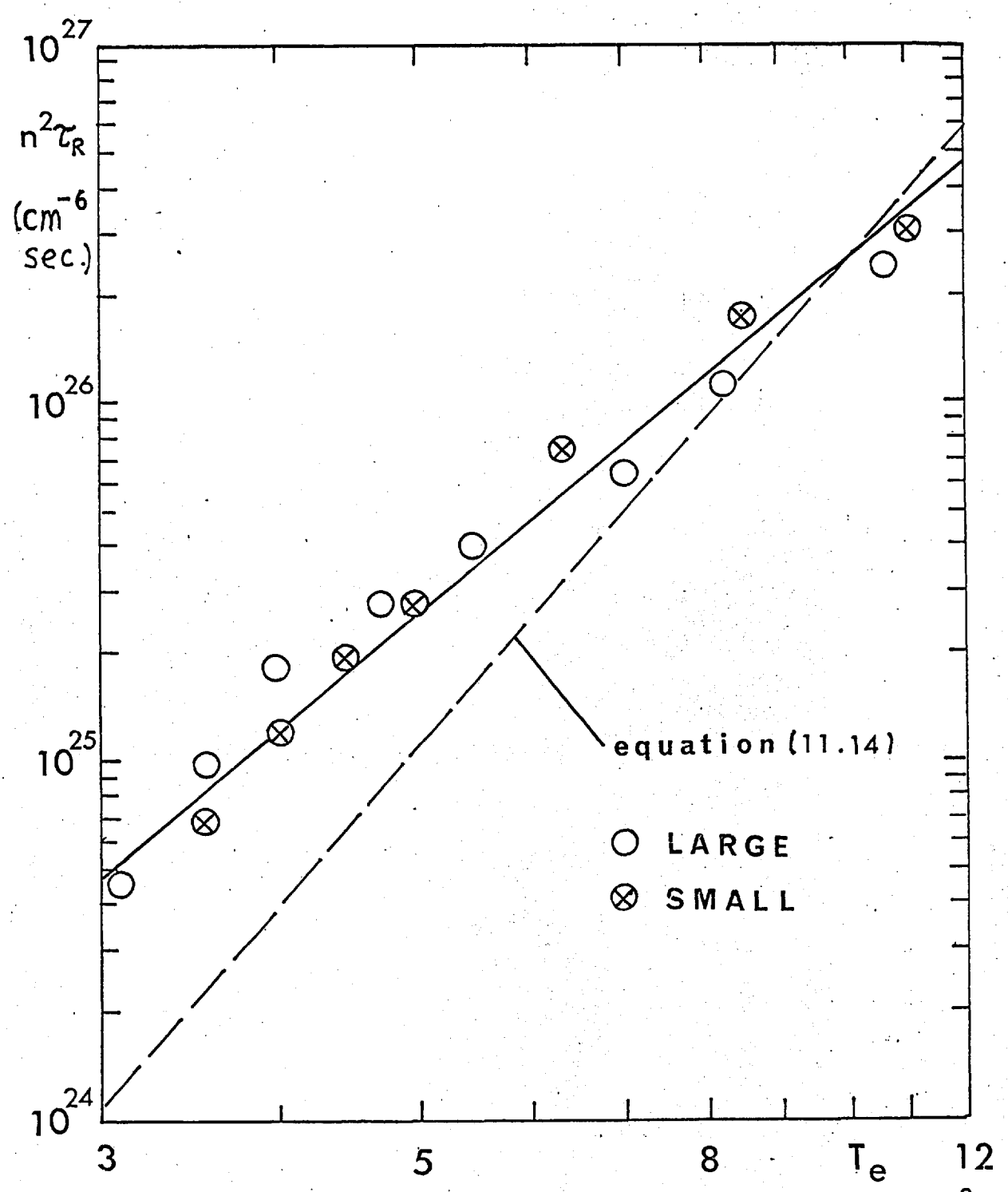

FIG (11.29) Plot of the experimental values of $n^2\tau_R$ versus T_e for helium plasmas.

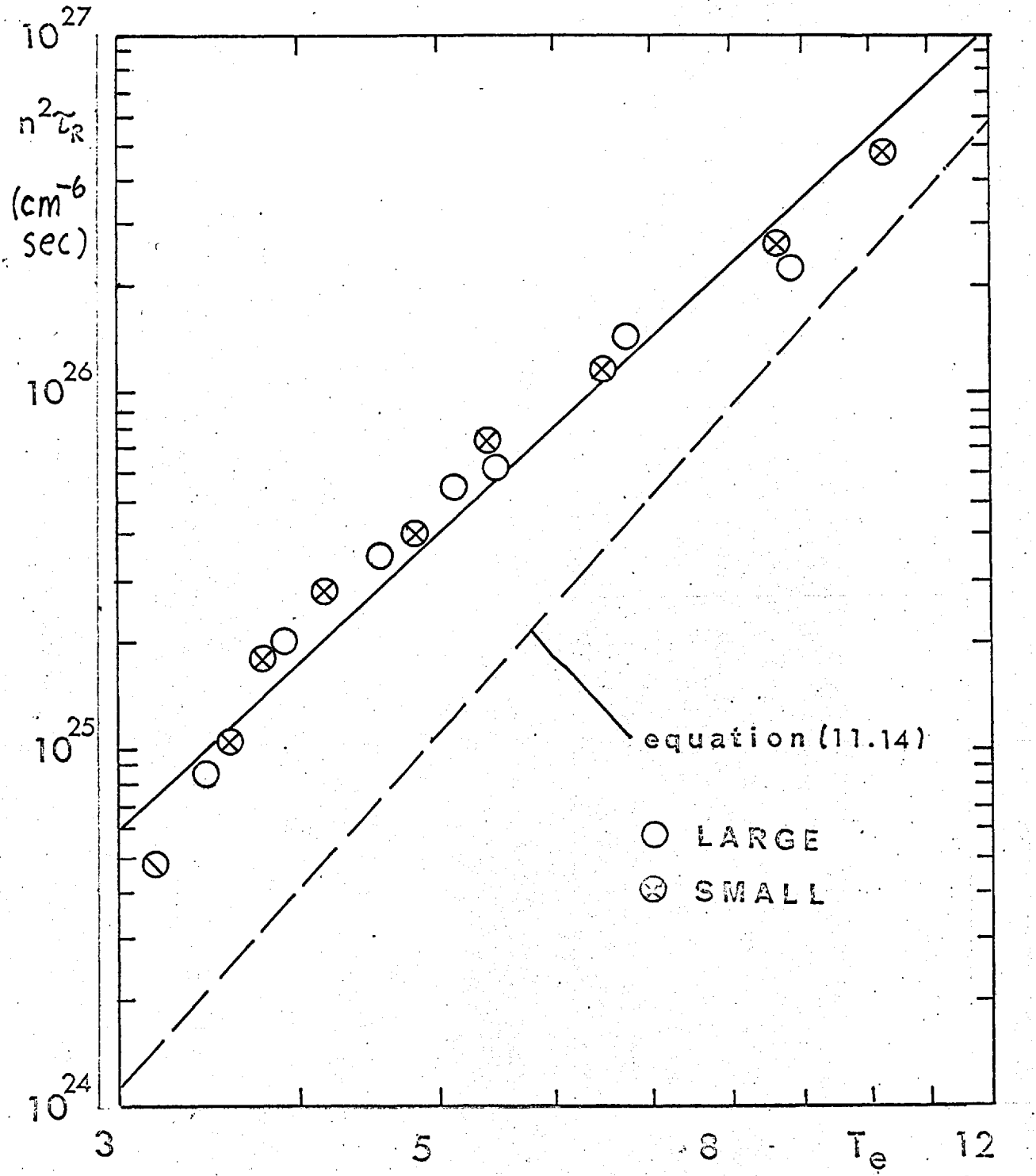

FIG (11.30) Plot of the experimental values of $n^2\tau_R$ versus T_e for neon plasmas.

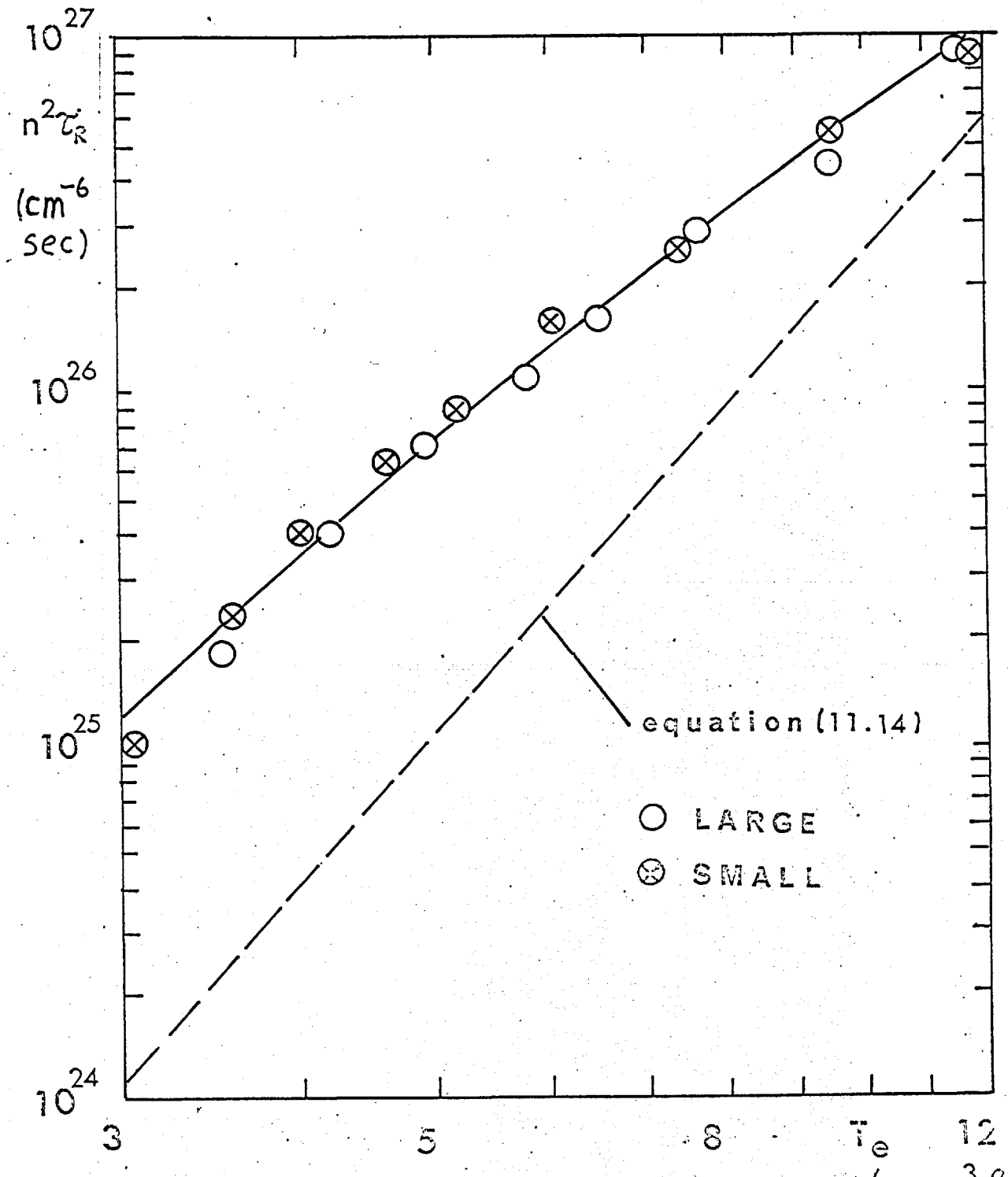

FIG (11.31) Plot of the experimental values of $n^2\tau_R$ versus T_e for argon plasmas.

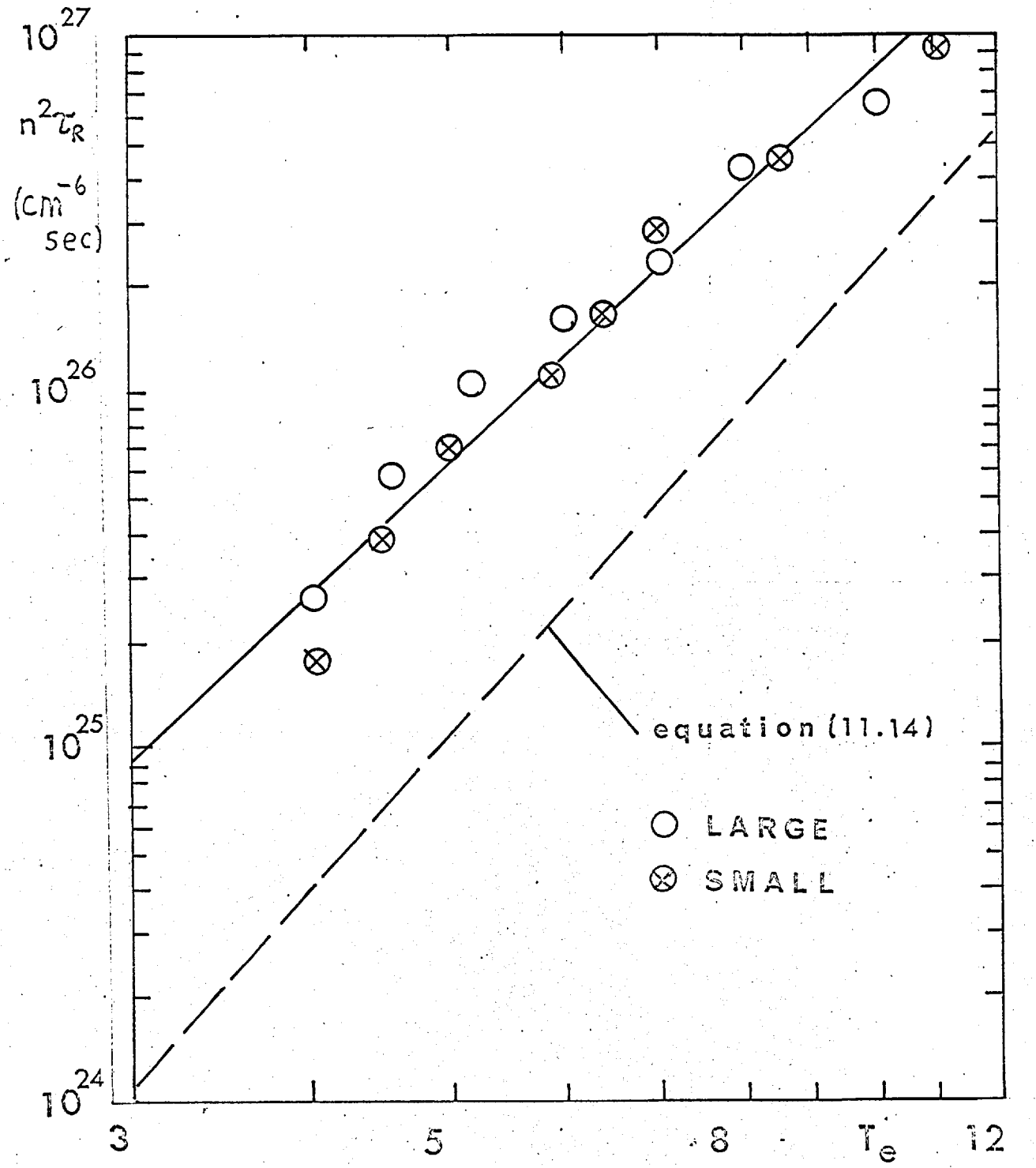

FIG (11.32) Plot of the experimental values of $n^2 \tau_R$ versus T_e for krypton plasmas.

In figs. (11.29) to (11.32) the experimental value of $n^2\tau_R$ has been plotted logarithmically against the corresponding experimental value of T_e, for each set of rare gas experiments in both sizes of torus. All the experimental results were for the low gas pressure region 50 to 150 m.torr. The gradients of the plots give the power relationship and the intercepts give the value of the multiplying constant. The line corresponding to equation (11.14) with $C = 3.9 \ 10^{-9}$ has been included on each plot for comparison purposes.

Inspection of figs. (11.29) to (11.32) shows that there is fair agreement of the experimental results with equation (11.14) in all cases. Detailed comparison of the results shows that the experimental values of the multiplying constant C lie in the range

$$4 \ 10^{-9} < C < 4 \ 10^{-8} \text{ (c.g.s. units)} \quad (11.15)$$

with a systematic trend towards larger values of C going up the atomic scale from helium to krypton. Also in the case of helium, the power dependence of temperature is closer to 4.0 than 4.5.

CHAPTER 12

COMPUTER SOLUTION OF THE CONSERVATION OF ENERGY - RECOMBINATION EQUATIONS IN A DECAYING PLASMA

The principle of conservation of energy is applied to an afterglow plasma for the case where three body electron-ion recombination is assumed to be the dominant plasma decay mechanism. The energy balance equations are formulated and they are solved together with the recombination equation both analytically, for simple limiting approximations, and more generally using a computer. The solutions are aimed at predicting the plasma recombination time or the recombination coefficient as a function of electron and atom density. The idea of calculating the recombination coefficient from a solution of the energy balance - recombination equations was first proposed by Byron et al (78). A review of their work and the later work of Bates and Kingston (74)(75) is given at the start of this chapter, which shows that both these solutions to the problem are completely unsuitable for estimating recombination coefficients in plasmas with electron densities $> 10^{13}$ cm^{-3}.

The new solutions to the energy balance - recombination equations that are presented, are specifically directed towards calculating the recombination times (and recombination coefficients) that exist in decaying hydrogen and rare gas plasmas throughout the density decay region $10^{13} - 10^{16}$ cm^{-3}.

(12.1) REVIEW OF THE WORK OF BYRON et al.

Byron, Stabler and Botz (78) have combined their work on

the evaluation of the C.R. recombination coefficient, described in section (9.11), with the equations for elastic energy transfer amongst the plasma particles. The electron energy equation was written as

$$\frac{3}{2} n k \frac{dT_e}{dt} = Q \text{ inel} - Q \text{ el} \qquad (12.1)$$

where Q el = rate of elastic energy transfer from electrons to atoms and ions

Q inel = rate of inelastic energy transfer to the electron gas by the recombination process.

$$\therefore Q \text{ inel} = \left(\bar{E} + \frac{5}{2} k T_e \right) \frac{dn}{dt} \qquad (12.2)$$

where $\bar{E}$ = mean energy given to the electron gas per ion recombined.

For many afterglow plasma conditions

$$\bar{E} \gg \frac{3}{2} k T_e \qquad (12.3)$$

and so $$Q \text{ inel} \gg \frac{3}{2} n k \frac{dT_e}{dt} \qquad (12.4)$$

hence, a quasi-equilibrium situation for electron temperature prevails and from equations (12.1) and (12.2) the recombination coefficient is given by

$$\alpha = \frac{1}{n^2} \cdot \frac{dn}{dt} = \frac{Q \text{ el}}{n^2 \left(\bar{E} + \frac{5}{2} k T_e \right)} \qquad (12.5)$$

Q el was assumed to be primarily due to elastic energy transfer to the ions and an expression given by Petschek and Byron (119) for Q el was substituted into equation (12.5).

The plasma recombination times and the electron densities existing at different points in a plasma decay were then found

by solving simultaneously equation (12.5) with the equation for elastic energy transfer in the ion gas and the three body recombination rate equation (9.22). Solutions were worked out only for hydrogen or helium afterglows and good agreement of the results was concluded in the density range 10^{12} to $5\ 10^{13}$ cm^{-3} with the experimental results of Motley and Kuckes (85), who measured α and T_e in a magnetically confined helium plasma at gas pressures of 0.5 and 4.0 m.torr.

(12.2) REVIEW OF THE WORK OF BATES AND KINGSTON

Bates and Kingston (74)(75) have also tackled recombination and energy balance in decaying hydrogen and helium plasmas. Their results have been widely quoted by experimental workers (92)(93)(88)(97)(87) in the comparison of C.R. recombination theory with experiment.

In formulating the energy balance equations, Bates and Kingston used a previously published paper (120) to express the nett power radiated by the plasma in the form

$$\text{Nett Power Radiated} = P + n(1)\, P_1 \qquad (12.6)$$

where P and P_1 are coefficients depending on n, T_e and the optical depth of the plasma.

The notation used to write the expressions for the rate of elastic energy transfer from particle species 1 to particle species 2 was of the form

$$Q_{12} = n_1 . n_2 . \eta_{12} . (T_1 - T_2) \qquad (12.7)$$

where Q_{12} = nett rate of elastic energy transfer from 1 to 2
n_1, T_1 = density, temperature of particle species 1
n_2, T_2 = density, temperature of particle species 2

η_{12} = elastic energy transfer coefficient.

In general η_{12} is a function of n_1, n_2, T_1 and T_2.

The energy balance equation for the plasma electrons was formulated by Bates and Kingston as

$$\frac{3}{2} n k \frac{dTe}{dt} = H_o - H_1 . n(1) - n^2 \eta_{ei}(T_e - T_i) - n\, n(1) \eta_{ea}(T_e - T_a) - L_e \qquad (12.8)$$

where $H_o = (I + 3/2\ k\ T_e)\ \alpha\ n^2 + P$ (12.9)

$H_1 = (I + 3/2\ k\ T_e)\ S\ n + P_1$ (12.10)

I = ionisation energy of atom in its ground state

α = C.R. recombination coefficient

S = C.R. ionisation coefficient

L_e = electron thermal conductivity loss rate.

Except for very dense plasmas, $H_1 . n(1)$ was shown to be negligible compared to H_o.

The energy balance equation corresponding to the ions was formulated as

$$\frac{3}{2} n k \frac{dT_i}{dt} = n^2 \eta_{ei}(T_e - T_i) - n\, n(1) \eta_{ia}(T_i - T_a) - \frac{3}{2} S\, n\, n(1) k (T_i - T_a) - L_i \qquad (12.11)$$

where L_i = rate of ionic thermal conductivity loss

similarly, the energy balance equation for the atoms was written as

$$\frac{3}{2} n(1)\ k \frac{dTa}{dt} = n\, n(1) \eta_{ea}(T_e - T_a) + n\, n(1) \eta_{ia}(T_i - T_a) + \frac{3}{2} k (T_i - T_a) \alpha n^2 - L_a \qquad (12.12)$$

where L_a = rate of atom thermal conductivity loss.

The assumptions made by Bates and Kingston in solving these equations are as follows:

1. The elastic energy transfer coefficients were found for

hydrogen and helium plasmas from the references (119) (121) (122) (123). Over the range of conditions encountered in decaying plasmas, the estimated error on the calculated coefficients was around 20%.

2. A magnetically confined plasma was considered so that the charged particle thermal conductivity loss was equated to zero.

$$\text{ie. } L_e = L_i = 0. \qquad (12.13)$$

The atom thermal conductivity loss rate was evaluated for a cylindrical plasma column where a plasma radius of 3 cm was taken as being representative of a typical laboratory plasma.

3. Consideration of the relaxation times of the electron and ion temperatures showed that providing

$$\frac{n}{n(1)} < \begin{cases} \frac{1}{3} & \text{optically thin plasma} \\ \frac{1}{10} & \text{optically thick plasma} \end{cases} \qquad (12.14)$$

Then the relaxation times for T_e and T_i were always much less than the relaxation times for n and n(1). This closely followed the proposal of Byron et al. described in section (12.1) and meant that the values of T_e and T_i were close to the quasi-equilibrium values obtained by putting dT_e/dt and dT_i/dt both equal to zero in equations (12.8) and (12.11). This assumption enormously simplified the solution of these equations.

4. Using their previously computed data (71) (72) (120) for α, S, P and P_1 in hydrogen plasmas, Bates and Kingston solved the quasi-equilibrium versions of equations (12.8) (12.11) and (12.12) by iteration using a computor to give T_e (n, n(1)) and hence α (n, n(1)). However, the very drastic assumption of setting

$$T_a = \text{constant} \qquad (12.15)$$

was used in order to facilitate the computation. Fixed values of

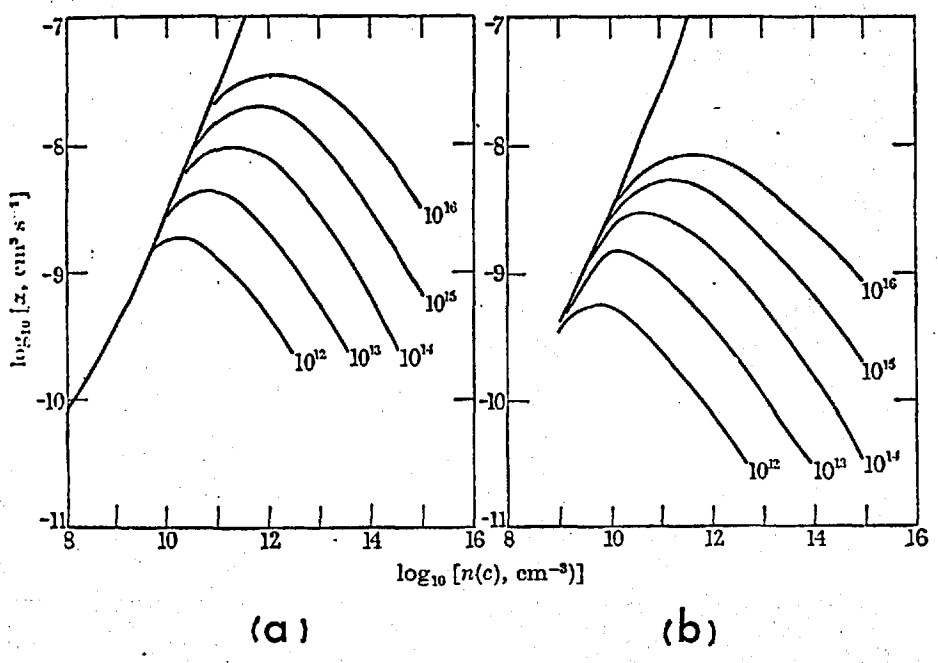

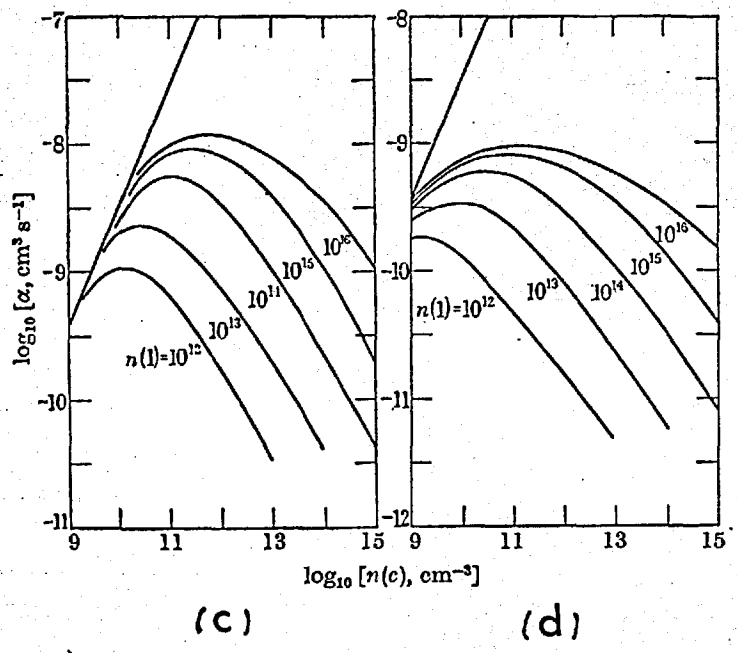

FIG (12.1) C.R. recombination coefficients in decaying plasmas with atom temperature held fixed at 250°K as found by Bates and Kingston.

(a) Optically thin hydrogen plasma.
(b) Optically thick hydrogen plasma.
(c) Optically thin helium plasma.
(d) Optically thick helium plasma.

The number density of normal atoms $n(1)$ is marked on each curve.

T_a = 250 ^oK, 1000 ^oK and 4000^oK were chosen in an attempt to cover as wide a range of plasma conditions as possible.

The results obtained for the variation of the recombination coefficient with electron density for fixed values of n(1) in optically thick and thin hydrogen and helium afterglows with atom temperature fixed at 250^oK have been reproduced in fig.(12.1)

(12.3) RANGE OF PLASMA CONDITIONS FOR WHICH BATES AND KINGSTON'S WORK IS VALID.

Bates and Kingston (74) have computed values of the electron density at which the atom temperature at the centre of the plasma rises 20% above fixed values of the wall temperature equal to 250^oK, 1000^oK and 4000^oK. This calculation was performed in an attempt to find the upper limit for electron density for which it is valid to assign a fixed value to the atom temperature in the decaying plasma. The results obtained are summarised in table (12.1) and they apply to both optically thin and thick plasma over a wide range of values of n(1).

TABLE (12.1)

FIXED WALL TEMPERATURE = T_w (^oK)	MAXIMUM VALUE OF ELECTRON DENSITY FOR $T_a \leqslant 1.2\ T_w$ (cm^{-3})
250	10^{12} - 12.5
1000	10^{13} - 13.5
4000	10^{14} - 14.5

For plasmas contained in discharge vessels having walls at room temperature ($300^{o}K$), table (12.1) shows that Bates and Kingston's solutions to the recombination-energy balance equations are only valid for electron densities $\leqslant 3 . 10^{12}$ cm^{-3}. A comparison made by Bates and Kingston between their computed recombination coefficients and the experimental results of Hinnov and Hirschberg (84) over the density range 10^{11} to $3 . 10^{13}$ cm^{-3} appears to confirm this upper limit to n. For $n \leqslant 3 . 10^{12}$ cm^{-3} good agreement was found between theory and experiment but going from $3 . 10^{12}$ to $3 . 10^{13}$ cm^{-3} the theoretical results showed an increasing trend towards overestimating the experimental results by nearly an order of magnitude at $3 . 10^{13}$ cm^{-3}.

At first sight, table (12.1) suggests that the interpolation of Bates and Kingston's calculations for fixed atom temperatures above $250^{o}K$ might enable the usefulness of their calculations to be extended to higher electron densities than $3 . 10^{12}$ cm^{-3}. This procedure is, however, in general not permissible, since the assumption of fixed atom temperature automatically means that

$$\frac{dT_a}{dt} = 0 \quad \text{in equation (12.12).}$$

Thus the interpolation procedure can only be used when the atom temperature is in a state of quasi-equilibrium: when the terms on the R.H.S. of equation (12.12) are very much greater than the term of the L.H.S. of the equation. An examination of the relaxation of atom temperature has been performed by Bates and Kingston (74) who have indicated that quasi-equilibrium values of T_a only exists for the conditions

$$\frac{n}{n(1)} > \begin{cases} \frac{1}{10} & \text{optically thin plasma} \\ \frac{1}{30} & \text{optically thick plasma} \end{cases} \qquad (12.16)$$

A comparison of the conditions (12.14) for quasi-equilibrium values of T_e and T_i with conditions (12.16) shows the very limited range of degrees of plasma ionisation over which T_e, T_i and T_a are all in a state of quasi-equilibrium.

From above, it can be seen that the approximation (12.15) inherent in Bates and Kingston's work limits the applicability of their solutions of energy balance to ranges of plasma densities which are well outside those encountered in our experiment, since our experimental ranges were

$$\left.\begin{aligned} 3\ 10^{12} < n < 3\ 10^{15} \quad cm^{-3} \\ 3\ 10^{14} < n(1) < 6\ 10^{16} \quad cm^{-3} \end{aligned}\right\} \qquad (12.17)$$

A further difficulty of using Bates and Kingstons work is the fact that their computations only apply to hydrogen and helium plasmas. We require a solution of the energy balance-recombination equations in neon, argon and krypton plasmas as well as the above two types of plasma.

Finally, it is apparent from our experimental measurements and from the theory of energy transport in a plasma discussed in Chapter 10, that the recombination rate of a decaying plasma varies quite strongly with the size of the plasma. Bates and Kingston assumed a discharge tube radius of 3 cm, and clearly an accurate comparison of their theory with experiment can only be made for experimental tube radii close to 3 cm. Whilst our experimental torus minor radii were close to this figure, being 2.20 and 3.55 cm, Bates and Kingston's computed solutions do not enable us to make separate theoretical comparison with experiment for either size of discharge tube.

(12.4) OUTLINE PROPOSALS FOR A NEW SET OF SOLUTIONS TO THE ENERGY BALANCE-RECOMBINATION EQUATIONS

We outline below the conditions which a general solution of

the energy balance-recombination equations in afterglow plasmas should satisfy.

1. The solutions should be valid at high electron densities especially in the region

$$10^{12} < n < 10^{16} \quad cm^{-3}$$

2. The solutions should be applicable to the full range of rare gas plasmas and not just to helium or hydrogen plasmas.

3. The energy balance equations must include, to the fullest extent, the effects of non-uniform distributions of the plasma parameters n, n(1), T_e, T_i and T_a throughout the plasma. This implies that the energy balance equations have to be formulated for the gradients of n, n(1), T_e, T_i and T_a that exist during plasma decay in a particular size of discharge tube. Also full account must be taken of the geometrical dependence of the physical processes occuring in decaying plasmas which affect the decay rate, such as the self absorption of radiation by the plasma and meta-stable atom diffusion.

4. The solutions of the equations should be derived in a form that can be most accurately compared with experimental data obtained from laboratory studies of plasma decays. This implies that the solutions are required in the form of either the recombination time τ_R, or the recombination coefficient α, expressed as a function of the parameters electron density, atom density, type of gas and radius of discharge tube.

(12.5) DETAILED PROPOSALS OF THE NEW THEORY

The main features of our approach to the conservation of energy in a decaying plasma satisfying the conditions 1 to 4 outlined in section (12.4) above are as follows:

1. The equations (12.8) (12.11) and (12.12) describing the rates of change of electron, ion and atom temperatures are taken as the starting point of the theory.

2. The plasma decay is assumed to be dominated by three body recombination and the recombination coefficient α is taken to be of the form given by equation (9.26)

ie $$\alpha = C\, n\, (T_e)^{-4.5}$$

where $C = 3.9 \quad 10^{-9}$ (n cm^{-3}, T_e ^{o}K)

Equation (9.26) is assumed to apply to all types of plasmas and justification for adopting this simple analytical expression has been given by D'Angelo (82).

3. Terms incolving the collisional ionisation coefficient S in equations (12.8) (12.11) and (12.12) are assumed to be negligible in comparison to the other terms. This is in agreement with Bates et al. (71)(72) numerical evaluation of S for a hydrogen plasma for the situation where

$$n \lesssim 10^{16} \quad \text{cm}^{-3}$$

In our experiment, the highest value of average electron density measured was $\leq 10^{16}$ cm^{-3}.

4. A comparison of atomic and plasma (Lorentz gas) coefficients of thermal conductivity has been given in Appendix (A.3), from which it can be seen that in afterglow plasmas

Atom thermal conductivity loss rate $\gg$ Plasma thermal conductivity loss rate

$$\therefore L_a \gg L_e \text{ or } L_i \qquad (12.18)$$

where inequality (12.18) applies to non-magnetically confined plasmas.

5. It is assumed that the plasma is nearly fully ionised initially, and that the plasma decay has proceeded to a situation

corresponding to inequality (12.14) where both the electron. and ion temperatures are in a state of quasi-equilibrium. A quasi-equilibrium or a fixed value for atom temperature is NOT assumed.

6. The factor q is introduced into equation (12.8) in order to replace H_o and H_1 where q is defined by

$$q = \frac{\text{Energy transferred to the plasma electrons per ion recombined}}{\text{Ionisation energy of the atom}} \qquad (12.19)$$

The factor q has to take into account all the physical processes leading to feed-back of the recombination energy and kinetic energy of the recombining particles to the plasma electrons, including electron collisions with metastable atoms and terms involving the self absorption of radiation by the plasma. Thus, in general, q is a very complex function of the plasma parameters n, n(1), T_e, T_a and the plasma geometry. A detailed discussion of the variation of q with these plasma parameters is given in the next chapter, where it is shown that q can vary between the limits

$q \sim 1.0$ for a high density, optically thick plasma (12.20)

to $q \sim \frac{5kT_e}{2I}$ for a low density, optically thin plasma (12.21)

The upper limited (1220) corresponds to most of the recombination energy being retained within the plasma, whilst the lower limit (12.21) corresponds to only a small fraction ($\sim$ 0.1) of the recombination energy being retained within the plasma.

Combining the features outlined above, equations (12.8) (12.11) and (12.12) can be re-written as follows.

Electron equation.

$$0 = q\,I\,\alpha\,n^2 - n^2\eta_{ei}(T_e-T_i) - n\,n(1)\eta_{ea}(T_e-T_a) - L_e \qquad (12.22)$$

Ion equation

$$0 = n^2\eta_{ei}(T_e-T_i) - n\,n(1)\eta_{ia}(T_i-T_a) - L_i \qquad (12.23)$$

Atom equation

$$\frac{3}{2}\,n(1)\,k\,\frac{dT_a}{dt} = n\,n(1)\eta_{ea}(T_e-T_a) + n\,n(1)\eta_{ia}(T_i-T_a) - L_a \qquad (12.24)$$

Adding equations (12.22) (12.23) and (12.24) and using inequality (12.18) we obtain

$$\frac{3}{2}\,n(1)\,k\,\frac{dT_a}{dt} = q\,I\,\alpha\,n^2 - L_a \qquad (12.25)$$

From equation (12.25) and inequality (12.18) it can be seen that for a wide range of conditions the terms L_e and L_i in equations (12.22) and (12.23) are small compared to the other terms and hence from (12.23) we can write

$$(T_e - T_i) = \frac{n(1)\ \eta_{ia}}{n\eta_{ei} + n(1)\eta_{ia}}\ (T_e - T_a) \qquad (12.26)$$

which on substitution into (12.22) gives

$$q\,I\,\alpha\,n = \left[\frac{n\,n(1)\ \eta_{ei}\,\eta_{ia}}{n\eta_{ei} + n(1)\eta_{ia}} + n(1)\eta_{ea}\right].\ (T_e - T_a) \qquad (12.27)$$

In deriving equations (12.25) and (12.27) we have ignored any spatial variation of n, n(1), T_e and T_a inside the plasma: these equations are strictly applicable only to infinite plasmas. We will now modify the equations above to take into account the spatial variation of n, n(1), T_e and T_a discussed in Chapter 10.

Comparison of equation (12.25) with equation (10.10) shows that the former is simply the energy transport equation written for a uniform plasma. The extension of equation (12.25) to include the case of non-uniform plasmas is therefore very straight forward. According to the work presented in section (10.1), the first order approximation density and temperature distribution profiles associated with non-uniform plasma decay are

$$\begin{aligned} n &= n_o \left(1 - (r/a)^2 \right) \\ T_e &= T_{eo} \left(1 - (r/a)^2 \right)^{\frac{1}{2}} \\ n(1) &= n(1)_o \left(1 - (r/a)^2 \right)^{-\frac{1}{2}} \end{aligned} \qquad (12.28)$$

and the energy transport equation for a plasma with the above distribution profiles can be written from (10.22) and (10.40) as

$$q\, I\, \alpha . n_o^2 - \frac{3}{4}\, \overline{n(1)}\, k \frac{d\, T_{ao}}{dt} = \frac{2K}{a^2} \left(T_{ao}^2 - T_w^2 \right) \qquad (12.29)$$

where equation (12.29) expresses the relationship between the AXIAL values of electron density and atom temperature and the AVERAGE value of atom density in a non-uniform plasma contained in a cylindrical vessel of radius a and of fixed wall temperature T_w.

Equation (12.27) can be re-written to express the relationship between the axial values of electron and atom temperatures in a non-uniform cylindrically symmetric plasma as

$$T_{eo} - T_{ao} = \frac{q\, I\, \alpha . n_o}{\dfrac{n_o\, \overline{n(1)}\, \eta_{ei}\, \eta_{ia}}{2\, n_o\, \eta_{ei} + \overline{n(1)}\, \eta_{ia}} + \dfrac{\overline{n(1)}\, \eta_{ea}}{2}} \qquad (12.30)$$

Similarly we can write the expression for the recombination coefficient $\alpha .$ existing in the plasma as

$$\alpha . = C\, n_o\, (T_{eo})^{-4.5} \qquad (12.31)$$

For a particular type of gas, expressions for the elastic energy rate transfer coefficients can be substituted into equation (12.30) and the radius of the cylindrical vessel can be substituted into equation (12.29), substitution of equation (12.31) into equations (12.29) and (12.30) therefore yields two equations linking the five plasma parameters n_o, $\overline{n(1)}$, T_{eo}, T_{ao} and q and hence we can solve for axial and atom temperatures in the form

$$\begin{aligned} T_{eo} &= T_{eo}\ (n_o, \overline{n(1)},\ q\ ) \\ T_{ao} &= T_{ao}\ (n_o, \overline{n(1)},\ q\ ) \end{aligned} \qquad (12.32)$$

and from equation (12.31) we can then express the plasma recombination coefficient or the plasma decay time $\tau_R = (\alpha\ n_o)^{-1}$ as

$$\alpha = \alpha\ (q,\ n_o,\ \overline{n(1)}\ ) \qquad (12.33)$$

$$\tau_R = \tau_R (q,\ n_o,\ \overline{n(1)}\ ) \qquad (12.34)$$

We note that the method of solving the energy balance equations as described above, enables us to calculate (to a first order approximation) the plasma recombination decay time existing THROUGHOUT the interior of a NON-UNIFORM cylindrical decaying plasma in terms of the variables q, n_o and $\overline{n(1)}$. The last two variables are easily measured experimentally from the interferometer output and the initial gas filling pressure respectively, and so, in cases where q can be reliably estimated (eg. optically thick or optically thin limits (12.20) and (12.21), an immediate comparison can be made between the experimentally measured recombination time $\tau_R(n_o, \overline{n(1)}\ )$ and the theoretical value given by (12.34). In cases where the value of q is intermediate between limits (12.20) and (12.21), an additional calculation of q has to be performed before the theoretical decay

time can be compared with the experimental decay time. The comparison of theory and experiment is discussed in detail in the next chapter.

(12.6) THE ELASTIC ENERGY TRANSFER COEFFICIENTS

Expressions for the elastic energy transfer coefficients η_{ei}, η_{ia} and η_{ea} are given in Appendices (A.4) (A.5) and (A.6). The forms of the quantities differ from those adopted by Bates and Kingston (74)(75) and the values of η_{ea} are based on more recent information (124).

For the case of the rare gases He, Ne, A and Kr it can be seen from (A.4), (A.5) and (A.6) that numerically

$$n(1)\eta_{ea} \ll \begin{cases} n\eta_{ei} & \text{when } n\eta_{ei} < n(1)\eta_{ia} \\ n(1)\eta_{ia} & \text{when } n\eta_{ei} > n(1)\eta_{ia} \end{cases} \qquad (12.35)$$

$$\text{subject to } \frac{n}{n(1)} \geqslant \begin{cases} 10^{-4} & \text{for } T_e < 10{,}000^{\circ}K \\ 10^{-5} & \text{for } T_e < 1{,}000^{\circ}K \end{cases} \qquad (12.36)$$

We are mainly concerned with the study of plasma decay for degrees of ionisation $> 10^{-5}$ (molecular ion formation is likely to dominate C.R. recombination for lower degrees of ionisation) and within this limit, the conditions prevailing in afterglow plasmas easily satisfy (12.36). From (12.35), it can be seen that the term $\overline{n(1)\eta_{ea}}$ makes a negligible contribution to equation (12.30) and the latter can be re-written as

$$T_{eo} - T_{ao} = q\,I\,\alpha\,n_o \left[\frac{2}{n(1)\,\eta_{ia}} + \frac{1}{n_o\,\eta_{ei}} \right] \qquad (12.37)$$

In physical terms, expression (12.35) shows that, for the rare gases, the elastic energy transferred by direct collisions between electrons and atoms is negligible compared to that transferred between electrons and atoms via intermediate collisions of each particle species with the ions. From Appendices (A.4) and (A.5) it can be seen that for the conditions in afterglow plasmas,

$$\eta_{ei} \simeq (\text{order of magnitude}) \times \eta_{ia} \qquad (12.38)$$

Hence, for the initial highly ionised stages of plasma decay where $n_o \sim \overline{n(1)}$, the term $\overline{n(1)}\,\eta_{ia}$ dominates equation (12.37) which corresponds to the ion temperature being much closer to T_e than to T_a. At later stages of plasma decay where $n_o \ll \overline{n(1)}$, the term $n_o \eta_{ei}$ dominates equation (12.37) corresponding to the ion temperature being much closer to T_a than to T_e.

Equation (12.37) is only valid for conditions (12.36) for the rare gases and is NOT valid for hydrogen in weakly ionised plasma since from Appendix (A.6)

$$\eta_{ea}\,(\text{hydrogen}) \sim (2 \text{ to } 3 \text{ orders of magnitude})\,\eta_{ea}\,(\text{rare gas}) \qquad (12.39)$$

so that for degrees of ionisation $< 10^{-3}$ direct elastic energy transfer between electrons and atoms plays a significant part in the total elastic energy transfer in hydrogen plasmas.

(12.7) ANALYTICAL SOLUTIONS TO THE CONSERVATION OF ENERGY EQUATIONS

The energy balance - recombination equations proposed in

section (12.5) are capable of being solved analytically for certain limiting cases of afterglow plasma parameters. For convenience, we will describe the relationship between electron and atom temperatures by the equation

$$T_a = f\ T_e \qquad (12.40)$$

where in general the factor f is a function of n, n(1), T_e and T_a.

Using this factor f, the energy transport equation (12.29) can be re-written as

$$q\ I\ \alpha\ n_o^2 - \frac{3}{4}\ \overline{n(1)}\ k\ \frac{d}{dt}\ (f\ T_{eo}) = \frac{2K}{a^2}\ f^2\ T_{eo}^2 \qquad (12.41)$$

where it is assumed $T_{eo} > 2\ T_w$.

We will now solve equation (12.41) for the two limiting conditions that correspond to either term on the L.H.S. of the equation being dominant over the other term.

(12.7.1) Quasi-Equilibrium Approximation

The quasi-equilibrium (Q.E.) approximation corresponds to the situation where

$$q\ I\ \alpha\ n_o^2 \gg \frac{3}{4}\ \overline{n(1)}\ k\ \frac{d}{dt}\ (f\ T_{eo}) \qquad (12.42)$$

In this case, the atom temperature is in a state of quasi-equilibrium, and since, for the values of electron temperatures typical of afterglow plasmas

$$I \sim 20\ k\ T_{eo} \qquad (12.43)$$

condition (12.42) should apply to the initial stages of optically thick plasma decay where

$$n_o \geq \frac{\overline{n(1)}}{40} \qquad (12.44)$$

Combining equations (12.41) and (12.31) for the Q.E. approximation, we obtain

$$q\ I\ C\ n_o^3 = \frac{2K}{a^2} f^2\ T_{eo}^{6.5} \qquad (12.45)$$

and the analytical expressions for axial electron temperature and recombination decay time in the Q.E. region are therefore

$$T_{eoQE} = \left[\frac{q\ I\ C\ a^2}{2\ K\ f^2}\right]^{2/13} \left[n_o\right]^{6/13} \qquad (12.46)$$

$$\tau_{RQE} = \left[\frac{q\ I\ a^2}{2\ K}\right]^{9/13} \frac{\left[n_o\right]^{1/13}}{\left[C\right]^{4/13}\left[f\right]^{18/13}} \qquad (12.47)$$

From equations (12.46) and (12.47) it can be seen that the electron temperature in the Q.E. region depends only slightly on the quantities q and f and is dominated by the value of n_o, whilst the plasma recombination time shows a negligible direct dependence upon n_o and only varies with changing n_o through the dependence of the quantities q and f upon n_o. At high electron densities where

$$n_o \geq 5\ 10^{14}\ cm^{-3} \qquad (12.48)$$

we would expect the plasma to be optically thick and the electron and atom temperatures to be closely coupled so that both q and f would be close to unity. For this case, equation (12.47) predicts that the recombination time is virtually independent of changing n_o and that consequently a plot of ln (electron density) would vary linearly with time. This prediction agrees well with the experimental decay plots of electron density, at high values of density, shown in figs. (11.4) to (11.14).

In table (12.2), the values of plasma recombination times obtained from equation (12.47) for f and q equal to unity and n_o equal to 10^{15} cm^{-3} have been listed for hydrogen and the rare gases in each size of torus. Values of the plasma recombination times obtained from the gradients of the p/τ versus p plots , for electron density = 10^{15} cm^{-3} (shown in figs. 11.17 to 11.27), have also been listed in table (12.2). The agreement between theory and experiment in the high density Q.E. limiting case can be seen to be quite good.

TABLE (12.2)

GAS	TORUS MINOR RADIUS (cm)	PLASMA RECOMBINATION TIME FROM EQN.(12.47) $n = 10^{15}$ cm^{-3} (μ. sec.)	PLASMA RECOMBINATION TIME (EXPERIMENTAL) $n = 10^{15}$ cm^{-3} (μ. sec.)
H	3.55	62	40
H	2.20	33	27
He	3.55	106	106
He	2.20	55	75
Ne	3.55	214	220
Ne	2.20	114	115
A	3.55	325	440
A	2.20	172	250
Kr	3.55	510	650
Kr	2.20	265	440

(12.7.2) Atomic Latent Heat Approximation

The atomic latent heat approximation (L.H.) corresponds to the situation where

$$q\,I \alpha n_o^2 \ll -\frac{3}{4}\,\overline{n(1)}\,k\,\frac{d}{dt}\,(f\,T_{eo}) \qquad (12.49)$$

Physically, inequality (12.49) is satisfied when the rate of energy being retained within the plasma due to electron-ion recombination is negligible compared to the rate of change of thermal energy of the atoms. This situation is analagous to the decay of atomic latent heat in a non-ionised gas with no heating mechanisms present. In afterglow plasmas, inequality (12.49) applies to the late stages of high atom density decay, and it is more easily satisfied when the plasma is optically thin. The energy transport equation (12.29) in the L.H. region is written as

$$-\frac{3}{4}\,\overline{n(1)}\,k\,\frac{d}{dt}\,(f\,T_{eo}) = \frac{2K}{a^2}\,f^2\,T_{eo}^{\,2} \qquad (12.50)$$

we will assume that T_e changes more rapidly with time than the quantity f so that

$$f\,\frac{dT_{eo}}{dt} \gg T_{eo}\,\frac{df}{dt} \qquad (12.51)$$

The validity of assumption (12.51) is examined later in section (12.8). Using (12.51) we can write

$$\frac{d}{dt}\,(f\,T_{eo}) \approx f\,.\,\frac{dT_{eo}}{dn_o}\,.\,\frac{dn_o}{dt} = -f\,C\,n_o^{\,3}\,(T_{eo})^{-4.5}\,\frac{dT_{eo}}{dn_o}$$

so that equation (12.50) becomes

$$\frac{3\,\overline{n(1)}\,k\,a^2\,C}{8\,K\,f}\;\frac{dT_{eo}}{dn_o} = \frac{(T_{eo})^{6.5}}{(n_o)^3} \qquad (12.52)$$

Integrating (12.52) (with f outside the integral) we obtain

$$\frac{2}{11}\,(T_{eo})^{-5.5} = \frac{4\,K\,f}{3\,\overline{n(1)}\,k\,a^2\,C\,n_o^2} + \text{constant} \qquad (12.53)$$

The constant of integration depends upon the boundary conditions existing at the start of the L.H. region. By considering the transition region between the initial Q.E. region and the later L.H. region which is defined by the equation

$$q\,I\,\alpha\,n_o^2 = -\frac{3}{4}\,\overline{n(1)}\,k\,\frac{d}{dt}\,(f\,T_{eo}) \qquad (12.54)$$

the constant of integration in equation (12.53) can be shown to be

$$\text{integration constant} = \frac{-3\,K\,f}{22\,(n_o^*)^2\,\overline{n(1)}\,k\,a^2\,C} \qquad (12.55)$$

where n_o^* is the value of n_o satisfying equation (12.54). From substitution of the integration constant (12.55) into (12.53), it can be seen that when

$$n_o \ll n_o^*$$

the value of the integration constant makes a negligible contribution to (12.53) so that the electron temperature and plasma recombination decay times well inside the L.H. region are given by the analytical expressions

$$T_{eoLH} = \left[\frac{3\,\overline{n(1)}\,k\,a^2\,C}{22\,K\,f}\right]^{2/11}\left[n_o\right]^{4/11} \qquad (12.56)$$

$$\tau_{RLH} = \frac{3\,\overline{n(1)}\,k\,a^2}{22\,K\,f\,T_{eo}} \qquad (12.57)$$

From equations (12.57) (12.56) and (12.40) we can write

$$\frac{\overline{n(1)}}{\tau_{RLH}} = \text{constant} \times \left[\overline{n(1)}\right]^{2/11} \left[f\right]^{9/11} \left[n_o\right]^{4/11} \qquad (12.58)$$

The average atom density $\overline{n(1)}$ is directly proportional to the gas filling pressure p for the degrees of ionisation associated with the L.H. region, and therefore from (12.58), the quantity p/τ, for fixed values of n_o can be seen to depend almost entirely on the quantity f. In section (12.8) it is shown that f can be a very slowly varying function with changing plasma conditions. Hence for the L.H. region, we would typically expect the value of p/τ, at a fixed value of electron density, to be a constant, to a first approximation, independent of the plasma conditions. This is in excellent agreement with the experimental plots of p/τ versus p shown in figs. (11.17) to (11.27), where, at the high gas pressures and low electron densities appropriate to L.H. decay region conditions, the quantity p/τ appears to assymptotically approach fixed values.

(12.8) ATOM TEMPERATURE DECAY TIMES IN AFTERGLOW PLASMAS

Above, we have derived analytical expressions for the axial electron temperature and plasma recombination time that can be applied in the Q.E. and L.H. regions. We would expect the decay of high density, highly ionised plasma to start in the Q.E. region and pass, with falling degree of ionisation, into the L.H. region.

Equations (12.46) and (12.40) show that providing the decay times for the quantities f and q in the Q.E. region are both much longer than the electron density decay time, then the decay time for atom temperature in the Q.E. region = τ_{TQE} bears a fixed relationship with the electron density recombination time given by

$$\tau_{TQE} = 2.166 \ \tau_{RQE} \qquad (12.59)$$

The decay time for atom temperature in the L.H. region = τ_{TLH} can be obtained directly from equation (12.50) as

$$\tau_{TLH} = \frac{3 \overline{n(1)} \ k \ a^2}{8 \ K \ T_{ao}} \qquad (12.60)$$

However, by assuming that the decay time for f is much greater than that for electron density, we have shown in section (12.7.2) that the plasma recombination time can be written according to equation (12.57). Comparison of (12.60) with (12.57) shows that in the L.H. region

$$\tau_{TLH} = 2.75 \ \tau_{RLH} \qquad (12.61)$$

It is apparent from equations (12.59) and (12.61) that the atom temperature decay time bears nearly the same fixed relationship with the electron density recombination time in both the Q.E. and L.H. plasma regions. We therefore propose that we can take the equation (12.62)

$$\tau_T = 2.5 \ (\pm 0.3) \tau_R \qquad (12.62)$$

as expressing the relationship between atom temperature decay time τ_T and recombination time τ_R throughout the whole of the plasma decay period subject to the following two conditions being satisfied:

1. The decay times for both the quantities q and f must be greater than the electron density decay time .

2. The atom temperature, at the plasma axis, must be greater than twice the wall temperature of the containing tube. This condition is implicit in dropping the term involving T_w from the energy transport equation in (12.41).

By adopting equation (12.62) we can make an enormous simplification to the method of solving the energy transport equation (12.29). Since the time differential term involving atom temperature can be replaced by a term involving density decay time

ie. $\frac{dT_{ao}}{dt}$ can be replaced by $\frac{T_{ao}}{2.5\tau_R}$ or $\frac{T_{ao}\ \alpha\ n_o}{2.5}$ (12.63)

The conditions 1 and 2 above, which enable the approximation (12.63) to be made will now be examined.

The quantity q is a complex plasma parameter for which no simple analytical expression is available. However, according to theory presented in section(13.5)of the next chapter, we can place upper and lower limits on q given by

$$1.0 \leqslant q \leqslant \frac{5\ k\ T_{eo}}{2\ I} \qquad (12.64)$$

For the conditions encountered in high density afterglow plasmas, we would expect q to change from 1.0 to around 0.1 for changes in the degree of ionisation of the plasma from 0.3 to around 10^{-4}. Thus the decay time of the factor q is unlikely to be less than the electron density decay time.

The factor f can be easily related to the electron density for rare gas plasmas using equation (12.37) which can be

re-written as

$$1 - f = \frac{q\,I}{\tau_R\, T_{eo}} \left[\frac{1}{n_o \eta_{ei}} + \frac{2}{\overline{n(1)}\,\eta_{ia}} \right] \qquad (12.65)$$

Substitution of the forms of η_{ei} and η_{ia} given in Appendices (A.4) and (A.5) together with values of T_{eo} and τ_R from equations (12.46) and (12.47) for the Q.E. region, and from equations (12.56) and (12.57) for the L.H. region yields the following

Q.E. region $$1 - f = \frac{Y\,(\overline{n\,(1)},\, q,\, T_e)}{n_o}\, f^{4/3} \qquad (12.66)$$

L.H. region $$1 - f = \frac{Z\,(\overline{n(1)},\, q,\, T_e)}{n_o}\, f^{3/4} \qquad (12.67)$$

where Y and Z are slowly varying functions.

Inspection of equations (12.66) and (12.67) shows that the decay time of the quantity $f = \tau_f$ depends upon the actual value of f. When f is large (near its maximum value of unity) $\tau_f \gg \tau_R$. When f is small, < 0.1, then $\tau_f \sim \tau_R$. By imposing a lower limit on the value of f around 0.3 we will always ensure that $\tau_f > \tau_R$.

Summarising, the two necessary conditions for the approximation (12.63) to be valid are

$$\left.\begin{aligned} T_{ao} &\geqslant 0.3\, T_{eo} \\ T_{ao} &\geqslant 2\, T_w \end{aligned}\right\} \qquad (12.68)$$

where $T_w = 300^{\circ}K$.

(12.9) COMPUTER SOLUTION OF ENERGY EQUATIONS IN HIGH DENSITY PLASMAS

The conditions (12.68) given above will only be satisfied in high density plasma afterglows where atom temperatures elevated above the wall temperature and close coupling of the electron and atom temperatures is predicted. This high density region satisfying (12.68) is the region which corresponds to most of our experimental results and it is certainly the region where the previous solutions (74)(75) to the energy balance-recombination equations are not valid.

The equations to be solved are (12.29), (12.30) or (12.37) and (12.31). In fact, equation (12.37) is used in preference to (12.30) for mathematical convenience. This choice places no limit on the accuracy of the results for rare gas plasma decays but it means that solutions for hydrogen are only valid for degrees of ionisation $> 10^{-2}$. For this reason, attention will be concentrated on rare gas plasmas henceforth. The elastic energy rate transfer coefficients as worked out in Appendices (A.4) and (A.5) have been shown to have the approximate forms

$$\eta_{ei} \simeq \frac{X_{ei}}{T_e^{3/2}} \quad \text{and} \quad \eta_{ia} \simeq X_{ia}$$

where X_{ei} and X_{ia} are constants for a particular type of gas as given by tables (A.4.3) and (A.5.2.) respectively. The approximation (12.63) is used in equation (12.29) and so the set of simultaneous equations expressing the energy balance and recombination are formulated from (12.29) (12.37) and (12.31) as

$$\left.\begin{aligned} (q\,I\,n_o + 0.30\,\overline{n(1)}\,k\,T_{ao})\,\alpha\,n_o &= \frac{2\,K\,T_{ao}^{\,2}}{a^2} \\ T_{eo} &= T_{ao} + q\,I\,\alpha\,n_o\left[\frac{T_{eo}^{\,1.5}}{n_o\,X_{ei}} + \frac{2}{\overline{n(1)}\,X_{ia}}\right] \\ \alpha &= C\,n_o\,T_{eo}^{\,-4.5} \end{aligned}\right\} \quad (12.69)$$

These simultaneous equations were solved by an iteration process on an IBM 1130 computer to provide two sets of results: the first set of results described in section (12.9.1) are concerned with defining the boundary line between the Q.E. and A.H. regions and the evaluation of the plasma parameters at this boundary. The second set of results described in section (12.9.2) are concerned with evaluating the plasma parameters T_{eo}, T_{ao}, f, and τ_R over a wide region of plasma decays defined by ranges of the parameters q, n_o and $\overline{n(1)}$.

(12.9.1) Computer Solution for Boundary between Q.E. and A.H. Plasma Regions

The plasma parameters associated with the boundary between the Q.E. region defined by (12.42) and the L.H. region defined by (12.49) have been computed so that a comparison can be made with the experimentally based plots of p/τ versus p given in figs. (11.17) to (11.27). These experimental plots show that there appears to be a fixed value of pressure or $\overline{n(1)}$ associated with the change from a straight line relationship to a curved relationship between P/τ and p at each fixed value of electron density. The straight line relationship occuring at high degrees of ionisation has been associated with the Q.E.

conditions as described in section (12.7.1). The non-linear relationship has been associated with the L.H. conditions as described in section (12.7.2). Thus, the plasma parameters associated with the boundary between the Q.E. and L.H. regions, should be identical to those associated with the transition from a linear to a non-linear relationship between P/τ and p.

The equation which defines the boundary between the Q.E. and L.H. regions is

$$q\, I\, \alpha\, n_o^2 = \frac{3}{4}\, \overline{n(1)}\, k\, \frac{d}{dt}\, T_{ao} \qquad (12.70)$$

which for the high density approximation (12.63) becomes

$$q\, I\, n_o = 0.30\, \overline{n(1)}\, k\, T_{ao} \qquad (12.71)$$

and so the plasma parameters associated with the boundary are found from the solution of (12.71) with the set of equations (12.69). We have three independent equations linking the five plasma variables q, n_o, $\overline{n(1)}$, T_{eo} and T_{ao}.

In solving these equations, it was found that for a given value of q, a boundary solution could only be obtained by having $\overline{n(1)}$ greater than some specific minimum quantity. These minimum values of $\overline{n(1)}$ were computed as a function of q, type of gas and radius of discharge tube and they are listed in table (12.3). The values listed in table (12.3), represent the lower limits on $\overline{n(1)}$ for the plasma decay to ever reach the boundary defined by equation (12.71). For values of $\overline{n(1)}$ less than those given in table (12.3), the plasma decay always lies in the Q.E. region for all values of electron density.

TABLE (12.3)

MINIMUM VALUES OF $\overline{n(1)}$ SATISFYING EQUATION (12.71)

TYPE OF GAS.	DISCHARGE TUBE RADIUS (cm)	q		
		1.0	0.4	0.1
H	2.20	$3.23\ 10^{15}$	$1.20\ 10^{15}$	$2.58\ 10^{14}$
H	3.55	$1.95\ 10^{15}$	$7.06\ 10^{14}$	$1.56\ 10^{14}$
He	2.20	$1.44\ 10^{16}$	$5.60\ 10^{15}$	$1.14\ 10^{15}$
He	3.55	$8.46\ 10^{15}$	$3.05\ 10^{15}$	$7.54\ 10^{14}$
Ne	2.20	$1.89\ 10^{16}$	$6.84\ 10^{15}$	$1.46\ 10^{15}$
Ne	3.55	$1.12\ 10^{16}$	$4.02\ 10^{15}$	$8.62\ 10^{14}$
A	2.20	$1.28\ 10^{16}$	$4.62\ 10^{15}$	$9.92\ 10^{14}$
A	3.55	$7.54\ 10^{15}$	$2.72\ 10^{15}$	$5.84\ 10^{14}$
Kr	2.20	$1.28\ 10^{16}$	$4.64\ 10^{15}$	$9.94\ 10^{14}$
Kr	3.55	$7.55\ 10^{15}$	$2.73\ 10^{15}$	$5.85\ 10^{14}$

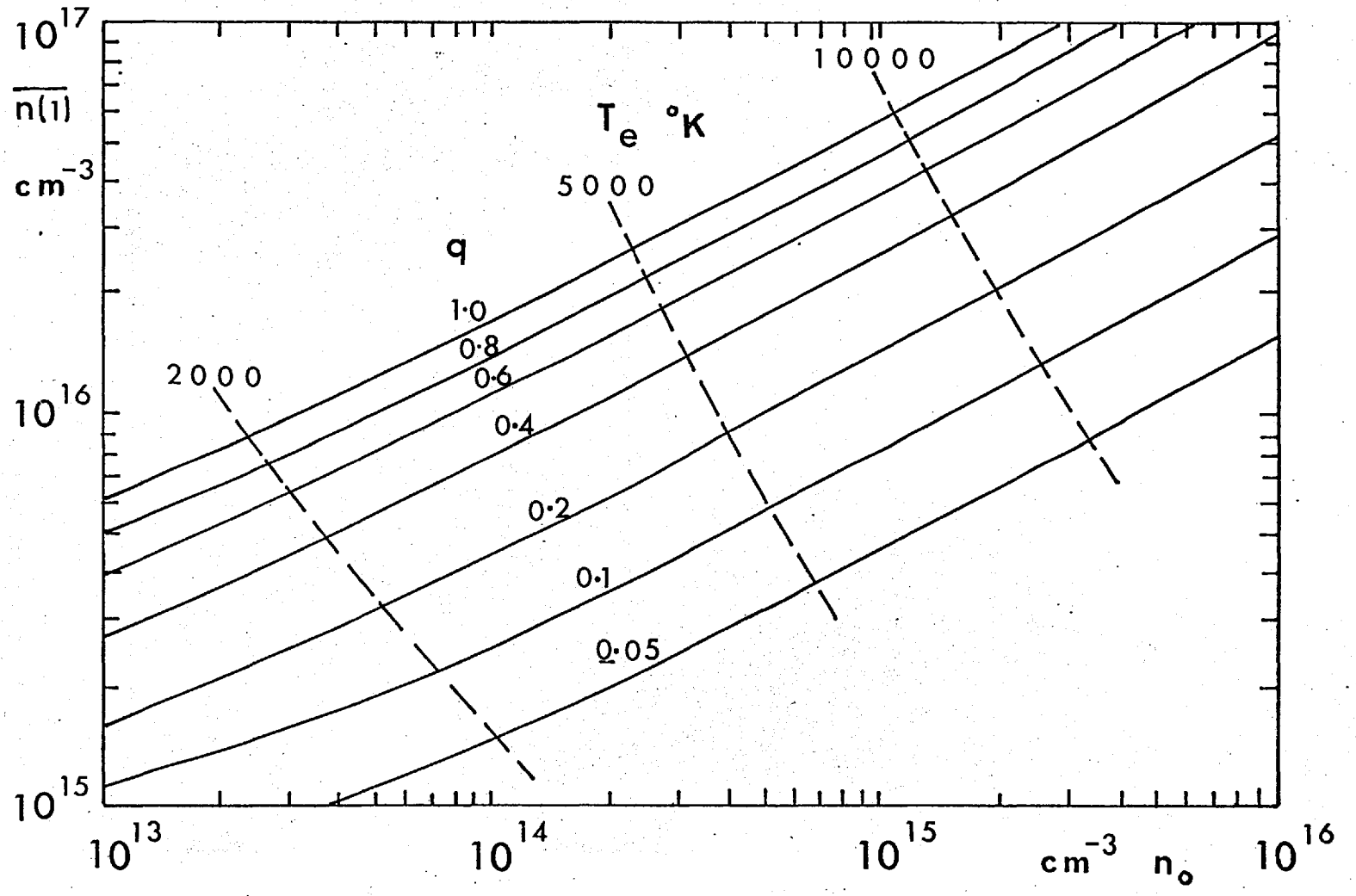

FIG (12.2) Q.E. - L.H. boundary parameters in large torus hydrogen plasmas.

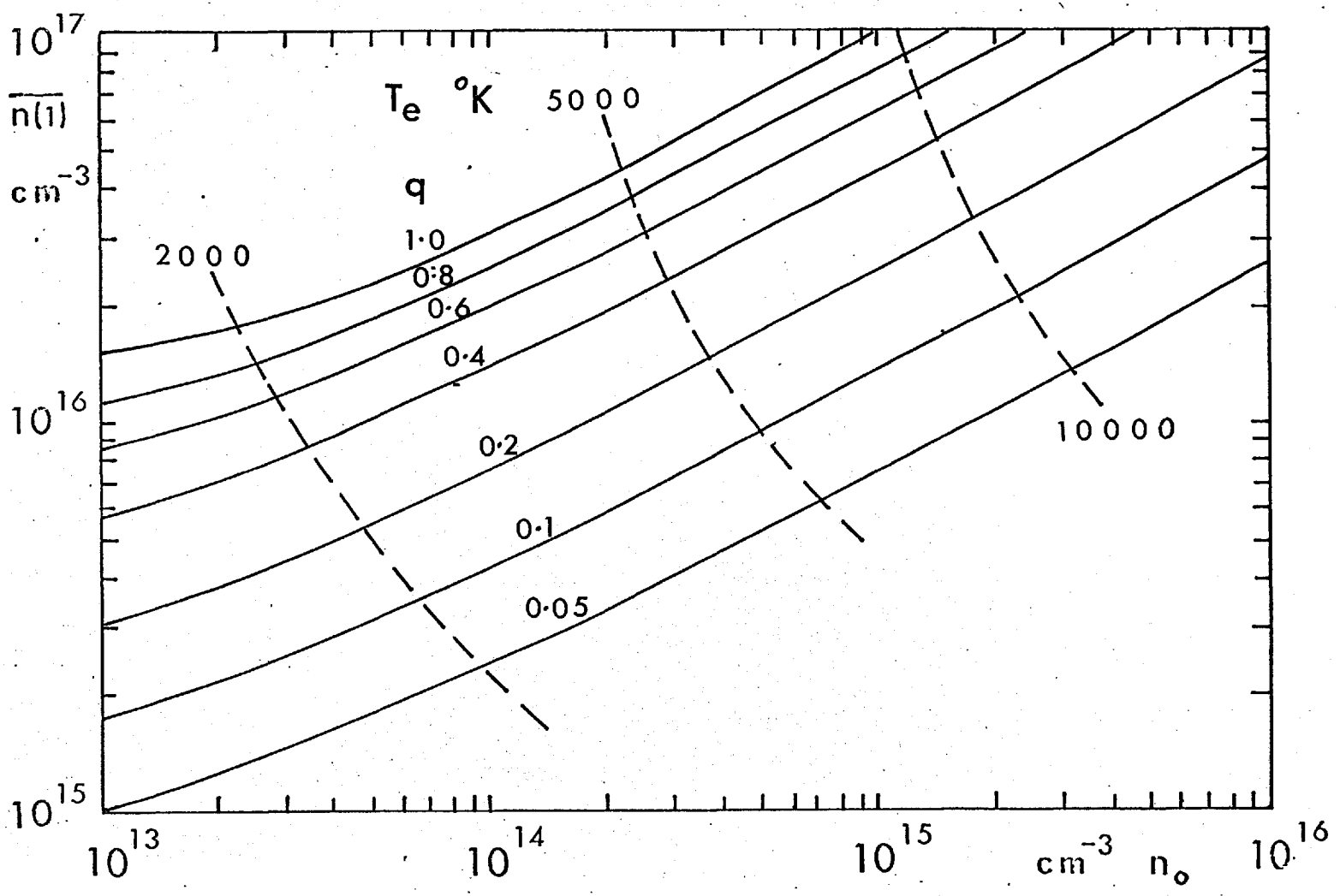

FIG (12.3) Q.E. - L.H. boundary parameters in large torus helium plasmas.

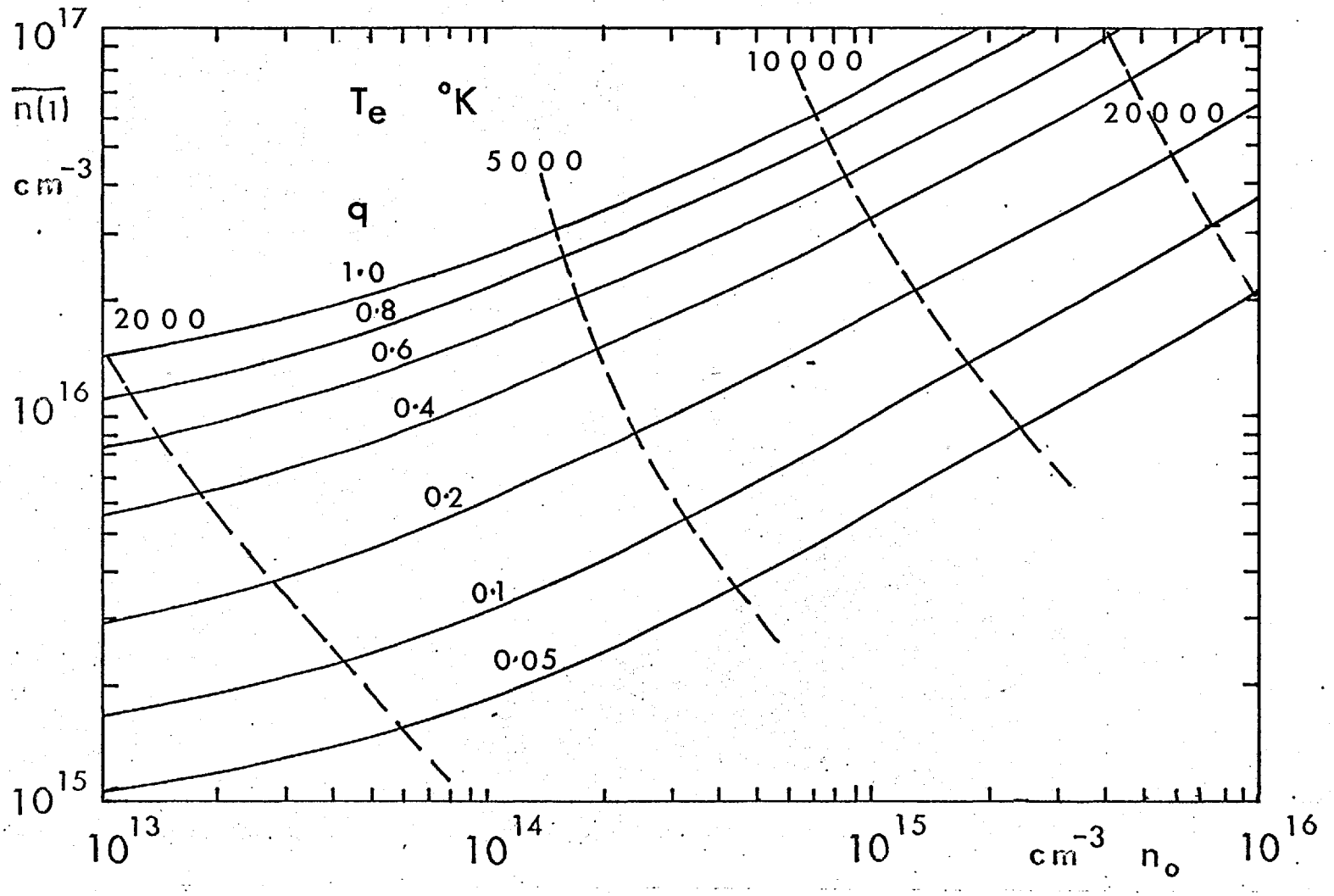

FIG (12.4) Q.E. - L.H. boundary parameters in large torus neon plasmas.

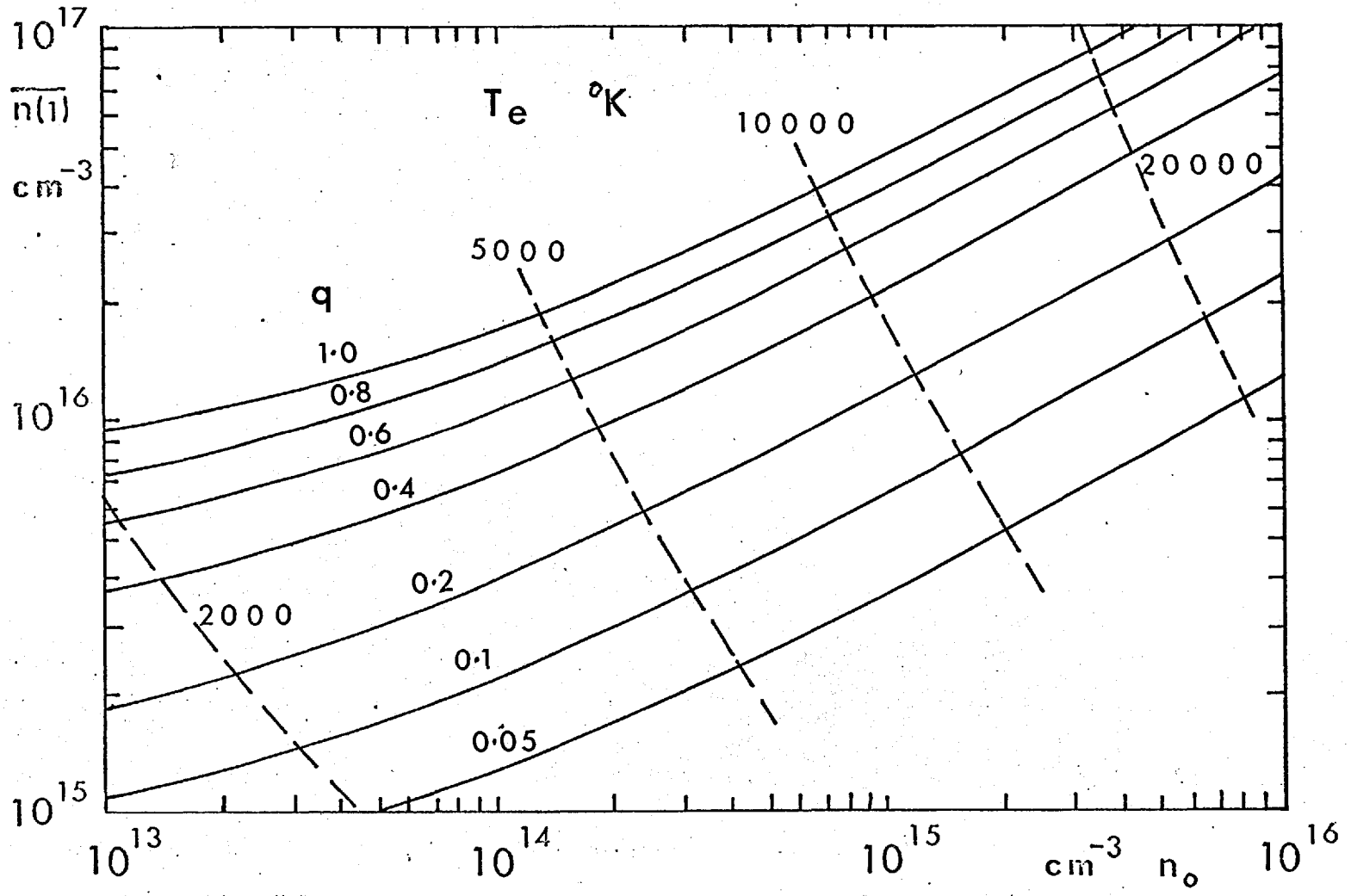

FIG (12.5) Q.E. - L.H. boundary parameters in large torus argon plasmas.

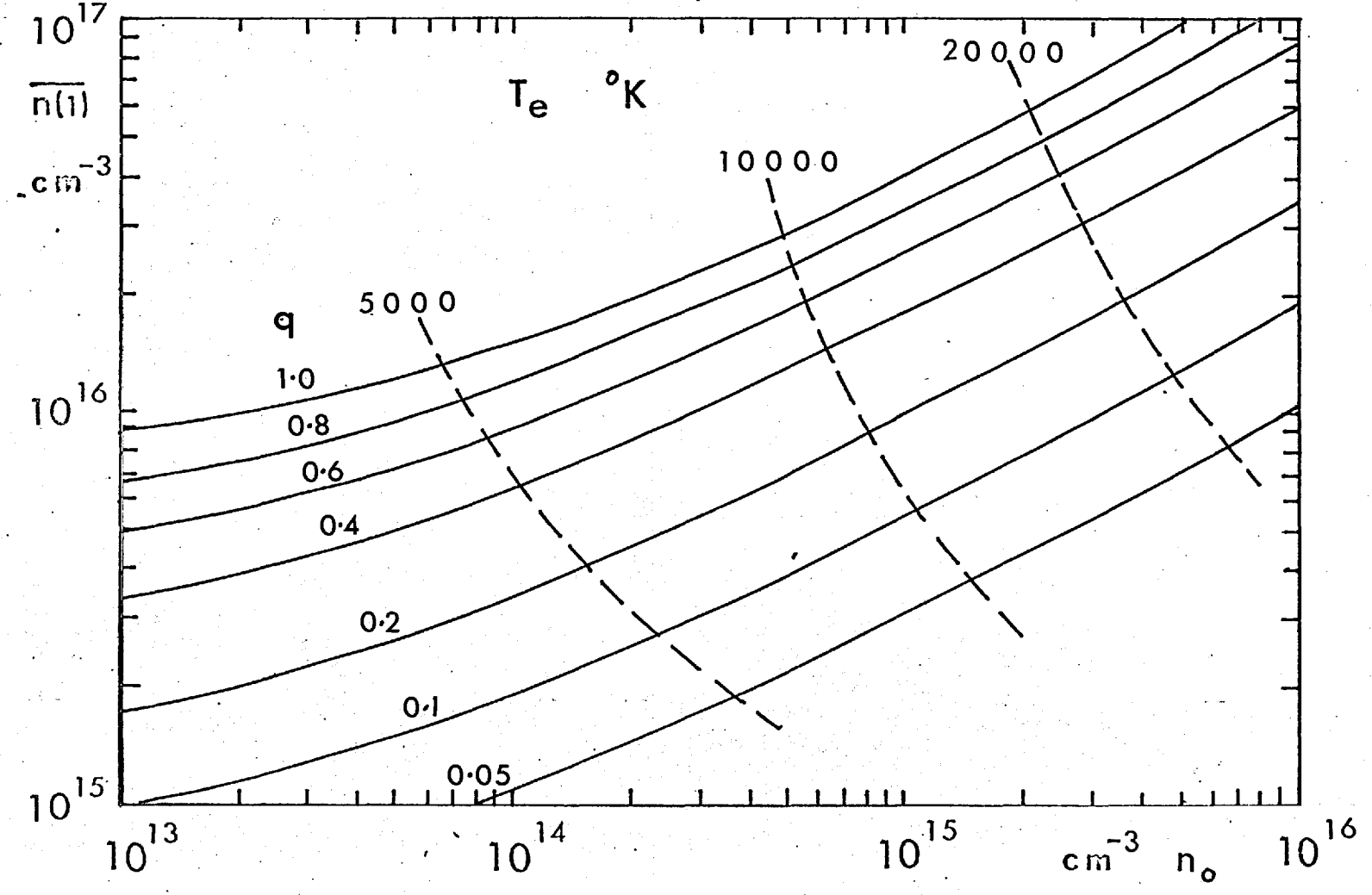

FIG (12.6) Q.E. - L.H. boundary parameters in large torus krypton plasmas.

For values of $\overline{n(1)}$ greater than those shown in table (12.3), the equations (12.69) and (12.71) were solved to give the parameters n_o, T_{eo}, T_{ao}, and τ_R associated with the boundary between the Q.E. and L.H. regions for specified values of q and $\overline{n(1)}$ over the ranges

$$q = 1.0,\ 0.8,\ 0.6,\ 0.4,\ 0.2,\ 0.1,\ 0.05$$
$$\overline{n(1)} = 3.\ 10^{15} \text{ to } 3.\ 10^{17} \text{ in logarithmic steps of X } 1.5.$$

The solutions for large torus dimensions are shown in figs. (12.2) to (12.6) where boundary line values of n_o have been plotted against $\overline{n(1)}$ for fixed values of q. Values of T_{eo} associated with the boundary have also been included on the same graphs. It was found from an examination of the computed values of T_{eo} and T_{ao} that the conditions (12.68) were satisfied in all gases when

$$\begin{aligned} n_o &\geqslant 3\ 10^{13}\ \text{cm}^{-3} \quad \text{tube radius} = 2.20\ \text{cm} \\ n_o &\geqslant 10^{13}\ \text{cm}^{-3} \quad \text{tube radius} = 3.55\ \text{cm} \end{aligned} \qquad (12.72)$$

(12.9.2) General Solution to the Set of Equations (12.69)

Equations (12.69) form a pair of independent equations linking five variable plasma parameters. In our computed solution to these equations, the parameters q, n_o and $\overline{n(1)}$ were specified over the ranges

$$q = 1.0,\ 0.8,\ 0.6,\ 0.4,\ 0.2,\ 0.1,\ 0.05$$
$$n_o = 10^{12} \text{ to } 10^{16}\ \text{cm}^{-3} \text{ in log steps of x } 3$$
$$\overline{n(1)} = 3\ 10^{15} \text{ to } 3\ 10^{17}\ \text{cm}^{-3} \text{ in log steps of x } 3$$

and the parameters T_{eo}, T_{ao} and the plasma recombination time were found for each combination of variables: a total of 315 sets of results for each gas in each size of torus. Inspection

of the computed values of T_{eo} and T_{ao} showed that conditions (12.68) were satisfied provided n_o satisfied the conditions (12.72). Thus the computor results obtained in this and the previous section are valid in the high density regions

$$\left.\begin{aligned} 10^{16} < n_o < 3\ 10^{13}\ \text{cm}^{-3} &\text{ for the small torus} \\ 10^{16} < n_o < 10^{13}\ \text{cm}^{-3} &\text{ for the large torus} \end{aligned}\right\} \quad (12.73)$$

It is physically impossible to tabulate or show graphically all the computed results and only plots of the recombination time versus n_o for fixed values of $\overline{n(1)}$ for the cases where $q = 1.0$ and 0.1 are shown in figs. (12.7) to (12.14). The plots where $q = 1.0$ can be taken to represent values of the recombination time as a function of n_o, $\overline{n(1)}$ in optically thick plasmas, and very approximately, the plots where $q = 0.1$ can be taken to represent the recombination time in optically thin plasmas. Within the electron density range (12.73), the recombination time $\tau_R\ (n, \overline{n(1)})$ should lie somewhere between the values predicted when $q = 1.0$ and $q = 0.1$.

The curves marked Q.E. in figs. (12.7) to (12.14) represent the plasma recombination time in the quasi-equilibrium atom temperature case. This was obtained by putting $\overline{n(1)}$ equal to zero in the first of equations (12.69) whilst putting $\overline{n(1)} = 10^{15}\ \text{cm}^{-3}$ in the second of (12.69). Thus this Q.E. case sets a lower limit to the value of the recombination time with decreasing $\overline{n(1)}$ and can be applied to the decay of plasmas at low gas pressures where $\overline{n(1)}$ is below the values quoted in table (12.3).

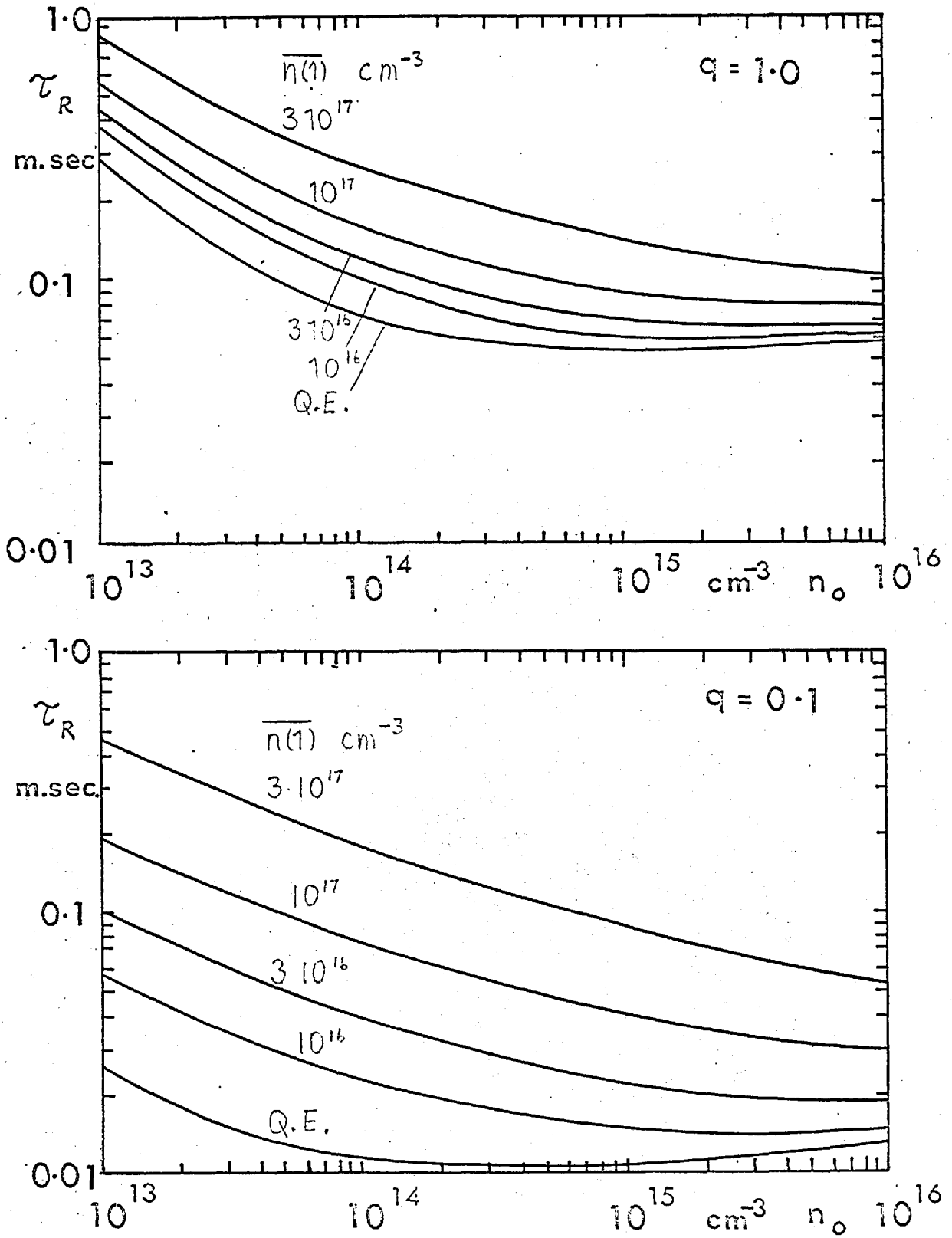

FIG (12.7) Computed recombination times in small torus helium plasmas.

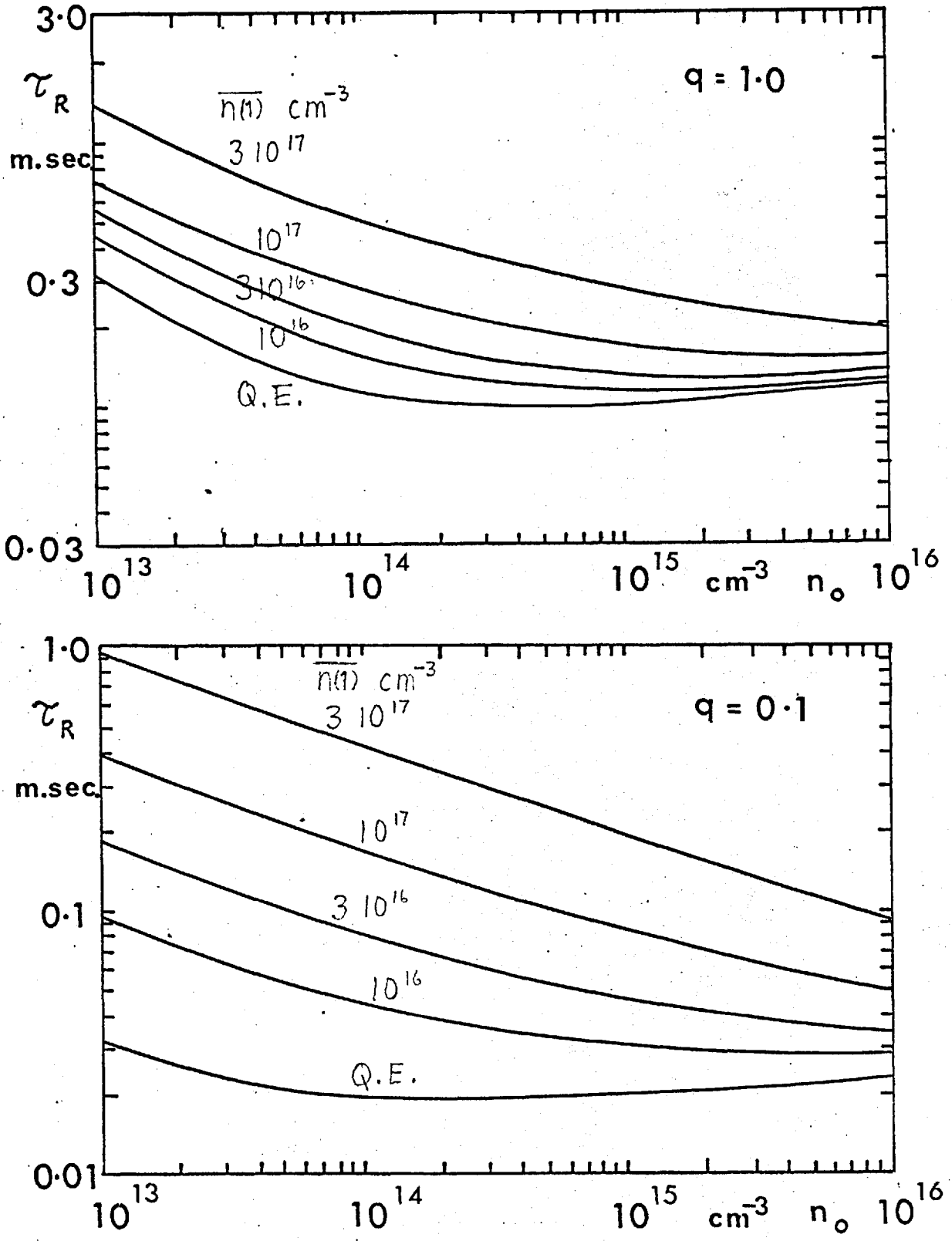

FIG (12.8) Computed recombination times in large torus helium plasmas.

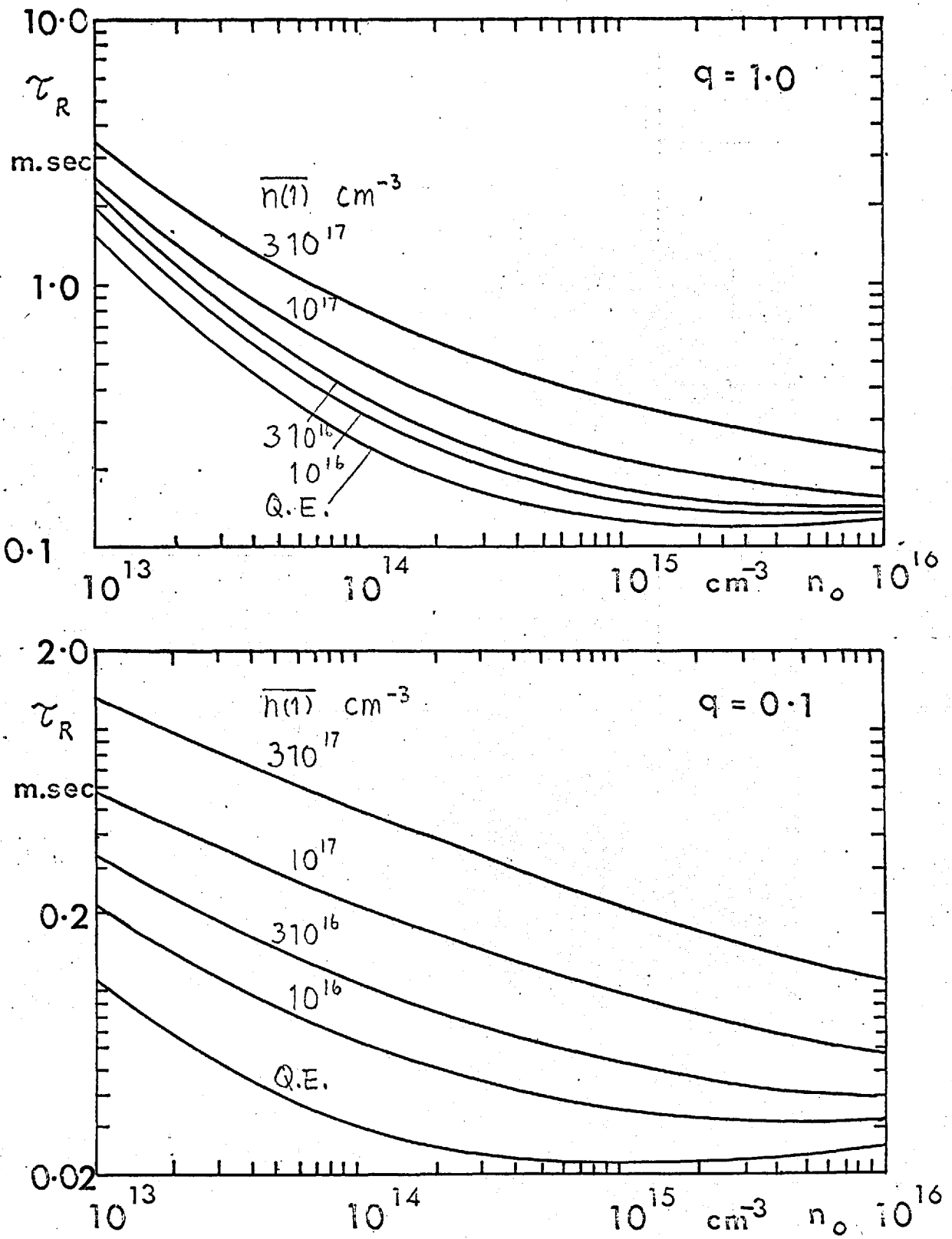

FIG (12.9) Computed recombination times in small torus neon plasmas.

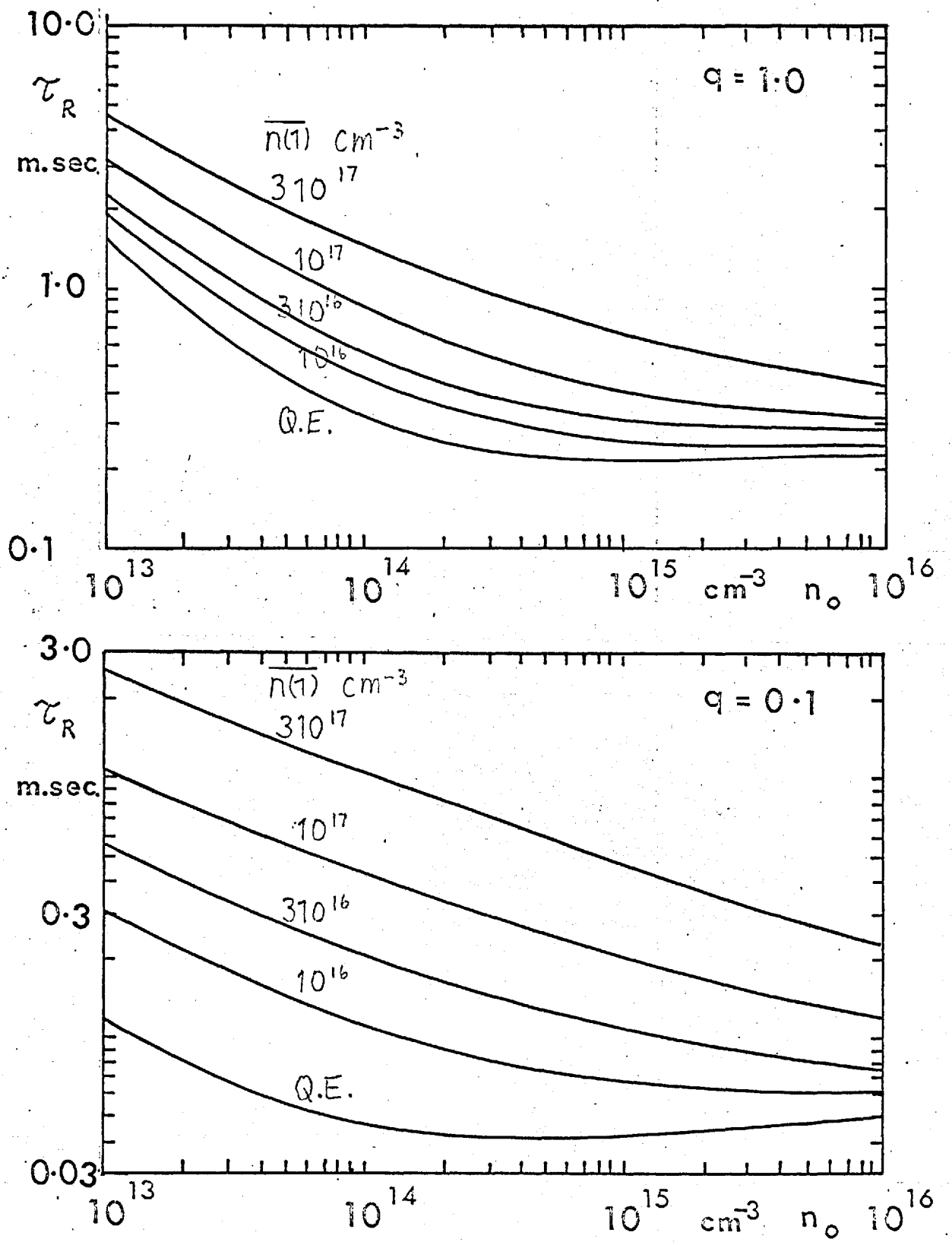

FIG (12.10) Computed recombination times in large torus neon plasmas.

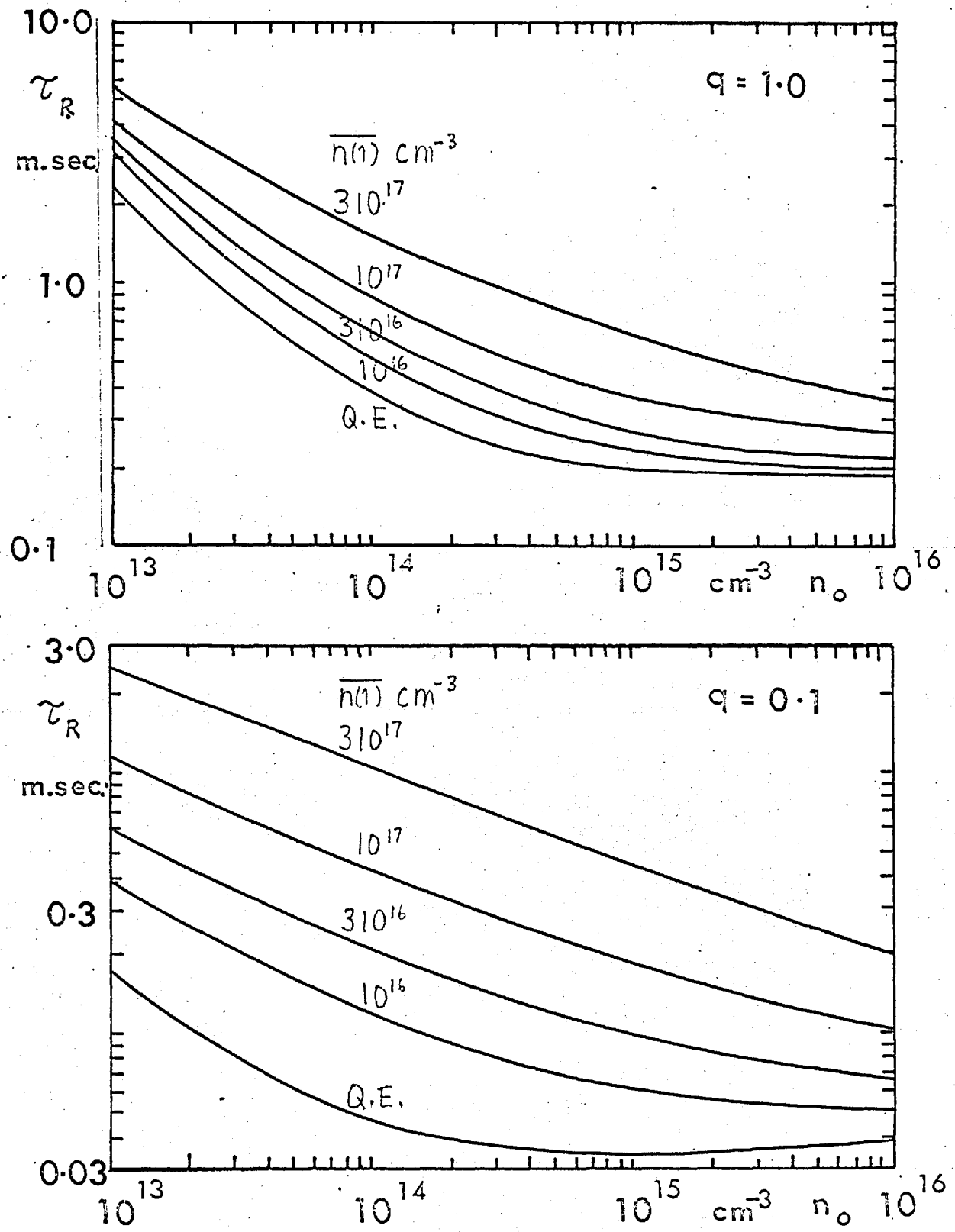

FIG (12.11) Computed recombination times in small torus argon plasmas.

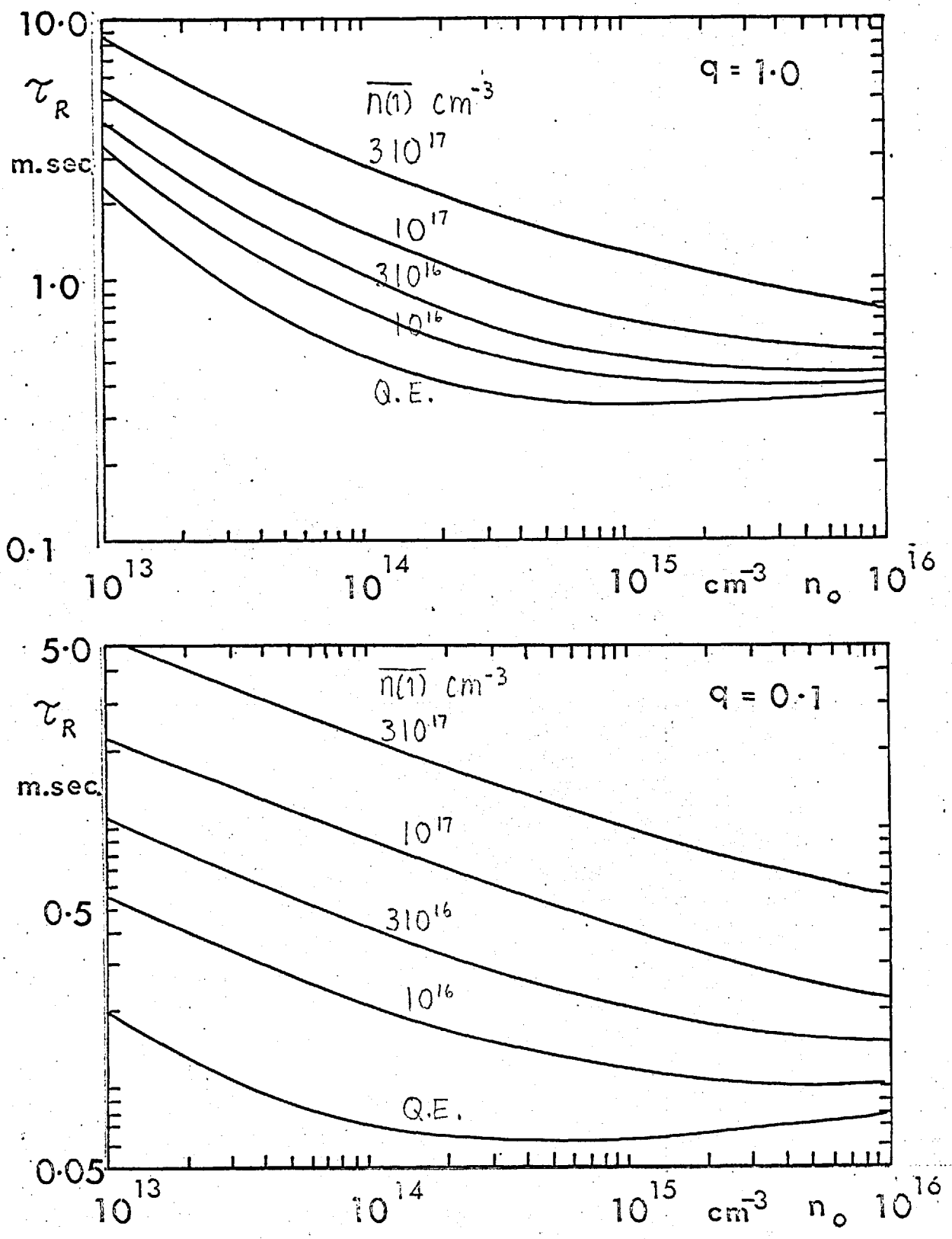

FIG (12.12) Computed recombination times in large torus argon plasmas.

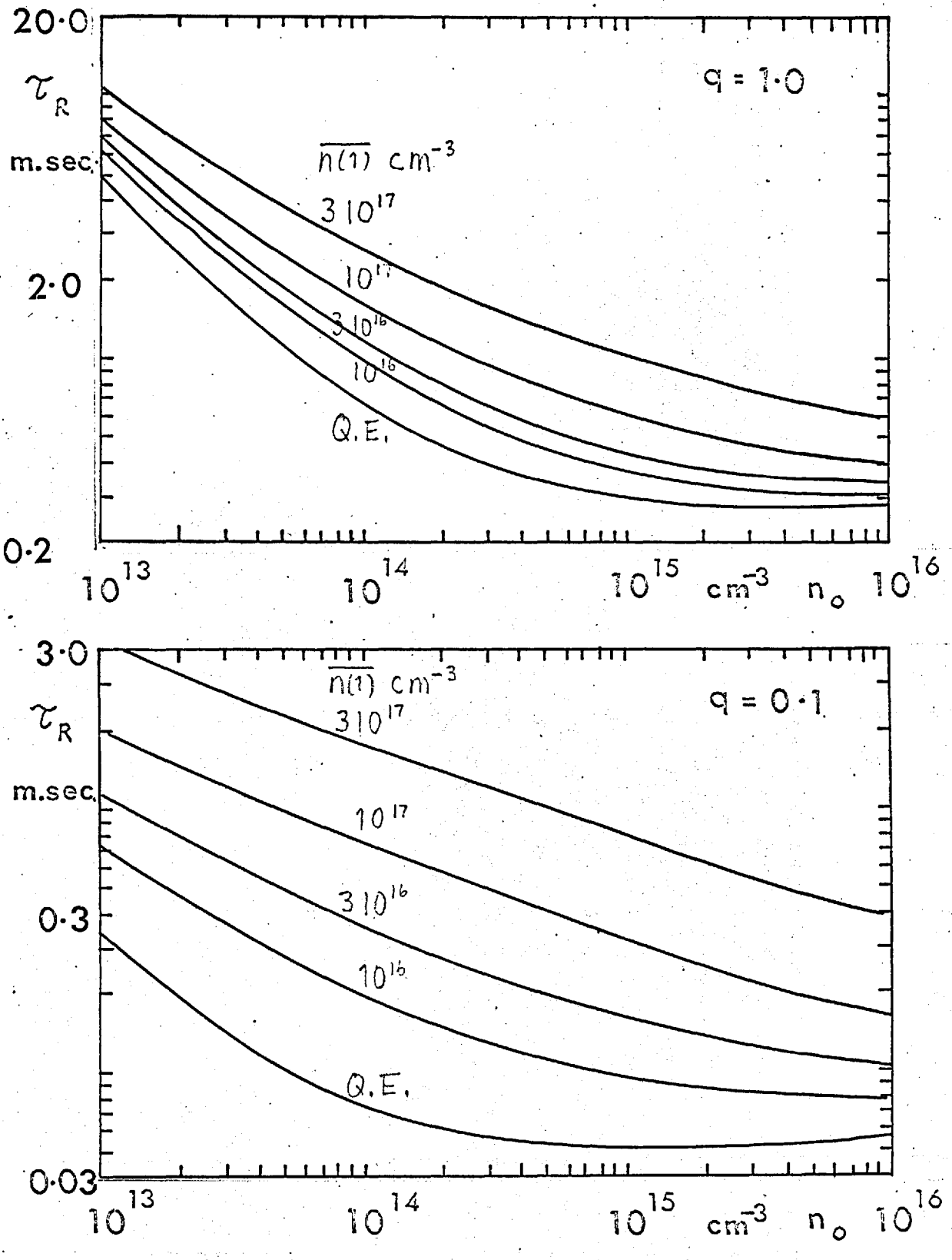

FIG (12.13) Computed recombination times in small torus krypton plasmas.

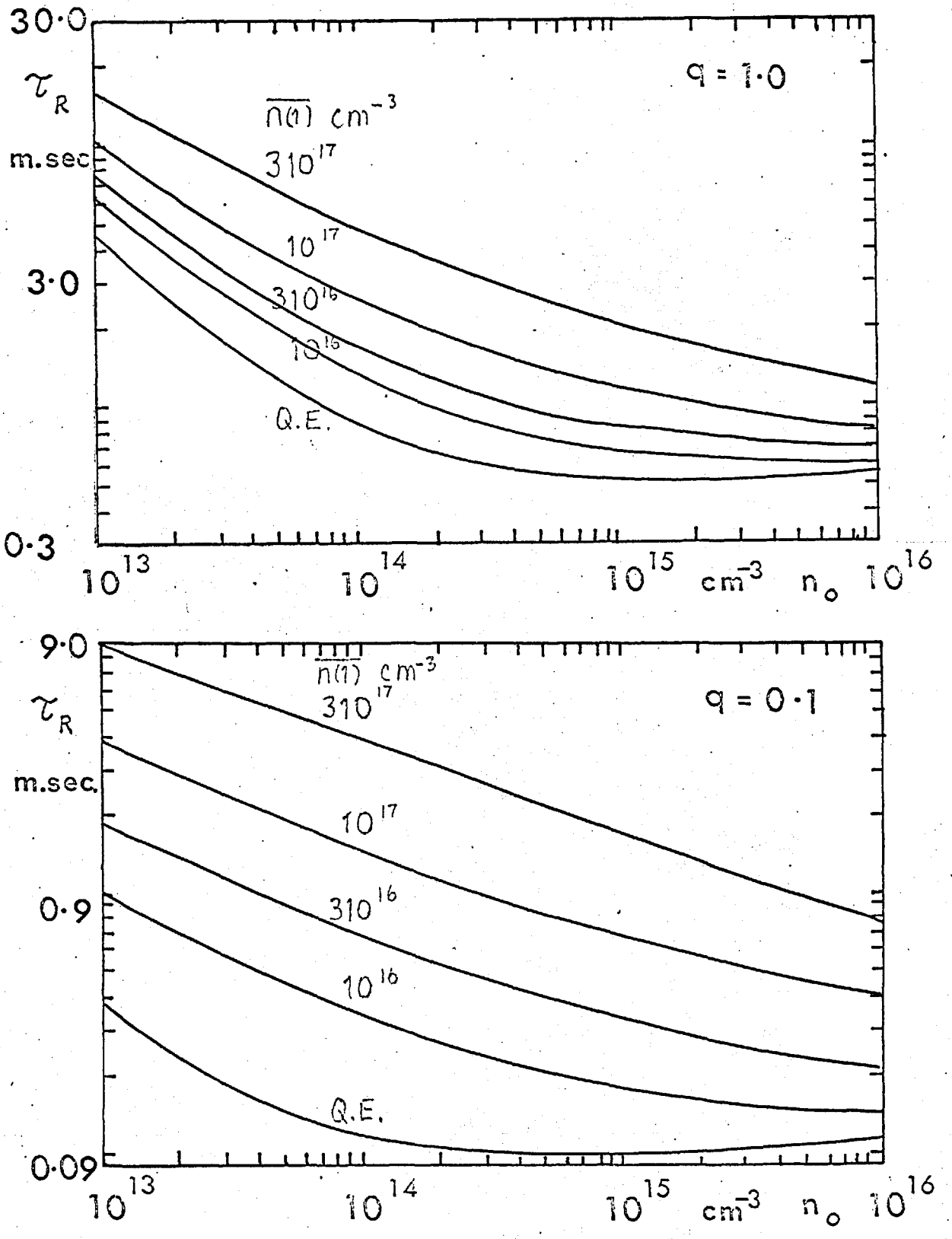

FIG (12.14) Computed recombination times in large torus krypton plasmas.

(12.10) COMPUTER SOLUTION OF ENERGY EQUATIONS IN LOW DENSITY PLASMAS

The results computed in section (12.9) rely on the validity of replacing the time differential term for T_{ao} with expression (12.63) and it has been shown that this procedure can only be applied to high electron density plasmas satisfying the conditions (12.73).

The solution of the energy balance - recombination equations (12.29) (12.37) and (12.31) has been performed for values of $n_o < 10^{13}$ cm^{-3} by choosing different approximations from those made in section (12.9).

At low electron densities, the coupling between the electron and atom temperatures via elastic energy transfer between particles is weak and as a result the atom temperature remains close to the tube wall temperature during the discharge heating phase. Consequently, we will assume that for $n_o < 10^{13}$ cm^{-3}

$$\left.\begin{aligned} T_{ao} &\lesssim 2\,T_w \\ T_{eo} &\gg T_{ao} \end{aligned}\right\} \qquad (12.74)$$

The low atom temperatures mean that the effects of atomic thermal energy in the energy transport equation (12.29) are negligible and the full set of energy balance-recombination equations are approximated to become

$$\left.\begin{aligned} q\,I\,\alpha\,n_o^2 &= \frac{2K}{a^2}\,(T_{ao}^2 - T_w^2) \\ T_{eo} &= q\,I\,\alpha\,n_o\left[\frac{T_{eo}^{1.5}}{n_o\,X_{ei}} + \frac{2}{n(1)\,X_{ia}}\right] + T_w \\ \alpha &= C\,n_o^2\,(T_{eo})^{-4.5} \end{aligned}\right\} \qquad (12.75)$$

The limits of plasma conditions for which the inequalities (12.74) hold true are given by substituting $T_a = 2\ T_w$ into the set of equations (12.75). The results obtained from doing this are shown in figs. (12.15) and (12.16) where the maximum allowed value of n_o has been plotted against $\overline{n(1)}$ for valuesof q of 1.0 and 0.1. For the rare gases, it can be seen from figs. (12.15) and (12.16) that the upper electron density limits to the solutions of the set of equations (12.75) are

$$\left.\begin{aligned} n_o &\leqslant 10^{13}\ \text{cm}^{-3} \text{ for the large torus} \\ n_o &\leqslant 2.10^{13}\ \text{cm}^{-3} \text{ for the small torus} \end{aligned}\right\} \qquad (12.76)$$

Comparison of these upper density limits of the low density approximation of the energy equations, with the lower density limits (12.72) and (12.73) found for the high density approximation, shows that there is good consistency amongst both sets of approximations.

Solutions to the set of equations (12.75) have been found for T_{eo}, T_{ao} and τ_R as a function of q, n_o and $\overline{n(1)}$ over the ranges

$$q = 1.0,\ 0.8,\ 0.6,\ 0.4,\ 0.2,\ 0.1,\ 0.05$$

$$n_o = 10^{12},\ 3\ 10^{12},\ 10^{13}\ \text{cm}^{-3}$$

$$\overline{n(1)} = 10^{14} \text{ to } 10^{17}\ \text{cm}^{-3} \text{ in log steps of x 3.}$$

The results obtained are not presented here because a direct comparison with our experimental results cannot be performed. Since our plasma was nearly fully ionised initially, condition (12.76) was always violated at the start of the plasma decay even at our lowest working pressure of 10 m.torr. Consequently, it is extremely unlikely that the atom temperatures remained $\leqslant 2\ T_w$ in our experiment.

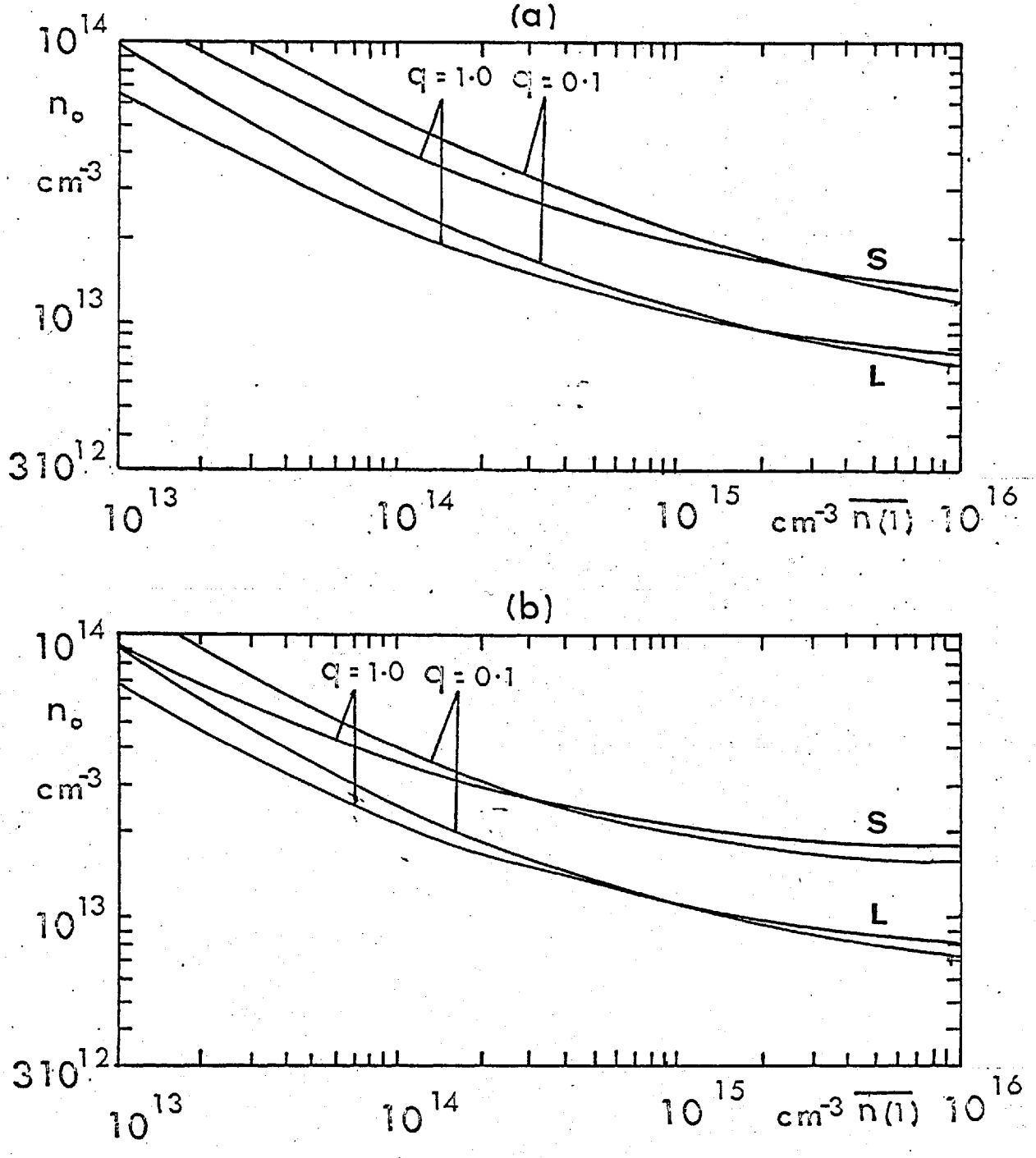

FIG (12.15) Plasma parameters associated with the condition $T_a = 2T_w$

(a) helium plasmas
(b) neon plasmas.

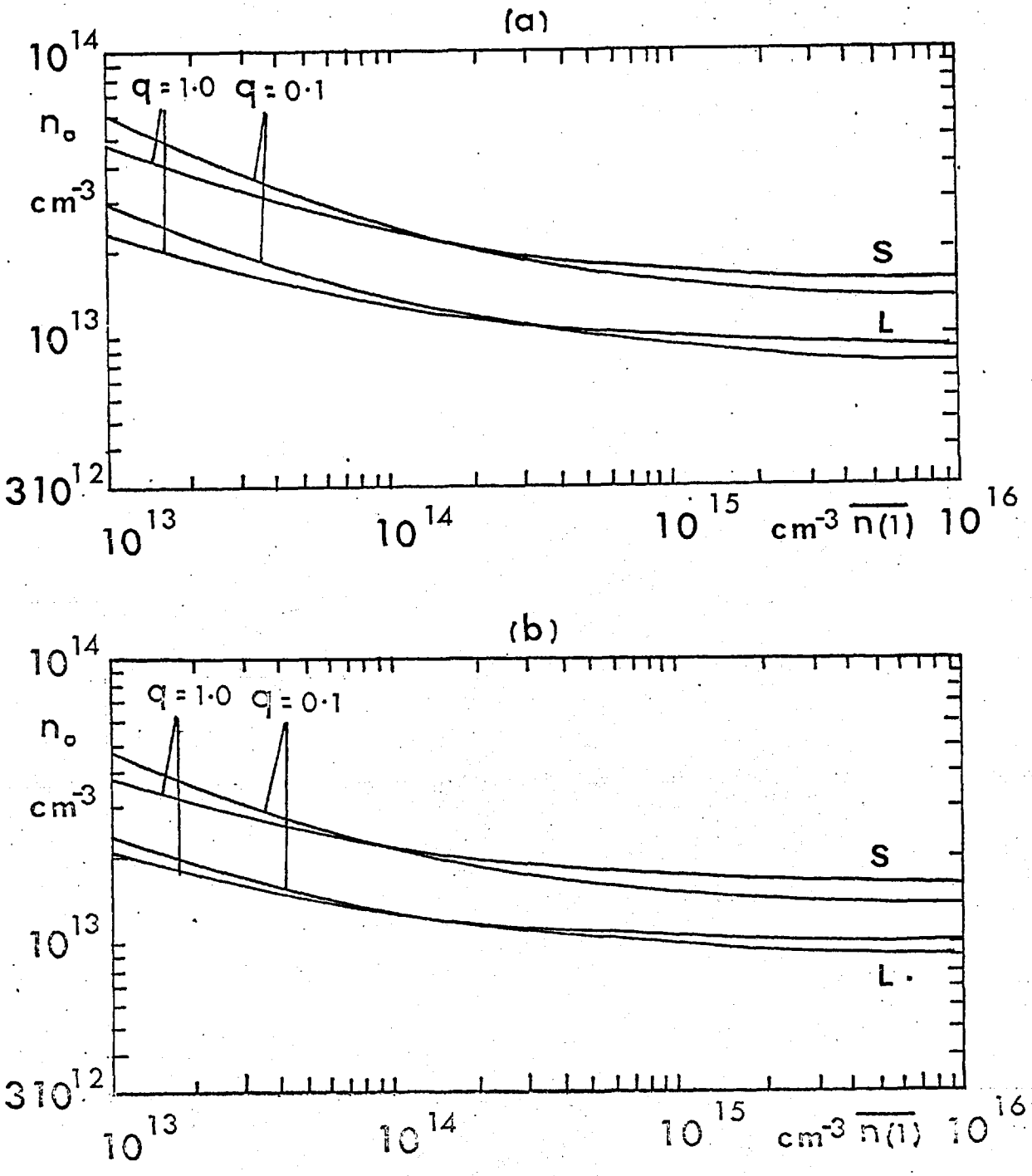

FIG (12.16) Plasma parameters associated with the condition $T_a = 2T_w$

(a) argon plasmas
(b) krypton plasmas.

(12.11) COMPARISON OF LOW DENSITY COMPUTOR SOLUTIONS WITH BATES AND KINGSTON'S SOLUTIONS OF THE ENERGY EQUATIONS.

The main modification made to the energy balance-recombination equations in our low density approximation, described in section (12.10) above, is that the atom temperature remains between the values of T_w and $2T_w$ (300 - 600°K for T_w = 300°K). This condition is very similar to the condition adopted by Bates and Kingston (74)(75) in their solutions of the same equations for a fixed atom temperature of 250°K which has already been described in sections (12.2) and (12.3).

Therefore, it is interesting to compare the values for the recombination time or recombination coefficient given by our low density approximation with the values given by Bates and Kingston. Since our set of equations (12.75) has a doubtful application to hydrogen, only the case of helium plasmas will be considered.

Bates and Kingston's results for helium in optically thick and optically thin plasma are reproduced in figs. (12.1) where they have plotted α against n over a range 10^9 to 10^{15} cm^{-3} for fixed values of n(1) from 10^{12} to 10^{16} cm^{-3}. In order that we can make a direct comparison between these results and our low density results, the upper limit condition (12.76) has to be ignored, and the set of equations (12.75) were solved by iteration on the computer for the following ranges of plasma parameters

$$n_o = 10^{12} \text{ to } 10^{15} \text{ cm}^{-3} \text{ in log steps of x 3}$$

$$\overline{n(1)} = 10^{14}, 10^{15}, 10^{16}, 10^{17} \text{ cm}^{-3}$$

$$q = 1.0 \text{ and } 0.1$$

The results were computed for the dimensions of the large torus only since its minor raidus of 3.55 cm is the closer to

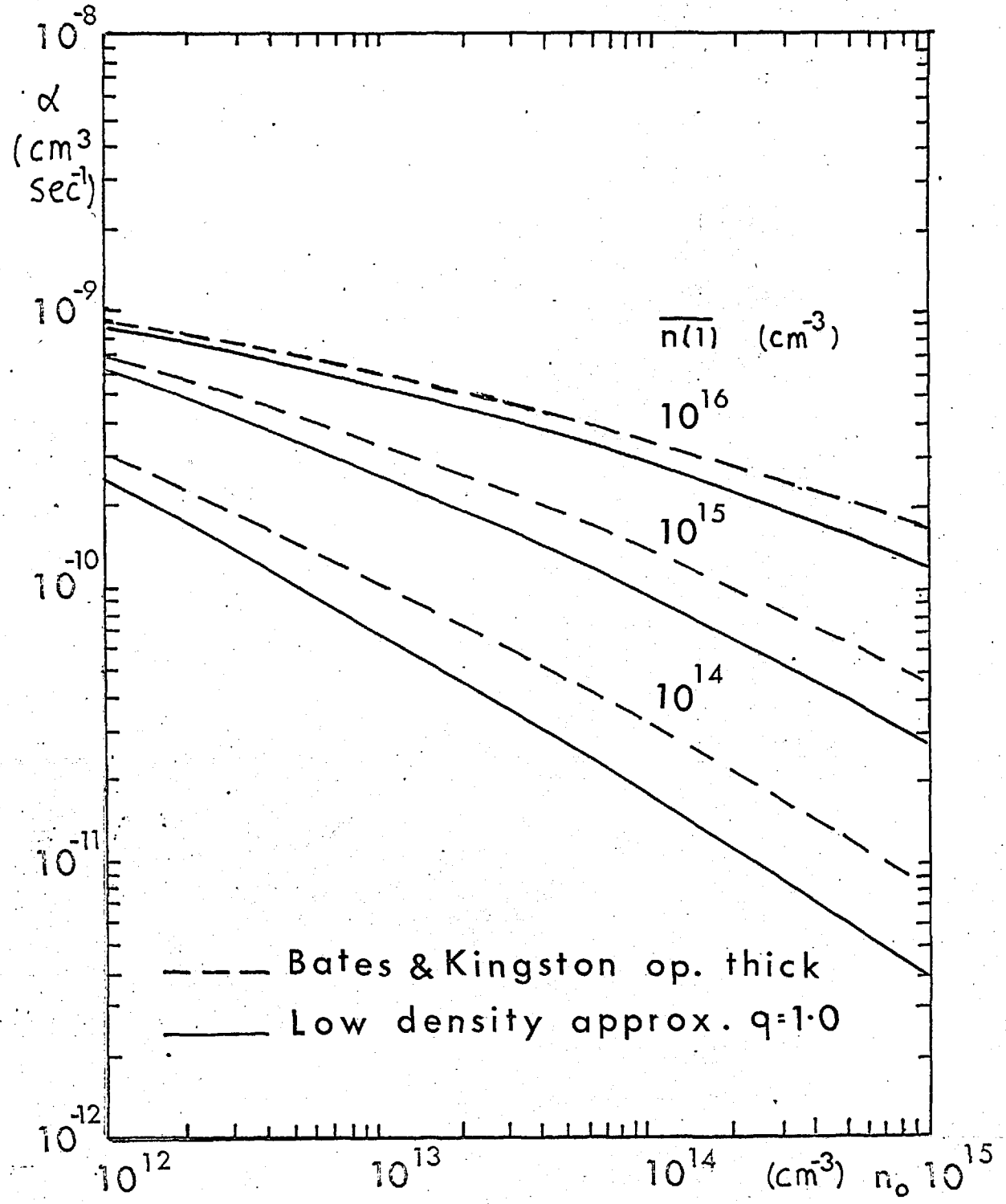

FIG (12.17) Comparison of the helium plasma recombination coefficients found for the q = 1.0 low density approximation with the optically thick results of Bates and Kingston.

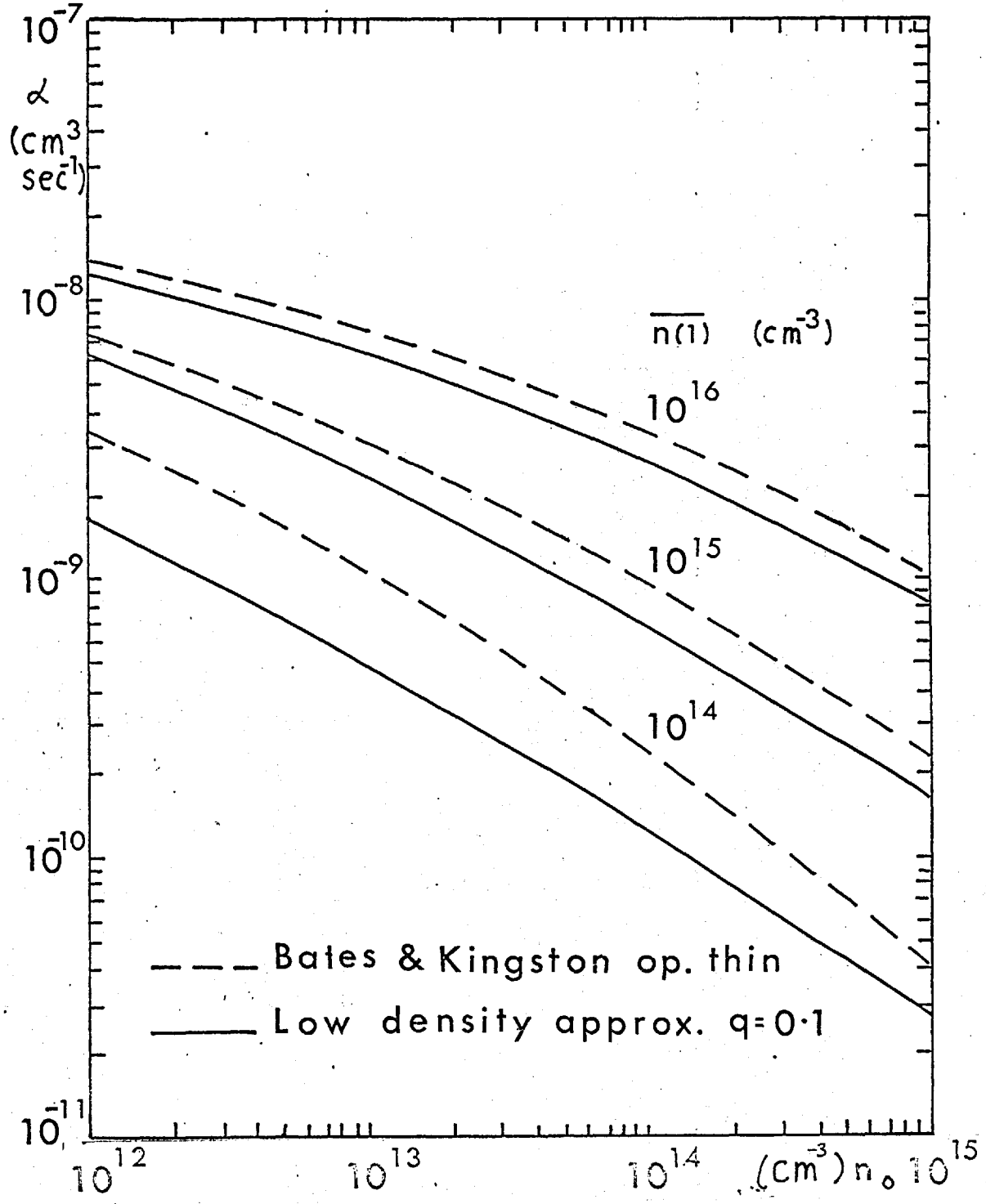

FIG (12.18) Comparison of the helium plasma recombination coefficients found for the q = 0.1 low density approximation with the optically thin results of Bates and Kingston.

Bates and Kingston's chosen radius of 3.0 cm than is the minor radius of our small torus. The results obtained for the variation of $\alpha(n_o)$ for fixed $\overline{n(1)}$ are shown in figs. (12.17) and (12.18) together with Bates and Kingston's results. We have chosen to compare our case of $q = 1.0$ with the optically thick case of Bates and Kingston and our case of $q = 0.1$ with their optically thin case. A comparison of the two sets of results in each case shows that there is an excellent agreement between our low density solutions and Bates and Kingston's solutions to the energy equations. However, we have already shown that our low density approximation is not valid for $n_o > 10^{13}$ cm^{-3} and therefore it seems even more certain that Bates and Kingston's results do not apply for electron densities $> 10^{13}$ cm^{-3} either.

(12.12) COMPARISON OF LOW DENSITY RESULTS, BATES AND KINGSTON'S RESULTS AND HIGH DENSITY RESULTS IN THE ELECTRON DENSITY REGION $10^{13} - 10^{15}$ cm^{-3}

The variation of recombination coefficient with electron density for fixed values of $\overline{n(1)}$ as given by the high density computation of section (12.9) have been plotted in figs. (12.19) and (12.20) for the case of helium gas in the large torus with $q = 1.0$ and 0.1. Comparison of figs. (12.17) and (12.18) with figs. (12.19) (12.20) shows the marked contrast between the different approximations of the energy balance-recombination equations in the density region 10^{13} to 10^{15} cm^{-3}. In particular, two opposite trends are noticeable:

1. In figs. (12.17) and (12.18) α at a fixed value of n_o increases with increasing $\overline{n(1)}$, whereas in figs. (12.19) and (12.2 α at a fixed value of n_o decreases with increasing $\overline{n(1)}$

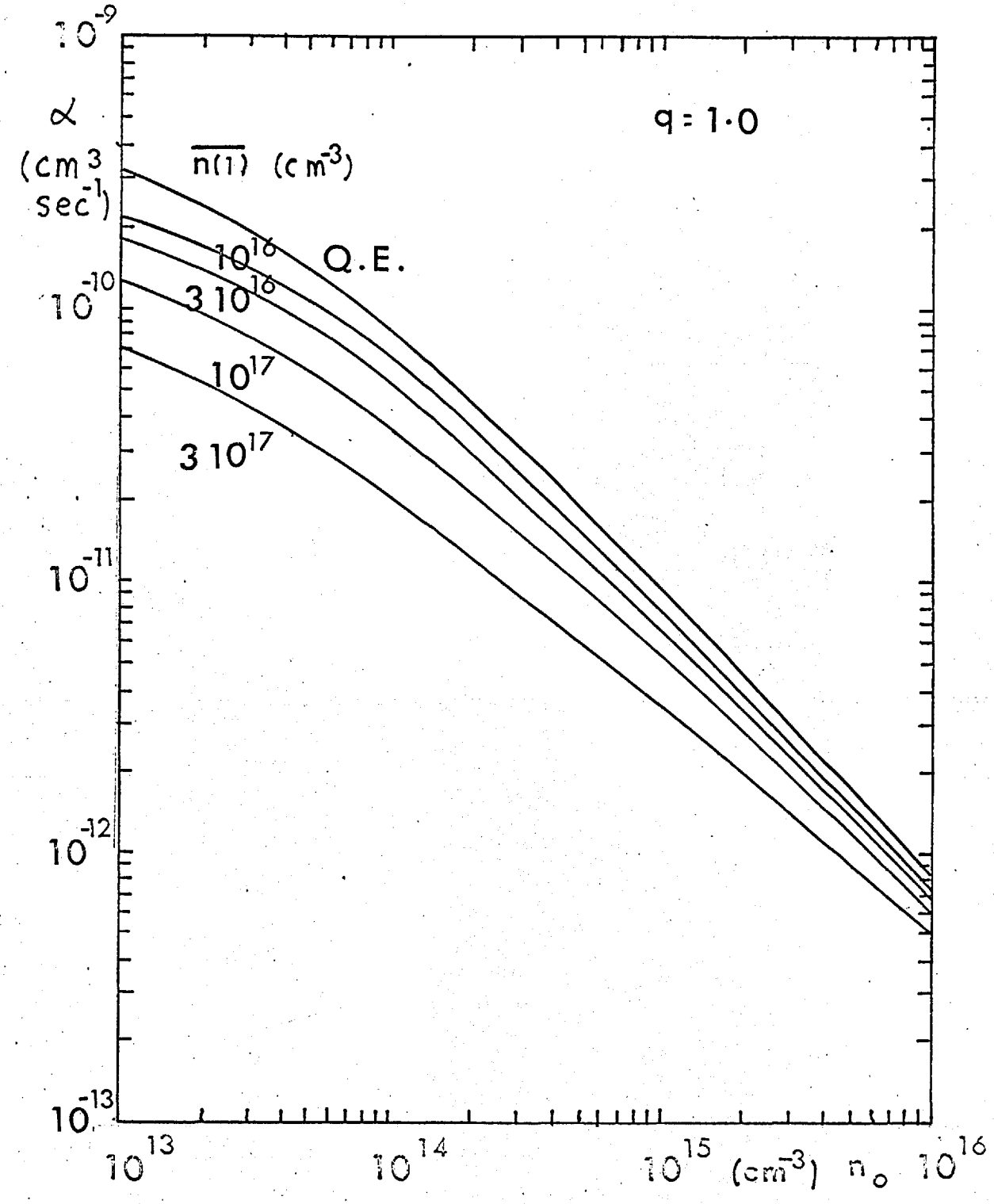

FIG (12.19) Helium plasma recombination coefficients found for the q = 1.0 high density approximation.

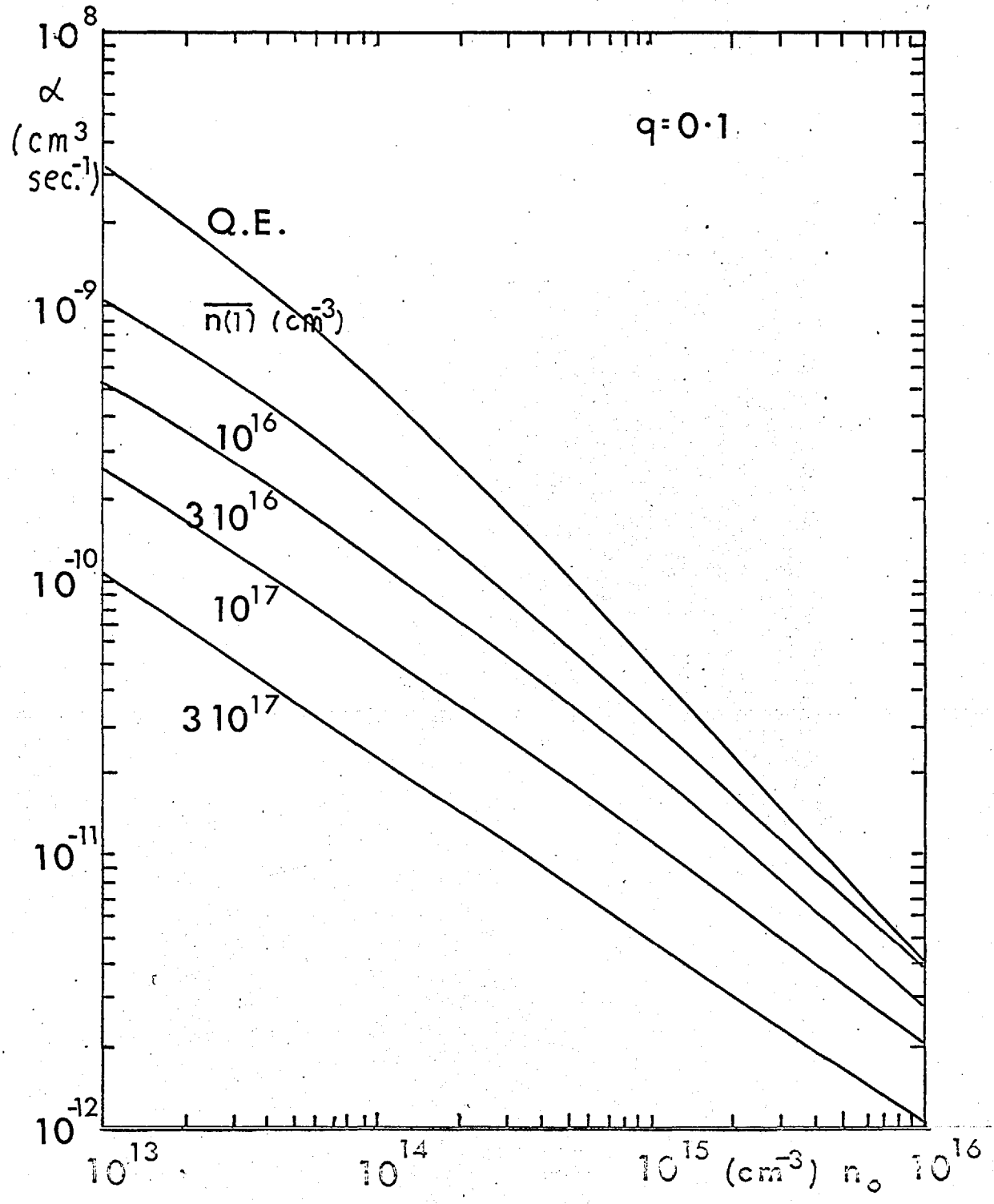

FIG (12.20) Helium plasma recombination coefficients found for the q = 0.1 high density approximation.

2. In figs. (12.17) and (12.18) the value of α is a diverging function of $\overline{n(1)}$ with increasing fixed values of n_o, whereas in figs. (12.19) and (12.20) the value of α is a converging function of $\overline{n(1)}$ with increasing n_o.

Inspection of the plasma electron density decay plots given in figs. (11.4) to (11.14) shows that at a fixed value of n, the decay time (ie. gradient of the decay plot) always increases with increasing $\overline{n(1)}$. Also, in figs. (11.4) to (11.14) it can be seen that the gradients of the decay plots are diverging functions of gas pressure with decreasing values of density, ie. α is a converging function of $\overline{n(1)}$ with increasing n_o. Allowance for diffusion effects does not alter these two experimentally observed trends, and the excellent agreement with the results shown in figs. (12.19) and (12.20) would appear to further confirm the correctness of the high density approximation presented in section (12.9) in the region $10^{13} < n_o < 10^{16}$ cm^{-3}.

CHAPTER 13

COMPARISON OF COMPUTED AND EXPERIMENTAL RESULTS

The experimental values of the recombination time found from the electron density decay plots are compared with the recombination times computed for the high density approximation described in the previous chapter. It is shown that, for plasma conditions between the optically thick and optically thin limits, this comparison leads to the numerical estimation of the factor q as a function of electron density, type of gas and radius of discharge tube. An entirely theoretical estimation of the factor q as a function of the same variables is also presented from the effects of variations in radiation trapping inside the plasma with changing n, n(1), T_e. As a result of a comparison of these two separate numerical estimations of the factor q, good overall agreement is concluded between the computed and experimental results.

(13.1) METHOD FOR COMPARING COMPUTED AND EXPERIMENTAL RESULTS

In performing a comparison of theory with experiment we have chosen to compare the plasma recombination times for each set of results. The reasons for making this choice are

1. The recombination time is a very strong function of electron temperature in the three body C.R. regime, as can be seen from equations (9.25) (9.26) and (9.27). Hence, the fractional difference between experimental and computed values of τ_R will be four to five times larger than the fractional difference

between the experimental and computed value of T_e.

2. It is generally true for the diagnostics of decaying plasmas that the recombination time can be measured with a greater accuracy and over a wider range of plasma conditions than the electron temperature can be measured.

3. The recombination time is to be preferred as a comparison standard over the recombination coefficient, especially in describing high density plasma decay. From the decay plots shown in figs. (11.4) to (11.14), and the Q.E. recombination theory presented in section (12.7), the conditions existing in afterglow plasma make τ_R only a very slowly varying function of n at high densities. This small variation of τ_R with n tends to be masked in the value of recombination coefficient by the inverse density dependence inherent in the derivation of α from τ_R.

$$\alpha = (n \tau_R)^{-1}$$

From the experimental measurements on decaying plasmas, τ_R is most accurately obtained as a function of n_o and $\overline{n(1)}$. In our computor calculations, τ_R has been obtained as a function of n_o, $\overline{n(1)}$ and q. Theoretical estimates of the value of q as a function of n, n(1), T_e can be made in decaying plasma conditions, as will be shown in section (13.9), but these estimates are very crude due to the complex physical processes inherent in the factor q. The only plasma region where we can be sure of the value of q is the high density region where n and n(1) are both $\geq 10^{15}$ cm^{-3}. In this region most of the recombination energy is retained within the plasma and $q \sim 1.0$ so that, at high densities, a comparison of theory and experiment is straight forward. For the decay region where $n < 10^{15}$ cm^{-3} we can compare theory and experiment by either of the following two methods.

(a) The crude theoretical estimation of $q\ (n_o, \overline{n(1)}, T_{eo})$ can be combined with the computer solutions of $T_{eo}(q, n_o, \overline{n(1)})$ and $\tau_R(q, n_o, \overline{n(1)})$ to yield $\tau_R\ (n_o, \overline{n(1)})$. In adopting this method, the errors on the values of $\tau_R\ (n_o, \overline{n(1)})$ are almost entirely determined by the errors in the factor $q\ (n_o, \overline{n(1)}, T_{eo})$ so that the accuracy of the computer calculations is completely overshadowed by the accuracy of the calculation of the factor q right from the start of this method of comparison.

(b) The experimental values of $\tau_R(n_o, \overline{n(1)})$ can be compared with the computed values of $\tau_R(q, n_o, \overline{n(1)})$ to yield values of q as a function of n_o, $\overline{n(1)}$. The accuracy of this evaluation of the factor $q\ (n_o, \overline{n(1)})$ depends solely upon the accuracies of the experimental results and the computer solutions to the energy balance - recombination equations. Hence $q\ (n_o, \overline{n(1)})$ should be obtained to a greater accuracy than would be possible by theory alone. For a comparison of theory with experiment, the value of $q\ (n_o, \overline{n(1)})$, found as above, can be compared with an entirely theoretical estimation of $q(n_o, \overline{n(1)})$ found from a combination of the crude calculation of $q\ (n_o, \overline{n(1)}, T_{eo})$ with the computed calculation $T_{eo}\ (q, n_o, \overline{n(1)})$.

The overall accuracy of the method of comparison (a) is, of course, the same as that for method (b), since in both cases it is largely determined by the error in the theoretical estimation of $q\ (n_o, \overline{n(1)}, T_{eo})$. However, method (b) was chosen as being preferable to method (a) since, in the former, the estimate of $q\ (n_o, \overline{n(1)}, T_{eo})$ is only introduced into the last stage of the comparison. Also from method (b) we obtain as experimental - theoretical estimate of $q\ (n_o, \overline{n(1)})$ which is a quantity of interest in its own right in the study of decaying plasmas.

(13.2) COMPARISON OF COMPUTED AND EXPERIMENTAL RESULTS IN THE Q.E. REGION.

At low gas pressures, and high electron densities, the experimental plots of p/τ versus p shown in figs. (11.17) to (11.27) can be seen to be linear. From equation (11.6), this linear relationship means that the plasma recombination time is independent of gas pressure or average atom density $\overline{n(1)}$ and τ_R is a function of q and n_o only. As a consequence, the experimental values of τ_R obtained from the gradients of the linear regions of the plots p/τ versus p can be compared with the values of τ_R computed for the Q.E. atom temperature case where theoretically τ_R is independent of $\overline{n(1)}$ and is a function of q and n_o only. This comparison yields values for q (n_o) in the Q.E. case for plasma decay in each type of gas in each size of discharge tube.

In column two of table (13.1), the experimental values of τ_R, found at fixed values of n_o, have been listed and in column three, the values of $q(n_o)$, found as described above, have been listed where q (n_o) was interpolated from the Q.E. values of τ_R computed in section (12.9.1) for q = 1.0, 0.8, 0.6, 0.4, 0.2, 0.1 and 0.05.

In the fourth column of table (13.1) the values of gas pressure p_B at which the plots of p/τ versus p depart from a linear relationship have been listed and these have been converted to values of average atom density $\overline{n(1)}_B$ as shown in column five.

In column six, the values of atom density corresponding to the boundary line between the Q.E. and L.H. regions as computed in section (12.9.1) have been listed. These values for

TABLE (13.1)

n_o (cm^{-3})	τ_R (μ.sec)	q	P_B (m.torr)	$\overline{n(1)}_B$ (cm^{-3})	$\overline{n(1)}$ (Q.E.-L.H.) (cm^{-3})
HELIUM,	LARGE	TORUS			
10^{15}	106	1.0	-	-	$9.4\ 10^{16}$
$3\ 10^{14}$	104	1.0	-	-	$5.3\ 10^{16}$
10^{14}	129	1.0	700	$2.5\ 10^{16}$	$3.0\ 10^{16}$
$3\ 10^{13}$	159	0.95	550	$1.9\ 10^{16}$	$1.8\ 10^{16}$
10^{13}	196	0.63	450	$1.6\ 10^{16}$	$8.8\ 10^{15}$
$3\ 10^{12}$	245	0.35	350	$1.2\ 10^{16}$	-
NEON	LARGE	TORUS			
10^{15}	222	1.0	-	-	$7.2\ 10^{16}$
$3\ 10^{14}$	213	0.82	-	-	$2.8\ 10^{16}$
10^{14}	217	0.62	600	$2.1\ 10^{16}$	$1.7\ 10^{16}$
$3\ 10^{13}$	235	0.38	450	$1.6\ 10^{16}$	$6.8\ 10^{15}$
10^{13}	250	0.20	350	$1.2\ 10^{16}$	$3.0\ 10^{15}$
$3\ 10^{12}$	345	0.11	150	$5.2\ 10^{15}$	-
ARGON	LARGE	TORUS			
10^{15}	440	1.0	-	-	$4.8\ 10^{16}$
$3\ 10^{14}$	440	1.0	-	-	$2.7\ 10^{16}$
10^{14}	430	0.81	-	-	$1.4\ 10^{16}$
$3\ 10^{13}$	555	0.58	550	$1.9\ 10^{16}$	$7.6\ 10^{15}$
10^{13}	590	0.30	300	$1.1\ 10^{16}$	$3.0\ 10^{15}$
$3\ 10^{12}$	1040	0.19	150	$5.2\ 10^{15}$	-

TABLE (13.1) CONTINUED

n_o (cm^{-3})	τ_R (μ.sec.)	q	P_B (m.torr)	$\overline{n(1)}_B$ (cm^{-3})	$\overline{n(1)}$ (Q.E.-L.H.) (cm^{-3})
KRYPTON	LARGE	TORUS			
10^{15}	650	1.0	-	-	$4.0\ 10^{16}$
$3\ 10^{14}$	645	1.0	-	-	$2.3\ 10^{16}$
10^{14}	700	0.78	600	$2.1\ 10^{16}$	$1.2\ 10^{16}$
$3\ 10^{13}$	960	0.52	400	$1.4\ 10^{16}$	$5.8\ 10^{15}$
10^{13}	1240	0.32	300	$1.05\ 10^{16}$	$1.8\ 10^{15}$
$3\ 10^{12}$	2330	0.21	200	$7.0\ 10^{15}$	-
HELIUM	SMALL	TORUS			
$2\ 10^{15}$	82	1.0			$1.6\ 10^{17}$
10^{15}	80	1.0			$1.1\ 10^{17}$
$3\ 10^{14}$	86	1.0			$6.2\ 10^{16}$
10^{14}	87	1.0	600	$2.1\ 10^{16}$	$3.8\ 10^{16}$
$3\ 10^{13}$	101	0.82	450	$1.6\ 10^{16}$	$2.1\ 10^{16}$
10^{13}	112	0.42	300	$1.05\ 10^{16}$	$8.4\ 10^{16}$
HELIUM	SMALL	TORUS	TOROIDAL	FIELD	= 2 k.v.
$2\ 10^{15}$	68	1.0	-	-	$1.6\ 10^{17}$
10^{15}	74	1.0	-	-	$1.1\ 10^{17}$
$3\ 10^{14}$	77	1.0	-	-	$6.2\ 10^{16}$
10^{14}	76	1.0	800	$2.9\ 10^{16}$	$3.8\ 10^{16}$
$3\ 10^{13}$	80	0.62	500	$1.8\ 10^{16}$	$1.6\ 10^{16}$
10^{13}	83	0.33	350	$1.2\ 10^{15}$	$6.7\ 10^{15}$

TABLE (13.1) CONTINUED

n_o (cm^{-3})	τ_R (μ.sec)	q	P_B (m.torr)	$\overline{n(1)}_B$ (cm^{-3})	$\overline{n(1)}$ (Q.E.-L.H.) (cm^{-3})
NEON	SMALL	TORUS			
$2\ 10^{15}$	123	1.0	-	-	$1.2\ 10^{17}$
10^{15}	115	0.90	-	-	$8.0\ 10^{16}$
$3\ 10^{14}$	114	0.62	-	-	$3.2\ 10^{16}$
10^{14}	116	0.42	500	$1.8\ 10^{16}$	$1.4\ 10^{16}$
$3\ 10^{13}$	118	0.22	350	$1.2\ 10^{16}$	$5.6\ 10^{15}$
10^{13}	131	0.12	250	$8.8\ 10^{15}$	$2.6\ 10^{15}$
ARGON	SMALL	TORUS			
$2\ 10^{15}$	230	1.0	-	-	$8.4\ 10^{16}$
10^{15}	250	1.0	-	-	$5.8\ 10^{16}$
$3\ 10^{14}$	275	1.0	-	-	$3.4\ 10^{16}$
10^{14}	285	0.77	450	$1.6\ 10^{16}$	$1.7\ 10^{16}$
$3\ 10^{13}$	305	0.38	350	$1.2\ 10^{16}$	$6.6\ 10^{16}$
10^{13}	385	0.20	250	$8.7\ 10^{15}$	$2.8\ 10^{16}$
KRYPTON	SMALL	TORUS			
$2\ 10^{15}$	440	1.0	-	-	$6.8\ 10^{16}$
10^{15}	435	1.0	-	-	$4.9\ 10^{16}$
$3\ 10^{14}$	455	1.0	-	-	$2.9\ 10^{16}$
10^{14}	520	0.76	700	$2.4\ 10^{16}$	$1.6\ 10^{16}$
$3\ 10^{13}$	570	0.38	350	$1.05\ 10^{16}$	$6.0\ 10^{15}$
10^{13}	630	0.18	120	$4.2\ 10^{15}$	$2.4\ 10^{15}$

$n(1)$ (Q.E. - L.H.) were obtained from figs. (12.2) to (12.6) for the large torus case and from the corresponding plots (not shown) for the small torus case using the values of n_o and q given in the first and third columns of table (13.1). This procedure assumes that the value of q at the boundary region is the same as that well inside the Q.E. region.

(13.3) COMPARISON OF COMPUTED AND EXPERIMENTAL RESULTS FOR $\overline{n(1)} = 10^{16}$ AND $3.\ 10^{16}\ cm^{-3}$.

At high gas pressures and low electron densities, the plots of p/τ versus p shown in figs. (11.17) to (11.27) can be seen to be non-linear. This non-linear relationship indicates that the experimental recombination time is a function of $\overline{n(1)}$ as well as n_o. Hence a comparison of theory with experiment requires that the experimental value of $\tau_R(n_o, \overline{n(1)})$ be compared with the computed values of τ_R $(q, n_o, \overline{n(1)})$ given in section (12.9.2).

The value of τ_R $(n_o, \overline{n(1)})$ cannot be obtained from the gradient of the p/τ versus p plots in the non-linear regime since from equation (11.6)

$$\frac{d}{dp}\left[p/\tau\right] = (\tau_R)^{-1} \text{ only when } \tau_R \text{ is independent of p or } \overline{n(1)}$$

Instead, the values of the term $(D_a.p\ /\ \Lambda_o^2)$ found for a fixed value of n_o from the intercepts at the $p = o$ axis shown in figs. (11.17) to (11.27) were taken to be representative of the plasma diffusion that occurred for all values of $\overline{n(1)}$, so that the experimental values of τ_R, were obtained from the modified version of equation (11.6) given below

$$\frac{1}{\tau_R} = \frac{1}{\tau} - \left[\frac{D_a.p}{\Lambda_o^2}\right].\frac{1}{p} \qquad (13.1)$$

where τ = plasma decay time measured at the gas pressure p.

Values of τ_R found using equation (13.1) for the rare gas decays where $\overline{n(1)} = 10^{16}$ cm^{-3} (p = 300 m.torr) and $\overline{n(1)} = 3.\ 10^{16}$ cm^{-3} (p = 1 torr) are listed in table (13.2). The corrections to the measured decay times due to diffusion at these atom densities were typically 10% and 3% respectively, and so, the errors involved in neglecting the variation of the term $(D_a.p\ /\ \Lambda_o^{\ 2})$ with $\overline{n(1)}$, via the dependence of T_{eo} on $\overline{n(1)}$, are negligible. The values of the quantity q $(n_o, \overline{n(1)})$ obtained from a comparison of τ_R $(n_o, \overline{n(1)})$ with the computed results of section (12.9.2) are also listed in table (13.2).

(13.4) COMMENTS ON TABLES (13.1) AND (13.2)

The following comments are made with regard to the results presented in tables (13.1) and (13.2).

1. In all cases for $n_o \geqslant 10^{15}$ cm^{-3}, the value of the factor q can be seen to be close to unity indicating that, for this plasma condition, most of the recombination energy is retained within the plasma.

2. The variations of the factor q with electron density for each set of results are shown graphically in figs. (13.1) to (13.4). Comparison of these plots of q versus n_o shows that, with decreasing n_o, the factor q falls much more rapidly in neon plasmas than in helium plasmas. The behaviours of q with n_o in argon and krypton plasmas are closely similar and are intermediate

TABLE (13.2)

n_o (cm^{-3})	$\overline{n(1)} = 10^{16}$ cm^{-3}		$\overline{n(1)} = 3.\ 10^{16}$ cm^{-3}	
	τ_R (μ.sec)	q	τ_R (μ.sec)	q
HELIUM	LARGE	TORUS		
10^{15}	112	1.0	146	1.0
$3\ 10^{14}$	112	1.0	146	1.0
10^{14}	133	0.95	174	0.95
$3\ 10^{13}$	154	0.60	220	0.65
10^{13}	205	0.40	330	0.50
HELIUM	SMALL	TORUS		
$2\ 10^{15}$	67	1.0	68	1.0
10^{15}	66	1.0	73	1.0
$3\ 10^{14}$	68	1.0	80	0.95
10^{14}	78	0.80	87	0.78
$3\ 10^{13}$	75	0.40	94	0.38
10^{13}	81	0.18	108	0.14
NEON	LARGE	TORUS		
10^{15}	200	0.70	280	0.85
$3\ 10^{14}$	200	0.55	280	0.60
10^{14}	190	0.30	280	0.28
$3\ 10^{13}$	230	0.18	300	0.18
10^{13}	300	0.10	540	0.10

TABLE (13.2) CONTINUED

n_o (cm^{-3})	$\overline{n(1)} = 10^{16}$ cm^{-3}		$\overline{n(1)} = 3.\ 10^{16}$ cm^{-3}	
	τ_R (μ.sec)	q	τ_R (μ.sec)	q
NEON	SMALL	TORUS		
$2\ 10^{15}$	116	1.0	146	1.0
10^{15}	116	0.8	146	0.85
$3\ 10^{14}$	102	0.5	145	0.60
10^{14}	106	0.25	154	0.30
$3\ 10^{13}$	114	0.10	170	0.10
10^{13}	150	0.07	200	0.08
ARGON	LARGE	TORUS		
10^{15}	400	1.0	490	1.0
$3\ 10^{14}$	400	0.70	490	0.60
10^{14}	390	0.40	470	0.30
$3\ 10^{13}$	610	0.35	830	0.25
10^{13}	820	0.19	1190	0.14
ARGON	SMALL	TORUS		
$2\ 10^{15}$	240	1.0	300	1.0
10^{15}	240	1.0	270	1.0
$3\ 10^{14}$	230	0.45	270	0.40
10^{14}	230	0.25	400	0.27
$3\ 10^{13}$	250	0.13	490	0.16
10^{13}	330	0.08	600	0.10

TABLE (13.2) CONTINUED

n_o (cm^{-3})	$\overline{n(1)} = 10^{16}$ cm^{-3}		$\overline{n(1)} = 3.10^{16}$ cm^{-3}	
	τ_R (μ.sec)	q	τ_R (μ.sec)	q
KRYPTON	LARGE	TORUS		
10^{15}	610	1.0	870	1.0
$3\ 10^{14}$	610	0.68	870	0.67
10^{14}	710	0.42	840	0.23
$3\ 10^{13}$	1010	0.28	1250	0.15
10^{13}	1500	0.18	1820	0.10
KRYPTON	SMALL	TORUS		
$2\ 10^{15}$	400	1.0	490	1.0
10^{15}	400	1.0	490	1.0
$3\ 10^{14}$	440	0.80	540	0.90
10^{14}	500	0.55	640	0.60
$3\ 10^{13}$	630	0.35	930	0.40
10^{13}	900	0.13	1220	0.12

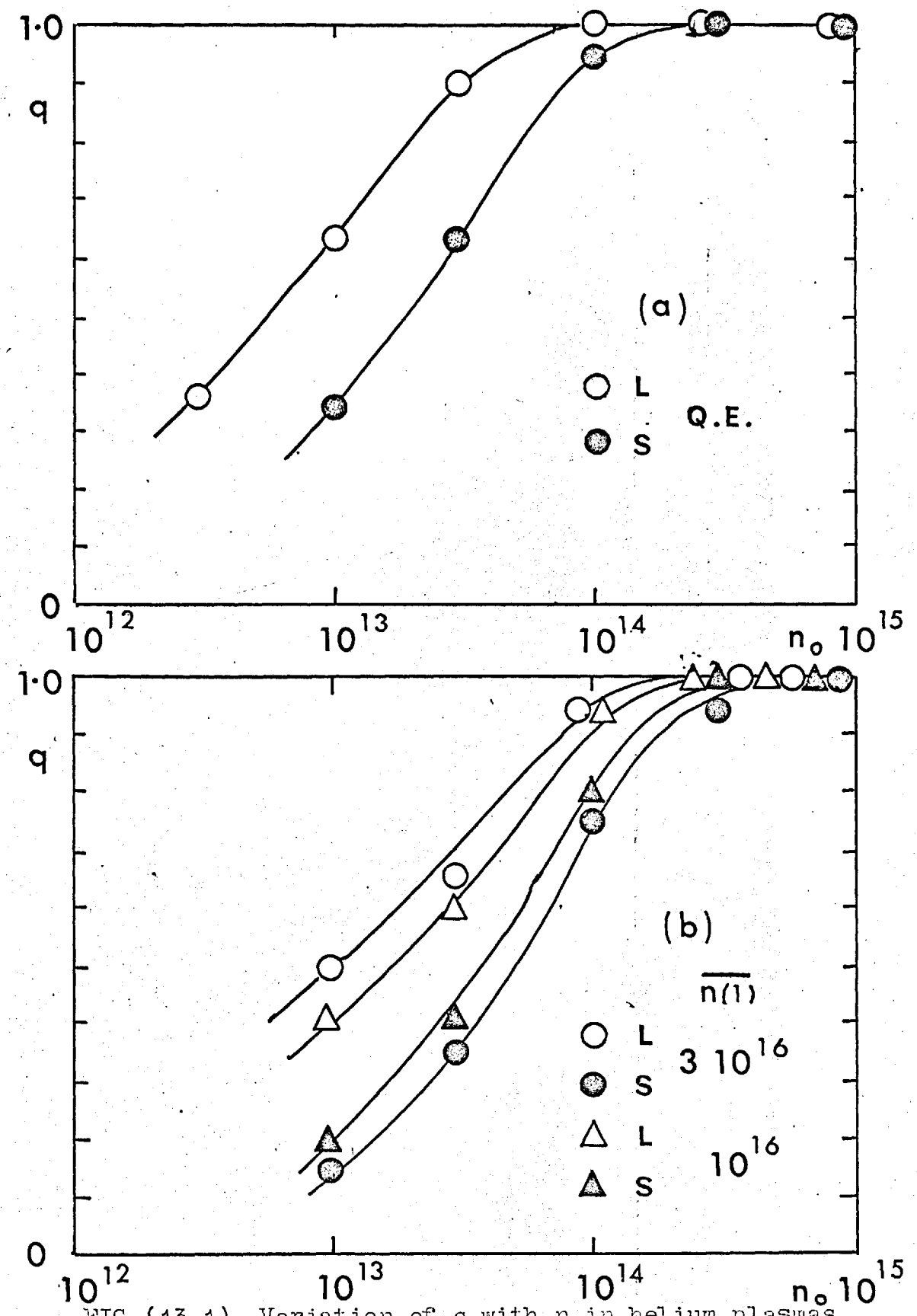

FIG (13.1) Variation of q with n in helium plasmas (a) Q.E. case (b) $\overline{n(1)} = 10^{16}$ and $3\ 10^{16}$ cm^{-3}.

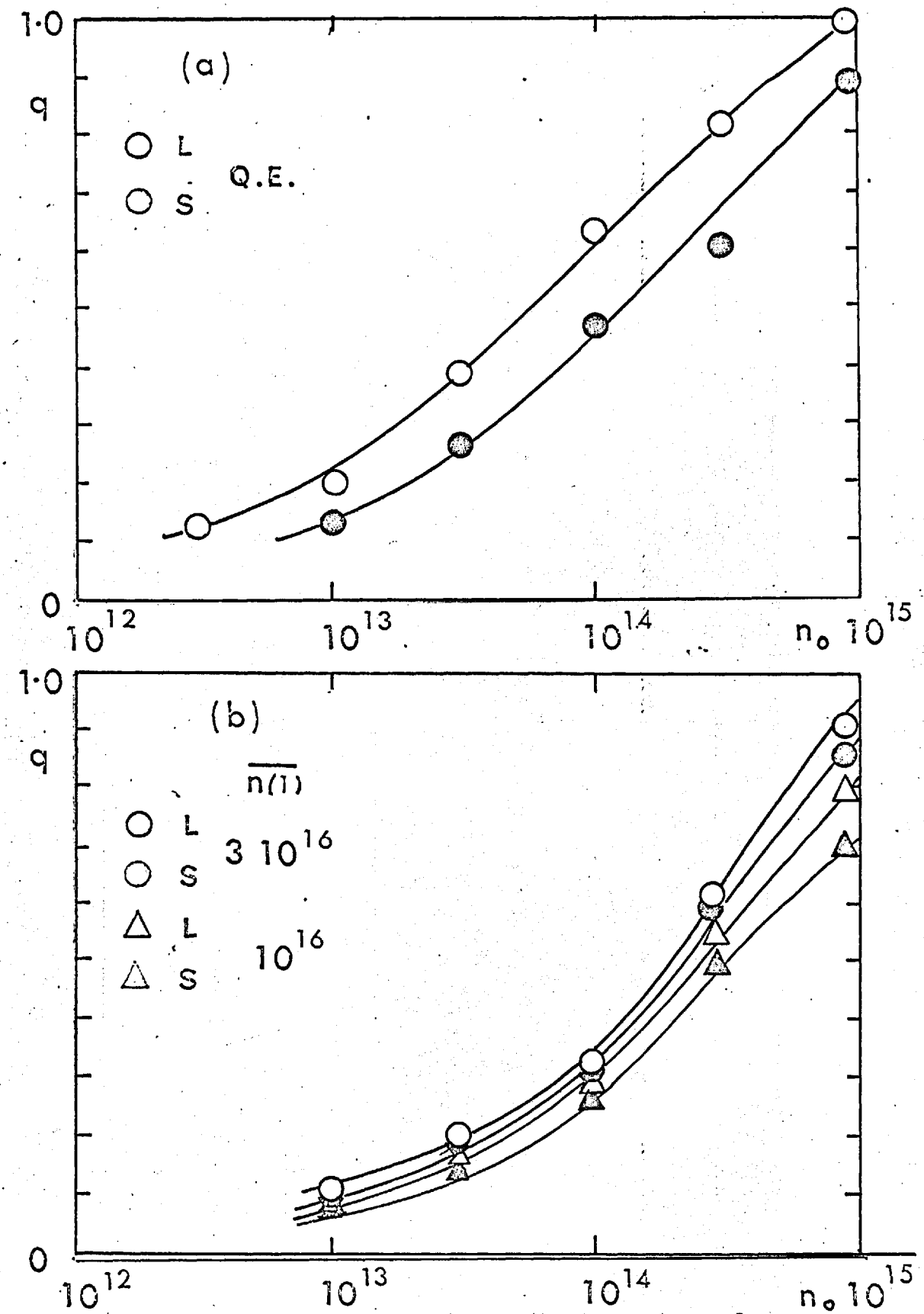

FIG (13.2) Variation of q with n in neon plasmas
(a) Q.E. case (b) $\overline{n(1)} = 10^{16}$ and $3\ 10^{16}$ cm^{-3}

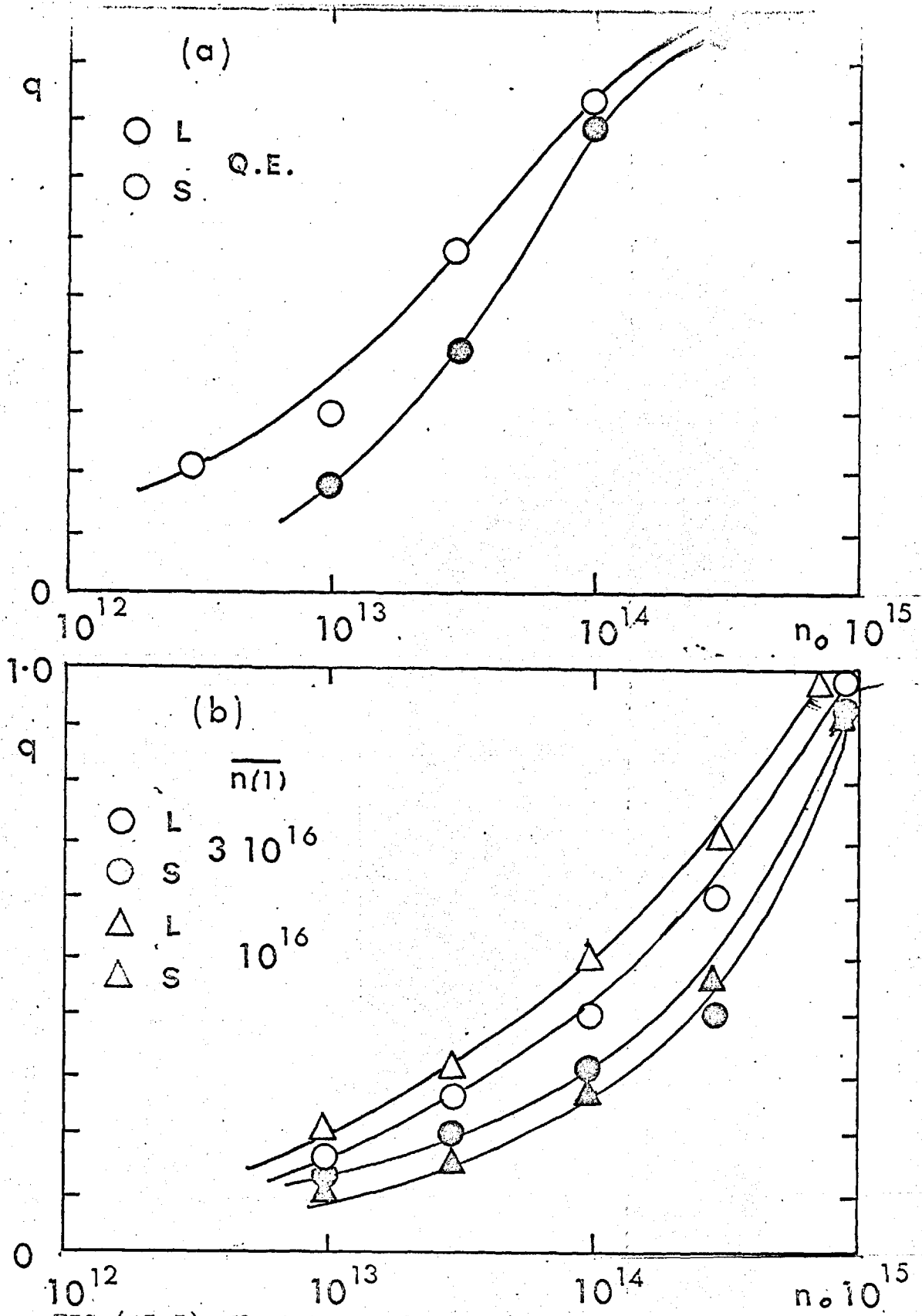

FIG (13.3) Variation of q with n in argon plasmas (a) Q.E. case (b) $\overline{n(1)} = 10^{16}$ and $3\ 10^{16}$ cm^{-3}

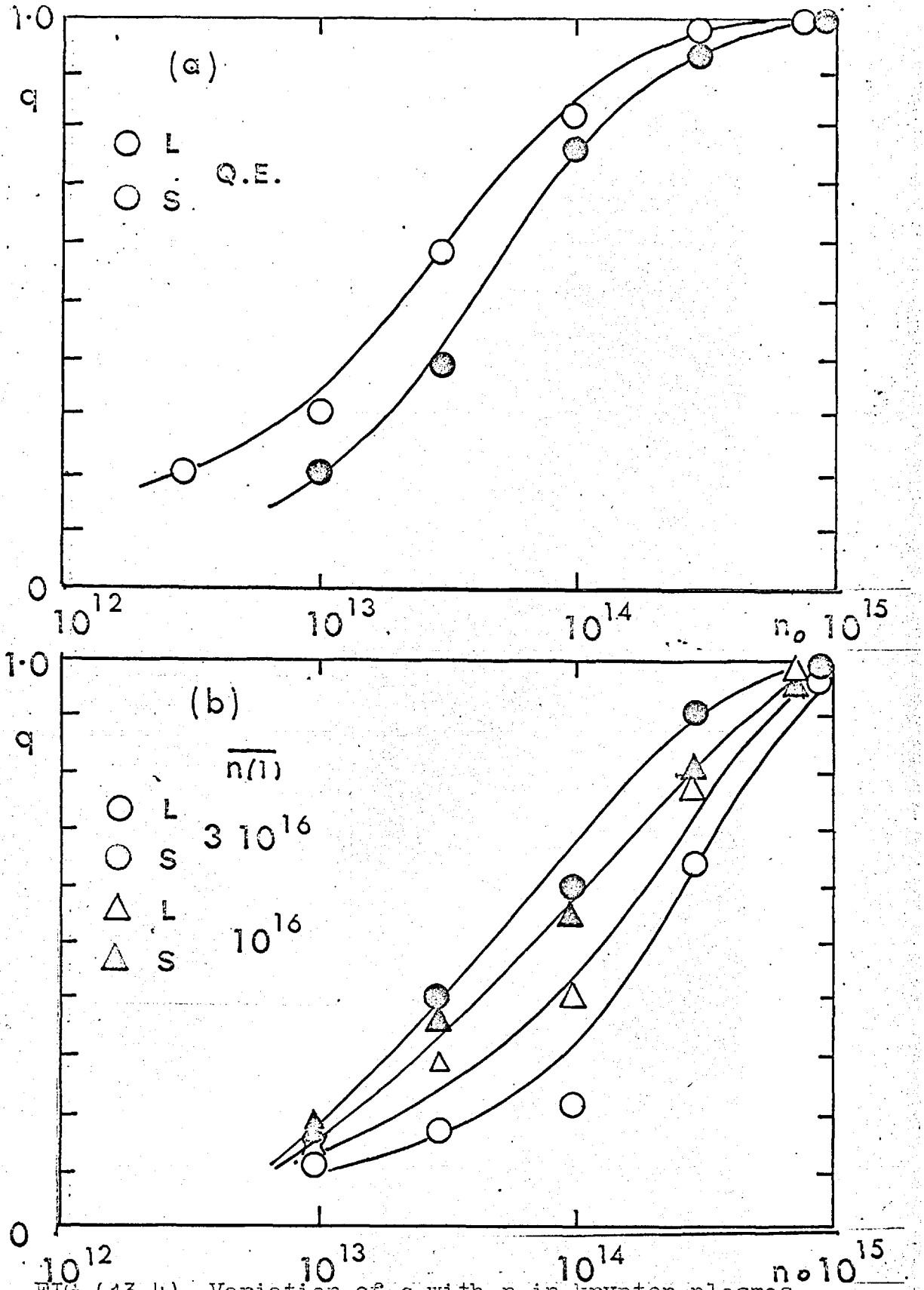

FIG (13.4) Variation of q with n in krypton plasmas.
(a) Q.E. case (b) $\overline{n(1)}$ = 10^{16} and 3 10^{16} cm^{-3}

between the cases of neon and helium plasmas.

3. With the exception of decays in krypton at high gas pressures, the values of the factor q, at fixed values of n_o, $\overline{n(1)}$ and the type of gas, are higher for the large torus results than for the small torus results.

4. The values of q (n_o) given in table (13.1) are systematically slightly larger than the values of q (n_o), corresponding to the same gas and torus size, given in table (13.2). This small variation is probably due to the approximations inherent in the Q.E. limiting case that are discussed in section (12.9.2). These approximations would in fact lead to an overestimation of the value of q (n_o) when the particle latent heat term in the real plasma is not completely negligible.

5. In table (13.2), the values of the factor q (n_o) are only marginally higher for $\overline{n(1)} = 3\ 10^{16}$ cm^{-3} than for $\overline{n(1)} = 10^{16}$ cm^{-3}. The closeness of corresponding values of q at these different atom densities would seem to suggest that the factor q is not a strongly dependent function of $\overline{n(1)}$.

(13.5) THE FACTOR q.

A detailed examination of the physical processes inherent in the factor q is now presented. Recalling the definition of q from equation (12.19).

$$q = \frac{\text{Energy retained by the Plasma Electrons per Ion Recombined}}{\text{Ionisation Energy of the Atom}}$$

The recombination energy retained by the electron gas arises from collisions between the plasma electrons and the excited atoms. The work of Byron et al. (78) discussed in section(9.11)

has shown that the populations of the energy levels of the atom between the crossing quantum number p_c and the continuum limit are primarily determined by collisional processes. Hence, we can assume that for every ion recombined, the plasma electrons always carry away an amount of energy equal to the energy gap between p_c and the continuum limit. The work of Makin and Keck discussed in section (9.12) has shown that the value of this energy gap is typically $5/2\ k\ T_e$, and so we can put a minimum value on the factor q

$$q\ (\text{minimum}) = \frac{5\ k\ T_e}{2\ I} \qquad (13.2)$$

The values of the ionisation energy I for hydrogen and the rare gases are so large (13.6 to 24.5 e.v.) that even for electron temperatures as high as 20,000°K we only obtain from equation (13.2) values for q between 0.1 and 0.2. In order to obtain larger values of q, (around unity for dense plasmas), we require that collisional de-excitation of some of the levels below p_c should be appreciable. In particular, since the energy gaps between the excited levels and the ground state in hydrogen and the rare gases are such large fractions of the total ionisation energy, a large value of q requires that the population densities of some of the first few excited levels in the atom must be considerably larger than those predicted by the collisional excitation $\rightleftharpoons$ radiative de-excitation equilibrium situation. Excited state populations for the lower levels which are enhanced above these particular equilibrium population values can arise in decaying plasmas in two ways.

1. Certain of the first excited states of the atom may be metastable states because the selection rules prevent radiative transitions to the ground state of the atom. The presence of

metastable states are well known in the rare gases.

2. For allowed radiative transitions to the ground state, the emitted quantum of radiation may be absorbed by a nearby ground state atom before it escapes from the plasma. This phenomena can be treated using the theory of radiation trapping in a plasma and concept of the plasma optical depth.

Both the processes outlined above will be considered below in detail with particular emphasis on the numerical evaluation of the factor q in a decaying plasma with changing plasma conditions.

(13.6) METASTABLE ATOM PRODUCTION AND DESTRUCTION IN DECAYING PLASMAS.

For the rare gases, the selection rules of radiative transitions produce metastable energy levels. The lifetimes of atoms in metastable states in decaying plasmas have been studied by several workers (107) (108) (109). The metastable levels in helium are the $2\,^3S_1$ and $2\,^3S_0$ levels, and in the other rare gases, the metastable levels are the $^3P_2$ and $^3P_0$ levels associated with the first excited state. The most likely processes by which atoms in metastable states are destroyed in decaying plasmas can be summarised:

1. Diffusion of the metastable atoms to the walls of the discharge tube followed by de-excitation at the walls.

2. Two body collisions with other plasma particles leading to excitation to an allowed radiating state.

3. Two body collisions with an electron in the form of a superelastic collision where the electron carries away the excitation energy of the metastable state.

4. Collisions between a pair of metastable atoms leading to the ionisation of one atom and the de-excitation of the other.

For helium plasmas, the lowest state that can radiate to the ground state is 1.4 e.v. above the 2^3S_1 state and so metastable atom destruction by process 2. is only likely to occur in hot plasmas. Byron et al (78) have shown that process 2. is a more probable path for destruction than process 3. only for electron temperatures $> 2000^{\circ}K$. The diffusion of helium metastable atoms has been discussed by Phelps and Molnar (107) and Kuckes et al. (85) and the latter authors have tentatively suggested that process 3. could account for the retention of recombination energy in the plasma.

For both argon and neon, the lowest states that can radiate to the ground states are only 0.1 e.v. above the lowest metastable states. Thus, destruction of the metastable atoms by process 2. can readily occur in afterglow plasmas via collisions that involve changes in energy that are less than the kinetic energy of the plasma particles.

Summarising the above statements, it appears that the superelastic collisions of process 3., which would lead to a large value of the factor q, are only possible in low temperature helium plasma decays where metastable atom diffusion to the walls is small.

(13.7) RADIATION TRAPPING IN A DECAYING PLASMA

The interaction of radiation produced inside a plasma with the surrounding plasma was first studied by Zemansky (110). The theory of radiation trapping is usually concerned with

transitions from the excited levels to the ground state: the so-called 'resonance' lines. The total reabsorption of the resonance lines in decaying hydrogen and rare gas plasmas could account for more than 75% of the recombination energy of the newly formed atoms being retained within the plasma.

Mitchell and Zemansky (111) in a classic book have discussed the forms of the absorption coefficient $k(\nu)$ for resonance radiation for the cases of natural, Doppler and pressure broadening of the line profiles. They have also derived simple expressions for the total amount of absorption of radiation occuring in a finite size plasma. Holstein (112) (113) has used Mitchell and Zemansky's expressions for $k(\nu)$ in considering the transport of quanta through a plasma, with a large number of repeated absorptions and emissions, in terms of a Boltzmann type integro-differential equation. He has derived expressions, in different geometries, for an 'escape factor' g, which is a dimensionless quantity equivalent to the number of absorptions and emissions experienced by an individual photon prior to its escape from the plasma. Walsh (114), following the theory of Holstein, has derived expressions for the density of resonance atoms and the imprisonment lifetime of resonance radiation for a parallel plate geometry plasma. Two approximate solutions have been given according to whether the electronic de-excitation rate of the resonance state is much smaller or larger than the imprisonment time of the photon. Hearn (115) has studied the radiative transfer of Doppler broadened resonance lines in a plasma, not in L.T.E., in terms of a two level atomic model and he has applied his results to Lyman α radiation.

For the plasma conditions existing in afterglows, we would expect Doppler broadening of the line profiles to be the dominant

line broadening mechanism. In Appendix (A.7), most of the above work is considered with regard to obtaining suitable analytical expressions for the plasma optical depth, the escape factor g and the absorption coefficient k_o in decaying hydrogen and rare gas plasmas. A first class review of the effects of radiation trapping in plasmas has already been given by McWhirter (125).

(13.8) BATES AND KINGSTON'S INCORPORATION OF RADIATION TRAPPING INTO THE C.R. MODEL

The incorporation of radiation trapping into the C.R. plasma model as performed by Bates and Kingston (74) has already been discussed in section (12.2). The very simple approximation was adopted that, when the plasma was optically thick towards certain lines, the corresponding transition probability was set equal to zero. Here, we discuss the results of this very simple procedure applied to a hydrogen plasma.

Bates and Kingston considered two cases: (a) the plasma optically thin towards all radiation, (b) the plasma optically thick towards Lyman α radiation. A quantity Λ was calculated for cases (a) and (b) where

$$\Lambda = 1 - \frac{P}{\alpha n^2 I} \qquad (13.4)$$

where P = nett power radiated by the plasma.

The quantity Λ defined by equation (13.4) can be seen to be identical with our quantity q defined by equation (12.19). Plots of the values of Λ for case (a) and case (b) plasmas are reproduced from (74) and shown in fig. (13.5) for fixed electron temperatures of 250, 1000, 4000 and 16000°K.

The following remarks are made about these results and their method of calculation:

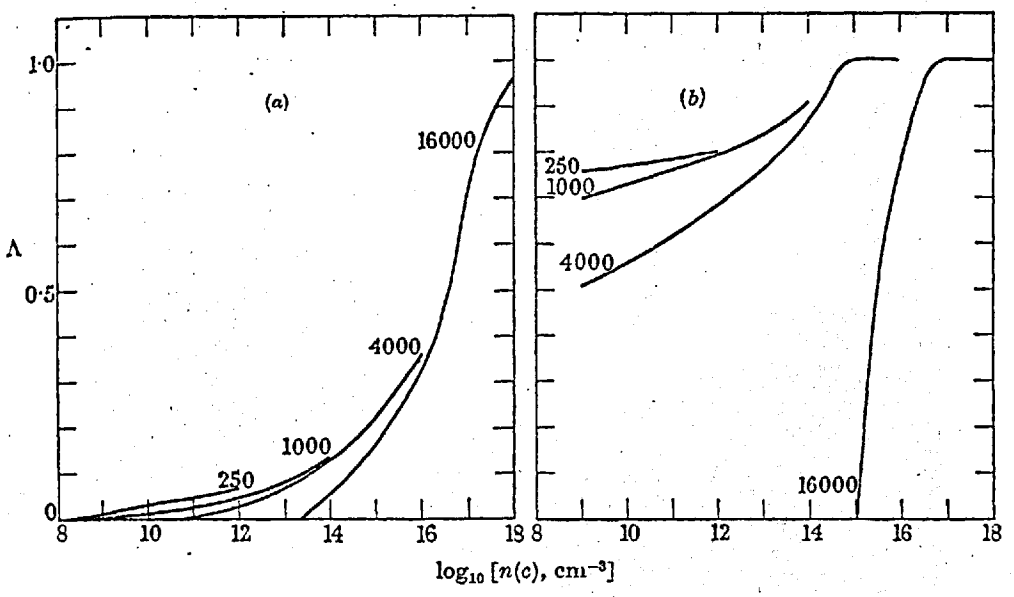

Ratio Λ of net rate at which decaying H—H⁺—e plasma gains thermal energy by collisions to net rate at which electronic energy is released by recombination: (*a*) optically thin (case i) plasma, (*b*) optically thick (case ii) plasma. The electron temperature in degrees K is indicated on each curve

FIG. (13.5)

1. There appears to be general agreement between the calculated values of Λ shown in fig. (13.5) and the values of q shown in figs. (13.1) to (13.4).

2. The assumption of infinite optical depth for the resonance line made by Bates and Kingston in their case (b) is only valid in cold dense plasmas. In high density, high temperature afterglows, the plasma is only marginally optically thick towards the resonance lines and, for these conditions, q or Λ will lie somewhere between the values of cases (a) and (b).

3. Bates and Kingston have only performed calculations for hydrogen and helium plasmas.

(13.9) GENERAL TREATMENT OF RADIATION TRAPPING IN THE C.R. PLASMA MODEL.

We develop in this section a theory for the incorporation of radiation trapping into the C.R. plasma model which takes full account of variations in the optical depth of the resonance lines with changing plasma conditions. The theory presented is aimed at finding an analytical expression for the factor q, which can be applied to high density, high temperature plasma decays in hydrogen and the rare gases.

The variation of optical depth for each radiative transition in a plasma can be simply incorporated into the C.R. model, discussed in section (9.6), by multiplying each transition probability $A(p,q)$ by its appropriate Holstein escape factor $g(\overline{\delta_{pq}})$ defined by equation (A.7.8). Thus, for a plasma which has a finite optical depth to all transitions directly into the atom ground state and a zero optical depth to all other transitions, the terms involving transition probability in equation (9.14), (describing the population rate of the pth bound level), are modified as follows:

The term $+ \sum_{q \neq p} n(q)\, A(q,p)$ in equation (9.14) is modified to become

$$+ \sum_{\substack{q \neq p \\ p \neq 1}} n(q)\, A(q,p) \quad + \quad \sum_{q \neq 1} n(q).g(\overline{\delta_{q1}}).A(q,1) \qquad (13.5)$$

and the term $- n(p) \sum_{p \neq q} A(p,q)$ in equation (9.14) is modified to become

$$-n(p)\sum_{\substack{p\neq q \\ q\neq 1}} A(p,q) \quad - \quad n(p).g(\overline{\delta_{p1}}).A(p,1) \qquad (13.6)$$

The solution of the complete set of population rate equations like equation (9.14) when modified as described above presents fearsome difficulties, (hence Bates and Kingston's assumption of putting $g(\delta) = 0$ for the resonance lines and $g(\delta) = 1$ for the other lines). However, we will show that it is not necessary to solve the complete set of population rate equations in order to find the factor $q\ (n,\ n(1),\ T_e)$ appropriate to decaying plasmas possessing medium to large optical depths towards the resonance lines. The factor $q\ (n,\ n(1),\ T_e)$ can be found with reasonable accuracy, whilst retaining the variable escape factors for the resonance transitions, on the following basis.

1. We first consider the total nett power P radiated from the decaying plasma, in terms of the sum of the following contributions:

$$P = P_{BB} + P_{FB} + P_{FF}$$

where P_{BB} = contribution from bound-bound transitions

P_{FB} = contribution from free-bound transitions

P_{FF} = contribution from free-free transitions

Detailed calculations of all these contributions to the power radiated from hydrogen plasmas have been performed by Bates and Kingston (120) who have shown that:

For optically thin plasma

$$P_{BB} \gg P_{FB} \quad \text{or} \quad P_{FF} \tag{13.8}$$

For plasma optically thick towards the resonance lines

$$\left.\begin{aligned} P_{BB} &\gg P_{FB} \quad \text{for} \quad T_e < 10{,}000^{\circ}K \\ P_{BB} &\sim P_{FB} \quad \text{for} \quad T_e > 10{,}000^{\circ}K \\ P_{BB} &\gg P_{FF} \quad \text{always} \end{aligned}\right\} \tag{13.9}$$

Hence, except for the very early stages of high density plasma decay when $T > 10{,}000^{\circ}K$ we can assume that bound-bound transitions in hydrogen plasmas make the dominant contribution to the nett power radiated by the plasma. For the cases of the rare gases, especially argon, the much larger number of bound-bound transitions should make the above approximation even more valid.

2. The nett power radiated from the plasma due to bound-bound transitions is written as

$$P_{BB} = \sum_{p>q}^{\infty} \sum_{q=1}^{\infty} n(p)\, g\, (\overline{\delta pq})\, A_{p,q}\, E_{pq} \tag{13.10}$$

and from equation (13.4) we can therefore write the factor $q\,(n, n(1)\, T_e)$ in the form

$$q\,(n, n(1), T_e) = 1 - \frac{P_{BB}}{a\, n^2\, I} \tag{13.11}$$

From equations (13.10) and (13.11) it can be seen that the value of the factor $q\,(n, n(1), T_e)$ depends almost entirely upon the trapping of resonance radiation within the plasma for the

cases of hydrogen and the rare gases. This situation arises in these gases because transitions to the ground state involve more than 3/4 of the total ionisation energy of the atom, and we can write

$$q\,(n,\, n(1),\, T_e) = 1 - \frac{\sum_{p>1} n(p)\, g(\overline{\delta_{p1}})\, A(p,1) E_{p1}}{\alpha\, n^2\, I} \qquad (13.12)$$

3. Expression (13.12) is capable of being simplified even further. We note that:

$A(p,1)$ is a rapidly decreasing function with increasing p.

E_{p1} is a very slightly increasing function with increasing p.

and for optically thin plasmas

$$n(2) > n(p) \qquad p \geqslant 3$$

and for plasmas possessing large optical depths for the resonance lines the fact that level 2 cannot radiate via an optically thin transition, whereas for levels $p \geqslant 3$ optically thin transitions are possible, means that

$$n(2) \gg n(p) \qquad p \geqslant 3$$

Therefore in both optically thin and optically thick plasmas, we see that the term

$$n(2)\, g\,(\overline{\delta_{21}})\, A_{21}\, E_{12}$$

makes the major contribution to the value of the summation in equation (13.12) and to a first approximation we can write

$$q\,(n,\, n(1),\, T_e) \approx 1 - \frac{n(2)\, g(\delta_{21})\, A_{21}\, E_{12}}{\alpha\, n^2\, I} \qquad (13.13)$$

4. In section (13.5), consideration of electron collisions with the upper L.T.E. populated bound levels gave a minimum value

for q of

$$q = \frac{5}{2I} k T_e$$

This contribution to the factor q can be incorporated into a modified version of equation (13.13) where we write

$$q(n, n(1), T_e) \approx \frac{5 k T_e}{2 I} + \frac{E_{12}}{I} \left[1 - \frac{n(2)\, g(\overline{\delta_{21}})\, A_{21}}{\alpha n^2} \right] \qquad (13.14)$$

The two terms of the R.H.S. of equation (13.14) represent the contributions to q from electron collisions with the upper bound levels above the crossing quantum number p_c and with the first excited level only. Thus, in this first approximation to the value of q, the effects of electron collisions with the bound levels whose principal quantum numbers lie between

$$p_c > p > 3 \qquad (13.15)$$

have been neglected.

(13.9.1) Calculation of the First Excited Level Population Density n(2).

The population density n(2) of the first excited level, in a form that is suitable for substituting into equation (13.14), is given by equation (9.14), modified according to (13.5) and (13.6), as

$$\frac{dn(2)}{dt} = n \sum_{p \neq 2}^{\infty} n(p).\, K(p,2) - n.n(2) \sum_{p \neq 2}^{\infty} K(2,p)$$

$$+ \sum_{p \geq 3}^{\infty} n(p).A(p,2) - n(2).g(\overline{\delta_{21}}).A_{21}$$

+ terms expressing the nett recombination rate directly into level 2 (13.16)

Except for very cold dense plasmas, which lie outside typical afterglow conditions, we have the situation where according to (72)

$$n(2) \ll n \tag{13.17}$$

so that n(2) rapidly reaches a quasi-equilibrium value given by setting the L.H.S. of equation (13.16) equal to zero.

For plasmas which have medium to large values of optical depths for the resonance lines, we have the conditions where

$$\left.\begin{aligned} n(1) &\gg n(p) \\ n(2) &\gg n(p) \end{aligned}\right\} \; p \geq 3 \tag{13.18}$$

As a consequence of (13.18) we will assume that excitation of the ground state atoms by electron impact forms the major part of the collisional populating summation in equation (13.16).

ie. $$n \sum_{p \neq 2}^{\infty} n(p)\, K(p,2) \approx n\, n(1)\, K(1,2) \tag{13.19}$$

Also, since level 2 lies well below the crossing quantum number p_c, we will assume that the rate of population of level 2 due to downward radiative transitions plus the terms expressing the nett recombination directly into level 2 simply equals the nett recombination rate of the plasma.

$$\text{ie.} \quad \sum_{p \neq 3}^{\infty} n(p)\, A(p, 2) + \begin{array}{l}\text{recombination}\\ \text{directly into}\\ \text{level 2}\end{array} = \alpha\, n^2 \qquad (13.20)$$

Using approximations (13.19) and (13.20) in equation (13.16), we can write the quasi-equilibrium population density of level 2 = $n_Q(2)$ as

$$n_Q(2) = \frac{n\, n(1)\, K(1, 2) + \alpha\, n^2}{n \sum_{p \neq 2} K(2, p) + g(\delta_{21})\, A_{21}} \qquad (13.21)$$

In the optically thick limit where $g(\delta_{21})$ goes to zero, we obtain the expression for the optically thick quasi-equilibrium population density of level 2 = $n_E(2)$ as

$$n_E(2) = \frac{n(1)\, K(1, 2) + \alpha\, n}{\sum_{p \neq 2} K(2, p)} \qquad (13.22)$$

The form of equation (13.22) can be seen intuitively to be correct, since $n_E(2)$ is determined solely by the ratio of the dominant collisional populating and depopulating terms.

Combining equations (13.21) and (13.22) we can re-write $n_Q(2)$ in terms of $n_E(2)$ as

$$n_Q(2) = \frac{n_E(2)}{1 + \dfrac{n_E(2)\, g(\delta_{21})\, A_{21}}{\alpha\, n^2 + n\, n(1)\, K(1, 2)}} \qquad (13.23)$$

The substitution of the value of level 2 population density given by equation (13.23) into the equation (13.14) yields an expression for the factor $q(n, n(1), T_e)$ of the form

$$q\,(n,\, n(1),\, T_e) = \frac{5\,k\,T_e}{2\,I} + \frac{E_{12}}{I}\left[\,1 - (\Phi + \Psi)^{-1}\,\right] \qquad (13.24)$$

where $$\Phi = \frac{\alpha\, n}{\alpha\, n \;+\; n(1)\, K\,(1,\, 2)} \qquad (13.25)$$

$$\Psi = \frac{\alpha\, n^2}{n_E(2)\; g\,(\overline{\delta_{21}})\; A_{21}} \qquad (13.26)$$

The numerical evaluation of the quantities Φ and Ψ defined by equations (13.25) and (13.26) will now be discussed.

(13.9.2) Evaluation of the Quantity Φ

We require suitable forms for α and $K(1, 2)$ for substitution into equation (13.25). The recombination coefficient α is taken to be that given by equation (9.26) for C.R. plasma recombination. Allen (116) has worked out the cross-section for atomic excitation due to collisional impact by electrons having a Maxwellian velocity distribution. Using Allen's cross-sections, Hamberger (117) has shown that the rate coefficient $K\,(p,\, q)$ for collisional excitation from level p to level q has the form

$$K\,(p,\, q) = 1.30\;\; 10^{-5}\; f_{pq}\; \frac{k\,T_e}{(E_{pq})^2}\;\; \exp\left[-\frac{E_{pq}}{k\,T_e}\right] \qquad (13.27)$$

where f_{pq} = absorption oscillator strength for the transition

E_{pq} = excitation energy in e.v.

$k\,T_e \ll E_{pq}$

Using equation (13.27), the rate coefficient $K\,(1,\, 2)$ for

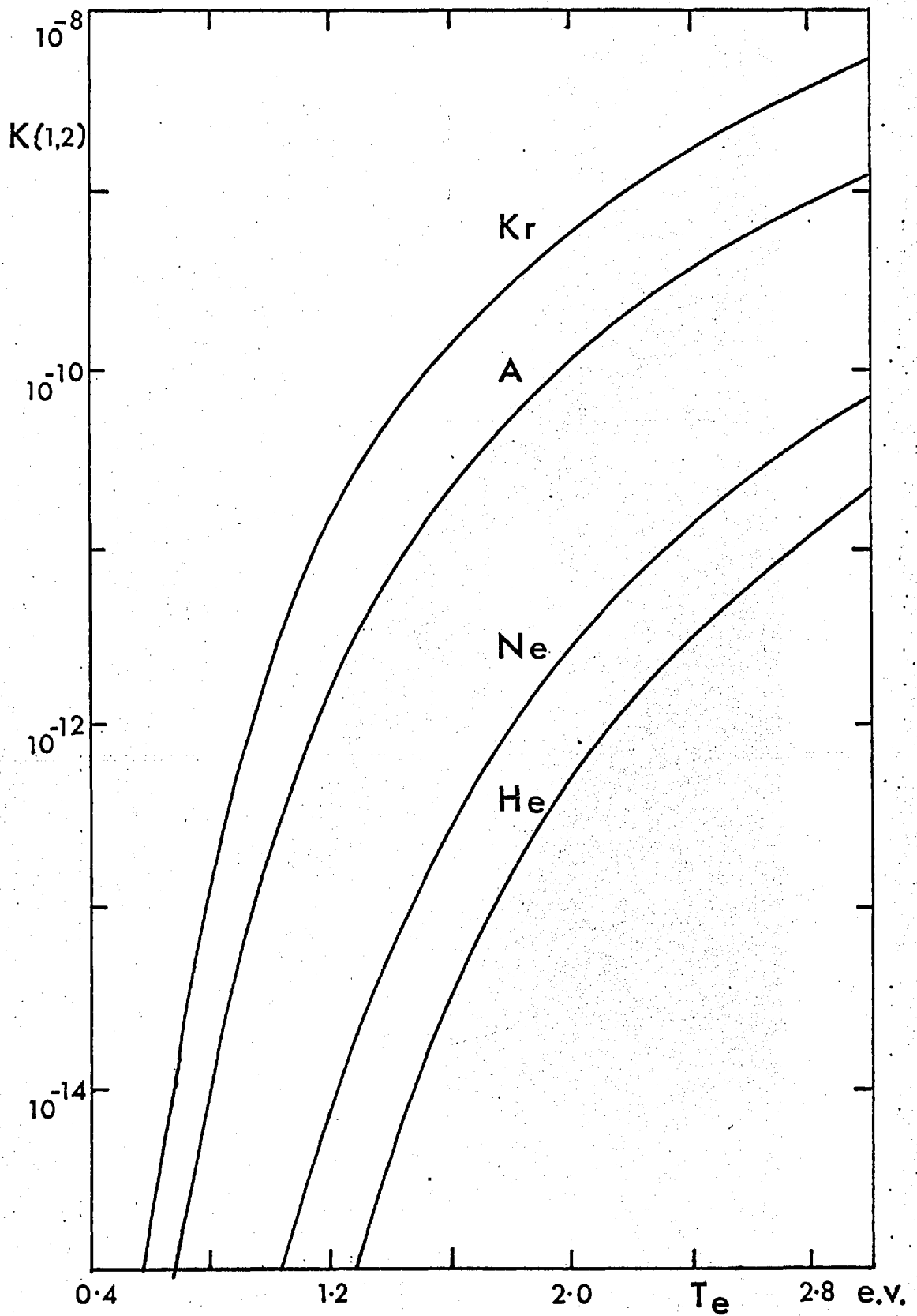

FIG (13.6) Collisional excitation rate coefficients K(1,2) for the rare gases.

collisional excitation from the atom ground state to the first excited state has been plotted as a function of T_e for the rare gases as shown in fig. (13.6).

The values of α given by equation (9.26) for decaying plasma conditions lie between the limits

$$10^{-12} < \alpha < 10^{-9} \quad \text{cm.}^3 \text{ sec.}^{-1} \qquad (13.28)$$

Hence from fig. (13.6) we can see that for highly ionised rare gas plasma decay

$$\left.\begin{aligned} \alpha\, n &>> n(1).K(1,2) \quad \text{for } T_e < 10{,}000^\circ\text{K} \\ \alpha\, n &\sim n(1).K(1,2) \quad \text{for } T_e > 10{,}000^\circ\text{K} \end{aligned}\right\} \qquad (13.29)$$

Hence at low temperatures the value of Φ given by equation (13.25) is very close to unity, whilst at high temperatures Φ is usually $<< 1$. If at high temperatures we also have a value for $\Psi << 1$, then from equation (13.24) negative values for the factor q are predicted. In physical terms, this latter situation corresponds to collisional excitation from the atom g.s. (small Φ in equation (13.25)) followed by radiative transition back to the atom g.s. (small Ψ in equation (13.26)) leading to a cooling of the plasma. In real plasmas, negative values for the factor q can only arise in the presence of external sources of heat. In plasma afterglows (no external sources of heat) the plasma conditions automatically adjust themselves so as to maintain a positive value of the factor q.

Since for most of the plasma decay region studied in our experiment the quasi-equilibrium values of T_e were $< 10{,}000^\circ$K, we will take the value of Φ to be

$$\Phi \approx 1.0 \qquad (13.30)$$

(13.9.3) Evaluation of the Quantity Ψ

From equation (13.26) defining Ψ , we require suitable expressions for the quantities $g(\overline{\delta_{21}})$ and $n_E(2)$. The Holstein escape factor $g(\overline{\delta_{21}})$ has been discussed in Appendix (A.7). The average optical depth $\overline{\delta_{21}}$ for the resonance line in a cylindrical plasma of radius a is given by

$$\overline{\delta_{21}} = k_{21}\, a \qquad (13.31)$$

where k_{21} = absorption coefficient for the line.

In afterglow plasmas, line profiles are usually determined by Doppler broadening and the expression for the absorption coefficient in this case is given by equation (A.7.15) as

$$k_{21} = \left[\frac{\pi e^2}{(2\pi k)^{\frac{1}{2}} m c}\right]\left[\frac{M}{T}\right]^{\frac{1}{2}} n(1)\ \lambda_{12}\, f_{12} \qquad (13.32)$$

Numerical values for k_{21} for the resonance lines in the rare gases are listed in table (13.3)

TABLE (13.3)

gas	k_{21} (c.g.s. units of $n(1)\ T^{-\frac{1}{2}}$)
He	$3.76\ 10^{-12}$
Ne	$4.64\ 10^{-12}$
A	$1.55\ 10^{-11}$
Kr	$4.50\ 10^{-11}$

In our experiment, we encountered minimum values of n(1) and a of 10^{15} cm^{-3} and 2.2 cm respectively. Hence from table (13.3) and equation (13.31) we can see that, even for T $\sim$ 20,000°K

$$\overline{\delta_{21}} \gg 1 \quad \text{throughout all plasma decays} \qquad (13.32)$$

Thus Holstein's expression for $g(\overline{\delta_{21}})$ in cylindrical geometry, equation (A.7.19), can be employed, or more simply, and with very little loss in accuracy

$$g(\overline{\delta_{21}}) \approx \frac{1}{\overline{\delta_{21}}} = \frac{1}{k_{12}\, a} \qquad (13.33)$$

The quasi-equilibrium population density $n_E(2)$ in the optically thick limiting case has already been shown to be determined entirely by collisional processes. We can therefore take the value of $n_E(2)$ to be that predicted by a modified form of Saha's equation (84).

$$n_E(2) = \frac{n^2\, b_2}{2\, b_i} \left[\frac{h^2}{2\pi\, m\, k\, T_e} \right]^{3/2} \exp\left[\frac{I_2}{k\, T_e} \right] \qquad (13.34)$$

where b_2 = statistical weight of level 2

b_i = statistical weight of ion ground state

I_2 = binding energy of level 2

and the other symbols have their usual meaning.

We will also use the equation expressing the inherent relationship between the oscillator strength and transition probability of a line which according to (111) is

$$f_{21} = \frac{m\, c}{8\pi^2\, e^2} \frac{b_2}{b_1} (\lambda_{21})^2\, A_{21} \qquad (13.35)$$

Using equations (9.26), (13.32), (13.33), (13.34) and (13.35)

we can write expression (13.26) for Ψ in the form

$$\Psi = \frac{C k b_{ia}}{2 b_1} \left[\frac{m}{h^2}\right]^{3/2} \left[M\right]^{\frac{1}{2}} \left[\lambda_{21}\right]^3 n\, n(1) \left[T_e\right]^{-7/2} \exp\left[\frac{-I_2}{k\, T_e}\right] \qquad (13.36)$$

where C = constant in equation (9.26)
(C = $3.9\ 10^{-9}$ cm^{-3} $sec.^{-1}$)
λ_{21} = wavelength of transition

Equation (13.36) can be re-written in a more manageable form by introducing a quantity G:

$$\Psi = G\, n\, n(1) \left[T_e\right]^{-7/2} \exp\left[\frac{-I_2}{k\, T_e}\right] \qquad (13.37)$$

where G is a function of the type of gas and the radius of the discharge tube only. Values of the quantity G for the rare gases and sizes of torus used in our experiments are given in table (13.4).

TABLE (13.4) : NUMERICAL VALUE OF G (c.g.s. units)

GAS	LARGE TORUS	SMALL TORUS
He	$1.61\ 10^{-14}$	$9.94\ 10^{-15}$
Ne	$7.17\ 10^{-14}$	$4.44\ 10^{-14}$
A	$2.97\ 10^{-13}$	$1.84\ 10^{-13}$
Kr	$7.21\ 10^{-13}$	$4.47\ 10^{-13}$

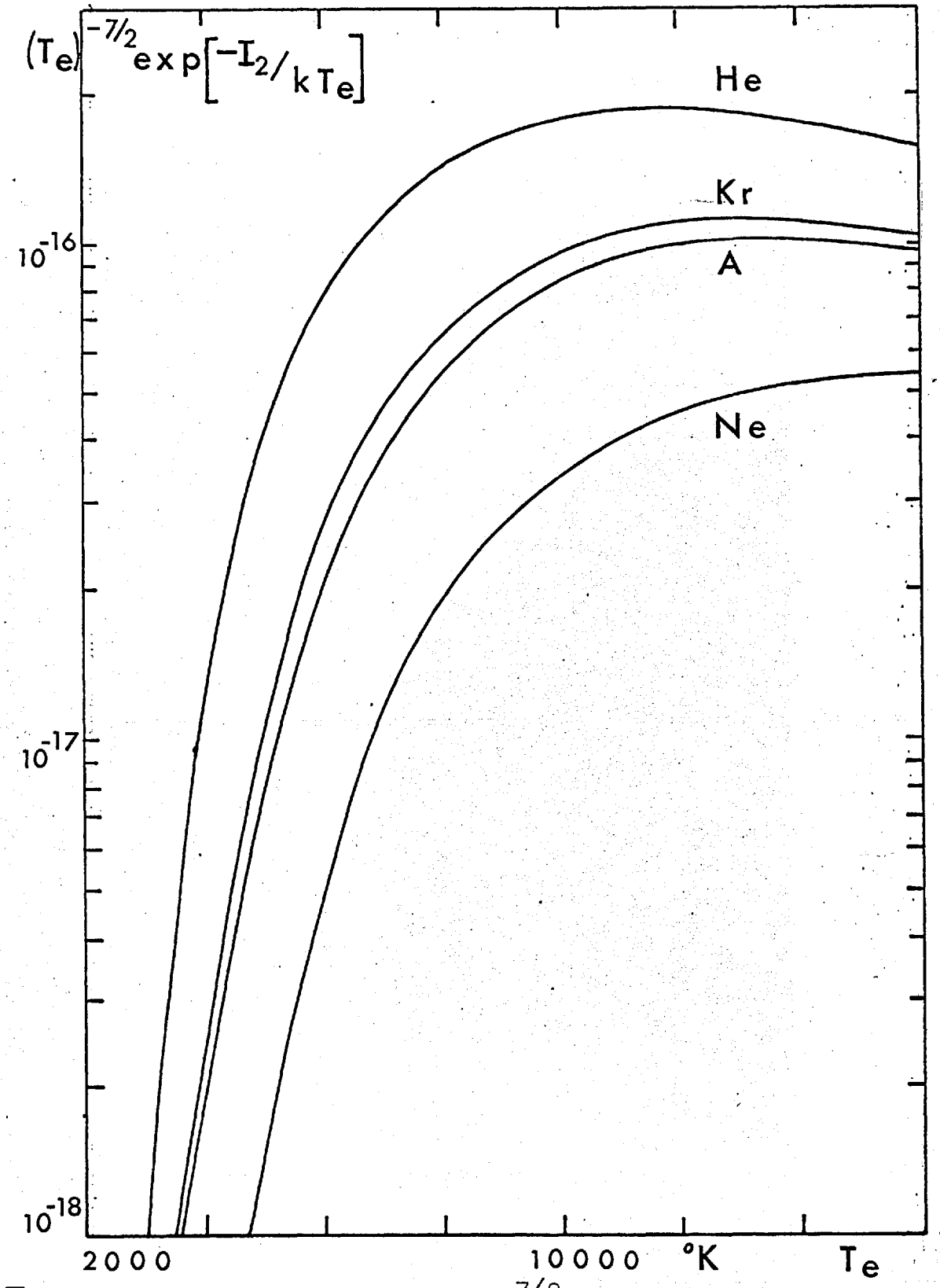

FIG (13.7) Plots of $(T_e)^{-7/2}$ exp $(-I_2/k\ T_e)$ versus T_e for the rare gases.

For each of the rare gases the quantity $(T_e)^{-7/2} \exp(-I_2/k\,T_e)$ has been plotted against T_e as shown in fig. (13.7). These plots are extremely interesting since they show that the above quantity falls much more rapidly with decreasing T_e for neon than for helium, with argon and krypton being intermediate and closely similar.

The value of Ψ for any specified values of n, n(1) and T_e can thus be obtained from equation (13.37) using table (13.4) and fig. (13.7).

(13.9.4) Evaluation of the Factor q.

As a result of the calculations presented in sections (13.9.2) and (13.9.3), we are now in a position to numerically evaluate the factor q from equation (13.24) in changing afterglow plasma conditions.

In the early afterglow plasma region characterised by the following conditions

$$\left.\begin{aligned} T_e &= 8000 - 12000^{\circ}K \\ n &= 10^{15}\ cm^{-3} \\ n(1) &= 3 \cdot 10^{15}\ cm^{-3} \end{aligned}\right\} \qquad (13.38)$$

the calculated values of the quantities Φ and Ψ are

$$\left.\begin{aligned} \Phi &\approx 1 \\ \Psi &\gg 1 \quad \text{for He, A, Kr plasmas} \\ \Psi &\gtrsim 1 \quad \text{for Ne. plasma} \end{aligned}\right\} \qquad (13.39)$$

and the corresponding ranges of values of the factor q are

$$\left.\begin{aligned} q &\approx 0.90 \text{ to } 1.0 \text{ in He, A, Kr plasmas} \\ q &\approx 0.75 \text{ to } 0.90 \text{ in Ne plasma} \end{aligned}\right\} \qquad (13.40)$$

These values of the factor q calculated in the early afterglow region agree very well with the values of q given in tables (13.1) and (13.2) for measurements made at high densities.

In the late afterglow plasma region characterised by the conditions

$$\left.\begin{aligned} n &\lesssim 10^{14} \text{ cm}^{-3} \\ T_e &\lesssim 6{,}000^{\circ}\text{K} \end{aligned}\right\} \qquad (13.41)$$

The value of the quantity Φ is always very close to one, and the expression for the factor q reduces to

$$q = \frac{5\,k\,T_e}{2\,I} + \frac{E_{12}}{I}\left[\,1 - (1+\Psi)^{-1}\,\right] \qquad (13.42)$$

For plasma decay in the region (13.41), we can see from fig. (13.7) that the value of the quantity Ψ is determined largely by the value of the quasi-equilibrium electron temperature existing in the plasma. In evaluating Ψ in the late afterglow region, we used the values of electron temperature that have been computed as a function of q, n and n(1) as described in section (12.9.1). For a first approximation, values of electron temperature computed for the condition q = 1 are used to find values for Ψ which, on substitution into equation (13.42), give the first order values of q. The second stage approximation involves finding the electron temperature corresponding to the first stage value of q, and repeating the above process. Iteration to further stages of approximation can be made indefinitely.

Using the method of calculation outlined above, the value of q (n, n(1)) has been worked out for plasma decays in each of the four rare gases and in each size of torus. The results are shown graphically in figs. (13.8) to (13.11) where the variation

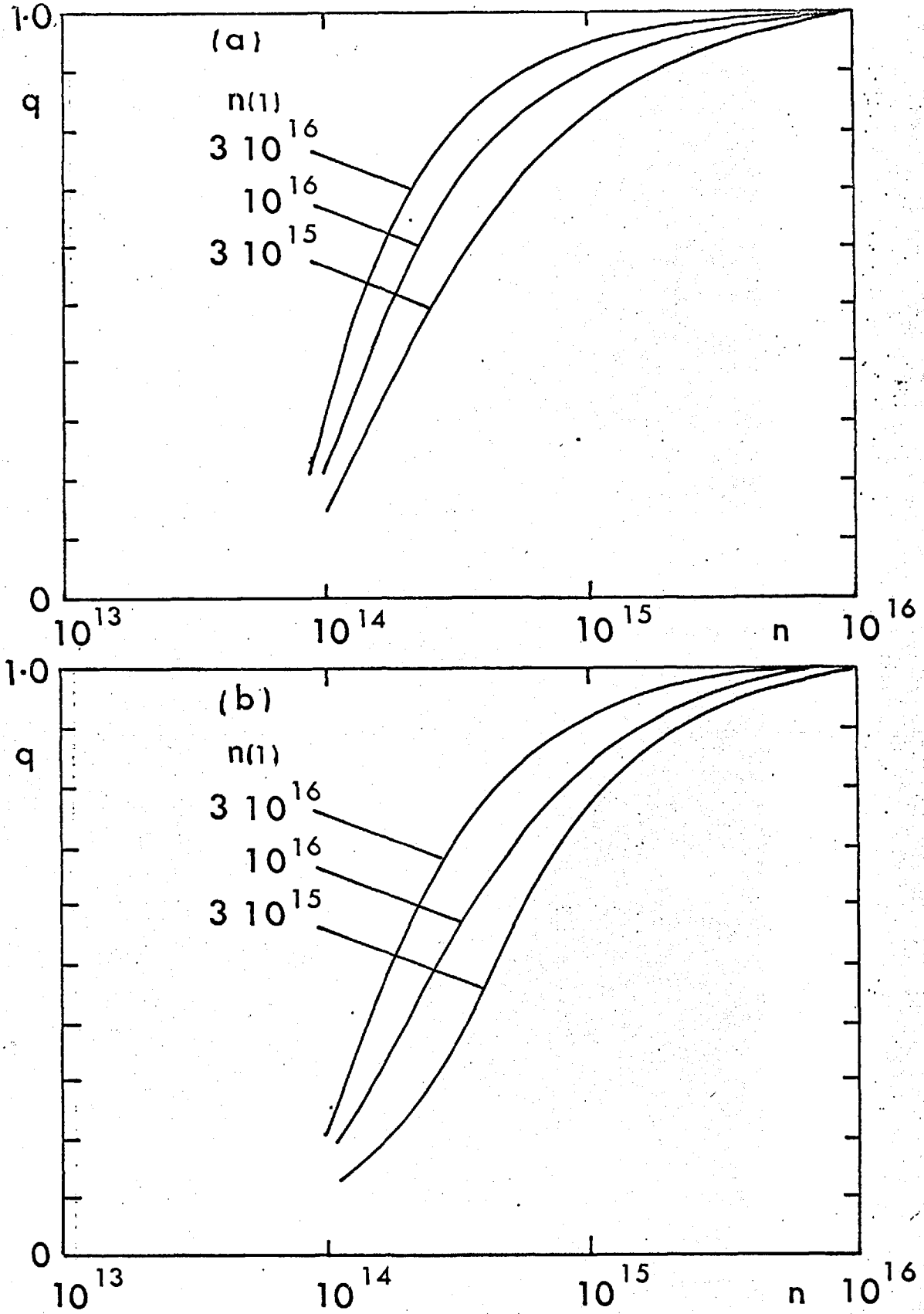

FIG (13.8) Plots of q (n, n(1)) for helium plasmas.
(a) large torus (b) small torus.

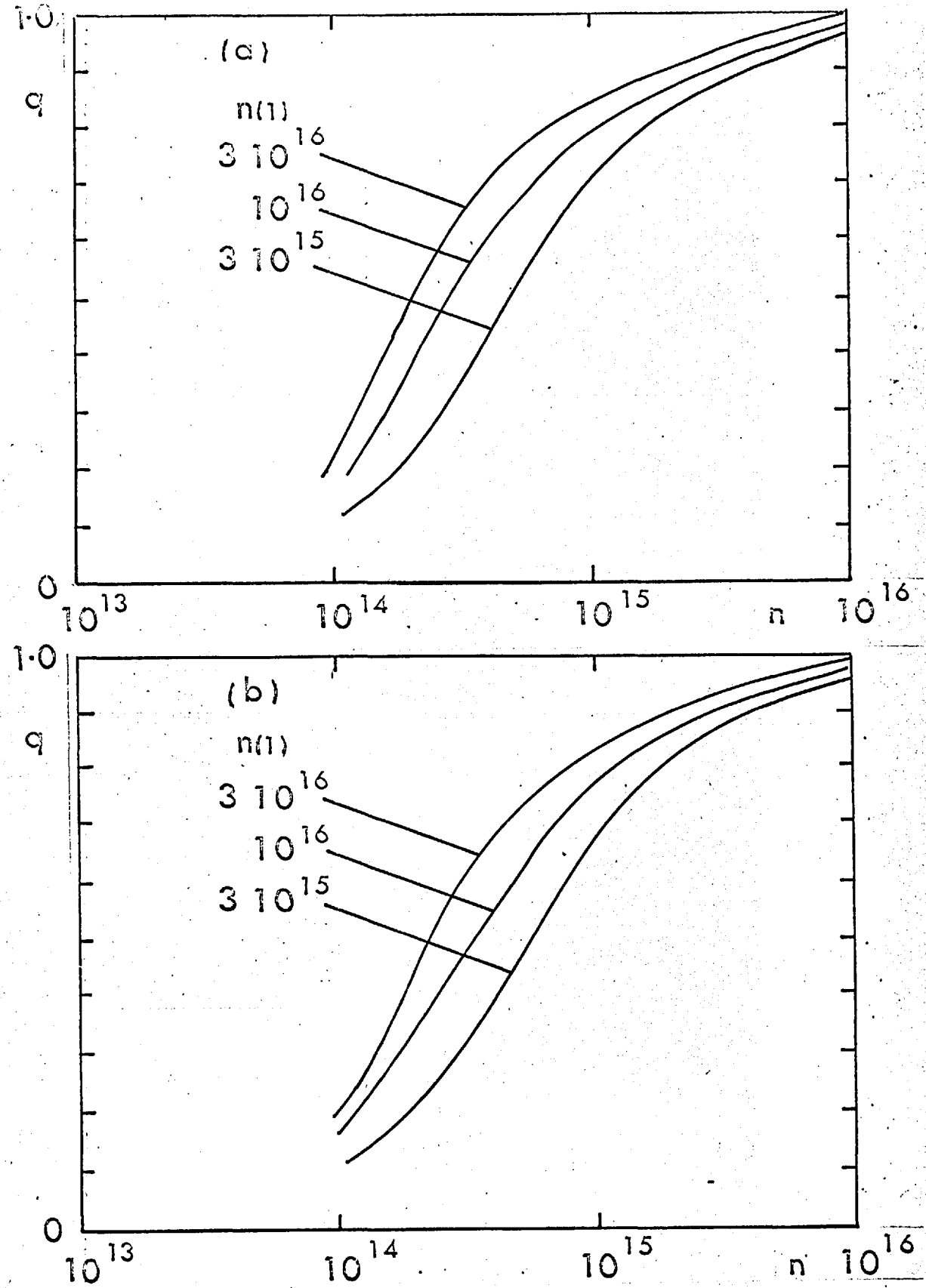

FIG (13.9) Plots of q (n, n(1)) for neon plasmas (a) large torus (b) small torus.

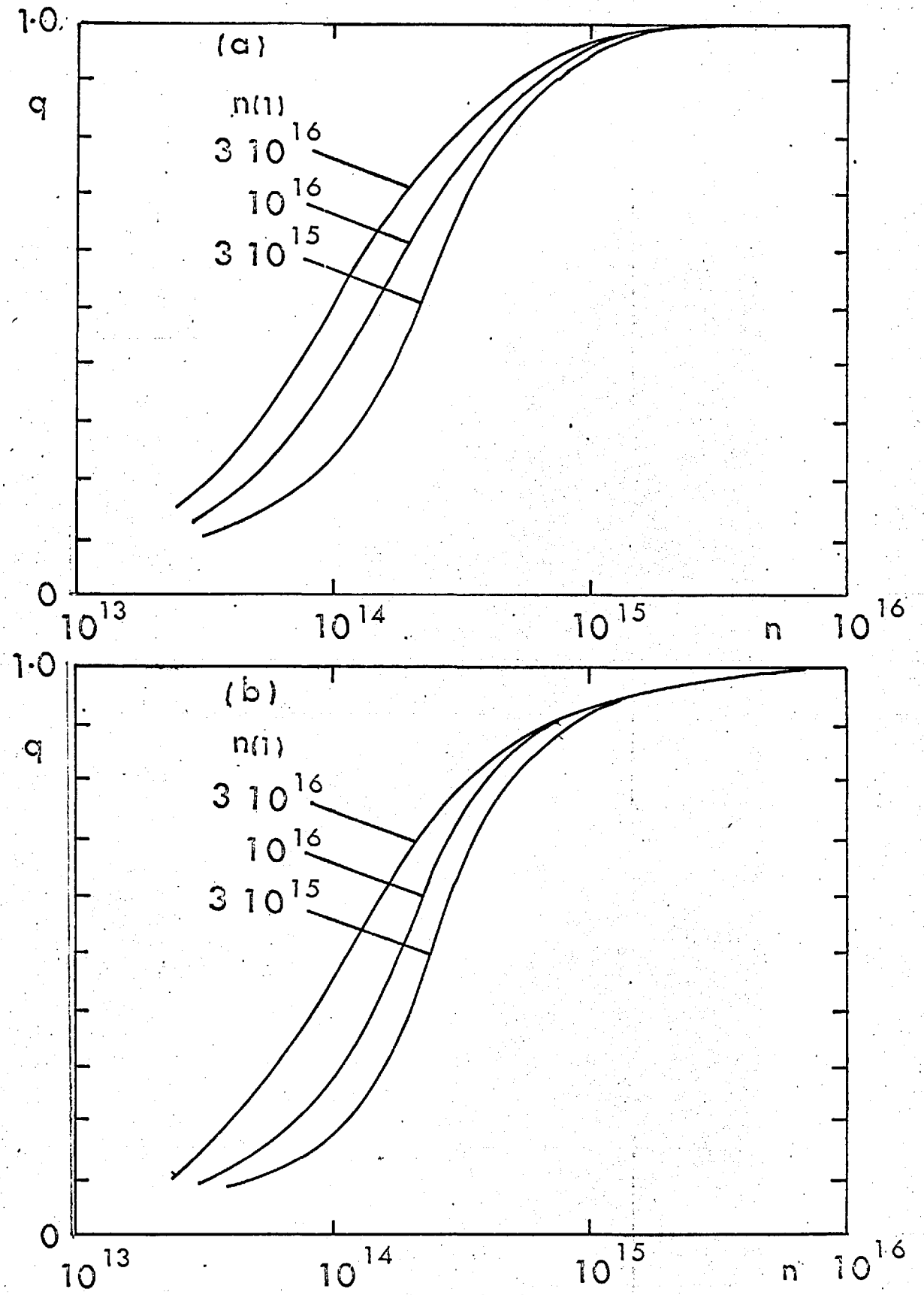

FIG (13.10) Plots of q (n, n(1)) for argon plasmas (a) large torus (b) small torus.

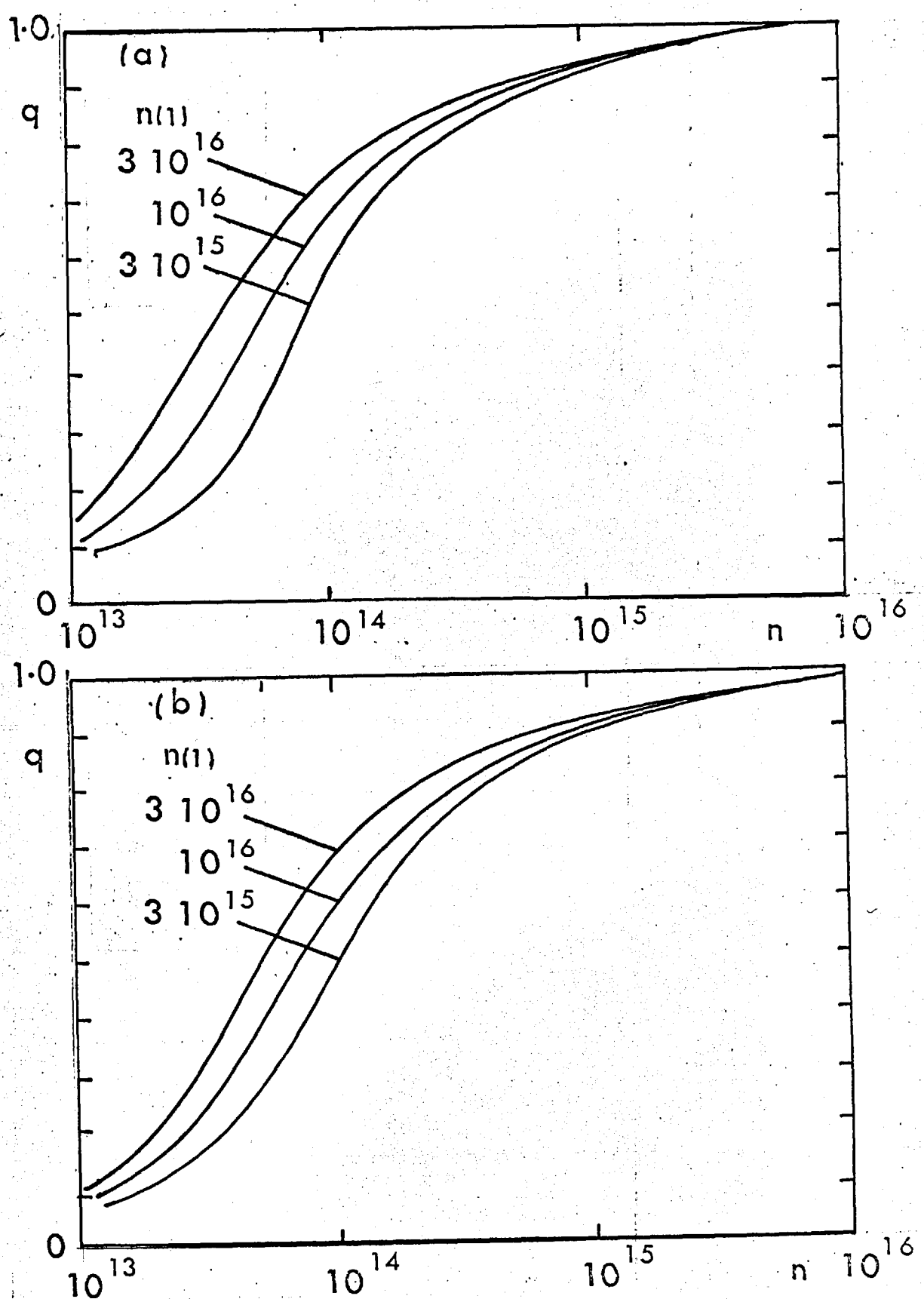

FIG (13.11) Plots of q (n, n(1)) for krypton plasmas.
(a) large torus (b) small torus

of q with n over a range 10^{13} to 10^{16} cm^{-3} has been plotted for fixed values of $n(1) = 3 . 10^{15}$, 10^{16} and $3 . 10^{16}$ cm^{-3} for each size of torus.

(13.10) COMPARISON OF THE TWO ESTIMATIONS OF THE FACTOR q (n, n(1))

The two estimations of the factor q (n, n(1)) presented above can be compared visually from an inspection of the graphs shown in figs. (13.1) to (13.4) and figs. (13.8) to (13.11). The following comments are made about this comparison.

1. The experimental-computed values of q (n, n(1)), which we will call case I results, apply at the axis of a non-uniform cylindrical plasma. The entirely theoretical values of q (n, n(1)), which we will call case II results, apply to uniform cylindrical plasma.

2. Good general agreement can be seen between both sets of results. The effects of electron collisions with the excited levels between p = 3 and the crossing level p_c are neglected in case II, and this approximation possibly accounts for the more rapid fall in q (n, n(1)) at low densities in case II than in case I.

3. Neon shows the most rapid decay of the value of q with decreasing n in both cases, whilst the elements showing the least rapid decay of q with decreasing n are helium in case I and krypton in case II. In case II the large G factor and the high quasi-equilibrium values of T_e for krypton more than offset the difference in behaviour between krypton and helium shown in fig. (13.7).

4. The dominant dependence of q upon T_e, shown theoretically in case II, yields results for q which have only a slight dependence on the value of neutral atom density n(1), although the actual value of the absorption coefficient, equation (13.32), is only slightly dependent on T_e and is proportional to n(1). However these case II results are in good agreement with case I results where an extremely small dependence of the factor q upon the value of n(1) was found.

CHAPTER 14

DISCUSSION AND CONCLUSIONS ON AFTERGLOW PLASMA WORK

The overall aim of the work presented in chapters 7 to 13 has been to give a comprehensive experimental and theoretical description of the decay of laboratory type plasma in the electron density range 10^{16} to 10^{13} cm^{-3}. In this chapter, we discuss the above work and state some conclusions that can be drawn from it.

On the experimental aspects of the work presented, we have shown that the 337 μm laser interferometer is a unique and powerful diagnostic for investigating high density plasma afterglows and it enables the decays of both electron density and electron temperature to be measured very accurately. The wide range of afterglow plasmas that have been studied (comprising 125 different afterglows in hydrogen and the rare gases in two sizes of torus) combined with the accuracy of the measurements of plasma parameters in the afterglows, make the present experimental work one of the most comprehensive experimental studies of afterglow plasmas that has so far been performed.

Right from the start of our work, detailed attention has been given to the non-uniform distributions of plasma parameters in laboratory type afterglows where the walls of the discharge vessel remain fixed at room temperature ($300^{o}K$). We have derived an equation for the transport of energy inside a cylindrical afterglow plasma which shows that the distribution profiles and the overall decay rates of the density and

temperature of each particle species in the plasma are interdependent quantities. Experimental measurements of electron density profiles in afterglow plasmas, made by two independent methods, have been shown to be in good agreement with theoretical calculations of electron density profiles obtained from the energy transport equation. The good agreement of experiment with theory on the electron density distribution in the plasma, also confirms the theoretical electron density decay equations obtained from the energy transport equation, because of the interdependence of the distribution and decay rate of each plasma parameter in the afterglow.

The above calculations performed on the decay of non-uniform plasma havebeen used in chapter 12 as the basis of a new series of calculations of the plasma recombination times in the electron density range 10^{16} to 10^{13} cm^{-3}. In this density range, the decay of plasma has been shown to be dominated by the three body recombination process with an electron as the third body. In our theoretical description of this three body recombination process, we have used the analytical expression for the recombination coefficient derived by D'Angelo (82) . According to D'Angelo, his expression for the three body recombination coefficient, though simple mathematically, is comparable in its accuracy with any of the more complex numerical calculations of the three body recombination coefficient (71)(72) that have been performed. The equations describing the energy balance and recombination processes in non-uniform rare gas plasmas have been solved with the aid of a computer to yield the equilibrium values of electron temperature, atom temperature and plasma recombination time throughout the high density range of plasma decay. An essential feature of our computer solutions to the energy balance and recombination

equations is that we have treated the atom temperature inside the plasma as a variable. The computed values of atom temperature at the centre of high density plasmas have been shown to be well above the value of the discharge tube wall temperature. A comparison has been made in chapter 12 between our new solutions of the energy balance and recombination equations and the solutions of similar equations given by Bates and Kingston (74)(75), who treated the atom temperature inside the plasma as a fixed constant throughout the afterglow. For the cases of both optically thick and optically thin helium afterglows, the above comparison has shown that the recombination coefficient for densities $> 10^{14}$ cm^{-3} predicted by our calculations is about an order of magnitude smaller than the recombination coefficient for corresponding densities predicted by Bates and Kingston's calculations.

One of the most useful aspects of the present work is that plasma decays have been studied in two sizes of discharge tube using the same diagnostic equipment. This study enables the variation of the plasma decay rate with the size of discharge tube to be assessed without the systematic errors inherent in a comparison of two independently performed experiments. We have shown that two main physical processes affecting the energy balance (and hence recombination rate) of the plasma are atomic thermal conduction to the walls of the discharge tube and the trapping of radiation inside the plasma. Since the effects of both these physical processes vary quite strongly with plasma radius, we expect the plasma decay rate, for fixed values of gas pressure and axial electron density, to also vary quite strongly with the radius of the discharge tube. For our two sizes of torus, the ratio of the minor radii was 1.6 and the ratio of the decay times measured experimentally for comparable values of gas pressure and axial electron density was found to vary from

1.5 to 2.8 with decreasing electron density in the range $3\ 10^{15}$ to $3\ 10^{12}$ cm^{-3}. A simple theoretical treatment of the effects of radiation trapping in an afterglow plasma has been combined with the computer solutions to the energy balance and recombination equations, where the radial dependence of the physical processes quoted above has been included into the theory. It has been shown in chapter 13 that this theory is in good consistent agreement with the experimental results for both sizes of torus.

With reference to the errors inherent in the theoretical work presented, the values of the recombination times computed in chapter 12 as a function of the variables q, n_o and $\bar{n}(\overline{1})$ are estimated to be correct to within $\pm$ 30%. The theoretical calculation of the value of the factor q, found as a function of n, n(1) in chapter 13, is much more approximate and the errors of the calculation increase fairly rapidly with the decreasing plasma optical depth of the resonance lines. Thus the overall accuracy of the theoretical work is limited by the accuracy of numerically evaluating the effects of radiation trapping in the plasma. This latter problem is not new (125) and it turns out to be a problem which it is difficult to treat in a realistic manner. So far, no accurate method of calculating the effects of radiation trapping, which can be applied to the plasma conditions encountered in laboratory afterglows, appears to have been published. However should an accurate calculation method become available at a future date, it could easily be combined with the existing computer calculations given in chapter 12.

Although the theoretical work presented in chapters 10, 12 and 13 is self contained, its origin and development owes a lot to results of the experimental work performed on plasma afterglows. The wide range of experimental data that has been

obtained served as an invaluable comparison standard by which new theoretical ideas could be checked.

In performing afterglow plasma experiments in apparatus originally intended for high temperature plasma containment, we have followed a trend set by previous workers. Kuckes et al (85) and Hinnov and Hirschberg (84)(86) performed studies of low density helium plasma decay in the models B1 and C stellarators and the hydrogen and helium afterglow studies of Quinn (99) and Newton and Sexton (92)(93) were both performed on the preionised discharge of the U.K.A.E.A. megajoule θ pinch experiment.

Following correspondence arising from the preliminary reports (141)(142) on the afterglow plasma work, several other workers are at the present time attempting to use a c.w. sub-millimetre wavelength laser interferometer as a plasma diagnostic At U.K.A.E.A. Culham, Newton and Sexton are applying this diagnostic to further afterglow plasma studies and at C.E.N. Fontenay-aux-Roses, Hesse is applying it to other plasma studies in the electron density region around 10^{15} cm^{-3}.

APPENDIX (A.1)

CALCULATION OF THE INDUCTANCE OF THE EIGHT ROD SYSTEM

The total inductance of the eight rod system which acted as the primary load for the main capacitor bank discharge with the small torus system was calculated as follows. The radius of curvature of the toroidal Z axis of the system was 25.4 cm (10.00 in.) and the rods were equally spaced around this axis on a circle of radius 3.81 cm (1.500 in.). The symmetry of the system meant that pairs of rods had the same radius of curvature and we will label the rods according to their radii of curvature as given in table (A.1.1).

TABLE (A.1.1)

RODS	RADIUS OF CURVATURE (c.m.)
1,2	21.91
3,4	23.98
5,6	26.90
7,8	28.97

From the symmetry of the eight rod system, the 64 components of mutual inductance can be described in terms of 16 different values and the 8 self inductances can be described in terms of 4 different values. Also the currents in pairs of rods with

the same radius of curvature are equal.

Thus, the eight equations relating the EMF across each rod to the rates of change of current in each rod using the coefficients of self inductance and mutual inductance, reduce to four simultaneous linear equations connecting the variables $\mathcal{E}$, di_1/dt, di_3/dt, di_5/dt, di_7/dt where $\mathcal{E}$ is the E.M.F. across each rod. The solution of these four simultaneous equations has the form

$$\frac{-\mathcal{E}}{\Delta} = \frac{di_1/dt}{\Delta_A} = \frac{di_3/dt}{\Delta_B} = \frac{di_5/dt}{\Delta_C} = \frac{di_7/dt}{\Delta_D} \qquad (A.1.1)$$

where determinant Δ has the form

$$\Delta = \begin{vmatrix} L_1 + M_{12} & M_{13} + M_{14} & M_{15} + M_{16} & M_{17} + M_{18} \\ M_{13} + M_{32} & L_3 + M_{34} & M_{35} + M_{36} & M_{37} + M_{38} \\ M_{15} + M_{56} & M_{53} + M_{54} & L_5 + M_{56} & M_{57} + M_{58} \\ M_{17} + M_{78} & M_{73} + M_{74} & M_{75} + M_{76} & L_7 + M_{78} \end{vmatrix} \qquad (A.1.2)$$

where : M refers to mutual inductance
L refers to self inductance.

The determinants Δ_A, Δ_B, Δ_C and Δ_D are obtained from Δ by setting successive columns equal to unity in expression (A.1.2).

Now the total inductance L_{ROD} of the eight rod system is defined by the equation

$$\frac{-\mathcal{E}}{L_{ROD}} = \sum_{x=1}^{8} \frac{di_x}{dt} \qquad (A.1.3)$$

Hence from (A.1.1) and (A.1.2.)

$$\frac{1}{L_{ROD}} = 2\,\frac{(\Delta_A + \Delta_B + \Delta_C + \Delta_D)}{\Delta} \qquad (A.1.4)$$

The values of the coefficients of mutual and self inductance appearing in equation (A.1.1) were worked out using Grover (126) and the five determinants were evaluated as

Δ_A = 1.990 μH

Δ_B = 1.5676 μH

Δ_C = 1.1079 μH

Δ_D = 0.9012 μH

Δ = 7.3457 μH

which according to (A.1.4) gives a value of L_{ROD} = 659.8 n.H.

It is interesting to compare the above value with the theoretical value of inductance for a solid rod and a thin tube which have the same toroidal radius and minor radius as our eight rod system. From Smythe (8) these inductance values are

L (solid toroidal rod) = 711.8 n.H.

L (thin toroidal tube) = 631.8 n.H.

APPENDIX (A.2)

COEFFICIENTS OF ATOMIC THERMAL CONDUCTIVITY

The thermal conductivity of atomic hydrogen has been calculated from classical scattering theory by Dalgarno and Smith (127) over the temperature range of interest in afterglow plasmas 300 to 10,000^{o}K. These calculations showed that the coefficient of atomic thermal conductivity χ could be written in the form

$$\chi = K T_a \qquad (A.2.1)$$

where K = constant (= 40 erg cm^{-1} sec^{-1} deg K^{-2} for hydrogen)

T_a = atom temperature

For rare gases, no theoretical calculations have been found, and the most comprehensive set of experimental measurements that have been found are reproduced from (128) in table (A.2.1). The coefficient of proportionality K was obtained from applying equation (A.2.1) to the results. Since the temperatures quoted in table (A.2.1) lie just below our main region of interest, (10^3 to 10^4 ^{o}K), the values found for K at any fixed atom temperature were multiplied by the factor which reduced the value of K for hydrogen at this particular temperature to 40.0. These values have been listed in table (A.2.1) under the column K*. The values of K* obtained for each gas show excellent consistency indicating the same form of atomic thermal conductivity dependence on temperature for the rare gases as for hydrogen. Consequently, the coefficient of atomic thermal conductivity was taken to be of the form of equation (A.2.1) for all gases where the coefficient of proportionality K is given in table (A.2.2)

TABLE (A.2.1.)

GAS	χ (10^{-4} watt cm^{-1} deg K^{-1})	T_a ($^\circ K$)	K (erg cm^{-1} sec^{-1} deg K^{-2})	K^* (see text)
H	18.2	300	60.7	40
	22.8	400	57.0	40
	32.0	500	53.0	40
	39.7	800	49.6	40
He	15.1	300	50.0	32.9
	18.2	400	45.5	31.9
	23.7	600	39.5	29.8
Ne	4.9	300	16.3	10.7
	5.9	400	14.8	10.4
	7.7	600	12.8	9.7
A	1.77	300	5.9	3.9
	2.23	400	5.6	3.9
	3.0	600	5.0	3.8
	3.7	800	4.6	3.7
	4.3	1000	4.3	-
	4.8	1200	4.0	-
Kr	0.94	300	3.12	2.06
	1.21	400	3.03	2.13
	1.68	600	2.80	2.11

TABLE (A.2.2)

GAS	K (erg cm^{-1} sec^{-1} deg k^{-2})
H	40
He	32
Ne	10
A	4.0
Kr	2.1

APPENDIX (A.3)

COMPARISON OF ATOMIC AND PLASMA COEFFICIENTS OF THERMAL CONDUCTIVITY

For the Lorentz gas plasma model the expression for the coefficient of plasma thermal conductivity χ_L is given by Spitzer (10) where Z = 1 as

$$\chi_L = \frac{\delta \epsilon \; 4.67 \; 10^{-12} \; T_e^{5/2}}{\ln \Lambda} \quad \text{cal. sec}^{-1} \text{ cm}^{-1} \text{ deg K}^{-1}$$

where $\delta = 0.225$, $\epsilon = 0.419$ } correction factors for Z = 1

Taking $\ln \Lambda \sim 10$ for afterglow plasma conditions this expression reduces to

$$\chi_L = 1.8 \; 10^{-6} \; T_e^{5/2} \quad \text{erg sec}^{-1} \text{ cm}^{-1} \text{ deg K}^{-1} \qquad \text{(A.3.1)}$$

From a comparison of equations (A.3.1) and (A.2.1) together with the values of K listed in table (A.2.2), the values of atom temperature at which $\chi = \chi_L$ have been listed in table (A.3.1).

TABLE (A.3.1)

GAS	T_a (^oK) when $\chi = \chi_L$
H	79000
He	68000
Ne	31000
A	17000
K	11000

Except for argon and krypton which are marginal, the values of atom temperature when $\chi = \chi_L$ are much larger than those encountered in decaying plasmas, showing that generally atomic thermal conductivity effects are dominant.

APPENDIX (A.4)

THE ELECTRON-ION ELASTIC ENERGY TRANSFER COEFFICIENT η_{ei}

The rate of elastic energy transfer Q_{ei} between electrons and ions due to Coulomb collisions between the particles has been calculated by Petschek and Byron (119). From these calculations and our definition of the elastic energy transfer coefficient equation (12.7) we can write

$$\eta_{ei} = \frac{e^4}{M}\left[\frac{8\pi m}{k}\right]^{\frac{1}{2}} \frac{2.3026}{T_e^{3/2}} \log_{10}\left[\frac{9\,(k\,T_e)^3}{8\pi n e^6}\right] \qquad (A.4.1)$$

where the symbols used have their usual meaning.

In table (A.4.1), values of the quantity $\frac{e^4}{M}\cdot\left[\frac{8\pi m}{k}\right]^{\frac{1}{2}}\cdot 2.3026$ have been calculated for various gases.

TABLE (A.4.1)

GAS	$2.3026\,\frac{e^4}{M}\left[\frac{8\pi m}{k}\right]^{\frac{1}{2}}$
H	$9.41\ 10^{-19}$
He	$2.35\ 10^{-19}$
Ne	$4.66\ 10^{-20}$
A	$2.35\ 10^{-20}$
K	$1.12\ 10^{-20}$

For the case of a decaying plasma where three body C.R, plasma recombination is dominant, we will assume that n and T_e are related by the equation (9.26) for the recombination coefficient so that we can write

$$\tau_R = (\alpha\, n)^{-1} = (C\, n^2)^{-1}\, T_e^{9/2} \qquad (A.4.2)$$

and using (A.4.2) the logrithmic term in equation (A.4.1) can be re-written as

$$\log_{10}\left[\frac{9\, k^3\, C^{\frac{1}{2}}}{8\,\pi\, e^6}\right] + \frac{3}{4}\log_{10}\left[T_e\right] + \log_{10}\left[\tau_R\right]$$

$$= 4.49 + \frac{3}{4}\log_{10} T_e + \log_{10}\tau_R \qquad (A.4.3)$$

We are mainly interested in finding a suitable expression for η_{ei} only in the decaying plasma region bounded by

$$\left.\begin{array}{l} 300 < T_e < 15000^{\circ}K \\ 10^{-5} < \tau_R < 3\ 10^{-3}\ \text{sec.} \end{array}\right\} \qquad (A.4.4)$$

where the highest values of T_e and the lowest values of τ_R occur together. From substitution of the typical range of values for T_e and τ_R encountered experimentally into expression (A.4.3) the value of the logrithmic term has been calculated as given in table (A.4.2).

TABLE (A.4.2)

Gas	Logrithmic term
H	3.0 ($\pm$ 0.8)
He	3.5 ($\pm$ 0.8)
Ne, A, Kr	4.0 ($\pm$ 0.8)

In the interest of simplifying the computer work, the mean values of the logrithmic term listed in table (A.4.2) were taken to apply throughout so that equation (A.4.1) was taken to be of the form

$$\eta_{ei} = \frac{X_{ei}}{[T_e]^{3/2}} \qquad (A.4.5)$$

where X_{ei} is a constant for a particular gas given by table (A.4.3).

TABLE (A.4.3)

GAS	X_{ei} (c.g.s. units)
H	$2.9\ 10^{-18}$
He	$8.4\ 10^{-19}$
Ne	$1.9\ 10^{-19}$
A	$9.4\ 10^{-20}$
Kr	$4.5\ 10^{-20}$

We note that in the final expression for Q_{ei}, which is

$$Q_{ei} = n^2 \eta_{ei} (T_e - T_i)$$

the varation in the values of the terms n^2 and $T_e^{3/2}$ over the ranges of interest in decaying plasmas are 10^{10} and 350 respectively which makes the neglection of the variation of the logrithmic term in (A.4.1) ($< 50\%$) over this region a very reasonable approximation.

APPENDIX (A.5)

THE ION-ATOM ELASTIC ENERGY TRANSFER COEFFICIENT η_{ia}

Here we are no longer dealing with a simple interaction law between particles as was the case of the Coulomb interaction between electrons and ions in appendix (A.4). Consequently, the errors involved in η_{ia} are likely to be much larger than those in η_{ei}.

Bates and Kingston (74) have given an expression for η_{ia} based on the calculations of Bates and Boyd (123) of the form

$$\eta_{ia} = 3.5\ 10^{-28}\ (T_i + T_a)^{3/2} \left[11.41 - \log_{10} (T_i + T_a) \right]^2 \qquad (A.5.1)$$

The same authors (75) have stated that the value of η_{ia} for helium derived from the charge exchange calculations of Moiseiwitsch (121) is roughly

$$\eta_{ia}\ (\text{helium}) \approx 0.25\ \eta_{ia}\ (\text{hydrogen}) \qquad (A.5.2)$$

In the general case, Bates and Kingston (74) have shown that η_{ia} can be related to the charge transfer cross-section σ_T by the relationship

$$\eta_{ia} = \left[\frac{8\ k^3\ (T_i + T_a)}{\pi\ M} \right]^{\frac{1}{2}} 2\sigma_T \qquad (A.5.3)$$

Dalgarno (118) has performed calculations of the charge transfer cross-sections over a wide range of conditions for atomic hydrogen and the rare gases, and combining his results with the expression (A.5.3), values of η_{ia} over the expected ranges of T_i and T_a in afterglow plasmas have been calculated as shown in table (A.5.1).

TABLE (A.5.1)

η_{ia} (erg cm^3 sec^{-1} deg K^{-1})

GAS	$T_i + T_a$ (^oK)		
	600	2000	20000
H	$6.8\ 10^{-25}$	$1.1\ 10^{-24}$	$2.7\ 10^{-24}$
He	$2.2\ 10^{-25}$	$3.2\ 10^{-25}$	$8.2\ 10^{-25}$
Ne	$1.1\ 10^{-25}$	$1.7\ 10^{-25}$	$4.2\ 10^{-25}$
A	$1.2\ 10^{-25}$	$2.1\ 10^{-25}$	$5.8\ 10^{-25}$
Kr	$1.1\ 10^{-25}$	$1.8\ 10^{-25}$	$5.0\ 10^{-25}$

In the expression for the rate of elastic energy transfer from the ions to the atoms Q_{ia}, which is

$$Q_{ia} = n\, n(1)\, \eta_{ia} (T_i - T_a) \qquad (A.5.4)$$

The variation of η_{ia} with ion and atom temperatures as shown in table (A.5.1) in afterglow plasma conditions is considerably less than the variation in Q_{ia} due to density changes. Hence, to simplify the computor work, we will take the form of η_{ia} for substitution into (A.5.4) to be

$$\eta_{ia} = X_{ia} \qquad (A.5.5)$$

where X_{ia} is a constant for a particular gas given by table (A.5.2).

TABLE (A.5.2)

GAS	X_{ia} (c.g.s. units)
H	$1.7 \ 10^{-24}$
He	$4.8 \ 10^{-25}$
Ne	$2.5 \ 10^{-25}$
A	$3.4 \ 10^{-25}$
Kr	$3.0 \ 10^{-25}$

APPENDIX (A.6)

THE ELECTRON-ATOM ELASTIC ENERGY TRANSFER COEFFICIENT η_{ea}

Using the work of Temkin and Lamkin (122), Bates and Kingston (74) have given an expression for η_{ea} for hydrogen of the form

$$\eta_{ea}\,(H) = 1.0\ 10^{-26}\ \phi(T)\ \text{erg cm}^3\ \text{sec}^{-1}\ \text{deg}^{-1} \qquad (A.6.1)$$

where $\phi(T)$ is 1.0 when $T = 300^{\circ}K$ and rises to 3.0 when $T = 10{,}000^{\circ}K$.

Bates and Kingston (75) have also used the work of Moiseiwitsch (121) to find η_{ea} for helium of the form

$$\eta_{ea}\,(He) = 2.53\ 10^{-29}\ T_e^{\frac{1}{2}}\ \text{erg cm}^3\ \text{deg}^{-1}\ \text{sec}^{-1} \qquad (A.6.2.)$$

Recently, Ovcharenko (124) has calculated the cross-section for the elastic scattering of electrons by atoms for a Maxwellian velocity distribution of electrons and the results for the rare gases are shown in fig. (A.6.1). Petschek and Byron (119) have shown that for electron collisions with heavy particles of type B (ions or atoms) the rate coefficient η_{eB} for elastic energy transfer from electrons to type B particles can be written as

$$\eta_{eB} = \frac{m^2}{M_B\ T_e} \int v_e^3\ f_e\ \sigma_{eB}\,(v_e)\ d^3v_e \qquad (A.6.3)$$

where f_e = normalised distribution function for electrons

$\sigma_{eB}(v_e)$ = cross-section as a function of electron velocity

M_B = mass of particles of type B.

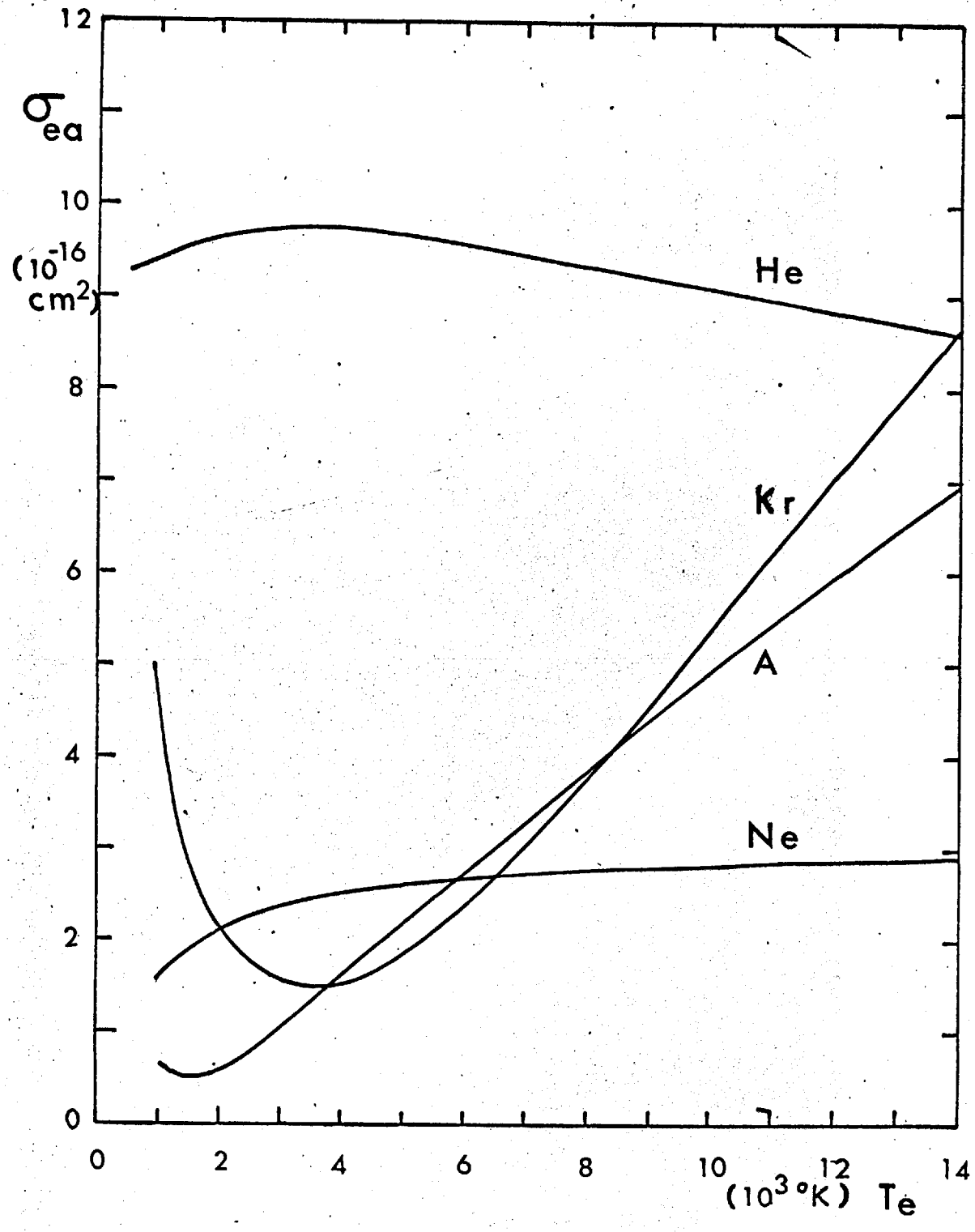

FIG (A.6.1) Cross-sections for the elastic scattering of electrons by rare gas atoms.

For the case of helium and neon, from fig. (A.6.1) we can see that the values of $\sigma(v_e)$ are approximately constant over the temperature range encountered in afterglow plasmas and therefore we can simplify (A.6.3) to become

$$\eta_{ea} = \frac{m^2}{M_B T_e} \overline{\sigma(v_e)} \left[\overline{(v_e)}\right]^3 \qquad \text{(A.6.4.)}$$

where $\overline{\sigma(v_e)}$ (Ne) = $2.8\ 10^{-16}$ cm^2 from fig. (A.6.1)

$\overline{\sigma(v_e)}$ (He) = $9.0\ 10^{-16}$ cm^2 " " "

$\overline{v_e} = \left(\frac{8kT}{\pi m}\right)^{\frac{1}{2}}$ = average electron velocity

Evaluating the expression (A.6.4) for the cases of helium and neon we therefore obtain expressions for η_{ia} of the forms

$$\eta_{ea}\ (He) = 2.70\ 10^{-29}\ T_e^{\frac{1}{2}} \text{ erg cm}^3 \text{ sec}^{-1} \text{ deg}^{-1} \qquad \text{(A.6.5)}$$

$$\eta_{ea}\ (Ne) = 0.16\ 10^{-29}\ T_e^{\frac{1}{2}} \quad " \qquad \text{(A.6.6)}$$

Expression (A.6.5) obtained in this way compares favourably with the expression (A.6.2) derived by Bates and Kingston.

The evaluation of the expressions for η_{ia} for argon and krypton gases requires the full integral expression (A.6.3) to be worked out. This has not been performed, however from the cross-sections shown in fig. (A.6.1) the expressions for η_{ia} for these two gases should not differ drastically from expressions (A.6.5) and (A.6.6).

For the case of hydrogen, Kolesnikov and Obukhov-Denisov (128) have evaluated the elastic scattering cross-section as a function of electron energy. For an electron energy of 0.7 e.v. they found

$$\sigma_{ea}(H) = 5.7\ 10^{-15}\ cm^2$$

which yields a value for η_{ea} according to equation (A.6.4) of

$$\eta_{ea}(H,\ 0.7\ e.v.) = 6.7\ 10^{-26}\ erg\ cm^3\ sec^{-1}\ deg^{-1}$$

This value compares favourably with the value of η_{ea} give by equation (A.6.1) for $T_e = 0.7$ e.v. which is

$$\eta_{ea}(H,\ 0.7\ e.v.) = 2.8\ 10^{-26}\ erg\ cm^3\ sec^{-1}\ deg^{-1}$$

Thus we can conclude that η_{ea} for the rare gases has the form

$$\eta_{ea} = X_{ea}\ T_e^{\frac{1}{2}}\ erg\ cm^3\ sec^{-1}\ deg^{-1} \qquad (A.6.7)$$

where X_{ea} is approximately constant for each gas and is given by (A.6.5) and (A.6.6) for helium and neon and is $\sim 10^{-30}$ erg cm^2 sec^{-1} deg^{-1} for argon and krypton.

APPENDIX (A.7)

RADIATION TRAPPING IN A PLASMA

The equation which describes the change in intensity $I(\nu)$ of radiation of frequency ν passing through a thin slab of plasma of thickness Δx is

$$\Delta I(\nu) = - I(\nu)\, k(\nu)\, \Delta x + j(\nu)\, \Delta x \qquad (A.7.1)$$

where $k(\nu)$ = absorption coefficient
$j(\nu)$ = coefficient of emissivity

We define the optical depth of the plasma $\delta(\nu)$ by the equation.

$$\delta(\nu) = \int k(\nu)\, dx \qquad (A.7.2)$$

In the limit as $\Delta x \to 0$, equation (A.7.1) can be written as

$$\frac{dI(\nu)}{d\delta(\nu)} = - I(\nu) + \frac{j(\nu)}{k(\nu)} \qquad (A.7.3)$$

Equation (A.7.3) is called the equation of radiative transfer and the ratio of the coefficients of emissivity and absorption is called the source function.

For a non-uniform plasma we will assume a mean optical depth $\overline{\delta(\nu)}$ which is related linearly to the absorption coefficient by the equation

$$\overline{\delta(\nu)} = k(\nu)\ \overline{D} \qquad (A.7.4)$$

where $\overline{D}$ is a characteristic distance of the plasma geometry and is independent of frequency.

For a non-uniform plasma, the intensity of isotropic radiation $\overline{I(\nu)}$ can be written as

$$\overline{I(\nu)} = \frac{j(\nu)}{k(\nu)} \left[1 - \exp\left(- k(\nu)\, \bar{D}\right) \right] \qquad (A.7.5)$$

For a two level atomic model where p, q are the quantum numbers and A(p, q), B(p, q) are the Einstein coefficients defined in terms of intensity of isotropic radiation, then the rate of change in the level p population due to photon transitions (neglecting stimulated emission) is

$$\frac{d\,n(p)}{dt} = - n(p)\, A(p, q) + n(q)\, \frac{B(q, p)}{4\pi} \int_0^\infty I(\nu)\, b(\nu)\, d\nu \qquad (A.7.6)$$

where $b(\nu)$ = normalised profile of spectral absorption.

Equation (A.7.6) can be re-written in terms of an escape probability factor g for photons which is analagous to that described by Holstein (112) (113), thus,

$$\frac{d\,n(p)}{dt} = - n(p)\, A(p, q)\, g \qquad (A.7.7)$$

$$\text{where } g = 1 - \frac{n(q)\, B(q, p)}{n(p)\, A(p, q)\, 4\pi} \int_0^\infty \bar{I}(\nu)\, b(\nu)\, d\nu \qquad (A.7.8)$$

By assuming that the frequency spectrum of the emitted radiation is directly proportional to the frequency spectrum for the absorption of radiation then,

$$j(\nu) = n(p)\, b(\nu)\, h\nu\, A(p, q) \qquad (A.7.9)$$

$$k(\nu) = \frac{n(q)}{4\pi}\, b(\nu)\, h\nu\, B(q, p) \qquad (A.7.10)$$

$$\text{Hence the source function } \frac{j(\nu)}{k(\nu)} = \frac{4\pi\, n(p)\, A(p, q)}{n(q)\, B(q, p)} \qquad (A.7.11)$$

Combining equations (A.7.8) and (A.7.11) and noting that the source function is independent of frequency, we can write the expression for g as

$$g = 1 - \int_0^\infty \left(1 - \exp\left(\overline{\delta(\nu)}\right)\right) . b(\nu) . d\nu \qquad (A.7.12)$$

The conditions existing in afterglow plasmas are such that the spectral line profile function $b(\nu)$ is determined by Doppler broadening with natural and pressure line broadening being negligible by comparison. The Doppler broadened line profile is of Gaussian type with the half width proportional to the atom thermal velocity, and a suitable normalised Gaussian profile for $b(\nu)$ is

$$b(\nu) = \frac{2}{\Delta\nu_D}\left[\frac{\ln 2}{\pi}\right]^{\frac{1}{2}} \exp(-w^2) \qquad (A.7.13)$$

where $w = 2(\ln 2)^{\frac{1}{2}} \dfrac{(\nu - \nu_o)}{\Delta\nu_D}$

$$\Delta\nu_D = \frac{2}{\lambda_o}\left[\frac{2 \ln 2\, k\, T}{M}\right]^{\frac{1}{2}}$$

and the subscript o refers to the centre profile frequency. Substituting equation (A.7.13) into (A.7.10), we obtain the expression for the Doppler broadened absorption coefficient as

$$k(\nu) = k_o \exp(-w^2) \qquad (A.7.14)$$

where $$k_o = \frac{2}{\Delta\nu_D}\left\{\frac{\ln 2}{\pi}\right\}^{\frac{1}{2}} \frac{n(q)\, h\, \nu_o\, B(q, p)}{4\pi} \qquad (A.7.15)$$

and the corresponding expression for the Doppler broadened mean optical depth is from equation (A.7.4)

$$\overline{\delta(\nu)} = \overline{\delta_o} \exp(-w^2) \qquad (A.7.16)$$

where $\delta_o = k_o \bar{D}$

The forms of $\overline{\delta(\nu)}$ and $b(\nu)$ given by equations (A.7.16) and (A.7.13) have been substituted into equation (A.7.12) and the

numerical value of g as a function of δ_o found as given in table (A.7.1). The values quoted in this table were obtained from the original evaluation of the integral expression for g performed by McWhirter (125).

TABLE (A.7.1)

δ_o	g
0.0	1.000
0.1	0.932
1.0	0.514
3.0	0.180
10.0	0.0359
30.0	0.00987
100.0	0.00253

Holstein (112)(113) has derived analytical expressions for the escape factor g which are valid in the optically thick case for plane parallel and cylindrical plasma geometry. His expressions are

$$g \text{ (plane parallel)} = \frac{1.875}{k_o L (\pi \log k_o L)^{\frac{1}{2}}} \qquad \text{(A.7.18)}$$

$$g \text{ (cylindrical)} = \frac{1.60}{k_o a (\pi \log k_o a)^{\frac{1}{2}}} \qquad \text{(A.7.19)}$$

where L = separation of parallel planes
a = radius of cyliner.

Recently Ingold (129) has extended Holstein's work to the optically thin case.

By using the relationship between the absorption oscillator

strength f_{pq} of the line and the Einstein coefficient $B(q, p)$ given by (111) of the form

$$B(q, p) = \frac{4\pi^2 e^2}{m c h \nu_o} f_{pq} \qquad (A.7.20)$$

The expression (A.7.15) for k_o can be re-written in the form

$$k_o = \left[\frac{\pi e^2}{(2\pi k)^{\frac{1}{2}} m c}\right]\left[\frac{M}{T}\right]^{\frac{1}{2}} n(q) \lambda_{pq} f_{pq} \qquad (A.7.21).$$

REFERENCES

(1) HAINES M.G., Conference on Plasma Physics and Controlled Fusion Research Salzburg 1961, I.A.E.A. Vienna, (1962)

(2) HAINES M.G., Proc. 6th Int. conf. of Ionization Phenomena in Gases. 1963, S.E.R.M.A. 4, 447, (1964).

(3) MEASURES R.M., Ph.D. Thesis, University of London, (1964)

(4) ETHERINGTON R.J., Ph.D. Thesis, University of London, (to be published).

(5) DUNNETT R.M., Ph.D. Thesis, University of London, (1968).

(6) DUNNETT R.M., Nuclear Fusion, 8, 287, (1968).

(7) FITCH, R.A., and McCORMICK N.R., Proc. I.E.E., 106 A, 117, (1959)

(8) SMYTHE W.R., Static and Dynamic Electricity (2nd edn.), McGraw-Hill, (1950)

(9) EDWARDS, F.S., HUSBANDS, A.S., and PERRY F.R. Proc. I.E.E. Conf. on High Voltage Impulse Generators, paper 1089, (1949)

(10) SPITZER, L., Physics of Fully Ionized Gases, (2nd edn.), Interscience Publishers N.Y., (1962)

(11) CHAPMAN S., and COWLING T.G., 'The Mathematical Theory of Non-Uniform Gases', C.U.P., (1939)

(12) GOLANT V.E., Soviet Phys. Uspekhi, 6, 161, (1963)

(13) BOSTICK W.H., and LEVINE MA., Phys. Rev., 97, 13, (1955)

(14) BOHM D., The Characteristics of Electrical Discharges in Magnetic Fields ed. GUTHRIE and WAKERLING, McGraw-Hill N.Y., (1949)

(15) GOLANT V.E., DANILOV O.B., and ZHILINSKII A.P., Soviet Phys. - Tech. Phys., 8, 778, (1964).

(16) KAGAN Y.M. and PEREL V.I., Usp. Fiz. Nank., 81, 409, (1963)

(17) ROGOWSKI W. and STEINHAUS W., Arch. Elektrotech., 1, 141, (1912).

(18) HUDDLESTONE R.H., and LEONARD S.L., 'Plasma Diagnostic Techniques,' Academic Press N.Y., (1965).

(19) COOPER J., Plasma Phys. (J. Nuc. Energy Pt. C), 5, 285, (1963).

(20) LOUBERG R.H., Ann. Phys., 8, 311, (1959).

(21) GERMANN C., Nuc. Instr. and Methods, 21, 17, (1963).

(22) SEGRE S.E., and ALLEN J.E., J. Sci. Instrum., 37, 369,(1960).

(23) ASHBY D.E.T.F., HOLMES L.S., and KASHA M.A., J. Sci. Instrum., 40, 364, (1963).

(24) HERZOG R.F.K., and TISCHLER O., Rev. Sci. Instr., 23, 1000, (1953).

(25) GAUTIER, P., Comptus Rendus Acad. Sci. Paris, 242, 1707, (1956).

(26) ASHBY D.E.T.F., GOODING T.J., HAYWORTH B.R., and LARSON A.V., A.I.A.A. Journal, 3, 1040, (1963).

(27) ASHBY D.E.T.F., and AVIS B.E., Report No. CLM-M28 U.K.A.E.A. (1964).

(28) ASHBY D.E.T.F., and PATON A., Plasma Phys., 9, 359, (1967).

(29) CROCKER A., GEBBIE H.A., KIMMETT M.F., and MATHIAS L.E.S., Nature, 201, 250, (1964).

(30) GEBBIE H.A., STONE N.W.B., and FINLAY F.D., Nature, 202, 685, (1964).

(31) MATTHIAS L.E.S., CROCKER A. and WILLS M.S., Electronics Letters, 1, 45 (1965).

(32) GEBBIE H.A., STONE N.W.B., SLOUGH W., CHAMBERLAIN J.E. and SHERATON W.A., Nature, 211, 62, (1966).

(33) MÜLLER W.M. and FLESHER G.T., App. Phys. Lett., 10, 93, (1967).

(34) GEBBIE H.A., Phys. Rev., 107, 1194 (1957).

(35) BURROUGHS W.J., PYATT E.C., and GEBBIE H.A., Nature, 212, 387, (1966).
(36) CHANTRY G.W., GEBBIE H.A., and CHAMBERLAIN J.E. Nature, 205, 377 (1965).
(37) LIDE D.R., and MAKI A.G., App. Phys. Lett., 11, 62, (1967).
(38) HOCKER L.O., and JAVAN A., Phys. Lett., 7, 489, (1967).
(39) HOCKER L.O., JAVAN A., RAO D.R., FRENKEL L. and SULLIVAN T., App. Phys. Lett., 10, 147, (1967).
(40) STRATTON J.A., 'Electromagnetic Theory,' McGraw-Hill N.Y. (1941).
(41) HEALD, M.A., and WHARTON C.B., 'Plasma Diagnostics with Microwaves,' John Wiley, (1965).
(42) GINZBERG V.L., 'The Propogation of Electromagnetic Waves in Plasmas', Pergamon Press, (1964).
(43) WORT D.J.H., Report No. CLM R-27 U.K.A.E.A. (1963).
(44) LI T., Bell System Tech. J., 44, 917, (1965).
(45) BOYD G.D., and KOGELNIK H., Bell System Tech. J., 41, 1347, (1962).
(46) GOLAY M.J.E., Rev. Sci. Instrum., 20, 816, (1949).
(47) PUTLEY E.H., Proc. Phys. Soc., 76, 802, (1960).
(48) PUTLEY E.H., Appl. Optics, 4, 649, (1965).
(49) SHAW N, and PUTLEY E.H., R.R.E., Memorandum No.2056, (1964).
(50) LUDLOW J.H., MITCHELL W.H., PUTLEY E.H., and SHAW N., J. Sci. Instrum., 44, 694 (1965)
(51) PAYNE C.D., and PREWER B.E., Proc. I.E.R.E. Conference on Laser Applications, 204, (1969).
(52) press release in Laser Focus Dec. (1968).
(53) GRIMES C.C., RICHARDS P.L., and SHAPIRO S., J. Appl. Phys., 39, 3905, (1968).
(54) VOGEL P., and GENZEL L., Infrared Physics, 4, 257, (1964).
(55) RESSLER G.M., and MÖLLER K.D., Appl. Optics, 6, 893, (1967).

(56) CHAMBERLAIN J.E., CHANTRY G.W., FINDLAY F.D., GEBBIE H.A., GIBBS J.E., STONE N.W.B., and WRIGHT A.J., Infrared Phys., 6, 195, (1966).

(57) GEBBIE H.A., and STONE N.W.B., Infrared Phys., 4, 85, (1963).

(58) KIMMITT M.F., and NIBLETT G.B.F., Proc. Phys. Soc., 82, 938, (1963).

(59) STUCKELBERGER E.C.G., and MORSE P.M., Phys. Rev., 36, 16, (1930).

(60) CILLIÉ G., M.N. Roy. Astron. Soc., 32, 820, (1932).

(61) MASSEY H.S.W., and BURHOP E.H.S., 'Electronic and Ionic Impact Phenomena,' Clarendon Press, Oxford, (1952).

(62) D'ANGELO N., Phys. Rev., 121, 505, (1961).

(63) GIOVANELLI R.G., Austr. J. Sci. Res., A1, 275, 289, (1948).

(64) BATES D.R., and KHARE S.P., Proc. Phys. Soc., 85, 231, (1965).

(65) DELOCHE R., Paper (1.1.8.), Proc. 8th Int. Conf. on Ionization Phenomena in Gases, Vienna, (1967).

(66) CRONIN J.C., and SEXTON M.C., Brit. J. Appl. Phys. (J.Phys.D.), sev.2. 1, 889, (1968).

(67) BATES D.R., Phys. Rev., 77, 718, (1950).

(68) OSKAM H.J. and MITTELSTADT V.R., Phys. Rev. 132, 1435,(1963).

(69) BATES D.R., and KINGSTON A.E., Nature, 189, 652, (1961).

(70) McWHIRTER R.W.P., Nature, 190, 902, (1961).

(71) BATES, D.R., KINGSTON A.E., and McWHIRTER R.W.P., Proc. Roy. Soc., A267, 297, (1962).

(72) BATES D.R., KINGSTON A.E., and McWHIRTER R.W.P., Proc. Roy. Soc., A270, 155, (1962).

(73) McWHIRTER R.W.P., and HEARN A.G., Proc. Phys. Soc., 82, 641, (1963).

(74) BATES D.R., and KINGSTON A.E., Proc. Roy. Soc., A279, 10, (1964).

(75) BATES D.R., and KINGSTON A.E., Proc. Roy. Soc., A279, 32, (1964).
(76) SEATON M.J., 'Atomic and Molecular Processes' (ed.D.R. Bates) Academic Press, N.Y., (1962).
(77) GRYZINSKI M., Phys. Rev., 115, 374, (1959).
(78) BYRON S., STABLER R.C., and BORTZ P.I., Phys. Rev. Lett., 8, 376, (1962).
(79) BETHE H.A., and SALPETER E.E., 'Quantum Mechanics of One and Two Electron Atoms,' Academic Press, N.Y., (1957).
(80) MAKIN B., and KECK J.C., Phys. Rev. Lett., 11, 281, (1963).
(81) KECK J.C., J. Chem. Phys., 32, 1035, (1952).
(82) D'ANGELO N., Phys. Rev., 140, A1488, (1965).
(83) THOMSON J.J. Phil. Mag., 47, 337, (1924).
(84) HINNOV E., and HIRSCHBERG J.G., Phys. Rev., 125, 795, (1962)
(85) KUCKES A.F., MOTLEY R.W., HINNOV E., and HIRSCHBERG J.G., Phys. Rev. Lett., 6, 337, (1961).
(86) HINNOV E., Princeton University Report No. MATT-420, (1966).
(87) ROBBEN F., KUNKEL W.B., and TALBOT L., Phys. Rev., 132, 2363, (1963).
(88) COOPER W.S., and KUNKEL W.B., Phys. Rev., 138, 1022, (1965).
(89) CHEN C.J., Phys. Rev., 163, 1, (1967).
(90) CHEN C.J., J. Chem. Phys., 50, 1560, (1969).
(91) CHEN C.J., Phys. Rev., 177, 245, (1969).
(92) NEWTON A.A., and SEXTON M.C., Proc. Phys. Soc. (J.Phys.B.)., Ser.2.1., 669, (1968).
(93) NEWTON A.A., Ph.D. Thesis, University of London, (1967).
(94) COLLINS C.B., and HURT W.B., Phys. Rev. 167, 166, (1968).
(95) COLLINS C.B., and HURT W.B., Phys. Rev., 177, 257, (1969).
(96) GUSINOW M.A., GERADO J.B., and VERDEYEN J.T., Phys. Rev., 149, 91, (1966).
(97) GERADO J.B., and GUSINOW M.A., J. Appl. Phys., 40, 2533, (1969).

(98) ANISIMOV A.E., VINOGRADOV N.I., GOLANT V.E., and KONSTANTINOV B.P., Sov. Phys.-Tech. Phys., 7, 884, (1963).

(99) QUINN J.M.P., Plasma Phys. (J. Nuc. Energy Pt. C), 7, 113, (1965).

(100) BRAND, G.R., J. Appl. Phys., 39, 1945, (1968).

(101) IRONS F.E., and MILLAR D.D., Austr. J. Phys., 18, 23, (1965).

(102) ALESKOVSKII Y.M., and GRANOVSKII V.L., Sov.Phys. - JETP, 16, 887, (1963).

(103) JONES H.W. and SAUNDERS P.A., Report no. A.E.R.E. - R3611, U.K.A.E.A.

(104) JOHNSON E.O., and MALTER L., Phys. Rev., 80, 58, (1950).

(105) WHARTON C.B., and SLAGER D.M., J. Appl. Phys., 31, 428, (1960).

(106) BROWN J., Microwave Lenses, Methuen, (1953).

(107) PHELPS A.V., and MOLNAR J.P., Phys. Rev., 89, 1202, (1953).

(108) PHELPS A.V., Phys. Rev., 99, 1307, (1955).

(109) SCHULZ G.J., and FOX R.E., Phys. Rev., 106, 1179, (1957).

(110) ZEMANSKY M.W., Phys. Rev., 29, 513, (1927).

(111) MITCHELL A.C.G., and ZEMANSKY M.W., 'Resonance Radiation and Excited Atoms,' Macmillan, (1934).

(112) HOLSTEIN T., Phys. Rev., 72, 1212, (1947).

(113) HOLSTEIN T., Phys. Rev., 83, 1159, (1951).

(114) WALSH P.J., Phys. Rev., 107, 338, (1957).

(115) HEARN A.G., Proc. Phys. Soc., 81, 648, (1963).

(116) ALLEN C.W., Astrophysical Quantities, Athlone Press, (1955)

(117) HAMBERGER S., Ph.D. Thesis, University of London, (1966).

(118) DALGARNO A., Phil. Trans. Roy. Soc. A., 250, 426, (1958).

(119) PETSCHEK B.E., and BYRON S., Ann. Phys. 1, 270, (1957).

(120) BATES D.R., and KINGSTON A.E., Planet Space Sci., 11, 1, (1963).

(121) MOISEIWITSCH B.L., Proc. Phys. Soc. A., 69, 653, (1956).
(122) TEMKIN A., and LAMKIN J.C., Phys. Rev., 121, 788, (1961).
(123) BATES D.R., and BOYD A.H., Proc. Phys. Soc. 80, 1301, (1962).
(124) OVCHARENKO V. (private communication).
(125) McWHIRTER R.W.P., Chapter 5 of reference (18).
(126) GROVER F.W., Inductance Calculations Working Formulas and Tables, Dover Publications Inc., (1962).
(127) DALGARNO A., and SMITH F.J., Proc. Roy. Soc. A., 267, 417, (1962).
(128) KOLESNIKOV V.N., and OBUKHOV-DENISOV V.V., Soviet Phys. - J.E.T.P., 15, 692, (1962).
(129) INGOLD J.H., J. Appl. Phys., 39, 5834, (1968).
(130) JAHN R.G., Phys. Fluids, 5, 678, (1962).
(131) BUDDEN K.G., Radio Waves in the Ionosphere, Cambridge Press, (1961).
(132) ALBINI F.A., and JAHN R.G., J. App. Phys., 32, 75, (1961).
(133) FRENCH I.P., CLOUTIER G.G., and BACHYNSKI M.P., Can. J. Phys., 39, 1273
(134) TAKEDA S., and ROUX M., J. Phys. Soc. of Japan, 16, 95, (1961).
(135) TAKEDA S., and TSUKISHIMA T., J. Phys. Soc. of Japan, 18, 426, (1963).
(136) KINNEY R.A., I.E.E.E. Trans. on Nuclear Science, 15, 6, (1968).
(137) ETHERINGTON R.J., and HAINES M.G., Phys. Rev. Lett., 14, 1019, (1965).
(138) THONEMANN P.C., and KOLB A.C., Phys. Fluids, 7, 1455, (1964).
(139) DANGOR A.E., PARKINSON G.J., DUNNETT R.M., HAINES M.G., and LATHAM R., Conf. Plasma Physics and Controlled Nuclear Fusion Research Novosibirsk (1968), published volume 1, 255, I.A.E.A. Vienna, (1969).

(140) DANGOR A.E., HAINES M.G., KILKENNY J., PARKINSON G.J., POTTER D.E., and WATKINS M.J., Third European Conference on Plasma Physics and Controlled Fusion Research, Utrecht (1969).

(141) PARKINSON G.J., and DANGOR A.E., International Conference on Plasma Diagnostics, Culham (1968), Paper B.3.

(142) PARKINSON G.J., DANGOR A.E., and CHAMBERLAIN J., Appl. Phys. Lett., 13, 233, (1968).

ACKNOWLEDGEMENTS

The author wishes to thank Dr. R. Latham for his enthusiastic supervision and guidance on all aspects of the plasma research. The research on the Polytron device was performed under the guidance of Dr. M. G. Haines and the author thanks him for many helpful discussions on this project. Much of the author's experimental experience was acquired whilst working in conjunction with Dr. A. E. Dangor and special thanks are due to him for inumerable suggestions concerning the diagnostics of both the Polytron and afterglow plasmas. Thanks are also due to Mr. D. A. Brown, Dr. M. Dunnett and Mr. P. Garne who all worked for various periods on the Polytron.

The fine workmanship apparent in the construction of the Polytron device was almost entirely due to the skill of Messrs. B. Boreham and P. Daly. Virtually all electronics aspects of the research were dealt with by Mr. L. Nyman, under the general supervision of Dr. A. Folkierski, and thanks are due to them both for producing nearly infallible electronics.

The author is indebted to Mr. D. Wort of the U.K.A.E.A. Culham Laboratory for arranging the loan of 70 G.H_Z microwave equipment, to Dr. J. Chamberlain of the National Physical Laboratory for arranging the loan of the HCN laser and to Mr. N. Shaw of the Royal Radar Establishment Malvern for arranging the loan of the Putley detector. The above three people are thanked for many helpful discussions on their respective pieces of equipment.

The assistance of Mrs. D. Jones with the computer work is gratefully acknowledged.

The author thanks Mrs. T. Law for sparing no effort in her careful typing of the manuscript.

Finally, the author is grateful to the Science Research Council for the provision of a maintenance grant during the period of study.

Reprinted from

Volume 13, Number 7 APPLIED PHYSICS LETTERS 1 October 1968

TIME RESOLVED MEASUREMENTS OF ELECTRON NUMBER DENSITY AND ELECTRON TEMPERATURE USING LASER INTERFEROMETRY AT 337-μm WAVELENGTH

G. J. Parkinson and *A. E. Dangor*
Imperial College, London S.W. 7, England
J. Chamberlain
National Physical Laboratory,
Teddington, Middx., England
(Received 29 July 1968)

An experiment is described where a cw HCN laser working primarily at 337-μm wavelength was used as the source of a Mach–Zehnder interferometer for the study of plasma decay in the electron number density region $5 \cdot 10^{15} > n_e > 5 \cdot 10^{13}$ cm^{-3}. It was found that an estimate of the electron temperature in the range 10^3–10^4°K could also be made from the amplitude of the interferometer fringes.

The development of the cw HCN laser working primarily at 337-μm wavelength (Ref. 1) has enabled measurements to be made of both the real refractive index and attenuation index of the complex refractive index of a plasma, in a range of conditions between the diagnostic limits of microwave wavelengths and near infrared wavelengths.

Plasma electron densities (up to a cutoff number density for $\lambda = 337$ μm of 10^{16} electrons cm^{-3}) can be measured to accuracies around 100 times greater than can be achieved using 3.39-μm radiation from a He-Ne laser over the same plasma path length. For $\omega \gg \omega_p$ the plasma frequency:

$$\overline{n_e}\,\ell = 0.664\ 10^{15}\,N \text{ for } \lambda = 337\ \mu\text{m}$$
$$\overline{n_e}\,\ell = 0.658\ 10^{17}\,N \text{ for } \lambda = 3.39\ \mu\text{m}$$

where $\overline{n_e}$ = average electron number density in cm^{-3}, ℓ = plasma path length in cm, and N = interferometer fringe number.

Plasma electron temperatures can be obtained from measurements of the amplitudes of the interferometer fringes which depend on reflection, refraction and attenuation of the radiation by the plasma. The attenuation length d of electromagnetic radiation inside a uniform plasma is given by (Ref. 2)

$$d = 2\frac{c}{\nu}\left(\frac{\omega}{\omega_p}\right)^2\left[1-\frac{\omega_p^2}{\omega^2}\right]^{1/2} \text{cm}, \qquad (1)$$

where

$$\omega_p = \left(\frac{4\pi n_e e^2}{m_e}\right)^{1/2} \text{ in rad sec}^{-1}$$
ν = electron collision frequency in sec^{-1}
c = velocity of light in cm sec^{-1}

subject to $\nu \ll \omega$ and $\omega > \omega_p$.

For most laboratory plasmas in the range $10^{16} > n_e > 5 \cdot 10^{13}$ cm^{-3}, Coulomb collisions between ions and electrons dominate other collision mechanisms and ν is given by (Ref. 3)

$$\nu = 2.6\, n_e\, Z\,(T_e)^{-3/2} \ln\Lambda \text{ sec}^{-1} \qquad (2)$$

where T_e = electron temperature in °K, Z = ionic charge, and $\ln\Lambda$ = Coulomb logarithm.

Electron temperatures were found from Eqs. (1) and (2) using the values of n_e and d calculated from the interferometer fringes. Figure 1 shows plots of n_e and T_e for a uniform plasma which give rise to attenuation lengths $d = 1$, 10, 100 cm for 337-μm radiation. The values of d that can be estimated from the experimental results usually lie between 0.3 and 20 times the radiation path length through the plasma. The effects of reflection of the beam from the plasma are usually small compared to the collisional attenuation, but a correction factor for reflection was made in working out the results. Typically about 5% of the radiation is reflected at

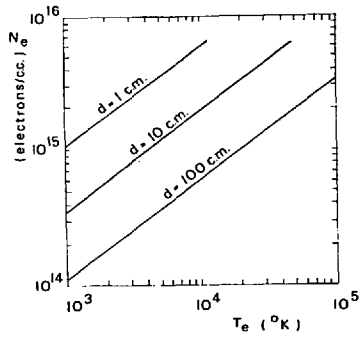

Fig. 1. Plot of n_e versus T_e for attenuation length d = 1, 10, and 100 cm in a uniform plasma.

$n_e = 5 \cdot 10^{15}$ cm^{-3} and 0.5% at $n_e = 2.5 \cdot 10^{15}$ cm^{-3}.

In the experiment the decay of plasma in a fused silica torus (major diameter 50 cm, minor diameter 4.4 cm) was studied using the HCN laser as the source of a Mach–Zehnder interferometer. The plasma was produced by a pulsed 10-kA discharge lasting about 15 μsec. To reduce refraction losses in the discharge, lenses situated outside the interferometer mirrors were used to focus the laser beam at the center of the discharge tube. The laser windows, beam splitters, and mirrors were constructed using the principles outlined in (Ref. 4). The interferometer was adjusted for destructive interference in the absence of plasma using a Golay cell detector. With suitable compensation for losses in the discharge tube walls, fringes with a visibility of 20:1 could be produced by movement of the reference beam mirror. For the study of plasma decay, a Putley indium antinomide detector (Ref. 5) in a screened room was used to monitor the interferometer output. The upper frequency response of the Putley detector and its amplifier was 0.5 MHz. Experiments have been performed using hydrogen, helium, neon, argon, and krypton gases in the measurement of electron-ion recombination coefficients in the region $5 \cdot 10^{15} > n_e > 5 \cdot 10^{13}$ cm^{-3} and $10^4 > T_e > 10^3$ °K (Ref. 6). Independent estimates of electron temperature were made using Langmuir probes and spectroscopically for hydrogen and helium.

Typical laser interferometry signals are shown in Figs. 2 and 3. The detector output is displayed downwards. Comparison of the relative amplitudes of the corresponding fringe maxima (which depends on the amplitude of the transmitted beam through the discharge) starting from the last fringe and working backwards in time, shows that a greater attenuation occurs in Fig. 3 than in Fig. 2. This cannot be due to fall off in detector frequency response as the fringes change more slowly with time in Fig. 3 than Fig. 2, and is in agreement with the assumption that at corresponding values of number density, the electron temperature is lower in Fig. 3 than Fig. 2 and this causes greater collisional attenuation of the transmitted beam. Plots of the decay curves for n_e and T_e calculated from the results shown in Figs. 2 and 3 are shown in Fig. 4. The increasing attenuation of fringe amplitude at a particular value of n_e with increasing gas pressure was observed in all gases: the extreme case being hydrogen at 1.0-Torr pressure where the attenuation length was less than the tube diameter at the third from last fringe. In the case of krypton, the collisional attenuation was extremely small, and almost constant amplitude fringes were recorded for pressures up to 0.1 Torr.

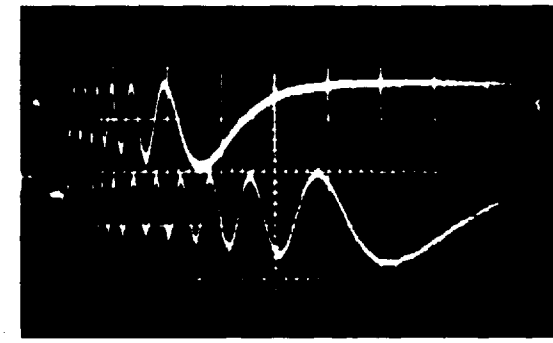

Fig. 2. 337-μm infrared fringes for plasma decay in argon at 100-μm pressure. Upper trace sweep speed 100 μsec per large division. Lower trace sweep speed 50 μsec per large division.

The electron number density was measured independently at 7.10^{13} cm^{-3} using 4.3-mm microwave equipment and there was excellent agreement with the laser results.

Further work including extending the frequency response of the detector and the use of the laser in other arrangements than the Mach–Zehnder is at present under way.

The authors with to thank Mr. P. Garnett of Imperial College and Mr. N. Shaw of the Royal Radar Establishment, Malvern, for their cooperation in carrying out this experiment.

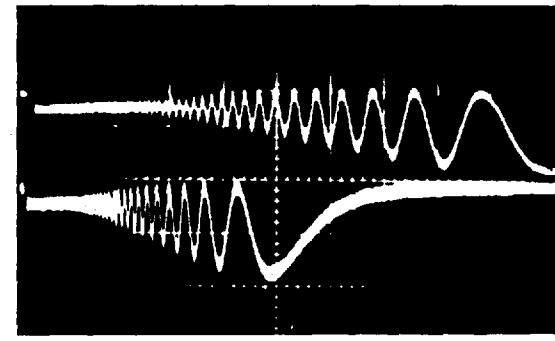

Fig. 3. 337-μm infrared fringes for plasma decay in argon at 500-μm pressure. Upper trace sweep speed 100 μsec per large division. Lower trace sweep speed 200 μsec per large division.

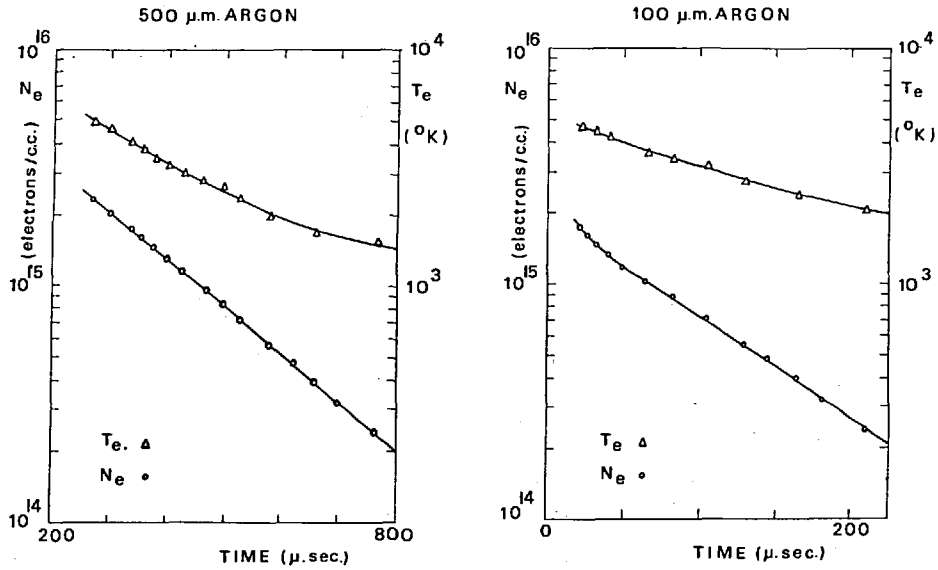

Fig. 4. Plots of the decay of electron number density and electron temperature derived from the fringes shown in Figs. 2 and 3.

[1]H. A. Gebbie, N. W. B. Stone, W. Slough, J. Chamberlain, W. A. Sheraton, Nature 211, 62 (1966).

[2]M. A. Heald and C. B. Wharton, *Plasma Diagnostics with Microwaves* (John Wiley & Sons, Inc., New York, 1965).

[3]J. L. Delcroix, *Introduction to the Theory of Ionized Gases* (Interscience Publishers, Inc., New York, 1960).

[4]J. Chamberlain, G. W. Chantry, F. D. Finlay, H. A. Gebbie, J. E. Gibbs, N. W. B. Stone, and A. J. Wright, Infrared Phys. 6, 195 (1966).

[5]E. H. Putley, Appl. Opt. 4, 649 (1965).

[6]G. J. Parkinson (unpublished work).